OMICS SOLUTIONS FOR ENDOCRINE DISORDERS

EDITED BY: Anna Halama and Stephen Atkin
PUBLISHED IN: Frontiers in Endocrinology

frontiers Research Topics

ISSN 1664-8714
ISBN 978-2-88976-578-2
DOI 10.3389/978-2-88976-578-2

About Frontiers

Frontiers is more than just an open-access publisher of scholarly articles: it is a pioneering approach to the world of academia, radically improving the way scholarly research is managed. The grand vision of Frontiers is a world where all people have an equal opportunity to seek, share and generate knowledge. Frontiers provides immediate and permanent online open access to all its publications, but this alone is not enough to realize our grand goals.

Frontiers Journal Series

The Frontiers Journal Series is a multi-tier and interdisciplinary set of open-access, online journals, promising a paradigm shift from the current review, selection and dissemination processes in academic publishing. All Frontiers journals are driven by researchers for researchers; therefore, they constitute a service to the scholarly community. At the same time, the Frontiers Journal Series operates on a revolutionary invention, the tiered publishing system, initially addressing specific communities of scholars, and gradually climbing up to broader public understanding, thus serving the interests of the lay society, too.

Dedication to Quality

Each Frontiers article is a landmark of the highest quality, thanks to genuinely collaborative interactions between authors and review editors, who include some of the world's best academicians. Research must be certified by peers before entering a stream of knowledge that may eventually reach the public - and shape society; therefore, Frontiers only applies the most rigorous and unbiased reviews.
Frontiers revolutionizes research publishing by freely delivering the most outstanding research, evaluated with no bias from both the academic and social point of view. By applying the most advanced information technologies, Frontiers is catapulting scholarly publishing into a new generation.

What are Frontiers Research Topics?

Frontiers Research Topics are very popular trademarks of the Frontiers Journals Series: they are collections of at least ten articles, all centered on a particular subject. With their unique mix of varied contributions from Original Research to Review Articles, Frontiers Research Topics unify the most influential researchers, the latest key findings and historical advances in a hot research area! Find out more on how to host your own Frontiers Research Topic or contribute to one as an author by contacting the Frontiers Editorial Office: frontiersin.org/about/contact

OMICS SOLUTIONS FOR ENDOCRINE DISORDERS

Topic Editors:
Anna Halama, Weill Cornell Medicine- Qatar, Qatar
Stephen Atkin, Royal College of Surgeons in Ireland, Bahrain

Citation: Halama, A., Atkin, S., eds. (2022). Omics Solutions for Endocrine Disorders. Lausanne: Frontiers Media SA. doi: 10.3389/978-2-88976-578-2

Table of Contents

frontiers | Frontiers in Endocrinology

EDITORIAL
published: 22 June 2022
doi: 10.3389/fendo.2022.948991

Editorial: Omics Solutions for Endocrine Disorders

Stephen L. Atkin[1*] *and Anna M. Halama*[2]

[1] Department of Research, Royal College of Surgeons in Ireland, Al Muharraq, Bahrain, [2] Department of Research, Weill Cornell Medicine- Qatar, Ar-Rayyan, Qatar

Keywords: omics, proteomic, transcriptomatics, systems biology, endocrinolgy, diabetes, genomics

Editorial on the Research Topic

Omics Solutions for Endocrine Disorders

Multifactorial processes contribute to the development of endocrinological disorders such as diabetes, polycystic ovary syndrome (PCOS) and some carcinomas. Frequently, standard clinical tests are insufficient for proper diagnosis and treatment. Therefore, strategies providing further insight into endocrinological disorders that support the clinical pipeline are required. Recently, omics technologies such as genomics, transcriptomics, proteomics, metabolomics and lipidomics have been introduced into the field of complex disorders to improve diagnostics and treatment (**Figure 1**). This special edition highlights the use of omic technologies in endocrinological disorders, including diabetes and its comorbidities, as well as obesity and PCOS, further emphasizing their potential to be implemented into the clinical pipeline. What this special edition also emphasizes is the differing methodology available for each of the "omic" approaches that may not be directly comparable, one example being in proteomics where some groups use aptamer-based technology whilst others may use mass spectroscopy, and therefore the need for standardization.

Hu et al utilized whole-exome sequencing and transcriptome sequencing (RNA-seq) of 41 patients with parathyroid adenomas, confirming mutations in the adenomas and, additionally, identified the somatic mutation of EZH1. Subsequent RNA-seq data clustering analysis identified factors that could contribute to the parathyroid adenoma gene expression profile and may contribute to a clinically useful diagnostic panel if replicated in a larger cohort.

The value of an "omics" approach to therapeutic efficacy was undertaken by Martin et al in a model of diabetic kidney disease. Here, the authors looked at the medications that would activate tubular fatty acid oxidation following an animal model of bariatric surgery (Roux-en-Y) using transcriptomic and urinary metabolomic profiling. Medication-specific transcriptomic responses following Roux-en-Y surgery were explored using a network pharmacology approach. Their integrative multi-omic analyses suggested fenofibrate, as an agonist of peroxisome proliferator activated receptor-alpha (PPARa)-stimulated fatty acid oxidation, had potential utility in a combinatorial approach for the treatment of diabetic kidney disease in the setting of obesity. These interesting data need replication and clinical evaluation in human disease and may contribute to future progress in the treatment of diabetic kidney disease.

A further contribution to diabetic kidney disease was provided by Wang et al. This study was conducted in a human renal proximal epithelial tubular cell line with the aim to investigate molecular pathways contributing to glucose homeostasis under lactate dehydrogenase inhibition (oxamate), which was shown previously to modulate glucose metabolism by impacting mitochondrial respiration. The authors identified 3,884 genes there were significantly altered in the cell line under oxamate treatment

OPEN ACCESS

Edited and reviewed by:
Ruth Andrew,
University of Edinburgh,
United Kingdom

***Correspondence:**
Stephen L. Atkin
satkin@rcsi.com

Specialty section:
This article was submitted to Systems Endocrinology, a section of the journal Frontiers in Endocrinology

Received: *20 May 2022*
Accepted: *25 May 2022*
Published: *22 June 2022*

Citation:
Atkin SL and Halama AM (2022) Editorial: Omics Solutions for Endocrine Disorders. Front. Endocrinol. 13:948991. doi: 10.3389/fendo.2022.948991

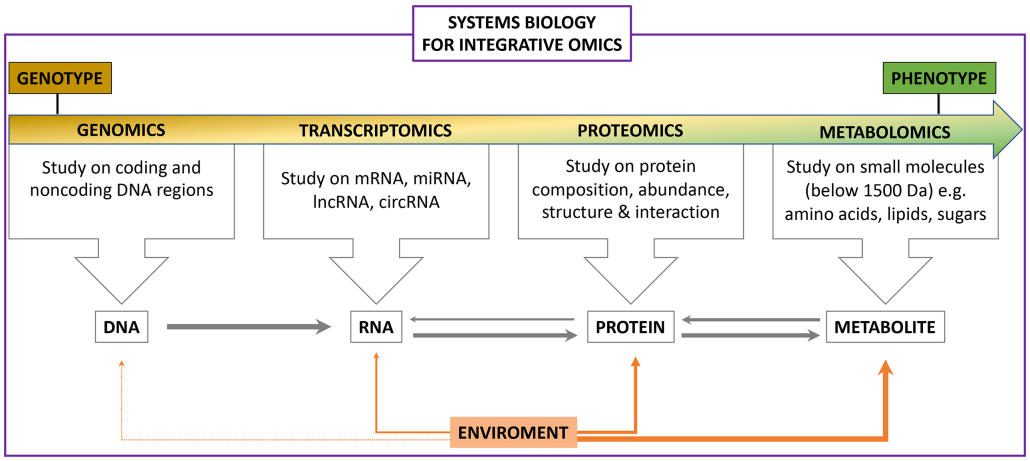

FIGURE 1 | The scope of Integrative Omics.

and they linked those alterations with mitochondrial biogenesis and mitophagy which, when prolonged, compromises stress resistance. These data may indicate a molecular survival pathway in these cells, but replication in primary human tissue is required to indicate whether this may have potential clinical relevance.

Further insights into insulin resistance (IR) were provided by Yang et al. who utilized a proteomic approach to determine molecular dysregulations in white adipose tissue (WAT), liver and skeletal muscle of mice in which IR was induced with a high fat diet. A network-based approach was developed to explore IR-related tissue communications. Tissue specific insulin resistance networks were constructed with functional analysis of the cross-tissue interface. The results of this analysis suggested that the liver is a key player in insulin resistance as the liver was the only tissue expressing abnormal glucose metabolic signals. Moreover, the authors identified the CD36–PPAR axis in liver and WAT and verified it as a bridge that links cross-tissue signals with intracellular metabolism, potentially contributing to IR. Whilst there are limitations to this approach (animal model, static experiments, no other validation studies in the literature), the importance to humans may be in the relevance of the mechanisms of central IR and thus future molecular therapeutic approaches.

Diboun et al. utilized metabolomics in pregnant women in their second trimester with and without polycystic ovary syndrome (PCOS) and showed that women with PCOS had lower birthweight babies marked by a unique metabolic signature of specific triglycerides that, if confirmed in a larger population, may have diagnostic relevance in these patients.

Ding et al. also used metabolomics to investigate perimenopausal obesity compared to non-obese women in a Chinese population. In total, forty-six different metabolites were identified that may be useful as a metabolic signature to identify women at risk for perimenopausal obesity. Moreover, the authors linked those metabolites to dysfunction in dimethylarginine dimethylaminohydrolase (DDAH)/asymmetric NG, NGdimethyl–L–arginine (ADMA)/nitric oxide synthase (NOS)/nitric oxide (NO) signaling pathway related to the onset of cardiovascular disease. Nevertheless, replication studies in larger populations and in different ethnic backgrounds would be required to further translate this finding into clinical settings.

Continuing to focus on obesity, Joshi et al. used a bioinformatic approach to identify differentially expressed genes relevant for obesity that potentially could serve as therapeutic targets. The authors established databases from the available gene expression datasets and translated them into protein-protein and miRNA regulatory networks to identify key hub genes for obesity. Further, the authors identified, through bioinformatics analysis combined with validation genes, STAT3, CORO1C, SERPINH1, MVP, ITGB5, PCM1, SIRT1, EEF1G, PTEN and RPS2 as critical components in the development and prognosis of obesity; those genes could be probed as potential drug targets.

The importance of advanced bioinformatic approaches was also shown by Tsai et al. who deployed whole genome and chromatin immunoprecipitation sequencing data to provide further insight into osteoporosis. The authors investigated the association between RUNX2, a key molecule for osteoblast development, and functional SNPs to find factors contributing to osteopenia/osteoporosis and identified SNP rs6086746 (located upstream of the PLCB4 gene) as one of the factors involved in the etiology of osteopenia/osteoporosis. This study enhances the current understanding of the susceptibility to osteoporosis and further suggests the role of PLCB4 regulation in osteoporosis.

Overall, this series has highlighted that the "omic" approach yields powerful and extensive data for each of the areas explored and can provide further insight into disease etiology and disease progression as well as highlighting molecular targets for their treatment. However, there are significant challenges that must be addresses going forward. These include comparability of methodologies applied to describe each "omic", strategies enabling integration of multi-omics, standardization of quality control, which will have to be applied to make the results

reported readily comparable to one another and to clinical parameters. Moreover, there is a need to translate the findings into the clinical pipeline that will require investment of effort and resources into future clinical studies that implement multi-omic platforms. Thus, if we view human "omics" as a carpet with a complex interwoven pattern, then we appear to still be looking at the underside and thus are only seeing a few threads.

AUTHOR CONTRIBUTIONS

All authors listed have made a substantial, direct, and intellectual contribution to the work and approved it for publication.

Conflict of Interest: The authors declare that the research was conducted in the absence of any commercial or financial relationships that could be construed as a potential conflict of interest.

frontiers in Endocrinology

ORIGINAL RESEARCH
published: 14 May 2021
doi: 10.3389/fendo.2021.631680

Integrated Whole-Exome and Transcriptome Sequencing of Sporadic Parathyroid Adenoma

Ya Hu[1†], Xiang Zhang[1†], Ou Wang[2], Ming Cui[1], Xiaobin Li[1], Mengyi Wang[1], Surong Hua[1] and Quan Liao[1]*

[1] Department of General Surgery, Peking Union Medical College Hospital, Chinese Academy of Medical Sciences & Peking Union Medical College, Beijing, China, [2] Laboratory of Endocrinology, Department of Endocrinology, National Health Commission, Peking Union Medical College Hospital, Chinese Academy of Medical Sciences & Peking Union Medical College, Beijing, China

OPEN ACCESS

Edited by:
Anna Halama,
Weill Cornell Medicine, Qatar

Reviewed by:
Matthias Kroiss,
Julius Maximilian University of Würzburg, Germany
Sumeet Pal Singh,
Université libre de Bruxelles, Belgium

***Correspondence:**
Quan Liao
lqpumc@126.com

[†]These authors have contributed equally to this work

Specialty section:
This article was submitted to Systems Endocrinology, a section of the journal Frontiers in Endocrinology

Received: 20 November 2020
Accepted: 15 March 2021
Published: 14 May 2021

Citation:
Hu Y, Zhang X, Wang O, Cui M, Li X, Wang M, Hua S and Liao Q (2021) Integrated Whole-Exome and Transcriptome Sequencing of Sporadic Parathyroid Adenoma. Front. Endocrinol. 12:631680. doi: 10.3389/fendo.2021.631680

Purpose: Hyperparathyroidism is the third most common endocrine disease. Parathyroid adenoma (PA) accounts for approximately 85% of cases of primary hyperparathyroidism, but the molecular mechanism is not fully understood. Herein, we aimed to investigate the genetic and transcriptomic profiles of sporadic PA.

Methods: Whole-exome sequencing (WES) and transcriptome sequencing (RNA-seq) of 41 patients with PA and RNA-seq of 5 normal parathyroid tissues were performed. Gene mutations and characterized expression changes were identified. To elucidate the molecular mechanism underlying PA, unsupervised consensus clustering of RNA-seq data was performed. The correlations between the sequencing data and clinicopathological features of these patients were analyzed.

Results: Previously reported PA driver gene mutations, such as *MEN1* (9/41), *mTOR* (4/41), *ZFX* (3/41), *CASR* (3/41), *EZH2* (2/41) and *FAT1* (2/41), were also identified in our cohort. Furthermore, somatic mutation of *EZH1*, which had not been reported in PA, was found in 4 samples. RNA-seq showed that the expression levels of 84 genes were upregulated and 646 were downregulated in PA samples compared with normal samples. Unsupervised clustering analysis of RNA-seq data clustered these patients into 10 subgroups related to mutation or abnormal expression of a group of potential pathogenic genes.

Conclusion: *MEN1*, *EZH2*, *CASR*, *EZH1*, *ZFX*, *mTOR* and *FAT1* mutations in PA were revealed. According to the RNA-seq data clustering analysis, cyclin D1, β-catenin, VDR, CASR and GCM2 may be important factors contributing to the PA gene expression profile.

Keywords: parathyroid diseases, hyperparathyroidism, high-throughput, nucleotide sequencing, gene expression profiling

INTRODUCTION

Primary hyperparathyroidism (pHPT) is a common endocrine disorder with an incidence of approximately 66 and 25 per 100000 person-years among women and men, respectively (1). It was reported that the prevalence of pHPT was as high as 2.1% in postmenopausal women (2). The parathyroid tumor tissue secretes excessive parathyroid hormone, which results in hypercalcemia and related complications, such as osteoporosis, bone fracture, urolithiasis and renal failure. Parathyroid adenoma (PA) accounts for approximately 85% of pHPT. The genetic mechanisms of PA are not fully known, even though tremendous efforts have been made in previous studies. In PA with a hereditary background, the most well-known driver gene of PA was multiple endocrine neoplasia type 1 (*MEN1*). Other possible driver genes for hereditary pHPT include *RET* in MEN-2, *CDKN1B* in MEN-4, *CDC73* in hyperparathyroidism-jaw tumor syndrome, *GCM2* in familial isolated pHPT, *CASR* in familial hypocalciuric hypercalcemia type 1, *GNA11* in familial hypocalciuric hypercalcemia type 2, and *AP2S1* in familial hypocalciuric hypercalcemia type 3. For sporadic PA, somatic mutation of *MEN1* was identified in approximately 35% of cases (3). Mutation of *CCND1* or overexpression of cyclin D1 was found in 30% of sporadic PA cases. Other genes, such as *CASR*, *EZH2*, *CDKI*, and *CTNNB1*, may also contribute to the tumorigenesis of PA. However, the driver genes could still not be identified in a substantial proportion of sporadic PA.

Several studies have explored the molecular mechanism of PA with next-generation sequencing (NGS) technologies, such as whole-exome sequencing (WES) or transcriptome sequencing (RNA-seq). In 2018, Wei et al. (4) used WES to explore genetic abnormalities in 20 specimens of PAs. In 2019, Chai et al. (5) performed RNA-seq to compare the differentially expressed genes (DEGs) between 10 PA and 5 normal parathyroid (PaN) samples, and 8 hub molecules, including RPL23, RPL26, RPN1, RPS25, SEC11A, SEC11C, SEC61G and SPCS2, were identified. All these previous studies focused on one platform for tumor genome profiling. However, a multiplatform NGS analysis combined with WES and RNA-seq provides a more comprehensive view of the genetic landscape. RNA-seq is adept for identifying gene expression changes, gene fusions and alternative splicing, while WES is good at detecting copy number variants and gene mutations with low expression levels. With the corresponding RNA-seq data, the functional effects of genetic variants from WES can be interpreted with confidence.

Here, we performed concomitant WES and RNA-seq in 41 PA samples to identify related genetic variants and the consequent transcriptomic changes. The somatic mutations and DEGs were identified, and integrated analysis was employed. Based on RNA-seq data, unsupervised clustering with consensus clustering was applied to classify the patients, and the possible underlying molecular mechanism was explored.

MATERIALS AND METHODS

Patients and Specimens

A total of 41 samples of PA were selected randomly from the tissue bank of parathyroid tumors in the present study. These patients received operations from 2013 to 2019 at Peking Union Medical College Hospital, a tertiary referral university hospital. All the patients had a single PA without a history of multiple endocrine neoplasia, familial hyperparathyroidism syndrome or neck irradiation. The diagnosis of PA was made pathologically according to the WHO 2017 criteria (6). During the operation, the tumor specimens were collected from the central portion of the tumors to avoid contamination from adjacent tissues. Then, the specimens were immediately immersed in RNAlater (Ambion Inc., USA) solution at 4°C and stored at -80°C until use. The peripheral blood samples were collected, and white blood cells (WBCs) were stored at -80°C. Tiny PaN tissues were incidentally obtained from 5 patients with normal parathyroid function during surgery for thyroid diseases. The clinical data, including age, sex, imaging results, biochemical results and pathological evaluation, were collected. Follow-up data was obtained by reviewing outpatient records and telephone interviews. This study was approved by the Institutional Ethics Review Board of Peking Union Medical College Hospital (S-K836).The written informed consent was obtained from all the participants.

WES and WES Data Analysis

Genomic DNA was extracted from tumor and WBC samples with a DNeasy Blood & Tissue Kit (QIAGEN, Germany). A total of 0.6 μg of DNA per sample was used to prepare the DNA libraries with the Agilent SureSelect Human All Exon V6 Kit (Agilent Technologies, CA, USA). Then, the DNA libraries of each sample were sequenced with the Illumina HiSeq platform, and 150-bp paired-end reads were produced. Low-quality reads and reads containing adapter contamination were filtered. With Burrows-Wheeler Aligner (BWA) software, valid sequencing reads were mapped to the reference human genome (B37). Samtools, ANNOVAR, 1000 Genomes and other related databases were used to identify and annotate SNPs and insertions and deletions (InDels). The somatic single-nucleotide variant (SNV) was detected by MuTect, and the somatic InDel was detected by Strelka (7, 8). Somatic variants in the segmental duplication or with a frequency > 0.01 in the 1000 Genomes Chinese database were excluded for further analysis. The copy number variant was identified with Control-FREEC (9). The significantly mutated genes (SMGs) were identified by MuSiC software (10).

Transcriptome Sequencing and RNA-seq Data Analysis

RNA was extracted from tissue samples with TRIzol™ Reagent (Invitrogen, USA). A total of 2 μg of RNA per sample was used to generate sequencing libraries with the NEBNext® UltraTM RNA Library Prep Kit for Illumina® (NEB, USA). RNA-seq was

completed on an Illumina HiSeq platform, and 150-bp paired-end reads were produced. Paired-end clean reads were aligned to the reference genome using HISAT2 v2.0.5. HTSeq was used to count the reads mapped to each gene, and the fragments per kilobase of transcript sequence per million base pairs sequenced (FPKM) value was calculated based on the length of the gene and the read count mapped for each gene. Gene set enrichment analysis (GSEA) was used for functional enrichment analysis of DEGs, including Gene Ontology (GO) and Kyoto Encyclopedia of Genes and Genomes (KEGG) analyses (11). Gene fusion was identified by STAR-Fusion (12). The expression network analysis based on the DEGs was performed using the OmicStudio tools (https://www.omicstudio.cn/tool). For each pair of analyzed DEGs, the Pearson correlation coefficient was greater than 0.95 ($p<0.001$).

Integrative WES and RNA-seq Analysis

To explore the possible molecular mechanism underlying PA, unsupervised clustering of RNA-seq data was performed with the R package ConsensusClusterPlus. Consensus clustering was used to aid in discovering the optimal class. The number of clusters was selected according to the delta area plot and consensus cumulative distribution function (CDF) plot. Furthermore, the clustering results were explored with the features of the expression profile and genes in each cluster. The flowchart of data analysis was shown in **Figure S1**.

Statistical Analysis

Continuous parameters are shown as the mean ± standard deviation (SD), and discrete data are reported as numbers or corresponding percentages. Differences in variables between groups were evaluated with the Mann-Whitney U test. Fisher's exact test was used to compare the categorical data. A two-sided p-value < 0.05 was set as the threshold for statistical significance. All statistical analyses were performed with SPSS version 16.0.

RESULTS

Clinical Characteristics of Patients With PA

A total of 41 patients were enrolled in the present study (**Figure 1A**). The average age at diagnosis was 53.9 ± 10.8 (28–72) years. An obvious female predominance was revealed, with a female-to-

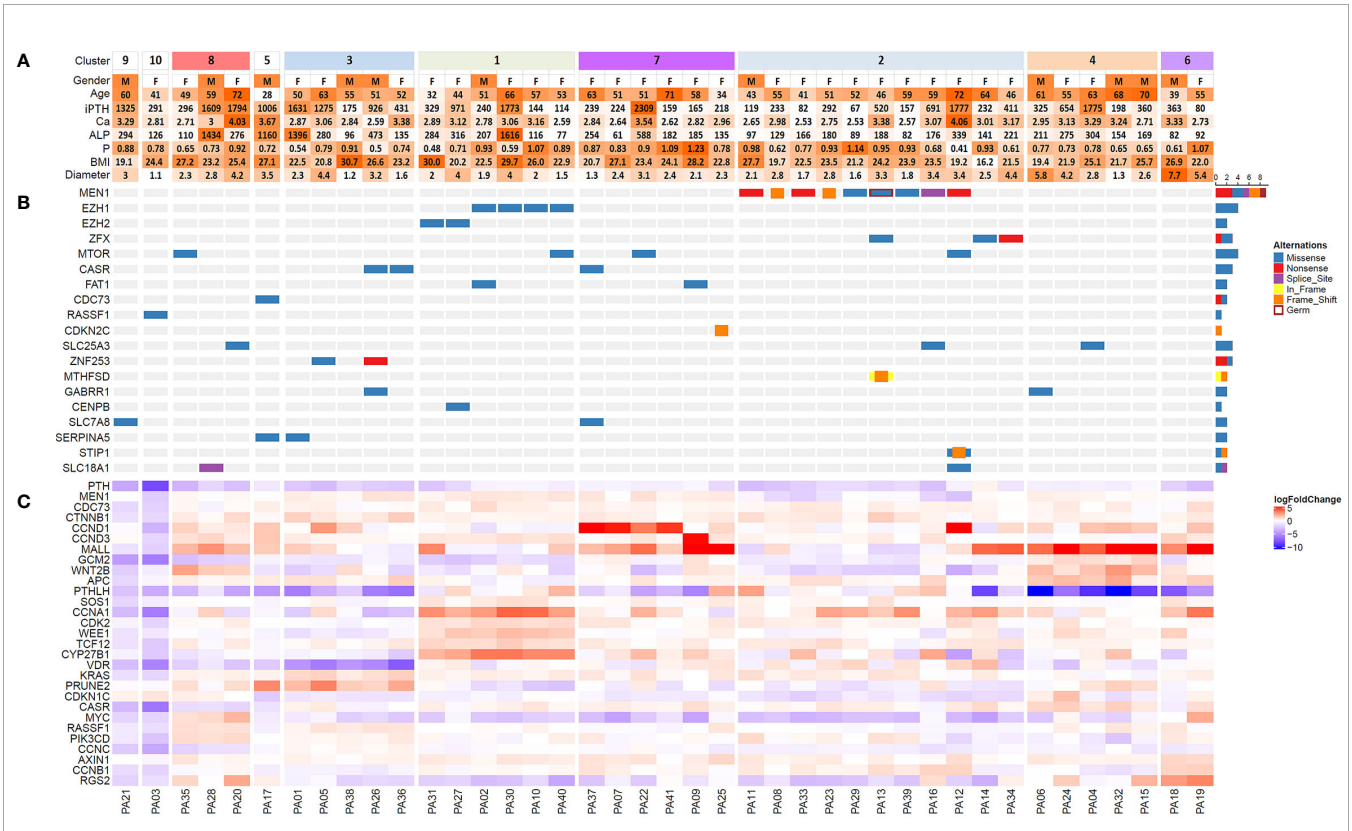

FIGURE 1 | Heatmap of clinical features **(A)**, significantly mutated genes **(B)** and differentially expressed genes **(C)** among 41 patients with parathyroid adenoma. Samples were clustered based on RNA-seq data by unsupervised clustering with the ConsensusClusterPlus package. Sample numbers are shown below the corresponding columns. In part **(C)** the logarithm of fold change in gene expression compared with the expression levels in normal parathyroid tissue is visualized by color intensity. Upregulation and downregulation of gene expression are represented by red and blue, respectively. iPTH, serum intact PTH level (12-67 pg/ml); Ca, serum calcium level (2.13-2.70 mmol/L); P, serum phosphorus level (0.81-1.45 mmol/L); ALP, alkaline phosphatase (35-100 U/L); BMI, body mass index; Diameter, maximum diameter of the tumor (cm).

male ratio of 30:11. The average serum levels of iPTH and Ca were 633.7 ± 628.1 (67.1-2309.2) pg/ml and 3.01 ± 0.37 (2.53-4.06) mmol/L, respectively.

Gene Mutations and Copy Number Variations With WES

For WES, we achieved a mean sequencing depth of 294× and 140× for the tumor and WBC control, respectively. Thereinto, 91.4% of the exome in tumors and 80.1% of the exome in WBC controls was sequenced with a depth of >50×. According to our filter criteria, a total of 668 nonsynonymous somatic mutations were detected, which included 636 SNVs and 32 InDels (**Table S1**). The top 7 recurrent mutated genes for PA were *MEN1* (9/41), *EZH1* (4/41), *mTOR* (4/41), *ZFX* (3/41), *CASR* (3/41), *EZH2* (2/41) and *FAT1* (2/41) (**Figure 1B**, **Table 1**). In this cohort, 8 somatic mutations and 1 germline mutation of *MEN1* were identified in 9 PA samples. Other potential driver genes reported in COSMIC, such as *RASSF1*, *CDKN2C* and *CDC73*, were found in one sample.

DEGs and Unsupervised Clustering With RNA-seq Data

In 41 PA and 5 PaN samples, a mean of 55.7 million reads were obtained by RNA-seq per sample, and 96.3% reads were successfully aligned to the reference genome. Compared with PaN samples, 84 genes were upregulated and 646 genes were downregulated (with a fold change of 1.5) in PA samples. GSEA showed that the DEGs were enriched in multiple biological processes, such as ribosome, lysosome, cell cycle and tight junction (**Figure 2**). Then, the DEGs were selected to build the expression network. The network comprised 113 network nodes and 500 network edges, indicating a complicated regulatory association in PA (**Figure S2**).

Integrative Analysis of WES and RNA-seq Data

Through consensus clustering, the RNA-seq data of PA samples could optimally be categorized into 10 clusters (**Figure S3**). Although unsupervised clustering is based merely on a mathematical calculation of gene expression data, prominent molecular features could be identified for most clusters based on existing knowledge (**Figure 1C**). On one hand, previously reported driver gene mutations could be identified in 3 clusters (Clusters 1, 2 and 5). In Cluster 2, all 9 samples with *MEN1* mutations (8 somatic mutations and 1 germline mutation) and 2 samples with *ZFX* mutations were included, which indicated that *MEN1* and *ZFX* mutations may result in a specific and similar expression profile. The expression of MEN1 in samples with *MEN1* mutations was decreased significantly ($p<0.001$).

TABLE 1 | Recurrently mutated genes and potential driver genes in parathyroid adenomas.

Gene	Sample ID	Somatic/Germline	Mutation type	Amino acid change
MEN1	8	Somatic	frameshift deletion	NM_000244: exon2:c.269_270del:p.Y90fs
MEN1	16	Somatic	splicing	NM_000244: exon8:c.928-1G>T
MEN1	23	Somatic	frameshift insertion	NM_000244: exon2:c.309dupG:p.S104fs
MEN1	29	Somatic	missense SNV	NM_000244: exon2:c.C95G:p.P32R
MEN1	33	Somatic	stopgain	NM_000244: exon3:c.C511T:p.Q171X
MEN1	39	Somatic	missense SNV	NM_000244: exon9:c.T1282A:p.W428R
MEN1	11	Somatic	stopgain	NM_000244: exon9:c.C1339T:p.Q447X
MEN1	12	Somatic	stopgain	NM_000244: exon4:c.C787T
MEN1	13	Germline	missense SNV	NM_000244: exon2:c.A1G:p.M1V
EZH1	2	Somatic	missense SNV	NM_001991: exon17:c.A1925T:p.Y642F
EZH1	10	Somatic	missense SNV	NM_001991: exon17:c.A1925T:p.Y642F
EZH1	30	Somatic	missense SNV	NM_001991: exon17:c.A1925T:p.Y642F
EZH1	40	Somatic	missense SNV	NM_001991: exon17:c.A1925T:p.Y642F
MTOR	22	Somatic	missense SNV	NM_004958: exon53:c.A7257T:p.E2419D
MTOR	35	Somatic	missense SNV	NM_004958: exon47:c.C6644T:p.S2215F
MTOR	40	Somatic	missense SNV	NM_004958: exon27:c.T4079C:p.L1360S
MTOR	12	Somatic	missense SNV	NM_004958: exon56:c.A7501T:p.I2501F
ZFX	13	Somatic	missense SNV	NM_001178086: exon4:c.A371G:p.K124R
ZFX	34	Somatic	stopgain	NM_001178086: exon6:c.G658T:p.E220X
ZFX	14	Somatic	missense SNV	NM_001178086: exon6:c.C1603T:p.R535W
CASR	26	Somatic	missense SNV	NM_000388: exon3:c.A307C:p.T103P
CASR	37	Somatic	missense SNV	NM_000388: exon3:c.C413T:p.T138M
CASR	36	Somatic	missense SNV	NM_000388: exon7:c.T1753C:p.C585R
EZH2	31	Somatic	missense SNV	NM_001203249: exon15:c.T1768A:p.Y590N
EZH2	27	Somatic	missense SNV	NM_001203249: exon15:c.A1769T:p.Y590F
FAT1	2	Somatic	missense SNV	NM_005245: exon10:c.G8140C:p.E2714Q
FAT1	9	Somatic	missense SNV	NM_005245: exon10:c.G8671T:p.D2891Y
CDC73	17	Somatic	missense SNV	NM_024529: exon3:c.G268T:p.D90Y
CDC73	17	Somatic	stopgain	NM_024529: exon1:c.G128A:p.W43X
RASSF1	3	Somatic	missense SNV	NM_170713: exon2:c.G157T:p.V53L
CDKN2C	25	Somatic	frameshift deletion	NM_078626: exon2:c.397_413del:p.R133fs

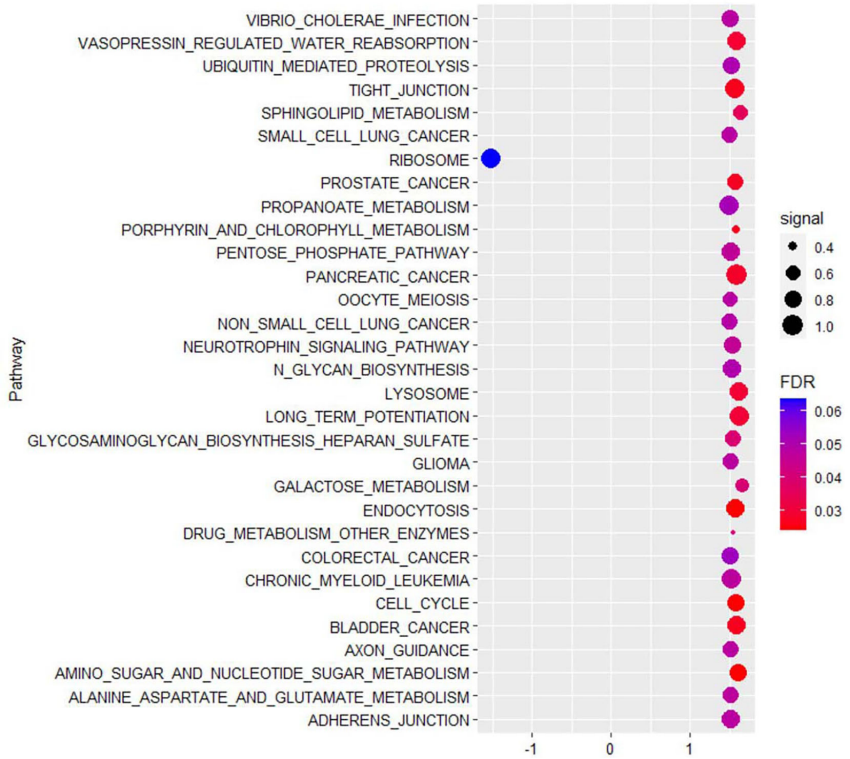

FIGURE 2 | The top 30 KEGG pathways enriched by gene set enrichment analysis (GSEA) showed that differentially expressed genes of parathyroid adenoma were enriched in multiple biological processes, such as ribosome, lysosome, cell cycle and tight junction. The horizontal axis represents the normalized enrichment score (NES), and the vertical axis represents the KEGG pathways. The false discovery rate (FDR) value and enrichment signal are represented by the color and circle diameter, respectively.

In Cluster 1, mutations in *EZH2* and *EZH1* were identified, and the expression levels of SOS1 (p= 0.002), CCNA1 (p < 0.001), CDK2 (p< 0.001), WEE1 (p< 0.001), TCF12 (p< 0.001) and CYP27B1 (p< 0.001) were significantly upregulated compared with those in the other subgroups (**Figure 3**). Double somatic mutations of *CDC73*, a stop-gain mutation (NM_024529:exon1:c.G128A:p.W43X) and a missense mutation (NM_024529:exon3:c.G268T:p.D90Y), were identified in PA17 (Cluster 5). Three samples with somatic mutations of *CASR* were distributed in Cluster 3 and Cluster 7.

On the other hand, prominent gene expression abnormalities were found in some clusters as previously reported in PA. The cyclin D1 (CCND1) mRNA level in Cluster 7 was much higher than that in any other cluster (p=0.006). For GCM2 and WNT2B, all 5 samples with the highest expression levels were clustered into Cluster 4, while no genetic mutation of known driver genes was identified. High expression levels of AXIN1 and CCNB1 were found in Cluster 6. High levels of KRAS (p=0.001) and PRUNE2 (p=0.001), as well as low levels of vitamin D receptor (VDR) (p=0.001), were prominent in Cluster 3. Low levels of CASR and high levels of MYC were found in the three samples in Cluster 8. Sample PA21 in Cluster 9 and sample PA03 in Cluster 10 had low levels of CDC73, CASR and SOS1, while no copy number or gene fusion abnormality of these genes was found.

Relationship Between Gene Expression and Clinical Features

The serum level of iPTH was correlated with serum Ca (p<0.001, rs=0.685), alkaline phosphatase (ALP) (p<0.001, rs=0.802), phosphorus (P) (p<0.001, rs=-0.525) and tumor diameter (p<0.001, rs=0.570), as well as the expression levels of VDR (p=0.009, rs=-0.403) and PRUNE2 (p=0.009, rs=0.401) (**Figure 4**). The expression level of the *PTH* gene was found to be correlated with the expression of multiple genes, such as *CTNNB1* (p=0.045, rs=-0.315), *MALL* (p=0.024, rs=0.352), and *GCM2* (p=0.002, rs=0.468).

DISCUSSION

To our knowledge, this study is the first integrative analysis of WES and RNA-seq in parathyroid neoplasia, providing new insight into the molecular mechanism of PA. Using WES, we revealed a group of mutations in genes such as *MEN1*, *EZH2*, *CDC73*, *ZFX*, *CASR*, *FAT1* and *RASSF1*, almost all of which had

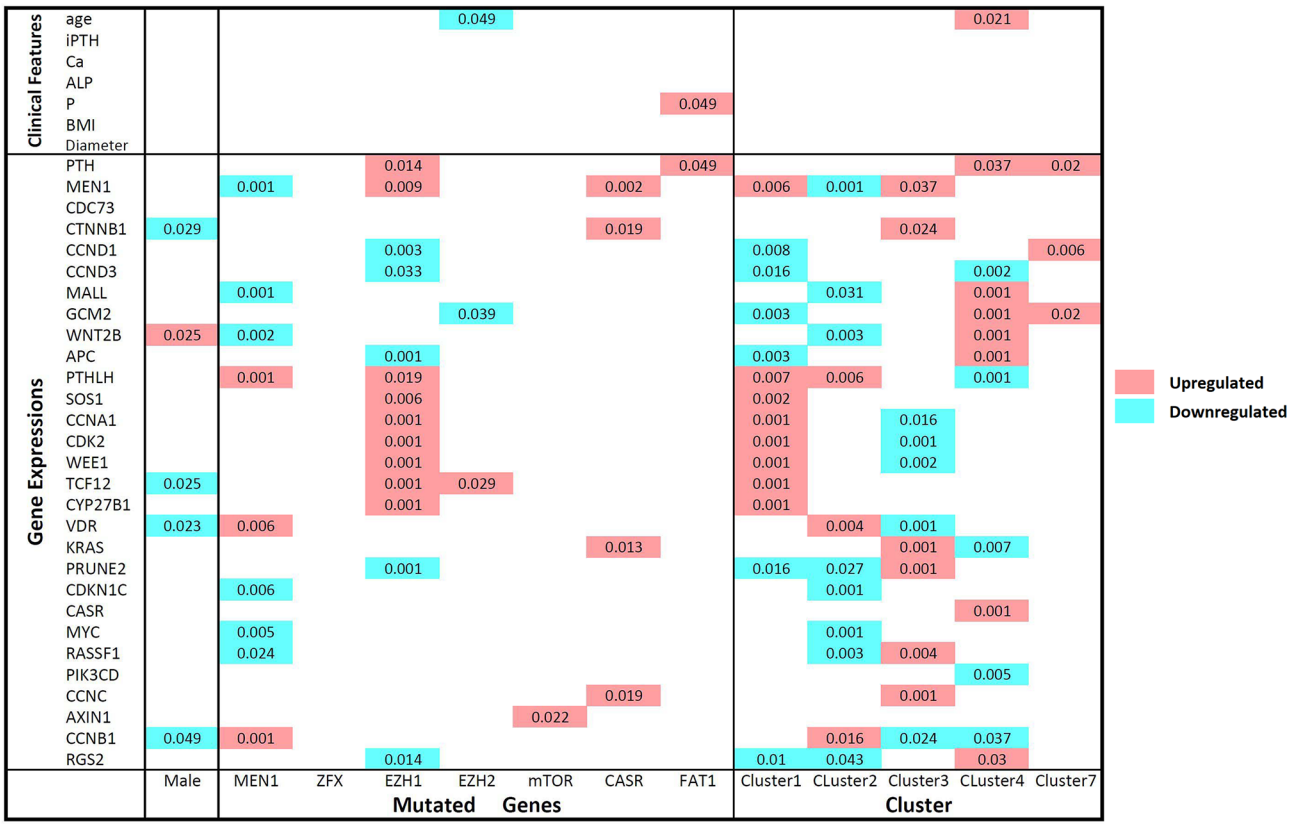

FIGURE 3 | Comparisons of gene expression levels and clinical features between mutant and wild-type parathyroid adenomas and between clusters according to the Mann-Whitney U test. The names of the mutated genes and clusters names are listed on the horizontal axis, and the gene expression level and clinical features are shown on the vertical axis. Comparisons of wild-type and mutant parathyroid adenomas and different clusters: upregulated and downregulated expression levels in samples with the mutant genotype or in certain clusters are represented by red and blue, respectively. P-values less than 0.05 are marked in the matrix. iPTH, serum intact parathyroid hormone level; Ca, serum calcium level; ALP, serum alkaline phosphatase level; P, serum phosphorus level; BMI, body mass index; Diameter, maximum diameter of the parathyroid adenoma.

been reported previously. In the RNA-seq analysis, overexpression of CCND1 and CTNNB1, which are recognized as vital factors for PA tumorigenesis, was also found (13, 14). KEGG analysis also found that ribosomal protein dysregulation was related to PA and is a known factor involved in tumor development (15). Previous work focused mainly on the mutation or expression of one or several of these related genes, which may be only one facet of the complex molecular mechanisms of PA tumorigenesis. However, contradictory results were occasionally reported in different publications. Therefore, we performed unsupervised clustering for the RNA-seq data, and 10 clusters were identified. Even though it is not easy to explain the intrinsic molecular mechanism underpinning these clusters from a single study with limited samples, we revealed some intriguing aspects.

In our cohort, 8 somatic mutations and 1 germline mutation of *MEN1* were identified, and the expression levels of *MEN1* in these 9 samples were significantly decreased. All these samples were clustered in one subgroup, indicating that the *MEN1* genotype might be related to the expression profile. *MEN1*, a tumor suppressor gene, was identified as a genetic driver of multiple endocrine neoplasia type 1 (16). Biallelic inactivation of *MEN1* is also found in approximately 12-35% sporadic PA cases (17, 18). We found that one patient with seemingly sporadic PA had a germline *MEN1* mutation, which was also reported by other authors (19). Three samples (7.3%) harboring somatic *ZFX* mutations were also included in Cluster 2, one of which carried a *MEN1* mutation concurrently. *ZFX*, a transcriptional target of cyclin D, was identified as a candidate driver gene for PA with a mutation rate of 5% (20, 21). In contrast to previous reports, all three mutations of *ZFX* in our cohort were not located at the R767 or R768 position.

Interestingly, 2 patients with the rare activating mutation Y464 of *EZH2* and 4 patients with the somatic mutation Y642F of *EZH1* were classified into one cluster (Cluster 1). Our results are consistent with previous reports showing that *EZH2* mutations are potential genetic drivers of PA. The activating mutation Y464N (previously described as Y641N) in *EZH2* was found previously in 2 of 193 sporadic PA samples (22). Although rare, 2 patients harbored the Y464 mutation in our cohort of 41.

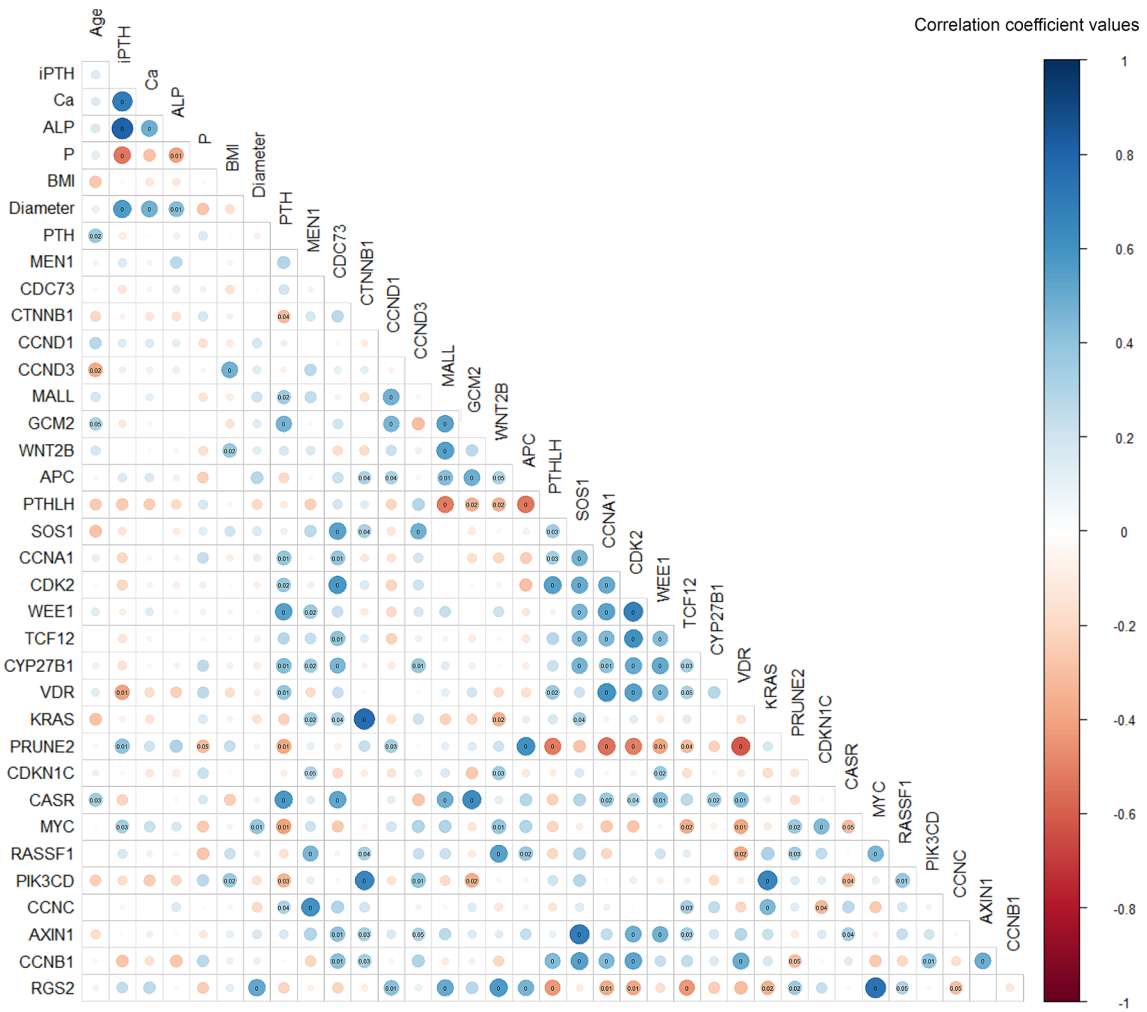

FIGURE 4 | Spearman's correlation matrix between gene expression and clinicopathological features in parathyroid adenoma. The correlation coefficient values are visualized by the size and color intensity of the circles. Positive and negative correlations are represented by blue and red, respectively. P-values below 0.05 are marked in the matrix, with P-values below 0.01 marked as zero. iPTH, serum intact parathyroid hormone level; Ca, serum calcium level; ALP, serum alkaline phosphatase; P, serum phosphorus level; BMI, body mass index; Diameter, maximum diameter of the parathyroid adenoma.

Furthermore, the somatic mutation Y642F of *EZH1* was identified in another 4 patients. Like *EZH2*, *EZH1* is also a component of the noncanonical polycomb repressive complex-2, which is recurrently mutated in multiple hematological malignancies (23). *EZH1* mutations were found in 20% of Hürthle cell adenomas and 10% of Hürthle cell carcinomas, and 53.8% of the mutations were Y642F (24). Though not reported previously, *EZH1* may be a potentially important gene for PA.

A somatic *CDC73* mutation was identified in one sample (PA17). Somatic inactivating mutations of *CDC73*, or loss of staining of the encoded parafibromin, occurred in approximately 60% of parathyroid carcinomas and in a few PAs (25, 26). In addition, significantly low expression of CDC73 was found in PA03 and PA21, while no mutation or copy number change was found in *CDC73*. Epigenetic changes may be the underlying cause.

In our cohort, overexpression of CCND1 was found in some samples, and the 4 samples with the highest expression levels were clustered in one group (Cluster 7). *CCND1*, encoding cyclin D1, was first identified as an oncogene in parathyroid tumors, and overexpression of this gene was found in 20-40% of PA samples (17, 27). Overexpression of CCND1 was caused by rearrangement of the PTH 5' regulatory region of the *CCND1* coding region in some PAs. However, this could not be identified by WES in the present study. Neither gene amplification nor mutation of *CCND1* was found in these samples. Furthermore, another cell cycle regulator factor, cyclin D3 (*CCND3*), may also be involved in sporadic PA, as we found that the expression level of cyclin D3 in PA09 was approximately 31 times higher than that in the normal control. This may be caused by the copy gain of *CCND3* identified in this sample. The partners of cyclin D1 in cell cycle regulation, such as *CDKN1B*, *CDKN1C*, *CDKN2C* and

other CDKI genes, were also reported to be involved in sporadic PA (28, 29). As reported, the expression of CDKN1B and CDKN1C was downregulated in some of our samples, while no somatic or germline variant of this gene was found (30). In addition, a frameshift deletion of *CDKN2C* was identified in one sample, and this mutation had been reported previously in a few PA samples (29, 31).

In the present cohort, somatic *CASR* mutations were identified in 3 samples, but the gene expression levels were not different from those in PaN. These 3 samples were clustered into different subgroups. *CASR* encodes a calcium sensing receptor, by which parathyroid cells monitor the extracellular calcium level. Inactivating germline mutations of *CASR* are responsible for familial hypocalciuric hypercalcemia and neonatal severe hyperparathyroidism. However, somatic inactivating *CASR* mutation was rarely found in sporadic PA (32–34). Therefore, *CASR* mutation was believed to be a predisposing factor rather than a genetic driver in PA (17). Another 3 specimens with low CASR expression were clustered into an independent subgroup (Cluster 8). Aberrant expression of *CASR* is frequently found in parathyroid tumors (35, 36). Five samples with the lowest VDR levels were clustered in Cluster 3, and VDR levels were negatively correlated with serum PTH levels, suggesting a vital role in PA. Decreased VDR expression was related to the high proliferation of pHPT, but no *VDR* mutation was found in our cohort (35, 37).

We could not identify any somatic or germline variants of *GCM2* in this Chinese cohort. However, a prominent increase in GCM2 levels was identified in 5 samples in an independent subgroup (Cluster 4). This was consistent with previous findings in which the GCM2 expression level was significantly upregulated in PA and correlated with a decrease in the response to hypocalcemia (38). *GCM2* encodes a transcription factor that is a critical regulator of the development of the parathyroid gland, and its activating germline variants are responsible for familial isolated hyperparathyroidism (39). In addition, Cluster 4 and 6 revealed no apparent driver mutation but showed aberrant expression of some tumor-related genes, such as GCM2 and AXIN1, indicating that driver gene plays an important, but not indispensable, role in the initiation of PA.

Another interesting mutation might be *SLC25A3*, which was identified in 3 of 41 samples. *SLC25A3* is essential for cytochrome c oxidase of the mitochondrial respiratory chain and *SLC25A3* deletion causes mitochondrial cardiomyopathy (40). Previously, mitochondrial variations may result in oncocytic phenotype of PA (41). However, *SLC25A3*-related studies were not available in PA.

There were several limitations to this study. The main shortcoming was the limited number of participants in this cohort, even though it was quite large considering recent sequencing studies on PA. Additional samples may help validate the gene mutation with low incidence. Second, due to the lack of normal parathyroid specimens for comparison, immunohistochemical staining or Western blot analysis were not suitable to confirm the protein levels of the related gene variants among PA samples. Third, bulk RNA-Seq data are heavily influenced by tissue cellular composition. The gene expression profile might contain not only the tumor-induced molecular alterations but also the interference from tumor heterogeneity.

CONCLUSIONS

This study revealed almost all previously reported molecular features of PA using integrated WES and RNA-seq analyses. In addition to the previously reported mutant genes, such as *MEN1*, *EZH2*, *CASR* and *CDC73*, somatic mutations of *EZH1* were also identified in the present PA cohort. With clustering based on RNA-seq, abnormal expression of cyclin D1, β-catenin, VDR, CASR and GCM2 may be an important factor influencing the gene expression profile of PA.

DATA AVAILABILITY STATEMENT

The data presented in the study are deposited in the Genome Sequence Archive (GSA) in BIG Data Center, Beijing Institute of Genomics (BIG), Chinese Academy of Sciences (CAS), publicly accessible at https://bigd.big.ac.cn/gsa-human/, accession number (HRA000665).

ETHICS STATEMENT

The studies involving human participants were reviewed and approved by the Institutional Ethics Review Board of Peking Union Medical College Hospital. The patients/participants provided their written informed consent to participate in this study.

AUTHOR CONTRIBUTIONS

YH and XZ designed the study and performed the experiments. YH, XL, and QL performed the surgery. XZ, OW, MC, XL, MW, and SH enrolled the patients and collected the samples. YH, XZ, OW and MC analyzed the data. YH, XZ and QL wrote and modified the manuscript. All authors contributed to the article and approved the submitted version.

FUNDING

This work was supported by the Chinese Academy of Medical Sciences (CAMS) Innovation Fund for Medical Sciences (CIFMS) (2017-I2M-1-001), the Nonprofit Central Research Institute Fund of the Chinese Academy of Medical Sciences (2018PT32014) and the Peking Union Medical College Innovative Team Development Program.

SUPPLEMENTARY MATERIAL

The Supplementary Material for this article can be found online at: https://www.frontiersin.org/articles/10.3389/fendo.2021.631680/full#supplementary-material

REFERENCES

1. Yeh MW, Ituarte PHG, Zhou HC, Nishimoto S, Liu I-LA, Harari A, et al. Incidence and Prevalence of Primary Hyperparathyroidism in a Racially Mixed Population. *J Clin Endocrinol Metab* (2013) 98:1122–9. doi: 10.1210/jc.2012-4022
2. Lundgren E, Rastad J, Thurfjell E, Åkerström G, Ljunghall S. Population-Based Screening for Primary Hyperparathyroidism with Serum Calcium and Parathyroid Hormone Values in Menopausal Women. *Surgery* (1997) 121:287–94. doi: 10.1016/s0039-6060(97)90357-3
3. Newey PJ, Nesbit MA, Rimmer AJ, Attar M, Head RT, Christie PT, et al. Whole-Exome Sequencing Studies of Nonhereditary (Sporadic) Parathyroid Adenomas. *J Clin Endocrinol Metab* (2012) 97:E1995–2005. doi: 10.1210/jc.2012-2303
4. Wei Z, Sun B, Wang ZP, He JW, Fu WZ, Fan YB, et al. Whole-Exome Sequencing Identifies Novel Recurrent Somatic Mutations in Sporadic Parathyroid Adenomas. *Endocrinology* (2018) 159:3061–8. doi: 10.1210/en.2018-00246
5. Chai YJ, Chae H, Kim K, Lee H, Choi S, Lee KE, et al. Comparative Gene Expression Profiles in Parathyroid Adenoma and Normal Parathyroid Tissue. *J Clin Med* (2019) 8:297. doi: 10.3390/jcm8030297
6. Lloyd RV, Osamura RY, Klöppel G, Rosai J. WHO/IARC Classification of Tumours. In: *WHO Classification of Tumours of Endocrine Organs. Lyon: IARC, 4th Edition*, Volume 10. France: International Agency for Research on Cancer (IARC) (2017).
7. Cibulskis K, Lawrence MS, Carter SL, Sivachenko A, Jaffe D, Sougnez C, et al. Sensitive Detection of Somatic Point Mutations in Impure and Heterogeneous Cancer Samples. *Nat Biotechnol* (2013) 31:213–9. doi: 10.1038/nbt.2514
8. Saunders CT, Wong WSW, Swamy S, Becq J, Murray LJ, Cheetham RK. Strelka: Accurate Somatic Small-Variant Calling from Sequenced Tumor–Normal Sample Pairs. *Bioinformatics* (2012) 28:1811–7. doi: 10.1093/bioinformatics/bts271
9. Boeva V, Popova T, Bleakley K, Chiche P, Cappo J, Schleiermacher G, et al. Control-FREEC: a Tool for Assessing Copy Number and Allelic Content Using Next-Generation Sequencing Data. *Bioinform (Oxf Engl)* (2012) 28:423–5. doi: 10.1093/bioinformatics/btr670
10. Dees ND, Zhang Q, Kandoth C, Wendl MC, Schierding W, Koboldt DC, et al. MuSiC: Identifying Mutational Significance in Cancer Genomes. *Genome Res* (2012) 22:1589–98. doi: 10.1101/gr.134635.111
11. Subramanian A, Tamayo P, Mootha VK, Mukherjee S, Ebert BL, Gillette MA, et al. Gene Set Enrichment Analysis: A Knowledge-Based Approach for Interpreting Genome-Wide Expression Profiles. *Proc Natl Acad Sci USA* (2005) 102:15545–50. doi: 10.1073/pnas.0506580102
12. Haas BJ, Dobin A, Li B, Stransky N, Pochet N, Regev A. Accuracy Assessment of Fusion Transcript Detection via Read-Mapping and de novo Fusion Transcript Assembly-Based Methods. *Genome Biol* (2019) 20:213. doi: 10.1186/s13059-019-1842-9
13. Arnold A. Major Molecular Genetic Drivers in Sporadic Primary Hyperparathyroidism. *Trans Am Clin Climatol Assoc* (2016) 127:235–44.
14. Alberto F. Genetics of Parathyroids Disorders: Overview. *Best Pract Res Clin Endocrinol Metab* (2018) 32:781–90. doi: 10.1016/j.beem.2018.09.011
15. Goudarzi KM, Lindström MS. Role of Ribosomal Protein Mutations in Tumor Development (Review). *Int J Oncol* (2016) 48:1313–24. doi: 10.3892/ijo.2016.3387
16. Chandrasekharappa SC. Positional Cloning of the Gene for Multiple Endocrine Neoplasia-type 1. *Science* (1997) 276:404–7. doi: 10.1126/science.276.5311.404
17. Costa-Guda J, Arnold A. Genetic and Epigenetic Changes in Sporadic Endocrine Tumors: Parathyroid Tumors. *Mol Cell Endocrinol* (2014) 386:46–54. doi: 10.1016/j.mce.2013.09.005
18. Farnebo F. Alterations of the MEN1 Gene in Sporadic Parathyroid Tumors. *J Clin Endocrinol Metab* (1998) 83:2627–30. doi: 10.1210/jc.83.8.2627
19. Starker LF, Åkerström T, Long WD, Delgado-Verdugo A, Donovan P, Udelsman R, et al. Frequent Germ-Line Mutations of the MEN1, CASR, and HRPT2/CDC73 Genes in Young Patients with Clinically Non-Familial Primary Hyperparathyroidism. *Horm Cancer* (2012) 3:44–51. doi: 10.1007/s12672-011-0100-8
20. Soong CP, Arnold A. Recurrent ZFX Mutations in Human Sporadic Parathyroid Adenomas. *Oncoscience* (2014) 1:360–6. doi: 10.18632/oncoscience.116
21. Casimiro MC, Crosariol M, Loro E, Ertel A, Yu Z, Dampier W, et al. ChIP Sequencing of Cyclin D1 Reveals a Transcriptional Role in Chromosomal Instability in Mice. *J Clin Investig* (2012) 122:833–43. doi: 10.1172/JCI60256
22. Cromer MK, Starker LF, Choi M, Udelsman R, Nelson-Williams C, Lifton RP, et al. Identification of Somatic Mutations in Parathyroid Tumors Using Whole-Exome Sequencing. *J Clin Endocrinol Metab* (2012) 97:E1774–81. doi: 10.1210/jc.2012-1743
23. Nakagawa M, Kitabayashi I. Oncogenic Roles of Enhancer of Zeste Homolog 1/2 in Hematological Malignancies. *Cancer Sci* (2018) 109:2342–8. doi: 10.1111/cas.13655
24. Jung CK, Kim Y, Jeon S, Jo K, Lee S, Bae JS. Clinical Utility of EZH1 Mutations in the Diagnosis of Follicular-Patterned Thyroid Tumors. *Hum Pathol* (2018) 81:9–17. doi: 10.1016/j.humpath.2018.04.018
25. Hu Y, Liao Q, Cao S, Gao X, Zhao Y. Diagnostic Performance of Parafibromin Immunohistochemical Staining for Sporadic Parathyroid Carcinoma: A Meta-Analysis. *Endocrine* (2016) 54:612–9. doi: 10.1007/s12020-016-0997-3
26. Cetani F, Banti C, Pardi E, Borsari S, Viacava P, Miccoli P, et al. CDC73 Mutational Status and Loss of Parafibromin in the Outcome of Parathyroid Cancer. *Endocr Connect* (2013) 2:186–95. doi: 10.1530/EC-13-0046
27. Motokura T, Bloom T, Kim HG, Jüppner H, Ruderman JV, Kronenberg HM, et al. A Novel Cyclin Encoded by a bcl1-linked Candidate Oncogene. *Nature* (1991) 350:512–5. doi: 10.1038/350512a0
28. Arya AK, Bhadada SK, Singh P, Sachdeva N, Saikia UN, Dahiya D, et al. Promoter Hypermethylation Inactivates CDKN2A, CDKN2B and RASSF1A Genes in Sporadic Parathyroid Adenomas. *Sci Rep* (2017) 7:3123. doi: 10.1038/s41598-017-03143-8
29. Costa-Guda J, Soong CP, Parekh VI, Agarwal SK, Arnold A. Germline and Somatic Mutations in Cyclin-Dependent Kinase Inhibitor Genes CDKN1A, CDKN2B, and CDKN2C in Sporadic Parathyroid Adenomas. *Horm Cancer* (2013) 4:301–7. doi: 10.1007/s12672-013-0147-9
30. Buchwald PC, Akerstrom G, Westin G. Reduced p18INK4c, p21CIP1/WAF1 and p27KIP1 mRNA Levels in Tumours of Primary and Secondary Hyperparathyroidism. *Clin Endocrinol* (2004) 60:389–93. doi: 10.1111/j.1365-2265.2004.01995.x
31. Gluick T, Yuan Z, Libutti SK, Marx SJ. Mutations in CDKN2C (p18) and CDKN2D (p19) May Cause Sporadic Parathyroid Adenoma. *Endocr Relat Cancer* (2013) 20:L27–9. doi: 10.1530/erc-13-0445
32. Hosokawa Y. Mutational Analysis of the Extracellular Ca(2+)-Sensing Receptor Gene in Human Parathyroid Tumors. *J Clin Endocrinol Metab* (1995) 80:3107–10. doi: 10.1210/jc.80.11.3107
33. Cetani F, Pinchera A, Pardi E, Cianferotti L, Vignali E, Picone A, et al. No Evidence for Mutations in the Calcium-Sensing Receptor Gene in Sporadic Parathyroid Adenomas. *J Bone Miner Res* (1999) 14:878–82. doi: 10.1359/jbmr.1999.14.6.878
34. Guarnieri V, Canaff L, Yun FHJ, Scillitani A, Battista C, Muscarella LA, et al. Calcium-Sensing Receptor (CASR) Mutations in Hypercalcemic States: Studies from a Single Endocrine Clinic Over Three Years. *J Clin Endocrinol Metab* (2010) 95:1819–29. doi: 10.1210/jc.2008-2430
35. Carling T, Rastad J, Szabó E, Westin G, Akerström G. Reduced Parathyroid Vitamin D Receptor Messenger Ribonucleic Acid Levels in Primary and Secondary Hyperparathyroidism. *J Clin Endocrinol Metab* (2000) 85:2000–3. doi: 10.1210/jc.85.5.2000
36. Aycicek GS, Aydogan BI, Sahin M, Cansız Ersoz C, Sak SD, Baskal N. Clinical Impact of p27Kip1 and CaSR Expression on Primary Hyperparathyroidism. *Endocr Pathol* (2018) 29:250–8. doi: 10.1007/s12022-018-9524-9
37. Yano S, Sugimoto T, Tsukamoto T, Chihara K, Kobayashi A, Kitazawa S, et al. Decrease in Vitamin D Receptor and Calcium-Sensing Receptor in Highly Proliferative Parathyroid Adenomas. *Eur J Endocrinol* (2003) 148:403–11. doi: 10.1530/eje.0.1480403
38. Kebebew E, Peng M, Wong MG, Ginzinger D, Duh QY, Clark OH. GCMB Gene, a Master Regulator of Parathyroid Gland Development, Expression, and Regulation in Hyperparathyroidism. *Surgery* (2004) 136:1261–6. doi: 10.1016/j.surg.2004.06.056

39. Guan B, Welch JM, Sapp JC, Ling H, Li Y, Johnston JJ, et al. GCM2-Activating Mutations in Familial Isolated Hyperparathyroidism. *Am J Hum Genet* (2016) 99:1034–44. doi: 10.1016/j.ajhg.2016.08.018
40. Mayr JA, Zimmermann FA, Horvath R, Schneider HC, Schoser B, Holinski-Feder E, et al. Deficiency of the Mitochondrial Phosphate Carrier Presenting as Myopathy and Cardiomyopathy in a Family with Three Affected Children. *Neuromuscul Disord* (2011) 21:803–8. doi: 10.1016/j.nmd.2011.06.005
41. Costa-Guda J, Tokura T, Roth SI, Arnold A. Mitochondrial DNA Mutations in Oxyphilic and Chief Cell Parathyroid Adenomas. *BMC Endocr Disord* (2007) 7:8. doi: 10.1186/1472-6823-7-8

Conflict of Interest: The authors declare that the research was conducted in the absence of any commercial or financial relationships that could be construed as a potential conflict of interest.

frontiers in Endocrinology

MINI REVIEW
published: 01 June 2021
doi: 10.3389/fendo.2021.659733

O-GlcNAcylation in Hyperglycemic Pregnancies: Impact on Placental Function

Jie Ning[1,2,3] *and Huixia Yang*[1,2,3]*

[1] Department of Obstetrics and Gynaecology, Peking University First Hospital, Beijing, China, [2] Beijing Key Laboratory of Maternal Foetal Medicine of Gestational Diabetes Mellitus, Beijing, China, [3] Peking University, Beijing, China

The dynamic cycling of *N*-acetylglucosamine, termed as O-GlcNAcylation, is a post-translational modification of proteins and is involved in the regulation of fundamental cellular processes. It is controlled by two essential enzymes, O-GlcNAc transferase and O-GlcNAcase. O-GlcNAcylation serves as a modulator in placental tissue; furthermore, increased levels of protein O-GlcNAcylation have been observed in women with hyperglycemia during pregnancy, which may affect the short-and long-term development of offspring. In this review, we focus on the impact of O-GlcNAcylation on placental functions in hyperglycemia-associated pregnancies. We discuss the following topics: effect of O-GlcNAcylation on placental development and its association with hyperglycemia; maternal-fetal nutrition transport, particularly glucose transport, *via* the mammalian target of rapamycin and AMP-activated protein kinase pathways; and the two-sided regulatory effect of O-GlcNAcylation on inflammation. As O-GlcNAcylation in the placental tissues of pregnant women with hyperglycemia influences near- and long-term development of offspring, research in this field has significant therapeutic relevance.

Keywords: O-GlcNAcylation, hyperglycemia in pregnancy, placental function, O-GlcNAc transferase, O-GlNAcase

OPEN ACCESS

Edited by:
Stephen Atkin,
Royal College of Surgeons in Ireland, Bahrain

Reviewed by:
Maria Mirabelli,
University Magna Graecia of Catanzaro, Italy
Ee Phie Tan,
Sanford Burnham Prebys Medical Discovery Institute, United States
Ewa Forma,
University of Łódź, Poland

***Correspondence:**
Huixia Yang
yanghuixia@bjmu.edu.cn

Specialty section:
This article was submitted to Systems Endocrinology, a section of the journal Frontiers in Endocrinology

Received: *16 February 2021*
Accepted: *17 May 2021*
Published: *01 June 2021*

Citation:
Ning J and Yang H (2021) O-GlcNAcylation in Hyperglycemic Pregnancies: Impact on Placental Function. Front. Endocrinol. 12:659733. doi: 10.3389/fendo.2021.659733

INTRODUCTION

Hyperglycemia in pregnancy (HIP), one of the most common medical conditions during pregnancy, may be classified as gestational diabetes mellitus (GDM) and diabetes mellitus in pregnancy. HIP is an important cause of adverse pregnancy outcomes and increasing incidences of metabolic syndromes in adulthood (1–3). The placenta is a key interface for maternal-fetal interaction, particularly for nutrition transport. It is instrumental in fetal intrauterine growth and long-term development of offspring. The placenta of women with HIP is exposed to a high concentration of blood glucose at different degrees and windows of time. This may affect numerous cellular pathways, leading to accumulation of advanced glycation end-products (4, 5) and induction of oxidative stress (6). The reported activation of the chronic hexosamine biosynthetic pathway (HBP) in placental tissue under similar conditions is also garnering attention (7).

O-linked β-N-acetylglucosamine (O-GlcNAc) glycosylation (O-GlcNAcylation) is a post-translational modification (PTM) of proteins that plays an essential role in regulating various cellular processes (**Figure 1**). In contrast to classical N-/O-linked glycosylation, which mostly occurs in the Golgi compartment and endoplasmic reticulum with the extraordinarily extracellular

complex array of glycans, the substrate for O-GlcNAcylation is uridine diphosphate N-acetylglucosamine (UDP-GlcNAc) generated from HBP. HBP is a pathway that integrates glucose, fatty acid, amino acid, and nucleotide metabolism. The GlcNAc moiety from UDP-GlcNAc can be transferred onto the serine and threonine residues of a wide variety of nuclear, cytoplasmic, and mitochondrial proteins through the catalytic activity of the enzyme O-GlcNAc transferase (OGT). The cleavage of O-GlcNAc from proteins is catalyzed by glycoside hydrolase O-GlcNAcase (OGA) (also named MGEA5). Similar to other PTMs, this process is dynamic and reversible (7).

It has been reported that O-GlcNAcylation occurs in the placenta and is involved in transcriptional regulation, signal transduction, and epigenetic modifications (8–11). OGA is expressed in most tissues, and one of the highest expression was found in the placenta (12). OGT acts as a placental biomarker of maternal stress, which affects fetal neurodevelopment (13). Studies in diabetes mellitus have shown that hyperglycemia directly increases protein O-GlcNAcylation, at least in part, by increasing the glucose flux through HBP, and that OGT/OGA expression may be regulated by chronic hyperglycemia (14). Studies on hyperglycemic rat models have also shown that O-GlcNAcylation levels increase in the placenta depending on the severity of hyperglycemia, and that trophoblast cells were the main target for O-GlcNAcylation (8). The focus of this review is to summarize the impact of O-GlcNAcylation in placenta exposed to HIP.

PLACENTA GROWTH AND DEVELOPMENT

The placenta is involved in the development, adaptation, and physiology of offspring in response to maternal growth and nutrient signals, primarily by regulating nutrient transport. O-GlcNAcylation seems to be an important modulator during placentation and placental development (15) (**Figure 2**). Studies on mouse embryos have demonstrated that the nuclear localization of Yes-associated protein 1 (YAP1) is glucose/HBP/O-GlcNAcylation-dependent, and this event is crucial for differentiation of the apical blastomeres to form the extraembryonic trophectoderm (TE) (16). During the incipient stages of trophoblast development at implantation, Ruane et al. (17) proposed that O-GlcNAcylation drives TE differentiation to the invasive trophoblast, as well as the differentiation of BeWo to syncytiotrophoblasts (STBs). Moreover, the O-GlcNAcylation of histone variant H2A was also shown to participate in the trophoblast stem cell differentiation process (18). A recent study on the placenta suggested that the O-GlcNAcylation of cystathionine γ-lyase (CSE) at Ser138 promotes its activity to produce H2S. Further, H2S inhibits androgen receptor dimerization and then represses trophoblast syncytialization (19). Glutamine fructose-6-phosphate amidotransferase (GFAT), an important rate-limiting enzyme of the HBP, regulates trophoblast cell proliferation in response to glucose through phosphatidylinositol 3-kinase (PI3K)-independent mammalian target of rapamycin (mTOR) activation (20). Furthermore, autophagy, a process which is governs the degradation of misfolded proteins and damaged organelles, is important for normal placental developmental activities, such as invasion and vascular remodeling of extravillous trophoblasts (EVT). Studies on HTR8/SVneo cells showed that mTOR signaling also plays a role in regulating autophagy *via* the modulation of Beclin1 and synaptosome associated protein 29 (SNAP29) O-GlcNAcylation (21). Enhanced autophagy levels have been observed in human and mouse placentas exposed to HIP, as well as trophoblast cells in high-glucose environments (22–24). With regard to HIP, it is worth studying the exact function of the O-GlcNAcylation-associated regulation of autophagy in placental development.

Placental OGT and OGA expression levels both affect placental development; however, maternal stress seems to be the pivotal regulator of OGT and is more critical for fetal neurodevelopment, rather than hyperglycemia (13, 25–27). And, as an X-linked gene, placental OGT levels and its biochemical marker, O-GlcNAcylation are higher in females than in males. Male fetuses are associated with an increased risk of GDM in the mother (28, 29), and there might be an O-GlcNAcylation-related sexual dimorphism in the placental response to maternal hyperglycemia. In contrast, the regulation of OGA expression is more associated with glycemia. Dela Justina et al. (8) observed that increased O-GlcNAcylation accumulation in placental tissue exposed to severe hyperglycemia might contribute to an increased placental index and morphometric alterations, which could be associated with placental dysfunction. Although there were no changes in OGT expression in all groups, OGA expression was augmented in placentas from the mild hyperglycemic group and reduced in placentas from hyperglycemic rats. This might be a biological compensation phenomenon as a result of being confronted with a mounting supply of glucose through HBP flux. Yang et al. (30) proposed that OGA deletion suppresses hypoxia-inducible factor-1α (HIF-1α) stabilization and the transcription of its target genes, leading to impaired placental vasculogenesis and consequent disorders in fetal growth and development. The possible mechanism of O-GlcNAcylation and OGT in the translation and stabilization of HIF-1α has been studied in cancer cells. It was observed that an increased level of O-GlcNAcylation and the overexpression of OGT reduced α-ketoglutarate, which assists hydroxylation and the degradation of HIF-1α (31). Moreover, unbalanced O-GlcNAcylation levels favor endothelial dysfunction in uterine arteries, which is important for uteroplacental circulation and this is partly modulated by OGT (32). These results might partly explain the structural and functional immaturity of placentas exposed to hyperglycemia and its effect on maternal-fetal interactions (33).

In addition to its influence on placenta, O-GlcNAcylation can directly affect embryonic development, including the regulation of oocyte meiotic division, embryo implantation and the survival and differentiation process of embryonic pluripotent stem cells. Besides, O-GlcNAcylation-related excessive induction of reactive oxygen species (ROS) and subsequent oxidative stress leads to embryo DNA damage, mitochondrial instability, and cell

apoptosis (34–36). A recent study also emphasized that the O-GlcNAc-dependent regulatory pathway is important for the DNA damage response required to maintain homeostasis in embryonic stem cells (37). Further, Muha et al. (38) proposed that the loss of OGA catalytic activity leads to widespread organ defects in mouse embryogenesis. Researchers have suggested that dysregulation of HBP and O-GlcNAcylation are major contributors toward the embryotoxic effects of hyperglycemia in early pregnancy (39). Another study also suggested that increased O-GlcNAcylation in metabolically compromised pregnancies, such as HIP, could be the underlying cause of defective neurodevelopmental outcomes (40).

NUTRIENT SENSING

The placenta contains an array of nutrient-sensing signaling pathways. Of these nutrient sensors, mTOR and AMP-activated protein kinase (AMPK) play a key role (41). Their involvement in placental O-GlcNAcylation is responsible for placental development and glucose and amino acid transport (42) (**Figure 1**).

The atypical serine/threonine kinase mTOR is part of two complexes with distinct functions and structures: mTOR complex 1 (mTORC1) and mTORC2 (43). mTORC1 is highly expressed in trophoblast cells (44). mTOR plays an important role in controlling trophoblast cell growth, proliferation, syncytialization and macropinocytosis (45). mTOR activity is regulated by the concentration of glucose, amino acids, and insulin, and is mediated by the PI3K/AKT signaling pathway. It stimulates cell growth through the phosphorylation of tuberous sclerosis complex 2 (TSC2), a negative regulator of mTORC1, and activation of Ras homolog enriched in brain (46, 47). mTORC1 promotes protein synthesis by directly phosphorylating the eukaryotic translation initiation factor 4E (eIF4E) binding protein 1 (4E-BP1) and ribosomal protein S6 kinase (p70S6K) (48). The activity of GSK3β, an enzyme that regulates glycogen synthesis, is inhibited by the activation of insulin-AKT signaling pathway, which executes diverse biological functions (49). Besides, GSK3 phosphorylation of TSC2 inhibits the mTOR signaling pathway and the regulation requires AMPK activity (50). Dynamic changes in the AMP: ATP ratio regulate the activation of AMPK. In addition to participating in a variety of cellular activities such as lipid metabolism, AMPK targets the mTORC1 pathway, which plays a direct/indirect inhibitory role (51). Several participants of the PI3K/AKT/mTOR signaling pathway have been found to be modified by O-GlcNAcylation, such as IRS-1, PI3K, AKT, AMPK, p70S6K, 4E-BP1, and GSK3β (52–54).

Increased mTOR activity and decreased AMPK activity can be observed in placentas exposed to HIP (55–57). In a variety of tissues including the placenta, it has been proven that the expression, localization and activation of the key enzymes of O-GlcNAcylation are regulated by these nutrient-sensing signaling pathways. Studies on cardiomyocytes demonstrated that GFAT can be directly phosphorylated by AMPK, thereby reducing its activity and lowering O-GlcNAcylation levels (58). The localization, expression, and substrate specificity of OGT are regulated by AMPK, which is highly dependent on various factors such as the physiological/pathological status and cell types. In several pathologies, O-GlcNAcylation levels are

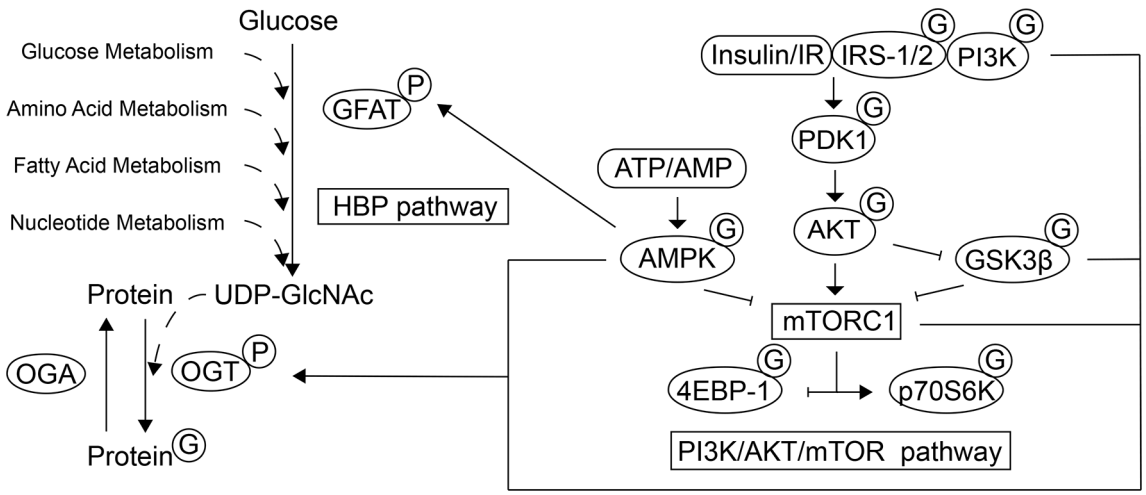

FIGURE 1 | Schematic representation of the interplay between the HBP, mTOR and AMPK pathways. O-GlcNAcylation, as a PTM of a wide variety of nuclear, cytoplasmic, and mitochondrial proteins, participates in various cellular processes. The HBP integrates glucose, fatty acid, amino acid, and nucleotide metabolism to generate the substrate for O-GlcNAcylation, UDP-GlcNAc. GFAT is the rate-limiting step of the HBP and its activity can be regulated by AMPK through phosphorylation. The O-GlcNAc moiety can be transferred to the target proteins and removed by OGT and OGA, respectively. The activity of mTOR and GSK3β can be mediated by the PI3K/AKT signaling pathway and mTORC1 promotes protein synthesis by directly phosphorylating 4E-BP1 and p70S6K. In response to energy state, AMPK also regulates the mTORC1 activity. The localization, activity, and substrate specificity of OGT are regulated through phosphorylation by AMPK, IR/PI3K and GSK3β, and the mTOR signaling regulates the expression of OGT. In contrast, several actors of the PI3K/AKT/mTOR signaling pathway have been found to be modified by O-GlcNAcylation, which leads to subsequent biological effects under different physiological conditions.

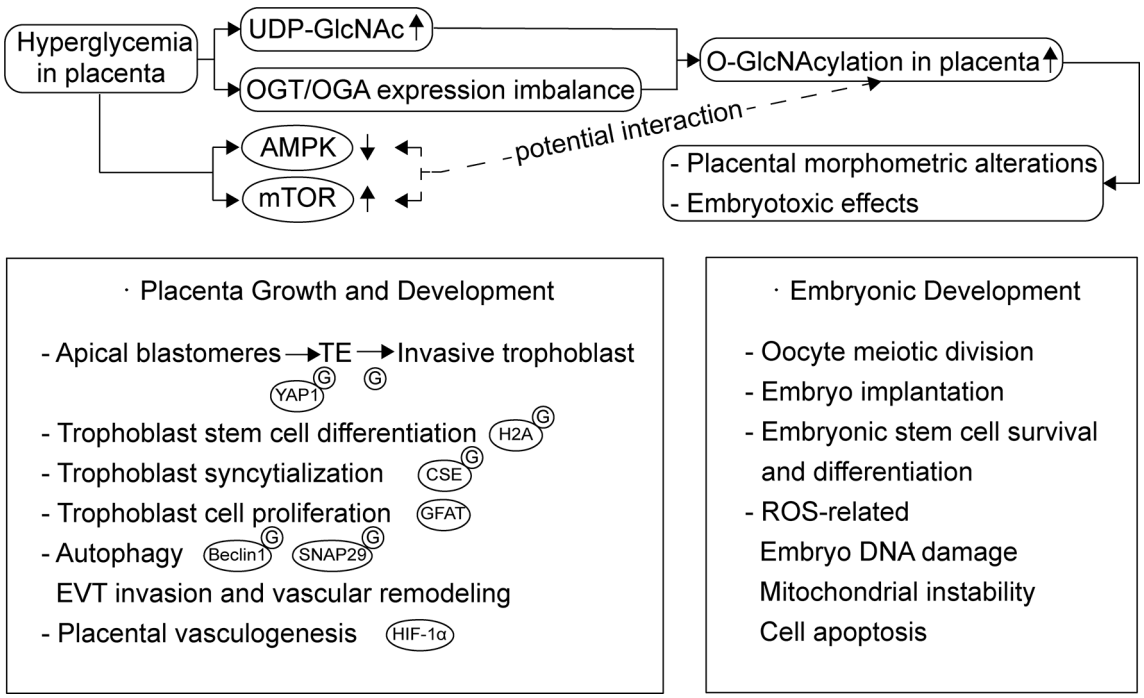

FIGURE 2 | Overview of the function of O-GlcNAcylation during placentation and placental development and O-GlcNAcylation dysregulation in placenta exposed to HIP. Besides embryonic development, O-GlcNAcylation also plays a role through all stages of placental development, including trophoblast cell proliferation, differentiation, syncytialization and autophagy. Hyperglycemia increases the glucose flux through HBP and affects placental OGA expression, which leads to increased O-GlcNAcylation accumulation in placenta. These changes may result in placental morphometric alterations and embryotoxic effects. mTOR and AMPK activity altered in HIP and their potential interaction with O-GlcNAcylation needs further studies.

reduced by AMPK activation to prevent adverse effects (59). Moreover, in Human HepG2 cells, it was observed that insulin stimulates the expression and activity of OGT and promotes its targeting to membranes which is dependent on activation of the PI3K pathway (60). Additionally, Kelly et al. (61) recently proved that the inhibition of mTOR signaling decreases the levels of OGT in the human placenta and affects development of the fetal brain. It was also proven in mouse brains that OGT is a substrate of GSK3β and that the phosphorylation of OGT by GSK3β increases OGT activity (62).

In contrast, OGT also acts as a nutrient sensor and regulates diverse cellular signaling pathways based on the metabolic status of cells by sensing glucose levels *via* UDP-GlcNAc concentrations and responding by dynamically O-GlcNAcylating proteins (63). Few studies have investigated the direct effects of O-GlcNAcylation on the PI3K/AKT/mTOR signaling pathway and its subsequent biological effects under physiological conditions. Under different disease states, O-GlcNAcylation has different activation/suppression effects on this signaling pathway (53, 54). Studies in the pancreas, liver, and skeletal muscle under diabetic conditions show that increased O-GlcNAcylation downregulates AKT and IRS-1 activity and inhibits the IRS-1/PI3K interaction. This leads to pancreatic β cell apoptosis, reduced glucose absorption through the downregulation of insulin-stimulated translocation of glucose transporter 4 (GLUT4) to the plasma membrane, and decreased gluconeogenesis through the regulation of GSK3β, which in turn contributes to blood glucose retention (64–69). The expression and activity of GLUTs in the placenta, which mediates maternal-fetal glucose transport, are also changed in HIP, but the influence of hyperglycemia has not been definitively concluded (70). Whereas GLUT1 was identified as the primary transporter in the placenta, James-Allan et al. demonstrated that (71) maternal insulin promotes GLUT4 trafficking to the fetal-facing basal plasma membrane of the STB. Moreover, during the entire process of gestation, the increase in the expression of GLUT4 meets the increased fetal nutrient demand and supports fetal growth. Further studies on skeletal muscle and adipose tissue proposed that GLUT4 could be directly O-GlcNAc modified, which might alter the translocation and transporter ability of GLUT4 (72). And Buller et al. found that basal glucose uptake and GLUT1 expression in rat LEF cell lines are inhibited by GSK3/TSC2/mTOR pathway (73). Whether O-GlcNAcylation can influence glucose uptake *via* direct modifications or the indirect regulation of GLUTs needs further investigation. The increase in protein O-GlcNAcylation in target tissues of diabetic patients might contribute to the maintenance of the pathological status of PI3K/AKT-mediated insulin resistance and could explain diabetic complications and adverse pregnancy outcomes (3, 74). O-GlcNAcylation of

proteins could enhance the sensitivity of the PI3K/AKT/mTOR signaling pathway to nutrients. In addition, metformin, a potentially effective drug that might improve pregnancy outcomes for HIP, has been proposed to causes the upstream activation of AMPK, resulting in the inhibition of mTOR signaling in the placenta (75–79). It has been proven that metformin reduces the levels of OGT and O-GlcNAcylation and reverses the decreased phosphorylation level of AMPK cause by O-GlcNAc modification in cervical cancer cells. Therefore, further exploration of the possible O-GlcNAcylation-related mechanisms of metformin treatment in placentas exposed to hyperglycemia is required (80).

There seems to be a complex dynamic relationship between these three pathways, and their dynamic changes and interactions may explain the changes in placental nutrient transport in the presence of HIP.

INFLAMMATORY REACTIONS

Hyperglycemia leads to increased expression of pro-inflammatory cytokines, such as IL-6 and TNF-α, which impairs placental functions (81). The transcriptional activity of NF-κB, a nuclear factor inducing the expression of these proinflammatory cytokines, is regulated not only by phosphorylation and acetylation, but also by site-specific O-GlcNAcylation (82). Studies on the placenta of hyperglycemic rats show that non-classical activation of NF-κB is elicited by O-GlcNAcylation and that the p65 subunit is the main target for O-GlcNAcylation. After O-GlcNAcylation, NF-κB showed higher nuclear translocation and transcriptional activity, which may explain why NF-κB activity increases sustainably under hyperglycemic conditions (82, 83). In addition to the O-GlcNAcylation of NF-κB, Pathak et al. (84) determined that the activation of transforming growth factor (TGF)-β-activated kinase 1 (TAK1) needs the O-GlcNAcylation of TAK1-binding protein 1 (TAB1) to activate NF-κB and finally lead to the production of IL-6 and TNF-α in IL-1R HEK293 cells. However, O-GlcNAcylation can also be a negative regulator of NF-κB activity. According to a study in rat aortic smooth muscle cells, O-GlcNAc modification of NF-κB p65 inhibited TNF-α-induced inflammatory mediator expression (85).

Currently, studies associated with O-GlcNAcylation of transcription factors, especially those related to inflammation are limited. A study on cardiac fibrosis caused by diabetes mellitus (86) revealed that hyperglycemia enhanced O-GlcNAcylation of transcription factor Sp1. This modification increased its transcriptional activity, and promoted the expression of transforming growth factor β1 (TGF-β1) and fibrosis-related proteins such as collagen in cardiac fibroblasts. In the placenta, O-GlcNAcylation of Sp1 possibly interrupted the interaction of Sp1 with its cooperative factor to reduce its transcription (87).

Moreover, macrophages, called Hofbauer cells in the placenta, play key roles in chronic inflammatory processes, and long-term exposure to hyperglycemia causes macrophages to exhibit a pro-inflammatory phenotype (88). It has been recently shown in mouse bone marrow-derived macrophages (BMMs) that enhanced UDP-GlcNAc generation caused by increased HBP activity is a trait of M2 macrophages (89). However, there has been no specific study of O-GlcNAcylation in Hofbauer cells to date. Further, the few studies using different macrophage cell models that have evaluated the effect of O-GlcNAcylation on macrophage function report conflicting results. One study reported that O-GlcNAcylation promotes antiviral innate immunity and inflammatory responses in BMMs (90). Another study based on THP-1 cells and mouse peritoneal macrophages revealed that O-GlcNAcylation suppresses innate immune activation and necroptosis of macrophages (91). Additionally, O-GlcNAcylation was also proposed to attenuate inflammatory processes in macrophages induced by LPS which was observed in RAW264.7 cells, BMMs and peritoneal mouse macrophages, as well as human monocyte-derived macrophages (92). Yang et al. (93) indicated that overnutrition stimulates O-GlcNAc signaling in macrophages of a mouse model of diet-induced obesity. Further, the activation of O-GlcNAc signaling has a suppressive effect on macrophage proinflammatory activation by restraining mTORC1/S6K1 signaling, which contributes to whole-body metabolic homeostasis. These conflicting observations in macrophages might be related to tissue residency or M1/M2 polarization, and prompt further research on Hofbauer cells is required.

O-GlcNAcylation may be a two-sided modulator of inflammation (94–96). Transcription factors and functional proteins may be modified in different cell types, stimulation conditions, and nutritional states, which may affect their activities and initiate pro-inflammatory or anti-inflammatory functions. The specific role of O-GlcNAcylation in HIP requires further exploration.

CONCLUSIONS

In summary, O-GlcNAcylation in the placental tissues of women with HIP plays an important role in placental development, nutrition sensing, and inflammatory response, and influences near- and long-term development of offspring. However, there are only a few relevant studies on the influence of O-GlcNAcylation on placental function. It is a process that has not been fully understood, particularly with regard to the regulation of transcription factors, intracellular signal transduction, and epigenetic modifications. As techniques to identify O-GlcNAcylation are increasingly being developed (97–101), further localization and quantitative analyses of O-GlcNAcylation in placental tissues exposed to hyperglycemia are required. This will facilitate the analysis of the effect of O-GlcNAcylation on the biological functions of placenta, as well as to understand the mechanistic details of the effect of maternal hyperglycemia on the development of offspring, particularly in relation to abnormalities in maternal-fetal nutrition transport and metabolism.

AUTHOR CONTRIBUTIONS

JN and HY wrote the manuscript. All authors contributed to the article and approved the submitted version.

FUNDING

This work was supported by the National Natural Science Foundation of China (81830044).

REFERENCES

1. Hod M, Kapur A, Sacks DA, Hadar E, Agarwal M, Di Renzo GC, et al. The International Federation of Gynecology and Obstetrics (FIGO) Initiative on Gestational Diabetes Mellitus: A Pragmatic Guide for Diagnosis, Management, and Care. *Int J Gynecol Obstet* (2015) 131:S173–211. doi: 10.1016/s0020-7292(15)30033-3
2. Wei Y, Xu Q, Yang H, Yang Y, Wang L, Chen H, et al. Preconception Diabetes Mellitus and Adverse Pregnancy Outcomes in Over 6.4 Million Women: A Population-Based Cohort Study in China. *PloS Med* (2019) 16: e1002926. doi: 10.1371/journal.pmed.1002926
3. Sun Y-Y, Juan J, Xu Q-Q, Su R-N, Hirst JE, Yang H-X. Increasing Insulin Resistance Predicts Adverse Pregnancy Outcomes in Women With Gestational Diabetes Mellitus. *J Diabetes* (2020) 12:438–46. doi: 10.1111/1753-0407.13013
4. Li S, Yang H. Relationship Between Advanced Glycation End Products and Gestational Diabetes Mellitus. *J Matern Fetal Neonatal Med* (2019) 32:2783–9. doi: 10.1080/14767058.2018.1449201
5. Li H, Dong A, Lv X. Advanced Glycation End Products and Adipocytokines and Oxidative Stress in Placental Tissues of Pregnant Women With Gestational Diabetes Mellitus. *Exp Ther Med* (2019) 18:685–91. doi: 10.3892/etm.2019.7623
6. Plows JF, Stanley JL, Baker PN, Reynolds CM, Vickers MH. The Pathophysiology of Gestational Diabetes Mellitus. *Int J Mol Sci* (2018) 19:3342. doi: 10.3390/ijms19113342
7. Yang X, Qian K. Protein O-GlcNAcylation: Emerging Mechanisms and Functions. *Nat Rev Mol Cell Biol* (2017) 18:452–65. doi: 10.1038/nrm.2017.22
8. Dela Justina V, Dos Passos Junior RR, Bressan AF, Tostes RC, Carneiro FS, Soares TS, et al. O-Linked N-acetyl-glucosamine Deposition in Placental Proteins Varies According to Maternal Glycemic Levels. *Life Sci* (2018) 205:18–25. doi: 10.1016/j.lfs.2018.05.013
9. Yao AY, Tang HY, Wang Y, Feng MF, Zhou RL. Inhibition of the Activating Signals in NK92 Cells by Recombinant GST-sHLA-G1a Chain. *Cell Res* (2004) 14:155–60. doi: 10.1038/sj.cr.7290215
10. Bale TL. Epigenetic and Transgenerational Reprogramming of Brain Development. *Nat Rev Neurosci* (2015) 16:332–44. doi: 10.1038/nrn3818
11. Wu D, Cai Y, Jin J. Potential Coordination Role Between O-GlcNAcylation and Epigenetics. *Protein Cell* (2017) 8:713–23. doi: 10.1007/s13238-017-0416-4
12. Gao Y, Wells L, Comer FI, Parker GJ, Hart GW. Dynamic O-glycosylation of Nuclear and Cytosolic Proteins: Cloning and Characterization of a Neutral, Cytosolic beta-N-acetylglucosaminidase From Human Brain. *J Biol Chem* (2001) 276:9838–45. doi: 10.1074/jbc.M010420200
13. Howerton CL, Morgan CP, Fischer DB, Bale TL. O-GlcNAc Transferase (OGT) as a Placental Biomarker of Maternal Stress and Reprogramming of CNS Gene Transcription in Development. *Proc Natl Acad Sci USA* (2013) 110:5169–74. doi: 10.1073/pnas.1300065110
14. Chen Y, Zhao X, Wu H. Metabolic Stress and Cardiovascular Disease in Diabetes Mellitus: The Role of Protein O-GlcNAc Modification. *Arterioscler Thromb Vasc Biol* (2019) 39:1911–24. doi: 10.1161/ATVBAHA.119.312192
15. Lima VV, Dela Justina V, Dos Passos RR Jr, Volpato GT, Souto PCS, San Martin S, et al. O-GlcNAc Modification During Pregnancy: Focus on Placental Environment. *Front Physiol* (2018) 9:1263. doi: 10.3389/fphys.2018.01263
16. Chi F, Sharpley MS, Nagaraj R, Roy SS, Banerjee U. Glycolysis-Independent Glucose Metabolism Distinguishes TE From ICM Fate During Mammalian Embryogenesis. *Dev Cell* (2020) 53:9–26.e4. doi: 10.1016/j.devcel.2020.02.015
17. Ruane PT, Tan CMJ, Adlam DJ, Kimber SJ, Brison DR, Aplin JD, et al. Protein O-GlcNAcylation Promotes Trophoblast Differentiation At Implantation. *Cells* (2020) 9:2246. doi: 10.3390/cells9102246
18. Hirosawa M, Hayakawa K, Yoneda C, Arai D, Shiota H, Suzuki T, et al. Novel O-GlcNAcylation on Ser(40) of Canonical H2A Isoforms Specific to Viviparity. *Sci Rep* (2016) 6:31785. doi: 10.1038/srep31785
19. Liu J, Shao X, Qin W, Zhang Y, Dang F, Yang Q, et al. Quantitative Chemoproteomics Reveals O-GlcNAcylation of Cystathionine γ-Lyase (CSE) Represses Trophoblast Syncytialization. *Cell Chem Biol* (2021) S2451-9456(21)00050-7. doi: 10.1016/j.chembiol.2021.01.024
20. Wen HY, Abbasi S, Kellems RE, Xia Y. mTOR: A Placental Growth Signaling Sensor. *Placenta* (2005) 26 Suppl A:S63–9. doi: 10.1016/j.placenta.2005.02.004
21. Zhang Q, Na Q, Song W. Moderate Mammalian Target of Rapamycin Inhibition Induces Autophagy in HTR8/SVneo Cells Via O-linked β-N-acetylglucosamine Signaling. *J Obstet Gynaecol Res* (2017) 43:1585–96. doi: 10.1111/jog.13410
22. He MY, Wang G, Han SS, Jin Y, Li H, Wu X, et al. Nrf2 Signalling and Autophagy Are Involved in Diabetes Mellitus-Induced Defects in the Development of Mouse Placenta. *Open Biol* (2016) 6:160064. doi: 10.1098/rsob.160064
23. Ji L, Chen Z, Xu Y, Xiong G, Liu R, Wu C, et al. Systematic Characterization of Autophagy in Gestational Diabetes Mellitus. *Endocrinology* (2017) 158:2522–32. doi: 10.1210/en.2016-1922
24. Nakashima A, Tsuda S, Kusabiraki T, Aoki A, Ushijima A, Shima T, et al. Current Understanding of Autophagy in Pregnancy. *Int J Mol Sci* (2019) 20:2342. doi: 10.3390/ijms20092342
25. Pantaleon M, Steane SE, McMahon K, Cuffe JSM, Moritz KM. Placental O-GlcNAc-Transferase Expression and Interactions With the Glucocorticoid Receptor Are Sex Specific and Regulated by Maternal Corticosterone Exposure in Mice. *Sci Rep* (2017) 7:2017. doi: 10.1038/s41598-017-01666-8
26. Howerton CL, Bale TL. Targeted Placental Deletion of OGT Recapitulates the Prenatal Stress Phenotype Including Hypothalamic Mitochondrial Dysfunction. *Proc Natl Acad Sci USA* (2014) 111:9639–44. doi: 10.1073/pnas.1401203111
27. Cowell W, Deyssenroth M, Chen J, Wright RJ. Maternal Stress in Relation to Sex-Specific Expression of Placental Genes Involved in Nutrient Transport, Oxygen Tension, Immune Response, and the Glucocorticoid Barrier. *Placenta* (2020) 96:19–26. doi: 10.1016/j.placenta.2020.05.004
28. Retnakaran R, Kramer CK, Ye C, Kew S, Hanley AJ, Connelly PW, et al. Fetal Sex and Maternal Risk of Gestational Diabetes Mellitus: The Impact of Having a Boy. *Diabetes Care* (2015) 38:844–51. doi: 10.2337/dc14-2551
29. Jaskolka D, Retnakaran R, Zinman B, Kramer CK. Sex of the Baby and Risk of Gestational Diabetes Mellitus in the Mother: A Systematic Review and Meta-Analysis. *Diabetologia* (2015) 58:2469–75. doi: 10.1007/s00125-015-3726-1
30. Yang YR, Jang H-J, Lee YH, Kim IS, Lee H, Ryu SH, et al. O-GlcNAc Cycling Enzymes Control Vascular Development of the Placenta by Modulating the Levels of HIF-1α. *Placenta* (2015) 36:1063–8. doi: 10.1016/j.placenta.2015.08.001
31. Makwana V, Ryan P, Patel B, Dukie SA, Rudrawar S. Essential Role of O-GlcNAcylation in Stabilization of Oncogenic Factors. *Biochim Biophys Acta Gen Subj* (2019) 1863:1302–17. doi: 10.1016/j.bbagen.2019.04.002
32. Dela Justina V, Priviero F, Dos Passos RR Jr, Webb RC, Lima VV, Giachini FR. O-GlcNAc Impairs Endothelial Function in Uterine Arteries From Virgin But Not Pregnant Rats: The Role of GSK3β. *Eur J Pharmacol* (2020) 880:173133. doi: 10.1016/j.ejphar.2020.173133
33. Sawy NAE, Alkushi AG. Histomorphological Study of Placenta in Gestational Diabetes Mellitus. *Int J Morphol* (2018) 36:687–92. doi: 10.4067/S0717-95022018000200687

34. Nagy T, Fisi V, Frank D, Kátai E, Nagy Z, Miseta A. Hyperglycemia-Induced Aberrant Cell Proliferation; A Metabolic Challenge Mediated by Protein O-GlcNAc Modification. *Cells* (2019) 8:999. doi: 10.3390/cells8090999
35. Brown HM, Green ES, Tan TCY, Gonzalez MB, Rumbold AR, Hull ML, et al. Periconception Onset Diabetes Is Associated With Embryopathy and Fetal Growth Retardation, Reproductive Tract Hyperglycosylation and Impaired Immune Adaptation to Pregnancy. *Sci Rep* (2018) 8:2114. doi: 10.1038/s41598-018-19263-8
36. Kim G, Cao L, Reece EA, Zhao Z. Impact of Protein O-GlcNAcylation on Neural Tube Malformation in Diabetic Embryopathy. *Sci Rep* (2017) 7:11107. doi: 10.1038/s41598-017-11655-6
37. Na H-J, Akan I, Abramowitz LK, Hanover JA. Nutrient-Driven O-GlcNAcylation Controls DNA Damage Repair Signaling and Stem/Progenitor Cell Homeostasis. *Cell Rep* (2020) 31:107632. doi: 10.1016/j.celrep.2020.107632
38. Muha V, Authier F, Szoke-Kovacs Z, Johnson S, Gallagher J, McNeilly A, et al. Loss of O-GlcNAcase Catalytic Activity Leads to Defects in Mouse Embryogenesis. *J Biol Chem* (2021) 296:100439. doi: 10.1016/j.jbc.2021.100439
39. Pantaleon M, Tan HY, Kafer GR, Kaye PL. Toxic Effects of Hyperglycemia are Mediated by the Hexosamine Signaling Pathway and O-Linked Glycosylation in Early Mouse Embryos. *Biol Reprod* (2010) 82:751–8. doi: 10.1095/biolreprod.109.076661
40. Parween S, Varghese DS, Ardah MT, Prabakaran AD, Mensah-Brown E, Emerald BS, et al. Higher O-GlcNAc Levels Are Associated With Defects in Progenitor Proliferation and Premature Neuronal Differentiation During Human Embryonic Cortical Neurogenesis. *Front Cell Neurosci* (2017) 11:415. doi: 10.3389/fncel.2017.00415
41. Gabory A, Roseboom TJ, Moore T, Moore LG, Junien C. Placental Contribution to the Origins of Sexual Dimorphism in Health and Diseases: Sex Chromosomes and Epigenetics. *Biol Sex Differ* (2013) 4:5. doi: 10.1186/2042-6410-4-5
42. Hart B, Morgan E, Alejandro EU. Nutrient Sensor Signaling Pathways and Cellular Stress in Fetal Growth Restriction. *J Mol Endocrinol* (2019) 62:R155–65. doi: 10.1530/JME-18-0059
43. Wullschleger S, Loewith R, Hall MN. TOR Signaling in Growth and Metabolism. *Cell* (2006) 124:471–84. doi: 10.1016/j.cell.2006.01.016
44. Zhang QX, Na Q, Song W. Altered Expression of mTOR and Autophagy in Term Normal Human Placentas. *Rom J Morphol Embryol* (2017) 58:517–26.
45. Shao X, Cao G, Chen D, Liu J, Yu B, Liu M, et al. Placental Trophoblast Syncytialization Potentiates Macropinocytosis Via mTOR Signaling to Adapt to Reduced Amino Acid Supply. *Proc Natl Acad Sci USA* (2021) 118:e2017092118. doi: 10.1073/pnas.2017092118
46. Laplante M, Sabatini DM. mTOR Signaling in Growth Control and Disease. *Cell* (2012) 149:274–93. doi: 10.1016/j.cell.2012.03.017
47. Manning BD, Toker A. AKT/PKB Signaling: Navigating the Network. *Cell* (2017) 169:381–405. doi: 10.1016/j.cell.2017.04.001
48. Ma XM, Blenis J. Molecular Mechanisms of mTOR-mediated Translational Control. *Nat Rev Mol Cell Biol* (2009) 10:307–18. doi: 10.1038/nrm2672
49. Golick L, Han Y, Kim Y, Park SW. BRD7 Regulates the Insulin-Signaling Pathway by Increasing Phosphorylation of GSK3β. *Cell Mol Life Sci* (2018) 75:1857–69. doi: 10.1007/s00018-017-2711-x
50. Inoki K, Ouyang H, Zhu T, Lindvall C, Wang Y, Zhang X, et al. TSC2 Integrates Wnt and Energy Signals Via a Coordinated Phosphorylation by AMPK and GSK3 to Regulate Cell Growth. *Cell* (2006) 126:955–68. doi: 10.1016/j.cell.2006.06.055
51. Liu X, Chhipa RR, Pooya S, Wortman M, Yachyshin S, Chow LML, et al. Discrete Mechanisms of mTOR and Cell Cycle Regulation by AMPK Agonists Independent of AMPK. *Proc Natl Acad Sci USA* (2014) 111:E435–44. doi: 10.1073/pnas.1311121111
52. Very N, Steenackers A, Dubuquoy C, Vermuse J, Dubuquoy L, Lefebvre T, et al. Cross Regulation Between mTOR Signaling and O-GlcNAcylation. *J Bioenerg Biomembr* (2018) 50:213–22. doi: 10.1007/s10863-018-9747-y
53. Very N, Vercoutter-Edouart AS, Lefebvre T, Hardiville S, El Yazidi-Belkoura I. Cross-Dysregulation of O-GlcNAcylation and PI3K/AKT/mTOR Axis in Human Chronic Diseases. *Front Endocrinol (Lausanne)* (2018) 9:602. doi: 10.3389/fendo.2018.00602
54. Shi J, Wu S, Dai C-I, Li Y, Grundke-Iqbal I, Iqbal K, et al. Diverse Regulation of AKT and GSK-3β by O-GlcNAcylation in Various Types of Cells. *FEBS Lett* (2012) 586:2443–50. doi: 10.1016/j.febslet.2012.05.063
55. Tsai K, Tullis B, Jensen T, Graff T, Reynolds P, Arroyo J. Differential Expression of mTOR Related Molecules in the Placenta From Gestational Diabetes Mellitus (GDM), Intrauterine Growth Restriction (IUGR) and Preeclampsia Patients. *Reprod Biol* (2021) 21:100503. doi: 10.1016/j.repbio.2021.100503
56. Hulme CH, Stevens A, Dunn W, Heazell AEP, Hollywood K, Begley P, et al. Identification of the Functional Pathways Altered by Placental Cell Exposure to High Glucose: Lessons From the Transcript and Metabolite Interactome. *Sci Rep* (2018) 8:5270. doi: 10.1038/s41598-018-22535-y
57. Nguyen-Ngo C, Jayabalan N, Salomon C, Lappas M. Molecular Pathways Disrupted by Gestational Diabetes Mellitus. *J Mol Endocrinol* (2019) 63:R51–72. doi: 10.1530/JME-18-0274
58. Gélinas R, Mailleux F, Dontaine J, Bultot L, Demeulder B, Ginion A, et al. AMPK Activation Counteracts Cardiac Hypertrophy by Reducing O-GlcNAcylation. *Nat Commun* (2018) 9:374. doi: 10.1038/s41467-017-02795-4
59. Gélinas R, Dontaine J, Horman S, Beauloye C, Bultot L, Bertrand L. AMP-Activated Protein Kinase and O-GlcNAcylation, Two Partners Tightly Connected to Regulate Key Cellular Processes. *Front Endocrinol* (2018) 9:519. doi: 10.3389/fendo.2018.00519
60. Perez-Cervera Y, Dehennaut V, Aquino Gil M, Guedri K, Solórzano Mata CJ, Olivier-Van Stichelen S, et al. Insulin Signaling Controls the Expression of O-GlcNAc Transferase and its Interaction With Lipid Microdomains. *FASEB J* (2013) 27:3478–86. doi: 10.1096/fj.12-217984
61. Kelly AC, Kramer A, Rosario FJ, Powell TL, Jansson T. Inhibition of Mechanistic Target of Rapamycin Signaling Decreases Levels of O-GlcNAc Transferase and Increases Serotonin Release in the Human Placenta. *Clin Sci (London Engl 1979)* (2020) 134:3123–36. doi: 10.1042/CS20201050
62. Kaasik K, Kivimäe S, Allen JJ, Chalkley RJ, Huang Y, Baer K, et al. Glucose Sensor O-GlcNAcylation Coordinates With Phosphorylation to Regulate Circadian Clock. *Cell Metab* (2013) 17:291–302. doi: 10.1016/j.cmet.2012.12.017
63. Lazarus MB, Nam Y, Jiang J, Sliz P, Walker S. Structure of Human O-GlcNAc Transferase and its Complex With a Peptide Substrate. *Nature* (2011) 469:564–7. doi: 10.1038/nature09638
64. Whelan SA, Dias WB, Thiruneelakantapillai L, Lane MD, Hart GW. Regulation of Insulin Receptor Substrate 1 (IRS-1)/AKT Kinase-Mediated Insulin Signaling by O-Linked beta-N-acetylglucosamine in 3T3-L1 Adipocytes. *J Biol Chem* (2010) 285:5204–11. doi: 10.1074/jbc.M109.077818
65. Park SY, Ryu J, Lee W. O-GlcNAc Modification on IRS-1 and Akt2 by PUGNAc Inhibits Their Phosphorylation and Induces Insulin Resistance in Rat Primary Adipocytes. *Exp Mol Med* (2005) 37:220–9. doi: 10.1038/emm.2005.30
66. Soesanto YA, Luo B, Jones D, Taylor R, Gabrielsen JS, Parker G, et al. Regulation of Akt Signaling by O-GlcNAc in Euglycemia. American Journal of Physiology. *Endocrinol Metab* (2008) 295:E974–80. doi: 10.1152/ajpendo.90366.2008
67. Parker GJ, Lund KC, Taylor RP, McClain DA. Insulin Resistance of Glycogen Synthase Mediated by O-Linked N-Acetylglucosamine. *J Biol Chem* (2003) 278:10022–7. doi: 10.1074/jbc.M207787200
68. Kang E-S, Han D, Park J, Kwak TK, Oh M-A, Lee S-A, et al. O-GlcNAc Modulation At Akt1 Ser473 Correlates With Apoptosis of Murine Pancreatic Beta Cells. *Exp Cell Res* (2008) 314:2238–48. doi: 10.1016/j.yexcr.2008.04.014
69. Ruan HB, Singh JP, Li MD, Wu J, Yang X. Cracking the O-GlcNAc Code in Metabolism. *Trends Endocrinol Metab* (2013) 24:301–9. doi: 10.1016/j.tem.2013.02.002
70. Stanirowski PJ, Szukiewicz D, Pazura-Turowska M, Sawicki W, Cendrowski K. Placental Expression of Glucose Transporter Proteins in Pregnancies Complicated by Gestational and Pregestational Diabetes Mellitus. *Can J Diabetes* (2018) 42:209–17. doi: 10.1016/j.jcjd.2017.04.008
71. James-Allan LB, Arbet J, Teal SB, Powell TL, Jansson T. Insulin Stimulates GLUT4 Trafficking to the Syncytiotrophoblast Basal Plasma Membrane in

the Human Placenta. *J Clin Endocrinol Metab* (2019) 104:4225–38. doi: 10.1210/jc.2018-02778
72. Bacigalupa ZA, Bhadiadra CH, Reginato MJ. O-GlcNAcylation: Key Regulator of Glycolytic Pathways. *J Bioenerg Biomembr* (2018) 50:189–98. doi: 10.1007/s10863-018-9742-3
73. Buller CL, Loberg RD, Fan MH, Zhu Q, Park JL, Vesely E, et al. A GSK-3/TSC2/mTOR Pathway Regulates Glucose Uptake and GLUT1 Glucose Transporter Expression. *Am J Physiol Cell Physiol* (2008) 295:C836–43. doi: 10.1152/ajpcell.00554.2007
74. Cork GK, Thompson J, Slawson C. Real Talk: The Inter-Play Between the mTOR, AMPK, and Hexosamine Biosynthetic Pathways in Cell Signaling. *Front Endocrinol (Lausanne)* (2018) 9:522. doi: 10.3389/fendo.2018.00522
75. Grace MR, Dotters-Katz SK, Zhou C, Manuck T, Boggess K, Bae-Jump V. Effect of a High-Fat Diet and Metformin on Placental mTOR Signaling in Mice. *AJP Rep* (2019) 9:e138–43. doi: 10.1055/s-0039-1683362
76. Feng Y, Yang H. Metformin - a Potentially Effective Drug for Gestational Diabetes Mellitus: A Systematic Review and Meta-Analysis. *J Matern Fetal Neonatal Med* (2017) 30:1874–81. doi: 10.1080/14767058.2016.1228061
77. Sivalingam VN, Myers J, Nicholas S, Balen AH, Crosbie EJ. Metformin in Reproductive Health, Pregnancy and Gynaecological Cancer: Established and Emerging Indications. *Hum Reprod Update* (2014) 20:853–68. doi: 10.1093/humupd/dmu037
78. Lindsay RS, Loeken MR. Metformin Use in Pregnancy: Promises and Uncertainties. *Diabetologia* (2017) 60:1612–9. doi: 10.1007/s00125-017-4351-y
79. Jiang S, Teague AM, Tryggestad JB, Jensen ME, Chernausek SD. Role of Metformin in Epigenetic Regulation of Placental Mitochondrial Biogenesis in Maternal Diabetes. *Sci Rep* (2020) 10:8314. doi: 10.1038/s41598-020-65415-0
80. Kim MY, Kim YS, Kim M, Choi MY, Roh GS, Lee DH, et al. Metformin Inhibits Cervical Cancer Cell Proliferation Via Decreased AMPK O-GlcNAcylation. *Anim Cells Syst (Seoul)* (2019) 23:302–9. doi: 10.1080/19768354.2019.1614092
81. Kawaharada R, Masuda H, Chen Z, Blough E, Kohama T, Nakamura A. Intrauterine Hyperglycemia-Induced Inflammatory Signalling Via the Receptor for Advanced Glycation End Products in the Cardiac Muscle of the Infants of Diabetic Mother Rats. *Eur J Nutr* (2018) 57:2701–12. doi: 10.1007/s00394-017-1536-6
82. Yang WH, Park SY, Nam HW, Kim DH, Kang JG, Kang ES, et al. NFkappaB Activation is Associated With its O-GlcNAcylation State Under Hyperglycemic Conditions. *Proc Natl Acad Sci USA* (2008) 105:17345–50. doi: 10.1073/pnas.0806198105
83. Dela Justina V, Gonçalves JS, de Freitas RA, Fonseca AD, Volpato GT, Tostes RC, et al. Increased O-Linked N-Acetylglucosamine Modification of NF-KB and Augmented Cytokine Production in the Placentas From Hyperglycemic Rats. *Inflammation* (2017) 40:1773–81. doi: 10.1007/s10753-017-0620-7
84. Pathak S, Borodkin VS, Albarbarawi O, Campbell DG, Ibrahim A, van Aalten DM. O-GlcNAcylation of TAB1 Modulates TAK1-mediated Cytokine Release. *EMBO J* (2012) 31:1394–404. doi: 10.1038/emboj.2012.8
85. Xing D, Gong K, Feng W, Nozell SE, Chen Y-F, Chatham JC, et al. O-GlcNAc Modification of NFκB p65 Inhibits TNF-α-Induced Inflammatory Mediator Expression in Rat Aortic Smooth Muscle Cells. *PloS One* (2011) 6: e24021. doi: 10.1371/journal.pone.0024021
86. Aguilar H, Fricovsky E, Ihm S, Schimke M, Maya-Ramos L, Aroonsakool N, et al. Role for High-Glucose-Induced Protein O-GlcNAcylation in Stimulating Cardiac Fibroblast Collagen Synthesis. *Am J Physiol Cell Physiol* (2014) 306:C794–804. doi: 10.1152/ajpcell.00251.2013
87. Lim K, Chang H-I. O-GlcNAc Inhibits Interaction Between Sp1 and Elf-1 Transcription Factors. *Biochem Biophys Res Commun* (2009) 380:569–74. doi: 10.1016/j.bbrc.2009.01.121
88. Sisino G, Bouckenooghe T, Aurientis S, Fontaine P, Storme L, Vambergue A. Diabetes During Pregnancy Influences Hofbauer Cells, a Subtype of Placental Macrophages, to Acquire a Pro-Inflammatory Phenotype. *Biochim Biophys Acta* (2013) 1832:1959–68. doi: 10.1016/j.bbadis.2013.07.009
89. Jha AK, Huang SC-C, Sergushichev A, Lampropoulou V, Ivanova Y, Loginicheva E, et al. Network Integration of Parallel Metabolic and Transcriptional Data Reveals Metabolic Modules That Regulate Macrophage Polarization. *Immunity* (2015) 42:419–30. doi: 10.1016/j.immuni.2015.02.005
90. Li T, Li X, Attri KS, Liu C, Li L, Herring LE, et al. O-GlcNAc Transferase Links Glucose Metabolism to MAVS-Mediated Antiviral Innate Immunity. *Cell Host Microbe* (2018) 24:791–803.e6. doi: 10.1016/j.chom.2018.11.001
91. Li X, Gong W, Wang H, Li T, Attri KS, Lewis RE, et al. O-GlcNAc Transferase Suppresses Inflammation and Necroptosis by Targeting Receptor-Interacting Serine/Threonine-Protein Kinase 3. *Immunity* (2019) 50:1115. doi: 10.1016/j.immuni.2019.01.007
92. Al-Mukh H, Baudoin L, Bouaboud A, Sanchez-Salgado J-L, Maraqa N, Khair M, et al. Lipopolysaccharide Induces GFAT2 Expression to Promote -Linked β–Acetylglucosaminylation and Attenuate Inflammation in Macrophages. *J Immunol (Baltimore Md 1950)* (2020) 205:2499–510. doi: 10.4049/jimmunol.2000345
93. Yang Y, Li X, Luan HH, Zhang B, Zhang K, Nam JH, et al. OGT Suppresses S6K1-mediated Macrophage Inflammation and Metabolic Disturbance. *Proc Natl Acad Sci U S A* (2020) 117:16616–25. doi: 10.1073/pnas.1916121117
94. Li Y, Xie M, Men L, Du J. O-GlcNAcylation in Immunity and Inflammation: An Intricate System (Review). *Int J Mol Med* (2019) 44:363–74. doi: 10.3892/ijmm.2019.4238
95. Baudoin L, Issad T. O-GlcNAcylation and Inflammation: A Vast Territory to Explore. *Front Endocrinol* (2014) 5:235. doi: 10.3389/fendo.2014.00235
96. Chang Y-H, Weng C-L, Lin K-I. O-GlcNAcylation and its Role in the Immune System. *J Biomed Sci* (2020) 27:57. doi: 10.1186/s12929-020-00648-9
97. Qin K, Zhu Y, Qin W, Gao J, Shao X, Wang YL, et al. Quantitative Profiling of Protein O-GlcNAcylation Sites by an Isotope-Tagged Cleavable Linker. *ACS Chem Biol* (2018) 13:1983–9. doi: 10.1021/acschembio.8b00414
98. Jia C, Zuo Y, Zou Q. O-GlcNAcPRED-II: An Integrated Classification Algorithm for Identifying O-GlcNAcylation Sites Based on Fuzzy Undersampling and a K-means PCA Oversampling Technique. *Bioinformatics (Oxford England)* (2018) 34:2029–36. doi: 10.1093/bioinformatics/bty039
99. Worth M, Li H, Jiang J. Deciphering the Functions of Protein O-GlcNAcylation With Chemistry. *ACS Chem Biol* (2017) 12:326–35. doi: 10.1021/acschembio.6b01065
100. Deracinois B, Camoin L, Lambert M, Boyer J-B, Dupont E, Bastide B, et al. O-GlcNAcylation Site Mapping by (Azide-Alkyne) Click Chemistry and Mass Spectrometry Following Intensive Fractionation of Skeletal Muscle Cells Proteins. *J Proteomics* (2018) 186:83–97. doi: 10.1016/j.jprot.2018.07.005
101. Leney AC, Rafie K, van Aalten DMF, Heck AJR. Direct Monitoring of Protein O-GlcNAcylation by High-Resolution Native Mass Spectrometry. *ACS Chem Biol* (2017) 12:2078–84. doi: 10.1021/acschembio.7b00371

Conflict of Interest: The authors declare that the research was conducted in the absence of any commercial or financial relationships that could be construed as a potential conflict of interest.

frontiers in Endocrinology

ORIGINAL RESEARCH
published: 10 June 2021
doi: 10.3389/fendo.2021.608183

Proteomics Analysis of the Spinal Dorsal Horn in Diabetic Painful Neuropathy Rats With Electroacupuncture Treatment

Xiangmei Yu[1], *Xiaomei Chen*[2], *Weiting Liu*[3], *Menghong Jiang*[3], *Zhifu Wang*[1]* *and Jing Tao*[2]*

[1] College of Integrated Traditional Chinese and Western Medicine, Fujian University of Traditional Chinese Medicine, Fuzhou, China, [2] College of Rehabilitation Medicine, Fujian University of Traditional Chinese Medicine, Fuzhou, China, [3] College of Acupuncture and Moxibustion, Fujian University of Traditional Chinese Medicine, Fuzhou, China

OPEN ACCESS

Edited by:
Anna Halama,
Weill Cornell Medicine-Qatar, Qatar

Reviewed by:
Philipp Antczak,
University Hospital of Cologne, Germany
Stephen Atkin,
Royal College of Surgeons in Ireland, Bahrain

***Correspondence:**
Zhifu Wang
2007015@fjtcm.edu.cn
Jing Tao
taojing01@fjtcm.edu.cn

Specialty section:
This article was submitted to Systems Endocrinology, a section of the journal Frontiers in Endocrinology

Received: 10 November 2020
Accepted: 12 April 2021
Published: 10 June 2021

Citation:
Yu X, Chen X, Liu W, Jiang M, Wang Z and Tao J (2021) Proteomics Analysis of the Spinal Dorsal Horn in Diabetic Painful Neuropathy Rats With Electroacupuncture Treatment. Front. Endocrinol. 12:608183. doi: 10.3389/fendo.2021.608183

Background: Clinical evidence demonstrates that electro-acupuncture (EA) of the Zu sanli (ST36) and Shen shu (BL23) acupoints is effective in relieving diabetic painful neuropathy (DPN); however, the underlying molecular mechanism requires further investigation, including the protein molecules associated with EA's effects on DPN.

Methods: Sprague-Dawley adult male rats (n =36) were randomly assigned into control, DPN, and EA groups (n=12 each). After four weeks of EA treatment, response to mechanical pain and fasting blood glucose were analyzed. A tandem mass tag (TMT) labeling approach coupled with liquid chromatography with tandem mass spectrometry was used to identify potential biomarkers in the spinal dorsal horn. Further, proteomics analysis was used to quantify differentially expressed proteins (DEPs), and gene ontology, KEGG pathways, cluster, and string protein network interaction analyses conducted to explore the main protein targets of EA.

Results: Compared with the DPN model group, the mechanical pain threshold was significantly increased, while the fasting blood glucose levels were clearly decreased in EA group rats. Proteomics analysis was used to quantify 5393 proteins, and DEPs were chosen for further analyses, based on a threshold of 1.2-fold difference in expression level ($P < 0.05$) compared with control groups. Relative to the control group, 169 down-regulated and 474 up-regulated proteins were identified in the DPN group, while 107 and 328 proteins were up- and down-regulated in the EA treatment group compared with the DPN group. Bioinformatics analysis suggested that levels of proteins involved in oxidative stress injury regulation were dramatically altered during the EA effects on DPN.

Conclusions: Our results provide the valuable protein biomarkers, which facilitates unique mechanistic insights into the DPN pathogenesis and EA analgesic, antioxidant stress and hypoglycemic effect.

Keywords: proteomics, electroacupuncture, oxidative phosphorylation, neuropathic pain, diabetes

INTRODUCTION

There are various types of chronic pain that can disturb the physical and mental health of individuals. Diabetic painful neuropathy (DPN) is a painful complication of diabetes, caused by constant high glucose levels. Approximately 20% of all diabetic patients present with neuropathic pain, manifesting as spontaneous pain, hyperalgesia, and allodynia (1). The streptozotocin (STZ)-diabetic rat model can be used to mimic the symptoms and pathological changes that occur during DPN. To date, the majority of studies have focused on peripheral sensory nerve function; however, the spinal cord is also important in the development of DPN (2). A number of morphological studies have demonstrated spinal cord damage and atrophy in patients with diabetes, and peripheral nerve stimulation can reduce blood-oxygen level-dependent activity in the dorsal horn of diabetic rats (3, 4).

Electroacupuncture (EA), as a beneficial acupuncture therapy, is effective in alleviating pain and improving quality of life in patients with diabetic peripheral neuropathy (5–7). Zusanli (ST36) and Shenshu (BL23) are common and effective acupoints used for treatment of diabetic peripheral neuropathy (8–10).

Proteomics analysis provides a valuable strategy for exploring the pathogenesis of diabetes mellitus, as well as therapeutic targets in this condition. Some proteomic studies have been performed in animal models of DPN or diabetic neuropathy, to search for differentially expressed proteins (DEPs) induced by STZ. Mitochondrial oxidative phosphorylation, metabolic dysregulation of mitochondrial complexes, and antioxidases are involved in DPN progression and represent potentially important therapeutic targets. However, previous studies have focused only on the proteomes of the sciatic nerve, lumbar 4/5 dorsal root ganglia, and trigeminal ganglia, while the exact spinal mechanism underlying DPN is far from clear and additional potential spinal biomarkers are needed (11–14).

MATERIALS AND METHODS

Animals and Ethics Statement

Male Sprague-Dawley rats weighing 160 ± 20g were obtained from the Experimental Animal Center of Fujian University of Chinese Medicine. Rats were housed under standard living conditions at 22°C and a 12 h light/dark cycle with sufficient food and water and acclimatized to the pain-testing environment before the experiments. All animal procedures were in strict accordance with relevant international laboratory animal use guidelines. After adaptive feeding, rats were randomly allocated into three groups as follows: Control group (n=12), DPN group (n=12), and EA group (n = 12).

According to the previous literature reports, diabetes was induced by a single intraperitoneal injection of STZ (65 mg/kg, Sigma Chemicals, USA) dissolved in citrate buffer (10 mmol/L, Na citrate, pH=4.3) (15). The control group received an equivalent volume of citrate buffer only. Two weeks later, tail venous fasting blood glucose (FBG) were measured using a glucometer (OEM, USA). Only rats with FBG >16.7 mmol/L and mechanical paw withdrawal threshold (PWT) <5 g were included in further experiments.

All experimental procedures and protocols were approved by the Animal Research and Ethics Committee of Fujian University of Traditional Chinese Medicine. At the endpoint of the experiment, all rats were euthanized, according to the Care Guidelines.

Electroacupuncture (EA) Procedure

In the EA group, the rats were loosely fixed on a wooden stand, where their head and limbs could move freely. After the rats were stabilized, the acupoints "Zu sanli" (ST36) and "Shen shu" (BL23) were selected for acupuncture and electrical stimulation (**Figure 1A**). EA intervention began at two weeks after STZ injection. ST36 is located at the posterolateral knee about 5mm below the fibula head (16), while BL23 is located in the depressions lateral to the lower border of the spinous processes of the second lumbar vertebrae, approximately 8mm from the midline of the adult rat (17). Needles inserted at ST36 and BL23 were connected to a G6805-1A multifunctional EA apparatus (Shanghai Medical Electronic Apparatus Company, Shanghai, China), with a stimulation intensity of 1mA, frequency 10 HZ. According to previous literature reports, EA stimulation was maintained for 30 min once every other day for a consecutive four weeks (15, 18).

Measurement of Paw Withdrawal Threshold

The mechanical PWT was examined before and after injection of STZ or citrate buffer (0, 2, 6 weeks after injection). The test environment was a 10 cm × 20 cm × 20 cm plastic cage with a plexiglass floor. After the rats were placed in the cage and allowed to stand for 10 minutes, the center of the feet of the rats were stimulated with different tense by von Frey Hairs (0.4, 0.6, 1.4, 2, 4, 6, 8, 10, and 15g) according to the up-down method described by Dixon (19). Each von Frey hair was held for about 1-2 s, with 10-min intervals between each stimulation. Testing was initiated with the 2.0 g hair.

The positive response was defined as a withdrawal of hind paw upon the stimulus. Whenever a positive response appeared, the next lower gram was applied, and whenever a negative response occurred, the next higher gram was applied. The testing consisted of five more stimuli after the first change in response occurred, and the pattern of response was converted to a 50% von Frey threshold using the method described by Dixon and based on our previous literature (20, 21). All data are presented as mean ± SE.

Sample Collection

To investigate DEPs in three groups, all rats were sacrificed under low dose isoflurane (0.5-1%) anesthesia, six weeks after STZ injection. The L_{4-5} spinal cords were rapidly dissected and immediately placed in -80°C refrigerator for the further proteomics detection.

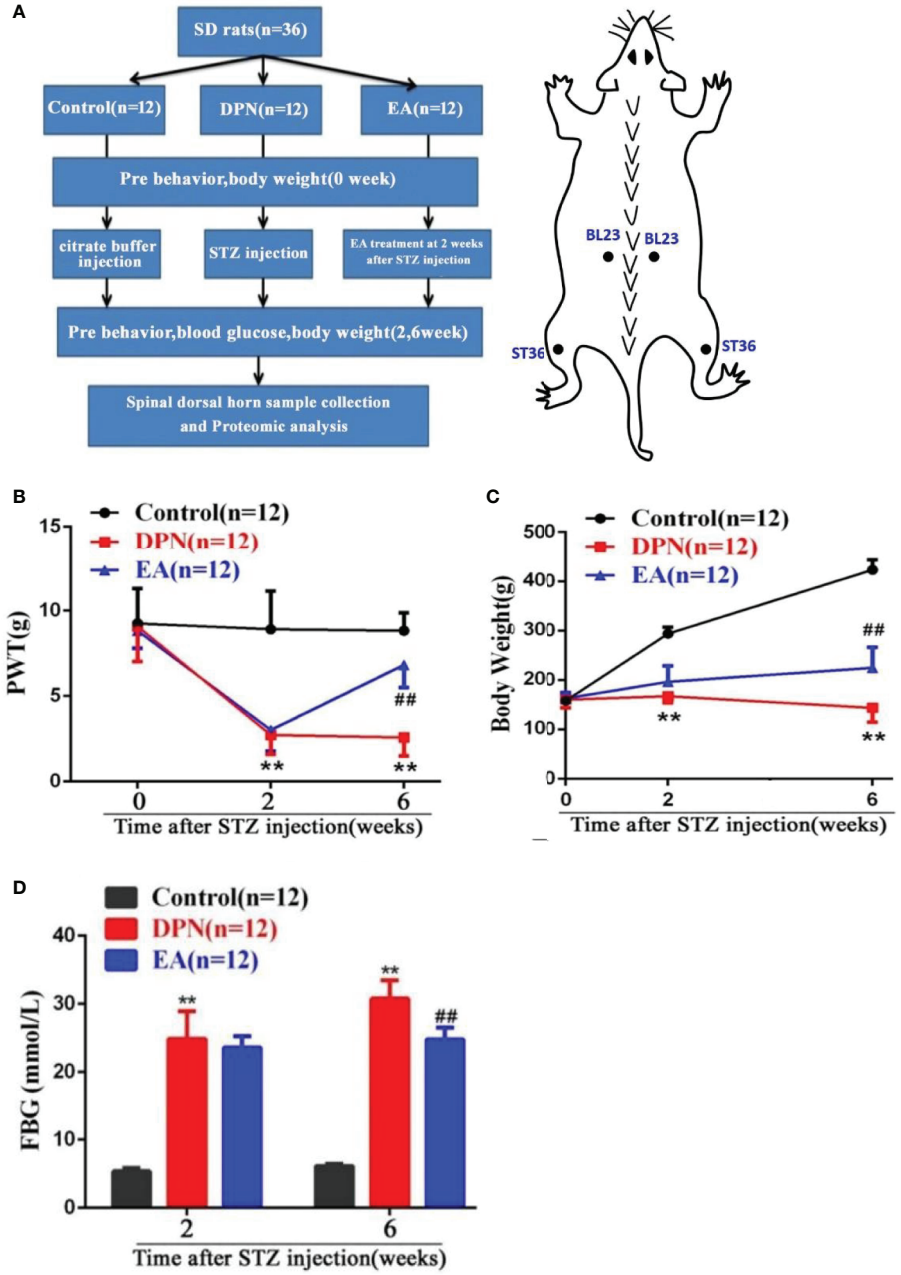

FIGURE 1 | Flow chart of the experiment and the changes of body weight, paw withdrawal threshold (PWT) and fast blood glucose (FBG) in DPN rats. **(A)** Flow chart of the experiment. **(B)** Body weight variation in Control, DPN, and EA groups rats. Two-way repeated ANOVA, F2, 33 = 237.4, P < 0.001; *post hoc* Turkey test: DPN compared with Control (**$P < 0.01$), EA compared with DPN ($^{\#\#}P < 0.01$). **(C)** Significant changes of PWT in different groups. Two-way repeated ANOVA, F2, 33 = 59.608, P < 0.001; *post hoc* Turkey test: DPN compared with Control (**$P < 0.01$), EA compared with DPN ($^{\#\#}P < 0.01$). **(D)** Significant changes of FBG in different groups. Two-way repeated ANOVA, F1, 33 = 299.3, P < 0.001; *post hoc* Turkey test: DPN compared with Control (**$P < 0.01$), EA compared with DPN ($^{\#\#}P < 0.01$).

Proteomics Experiment and Proteomics Data Analysis

Protein Extraction and Trypsin Digestion

The $L_{4\text{-}5}$ spinal cord tissue samples were removed from -80°C freezer, and an appropriate amount of sample was added to a pre-chilled mortar with liquid nitrogen and ground to powder. Proteins were then extracted from samples in lysis buffer (8 M urea, 1% protease inhibitor) using a high-intensity ultrasonic processor. Remaining debris was removed by centrifugation at 12,000g for 10min at 4°C. The protein concentration of the supernatant was detected with BAC kits.

For trypsin digestion, protein solution was reduced with dithiothreitol (final concentration, 5mM) for 30 min at 56°C, then incubated with iodoacetamide (final concentration, 11mM) for 15min at 37°C in darkness. Then, the protein samples were diluted with mM triethylamonium bicarbonate (TEAB), until the urea concentration was < 2 M. Finally, trypsin was added at a mass ratio (trypsin: protein) of 1:50 for the first digestion at 37°C overnight, then of 1:100 for the second digestion (4h, 37°C).

TMT Labeling

After trypsin digestion, peptides were desalted and vacuum-dried with the strata X C18 SPE column. Peptides were reconstituted in 0.5M TEAB and marked according to the TMT kit protocols.

LC-MS/MS Analysis

Separated peptides were subjected to sodium/iodide symporter sources. Tandem mass spectrometry (MS/MS) was performed using a Q ExactiveTM Plus (Thermo) instrument, coupled online to an ultra-performance liquid chromatography system.

Electrospray voltage was 2.0 kV, and intact peptides were detected in the Orbitrap at 70,000 mass resolution. The primary MS scan range was 350–1600 m/z. Collected data were processed using a data-dependent scanning program (DDA). Automatic gain control was set at 5E4, signal threshold as 5000 ions/s, maximum time 200 s, and dynamic exclusion time of the tandem mass scan 15 s, to avoid repeated scanning of precursor ions.

Database Search

MS/MS data were analyzed using the max quant search engine (v.1.5.2.8), with parameters as follows: Rat_Uniprot was first screened, then a reverse library added to calculate the false positive ratio (FPR); Trypsin/P was specified as the cleavage enzyme, allowing up to two missing cleavages; minimum peptide length was seven amino acid residues; maximum number of peptide modifications was five; mass tolerance for the primary precursor ions search was 20 ppm and 5 ppm for the main search; mass tolerance for fragment ions was 0.02 Da; the quantitative method was set to TMT-10plex; and the FPR for peptide-spectrum match identification was 1%.

Bioinformatics Annotation

Gene Ontology (GO) annotations were derived from the UniProt-GOA database (http://www.ebi.ac.uk/GOA/). InterProScansoft was used to elucidate the GO categories: molecular function, cellular component, and biological process. KEGG online service tools were used to annotate protein descriptions, which were matched into corresponding pathways using KEGG mapper. Wolfpsort (https://wolfpsort.hgc.jp/) was used to investigate subcellular localization. KEGG database pathway enrichment analysis was conducted using a two-tailed Fisher's exact test. Pathways were classified according to the KEGG website.

Further cluster analysis of function enrichment was conducted to explore potential connections and differences in specific functions. First, all categories were collected after enrichment, according to their P values, then filtered for those categories with P value < 0.05. This filtered P value matrix was transformed using the function x = –log10 (P value). Finally, these x values were z-transformed for each functional category. Cluster membership was visualized using a heat map.

Protein-Protein Interaction Network

Numbers or sequences of DEPs were compared using the STRING (v.10.5) protein network interaction database. An interaction relationship was extracted according to a confidence score > 0.7 (high confidence).

Statistical Analysis

All data are presented as the mean ± standard deviation (SD). The three groups were analyzed by the Analysis Of Variance (ANOVA) and *post hoc* Tukey test in the SPSS 21.0 software (SPSS, Armonk, NY, USA). Graphs were generated by using GraphPad Prism 7.0 software.

RESULTS

Electroacupuncture Significantly Reduced Mechanical Hypersensitivity and Fasting Blood Glucose Levels During the Development of DPN.

As shown in the flow chart of the experiment and acupoint diagram (**Figure 1A**), DPN model of rats and EA intervention were established and fasting blood glucose and behavioral tests conducted before and after STZ injection and EA intervention. Compared with the control group, body weight and mechanical pain threshold were significantly reduced while fasting blood glucose was dramatically increased at 2 weeks after STZ injection(***P*<0.01).

However, compared with the DPN model group, the body weight and mechanical pain threshold were obviously upgraded, while the fasting blood glucose was soothingly downgraded after four weeks of EA treatment(##*P*<0.01) (**Figures 1B–D**).

Quantitative of Differentially Expressed Proteins

A total 5744 proteins were identified from spinal dorsal horn samples from the three experimental groups, and 5393 proteins were quantified after proteomic analysis. Molecules with expression ratios showing a > 1.2-fold change and p-values < 0.05 were considered DEPs.

Compared with the control group, levels of 435 proteins were significantly changed (328 down- and 107 up-regulated) in DPN rats and 643 proteins changed in EA rats ($p < 0.05$ and fold-change > 1.5) (**Figure 2A**). Further analysis showed that 118 proteins were significantly changed (25 down- and 93 up-regulated) in DPN rats while 14 proteins were up-regulated and 83 proteins down-regulated after EA treatment ($p < 0.05$ and fold-change > 1.5) (**Figure 2B**). There were 51 common positive proteins when DPN up-regulated and EA down-regulated ($p < 0.05$ and fold-change > 1.5), while 8 common positive proteins were found which DPN down-regulated and EA-upregulated ($p < 0.05$ and fold-change > 1.5). There were

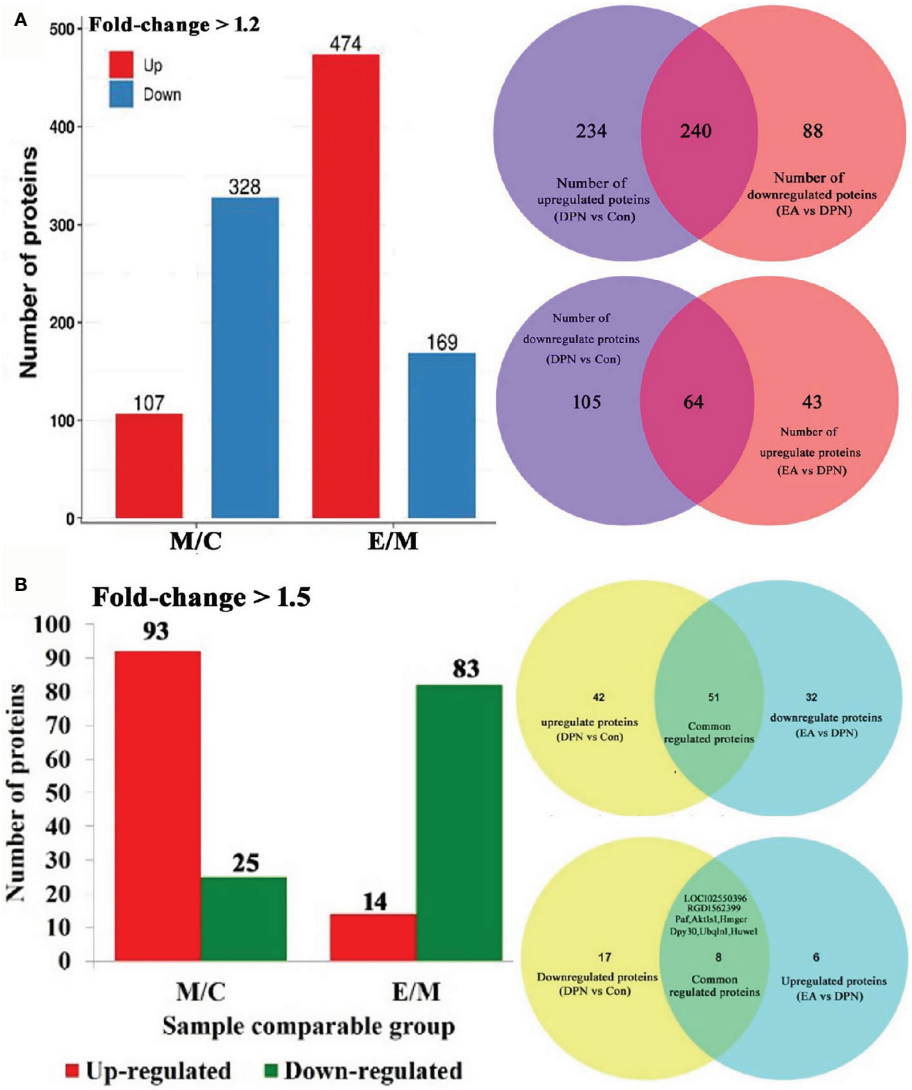

FIGURE 2 | Quantitative of differentially expressed proteins in three groups. **(A)** Number of differential protein set at 1.2-fold (M/C, DPN group compared with control group E/M; EA group compared with DPN group). 240 common positive proteins when DPN up-regulated and EA down-regulated set at 1.5-fold. 64 common positive proteins when DPN down-regulated and EA up-regulated set at 1.5-fold. **(B)** Number of differential protein set at 1.5-fold (M/C, DPN group compared with control group E/M; EA group compared with DPN group). 51 common positive proteins when DPN up-regulated and EA down-regulated set at 1.5-fold. 8 common positive proteins when DPN down-regulated and EA up-regulated set at 1.5-fold.

total 59 common changed proteins shown in the **Table 1** ($p < 0.05$ and fold-change > 1.5).

Molecular Function, Cellular Component, and Biological Process in Control, DPN, and EA Group Rats

GO analysis was used to evaluate the molecular function, cellular component, and biological processes enriched for DEPs.

In terms of biological processes, the top five enriched for DPN-associated proteins were cellular process, single-organism process, biological regulation, metabolic process, and response to stimulus, while the top five enriched for EA-regulated proteins were single-organism process, cellular process, metabolic process, biological regulation, and response to stimulus. Cell component analysis indicated the most enriched for DPN-associated proteins were cell, organelle, membrane, extracellular region, and macromolecular complex, among others, while EA-regulated proteins were mainly involved in the cell, organelle, membrane, macromolecular complex, and extracellular region. Molecular functions analysis suggested that the most common molecular functions of DPN-associated and EA-regulated proteins were binding and catalytic activity (**Figures 3A, B**).

According to subcellular structural localization analysis, the main subcategories (> 10%) in DPN-associated proteins were

TABLE 1 | The common significant differences of EA-regulated and DPN-associated proteins ($p < 0.05$ and changes >1.5-fold).

Protein accession	Protein description	Gene name	DPN/CON Ratio	P value	EA/DPN Ratio	P value
F7F9X9	—	Slc26a8	14.35	2.28E-06	0.076	1.61E-05
D3ZUF8	—	Vrk2	4.899	3.56E-05	0.216	0.000162
F7EUK4	T-kininogen 2	Kng1l1	4.212	2.17E-05	0.449	4.18E-05
Q5YIR9	—	Clec4a1	3.793	1.69E-08	0.225	0.001378
P17712	Glucokinase	Gck	3.655	6.97E-07	0.311	0.003456
P01048	T-kininogen 1	Map1	3.457	3.28E-06	0.528	4.31E-05
A0A0H2UHM3	Haptoglobin	Hp	2.313	0.035243	0.451	0.000338
M0RAV0	—	—	2.242	0.000317	0.646	0.001018
F1M5A4	Katanin p60 ATPase-containing subunit A-like 2	Katnal2	2.238	1.69E-05	0.48	2.22E-05
M0R4Z4	—	LOC682352	2.207	4.27E-05	0.636	0.000698
P20767	Ig lambda-2 chain C region	—	1.995	0.013403	0.642	5.97E-05
G3V9P3	—	MGC112715	1.95	2.46E-05	0.499	3.88E-05
D3ZNA5	Class I histocompatibility antigen, Non-RT1.A alpha-1 chain	LOC686860	1.878	4.33E-05	0.519	4.1E-05
B1WBQ8	Glyceraldehyde-3-phosphate dehydrogenase	Gapdhs	1.848	0.007075	0.626	0.001681
Q7TQ70	Fibrinogen alpha chain	Fga	1.823	1.17E-06	0.647	3.94E-06
D3ZV51	Olfactory receptor	LOC100909611	1.822	0.010757	0.427	0.000603
D4A6F2	—	Lynx1	1.822	0.000436	0.605	0.000517
A0A0G2KB63	Prohibitin-2	Phb2	1.821	3.07E-06	0.55	4.52E-06
P02680	Fibrinogen gamma chain	Fgg	1.796	4.31E-05	0.664	0.000184
P14480	Fibrinogen beta chain	Fgb	1.789	1.58E-05	0.644	1.64E-05
P67779	Prohibitin	Phb	1.751	3.53E-05	0.555	0.000384
F1M4J0	—	Rictor	1.748	0.00012	0.59	9.54E-05
A0A096MJ90	—	Ly6h	1.713	8.48E-05	0.529	6.06E-05
Q7TPI6	—	rCG_62991	1.69	0.001398	0.643	0.010803
Q66HL0	5-nucleotidase	Nt5e	1.689	0.003575	0.644	0.008803
P11951	Cytochrome c oxidase subunit 6C-2	Cox6c2	1.647	1.33E-06	0.495	4.16E-05
G3V851	—	Slc17a6	1.64	0.001939	0.608	9.99E-05
P80431	Cytochrome c oxidase subunit 7B, mitochondrial	Cox7b	1.634	1.48E-06	0.537	8.1E-07
B0BNE6	—	Ndufs8	1.62	0.000135	0.647	0.000305
P01836	Ig kappa chain C region, A allele	—	1.597	0.002182	0.362	0.000221
P10888	Cytochrome c oxidase subunit 4 isoform 1, mitochondrial	Cox4i1	1.574	4.74E-06	0.573	1.62E-06
P11661	NADH-ubiquinone oxidoreductase chain 5	Mtnd5	1.572	0.001844	0.597	5.64E-05
P80432	Cytochrome c oxidase subunit 7C, mitochondrial	Cox7c	1.562	0.000196	0.5	0.000103
D3ZLT1	—	Ndufb7	1.559	5.66E-05	0.585	8.2E-05
D4A565	—	Ndufb5	1.557	2.11E-05	0.582	4.47E-06
F1LXA0	—	Ndufa12	1.555	1.88E-05	0.625	3.16E-06
D3ZYX8	—	Cox7a2l	1.547	0.000164	0.631	0.000143
F1LTP5	Coiled-coil domain-containing protein 63	Ccdc63	1.546	8.42E-05	0.622	0.00018
A0A0G2K7D4	Dynein heavy chain 12, axonemal	Dnah12	1.545	2.08E-05	0.611	0.000599
Q5M7T6	—	Atp6v0d1	1.545	3.57E-05	0.58	4.5E-05
D4ACP8	—	Serac1	1.542	0.000463	0.664	0.00038
D4A463	—	Tpgs1	1.535	0.024738	0.579	0.006541
D3ZG43	—	Ndufs3	1.521	1.75E-05	0.641	1.69E-06
A0A2U3UXS5	—	Igsf21	1.519	0.006782	0.583	0.00152
A0A0H2UHV2	Mediator of RNA polymerase II transcription subunit 23	Med23	1.514	0.000217	0.666	0.000244
F1M0G0	—	Rgs17	1.51	0.006183	0.579	0.001856
P12075	Cytochrome c oxidase subunit 5B, mitochondrial	Cox5b	1.507	3.79E-05	0.587	4.56E-06
F1M9G7	CREB-binding protein	Crebbp	1.506	0.00094	0.623	6.26E-05
B0BN66	—	Sapcd2	1.505	0.005243	0.635	0.003216
B5DEL8	—	LOC100363268	1.504	0.000462	0.663	0.000245
F1LPG5	—	LOC688963	1.5	6.33E-05	0.637	0.000138
Protein accession	**Protein description**	**Gene name**	**DPN/CON Ratio**	**P value**	**EA/DPN Ratio**	**P value**
A0A0G2JUM9	—	LOC102550396	0.366	2.4303E-05	2.492	0.0001
D3ZAS1	—	RGD1562399	0.419	3.5258E-05	2.183	0.000136
Q6RIA2	PCNA-associated factor	Paf	0.468	5.7355E-05	1.548	0.001543
D3ZH75	—	Akt1s1	0.525	0.0183551		
P51639	3-hydroxy-3-methylglutaryl-coenzyme A reductase	Hmgcr	0.601	0.0025202	1.573	0.007535
G3V946	—	Dpy30	0.639	0.0141759	1.757	0.005797
A0A140TAI1	—	Ubqln1	0.647	4.0053E-05	1.54	0.000103
P51593	E3 ubiquitin-protein ligase HUWE1	Huwe1	0.665	5.9014E-05	1.543	0.00098

cytoplasm (26.59%), extracellular (21.46%), nucleus (18.35%), plasma membrane (14.31%), and mitochondria (10.42%). The same analysis of EA-associated proteins also identified the cytoplasm (27.36%), extracellular (18.62%), nucleus (17.47%), plasma membrane (15.4%), and mitochondria (13.56%) subcategories (**Figures 3C, D**).

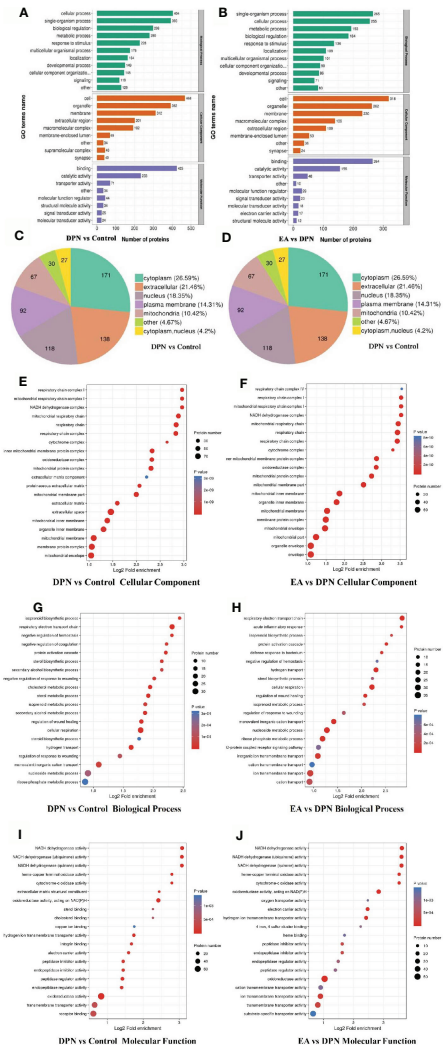

FIGURE 3 | GO annotation analysis showed the potential biomarkers mainly involved in DPN pathology and EA treatment **(A)** GO terms name of molecular function, cellular component, and biological process in DPN-associated proteins **(B)** GO terms name of molecular function, cellular component, and biological process in EA-regulated proteins **(C)** Subcellular structural localization analysis in DPN-associated proteins **(D)** Subcellular structural localization analysis in EA-regulated proteins. **(E–J)** GO annotation summarizing in cellular component, molecular function and biological process in different compared groups.

Last, GO analysis demonstrated that the cellular component, biological process molecular function of DPN and EA treatment were closely related to the mitochondrial respiratory chain and NADH dehydrogenase activity (**Figures 3E–J**).

Functional Enrichment Analysis With KEGG Pathway and Cluster Analysis of KEGG Pathway Functional Correlation of the DEPs

To further explore pathways significantly enriched for DEPs (DPN *vs.* Control, n = 643; EA *vs.* DPN, n = 435), DEPs were mapped to the KEGG database and enrichment levels calculated (Fisher's exact test; -log 10[p-value]), where a higher p-value indicates more DEPs enriched in a category. As shown in **Figures 4A, B**, KEGG pathway enrichment analysis demonstrated that DPN-associated and EA-regulated DEPs were mainly enriched in several pathways, particularly oxidative phosphorylation (**Figure 4C**). Further, remarkable changes were observed in ten proteins closely related to oxidative phosphorylation during EA treatment of DPN rats (**Table 2** and **Figure 4D**).

DISCUSSION

In our research, we found that four weeks EA can improve weight loss, blood glucose, and sensitivity to mechanical pain in DPN rats. We generated proteomics data from DPN rat spinal dorsal horn samples treated with repeated EA stimulation. A total of 5393 proteins were quantified using the TMT labeling proteomics method. Of these proteins, 93 were down-regulated,

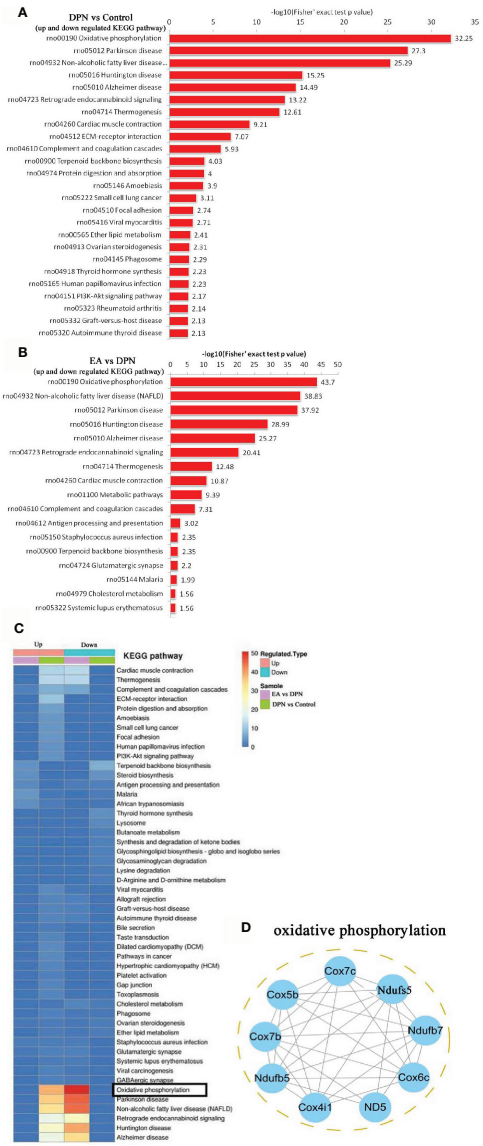

FIGURE 4 | KEGG pathway and related oxidative phosphorylated proteins analysis **(A)** the KEGG pathway enrichment analysis in DPN rats compared with control rats. **(B)** The KEGG pathway enrichment analysis in EA group rats compared with DPN rats. **(C)** The KEGG pathway analysis in different group rats. **(D)** Networks Analysis of major proteins in oxidative phosphorylation.

TABLE 2 | The prominent changes of oxidative phosphorylated proteins during EA treatment with DPN rat.

Protein accession	String gene	Protein description	DPN vs Control	EA vs DPN
P80432	Cox7c	Cytochrome c oxidase subunit 7C, mitochondria	1.562 up	0.5 down
P12075	Cox5b	Cytochrome c oxidase subunit 5B, mitochondria	1.507 up	0.587 down
P80431	Cox7b	Cytochrome c oxidase subunit 7B, mitochondria	1.634 up	0.537 down
D4A565	Ndufb5	NADH dehydrogenase (Ubiquinone) 1 beta subcomplex 5	1.557 up	0.582 down
P10888	Cox4i1	Cytochrome c oxidase subunit 4 isoform 1, mitochondria	1.574 up	0.573 down
P11661	ND5(Mtnd5)	NADH-ubiquinone oxidoreductase chain 5	1.572 up	0.597 down
P11951	Cox6c2	Cytochrome c oxidase subunit 6C-2	1.647 up	0.495 down
D3ZLT1	Ndufb7	“NADH dehydrogenase (Ubiquinone) 1 beta subcomplex, 7	1.559 up	0.585 down
B5DEL8	Ndufs5	NADH dehydrogenase (Ubiquinone) Fe-S protein 5	1.504 up	0.663 down

while 25were up-regulated during the development of DPN. After EA stimulation intervention, 14 up-regulated and down-regulated 83 proteins were detected in the spinal dorsal horn. KEGG pathway enrichment analysis suggested that oxidative phosphorylation was a major factor involved in the effects of EA therapy on DPN. The results of this study provide a potentially valuable theoretical underpinning of the mechanisms underlying DPN pathophysiology and the clinical application of acupuncture.

The occurrence of diabetes and its complications are closely related to the mechanism of oxidative phosphorylation *via* the disturbances of mitochondrial ATP, complex IV and reactive oxygen species (ROS) metabolism (22–24). Upregulated expression of complexes I, III, IV, and V was found in the sciatic nerve of diabetic neuropathy rats (11). In addition, mitochondrial complex III of dorsal root ganglia was significantly decreased, while glutathione peroxidase and peroxidase were increased during STZ induced diabetic peripheral neuropathy (13).

Our results indicate that cytochrome c oxidase (Cox, Complex IV) factors, including Cox4i1, Cox5b, Cox6c2, Cox7b, and Cox7c, were significantly upregulated in spinal dorsal horn during DPN, as were NADH-ubiquinone oxidoreductase (Complex I) factors, including Ndufb5, Ndufb7, andNdufs5. Further, treatment with EA could decrease the up-regulation of Cox and NADH oxidoreductase. As we know, abnormal function of mitochondrial Cox and NADH oxidoreductase could induce ROS overproduction, caspase 3 activation cell apoptosis (25, 26). Spinal ROS overproduction and activated caspase-3 induced by Cox play a critical role in microglial activation and neuronal apoptosis in several neuropathic pain models included DPN (27, 28). Blocking NADPH oxidase, scavenging ROS, and reducing oxidative phosphorylation by various pharmacotherapy could prevent the induction of spinal long-term potentiation and relieve the persistent pain (29–31).

In addition, EA can also inhibit oxidative phosphorylation and ROS production through different pathways in neuropathic pain and other chronic diseases. For example,

Neuronal ATP receptor P2X7 activation leads to ROS production and subsequent nociceptive pain (32, 33). EA can improve neuropathic pain by inhibiting oxidative phosphorylation, reducing ATP production, and suppressing central sensitization in the spinal dorsal horn (34). In middle cerebral artery occlusion rats, EA treatment could significantly improve the respiratory control ratio, and increase the activities of NADH dehydrogenase and Cox in the perifocal penumbra zone (35). In the state of ischemia reperfusion injury, EA can inhibit cardiac Cox and indirectly inhibit the activation of caspase 3 (36). However, EA can alleviate bupivacaine-induced myocardial injury by upregulating enzymatic activity of Cox (37). In a word, EA can biaxially regulate oxidative phosphorylation of Cox and NADH dehydrogenase with bidirectional properties in different diseases and tissues.

According to the above research reports, combined with our results, we speculated that EA can reduce diabetic neuropathic pain by downregulating Cox and NADH dehydrogenase in the spinal cord, which may mainly be through the following ways: (1) inhibiting the spinal ATP release and P2X7 activation, reducing the spinal neuronal abnormal excitability and microglial activation; (2) reducing spinal ROS production and oxidative phosphorylation injury, inhibiting cell injury and even apoptosis. In the next experiment, we will further explore the mechanism of EA regulating ROS and oxidative phosphorylation in DPN.

CONCLUSION

In conclusion, we used a TMT labeling approach coupled with liquid chromatography with tandem mass spectrometry to show that DPN and EA stimulation drive significant changes in spinal proteins, particularly those involved in oxidative phosphorylation. Our results highlight potential candidate protein biomarkers for DPN diagnosis and treatment.

DATA AVAILABILITY STATEMENT

The datasets presented in this study can be found in online repositories. The names of the repository/repositories and accession number(s) can be found in the article/supplementary material.

ETHICS STATEMENT

The animal study was reviewed and approved by Fujian University of Traditional Chinese Medicine Animal Ethics Committee.

AUTHOR CONTRIBUTIONS

XY and XC made an equal contribution to this research. ZW and JT are the co-corresponding authors and they completed the project design, data analysis, and drafted part of the manuscript. All authors contributed to the article and approved the submitted version.

FUNDING

This study was jointly supported by the National Natural Science Foundation of China (81774385, 81704149), the Science and technology platform construction project of Fujian science and Technology Department(Grant No.2018Y2002), the Key Project of "Traditional Chinese Medicine modernization research" in the National Key Research and Development plan (2019YFC1710301).

REFERENCES

1. Van H O, Audtin SK, Khan RA, Smith BH, Torrance N. Neuropathic Pain in the General Population: A Systematic Review of Epidemiological Studies. *Pain* (2014) 155:654–62. doi: 10.1016/j.pain.2013.11.013
2. Lee-Kubli Corinne A CNA. Painful Neuropathy: Mechanisms. *Handb Clin Neurol* (2014) 126:533–57. doi: 10.1016/B978-0-444-53480-4.00034-5
3. Malisza KL, Jones C, Gruwel MLH, Foreman D, Fernyhough P, Calcutt NA. Functional Magnetic Resonance Imaging of the Spinal Cord During Sensory Stimulation in Diabetic Rats. *J Magn Reson Imaging* (2009) 30:271–6. doi: 10.1002/jmri.21856
4. Eaton SE, ND H, Rajbhandari SM, Greenwood P, Wilkinson ID, Ward JD, et al. Spinal-Cord Involvement in Diabetic Peripheral Neuropathy. *Lancet* (2001) 358:35–6. doi: 10.1016/S0140-6736(00)05268-5
5. Shin K-M, Lee S, Lee EY, Kim CH, Kang JW, Lee CK, et al. Electroacupuncture for Painful Diabetic Peripheral Neuropathy: A Multicenter, Randomized, Assessor-Blinded, Controlled Trial. *Diabetes Care* (2018) 41:e141–2. doi: 10.2337/dc18-1254
6. Bailey A, Wingard D, Allison M, Summers P, Calac D. Acupuncture Treatment of Diabetic Peripheral Neuropathy in an American Indian Community. *J Acupunct Meridian Stud* (2017) 10(2):90–5. doi: 10.1016/j.jams.2016.10.004
7. Zhang YJ LF. Effectiveness of Acupuncture for Treatment of Diabetic Peripheral Neuropathy. *Med (Baltimore)* (2019) 98(39):e17282. doi: 10.1097/MD.0000000000017282
8. Tong Y GH, Han B. Fifteen-Day Acupuncture Treatment Relieves Diabetic Peripheral Neuropathy. *J Acupunct Meridian Stud* (2010) 3(2):95–103. doi: 10.1016/S2005-2901(10)60018-0
9. Zhang C MY, Yan Y. Clinical Effects of Acupuncture for Diabetic Peripheral Neuropathy. *J Tradit Chin Med* (2010) 30(1):13–4. doi: 10.1016/s0254-6272(10)60003-9
10. Feng Y FY, Wang Y, Hao Y. Acupoint Therapy on Diabetes Mellitus and Its Common Chronic Complications: A Review of Its Mechanisms. *BioMed Res Int* (2018) 22:1–9. doi: 10.1155/2018/3128378
11. Freeman OJ, Unwin RD, Dowsey AW, Begley P, Ali S, Hollywood KA, et al. Metabolic Dysfunction Is Restricted to the Sciatic Nerve in Experimental Diabetic Neuropathy. *Diabetes* (2016) 65(1):228–38. doi: 10.2337/db15-0835
12. Akude E, Zherebitskaya E, Chowdhury SK, Smith DR, Dobrowsky RT, Fernyhough P. Diminished Superoxide Generation Is Associated With Respiratory Chain Dysfunction and Changes in the Mitochondrial Proteome of Sensory Neurons From Diabetic Rats. *Diabetes* (2011) 60(1):288–97. doi: 10.2337/db10-0818
13. Zhang T, Gao Y, Gong Y, Zhou H, Xie P, Guan S, et al. Tang-Luo-Ning Improves Mitochondrial Antioxidase Activity in Dorsal Root Ganglia of Diabetic Rats: A Proteomics Study. *BioMed Res Int* (2017) 2017:8176089. doi: 10.1155/2017/8176089
14. Chowdhury SK DR, Fernyhough P. Nutrient Excess and Altered Mitochondrial Proteome and Function Contribute to Neurodegeneration in Diabetes. *Mitochondrion* (2011) 11(6):845–54. doi: 10.1016/j.mito.2011.06.007
15. Shi L, Zhang HH, Xiao Y, Hu J, Xu GY. Electroacupuncture Suppresses Mechanical Allodynia and Nuclear Factor κ B Signaling in Streptozotocin-Induced Diabetic Rats. *CNS Neurosci Ther* (2013) 19(2):83–90. doi: 10.1111/cns.12035
16. Zhang Z, Shi Y, Cai D, Jin S, Zhu C, Shen Y, et al. Effect of Electroacupuncture at ST36 on the Intestinal Mucosal Mechanical Barrier and Expression of Occludin in a Rat Model of Sepsis. *Acupunct Med* (2018) 36(5):333–8. doi: 10.1136/acupmed-2016-011187
17. Li J, Wu S, Tang H, Huang W, Wang L, Zhou H, et al. Long-Term Effects of Acupuncture Treatment on Airway Smooth Muscle in a Rat Model of Smoke-Induced Chronic Obstructive Pulmonary Disease. *Acupunct Med* (2016) 34(2):107–13. doi: 10.1136/acupmed-2014-010674
18. Cao BY, Li R, Tian HH, Ma YJ, Hu XG, Jia N, et al. Pi3k-Glut4 Signal Pathway Associated With Effects of EX-B3 Electroacupuncture on Hyperglycemia and Insulin Resistance of T2DM Rats. *Evid Based Complement Alternat Med* (2016) 7914387:1–10. doi: 10.1155/2016/7914387
19. Dixon WJ. Efficient Analysis of Experimental Observations. *Annu Rev Pharmacol Toxicol* (1980) 20:441–62. doi: 10.1146/annurev.pa.20.040180.002301
20. Wang ZF, Li Q, Liu SB, Mi WL, Hu S, Zhao J, et al. Aspirin-Triggered Lipoxin A4 Attenuates Mechanical Allodynia in Association With Inhibiting Spinal JAK2/STAT3 Signaling in Neuropathic Pain in Rats. *Neuroscience* (2014) 25(273):65–78. doi: 10.1016/j.neuroscience.2014.04.052
21. Mao-Ying QL, Zhao J, Dong ZQ, Wang J, Yu J, Yan MF, et al. A Rat Model of Bone Cancer Pain Induced by Intra-Tibia Inoculation of Walker 256 Mammary Gland Carcinoma Cells. *Biochem Biophys Res Commun* (2006) 345(4):1292–8. doi: 10.1016/j.bbrc.2006.04.186
22. Lewis MT, Kasper JD, Bazil JN, Frisbee JC, Wiseman RW. Quantification of Mitochondrial Oxidative Phosphorylation in Metabolic Disease: Application to Type 2 Diabetes. *Int J Mol Sci* (2019) 20(21):5271–301. doi: 10.3390/ijms20215271
23. Hunter CA, Kartal F, Koc ZC, Murphy T, Kim JH, Denvir J, et al. Mitochondrial Oxidative Phosphorylation Is Impaired in TALLYHO Mice, a New Obesity and Type 2 Diabetes Animal Model. *Int J Biochem Cell Biol* (2019) 116(105616):1–25. doi: 10.1016/j.biocel.2019.105616
24. Victor VM, Rocha M, Herance R, Hernandez-Mijares A. Oxidative Stress and Mitochondrial Dysfunction in Type 2 Diabetes. *Curr Pharm Des* (2011) 17(36):3947–58. doi: 10.2174/138161211798764915
25. Portt L, Norman G, Clapp C, Greenwood M, Greenwood MT. Anti-Apoptosisand Cell Survival: A Review. *Biochim Biophys Acta* (2011) 1813(1):238–59. doi: 10.1016/j.bbamcr.2010.10.010
26. Ye L, Xiao L, Bai X, Yang SY, Li Y, Chen Y, et al. Spinal Mitochondrial-Derived ROS Contributes to Remifentanil-Induced Postoperative Hyperalgesia Via Modulating NMDA Receptor in Rats. *Neurosci Lett* (2016) 10(634):79–86. doi: 10.1016/j.neulet.2016.09.016
27. Zhao WC, Zhang B, Liao MJ, Zhang WX, He WY, Wang HB, et al. Curcumin Ameliorated Diabetic Neuropathy Partially by Inhibition of NADPH Oxidase Mediating Oxidative Stress in the Spinal Cord. *Neurosci Lett* (2014) 560(7):81–5. doi: 10.1016/j.neulet.2013.12.019
28. Rasoulian B, Hajializadeh Z, Esmaeili-Mahani S, Rashidipour M, Fatemi I, Kaeidi A. Neuroprotective and Antinociceptive Effects of Rosemary (Rosmarinus Officinalis L.) Extract in Rats With Painful Diabetic Neuropathy. *J Physiol Sci* (2019) 69(1):57–64. doi: 10.1007/s12576-018-0620-x
29. Xu J, Wei X, Gao F, Zhong X, Guo R, Ji Y, et al. Nicotinamide Adenine Dinucleotide Phosphate Oxidase 2-Derived Reactive Oxygen Species Contribute to Long-Term Potentiation of C-Fiber-Evoked Field Potentials in Spinal Dorsal Horn and Persistent Mirror-Image Pain Following High-Frequency Stimulus of the Sciatic Nerve. *Pain* (2020) 161(4):758–72. doi: 10.1097/j.pain.0000000000001761
30. Schwartz ES, Kim HY, Wang J, Lee I, Klann E, Chung JM, et al. Persistent Pain Is Dependent on Spinal Mitochondrial Antioxidant Levels. *J Neurosci* (2009) 29(1):159–68. doi: 10.1523/JNEUROSCI.3792-08.2009
31. Ludman T, Melemedjian OK. Bortezomib-Induced Aerobic Glycolysis Contributes to Chemotherapy-Induced Painful Peripheral Neuropathy. *Mol Pain* (2019) 15:1–17. doi: 10.1177/1744806919837429
32. Ni CM, Sun HP, Xu X, Ling BY, Jin H, Zhang YQ, et al. Spinal P2X7R Contributes to Streptozotocin-Induced Mechanical Allodynia in Mice. *J Zhejiang Univ Sci B* (2020) 21(2):155–65. doi: 10.1631/jzus.B1900456
33. Munoz FM, Gao R, Tian Y, Henstenburg BA, Barrett JE, Hu H. Neuronal P2X7 Receptor-Induced Reactive Oxygen Species Production Contributes to Nociceptive Behavior in Mice. *Sci Rep* (2017) 7(1):1–12. doi: 10.1038/s41598-017-03813-7
34. Xu J, Chen XM, Zheng BJ, Wang XR. Electroacupuncture Relieves Nerve Injury-Induced Pain Hypersensitivity Via the Inhibition of Spinal P2x7 Receptor-Positive Microglia. *Anesth Analg* (2016) 122(3):882–92. doi: 10.1213/ANE.0000000000001097
35. Zhong S, Li Z, Huan L, Chen BY. Neurochemical Mechanism of Electroacupuncture: Anti-Injury Effect on Cerebral Function After Focal Cerebral Ischemia in Rats. *Evid Based Complement Alternat Med* (2009) 6(1):51–6. doi: 10.1093/ecam/nem062
36. Lu SF, Huang Y, Wang N, Shen WX, Fu SP, Li Q, et al. Cardioprotective Effect of Electroacupuncture Pretreatment on Myocardial Ischemia/Reperfusion Injury Via Antiapoptotic Signaling. *Evid Based Complement Alternat Med* (2016) 4609784:1–9. doi: 10.1155/2016/4609784
37. Wang C, Liang X, Yu Y, Li Y, Wen X, Liu M. Electroacupuncture Pretreatment Alleviates Myocardial Injury Through Regulating

Mitochondrial Function. *Eur J Med Res* (2020) 25(1):1–10. doi: 10.1186/s40001-020-00431-4

Conflict of Interest: The authors declare that the research was conducted in the absence of any commercial or financial relationships that could be construed as a potential conflict of interest.

frontiers in Endocrinology

ORIGINAL RESEARCH
published: 15 June 2021
doi: 10.3389/fendo.2021.638727

Metabolomic Profiling of Pregnancies With Polycystic Ovary Syndrome Identifies a Unique Metabolic Signature and Potential Predictive Biomarkers of Low Birth Weight

OPEN ACCESS

Edited by:
Ioannis Kyrou,
Aston Medical School,
United Kingdom

Reviewed by:
Johnny Awwad,
American University of Beirut,
Lebanon
Eva Kassi,
National and Kapodistrian
University of Athens
Medical School, Greece

***Correspondence:**
Nayef A. Mazloum
nam2016@qatar-med.cornell.edu
Mohamed A. Elrayess
m.elrayess@qu.edu.qa

Specialty section:
This article was submitted to Systems Endocrinology, a section of the journal Frontiers in Endocrinology

Received: *07 December 2020*
Accepted: *10 May 2021*
Published: *15 June 2021*

Citation:
Diboun I, Ramanjaneya M, Ahmed L, Bashir M, Butler AE, Albagha O, Abou-Samra AB, Atkin SL, Mazloum NA and Elrayess MA (2021) Metabolomic Profiling of Pregnancies With Polycystic Ovary Syndrome Identifies a Unique Metabolic Signature and Potential Predictive Biomarkers of Low Birth Weight. Front. Endocrinol. 12:638727. doi: 10.3389/fendo.2021.638727

Ilhame Diboun[1], Manjunath Ramanjaneya[2,3], Lina Ahmed[4], Mohammed Bashir[2], Alexandra E. Butler[5], Omar Albagha[1,6], Abdul Badi Abou-Samra[2], Stephen L. Atkin[7], Nayef A. Mazloum[4] and Mohamed A. Elrayess[8]**

[1] College of Health and Life Sciences, Hamad Bin Khalifa University (HBKU), Doha, Qatar, [2] Qatar Metabolic Institute, Hamad Medical Corporation, Doha, Qatar, [3] Translational Research Institute, Hamad Medical Corporation, Doha, Qatar, [4] Department of Microbiology and Immunology, Weill Cornell Medicine-Qatar, Qatar Foundation, Doha, Qatar, [5] Diabetes Research Center (DRC), Qatar Biomedical Research Institute (QBRI), Hamad Bin Khalifa University (HBKU), Qatar Foundation (QF), Doha, Qatar, [6] Centre for Genomic and Experimental Medicine, Institute of Genetics and Molecular Medicine, University of Edinburgh, Edinburgh, United Kingdom, [7] Post Graduate Studies and Research, Royal College of Surgeons in Ireland Bahrain, Adliya, Bahrain, [8] Biomedical Research Center (BRC), Qatar University, Doha, Qatar

Background: Polycystic ovary syndrome (PCOS) is a complex syndrome with clinical features of an endocrine/metabolic disorder. Various metabolites show significant association with PCOS; however, studies comparing the metabolic profile of pregnant women with and without PCOS are lacking. In this study, metabolomics analysis of blood samples collected from PCOS women and age and BMI matched controls in the second trimester of pregnancy was performed to identify metabolic differences between the two groups and determine their association with pregnancy outcome.

Methods: Sixteen PCOS and fifty-two healthy women in their second trimester underwent targeted metabolomics of plasma samples using tandem mass spectrometry with the Biocrates MxP® Quant 500 Kit. Linear regression models were used to identify the metabolic alterations associated with PCOS, followed by enrichment and Receiver Operating Characteristic (ROC) analyses to determine the best indicators of pregnancy outcomes.

Results: PCOS women had lower birth weight babies compared to healthy controls. As a group, systolic blood pressure (SBP) at both second trimester and at delivery negatively correlated with birth weight. Regression models indicated significant increases in the triglycerides C20:4_C34:3 and C18:2_C38:6 in the PCOS group [false discovery rate (FDR) <0.05]. Enrichment analysis revealed significant elevations in triglycerides containing arachidonic acid, linoleic acid and palmitic acid in the PCOS group. A number of indicators of baby birth weight were identified including SBP at delivery, hexosylceramide (d18:2/

24:0), ceramide (d18.0/24.1) and serine, with an AUC for all predictors combined for low birth weight (≤2500grams) of 0.88 (95%CI: 0.75-1.005, p<0.001).

Conclusions: PCOS pregnancies resulted in babies with a lower birth weight, marked by a unique metabolic signature that was enriched with specific triglycerides and unsaturated fatty acids. The functional significance of these associations needs further investigation.

Keywords: metabolomics, pregnancy, polycystic ovary syndrome (PCOS), birth weight, arachidonic acid, linoleic acid, palmitic acid

INTRODUCTION

Pregnancy triggers significant metabolic alterations to meet the increasing physiological demands of the mother and her developing fetus (1). In early pregnancy, these alterations reflect the whole body's anabolic status to fulfill the increasing nutritional needs; however, these physiological metabolic changes may be greatly influenced by various underlying health conditions (2). Among these, polycystic ovary syndrome (PCOS) affecting up to 10% of reproductively active women (3), causes anovulatory infertility (4) and increased risk of adverse pregnancy outcomes, including gestational diabetes, miscarriage and low birth weight (5, 6). Metabolic changes associated with PCOS in pregnant women and their impact on birth weight have not been fully explored.

Significant advances in mass spectrometry technologies have revolutionized the discovery of metabolic pathways that underlie the progression of various diseases such as insulin resistance, type 2 diabetes (7–9), cancer (10) and cardiovascular disease (11), giving a deeper insight into their disease etiologies. Studies have investigated changes in metabolites in different biofluids and tissues and have identified various potential markers with significant diagnostic and therapeutic utility (12). Studies of reproductive diseases, such as PCOS, GDM and poor pregnancy outcomes, have received increasing interest (13–15). A recent study investigating the metabolic changes associated with PCOS in pregnant women indicated abnormalities in lipid metabolism and beta-oxidation of fatty acids, causing increased risk of miscarriage (16). However, metabolic profiling to predict risk of low birth weight deliveries has not yet been explored.

In this study, targeted metabolomics analysis of blood samples from age and weight matched pregnant women in their second trimester with and without PCOS was related to pregnancy outcomes, including birth weight and gestational age at delivery. The emerging data indicate a unique metabolic signature of PCOS pregnant women at second trimester and identify metabolic markers of low birth weight.

METHODS

Study Design

This is a cross-sectional study that included 68 pregnant women (52 controls and 16 with PCOS) recruited during their second trimester at the antenatal clinic at The Women Wellness and Research Center (WWRC) of Hamad Medical Corporation in Doha, Qatar. The diagnosis of PCOS was based on the NIH criteria of biochemical evidence of hyperandrogenemia (free androgen index >4.5) or a raised testosterone greater than 2.7nmol/l, and oligomenorrhea or amenorrhea. Transvaginal ultrasound was not culturally acceptable and the abdominal ultrasounds in this obese population inaccurate enough to confirm polycystic ovaries. Non-classical 21-hydroxylase deficiency, hyperprolactinemia, Cushing's disease and androgen-secreting tumors were excluded by appropriate tests. All subjects had an oral glucose tolerance test to exclude diabetes. Protocols were approved by Institutional Review Boards (IRBs) of the Hamad Medical Corporation (15101/15) and Weill Cornell Medicine in Qatar (15-00016). All patients gave their written informed consent and the study was conducted in accordance with ICH GCP and the Declaration of Helsinki. Anthropometrics, medical history and demographics data were collected. Blood samples were collected by venipuncture during the regular follow-up second trimester visits and transported to the main HMC laboratory for the routine patient tests including biochemical profile. Additional samples serum were stored at -80°C until analysis was undertaken. Laboratory tests included second trimester biochemical profile and thyroid function tests. Blood samples were also collected for metabolomics analysis. Pregnancy outcomes including gestational age at delivery, birth weight, maternal weight and blood pressure were collated with the metabolomic profile for all participants.

Metabolomics

Tandem mass spectrometry was performed for targeted metabolomics of plasma samples using Biocrates MxP® Quant 500 Kit (Biocrates, Innsbruck, Austria) at the Fraunhofer Institute for Toxicology and Experimental Medicine (ITEM). FIA-MS/MS was utilized to measure lipids using a 5500 QTRAP® instrument with an ESI source (AB Sciex, Darmstadt, Germany). LC-MS/MS utilizing the same 5500 QTRAP® instrument was used for measuring small molecules as described previously (17). Appropriate MS software (Sciex Analyst®) was used to quantify data that was then imported into Biocrates MetIDQ™ software for calculation of analyte concentrations, assessment and compilation of data.

Statistical Analysis

Statistical analyses of demographic traits were performed using IBM SPSS version 25, R version 3.2.1 and SIMCA 14.0 software

(Umetrics, Sweden). Variables with skewed distributions were log transformed to ensure normality (18). Differences between controls and PCOS were tested by independent sample t test (normally distributed variables) or Mann-Whitney U (variables with skewed distribution) test. A p-value significance level of 0.05 was used. Data are presented as mean (SD) in tables or median (interquartile range) in figures. For metabolomics data analysis, principle component analysis (PCA) was performed using R version 2.14, www.r-project.org/. PCA revealed two main components (PC1 and PC2) that together captured 24% of the variance in the data (not shown). Orthogonal partial least square discriminant analysis (OPLS-DA), implemented as part of the software SIMCA, was used to compare controls and PCOS groups. All metabolites with greater than 50% missing values were omitted from SIMCA analysis. Linear regression was performed to identify significant metabolites differentiating PCOS from matching controls using the R statistical package (version 2.14, www.r-project.org/) after correcting for age, BMI and principle components (PC1 and PC2). Function enrichment analysis was performed using Chi square test by considering metabolites with a nominal p-value less than 0.05 from linear regression analysis by assessing the probability of observing the associated nominally-significant metabolites from the linear model by pure chance. The biological categories tested for enrichment were provided by Biocrates and expanded manually by reference to the Human Metabolome Database (19). An automated linear regression model, followed by Receiver Operating Characteristic (ROC) analysis, was utilized to determine the best predictors of pregnancy outcomes using IBM SPSS version 25.

RESULTS

General Characteristics of Participants

PCOS women in their second trimester of pregnancy were insulin resistant accordingly to their homeostatic model assessment for insulin resistance (HOMA-IR), and had on average 339.3 gram lighter babies compared to gestational-age and weight matched healthy controls on delivery ($p<0.05$) (**Table 1** and **Figure 1A**). The birth weights correlated negatively with overall maternal SBP at second trimester (R=-0.3, p=0.01) (**Figure 1B**) as well as SBP (R=-0.4, p=0.003) and DBP (R=-0.3, p=0.03) at delivery (**Figures 1C, D** respectively). As expected, there was a significant positive correlation between gestational age at delivery and birth weight (R=0.4, $p<0.001$). There were no significant differences in other pregnancy outcomes including the gestational age at delivery.

TABLE 1 | General characteristics of study participants.

Time	Variables	Total (N=68)	Controls (N=52)	PCOS (N=16)	P valueControl *vs* PCOS
Second Trimester	**Age (years)**	31.8 (5.7)	31.2 (5.8)	33.9 (4.9)	0.09
	BMI (kg/m2)	32.2 (7.1)	31.6 (7.2)	34.3 (6.5)	0.18
	SBP (mmHg)	111.9 (12.5)	111.2 (12.7)	114.0 (12.0)	0.44
	DBP (mmHg)	63.8 (7.7)	63.6 (7.6)	64.4 (8.3)	0.70
	Cholesterol (mmol.L)	4.8 (1.1)	4.8 (1.1)	4.8 (0.9)	0.99
	Triglycerides (mmol.L)	1.5 (0.8)	1.4 (0.7)	1.7 (0.9)	0.36
	HDL (mmol.L)	1.3 (0.4)	1.3 (0.40)	1.3 (0.6)	0.92
	LDL (mmol.L)	2.8 (0.9)	2.9 (0.9)	2.8 (1.0)	0.86
	Insulin (uIU.L)	0.5 (0.4)	0.4 (0.3)	0.6 (0.4)	0.06
	HbA1c(%)	5.3 (0.5)	5.3 (0.5)	5.3 (0.5)	0.87
	HOMA-IR	1.8 (1.7)	1.5 (1.7)	2.7 (1.3)	0.04
	Vitamin D_3 (IU.L)	15.1 (5.9)	14.9 (6.1)	15.9 (5.6)	0.60
	Urea (nmol.L)	3.1 (1.2)	3.1 (1.1)	2.9 (1.2)	0.43
	Creatinine (nmol.L)	49.7 (9.1)	49.4 (9.7)	51.7 (6.7)	0.39
	ALT(mmol.l)	15.1 (10.0)	13.9 (8.6)	18.9 (12.8)	0.08
	AST(mmol.l)	17.1 (7.1)	16.7 (6.9)	16.5 (7.8)	0.91
	Bilirubin (umol.L)	7.5 (4.4)	7.3 (3.9)	8.1 (5.6)	0.54
	ALP (iu.L)	83.3 (35.2)	84.3 (33.8)	80.3 (40.2)	0.70
	Albumin (g.L)	34.6 (6.7)	34.9 (7.0)	33.8 (5.9)	0.56
	TSH (mU.L)	2.4 (3.4)	2.7 (3.8)	1.6 (0.7)	0.29
	Thyroxine (pmol.L)	12.5 (1.8)	12.4 (1.6)	12.9 (2.3)	0.32
	Total Protein (g.L)	66.3 (5.3)	66.3 (5.6)	66.2 (4.8)	0.96
	Gestational age (weeks)	21.0 (4.4)	21.1 (4.6)	20.8 (4.0)	0.79
At Birth	**Newborn weight (grams)**	3053.7 (549.6)	3133.4 (528.6)	2794.4 (552.8)	0.03
	SBP (mmHg)	120.0 (11.7)	120.2 (11.3)	119.3 (13.3)	0.79
	DBP (mmHg)	72.1 (9.6)	72.3 (9.2)	71.3 (10.9)	0.70
	Maternal weight (Kg)	83.5 (15.1)	82.7 (14.4)	86.2 (17.3)	0.43
	Gestational age (weeks)	38.1 (1.8)	38.3 (1.4)	37.6 (2.0)	0.11

BMI (body mass index), SBP (systolic blood pressure), DBP (diastolic blood pressure), LDL (low density lipoprotein), HDL (high density lipoprotein), HbA1c (Hemoglobin A1c), HOMA-IR (Homeostatic model assessment for insulin resistance), ALP (alkaline phosphatase), ALT (alanine transaminase) or AST (aspartate aminotransferase).

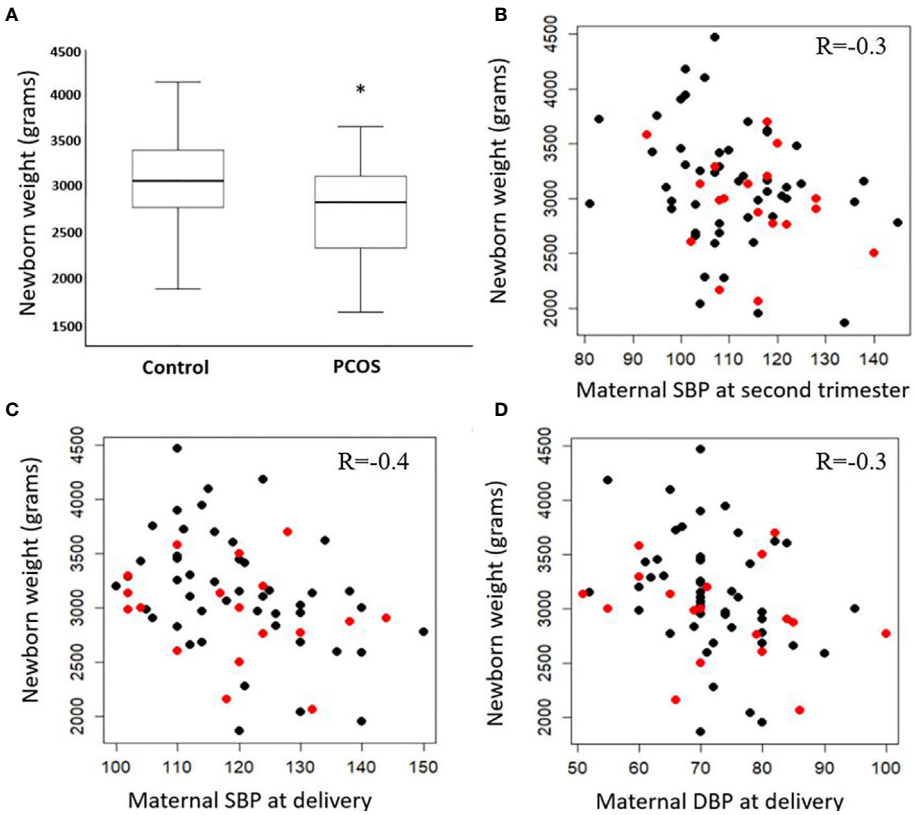

FIGURE 1 | Difference in birth weight at delivery in control and PCOS groups **(A)** median, interquartile range and maximum and minimum values). Correlations between birth weight (PCOS in red, controls in black) and systolic blood pressure (SBP) of mothers at second trimester **(B)**, SBP at delivery **(C)**, and diastolic blood pressure (DBP) at delivery **(D)**. Significance level (*) ≤ 0.05.

Global Metabolic Differences Between Control and PCOS Participants at Second Trimester

An OPLS-DA model comparing the metabolic profile of PCOS and control mothers indicated one class-discriminatory component and one orthogonal component, accounting for 40% of the variation in the study group Y-variable (PCOS groups). The Variable Importance in Projection (VIP) list indicated the discriminatory effects of triacylglycerols containing the following fatty acids (C20:4, C18:2 and C16:0) (**Supplementary Table S1**). The score plot exhibits an x-axis that separates the controls from PCOS group (**Figure 2A**) and the corresponding loading plot indicates triacylglycerols containing these fatty acids from the VIP list (C20:4, C18:2 and C16:0) (**Figure 2B**).

Metabolites Differentiating Controls From PCOS Participants

Following the OPLS-DA multivariate analysis, univariate regression models were utilized to identify metabolites that differentiate PCOS from controls (**Table S3**). First analysis showed metabolites (mostly triacylglycerols) exhibiting significant differences between PCOS and controls at FDR (<0.1) level of significance (**Table 2**), with two (TG.20.4_36.3, TG.18.2_38.6) reaching FDR level of significance (<0.05) (**Figure 3**). A second analysis considering fatty acid composition of nominally significant triacylglycerols, revealed enrichment of triacylglycerols containing C20:4, C18:2 and C16:0 in the PCOS group (p=0.0003, <0.00001 and 0.03, respectively) (also highlighted in **Figure 2B**).

Indicative Biomarkers of Birth Weight

An automatic linear regression model was utilized to identify best predictors of birth weight regardless of study groups. The model revealed 4 indicators, three of which were lipids, that varied in their importance and direction (positive and negative) in indicating the birth weight (**Table 3**) with a combined AUC for all indicators of low birth weight (≤2500 grams, n=8) of 0.88 (95%CI: 0.75-1.005, p<0.001) (**Figure 4**).

DISCUSSION

In the present study, we identified a distinct metabolic signature differentiating PCOS women from age, BMI and gestational age-matched controls, and revealed potential indicative metabolic

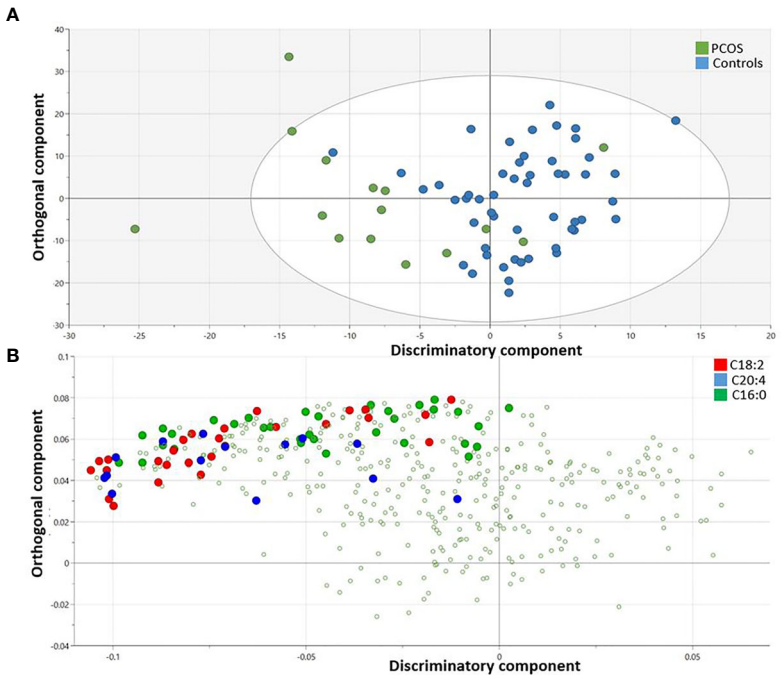

FIGURE 2 | OPLS-DA model comparing metabolites from controls and PCOS mothers. Score plot shows one dimensional separation on the x-axis between controls and PCOS mothers **(A)** and the corresponding loading plot indicates triacylglycerols containing enriched fatty acids (C20:4, C18:2 and C16:0) that are responsible for the group separation **(B)**.

biomarkers for the low birth weight of babies associated with PCOS. Our novel data indicate significant elevation in various serum triglycerides, particularly the polyunsaturated triglycerides C20:4_C34:3 and C18:2_C38:6, in the PCOS pregnant women. Although, triacylglycerols are not metabolically active, their breakdown products, including fatty acids and diacylglycerols, play important roles in cell signaling (8, 20). Indeed, our subsequent enrichment analysis showed significant elevations in triglycerides containing essential polyunsaturated fatty acid (PUFA) with critical cell signaling properties, namely C20:4 (arachidonic acid), C18:0 (linoleic acid) and C16:0 (palmitic acid) in the PCOS group. Several mass spectrometry-based studies have shown alterations in certain free fatty acids in the serum of PCOS women, including palmitoleic and oleic acids (21, 22). Furthermore, increased serum levels of linoleic acid were reported in PCOS obese patients (21), whereas elevated oleic acid and stearic acid levels were associated with the developmental competence of oocytes, which could contribute to lower pregnancies in PCOS women (21). These PUFAs were previously reported to play important roles in reproductive performance (23–25). Studies have shown that serum levels of arachidonic acid, linoleic acid, and docosahexaenoic acid were decreased in obese PCOS women compared to lean controls (14). This data highlights the important roles of these bioactive lipids in obesity-associated PCOS and PCOS in pregnant women. Previous studies have indicated that free fatty acids represent essential molecular mediators of various metabolic diseases including PCOS as they play a critical role in lipid metabolism with significant impact on cell growth, differentiation and metabolism (14). Oocyte fatty acid composition and their levels in the microenvironment could influence embryogenesis and pregnancy outcome (26, 27), by triggering endoplasmic reticulum stress and influencing oocyte maturation (21).

Our study has also revealed a 10% lower birth weight of babies in PCOS women compared to their matching controls: low birth weight is associated with a range of poor fetal outcomes including increased risk of neonatal death (28). Our data is in accord with previous studies that have reported an increased prevalence of small-for-gestational-age offspring in women with PCOS (5, 29) with no difference in gestational age at delivery. It is recognized that mothers with higher blood pressure had offspring with lower birth weight (30, 31) that we also showed here; however, in addition we report the novel finding of a negative correlation between maternal blood pressure in the second trimester and baby birth weight at delivery that may suggest a functional relationship between baby birth weight and maternal blood pressure as early as the second trimester. When considering potential indicative metabolic biomarkers of birth weight, our data revealed that SBP at delivery was the strongest predictor of low birth weight. Combined with the sphingolipids including the hexosylceramide HexCer (d18:2/24:0), the dihydroceramides Cer (d18:0/24:1) as well as the amino acid serine, these 4 markers best indicated low birth weight in our study.

The underlying mechanism of increased maternal blood pressure and associated lower birth weight is not well

TABLE 2 | Metabolites differentiating controls from PCOS women in their second trimester.

Metabolite	Sup-pathway	Super pathway	Estimate	SE	P value	FDR
TG.20.4_36.3	Triacylglycerols	Lipids	3.8	0.9	0.00007	0.031
TG.18.2_38.6	Triacylglycerols	Lipids	1.4	0.4	0.00020	0.047
TG.20.4_36.4	Triacylglycerols	Lipids	1.9	0.5	0.00036	0.052
TG.22.5_34.2	Triacylglycerols	Lipids	3.0	0.8	0.00067	0.052
TG.18.1_38.6	Triacylglycerols	Lipids	1.8	0.5	0.00083	0.052
TG.20.4_36.2	Triacylglycerols	Lipids	3.7	1.1	0.00087	0.052
TG.20.3_36.3	Triacylglycerols	Lipids	0.7	0.2	0.00109	0.052
TG.18.2_34.2	Triacylglycerols	Lipids	91.6	27.3	0.00133	0.052
DG.16.0_18.2	Diacylglycerols	Lipids	1.4	0.4	0.00136	0.052
DG.18.2_18.2	Diacylglycerols	Lipids	2.7	0.8	0.00167	0.052
TG.20.4_34.2	Triacylglycerols	Lipids	7.6	2.3	0.00169	0.052
TG.20.3_36.4	Triacylglycerols	Lipids	0.4	0.1	0.00176	0.052
TG.18.2_38.4	Triacylglycerols	Lipids	1.7	0.5	0.00182	0.052
TG.22.4_32.0	Triacylglycerols	Lipids	0.7	0.2	0.00183	0.052
TG.16.0_38.6	Triacylglycerols	Lipids	2.7	0.8	0.00187	0.052
Lactate	Carboxylic acids	Glycolysis	838.6	262.8	0.00218	0.052
TG.18.2_38.5	Triacylglycerols	Lipids	1.6	0.5	0.00222	0.052
TG.18.2_36.4	Triacylglycerols	Lipids	15.3	4.8	0.00226	0.052
TG.22.6_34.2	Triacylglycerols	Lipids	3.7	1.2	0.00227	0.052
AconAcid	Carboxylic acids	TCA cycle	0.3	0.1	0.00231	0.052
TG.16.0_40.8	Triacylglycerols	Lipids	0.9	0.3	0.00236	0.052
TG.22.5_32.0	Triacylglycerols	Lipids	1.4	0.4	0.00243	0.052
TG.16.0_38.5	Triacylglycerols	Lipids	4.4	1.4	0.00284	0.058
TG.18.2_36.3	Triacylglycerols	Lipids	30.8	10.1	0.00345	0.067
TG.16.0_40.7	Triacylglycerols	Lipids	1.7	0.6	0.00364	0.067
TG.22.4_34.2	Triacylglycerols	Lipids	1.2	0.4	0.00368	0.067
TG.22.6_32.0	Triacylglycerols	Lipids	1.6	0.5	0.00388	0.067
TG.20.2_34.2	Triacylglycerols	Lipids	1.6	0.5	0.00409	0.067
TG.18.0_38.6	Triacylglycerols	Lipids	0.4	0.1	0.00413	0.067
TG.22.5_34.1	Triacylglycerols	Lipids	2.9	1.0	0.00451	0.071
TG.18.2_32.0	Triacylglycerols	Lipids	33.5	11.4	0.00464	0.071
TG.20.4_32.0	Triacylglycerols	Lipids	3.5	1.2	0.00507	0.075
TG.16.0_40.6	Triacylglycerols	Lipids	1.8	0.6	0.00601	0.086
TG.16.0_36.4	Triacylglycerols	Lipids	49.8	17.7	0.00642	0.086
TG.18.1_36.4	Triacylglycerols	Lipids	18.3	6.5	0.00646	0.086
TG.20.3_34.2	Triacylglycerols	Lipids	2.2	0.8	0.00654	0.086
TG.20.4_34.1	Triacylglycerols	Lipids	7.3	2.6	0.00697	0.089
PC.aa.C36.4	Phosphatidylcholine	Lipids	50.1	18.0	0.00718	0.089
TG.17.0_36.4	Triacylglycerols	Lipids	0.6	0.2	0.00787	0.091
TG.20.4_34.3	Triacylglycerols	Lipids	0.8	0.3	0.00787	0.091
TG.22.6_34.1	Triacylglycerols	Lipids	4.2	1.5	0.00792	0.091
TG.20.4_34.0	Triacylglycerols	Lipids	1.1	0.4	0.00847	0.095
TG.20.3_32.0	Triacylglycerols	Lipids	1.2	0.5	0.00908	0.100

Linear regression was performed to identify significant metabolites differentiating Controls from PCOS using the R statistical package after correcting for age, BMI and principle components (PC1 and PC2). Estimate (beta value), SE (standard error), FDR (False Discovery Rate).

characterized. Elevated maternal blood pressure could potentially reflect a compensatory mechanism for placental dysfunction and a consequence of restricted fetal growth (32). The relationship between the two identified ceramides (HexCer.d18.2.24.0 and Cer.d18.0.24) and low birthweight could be reflecting their association with maternal insulin resistance, as our data has shown, causing lower gestational weight. Elevated levels of hexCer were previously shown to be associated with insulin resistance its driven lipotoxicity (33). Previous studies in rats have indicated that high muscle stearoyl- and oleoyl-ceramide content is associated with increased insulin resistance (34). Increased serine levels with lower gestational age could reflect the close correlation between serine levels and IR and obesity. Increased glycolysis may represent the key factor for increased serine serum levels in PCOS patients (35). Whether serine is an independent predictor of low birth weight, or simply an indirect marker for glucose intolerance, abnormal glucose metabolism and insulin resistance, it remains to be investigated. Serine phosphorylation hypothesis may provide a common biological mechanism for the two principal features of PCOS hyperandrogenemia and insulin resistance, however it t remains to be proven (36), however it remains to be verified. Further studies are warranted to characterize the functional relevance and the predictive value of the identified indicators of low birth weight at second trimester for diagnostic and potentially therapeutic interventions.

Study Limitations

Despite the relative low number of participants in the PCOS group, the metabolic differences between PCOS and matching

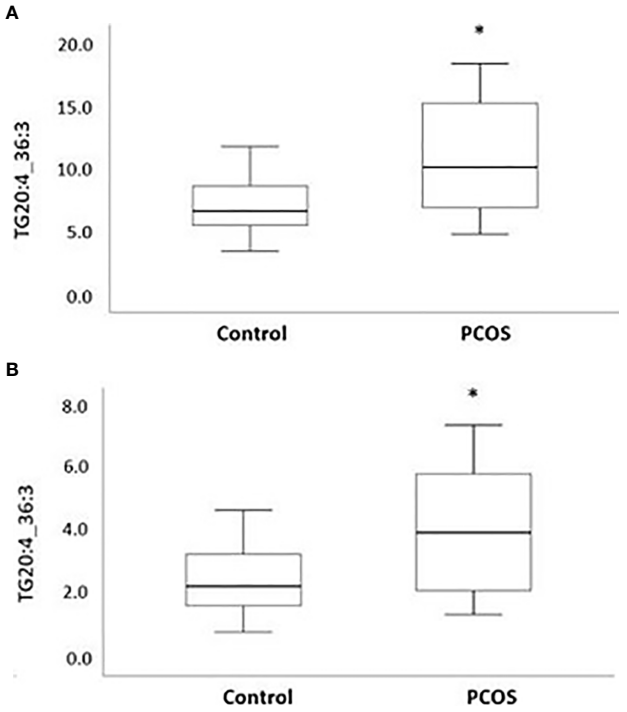

FIGURE 3 | Boxplots representing metabolites increased with PCOS. Differences between controls and PCOS were tested by linear regression. Medians and interquartile range (arbitrary units) are shown for plasma levels of TG20.4_36.3 **(A)** and TG.18.2_38.6 **(B)**. (*) FDR level of significance of ≤ 0.05 was used.

TABLE 3 | List of indicators associated with birth weight.

Predictor	Importance	Beta	P value	AUC (≤2500g)	Adjusted R^2
SBP at delivery	0.22	-0.49	0.003	0.7	0.44
HexCer.d18.2.24.0.	0.14	-0.36	0.02	0.6	
Cer.d18.0.24.1.	0.08	-0.28	0.05	0.6	
Serine	0.06	0.51	0.001	0.4	

controls were large enough to be detected following multiple testing correction. However, larger studies are warranted to rule out the possibility of false negatives due to low study power. Furthermore, the cross-sectional design may have reduced the ability to assess the metabolic changes during pregnancy and the interpretation of data from a pathophysiological angle. Additionally, the observational nature of the study warrants functional validation before inferring any functionality. Other unmeasured factors were not accounted for such as dietary habits, medication and other unknown environmental factors; however, correcting for principle components may have partially accounted for some of these confounders. Larger studies with dynamic measurement of metabolites during pregnancy in different matrixes, combined with functional validation, would certainly improve our understanding of the metabolic signature of PCOS and its impact on pregnancy outcome.

In conclusion, these data indicate differences in the metabolic signature between PCOS and control pregnant women at second trimester, and highlight the indicative potential of triacylglycerols as metabolic markers of low birth weight. This data needs further validation to improve our understanding of

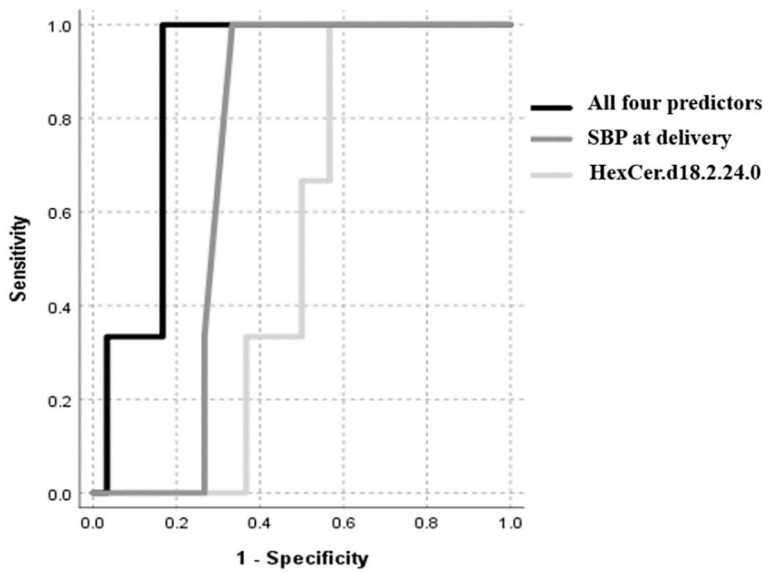

FIGURE 4 | ROC curve of low birth weight (≤2500 grams), including maternal SBP at delivery, HexCer.d18.2.24.0, Cer.d18.0.24.1 and serine.

the pathophysiology of PCOS in pregnancy and its impact on pregnancy outcome.

DATA AVAILABILITY STATEMENT

The datasets used and/or analyzed during the current study are available from the corresponding author on reasonable request.

ETHICS STATEMENT

The studies involving human participants were reviewed and approved by Institutional Review Boards (IRBs) of the Hamad Medical Corporation (15101/15) and Weill Cornell Medicine in Qatar (15-00016). The patients/participants provided their written informed consent to participate in this study.

AUTHOR CONTRIBUTIONS

ID carried out the statistical analysis and wrote the paper. YM, MR, OB, LA, AB, and AA-S helped with data analysis and reviewing the paper. MB and SA were involved in study design, sample collection and data analysis. ME and NM were lead principle investigators, designed the experiments, supervised progress, analyzed data and wrote and approved the final version of the article. ME and NM are responsible for the integrity of the work as a whole. All authors contributed to the article and approved the submitted version.

FUNDING

This research was sponsored by QNRF, Grant no. NPRP10-1205-160010 (NM) and NPRP13S-1230-190008 (ME and NM).

ACKNOWLEDGMENTS

We thank Qatar National Research Fund (QNRF; Grant no. NPRP10-1205-160010) and the Biomedical Research Program funds of Weill Cornell Medicine - Qatar, a program funded by the Qatar Foundation for funding this project. The statements made herein are solely the responsibility of the authors.

SUPPLEMENTARY MATERIAL

The Supplementary Material for this article can be found online at: https://www.frontiersin.org/articles/10.3389/fendo.2021.638727/full#supplementary-material

REFERENCES

1. Soma-Pillay P, Nelson-Piercy C, Tolppanen H, Mebazaa A. Physiological Changes in Pregnancy. *Cardiovasc J Afr* (2016) 27:89–94. doi: 10.5830/CVJA-2016-021
2. Grieger JA, Bianco-Miotto T, Grzeskowiak LE, Leemaqz SY, Poston L, McCowan LM, et al. Metabolic Syndrome in Pregnancy and Risk for Adverse Pregnancy Outcomes: A Prospective Cohort of Nulliparous Women. *PloS Med* (2018) 15:e1002710. doi: 10.1371/journal.pmed.1002710
3. Azziz R, Woods KS, Reyna R, Key TJ, Knochenhauer ES, Yildiz BO. The Prevalence and Features of the Polycystic Ovary Syndrome in an Unselected Population. *J Clin Endocrinol Metab* (2004) 89:2745–9. doi: 10.1210/jc.2003-032046
4. Palomba S, Falbo A, Russo T, Tolino A, Orio F, Zullo F. Pregnancy in Women With Polycystic Ovary Syndrome: The Effect of Different Phenotypes and Features on Obstetric and Neonatal Outcomes. *Fertil Steril* (2010) 94:1805–11. doi: 10.1016/j.fertnstert.2009.10.043
5. Sir-Petermann T, Hitchsfeld C, Maliqueo M, Codner E, Echiburu B, Gazitua R, et al. Birth Weight in Offspring of Mothers With Polycystic Ovarian Syndrome. *Hum Reprod* (2005) 20:2122–6. doi: 10.1093/humrep/dei009
6. Ghazeeri GS, Nassar AH, Younes Z, Awwad JT. Pregnancy Outcomes and the Effect of Metformin Treatment in Women With Polycystic Ovary Syndrome: An Overview. *Acta Obstet Gynecol Scand* (2012) 91:658–78. doi: 10.1111/j.1600-0412.2012.01385.x
7. Guasch-Ferre M, Hruby A, Toledo E, Clish CB, Martinez-Gonzalez MA, Salas-Salvado J, et al. Metabolomics in Prediabetes and Diabetes: A Systematic Review and Meta-Analysis. *Diabetes Care* (2016) 39:833–46. doi: 10.2337/dc15-2251
8. Al-Sulaiti H, Diboun I, Banu S, Al-Emadi M, Amani P, Harvey TM, et al. Triglyceride Profiling in Adipose Tissues From Obese Insulin Sensitive, Insulin Resistant and Type 2 Diabetes Mellitus Individuals. *J Transl Med* (2018) 16:175. doi: 10.1186/s12967-018-1548-x
9. Al-Sulaiti H, Diboun I, Agha MV, Mohamed FFS, Atkin S, Domling AS, et al. Metabolic Signature of Obesity-Associated Insulin Resistance and Type 2 Diabetes. *J Transl Med* (2019) 17:348. doi: 10.1186/s12967-019-2096-8
10. Serkova NJ, Glunde K. Metabolomics of Cancer. *Methods Mol Biol* (2009) 520:273–95. doi: 10.1007/978-1-60327-811-9_20
11. Barderas MG, Laborde CM, Posada M, de la Cuesta F, Zubiri I, Vivanco F, et al. Metabolomic Profiling for Identification of Novel Potential Biomarkers in Cardiovascular Diseases. *J BioMed Biotechnol* (2011) 2011:790132. doi: 10.1155/2011/790132
12. Zhang A, Sun H, Yan G, Wang P, Wang X. Metabolomics for Biomarker Discovery: Moving to the Clinic. *BioMed Res Int* (2015) 2015:354671. doi: 10.1155/2015/354671
13. Zhao X, Xu F, Qi B, Hao S, Li Y, Li Y, et al. Serum Metabolomics Study of Polycystic Ovary Syndrome Based on Liquid Chromatography-Mass Spectrometry. *J Proteome Res* (2014) 13:1101–11. doi: 10.1021/pr401130w
14. Li S, Chu Q, Ma J, Sun Y, Tao T, Huang R, et al. Discovery of Novel Lipid Profiles in PCOS: do Insulin and Androgen Oppositely Regulate Bioactive Lipid Production? *J Clin Endocrinol Metab* (2017) 102:810–21. doi: 10.1210/jc.2016-2692
15. Leite DFB, Morillon AC, Melo Junior EF, Souza RT, McCarthy FP, Khashan A, et al. Examining the Predictive Accuracy of Metabolomics for Small-for-Gestational-Age Babies: A Systematic Review. *BMJ Open* (2019) 9:e031238. doi: 10.1136/bmjopen-2019-031238
16. Feng X, Chen L, Li N, Zhao Y, Han Q, Wang X, et al. Metabolomics Biomarker Analysis of Threatened Abortion in Polycystic Ovary Syndrome: A Clinical Discovery Study. *RSC Adv* (2017) 7:52923–9. doi: 10.1039/C6RA27357B
17. Mahajan UV, Varma VR, Huang CW, An Y, Tanaka T, Ferrucci L, et al. Blood Metabolite Signatures of Metabolic Syndrome in Two Cross-Cultural Older Adult Cohorts. *Int J Mol Sci 21* (2020) 21:1324. doi: 10.3390/ijms21041324
18. Feng C, Wang H, Lu N, Chen T, He H, Lu Y, et al. Log-Transformation and its Implications for Data Analysis. *Shanghai Arch Psychiatry* (2014) 26:105–9. doi: 10.3969/j.issn.1002-0829.2014.02.009
19. Wishart DS, Tzur D, Knox C, Eisner R, Guo AC, Young N, et al. HMDB: The Human Metabolome Database. *Nucleic Acids Res* (2007) 35:D521–6. doi: 10.1093/nar/gkl923

20. Al-Sulaiti H, Diboun I, Domling AS, Elrayess MA. Mediators of Impaired Adipogenesis in Obesity-Associated Insulin Resistance and T2DM, Adipose Tissue - An Update. *IntechOpen* (2019) Book chapter:10.5772/intechopen.88746. doi: 10.5772/intechopen.88746
21. Niu Z, Lin N, Gu R, Sun Y, Feng Y. Associations Between Insulin Resistance, Free Fatty Acids, and Oocyte Quality in Polycystic Ovary Syndrome During In Vitro Fertilization. *J Clin Endocrinol Metab* (2014) 99:E2269–76. doi: 10.1210/jc.2013-3942
22. Pirwany IR, Fleming R, Greer IA, Packard CJ, Sattar N. Lipids and Lipoprotein Subfractions in Women With PCOS: Relationship to Metabolic and Endocrine Parameters. *Clin Endocrinol (Oxf)* (2001) 54:447–53. doi: 10.1046/j.1365-2265.2001.01228.x
23. Szczuko M, Zapalowska-Chwyc M, Drozd A, Maciejewska D, Starczewski A, Stachowska E. Metabolic Pathways of Oleic and Palmitic Acid are Intensified in PCOS Patients With Normal Androgen Levels. *Prostaglandins Leukot Essent Fatty Acids* (2017) 126:105–11. doi: 10.1016/j.plefa.2017.09.001
24. Wathes DC, Abayasekara DR, Aitken RJ. Polyunsaturated Fatty Acids in Male and Female Reproduction. *Biol Reprod* (2007) 77:190–201. doi: 10.1095/biolreprod.107.060558
25. Ciepiela P, Baczkowski T, Drozd A, Kazienko A, Stachowska E, Kurzawa R. Arachidonic and Linoleic Acid Derivatives Impact Oocyte ICSI Fertilization–a Prospective Analysis of Follicular Fluid and a Matched Oocyte in a 'One Follicle–One Retrieved Oocyte–One Resulting Embryo' Investigational Setting. *PloS One* (2015) 10:e0119087. doi: 10.1371/journal.pone.0119087
26. Baka S, Malamitsi-Puchner A. Novel Follicular Fluid Factors Influencing Oocyte Developmental Potential in IVF: A Review. *Reprod BioMed Online* (2006) 12:500–6. doi: 10.1016/S1472-6483(10)62005-6
27. Marei WF, Wathes DC, Fouladi-Nashta AA. Impact of Linoleic Acid on Bovine Oocyte Maturation and Embryo Development. *Reproduction* (2010) 139:979–88. doi: 10.1530/REP-09-0503
28. Negrato CA, Gomes MB. Low Birth Weight: Causes and Consequences. *Diabetol Metab Syndr* (2013) 5:49. doi: 10.1186/1758-5996-5-49
29. Anderson H, Fogel N, Grebe SK, Singh RJ, Taylor RL, Dunaif A. Infants of Women With Polycystic Ovary Syndrome Have Lower Cord Blood Androstenedione and Estradiol Levels. *J Clin Endocrinol Metab* (2010) 95:2180–6. doi: 10.1210/jc.2009-2651
30. Walker BR, McConnachie A, Noon JP, Webb DJ, Watt GC. Contribution of Parental Blood Pressures to Association Between Low Birth Weight and Adult High Blood Pressure: Cross Sectional Study. *BMJ* (1998) 316:834–7. doi: 10.1136/bmj.316.7134.834
31. Lim WY, Lee YS, Tan CS, Kwek K, Chong YS, Gluckman PD, et al. The Association Between Maternal Blood Pressures and Offspring Size At Birth in Southeast Asian Women. *BMC Pregnancy Childbirth* (2014) 14:403. doi: 10.1186/s12884-014-0403-1
32. Parmar P, Lowry E, Vehmeijer F, El Marroun H, Lewin A, Tolvanen M, et al. Understanding the Cumulative Risk of Maternal Prenatal Biopsychosocial Factors on Birth Weight: A DynaHEALTH Study on Two Birth Cohorts. *J Epidemiol Community Health* (2020) 74:933–41. doi: 10.1136/jech-2019-213154
33. Lair B, Laurens C, Van Den Bosch B, Moro C. Novel Insights and Mechanisms of Lipotoxicity-Driven Insulin Resistance. *Int J Mol Sci* (2020) 21(17):6358. doi: 10.3390/ijms21176358
34. Blachnio-Zabielska AU, Chacinska M, Vendelbo MH, Zabielski P. The Crucial Role of C18-Cer in Fat-Induced Skeletal Muscle Insulin Resistance. *Cell Physiol Biochem* (2016) 40:1207–20. doi: 10.1159/000453174
35. Zhao Y, Fu L, Li R, Wang LN, Yang Y, Liu NN, et al. Metabolic Profiles Characterizing Different Phenotypes of Polycystic Ovary Syndrome: Plasma Metabolomics Analysis. *BMC Med* (2012) 10:153. doi: 10.1186/1741-7015-10-153
36. Bremer AA, Miller WL. The Serine Phosphorylation Hypothesis of Polycystic Ovary Syndrome: A Unifying Mechanism for Hyperandrogenemia and Insulin Resistance. *Fertil Steril* (2008) 89:1039–48. doi: 10.1016/j.fertnstert.2008.02.091

Conflict of Interest: The authors declare that the research was conducted in the absence of any commercial or financial relationships that could be construed as a potential conflict of interest.

The handling editor declared a past co-authorship with one of the authors MR.

frontiers in Endocrinology

ORIGINAL RESEARCH
published: 24 June 2021
doi: 10.3389/fendo.2021.628907

Identification of Key Pathways and Genes in Obesity Using Bioinformatics Analysis and Molecular Docking Studies

Harish Joshi[1†], *Basavaraj Vastrad*[2†], *Nidhi Joshi*[3†], *Chanabasayya Vastrad*[4*†], *Anandkumar Tengli*[5†] *and Iranna Kottureshetti*[6†]

[1] Department of Endocrinology, Endocrine and Diabetes Care Center, Hubbali, India, [2] Department of Biochemistry, Basaveshwar College of Pharmacy, Gadag, India, [3] Department of Medicine, Dr. D. Y. Patil Medical College, Kolhapur, India, [4] Biostatistics and Bioinformatics, Chanabasava Nilaya, Bharthinagar, Dharwad, India, [5] Department of Pharmaceutical Chemistry, JSS College of Pharmacy, Mysuru and JSS Academy of Higher Education & Research, Mysuru, India, [6] Department of Ayurveda, Rajiv Gandhi Education Society's Ayurvedic Medical College, Ron, India

OPEN ACCESS

Edited by:
Stephen Atkin,
Royal College of Surgeons in Ireland, Bahrain

Reviewed by:
Weidong Zhao,
Dali University, China
Jinhui Liu,
Nanjing Medical University, China

***Correspondence:**
Chanabasayya Vastrad
channu.vastrad@gmail.com

†ORCID:
Harish Joshi
orcid.org/0000-0002-3817-5194
Basavaraj Vastrad
orcid.org/0000-0003-2202-7637
Nidhi Joshi
orcid.org/0000-0001-8067-3448
Chanabasayya Vastrad
orcid.org/0000-0003-3615-4450
Anandkumar Tengli
orcid.org/0000-0001-8076-928X
Iranna Kottureshetti
orcid.org/0000-0003-1988-7345

Specialty section:
This article was submitted to Systems Endocrinology, a section of the journal Frontiers in Endocrinology

Received: 13 November 2020
Accepted: 19 May 2021
Published: 24 June 2021

Citation:
Joshi H, Vastrad B, Joshi N, Vastrad C, Tengli A and Kottureshetti I (2021) Identification of Key Pathways and Genes in Obesity Using Bioinformatics Analysis and Molecular Docking Studies. Front. Endocrinol. 12:628907. doi: 10.3389/fendo.2021.628907

Obesity is an excess accumulation of body fat. Its progression rate has remained high in recent years. Therefore, the aim of this study was to diagnose important differentially expressed genes (DEGs) associated in its development, which may be used as novel biomarkers or potential therapeutic targets for obesity. The gene expression profile of E-MTAB-6728 was downloaded from the database. After screening DEGs in each ArrayExpress dataset, we further used the robust rank aggregation method to diagnose 876 significant DEGs including 438 up regulated and 438 down regulated genes. Functional enrichment analysis was performed. These DEGs were shown to be significantly enriched in different obesity related pathways and GO functions. Then protein–protein interaction network, target genes - miRNA regulatory network and target genes - TF regulatory network were constructed and analyzed. The module analysis was performed based on the whole PPI network. We finally filtered out STAT3, CORO1C, SERPINH1, MVP, ITGB5, PCM1, SIRT1, EEF1G, PTEN and RPS2 hub genes. Hub genes were validated by ICH analysis, receiver operating curve (ROC) analysis and RT-PCR. Finally a molecular docking study was performed to find small drug molecules. The robust DEGs linked with the development of obesity were screened through the expression profile, and integrated bioinformatics analysis was conducted. Our study provides reliable molecular biomarkers for screening and diagnosis, prognosis as well as novel therapeutic targets for obesity.

Keywords: adiposities, obesity, differentially expressed genes, modules, protein–protein interaction network

INTRODUCTION

Obesity has long been part of the larger metabolic disorder and affects a large proportion of the global population particularly in the Western World (1). Obesity is diagnosed on the basis of body mass index (1). Obesity occurs in children age between 5 to 19 years as well as more common in women than in men (2). Countless surveys have proved that obesity is an key risk factor for heart

disease (3), hyperlipidaemia (4), hyperinsulinaemia (5), hypertension (6), atherosclerosis (7), insulin resistance (8) and cancer (9). Important candidate genes and relevant signaling pathways linked with obesity remains largely unknown. As a result, seek of an earlier diagnosis and better prognosis, deeper understanding of genetic and molecular mechanisms about obesity is necessary.

Previous reports demonstrate that many genes and signaling pathways participate in obesity. Polymorphisms in UCP2 and UCP3 were responsible for development of obesity (10). TNFα and lipoprotein lipase were important for advancement of obesity (11). SLC6A14 (12) and JHDM2A (13) were lined with pathogenesis of obesity. Human salivary (AMY1) and pancreatic (AMY2) amylase genes were diagnosed with growth of obesity (14). Signaling pathways such as inflammatory signaling pathway (15), TLR4 signaling pathway (16), calcineurin-dependent signaling pathways (17), mTOR Complex1–S6K1 signaling pathway (18) and leptin-signaling pathway (19) were important for development of obesity. Therefore, it is meaningful to explore the precise molecular mechanisms involved in obesity and thus find a valid diagnostic way and generate an advance therapeutic strategy.

In present trends, the application of high-throughput analysis in gene expression profiling is becoming more valuable in clinical and medical research (20), molecular classification (21), prognosis prediction (22), diagnoses (23) and new targeted drug discovery (24). In this study, the original microarray data (E-MTAB-6728) was downloaded from ArrayExpress database (https://www.ebi.ac.uk/) and analyzed to get differently expressed genes (DEGs) between obesity persons and lean persons (normal controls). Subsequently, gene ontology (GO), pathway enrichment analysis, protein–protein interaction network construction and analysis, module analysis, target gene - miRNA interaction network construction and analysis, and target gene - TF interaction network construction and analysis to discover the key genes and pathways closely related to obesity. Finally, selected hub genes were validated by immunohistochemical (IHC) analysis, receiver operating characteristic curve (ROC) analysis and RT-PCR. This current investigation aimed at using bioinformatics tools to predict the key pathways and genes in obesity that can hold a value for target based therapeutic means.

MATERIALS AND METHODS

Microarray Data

The microarray expression profile of E-MTAB-6728 was downloaded from ArrayExpress (https://www.ebi.ac.uk/). E-MTAB-6728 was based on A-MEXP-1171 - Illumina HumanHT-12 v3.0 Expression BeadChip and was submitted by Bjune et al. (25). The E-MTAB-6728 dataset about expression of genes from obesity persons compared to lean persons (normal controls).There are twenty-four samples including twelve obesity persons and lean persons (normal controls). The overall design of the experiment was microarray analysis of adiposities from obese patients versus adipocytes from lean persons (controls).

Identification of DEGs

The raw data files were acquired for the analysis as IDAT files (Illumina platform) forms and were converted into gene symbols and then processed to background correction and quantile data normalization using the effective multiarray average algorithm in the beadarray package (26). The analysis was carried out *via* R software (version 3.5.2). Hierarchical clustering analysis was applied to categorize the samples into two groups with similar expression patterns in obesity persons and lean persons (normal controls). The paired Student's t-test based on the Limma package in R bioconductor was used to diagnose DEGs between two experimental conditions (27). Multiple testing corrections were performed by the Benjamini–Hochberg method (28). Then, the Log2 Fold change (log_2FC) was determined. We selected up regulated DEGs with $| log_2FC | > 0.524$ and FDR < 0.05, and down regulated DEGs with $| log_2FC | < -0.394$ and FDR < 0.05 were considered as the cutoff values.

Pathway and Gene Ontology (GO) Enrichment Analysis of DEGs

The BIOCYC, Kyoto Encyclopedia of Genes and Genomes (KEGG), REACTOME, Pathway Interaction Database (PID), GenMAPP, MSigDB C2 BIOCARTA, PantherDB, Pathway Ontology and Small Molecule Pathway Database (SMPDB) databases are a knowledge base for systematic analysis, annotation, and visualization of gene functions. The GO database can add functional classification for genomic data, including categories of biological processes (BP), cellular component (CC), and molecular function (MF). GO analysis is a prevalent genes and gene products annotating approach. ToppCluster (https://toppcluster.cchmc.org/) (29) is an online tool for gene functional classification, which is a key foundation for high-throughput gene analysis to understand the biological importance of genes. In the current investigation, in order to analyze the functions of DEGs, Pathway and GO enrichment analysis were conducted using the ToppCluster online tool; $p<0.05$ was set as the cutoff point.

Integration of PPI Network and Module Analysis

The mentha (https://mentha.uniroma2.it/) (30) is a biological database designed to predict protein-protein interaction (PPI) information. The DEGs were mapped to STRING to evaluate the interactive relationships, with a confidence score >0.9 defined as significant. Then, integration of protein-protein interaction (PPI) network was visualized using cytoscape software (version 3.8.2) (http://www.cytoscape.org/) (31). The plug-in Network Analyzer identified hub genes based on mathematical calculation methods such as node degree (32), betweenness (33), stress (34) and closeness (35) the number of genes within centrality mathematical calculation methods were represented the significance of the disorder. The PEWCC1 was applied to screen modules of PPI network with degree cutoff = 2, node score cutoff = 0.2, k-core = 2, and max. depth = 100 (36). The functional enrichment analysis in the module was performed by ToppCluster.

Construction of Target Genes - miRNA Regulatory Network

MiRNA of target genes were explored combined with the human miRNA information (miRNet database, (https://www.mirnet.ca/) (37), recorded using TarBase, miRTarBase, miRecords, miR2Disease, HMDD, SM2miR, PhenomiR, PharmacomiR, EpimiR and starBase databases, and visualized using the Cytoscape software (31).

Construction of Target Genes - TF Regulatory Network

TFs of hub genes were explored combined with the human TF information (NetworkAnalyst database, http://www.networkanalyst.ca) (38), recorded using ENCODE database, and visualized using the Cytoscape software (31).

Validation of Hub Genes

Immunohistochemical (IHC) analysis of adipose tissues was performed utilizing human protein atlas (www.proteinatlas.org) (39). ROC analysis was performed using pROC package (40) in R. ROC analyses were estimated for diagnostic value of hub genes. When the AUC value was > 0.7, the hub genes were considered to be capable of distinguishing obesity persons from normal lean with excellent specificity and sensitivity.

Detection of the mRNA Expression of the Hub Genes by RT-PCR

D12 (ATCC CRL-3280) cell line for obesity and D16 (ATCC CRL-3281) cell line a normal control were purchased from the American Type Culture Collection (ATCC) (Maryland, USA). D12 cells were cultured in Dulbecco's modified Eagle's medium (DMEM) F12 medium, which contains 10% fetal bovine serum. D16 cells were cultured in Dulbecco's modified Eagle's medium (DMEM) F12 medium, which contains 10% fetal bovine serum. The culture temperature is 37°C and CO2 concentration is 5%. Total cellular RNA was extracted from cell culture with 1 ml TRI Reagent® (Sigma, USA). Reverse transcription cDNA kit (Thermo Fisher Scientific, Waltham, MA, USA) and random primers were used to synthesize cDNA. RT-PCR was performed using QuantStudio 7 Flex real-time PCR system (Thermo Fisher Scientific, Waltham, MA, USA). The conditions for RT-PCR amplification were as follows: 95°C for 120 seconds followed by 40 cycles of 95°C for 15 seconds, annealing temperature for 45 seconds. Each sample was run in triplicate. Relative expression level for each target gene was normalized by the Ct value of β-actin (internal control) using a $2^{-\Delta\Delta CT}$ relative quantification method (41). The primer pairs used in the experiments are listed in **Supplementary Table 1**.

Molecular Docking Studies

The module SYBYL-X 2.0 perpetual software was used for Surflex-Docking of the designed molecules. The molecules were sketched by using ChemDraw Software and imported and saved in sdf. format using Openbabelfree software. The one co-crystallized protein from each of ERBB2, STAT3 and HSPAB8 were selected for docking studies. The protein structures of ERBB2, STAT3 and HSPAB8 of PDB code 1MFL, 5OOW and 3CWG was retrieved from Protein Data Bank (42–44). Together with the TRIPOS force field, GasteigerHuckel (GH) charges were added to all designed molecules and the standard ant-obesity drug Orlistat, for the structure optimization process. In addition, energy minimization was carried out using MMFF94s and MMFF94 algorithm process. Protein processing was carried out after the incorporation of protein. The co-crystallized ligand and all water molecules were removed from the crystal structure; more hydrogen's were added and the side chain was set. TRIPOS force field was used for the minimization of structure. The designed molecules interaction efficiency with the receptor was represented by the Surflex-Dock score in kcal/mol units. The interaction between the protein and the ligand, the best pose was incorporated into the molecular area. The visualization of ligand interaction with receptor is done by using discovery studio visualizer.

RESULTS

Data Normalization

Each array was normalized (centered) by quantile data normalization using the beadarray package in R bioconductor. As shown in **Figures 1A, B**, raw expression data were normalized after preprocessing; median-centered values demonstrated that the data were normalized and thus it was possible to cross-compare between obesity persons and lean persons (normal controls).

Identification of DEGs Between Obese Patients and Lean Persons

To preliminarily understand the mechanism contributing to the obesity, 24 patients [12 obesity persons and 12 lean persons (normal controls)] were selected for subsequent analysis. Based on the analysis, a total of 876 DEG compose of 438 genes had been expressed highly and about 438 genes had been shown to decrease expression in obesity and are listed in **Supplementary Table 2**. The FDR <0.05 was as a threshold value. Heat map is shown in **Figure 2**. Volcano plot for DEGs is shown in **Figure 3**.

Pathway and Gene Ontology (GO) Enrichment Analysis of DEGs

To further investigate the biologic functions and mechanisms of the DEGs, pathway and GO enrichment analyses were performed using ToppCluster tool. Pathway enrichment analysis revealed that the up regulated genes were mainly enriched in thyroid hormone metabolism II (via conjugation and/or degradation), ECM-receptor interaction, IL6-mediated signaling events, collagen formation, C21 steroid hormone metabolism, genes encoding collagen proteins, integrin signalling pathway, hypertension and suprofen pathway, and are listed in **Supplementary Table 3**. Similarly, down regulated genes were mainly enriched in superpathway of methionine degradation, ribosome, FoxO family signaling, eukaryotic translation elongation, propanoate metabolism, CDK regulation of DNA replication, p38 MAPK pathway, glycine, serine and threonine metabolic, and glycine, serine and

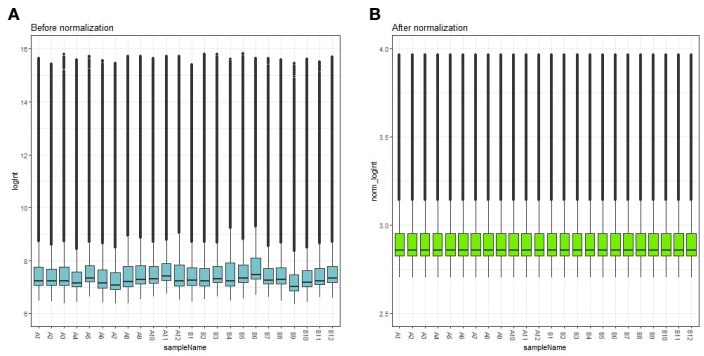

FIGURE 1 | Box plots of the gene expression data before **(A)** and after normalization **(B)**. Horizontal axis represents the sample symbol and the vertical axis represents the gene expression values. The black line in the box plot represents the median value of gene expression. (A1-A12 = adipocytes from lean persons; B1-B12 = adipocytes from obese patients).

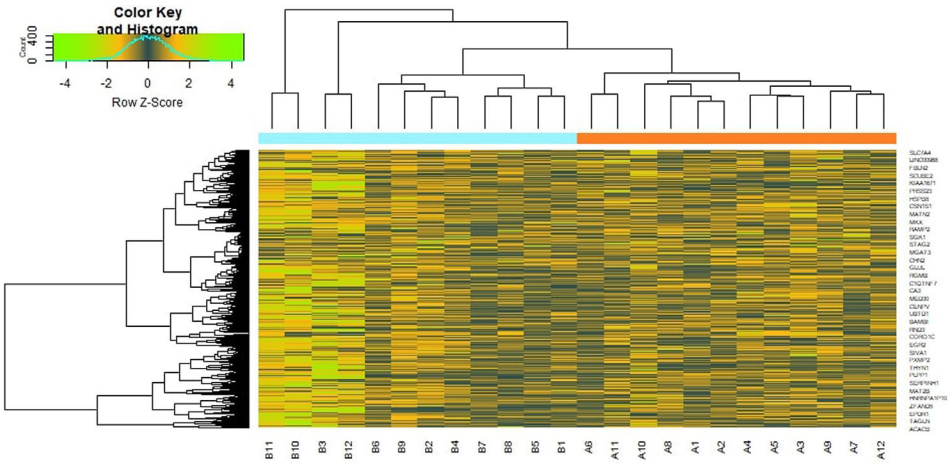

FIGURE 2 | Heat map of differentially expressed genes.

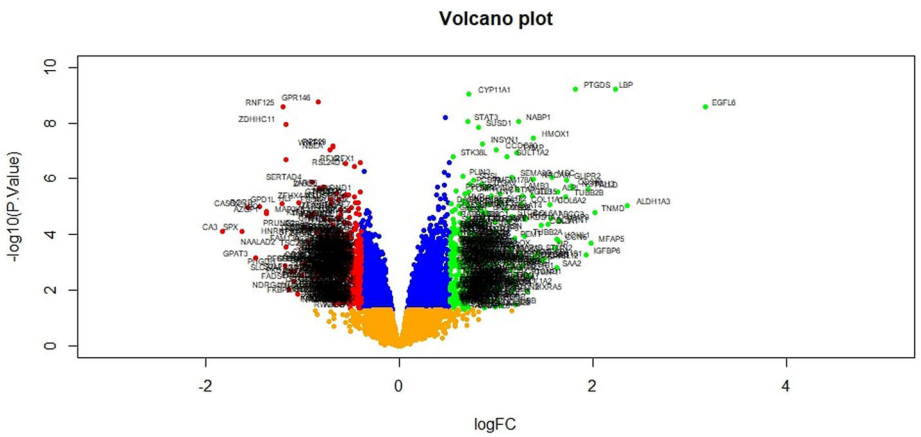

FIGURE 3 | Volcano plot of differentially expressed genes. Genes with a significant change of more than two-fold were selected.

threonine metabolism, and are listed in **Supplementary Table 4**. GO analysis results showed that up regulated genes were significantly enriched in blood vessel morphogenesis, extracellular matrix and growth factor binding, and are listed in **Supplementary Table 5**. Similarly, down regulated genes were mainly enriched in organic acid biosynthetic process, cytosolic small ribosomal subunit and structural constituent of ribosome, and are listed in **Supplementary Table 6**.

Integration of PPI Network and Module Analysis

The PPI network of up regulated genes consisted of 7271 nodes and 16270 edges (**Figure 4**) and down regulated genes consisted of 7276 nodes and 19862 edges (**Figure 5**) constructed in the mentha database and visualized using Cytoscape software. Based on the mentha database, the DEGs with the highest PPI scores identified by the four centrality methods are shown in **Supplementary Table 7**. There are 5 up regulated genes selected as hub genes, such as HSPA8, HSPA5, YWHAH, STAT3 and ERBB2, and 5 down regulated genes selected as hub genes, such as ESR1, ARRB1, CSNK2A2, RBBP4 and NR3C1. A significant module was obtained from PPI network of DEGs using PEWCC1, including module 1 contains 49 nodes and 99 edges (**Figure 6A**) and module 2 contains 66 nodes and 754 edges (**Figure 6B**). Functional enrichment analysis revealed that genes in these modules were mainly involved in PI3K-Akt signaling pathway, regulation of nuclear SMAD2/3 signaling, ribosome, eukaryotic translation elongation, metabolism of amino acids and derivatives, disease,

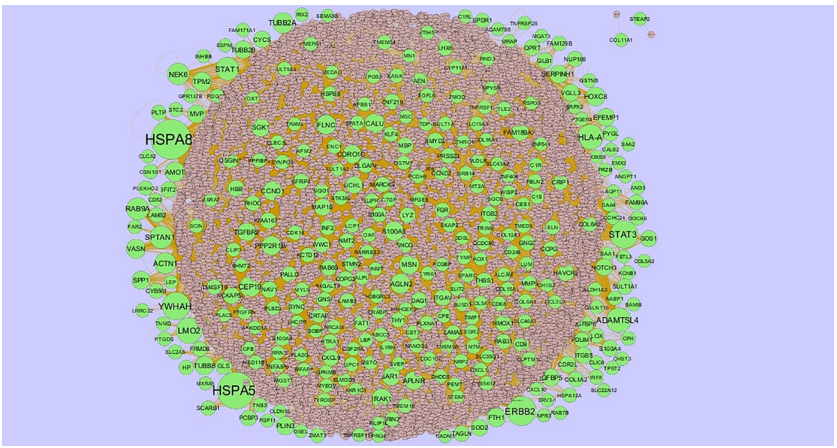

FIGURE 4 | Protein–protein interaction network of up regulated genes. Green nodes denotes up regulated genes.

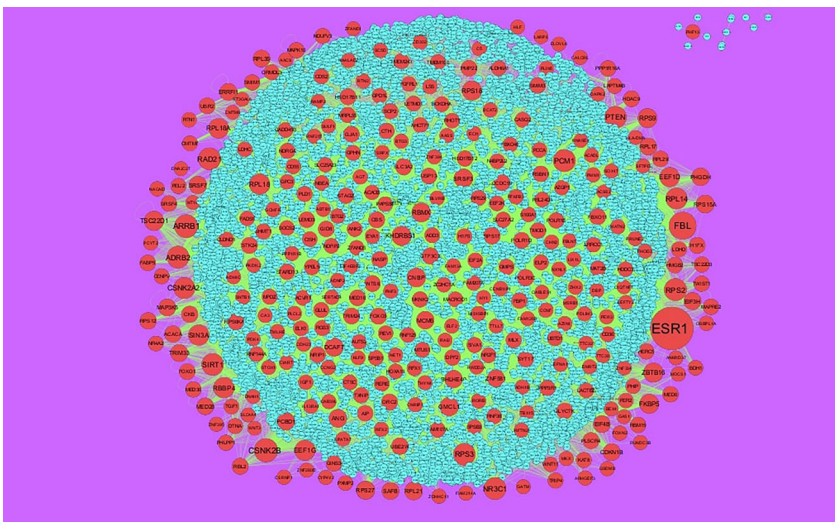

FIGURE 5 | Protein–protein interaction network of down regulated genes.

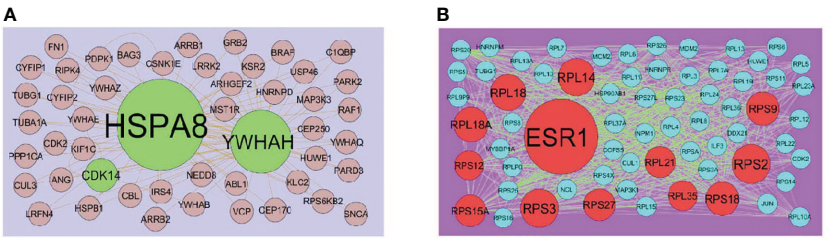

FIGURE 6 | **(A)** Module of up regulated genes. The green nodes denote the up regulated genes **(B)** Module of down regulated genes. The red nodes denote the down regulated genes.

cellular amide metabolic process, establishment of protein localization to endoplasmic reticulum, monocarboxylic acid biosynthetic process translation, translational initiation, macromolecule catabolic process and cytosolic small ribosomal subunit.

Construction of Target Genes - miRNA Regulatory Network

To further understand the regulatory network between miRNAs and target genes, through miRNet database were constructed by Cytoscape. As shown in **Figure 7**, the miRNA-regulated network with 2613 nodes (miRNA: 2261; target gene: 352) and 17260 edges was obtained for up regulated target genes and **Figure 8**, the miRNA-regulated network with 2685 nodes (miRNA: 2327; target gene: 358) and 19827 edges was obtained for down regulated target genes. Different target genes regulated by miRNAs are shown in **Supplementary Table 8**. SOD2 had been predicted to regulate 257 miRNAs (ex; hsa-mir-3144-3p), CCND1 had been predicted to regulate 251 miRNAs (ex; hsa-mir-7706), TUBB2A had been predicted to regulate 193 miRNAs (ex; hsa-mir-5692c), CCND2 had been predicted to regulate 179 miRNAs (ex; hsa-mir-7162-3p), TMEM189 had been predicted to regulate 146 miRNAs (ex; hsa-mir-548z), BTG2 had been predicted to regulate 247 miRNAs (ex; hsa-mir-6075), TXNIP had been predicted to regulate 228 miRNAs (ex; hsa-mir-3194-3p), MED28 had been predicted to regulate 203 miRNAs (ex; hsa-mir-6861-5p), CNBP had been predicted to regulate 197 miRNAs (ex; hsa-mir-4651) and MKNK2 had been predicted to regulate 195 miRNAs (ex; hsa-mir-3650).

Construction of Target Genes - TF Regulatory Network

To further understand the regulatory network between TFs and target genes, through NetworkAnalyst database were constructed by Cytoscape. As shown in **Figure 9**, the TF-regulated network with 629 nodes (TF: 336; Gene: 293) and 6293 edges was obtained for up regulated target genes and **Figure 10**, the TF-regulated network with 2685 nodes (TF: 342; Gene: 299) and 8597 edges was obtained for down regulated target genes. Different target genes regulated by TFs are shown in **Supplementary Table 9**. YWHAH had been predicted to regulate 70 TFs (ex; MAZ), LYZ had been predicted to regulate 62 TFs (ex; TFDP1), HP had been predicted to regulate 60 TFs (ex; KLF9), TRAM2 had been predicted to regulate 54 TFs (ex; KLF16), CCND1 had been predicted to regulate 51 TFs

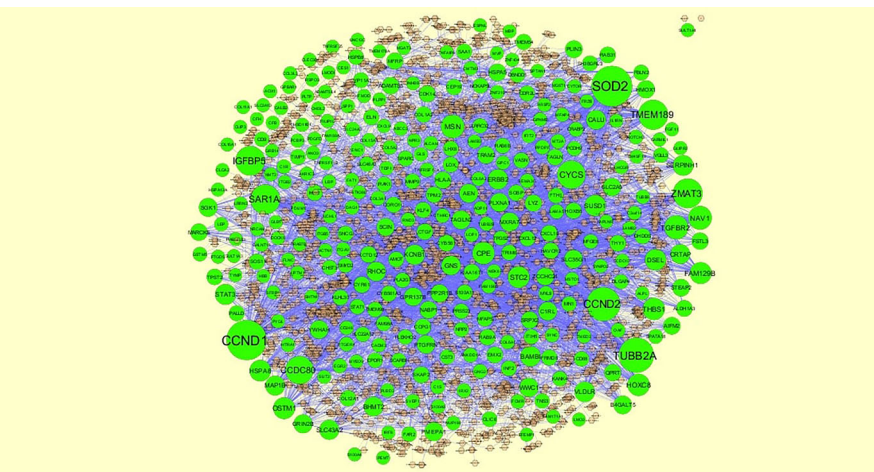

FIGURE 7 | The network of up regulated genes and their related miRNAs. The green circles nodes are the up regulated genes, and chocolate diamond nodes are the miRNAs.

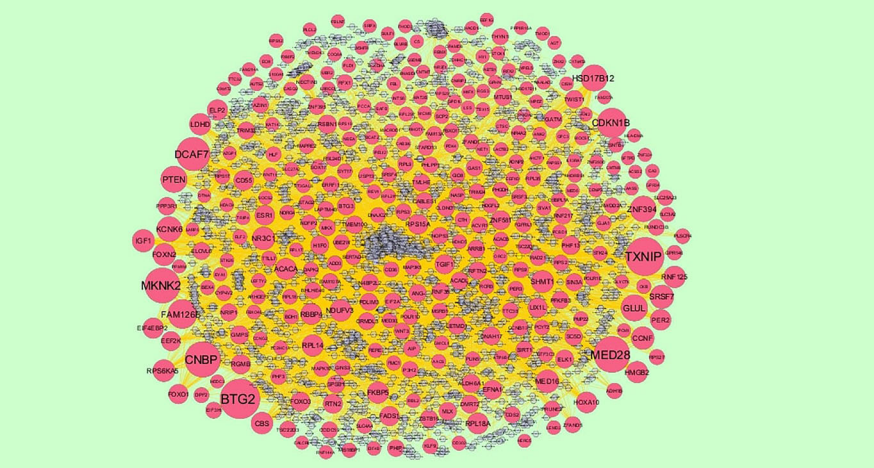

FIGURE 8 | The network of down regulated genes and their related miRNAs. The red circles nodes are the down regulated genes, and chocolate diamond nodes are the miRNAs.

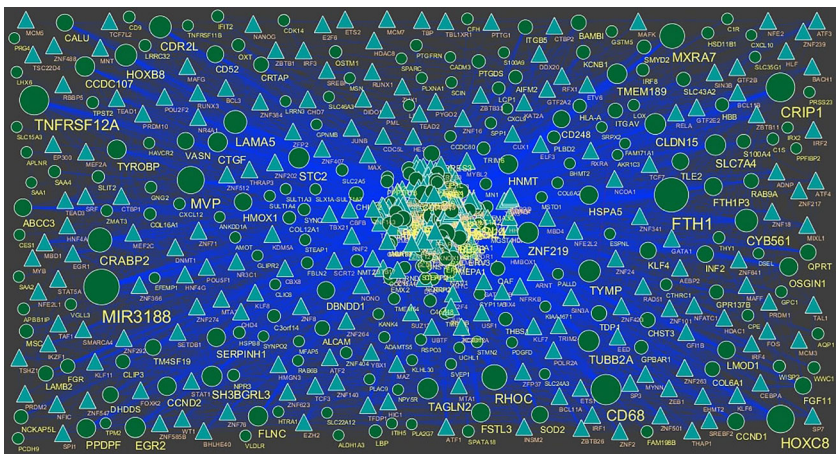

FIGURE 9 | TF - gene network of predicted target up regulated genes. (Blue triangle - TFs and green circles- target up regulated genes).

(ex; EZH2), EFNA1 had been predicted to regulate 91 TFs (ex; TFDP1), MED16 had been predicted to regulate 85 TFs (ex; MAZ), RWDD2A had been predicted to regulate 82 TFs (ex; KDM5B), ADD3 had been predicted to regulate 82 TFs (ex; SAP30) and AIP had been predicted to regulate 82 TFs (ex; PHF8).

Validation of Hub Genes

Immunohistochemical analysis demonstrated that the expression of STAT3, CORO1C, SERPINH1, MVP and ITGB5 were highly expressed in adipose tissues, whereas PCM1, SIRT1, EEF1G, PTEN and RPS2 were low expressed in adipose tissue (**Figure 11I**) and Box plots is showed in **Figure 11II**. Validated by ROC curves, we found that 10 hub genes had high sensitivity and specificity, including STAT3 (0.951), CORO1C (0.799), SERPINH1 (0.924), MVP (0.938), ITGB5 (0.938), PCM1 (0.826), SIRT1 (0.799), EEF1G (0.913), PTEN (0.833) and RPS2 (0.840) (**Figure 12**). The 10 hub genes might be biomarkers of obesity and have positive implications for early medical intervention of the disease.

Detection of the mRNA Expression of the Hub Genes by RT-PCR

The adipocytes were removed to detect the mRNA expression levels of hub genes in the PPI network, including STAT3, CORO1C, SERPINH1, MVP, ITGB5, PCM1, SIRT1, EEF1G, PTEN and RPS2. It was found that the mRNA expression levels of STAT3, CORO1C, SERPINH1, MVP and ITGB5 were significantly increased in the obesity compared with the control group. Furthermore, the results illustrate that the mRNA expression levels of PCM1, SIRT1, EEF1G, PTEN and

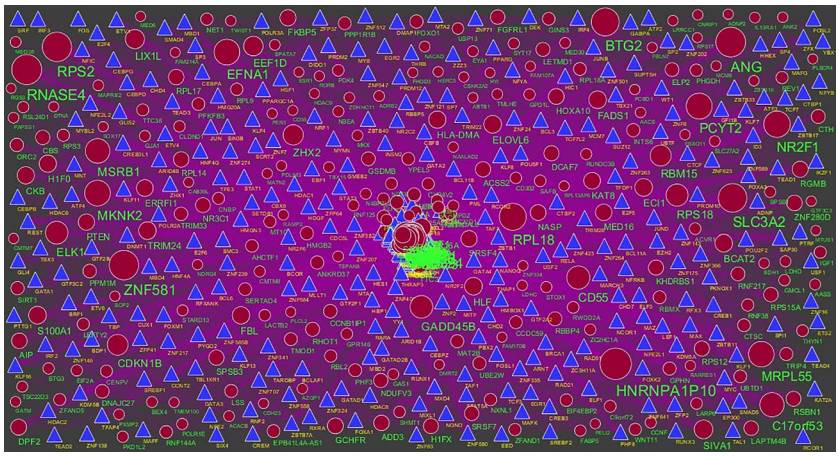

FIGURE 10 | TF-gene network of predicted target down regulated genes. (Blue triangle - TFs and red circles- target up regulated genes).

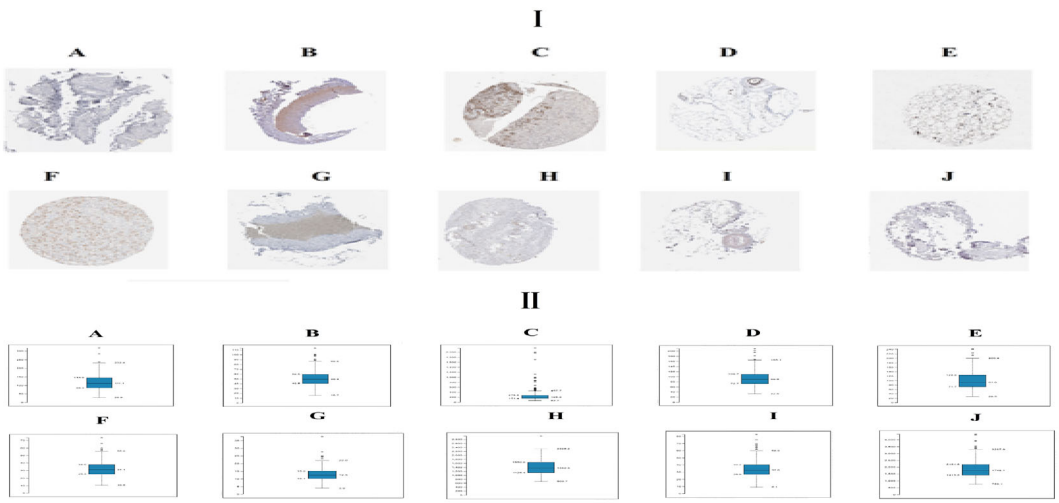

FIGURE 11 | I) Immunohisto chemical I (IHC) analyses of hub genes were produced using the human protein atlas (HPA) online platform. II) Box plot for IHC analysis of hub genes **(A)** STAT3 **(B)** CORO1C **(C)** SERPINH1 **(D)** MVP **(E)** ITGB5 **(F)** PCM1 **(G)** SIRT1 **(H)** EEF1G **(I)** PTEN **(J)** RPS2.

RPS2 were significantly decreased in the obesity compared with the control group (**Figure 13**). Therefore, the RT-PCR results of the hub genes were consistent with the bioinformatics analysis.

Molecular Docking Studies

In the present research, the docking simulations are performed to identify the active site conformation and major interactions responsible for complex stability with the ligand receptor. Designed novel molecules containing four membered more sensitive β-lactam ring, the four membered and performed docking studies using Sybyl X 2.1 drug design software. Molecules containing β-lactam ring is designed which is easily reacting group **Figure 14A**, based on the structure of anti-obesity drug orlistatfour membered ring **Figure 14B**, has potent pancreatic lipase inhibitory activity. The molecules were designed based on the structure of the standard anti-obesity drug orlistat. The one protein in each of three over expressed genes of ERBB2, its co-crystallized protein of PDB code 1MFL,HSPAB 8its co-crystallized protein of PDB code 5OOW and STAT 3its co-crystallized protein of PDB code of 3CWG respectively selected for docking studies. The investigation of designed molecules was performed to identify the potential molecule. The most of the designed molecules with respect to the standard anti-obesity drug orlistat, obtained C-score greater than 5. The C-score greater than 5 are said to be an active, among total of 32 designed molecules few molecules have excellent good binding energy (C-score) greater than 7 respectively.

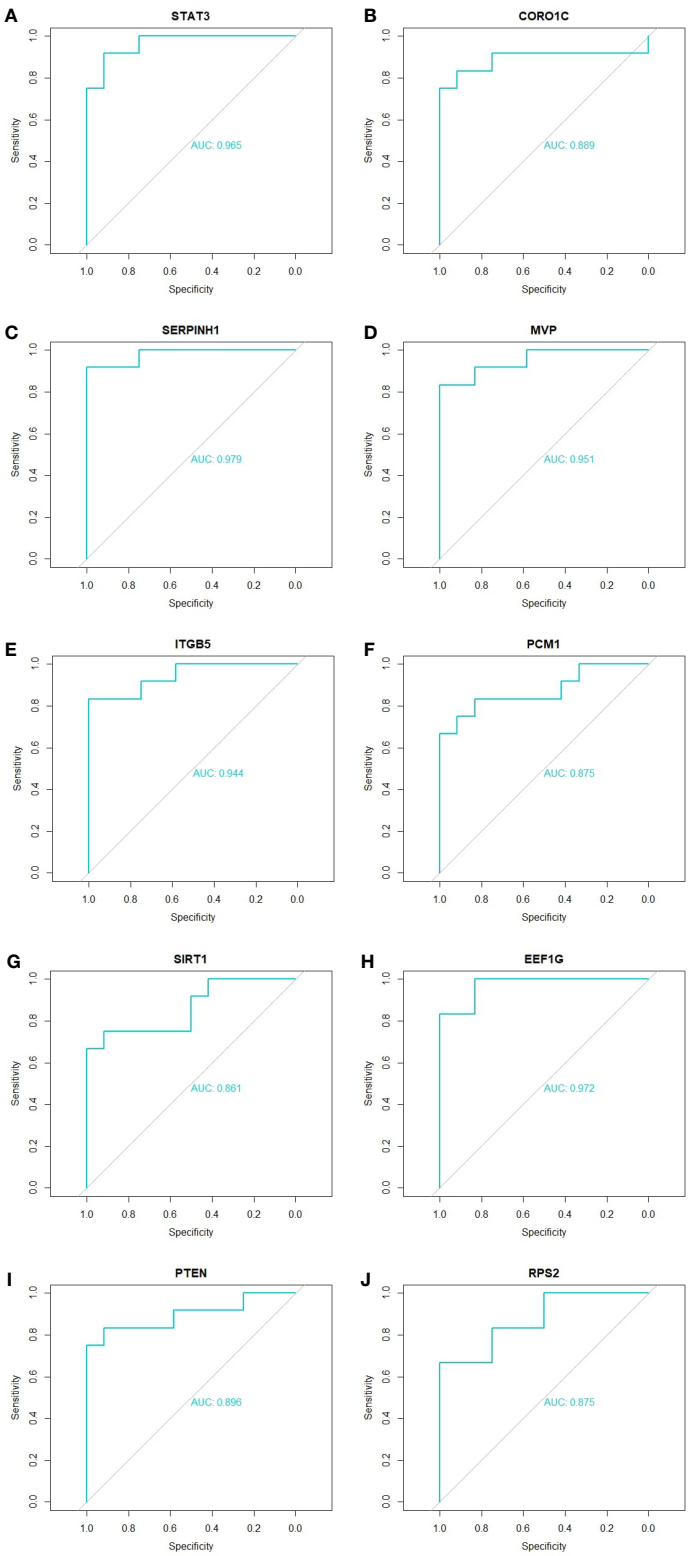

FIGURE 12 | ROC curve validated the sensitivity, specificity of hub genes as a predictive biomarker for obesity prognosis. **(A)** STAT3 **(B)** CORO1C **(C)** SERPINH1 **(D)** MVP **(E)** ITGB5 **(F)** PCM1 **(G)** SIRT1 **(H)** EEF1G **(I)** PTEN **(J)** RPS2.

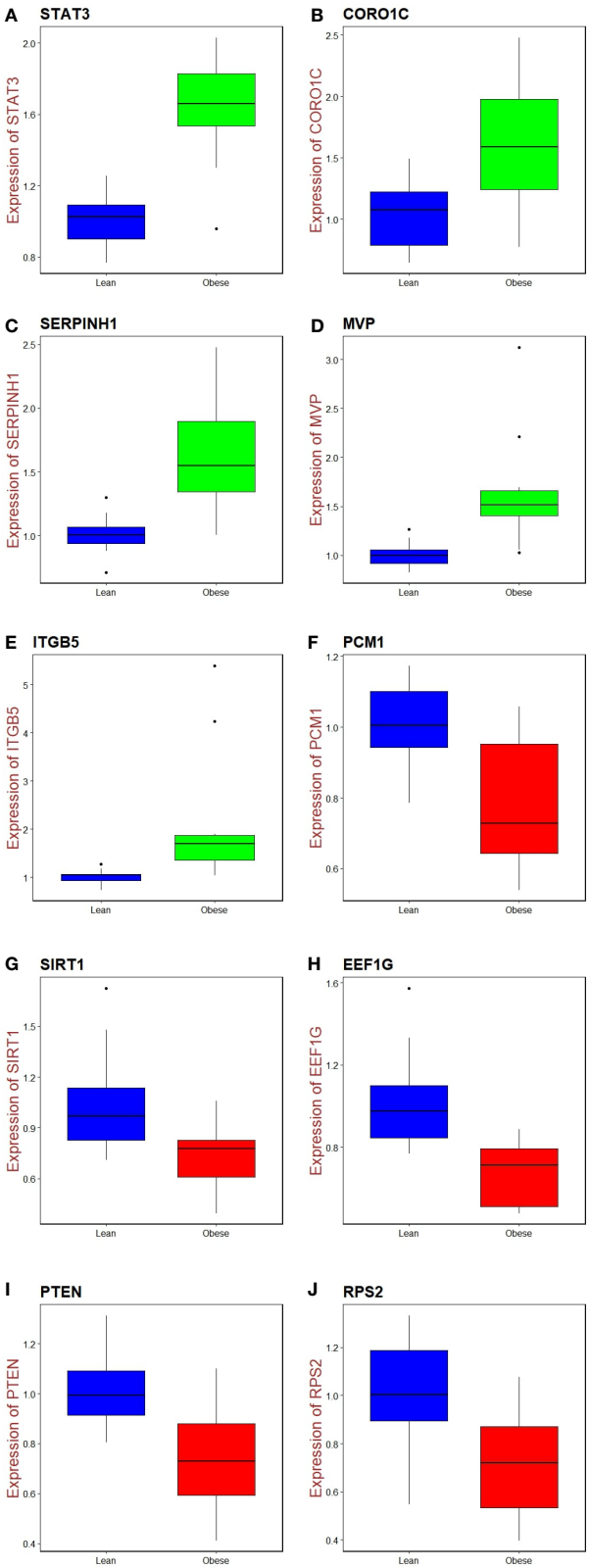

FIGURE 13 | Validation of hub genes by RT- PCR. **(A)** STAT3 **(B)** CORO1C **(C)** SERPINH1 **(D)** MVP E) ITGB5 **(F)** PCM1 **(G)** SIRT1 **(H)** EEF1G **(I)** PTEN **(J)** RPS2.

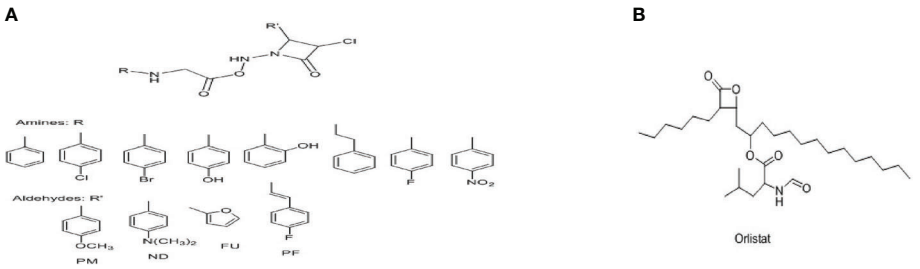

FIGURE 14 | **(A)** Scheme of designed molecule **(B)** Structure of orlistat.

The molecule ND4, FU5 and PF5 obtained score of 7.242, 7.659 and 7.842 with 1MFL and the molecules PM6, ND1, ND3, ND5, ND6, PF5 and PF6 obtained score of 7.5269, 7.6271, 8.0824, 7.6595, 7.0792 and 7.2659 with 3 CWG and the molecules PM4, PM6, ND1, ND5, ND6, PF4, and PF obtained good binding score of 7.1631, 8.8312, 7.3781, 7.9872, 7.9567, 7.0213 and 7.0386 with 5OOW respectively. The molecules found binding score 5-6 is PM1, PM2, PM3, PM4, PM5, PM6, PM7, PM8, ND1, ND2, ND3, ND5, ND6, ND7, ND8, FU1, FU2, FU3, FU4, FU7, FU8, PF1, PF2, PF3, PF4, PF6, PF7, PF8 and standard olistat (STD) with 1MFL and PM2, PM6, FU17, FU18, FU19, FU20, FU23, PF26, PF27, PF28 and PF32 with 3CWG, and PM1, PM2, PM3, PM5, PM7, PM8, ND2, ND3, ND4, ND7, ND8, FU1, FU2, FU3, FU4, FU5, FU6, FU7, FU8, PF1, PF2, PF3, PF6, PF7 and PF8 5OOW respectively. No molecules obtained binding score with less than 5 respectively; the values are depicted in **Supplementary Table 10**. The molecule PF5 has good binding score with all three proteins and ND1, ND3, ND5 and ND6 obtained good binding score with 3CWG and 5OOW. The molecule ND5 has highest binding score and is very close with standard olistat, the interaction with protein 5OOW and hydrogen bonding and other bonding interactions with amino acids are depicted by 3D (**Figure 15**) and 2D (**Figure 16**) images.

DISCUSSION

Due to the heterogeneity of obesity, obesity was still a disease with high rates of prevalence. This might be due to the scarcity of

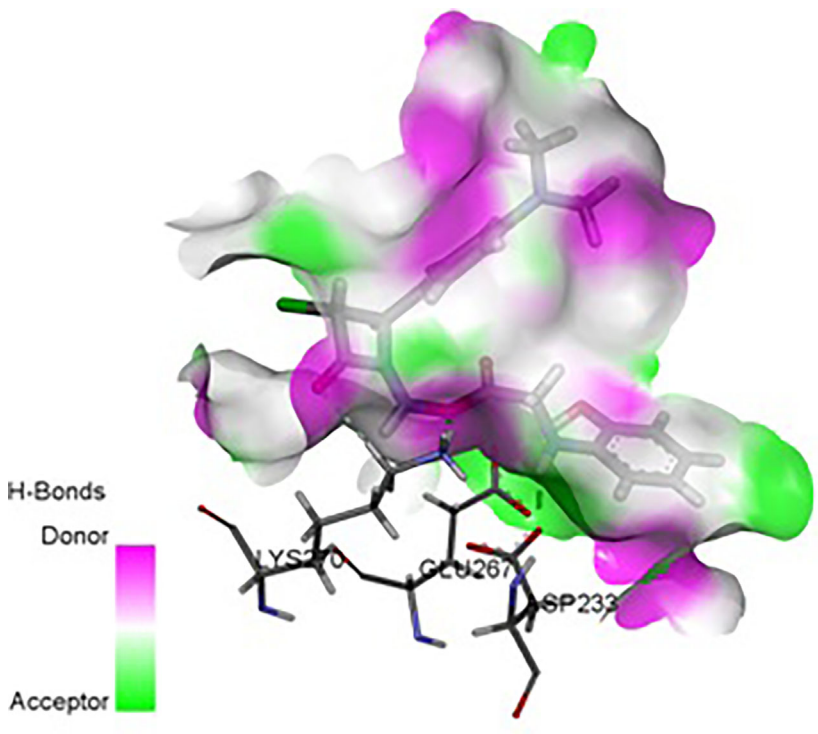

FIGURE 15 | 3D Interaction of ND5 with 5OOW.

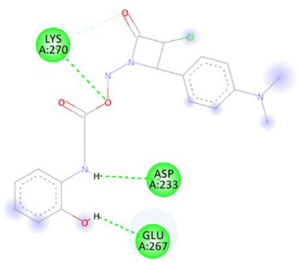

FIGURE 16 | 2D Interaction of ND5 with 5OOW.

valid biomarkers for detection of obesity and of valid treatment for obesity. Therefore, molecular mechanisms of obesity are necessary for scientists to find the treat and diagnosis method of obesity. Because of the fast advancement of bioinformatics analysis, it is more convenient to find out the genetic modification in obesity. Bioinformatics analysis enables us to explore the gene, the genetic change in obesity, which had been proved to be a better approach to identify novel biomarkers.

In our study, a total of 876 DEGs were diagnosed from gene expression dataset, consisting of 438 up regulated genes and 438 down regulated genes in obese patients compared to lean persons. Study showed that PTGDS (prostaglandin D2 synthase) (45), LBP (lipopolysaccharide binding protein) (46), EGFL6 (47), STAT3 (48) and HDAC9 (49) were closely associated with obesity. The expression level of CYP11A1 (50) and WNT11 (51) were linked to cancer progression, but these genes might be novel target for obesity. A previous study showed that expression of GPR146 played an important role in insulin resistance (52), but these genes might be novel target for obesity. Aberrant expression of RFX1 (53) and (54) are noticeable factors in the heart disease, but these genes might be novel target for obesity. CLDND1 expression predicted poor therapeutic outcomes of hypertension patients (55).

Functional enrichment analysis of DEGs was implemented. SULT1A1 (56), SULT1A2 (56), COL6A1 (57), COL6A2 (58), SOS1 (59), STAT1 (60), COL5A2 (61), RND3 (62), COL15A1 (63), CBS (cystathionine-beta-synthase) (64), MCM6 (65), TNFRSF12A (66), FMOD (fibromodulin) (67), TYMP (thymidine phosphorylase) (68), ALPL (alkaline phosphatase, biomineralization associated) (69), EFEMP1 (70), MFAP4 (71), IGFBP5 (72), GLUL (glutamate-ammonia ligase) (73), HACD1 (74) and SCP2 (75) have been reported to be biomarkers of heart disease or play a vital role in its pathogenesis, but these genes might be novel target for obesity. Several studies have shown that expressions of COL1A2 (76), COL3A1 (77), EEF2K (78), ANGPT1 (79), NOTCH3 (80) and TGFBR2 (81) can be a strong prognosis biomarker in patients with hypertension, but these genes might be novel target for obesity. DAG1 (82), ITGAV (integrin subunit alpha V) (83), LAMA5 (84), SPP1 (85), COL11A1 (86), COL12A1 (87), SERPINH1 (88), RHOC (89), RPL14 (90), RPL29 (91), RPS12 (92), RPS15A (93), RPS2 (94), RPS27 (95), RPS3 (96), RBL2 (97), EEF1D (98), ACACA (acetyl-CoA carboxylase alpha) (99), ORC2 (100), PHGDH (phosphoglycerate dehydrogenase) (101), SHMT1 (102), NRCAM (neuronal cell adhesion molecule) (103), NRP2 (104), RSPO3 (105), SRPX2 (106), THY1 (107), CD248 (108), CLEC3B (109), CST3 (110), CTHRC1 (111), GPC1 (112), ACSS2 (113) and HSD17B12 (114) have been extensively reported as a tumor biomarkers, but these genes might be novel target for obesity. The results obtained were consistent with studies that role of LAMB3 (115), THBS1 (116), TIMP1 (117), LOX (lysyl oxidase) (118), MMP9 (119), HSD11B1 (120), ITGB2 (121), HMOX1 (122), SOD2 (123), AKR1C3 (124), MAT2B (125), FOXO1 (126), FOXO3 (127), SIRT1 (128), ACACB (acetyl-CoA carboxylase beta) (129), ELK1 (130), MAP3K5 (131), CTH (cystathionine gamma-lyase) (132), AMOT (angiomotin) (133), CCDC80 (134), CXCL10 (135), ERBB2 (136), KLF4 (137), LEP (leptin) (138), MFGE8 (139), SLIT2 (140), TNMD (tenomodulin) (141), ADAMTS5 (142), ELN (elastin) (143), HTRA1 (144), LUM (lumican) (145), MFAP5 (146), IL1RN (147), ACADL (acyl-CoA dehydrogenase long chain) (148), AGT (angiotensinogen) (149), FADS1 (150), PDK4 (151), PER2 (152) and SLC27A2 (153) in obesity. CDKN1B was shown to be a potential predictor of advanced hyperinsulinemia (154), but this gene might be novel target for obesity. Reports illustrate that CXCL12 (155) and IGFBP6 (156) and ELOVL6 (157) were expressed in patients with insulin resistance, but these genes might be novel target for obesity.

Furthermore, by constructing PPI networks and moduleas, we identified some key genes that provide new insights for obesity diagnosis, prognosis, and drug target identification. Expression of the HSPA8 (158) and CKB (159) were correlated with disease grades of hypertension, but these genes might be novel target for obesity. Recent studies have proposed that HSPA5 (160), YWHAH (161), ESR1 (162), PTEN (163), IRAK1 (164), CYR61 (165) and ZBTB16 (166) are involved in obesity. Previous reports demonstrate that SPTAN1 (167), STEAP2 (168), NEK6 (169), ARRB1 (170), FBXO11 (171), UBR2 (172), INTS6 (173), CDK14 (174). LMO2 (175), MSN (176), TAGLN2 (177), SRSF3 (178), SAFB (179), SIN3A (180), TRIM24 (181) and AUTS2 (182) appears to be constitutively activated in cancer, but these genes might be novel target for obesity. CSNK2A2 expression might be regarded as an indicator of susceptibility to heart disease (183), but this gene might be novel target for obesity. COPG2, FBL, CSNK2B, PCM1, ZNF581, KHDRBS1, RBMX, RBBP4 and DCAF7 are novel biomarkers for obesity.

Target genes - miRNA regulatory network and target genes - TF regulatory network were constructed and analyzed. A previous study reported that CCND1 (184) and HP (185) were expressed in obesity. CCND2 (186) and TXNIP (187) are a potential marker for the detection and prognosis of insulin resistance, but these genes might be novel target for obesity. Other research has revealed that BTG2 was expressed in obesity (188). Expression of MED28 (189) and EFNA1 (190) might participate in cancer progression, but these genes might be novel target for obesity. TUBB2A,

TMEM189, CNBP, LYZ, TRAM2, MED16, RWDD2A, ADD3 and AIP are a novel biomarkers for obesity.

However, this investigation had some limitations. Primarily, the mechanisms of several hub genes in the pathological process of obesity remain unclear, warranting needs further investigation. Moreover, the success of our small molecule drug compound screening in reducing obesity remains to be assessed.

In conclusion, in this study, we determined that STAT3, CORO1C, SERPINH1, MVP, ITGB5, PCM1, SIRT1, EEF1G, PTEN and RPS2 might be critical genes in the development and prognosis of obesity through bioinformatics analysis combined with validations. However, it is essential that further experiments are carried out and clinical data made available to confirm the results of our investigation and guide the discovery of future gene therapies against obesity.

DATA AVAILABILITY STATEMENT

The datasets supporting the conclusions of this article are available in the ArrayExpress (https://www.ebi.ac.uk/arrayexpress/) repository. [E-MTAB-6728) (https://www.ebi.ac.uk/arrayexpress/experiments/E-MTAB-6728/)].

AUTHOR CONTRIBUTIONS

HJ: Methodology and validation. BV: Writing original draft, and review and editing. NJ: Software and resources. CV: Investigation and resources. AT: Formal analysis and validation. IK: Supervision and resources. All authors contributed to the article and approved the submitted version.

ACKNOWLEDGEMENTS

We thank Jan-Inge Bjune, Gunnar Mellgren and Simon N Dankel UNIVERSITY IN BERGEN, The Hormone Laboratory, 8.etg Lab Building, Jonas Lies road 91B, 5021 Bergen very much, the authors who deposited their microarray dataset, E-MTAB-6728, into the public Array Express database.

SUPPLEMENTARY MATERIAL

The Supplementary Material for this article can be found online at: https://www.frontiersin.org/articles/10.3389/fendo.2021.628907/full#supplementary-material

REFERENCES

1. Cole TJ, Bellizzi MC, Flegal KM, Dietz WH. Establishing a Standard Definition for Child Overweight and Obesity Worldwide: International Survey. *BMJ* (2000) 320(7244):1240–3. doi: 10.1136/bmj.320.7244.1240
2. Krotkiewski M, Björntorp P, Sjöström L, Smith U. Impact of Obesity on Metabolism in Men and Women. Importance of Regional Adipose Tissue Distribution. *J Clin Invest* (1983) 72(3):1150–62. doi: 10.1172/JCI111040
3. Freedman DS, Khan LK, Dietz WH, Srinivasan SR, Berenson GS. Relationship of Childhood Obesity to Coronary Heart Disease Risk Factors in Adulthood: The Bogalusa Heart Study. *Pediatrics* (2001) 108 (3):712–8. doi: 10.1542/peds.108.3.712
4. Locsey L, Asztalos L, Kincses Z, Berczi C, Paragh G. The Importance of Obesity and Hyperlipidaemia in Patients With Renal Transplants. *Int Urol Nephrol* (1998) 30(6):767–75. doi: 10.1007/BF02564866
5. Becker S, Dossus L, Kaaks R. Obesity Related Hyperinsulinaemia and Hyperglycaemia and Cancer Development. *Arch Physiol Biochem* (2009) 115(2):86–96. doi: 10.1080/13813450902878054
6. Rahmouni K, Correia ML, Haynes WG, Mark AL. Obesity-Associated Hypertension: New Insights Into Mechanisms. *Hypertension* (2005) 45 (1):9–14. doi: 10.1161/01.HYP.0000151325.83008.b4
7. Lovren F, Teoh H, Verma S. Obesity and Atherosclerosis: Mechanistic Insights. *Can J Cardiol* (2015) 31(2):177–83. doi: 10.1016/j.cjca.2014.11.031
8. Steppan CM, Bailey ST, Bhat S, Brown EJ, Banerjee RR, Wright CM, et al. The Hormone Resistin Links Obesity to Diabetes. *Nature* (2001) 409 (6818):307–12. doi: 10.1038/35053000
9. Calle EE, Kaaks R. Overweight, Obesity and Cancer: Epidemiological Evidence and Proposed Mechanisms. *Nat Rev Cancer* (2004) 4(8):579–91. doi: 10.1038/nrc1408
10. Jia JJ, Zhang X, Ge CR, Jois M. The Polymorphisms of UCP2 and UCP3 Genes Associated With Fat Metabolism, Obesity and Diabetes. *Obes Rev* (2009) 10(5):519–26. doi: 10.1111/j.1467-789X.2009.00569.x
11. Kern PA. Potential Role of TNFalpha and Lipoprotein Lipase as Candidate Genes for Obesity. *J Nutr* (1997) 127(9):1917S–22S. doi: 10.1093/jn/127.9.1917S
12. Suviolahti E, Oksanen LJ, Ohman M, Cantor RM, Ridderstrale M, Tuomi T, et al. The SLC6A14 Gene Shows Evidence of Association With Obesity. *J Clin Invest.* (2003) 112(11):1762–72. doi: 10.1172/JCI17491
13. Okada Y, Tateishi K, Zhang Y. Histone Demethylase JHDM2A is Involved in Male Infertility and Obesity. *J Androl* (2010) 31(1):75–8. doi: 10.2164/jandrol.109.008052
14. Carpenter D, Dhar S, Mitchell LM, Fu B, Tyson J, Shwan NA, et al. Obesity, Starch Digestion and Amylase: Association Between Copy Number Variants at Human Salivary (AMY1) and Pancreatic (AMY2) Amylase Genes. *Hum Mol Genet* (2015) 24(12):3472–80. doi: 10.1093/hmg/ddv098
15. Tanti JF, Ceppo F, Jager J, Berthou F. Implication of Inflammatory Signaling Pathways in Obesity-Induced Insulin Resistance. *Front Endocrinol (Lausanne)* (2013) 3:181. doi: 10.3389/fendo.2012.00181
16. Kim KA, Gu W, Lee IA, Joh EH, Kim DH. High Fat Diet-Induced Gut Microbiota Exacerbates Inflammation and Obesity in Mice *Via* the TLR4 Signaling Pathway. *PloS One* (2012) 7(10):e47713. doi: 10.1371/journal.pone.0047713
17. Briones AM, Nguyen Dinh Cat A, Callera GE, Yogi A, Burger D, He Y, et al. Adipocytes Produce Aldosterone Through Calcineurin-Dependent Signaling Pathways: Implications in Diabetes Mellitus-Associated Obesity and Vascular Dysfunction. *Hypertension* (2012) 59(5):1069–78. doi: 10.1161/HYPERTENSIONAHA.111.190223
18. Dann SG, Selvaraj A, Thomas G. Mtor Complex1-S6K1 Signaling: At the Crossroads of Obesity, Diabetes and Cancer. *Trends Mol Med* (2007) 13 (6):252–9. doi: 10.1016/j.molmed.2007.04.002
19. Mattevi VS, Zembrzuski VM, Hutz MH. Association Analysis of Genes Involved in the Leptin-Signaling Pathway With Obesity in Brazil. *Int J Obes Relat Metab Disord* (2002) 26(9):1179–85. doi: 10.1038/sj.ijo.0802067
20. Li H, Li X, Guo J, Wu G, Dong C, Pang Y, et al. Identification of Biomarkers and Mechanisms of Diabetic Cardiomyopathy Using Microarray Data. *Cardiol J* (2018) 27(6):807–16. doi: 10.5603/CJ.a2018.0113
21. Wei L, Wang J, Lampert E, Schlanger S, DePriest AD, Hu Q, et al. Intratumoral and Intertumoral Genomic Heterogeneity of Multifocal Localized Prostate Cancer Impacts Molecular Classifications and Genomic Prognosticators. *Eur Urol* (2017) 71(2):183–92. doi: 10.1016/j.eururo.2016.07.008
22. Yan Y, Xu Z, Qian L, Zeng S, Zhou Y, Chen X, et al. Identification of CAV1 and DCN as Potential Predictive Biomarkers for Lung Adenocarcinoma. *Am J Physiol Lung Cell Mol Physiol* (2019) 316(4):L630–43. doi: 10.1152/ajplung.00364.2018
23. Fan G, Tu Y, Chen C, Sun H, Wan C, Cai X. DNA Methylation Biomarkers for Hepatocellular Carcinoma. *Cancer Cell Int* (2018) 18:140. doi: 10.1186/s12935-018-0629-5

24. Jia L, Jia R, Li Y, Li X, Jia Q, Zhang H. LCK as a Potential Therapeutic Target for Acute Rejection After Kidney Transplantation: A Bioinformatics Clue. *J Immunol Res* (2018) 2018:6451298. doi: 10.1155/2018/6451298
25. Bjune JI, Haugen C, Gudbrandsen O, Nordbø OP, Nielsen HJ, Våge V, et al. IRX5 Regulates Adipocyte Amyloid Precursor Protein and Mitochondrial Respiration in Obesity. *Int J Obes (Lond)* (2018) 43(11):2151–62. doi: 10.1038/s41366-018-0275-y
26. Dunning MJ, Smith ML, Ritchie ME, Tavaré S. Beadarray: R Classes and Methods for Illumina Bead-Based Data. *Bioinformatics* (2007) 23(16):2183–4. doi: 10.1093/bioinformatics/btm311
27. Ritchie ME, Phipson B, Wu D, Hu Y, Law CW, Shi W, et al. Limma Powers Differential Expression Analyses for RNA-Sequencing and Microarray Studies. *Nucleic Acids Res* (2015) 43(7):e47. doi: 10.1093/nar/gkv007
28. Abbas A, Kong XB, Liu Z, Jing BY, Gao X. Automatic Peak Selection by a Benjamini-Hochberg-based Algorithm. *PloS One* (2013) 8(1):e53112. doi: 10.1371/journal.pone.0053112
29. Kaimal V, Bardes EE, Tabar SC, Jegga AG, Aronow BJ. ToppCluster: A Multiple Gene List Feature Analyzer for Comparative Enrichment Clustering and Network-Based Dissection of Biological Systems. *Nucleic Acids Res* (2010) 38(Web Server issue):W96–W102. doi: 10.1093/nar/gkq418
30. Calderone A, Castagnoli L, Cesareni G. Mentha: A Resource for Browsing Integrated Protein-Interaction Networks. *Nat Methods* (2013) 10(8):690–1. doi: 10.1038/nmeth.2561
31. Shannon P, Markiel A, Ozier O, Baliga NS, Wang JT, Ramage D, et al. Cytoscape: A Software Environment for Integrated Models of Biomolecular Interaction Networks. *Genome. Res* (2003) 3(11):2498–504. doi: 10.1101/gr.1239303
32. Przulj N, Wigle DA, Jurisica I. Functional Topology in a Network of Protein Interactions. *Bioinformatics* (2004) 20(3):340–8. doi: 10.1093/bioinformatics/btg415
33. Nguyen TP, Liu WC, Jordán F. Inferring Pleiotropy by Network Analysis: Linked Diseases in the Human PPI Network. *BMC Syst Biol* (2011) 5:179. doi: 10.1186/1471-2105-12-149
34. Shi Z, Zhang B. Fast Network Centrality Analysis Using Gpus. *BMC Bioinf* (2011) 12:149. doi: 10.1186/1471-2105-12-149
35. Fadhal E, Gamieldien J, Mwambene EC. Protein Interaction Networks as Metric Spaces: A Novel Perspective on Distribution of Hubs. *BMC Syst Biol* (2014) 8:6. doi: 10.1186/1752-0509-8-6
36. Zaki N, Efimov D, Berengueres J. Protein Complex Detection Using Interaction Reliability Assessment and Weighted Clustering Coefficient. *BMC. Bioinf* (2013) 14:163. doi: 10.1186/1471-2105-14-163
37. Fan Y, Xia J. Mirnet-Functional Analysis and Visual Exploration of miRNA-Target Interactions in a Network Context. *Methods Mol Biol* (2018) 1819:215–33. doi: 10.1007/978-1-4939-8618-7_10
38. Zhou G, Soufan O, Ewald J, Hancock REW, Basu N, Xia J. NetworkAnalyst 3.0: A Visual Analytics Platform for Comprehensive Gene Expression Profiling and Meta-Analysis. *Nucleic Acids Res* (2019) 47(W1):W234–41. doi: 10.1093/nar/gkz240
39. Uhlen M, Oksvold P, Fagerberg L, Lundberg E, Jonasson K, Forsberg M, et al. Towards a Knowledge-Based Human Protein Atlas. *Nat Biotechnol* (2010) 28(12):1248–50. doi: 10.1038/nbt1210-1248
40. Robin X, Turck N, Hainard A, Tiberti N, Lisacek F, Sanchez JC, et al. pROC: An Open-Source Package for R and S+ to Analyze and Compare ROC Curves. *BMC Bioinf* (2011) 12:77. doi: 10.1186/1471-2105-12-77
41. Livak KJ, Schmittgen TD. Analysis of Relative Gene Expression Data Using Real-Time Quantitative PCR and the 2(-Delta Delta C(T)) Method. *Methods* (2001) 25(4):402–8. doi: 10.1006/meth.2001.1262
42. El-Saadi MW, Williams-Hart T, Salvatore BA, Mahdavian E. Use of in-Silico Assays to Characterize the ADMET Profile and Identify Potential Therapeutic Targets of Fusarochromanone, a Novel Anti-Cancer Agent. *In Silico Pharmacol* (2015) 3(1):6. doi: 10.1186/s40203-015-0010-5
43. Li J, Ma X, Liu C, Li H, Zhuang J, Gao C, et al. Exploring the Mechanism of Danshen Against Myelofibrosis by Network Pharmacology and Molecular Docking. *Evid Based Complement Alternat Med* (2018) 2018:8363295. doi: 10.1155/2018/8363295
44. Veeramachaneni GK, Raj KK, Chalasani LM, Annamraju SK, Js B, Talluri VR. Shape Based Virtual Screening and Molecular Docking Towards Designing Novel Pancreatic Lipase Inhibitors. *Bioinformation* (2015) 11(12):535–42. doi: 10.6026/97320630011535
45. Urbanet R, Nguyen Dinh Cat A, Feraco A, Venteclef N, El Mogrhabi S, Sierra-Ramos C, et al. Adipocyte Mineralocorticoid Receptor Activation Leads to Metabolic Syndrome and Induction of Prostaglandin D2 Synthase. *Hypertension* (2015) 66(1):149–57. doi: 10.1161/HYPERTENSIONAHA
46. Moreno-Navarrete JM, Ortega F, Serino M, Luche E, Waget A, Pardo G, et al. Circulating Lipopolysaccharide-Binding Protein (LBP) as a Marker of Obesity-Related Insulin Resistance. *Int J Obes (Lond)* (2012) 36(11):1442–9. doi: 10.1038/ijo.2011.256
47. Oberauer R, Rist W, Lenter MC, Hamilton BS, Neubauer H. EGFL6 is Increasingly Expressed in Human Obesity and Promotes Proliferation of Adipose Tissue-Derived Stromal Vascular Cells. *Mol Cell Biochem* (2010) 343(1-2):257–69. doi: 10.1007/s11010-010-0521-7
48. Ernst MB, Wunderlich CM, Hess S, Paehler M, Mesaros A, Koralov SB, et al. Enhanced Stat3 Activation in POMC Neurons Provokes Negative Feedback Inhibition of Leptin and Insulin Signaling in Obesity. *J Neurosci* (2009) 29(37):11582–93. doi: 10.1523/JNEUROSCI.5712-08.2009
49. Chatterjee TK, Basford JE, Knoll E, Tong WS, Blanco V, Blomkalns AL, et al. HDAC9 Knockout Mice are Protected From Adipose Tissue Dysfunction and Systemic Metabolic Disease During High-Fat Feeding. *Diabetes* (2014) 63(1):176–87. doi: 10.2337/db13-1148
50. Zhao L, Triche EW, Walsh KM, Bracken MB, Saftlas AF, Hoh J, et al. Genome-Wide Association Study Identifies a Maternal Copy-Number Deletion in PSG11 Enriched Among Preeclampsia Patients. *BMC Pregnancy Childbirth* (2012) 12:61. doi: 10.1186/1471-2393-12-61
51. Li W, Geng L, Liu X, Gui W, Qi H. Recombinant Adiponectin Alleviates Abortion in Mice by Regulating Th17/Treg Imbalance *Via* P38mapk-STAT5 Pathway. *Biol Reprod* (2019) 100(4):1008–17. doi: 10.1093/biolre/ioy251
52. Kolar GR, Grote SM, Yosten GL. Targeting Orphan G Protein-Coupled Receptors for the Treatment of Diabetes and Its Complications: C-Peptide and GPR146. *J Intern Med* (2017) 281(1):25–40. doi: 10.1111/joim.12528
53. Du P, Gao K, Cao Y, Yang S, Wang Y, Guo R, et al. RFX1 Downregulation Contributes to TLR4 Overexpression in CD14+ Monocytes Via Epigenetic Mechanisms in Coronary Artery Disease. *Clin Epigenet* (2019) 11(1):44. doi: 10.1186/s13148-019-0646-9
54. Erbilgin A, Seldin MM, Wu X, Mehrabian M, Zhou Z, Qi H, et al. Transcription Factor Zhx2 Deficiency Reduces Atherosclerosis and Promotes Macrophage Apoptosis in Mice. *Arterioscler Thromb Vasc Biol* (2018) 38(9):2016–27. doi: 10.1161/ATVBAHA.118.311266
55. Matsuoka H, Tamura A, Kinehara M, Shima A, Uda A, Tahara H, et al. Levels of Tight Junction Protein CLDND1 Are Regulated by microRNA-124 in the Cerebellum of Stroke-Prone Spontaneously Hypertensive Rats. *Biochem Biophys Res Commun* (2018) 498(4):817–23. doi: 10.1016/j.bbrc.2018.03.063
56. O'Halloran AM, Patterson CC, Horan P, Maree A, Curtin R, Stanton A, et al. Genetic Polymorphisms in Platelet-Related Proteins and Coronary Artery Disease: Investigation of Candidate Genes, Including N-acetylgalactosaminyltransferase 4 (GALNT4) and Sulphotransferase 1A1/2 (SULT1A1/2). *J Thromb Thrombolysis* (2009) 27(2):175–84. doi: 10.1007/s11239-008-0196-z
57. Davies GE, Howard CM, Farrer MJ, Coleman MM, Bennett LB, Cullen LM, et al. Genetic Variation in the COL6A1 Region is Associated With Congenital Heart Defects in Trisomy 21 (Down's Syndrome). *Ann Hum Genet* (1995) 59(3):253–69. doi: 10.1111/j.1469-1809.1995.tb00746.x
58. Grossman TR, Gamliel A, Wessells RJ, Taghli-Lamallem O, Jepsen K, Ocorr K, et al. Over-Expression of DSCAM and COL6A2 Cooperatively Generates Congenital Heart Defects. *PloS Genet* (2011) 7(11):e1002344. doi: 10.1371/journal.pgen.1002344
59. Roberts AE, Araki T, Swanson KD, Montgomery KT, Schiripo TA, Joshi VA, et al. Germline Gain-of-Function Mutations in SOS1 Cause Noonan Syndrome. *Nat Genet* (2007) 39(1):70–4. doi: 10.1038/ng1926
60. Chmielewski S, Piaszyk-Borychowska A, Wesoly J, Bluyssen HA. STAT1 and IRF8 in Vascular Inflammation and Cardiovascular Disease: Diagnostic and Therapeutic Potential. *Int Rev Immunol* (2016) 35(5):434–54. doi: 10.3109/08830185.2015.1087519

61. Azuaje F, Zhang L, Jeanty C, Puhl SL, Rodius S, Wagner DR. Analysis of a Gene Co-Expression Network Establishes Robust Association Between Col5a2 and Ischemic Heart Disease. *BMC Med Genomics* (2013) 6:13. doi: 10.1186/1755-8794-6-13
62. Yue X, Yang X, Lin X, Yang T, Yi X, Dai Y, et al. Rnd3 Haploinsufficient Mice are Predisposed to Hemodynamic Stress and Develop Apoptotic Cardiomyopathy With Heart Failure. *Cell Death Dis* (2014) 5:e1284. doi: 10.1038/cddis.2014.235
63. Connelly JJ, Cherepanova OA, Doss JF, Karaoli T, Lillard TS, Markunas CA, et al. Epigenetic Regulation of COL15A1 in Smooth Muscle Cell Replicative Aging and Atherosclerosis. *Hum Mol Genet* (2013) 22(25):5107–20. doi: 10.1093/hmg/ddt365
64. Karamat FA, Oudman I, Ris-Stalpers C, Afink GB, Keijser R, Clark JF, et al. Resistance Artery Creatine Kinase mRNA and Blood Pressure in Humans. *Hypertension* (2014) 63(1):68–73. doi: 10.1161/HYPERTENSIONAHA.113.01352
65. Smith CE, Coltell O, Sorlí JV, Estruch R, Martínez-González MÁ, Salas-Salvadó J, et al. Associations of the MCM6-rs3754686 Proxy for Milk Intake in Mediterranean and American Populations With Cardiovascular Biomarkers, Disease and Mortality: Mendelian Randomization. *Sci Rep* (2016) 6:33188. doi: 10.1038/srep33188
66. Lyu M, Cui Y, Zhao T, Ning Z, Ren J, Jin X, et al. Tnfrsf12a-Mediated Atherosclerosis Signaling and Inflammatory Response as a Common Protection Mechanism of Shuxuening Injection Against Both Myocardial and Cerebral Ischemia-Reperfusion Injuries. *Front Pharmacol* (2018) 9:312. doi: 10.3389/fphar.2018.00312
67. Shami A, Tengryd C, Asciutto G, Bengtsson E, Nilsson J, Hultgårdh-Nilsson A, et al. Expression of Fibromodulin in Carotid Atherosclerotic Plaques is Associated With Diabetes and Cerebrovascular Events. *Atherosclerosis* (2015) 241(2):701–8. doi: 10.1016/j.atherosclerosis.2015.06.023
68. Li W, Yue H. Thymidine Phosphorylase: A Potential New Target for Treating Cardiovascular Disease. *Trends Cardiovasc Med* (2018) 28(3):157–71. doi: 10.1016/j.tcm.2017.10.003
69. Haarhaus M, Brandenburg V, Kalantar-Zadeh K, Stenvinkel P, Magnusson P. Alkaline Phosphatase: A Novel Treatment Target for Cardiovascular Disease in CKD. *Nat Rev Nephrol* (2017) 13(7):429–42. doi: 10.1038/nrneph.2017.60
70. Ellinghaus E, Ellinghaus D, Krusche P, Greiner A, Schreiber C, Nikolaus S, et al. Genome-Wide Association Analysis for Chronic Venous Disease Identifies EFEMP1 and KCNH8 as Susceptibility Loci. *Sci Rep* (2017) 7:45652. doi: 10.1038/srep45652
71. Wulf-Johansson H, Lock Johansson S, Schlosser A, Trommelholt Holm A, Rasmussen LM, Mickley H, et al. Localization of Microfibrillar-Associated Protein 4 (MFAP4) in Human Tissues: Clinical Evaluation of Serum MFAP4 and its Association With Various Cardiovascular Conditions. *PloS One* (2013) 8(12):e82243. doi: 10.1371/journal.pone.0082243
72. Song SE, Kim YW, Kim JY, Lee DH, Kim JR, Park SY. IGFBP5 Mediates High Glucose-Induced Cardiac Fibroblast Activation. *J Mol Endocrinol* (2013) 50(3):291–303. doi: 10.1530/JME-12-0194
73. Huggins GS, Berkowitz RI, Blackburn GL, Bray GA, Cheskin L, Clark JM, et al. Prospective Association of GLUL Rs10911021 With Cardiovascular Morbidity and Mortality Among Individuals With Type 2 Diabetes: The Look Ahead Study. *Diabetes* (2016) 65(1):297–302. doi: 10.2337/db15-0890
74. Konishi H, Okuda A, Ohno Y, Kihara A. Characterization of HACD1 K64Q Mutant Found in Arrhythmogenic Right Ventricular Dysplasia Patients. *J Biochem* (2010) 148(5):617–22. doi: 10.1093/jb/mvq092
75. He H, Wang J, Yannie PJ, Kakiyama G, Korzun WJ, Ghosh S. Sterol Carrier Protein-2 Deficiency Attenuates Diet-Induced Dyslipidemia and Atherosclerosis in Mice. *J Biol Chem* (2018) 293(24):9223–31. doi: 10.1074/jbc.RA118.002290
76. Tian DZ, Wei W, Dong YJ. Influence of COL1A2 Gene Variants on the Incidence of Hypertensive Intracerebral Hemorrhage in a Chinese Population. *Genet Mol Res* (2016) 15(1). doi: 10.4238/gmr.15017369
77. Samokhin AO, Stephens T, Wertheim BM, Wang RS, Vargas SO, Yung LM, et al. NEDD9 Targets COL3A1 to Promote Endothelial Fibrosis and Pulmonary Arterial Hypertension. *Sci Transl Med* (2018) 10(445). doi: 10.1126/scitranslmed.aap7294
78. Usui T, Okada M, Hara Y, Yamawaki H. Eukaryotic Elongation Factor 2 Kinase Regulates the Development of Hypertension Through Oxidative Stress-Dependent Vascular Inflammation. *Am J Physiol Heart Circ Physiol* (2013) 305(5):H756–68. doi: 10.1152/ajpheart.00373.2013
79. Andraweera PH, Dekker GA, Thompson SD, North RA, McCowan LM, Roberts CT. A Functional Variant in ANGPT1 and the Risk of Pregnancies With Hypertensive Disorders and Small-for-Gestational-Age Infants. *Mol Hum Reprod* (2012) 18(6):325–32. doi: 10.1093/molehr/gar081
80. Li X, Zhang X, Leathers R, Makino A, Huang C, Parsa P, et al. Notch3 Signaling Promotes the Development of Pulmonary Arterial Hypertension. *Nat Med* (2009) 15(11):1289–97. doi: 10.1038/nm.2021
81. Chen J, Zhao X, Wang H, Chen Y, Wang W, Zhou W, et al. Common Variants in TGFBR2 and miR-518 Genes Are Associated With Hypertension in the Chinese Population. *Am J Hypertens* (2014) 27(10):1268–76. doi: 10.1093/ajh/hpu047
82. Champelovier P, Besse A, Boucard N, Simon A, Leroux D, Pinel N, et al. Dag-1 Carcinoma Cell in Studying the Mechanisms of Progression and Therapeutic Resistance in Bladder Cancer. *Eur Urol* (2001) 39(3):343–8. doi: 10.1159/000052465
83. Flum M, Kleemann M, Schneider H, Weis B, Fischer S, Handrick R, et al. miR-217-5p Induces Apoptosis by Directly Targeting PRKCI, Bag3, ITGAV and MAPK1 in Colorectal Cancer Cells. *J Cell Commun Signal* (2018) 12(2):451–66. doi: 10.1007/s12079-017-0410-x
84. Bartolini A, Cardaci S, Lamba S, Oddo D, Marchiò C, Cassoni P, et al. BCAM and LAMA5 Mediate the Recognition Between Tumor Cells and the Endothelium in the Metastatic Spreading of KRAS-Mutant Colorectal Cancer. *Clin Cancer Res* (2016) 22(19):4923–33. doi: 10.1158/1078-0432.CCR-15-2664
85. Junnila S, Kokkola A, Mizuguchi T, Hirata K, Karjalainen-Lindsberg ML, Puolakkainen P, et al. Gene Expression Analysis Identifies Over-Expression of CXCL1, SPARC, SPP1, and SULF1 in Gastric Cancer. *Genes Chromosomes Cancer* (2010) 49(1):28–39. doi: 10.1002/gcc.20715
86. García-Pravia C, Galván JA, Gutiérrez-Corral N, Solar-García L, García-Pérez E, García-Ocaña M, et al. Overexpression of COL11A1 by Cancer-Associated Fibroblasts: Clinical Relevance of a Stromal Marker in Pancreatic Cancer. *PloS One* (2013) 8(10):e78327. doi: 10.1371/journal.pone.0078327
87. Duan S, Gong B, Wang P, Huang H, Luo L, Liu F. Novel Prognostic Biomarkers of Gastric Cancer Based on Gene Expression Microarray: COL12A1, GSTA3, FGA and FGG. *Mol Med Rep* (2018) 18(4):3727–36. doi: 10.3892/mmr.2018.9368
88. Kamikawaji K, Seki N, Watanabe M, Mataki H, Kumamoto T, Takagi K, et al. Regulation of LOXL2 and SERPINH1 by Antitumor microRNA-29a in Lung Cancer With Idiopathic Pulmonary Fibrosis. *J Hum Genet* (2016) 61(12):985–93. doi: 10.1038/jhg.2016.99
89. Liu BL, Sun KX, Zong ZH, Chen S, Zhao Y. MicroRNA-372 Inhibits Endometrial Carcinoma Development by Targeting the Expression of the Ras Homolog Gene Family Member C (Rhoc). *Oncotarget* (2016) 7(6):6649–64. doi: 10.18632/oncotarget.6544
90. Shriver SP, Shriver MD, Tirpak DL, Bloch LM, Hunt JD, Ferrell RE, et al. Trinucleotide Repeat Length Variation in the Human Ribosomal Protein L14 Gene (RPL14): Localization to 3p21.3 and Loss of Heterozygosity in Lung and Oral Cancers. *Mutat Res* (1998) 406(1):9–23. doi: 10.1016/S1383-5726(98)00006-5
91. Liu JJ, Huang BH, Zhang J, Carson DD, Hooi SC. Repression of HIP/RPL29 Expression Induces Differentiation in Colon Cancer Cells. *J Cell Physio* (2006) 207(2):287–92. doi: 10.1002/jcp.20589
92. Chen D, Zhang R, Shen W, Fu H, Liu S, Sun K, et al. RPS12-Specific shRNA Inhibits the Proliferation, Migration of BGC823 Gastric Cancer Cells With S100A4 as a Downstream Effector. *Int J Oncol* (2013) 42(5):1763–9. doi: 10.3892/ijo.2013.1872
93. Zhao X, Shen L, Feng Y, Yu H, Wu X, Chang J, et al. Decreased Expression of RPS15A Suppresses Proliferation of Lung Cancer Cells. *Tumour Biol* (2015) 36(9):6733–40. doi: 10.1007/s13277-015-3371-9
94. Wang M, Hu Y, Stearns ME. RPS2: A Novel Therapeutic Target in Prostate Cancer. *J Exp Clin Cancer Res* (2009) 28:6. doi: 10.1186/1756-9966-28-6
95. Dutton-Regester K, Gartner JJ, Emmanuel R, Qutob N, Davies MA, Gershenwald JE, et al. A Highly Recurrent RPS27 5'UTR Mutation in Melanoma. *Oncotarget* (2014) 5(10):2912–7. doi: 10.18632/oncotarget.2048

96. Youn H, Son B, Kim W, Jun SY, Lee JS, Lee JM, et al. Dissociation of MIF-rpS3 Complex and Sequential NF-κB Activation is Involved in IR-induced Metastatic Conversion of NSCLC. *J Cell Biochem* (2015) 116(11):2504–16. doi: 10.1002/jcb.25195
97. Zhu Y, Gu J, Li Y, Peng C, Shi M, Wang X, et al. MiR-17-5p Enhances Pancreatic Cancer Proliferation by Altering Cell Cycle Profiles *Via* Disruption of RBL2/E2F4-Repressing Complexes. *Cancer Lett* (2018) 412:59–68. doi: 10.1016/j.canlet.2017.09.044
98. Flores IL, Kawahara R, Miguel MC, Granato DC, Domingues RR, Macedo CC, et al. EEF1D Modulates Proliferation and Epithelial-Mesenchymal Transition in Oral Squamous Cell Carcinoma. *Clin Sci (Lond)* (2016) 130 (10):785–99. doi: 10.1042/CS20150646
99. Svensson RU, Parker SJ, Eichner LJ, Kolar MJ, Wallace M, Brun SN, et al. Inhibition of Acetyl-CoA Carboxylase Suppresses Fatty Acid Synthesis and Tumor Growth of Non-Small-Cell Lung Cancer in Preclinical Models. *Nat Med* (2016) 22(10):1108–19. doi: 10.1038/nm.4181
100. Song B, Liu XS, Rice SJ, Kuang S, Elzey BD, Konieczny SF, et al. Plk1 Phosphorylation of Orc2 and Hbo1 Contributes to Gemcitabine Resistance in Pancreatic Cancer. *Mol Cancer Ther* (2013) 12(1):58–68. doi: 10.1158/1535-7163.MCT-12-0632
101. Mullarky E, Mattaini KR, Vander Heiden MG, Cantley LC, Locasale JW. PHGDH Amplification and Altered Glucose Metabolism in Human Melanoma. *Pigment Cell Melanoma Res* (2011) 24(6):1112–5. doi: 10.1111/j.1755-148X.2011.00919.x
102. Komlósi V, Hitre E, Pap E, Adleff V, Réti A, Székely E, et al. SHMT1 1420 and MTHFR 677 Variants Are Associated With Rectal But Not Colon Cancer. *BMC Cancer* (2010) 10:525. doi: 10.1186/1471-2407-10-525
103. Górka B, Skubis-Zegadło J, Mikula M, Bardadin K, Paliczka E, Czarnocka B. NrCAM, a Neuronal System Cell-Adhesion Molecule, Is Induced in Papillary Thyroid Carcinomas. *Br J Cancer* (2007) 97(4):531–8. doi: 10.1038/sj.bjc.6603915
104. Yasuoka H, Kodama R, Tsujimoto M, Yoshidome K, Akamatsu H, Nakahara M, et al. Neuropilin-2 Expression in Breast Cancer: Correlation With Lymph Node Metastasis, Poor Prognosis, and Regulation of CXCR4 Expression. *BMC Cancer* (2009) 9:220. doi: 10.1186/1471-2407-9-220
105. Gong X, Yi J, Carmon KS, Crumbley CA, Xiong W, Thomas A, et al. Aberrant RSPO3-LGR4 Signaling in Keap1-deficient Lung Adenocarcinomas Promotes Tumor Aggressiveness. *Oncogene* (2015) 34 (36):4692–701. doi: 10.1038/onc.2014.417
106. Tanaka K, Arao T, Maegawa M, Matsumoto K, Kaneda H, Kudo K, et al. SRPX2 is Overexpressed in Gastric Cancer and Promotes Cellular Migration and Adhesion. *Int J Cancer* (2009) 124(5):1072–80. doi: 10.1002/ijc.24065
107. Abeysinghe HR, Cao Q, Xu J, Pollock S, Veyberman Y, Guckert NL, et al. THY1 Expression is Associated With Tumor Suppression of Human Ovarian Cancer. *Cancer Genet Cytogenet* (2003) 143(2):125–32. doi: 10.1016/S0165-4608(02)00855-5
108. Aquea G, Bresky G, Lancellotti D, Madariaga JA, Zaffiri V, Urzua U, et al. Increased Expression of P2RY2, CD248 and EphB1 in Gastric Cancers From Chilean Patients. *Asian Pac J Cancer Prev* (2014) 15(5):1931–6. doi: 10.7314/APJCP.2014.15.5.1931
109. Liu J, Liu Z, Liu Q, Li L, Fan X, Wen T, et al. CLEC3B is Downregulated and Inhibits Proliferation in Clear Cell Renal Cell Carcinoma. *Oncol Rep* (2018) 40(4):2023–35. doi: 10.3892/or.2018.6590
110. Yan Y, Fan Q, Wang L, Zhou Y, Li J, Zhou K. LncRNA Snhg1, a Non-Degradable Sponge for miR-338, Promotes Expression of Proto-Oncogene CST3 in Primary Esophageal Cancer Cells. *Oncotarget* (2017) 8(22):35750–60. doi: 10.18632/oncotarget.16189
111. Kim HC, Kim YS, Oh HW, Kim K, Oh SS, Kim JT, et al. Collagen Triple Helix Repeat Containing 1 (CTHRC1) Acts *Via* ERK-Dependent Induction of MMP9 to Promote Invasion of Colorectal Cancer Cells. *Oncotarget* (2014) 5(2):519–29. doi: 10.18632/oncotarget.1714
112. Duan L, Hu XQ, Feng DY, Lei SY, Hu GH. GPC-1 May Serve as a Predictor of Perineural Invasion and a Prognosticator of Survival in Pancreatic Cancer. *Asian J Surg* (2013) 36(1):7–12. doi: 10.1016/j.asjsur.2012.08.001
113. Hur H, Kim YB, Ham IH, Lee D. Loss of ACSS2 Expression Predicts Poor Prognosis in Patients With Gastric Cancer. *J Surg Oncol* (2015) 112(6):585–91. doi: 10.1002/jso.24043
114. Szajnik M, Szczepanski MJ, Elishaev E, Visus C, Lenzner D, Zabel M, et al. 17β Hydroxysteroid Dehydrogenase Type 12 (HSD17B12) is a Marker of Poor Prognosis in Ovarian Carcinoma. *Gynecol Oncol* (2012) 127(3):587–94. doi: 10.1016/j.ygyno.2012.08.010
115. Jiao H, Kulyté A, Näslund E, Thorell A, Gerdhem P, Kere J, et al. Whole-Exome Sequencing Suggests LAMB3 as a Susceptibility Gene for Morbid Obesity. *Diabetes* (2016) 65(10):2980–9. doi: 10.2337/db16-0522
116. Matsuo Y, Tanaka M, Yamakage H, Sasaki Y, Muranaka K, Hata H, et al. Thrombospondin 1 as a Novel Biological Marker of Obesity and Metabolic Syndrome. *Metabolism* (2015) 64(11):1490–9. doi: 10.1016/j.metabol.2015.07.016
117. Meissburger B, Stachorski L, Röder E, Rudofsky G, Wolfrum C. Tissue Inhibitor of Matrix Metalloproteinase 1 (TIMP1) Controls Adipogenesis in Obesity in Mice and in Humans. *Diabetologia* (2011) 54(6):1468–79. doi: 10.1007/s00125-011-2093-9
118. Chen JY, Tsai PJ, Tai HC, Tsai RL, Chang YT, Wang MC, et al. Increased Aortic Stiffness and Attenuated Lysyl Oxidase Activity in Obesity. *Arterioscler Thromb Vasc Biol* (2013) 33(4):839–46. doi: 10.1161/ATVBAHA.112.300036
119. Derosa G, Ferrari I, D'Angelo A, Tinelli C, Salvadeo SA, Ciccarelli L, et al. Matrix Metalloproteinase-2 and -9 Levels in Obese Patients. *Endothelium* (2008) 15(4):219–24. doi: 10.1080/10623320802228815
120. Nascimento FV, Piccoli V, Beer MA, Frankenberg AD, Crispim D, Gerchman F. Association of HSD11B1 Polymorphic Variants and Adipose Tissue Gene Expression With Metabolic Syndrome, Obesity and Type 2 Diabetes Mellitus: A Systematic Review. *Diabetol Metab Syndr* (2015) 7:38. doi: 10.1186/s13098-015-0036-1
121. Awaya T, Yokosaki Y, Yamane K, Usui H, Kohno N, Eboshida A. Gene-Environment Association of an ITGB2 Sequence Variant With Obesity in Ethnic Japanese. *Obes (Silver Spring)* (2008) 16(6):1463–6. doi: 10.1038/oby.2008.68
122. Moreno-Navarrete JM, Ortega F, Rodríguez A, Latorre J, Becerril S, Sabater-Masdeu M, et al. HMOX1 as a Marker of Iron Excess-Induced Adipose Tissue Dysfunction, Affecting Glucose Uptake and Respiratory Capacity in Human Adipocytes. *Diabetologia* (2017) 60(5):915–26. doi: 10.1007/s00125-017-4228-0
123. Aguer C, Pasqua M, Thrush AB, Moffat C, McBurney M, Jardine K, et al. Increased Proton Leak and SOD2 Expression in Myotubes From Obese Non-Diabetic Subjects With a Family History of Type 2 Diabetes. *Biochim Biophys Acta* (2013) 1832(10):1624–33. doi: 10.1016/j.bbadis.2013.05.008
124. Svensson PA, Gabrielsson BG, Jernås M, Gummesson A, Sjöholm K. Regulation of Human Aldoketoreductase 1C3 (AKR1C3) Gene Expression in the Adipose Tissue. *Cell Mol Biol Lett* (2008) 13(4):599–613. doi: 10.2478/s11658-008-0025-6
125. Zhao C, Chen X, Wu W, Wang W, Pang W, Yang G. MAT2B Promotes Adipogenesis by Modulating SAMe Levels and Activating AKT/ERK Pathway During Porcine Intramuscular Preadipocyte Differentiation. *Exp Cell Res* (2016) 344(1):11–21. doi: 10.1016/j.yexcr.2016.02.019
126. Farmer SR. The Forkhead Transcription Factor Foxo1: A Possible Link Between Obesity and Insulin Resistance. *Mol Cell* (2003) 11(1):6–8. doi: 10.1016/S1097-2765(03)00003-0
127. Boal F, Roumegoux J, Alfarano C, Timotin A, Calise D, Anesia R, et al. Apelin Regulates FoxO3 Translocation to Mediate Cardioprotective Responses to Myocardial Injury and Obesity. *Sci Rep* (2015) 5:16104. doi: 10.1038/srep16104
128. Zillikens MC, Meurs JB, Rivadeneira F, Amin N, Hofman A, Oostra BA, et al. SIRT1 Genetic Variation is Related to BMI and Risk of Obesity. *Diabetes* (2009) 58(12):2828–34. doi: 10.2337/db09-0536
129. Riancho JA, Vázquez L, García-Pérez MA, Sainz J, Olmos JM, Hernández JL, et al. Association of ACACB Polymorphisms With Obesity and Diabetes. *Mol Genet Metab* (2011) 104(4):670–6. doi: 10.1016/j.ymgme.2011.08.013
130. Pang L, You L, Ji C, Shi C, Chen L, Yang L, et al. miR-1275 Inhibits Adipogenesis *Via* ELK1 and Its Expression Decreases in Obese Subjects. *J Mol Endocrinol* (2016) 57(1):33–43. doi: 10.1530/JME-16-0007
131. Haim Y, Blüher M, Konrad D, Goldstein N, Klöting N, Harman-Boehm I, et al. ASK1 (MAP3K5) is Transcriptionally Upregulated by E2F1 in Adipose Tissue in Obesity, Molecularly Defining a Human Dys-Metabolic Obese

Phenotype. *Mol Metab* (2017) 6(7):725–36. doi: 10.1016/j.molmet.2017.05.003
132. Cai J, Shi X, Wang H, Fan J, Feng Y, Lin X, et al. Cystathionine γ Lyase-Hydrogen Sulfide Increases Peroxisome Proliferator-Activated Receptor γ Activity by Sulfhydration at C139 Site Thereby Promoting Glucose Uptake and Lipid Storage in Adipocytes. *Biochim Biophys Acta* (2016) 1861(5):419–29. doi: 10.1016/j.bbalip.2016.03.001
133. Roudier E, Chapados N, Decary S, Gineste C, Le Bel C, Lavoie JM, et al. Angiomotin p80/p130 Ratio: A New Indicator of Exercise-Induced Angiogenic Activity in Skeletal Muscles From Obese and Non-Obese Rats? *J Physiol* (2009) 587(Pt 16):4105–19. doi: 10.1113/jphysiol.2009.175554
134. Grill JI, Neumann J, Herbst A, Ofner A, Hiltwein F, Marschall MK, et al. Loss of DRO1/CCDC80 Results in Obesity and Promotes Adipocyte Differentiation. *Mol Cell Endocrinol* (2017) 439:286–96. doi: 10.1016/j.mce.2016.09.014
135. Herder C, Hauner H, Kempf K, Kolb H, Skurk T. Constitutive and Regulated Expression and Secretion of Interferon-Gamma-Inducible Protein 10 (IP-10/CXCL10) in Human Adipocytes. *Int J Obes (Lond)* (2007) 31(3):403–10. doi: 10.1038/sj.ijo.0803432
136. Mousa U, Onur H, Utkan G. Is Obesity Always a Risk Factor for All Breast Cancer Patients? c-erbB2 Expression is Significantly Lower in Obese Patients With Early Stage Breast Cancer. *Clin Transl Oncol* (2012) 14(12):923–30. doi: 10.1007/s12094-012-0878-z
137. Wang C, Ha X, Li W, Xu P, Gu Y, Wang T, et al. Correlation of A2bAR and KLF4/KLF15 With Obesity-Dyslipidemia Induced Inflammation in Uygur Population. *Mediators Inflammation* (2016) 2016:7015620. doi: 10.1155/2016/7015620
138. Mammès O, Betoulle D, Aubert R, Giraud V, Tuzet S, Petiet A, et al. Novel Polymorphisms in the 5' Region of the LEP Gene: Association With Leptin Levels and Response to Low-Calorie Diet in Human Obesity. *Diabetes* (1998) 47(3):487–9. doi: 10.2337/diabetes.47.3.487
139. Khalifeh-Soltani A, McKleroy W, Sakuma S, Cheung YY, Tharp K, Qiu Y, et al. Mfge8 Promotes Obesity by Mediating the Uptake of Dietary Fats and Serum Fatty Acids. *Nat Med* (2014) 20(2):175–83. doi: 10.1038/nm.3450
140. Lim R, Lappas M. Slit2 Exerts Anti-Inflammatory Actions in Human Placenta and is Decreased With Maternal Obesity. *Am J Reprod Immunol* (2015) 73(1):66–78. doi: 10.1111/aji.12334
141. Saiki A, Olsson M, Jernås M, Gummesson A, McTernan PG, Andersson J, et al. Tenomodulin is Highly Expressed in Adipose Tissue, Increased in Obesity, and Down-Regulated During Diet-Induced Weight Loss. *J Clin Endocrinol Metab* (2009) 94(10):3987–94. doi: 10.1210/jc.2009-0292
142. Bauters D, Spincemaille P, Geys L, Cassiman D, Vermeersch P, Bedossa P, et al. ADAMTS5 Deficiency Protects Against Non-Alcoholic Steatohepatitis in Obesity. *Liver Int* (2016) 36(12):1848–59. doi: 10.1111/liv.13181
143. Martinez-Santibanez G, Singer K, Cho KW, DelProposto JL, Mergian T, Lumeng CN. Obesity-Induced Remodeling of the Adipose Tissue Elastin Network is Independent of the Metalloelastase MMP-12. *Adipocyte* (2015) 4(4):264–72. doi: 10.1080/21623945.2015.1027848
144. Tiaden AN, Bahrenberg G, Mirsaidi A, Glanz S, Blüher M, Richards PJ. Novel Function of Serine Protease HTRA1 in Inhibiting Adipogenic Differentiation of Human Mesenchymal Stem Cells *Via* MAP Kinase-Mediated MMP Upregulation. *Stem Cells* (2016) 34(6):1601–14. doi: 10.1002/stem.2297
145. Wolff G, Taranko AE, Meln I, Weinmann J, Sijmonsma T, Lerch S, et al. Diet-Dependent Function of the Extracellular Matrix Proteoglycan Lumican in Obesity and Glucose Homeostasis. *Mol Meta* (2019) 19:97–106. doi: 10.1016/j.molmet.2018.10.007
146. Vaittinen M, Kolehmainen M, Rydén M, Eskelinen M, Wabitsch M, Pihlajamäki J, et al. MFAP5 is Related to Obesity-Associated Adipose Tissue and Extracellular Matrix Remodeling and Inflammation. *Obes (Silver Spring)* (2015) 23(7):1371–8. doi: 10.1002/oby.21103
147. Somm E, Cettour-Rose P, Asensio C, Charollais A, Klein M, Theander-Carrillo C, et al. Interleukin-1 Receptor Antagonist is Upregulated During Diet-Induced Obesity and Regulates Insulin Sensitivity in Rodents. *Diabetologia* (2006) 49(2):387–93. doi: 10.1007/s00125-005-0046-x
148. Zhang D, Christianson J, Liu ZX, Tian L, Choi CS, Neschen S, et al. Resistance to High-Fat Diet-Induced Obesity and Insulin Resistance in Mice With Very Long-Chain acyl-CoA Dehydrogenase Deficiency. *Cell Metab* (2010) 11(5):402–11. doi: 10.1016/j.cmet.2010.03.012
149. Giacchetti G, Faloia E, Sardu C, Camilloni MA, Mariniello B, Gatti C, et al. Gene Expression of Angiotensinogen in Adipose Tissue of Obese Patients. *Int J Obes Relat Metab Disord* (2000) 24 Suppl 2:S142–3. doi: 10.1038/sj.ijo.0801305
150. Dumont J, Goumidi L, Grenier-Boley B, Cottel D, Marécaux N, Montaye M, et al. Dietary Linoleic Acid Interacts With FADS1 Genetic Variability to Modulate HDL-cholesterol and Obesity-Related Traits. *Clin Nutr* (2018) 37(5):1683–9. doi: 10.1016/j.clnu.2017.07.012
151. Wan Z, Frier BC, Williams DB, Wright DC. Epinephrine Induces PDK4 mRNA Expression in Adipose Tissue From Obese, Insulin Resistant Rats. *Obes (Silver Spring)* (2012) 20(2):453–6. doi: 10.1038/oby.2011.252
152. Milagro FI, Gómez-Abellán P, Campión J, Martínez JA, Ordovás JM, Garaulet M. Clock, PER2 and BMAL1 DNA Methylation: Association With Obesity and Metabolic Syndrome Characteristics and Monounsaturated Fat Intake. *Chronobiol Int* (2012) 29(9):1180–94. doi: 10.3109/07420528.2012.719967
153. Caimari A, Oliver P, Rodenburg W, Keijer J, Palou A. Slc27a2 Expression in Peripheral Blood Mononuclear Cells as a Molecular Marker for Overweight Development. *Int J Obes (Lond)* (2010) 34(5):831–9. doi: 10.1038/ijo.2010.17
154. Uchida T, Nakamura T, Hashimoto N, Matsuda T, Kotani K, Sakaue H, et al. Deletion of Cdkn1b Ameliorates Hyperglycemia by Maintaining Compensatory Hyperinsulinemia in Diabetic Mice. *Nat Med* (2005) 11(2):175–82. doi: 10.1038/nm1187
155. Kim D, Kim J, Yoon JH, Ghim J, Yea K, Song P, et al. CXCL12 Secreted From Adipose Tissue Recruits Macrophages and Induces Insulin Resistance in Mice. *Diabetologia* (2014) 57(7):1456–65. doi: 10.1007/s00125-014-3237-5
156. Lu S, Purohit S, Sharma A, Zhi W, He M, Wang Y, et al. Serum Insulin-Like Growth Factor Binding Protein 6 (IGFBP6) is Increased in Patients With Type 1 Diabetes and Its Complications. *Int J Clin Exp Med* (2012) 5(3):229–37.
157. Matsuzaka T, Shimano H, Yahagi N, Kato T, Atsumi A, Yamamoto T, et al. Crucial Role of a Long-Chain Fatty Acid Elongase, Elovl6, in Obesity-Induced Insulin Resistance. *Nat Med* (2007) 13(10):1193–202. doi: 10.1038/nm1662
158. Oguri M, Kato K, Yokoi K, Watanabe S, Metoki N, Yoshida H, et al. Association of Polymorphisms of THBS2 and HSPA8 With Hypertension in Japanese Individuals With Chronic Kidney Disease. *Mol Med Rep* (2009) 2(2):205–11. doi: 10.3892/mmr_00000085
159. Karamat FA, Oudman I, Ris-Stalpers C, Afink GB, Keijser R, Clark JF, et al. Resistance Artery Creatine Kinase mRNA and Blood Pressure in Humans. *Hypertension* (2014) 63(1):68–73. doi: 10.1161/HYPERTENSIONAHA.113.01352
160. Xiang R, Fan LL, Huang H, Chen YQ, He W, Guo S, et al. Increased Reticulon 3 (Rtn3) Leads to Obesity and Hypertriglyceridemia by Interacting With Heat Shock Protein Family A (Hsp70) Member 5 (HSPA5). *Circulation* (2018) 138(17):1828–38. doi: 10.1161/CIRCULATIONAHA.117.030718
161. Capobianco V, Nardelli C, Ferrigno M, Iaffaldano L, Pilone V, Forestieri P, et al. miRNA and Protein Expression Profiles of Visceral Adipose Tissue Reveal miR-141/YWHAG and miR-520e/RAB11A as Two Potential miRNA/protein Target Pairs Associated With Severe Obesity. *J Proteome Res* (2012) 11(6):3358–69. doi: 10.1021/pr300152z
162. Liou TH, Chen HH, Wang W, Wu SF, Lee YC, Yang WS, et al. ESR1, FTO, and UCP2 Genes Interact With Bariatric Surgery Affecting Weight Loss and Glycemic Control in Severely Obese Patients. *Obes Surg* (2011) 21(11):1758–65. doi: 10.1007/s11695-011-0457-3
163. Pal A, Barber TM, Bunt M, Rudge SA, Zhang Q, Lachlan KL, et al. PTEN Mutations as a Cause of Constitutive Insulin Sensitivity and Obesity. *N Engl J Med* (2012) 367(11):1002–11. doi: 10.1056/NEJMoa1113966
164. Ahmad R, Shihab PK, Thomas R, Alghanim M, Hasan A, Sindhu S, et al. Increased Expression of the Interleukin-1 Receptor-Associated Kinase (IRAK)-1 is Associated With Adipose Tissue Inflammatory State in Obesity. *Diabetol Metab Syndr* (2015) 7:71. doi: 10.1186/s13098-015-0067-7
165. Bouchard L, Tchernof A, Deshaies Y, Lebel S, Hould FS, Marceau P, et al. CYR61 Polymorphisms Are Associated With Plasma HDL-cholesterol Levels in Obese Individuals. *Clin Genet* (2007) 72(3):224–9. doi: 10.1111/j.1399-0004.2007.00855.x
166. Bendlová B, Vaňková M, Hill M, Vacínová G, Lukášová P, VejraŽková D, et al. ZBTB16 Gene Variability Influences Obesity-Related Parameters and

Serum Lipid Levels in Czech Adults. *Physiol Res 66(Supplementum* (2017) 3): S425–31. doi: 10.33549/physiolres.933731
167. Hinrichsen I, Ernst BP, Nuber F, Passmann S, Schäfer D, Steinke V, et al. Reduced Migration of MLH1 Deficient Colon Cancer Cells Depends on SPTAN1. *Mol Cancer* (2014) 13:11. doi: 10.1186/1476-4598-13-11
168. Whiteland H, Spencer-Harty S, Morgan C, Kynaston H, Thomas DH, Bose P, et al. A Role for STEAP2 in Prostate Cancer Progression. *Clin Exp Metastasis* (2014) 31(8):909–20. doi: 10.1007/s10585-014-9679-9
169. Cao X, Xia Y, Yang J, Jiang J, Chen L, Ni R, et al. Clinical and Biological Significance of Never in Mitosis Gene A-Related Kinase 6 (NEK6) Expression in Hepatic Cell Cancer. *Pathol Oncol Res* (2012) 18(2):201–7. doi: 10.1007/s12253-011-9429-0
170. Zecchini V, Madhu B, Russell R, Pértega-Gomes N, Warren A, Gaude E, et al. Nuclear ARRB1 Induces Pseudohypoxia and Cellular Metabolism Reprogramming in Prostate Cancer. *EMBO J* (2014) Jun 1733(12):1365–82. doi: 10.15252/embj.201386874
171. Xue J, Chi Y, Chen Y, Huang S, Ye X, Niu J, et al. MiRNA-621 Sensitizes Breast Cancer to Chemotherapy by Suppressing FBXO11 and Enhancing p53 Activity. *Oncogene* (2016) 35(4):448–58. doi: 10.1038/onc.2015.96
172. Mao J, Liang Z, Zhang B, Yang H, Li X, Fu H, et al. Ubr2 Enriched in P53 Deficient Mouse Bone Marrow Mesenchymal Stem Cell-Exosome Promoted Gastric Cancer Progression *Via* Wnt/β-Catenin Pathway. *Stem Cells* (2017) 35(11):2267–79. doi: 10.1002/stem.2702
173. Peng H, Ishida M, Li L, Saito A, Kamiya A, Hamilton JP, et al. Pseudogene INTS6P1 Regulates Its Cognate Gene INTS6 Through Competitive Binding of miR-17-5p in Hepatocellular Carcinoma. *Oncotarget* (2015) 6(8):5666–77. doi: 10.18632/oncotarget.3290
174. Liou TH, Chen HH, Wang W, Wu SF, Lee YC, Yang WS, et al. Esr1, FTO, and UCP2 Genes Interact With Bariatric Surgery Affecting Weight Loss and Glycemic Control in Severely Obese Patients. *Obes Surg* (2011) 21(11):1758–65. doi: 10.1007/s11695-011-0457-3
175. Ma S, Guan XY, Beh PS, Wong KY, Chan YP, Yuen HF, et al. The Significance of LMO2 Expression in the Progression of Prostate Cancer. *J Pathol* (2007) 211(3):278–85. doi: 10.1002/path.2109
176. Wang CC, Liau JY, Lu YS, Chen JW, Yao YT, Lien HC. Differential Expression of Moesin in Breast Cancers and Its Implication in Epithelial-Mesenchymal Transition. *Histopathology* (2012) 61(1):78–87. doi: 10.1111/j.1365-2559.2012.04204.x
177. Yoshino H, Chiyomaru T, Enokida H, Kawakami K, Tatarano S, Nishiyama K, et al. The Tumour-Suppressive Function of miR-1 and miR-133a Targeting TAGLN2 in Bladder Cancer. *Br J Cancer* (2011) 104(5):808–18. doi: 10.1038/bjc.2011.23
178. Gautrey H, Jackson C, Dittrich AL, Browell D, Lennard T, Tyson-Capper A. SRSF3 and Hnrnp H1 Regulate a Splicing Hotspot of HER2 in Breast Cancer Cells. *RNA Biol* (2015) 12(10):1139–51. doi: 10.1080/15476286.2015.1076610
179. Hammerich-Hille S, Bardout VJ, Hilsenbeck SG, Osborne CK, Oesterreich S. Low SAFB Levels Are Associated With Worse Outcome in Breast Cancer Patients. *Breast Cancer Res Treat* (2010) 121(2):503–9. doi: 10.1007/s10549-008-0297-6
180. Ellison-Zelski SJ, Alarid ET. Maximum Growth and Survival of Estrogen Receptor-Alpha Positive Breast Cancer Cells Requires the Sin3A Transcriptional Repressor. *Mol Cancer* (2010) 9:263. doi: 10.1186/1476-4598-9-263
181. Tsai WW, Wang Z, Yiu TT, Akdemir KC, Xia W, Winter S, et al. TRIM24 Links a non-Canonical Histone Signature to Breast Cancer. *Nature* (2010) 468(7326):927–32. doi: 10.1038/nature09542
182. Han Y, Ru GQ, Mou X, Wang HJ, Ma Y, He XL, et al. AUTS2 is a Potential Therapeutic Target for Pancreatic Cancer Patients With Liver Metastases. *Med Hypotheses* (2015) 85(2):203–6. doi: 10.1016/j.mehy.2015.04.029
183. Saxena R, Bjonnes A, Prescott J, Dib P, Natt P, Lane J, et al. Genome-Wide Association Study Identifies Variants in Casein Kinase II (CSNK2A2) to be Associated With Leukocyte Telomere Length in a Punjabi Sikh Diabetic Cohort. *Circ Cardiovasc Genet* (2014) 7(3):287–95. doi: 10.1161/CIRCGENETICS.113.000412
184. Thun GA, Imboden M, Berger W, Rochat T, Probst-Hensch NM. The Association of a Variant in the Cell Cycle Control Gene CCND1 and Obesity on the Development of Asthma in the Swiss SAPALDIA Study. *J Asthma.* (2013) 50(2):147–54. doi: 10.3109/02770903.2012.757776
185. Chiellini C, Bertacca A, Novelli SE, Görgün CZ, Ciccarone A, Giordano A, et al. Obesity Modulates the Expression of Haptoglobin in the White Adipose Tissue *Via* TNFalpha. *J Cell Physiol* (2002) 190(2):251–8. doi: 10.1002/jcp.10061
186. Yaghootkar H, Stancáková A, Freathy RM, Vangipurapu J, Weedon MN, Xie W, et al. Association Analysis of 29,956 Individuals Confirms That a Low-Frequency Variant at CCND2 Halves the Risk of Type 2 Diabetes by Enhancing Insulin Secretion. *Diabetes* (2015) 64(6):2279–85. doi: 10.2337/db14-1456
187. Chutkow WA, Birkenfeld AL, Brown JD, Lee HY, Frederick DW, Yoshioka J, et al. Deletion of the Alpha-Arrestin Protein Txnip in Mice Promotes Adiposity and Adipogenesis While Preserving Insulin Sensitivity. *Diabetes* (2010) 59(6):1424–34. doi: 10.2337/db09-1212
188. Kim S, Hong JW, Park KW. B Cell Translocation Gene 2 (Btg2) is Regulated by Stat3 Signaling and Inhibits Adipocyte Differentiation. *Mol Cell Biochem* (2016) 413(1-2):145–53. doi: 10.1007/s11010-015-2648-z
189. Lee MF, Pan MH, Chiou YS, Cheng AC, Huang H. Resveratrol Modulates MED28 (Magicin/Eg-1) Expression and Inhibits Epidermal Growth Factor (EGF)-Induced Migration in MDA-MB-231 Human Breast Cancer Cells. *J Agric Food Chem* (2011) 59(21):11853–61. doi: 10.1021/jf202426k
190. Nakamura R, Kataoka H, Sato N, Kanamori M, Ihara M, Igarashi H, et al. EPHA2/EFNA1 Expression in Human Gastric Cancer. *Cancer Sci* (2005) 96 (1):42–7. doi: 10.1111/j.1349-7006.2005.00007.x

Conflict of Interest: The authors declare that the research was conducted in the absence of any commercial or financial relationships that could be construed as a potential conflict of interest.

frontiers in Endocrinology

ORIGINAL RESEARCH
published: 06 August 2021
doi: 10.3389/fendo.2021.648844

Vitamin D Level and Vitamin D Receptor Genetic Variation Were Involved in the Risk of Non-Alcoholic Fatty Liver Disease: A Case-Control Study

Ru Zhang[1†], Minxian Wang[1†], Min Wang[1], Liuxin Zhang[2], Yajie Ding[1], Zongzhe Tang[1], Zuqiang Fu[3], Haozhi Fan[4], Wei Zhang[5] and Jie Wang[1]*

[1] Department of Fundamental and Community Nursing, School of Nursing, Nanjing Medical University, Nanjing, China, [2] Department of Nursing, The Affiliated Brain Hospital of Nanjing Medical University, Nanjing, China, [3] Department of Epidemiology, School of Public Health, Nanjing Medical University, Nanjing, China, [4] Department of Information, The First Affiliated Hospital of Nanjing Medical University, Nanjing, China, [5] Department of Epidemiology, Shanghai Cancer Institute, Shanghai, China

OPEN ACCESS

Edited by:
Stephen Atkin,
Royal College of Surgeons in Ireland, Bahrain

Reviewed by:
Maximilian Zeyda,
Medical University of Vienna, Austria
Ilaria Barchetta,
Sapienza University of Rome, Italy

****Correspondence:***
Jie Wang
wangjienjmu@126.com

[†]These authors have contributed equally to this work and share first authorship

Specialty section:
This article was submitted to Systems Endocrinology, a section of the journal Frontiers in Endocrinology

Received: *02 February 2021*
Accepted: *20 July 2021*
Published: *06 August 2021*

Citation:
Zhang R, Wang M, Wang M, Zhang L, Ding Y, Tang Z, Fu Z, Fan H, Zhang W and Wang J (2021) Vitamin D Level and Vitamin D Receptor Genetic Variation Were Involved in the Risk of Non-Alcoholic Fatty Liver Disease: A Case-Control Study. Front. Endocrinol. 12:648844. doi: 10.3389/fendo.2021.648844

Background: It has been demonstrated that vitamin D receptor (*VDR*), a key gene in the metabolism of vitamin D (VD), may affect the development of Non-alcoholic fatty liver disease (NAFLD) by regulating VD level and its biological effects.

Objectives: To investigate the effects of serum VD level, *VDR* variation, and a combination of *VDR* SNP and environmental behavior factor on the risk of NAFLD.

Methods: A total of 3023 subjects from a community in Nanjing were enrolled, including 1120 NAFLD cases and 1903 controls. Serum 25(OH)D_3 levels were measured and eight single nucleotide polymorphisms (SNPs) in *VDR* gene were genotyped.

Results: Logistic regression analyses indicated that VD sufficiency and VD insufficiency were significantly associated with a low risk of NAFLD (all $P<0.05$; all $P_{trend}<0.05$, in a locus-dosage manner). After adjusting for gender and age, *VDR* rs2228570-A and rs11168287-A alleles were all reduced the risk of NAFLD (all $P_{FDR}=0.136$, in dominant model; $P_{trend}=0.039$, combined effects in a locus-dosage manner). The protective effects of two favorable alleles were more evident among subjects ≤40 years, non-hypertension, non-hyperglycemia and non-low high density lipoprotein-cholesterol (all $P<0.05$). The area under the receiver operating curve of the combination of *VDR* SNP and exercise time for assessing NAFLD risk was slightly higher than that of only including exercise time or neither (all $P<0.05$).

Conclusion: High serum VD levels and *VDR* variants (rs2228570-A and rs11168287-A) might contribute to a low risk of NAFLD in Chinese Han population. The inclusion of *VDR* SNP and exercise time could improve the efficiency in assessment of NAFLD risk, which might provide a novel perspective for early screening and preventing NAFLD.

Keywords: non-alcoholic fatty liver disease (NAFLD), vitamin D (VD) deficiency, 25-hydroxyvitamin D3, vitamin D receptor (VDR), genetic variation, risk assessment

INTRODUCTION

Non-alcoholic fatty liver disease (NAFLD), as the most prevalent liver disease worldwide, comprises a wide disease spectrum ranging from steatosis to nonalcoholic steatohepatitis (NASH) and NASH-related cirrhosis (1, 2). The reported prevalence reaches 10-30% in the United States, Europe and Asia (3, 4). Most patients with NAFLD are asymptomatic, and only few may complain of nonspecific symptoms, like discomfort, fatigue, and vague right upper abdominal pain (5), but NAFLD can increase the risk of type 2 diabetes mellitus (T2DM) as well as cardiovascular disease (6), and NASH may develop into fibrosis, even causing cirrhosis and hepatocellular carcinoma (7). There are currently no approved therapies for NAFLD (8, 9), and it is still necessary to explore the potential influencing factors affecting the development and progression of NAFLD.

Many factors are associated with NAFLD including insulin resistance (IR), metabolic syndrome and genetic variation (10, 11). Studies have increasingly found that vitamin D (VD) can affect the development of NAFLD by regulating IR (12), immune inflammation (13), lipid metabolism and target gene expression (14). Vitamin D deficiency is implicated in NAFLD etiology (15, 16), insulin resistance (17), visceral obesity, and metabolic syndrome (18). A meta-analysis found that compared to controls, patients with NAFLD had a lower level of VD (0.36 ng/mL) and were 1.26 times more likely to be VD-deficient (19). A population-based case-control study in China found that low serum VD was associated with advanced liver fibrosis in NAFLD patients (20). However, another systematic review and meta-analysis suggested that serum VD level might not change with NAFLD histologic severity (21). A randomized, double-blind, placebo-controlled trial in Italy suggested that although high-dose oral VD supplementation could increase the serum VD level, no effect was shown on hepatic steatosis or metabolic/cardiovascular parameters in T2DM patients with NAFLD (22). Thus, the relationship between VD and NAFLD was controversial.

VD must be transported, hydroxylated and finally combined with vitamin D receptor (VDR) to accomplish its biological roles (23). Serum VD may produce different biological effects due to genetic heterogeneity, which may help to explain why some people are prone to NAFLD, while others are not (even if they have metabolic syndrome components). Thus, exploring the influence of genetic variation on NAFLD related to VD metabolism is necessary. *VDR*, a key gene in VD metabolic pathway and a member of steroid/thyroid hormone receptor family (24), transcriptionally activates target genes after binding to vitamin D responsive elements localized in the promoter regions (25). These target genes mediate various NAFLD-associated processes, including lipid and glucose metabolism, cholesterol efflux and bile acid homeostasis, hepatic fibrogenesis, cellular differentiation, apoptosis and immune response (26, 27).

Notably, NAFLD is considered a complex disease trait such that interactions between the environment and a susceptible genetic host background influence disease development and progression (2). Studying data suggests that genetic background may influence the response to lifestyle modification. For example, reduction in liver fat and liver enzyme levels in response to weight loss was larger in subjects homozygous for the PNPLA3 I148M variant compared to non-carriers (28, 29). However, there is little information available on the association between environmental behaviors and *VDR* polymorphisms in the development and progression of NAFLD. Therefore, the aim of this study was to explore the effects of serum VD level, *VDR* variation, and a combination of *VDR* SNP and environmental behavior factor on the risk of NAFLD.

METHODS

Participants and Study Design

A total of 3023 subjects from a community in Nanjing (Jiangsu, China) were enrolled in this case-control study during July to September 2018. The NAFLD cases were recruited from those diagnosed based on "*Guideline of prevention and treatment for nonalcoholic fatty liver disease: a 2018 update*". NAFLD can be diagnosed if the following items 1-4 coexist with the fifth or sixth item: (1) no drinking or history of overdose drinking (less than 210g/week ethanol for men and 140g/week for women in the past 12 months); (2) excluding drug hepatitis, hepatitis C virus genotype 3 infection, hepatolenticular degeneration and other specific diseases that could result in fatty liver; (3) serum levels of transaminase and γ-glutamyl transpeptidase (γ-GT) increase mildly to moderately (<5 times above the upper normal limit), usually presenting as an increase of alanine aminotransferase (ALT); (4) metabolic syndrome constituents such as visceral obesity, hyperglycemia, blood lipid disorder and hypertension; (5) the result of liver imaging study meets the imaging diagnostic criteria of diffuse fatty liver; (6) the histological findings of liver biopsy meet the pathological diagnostic criteria of fatty liver disease. The non-NAFLD controls were collected from the same community during the study period and randomly assigned to the control group. The constituent ratios of gender and age between cases and controls were considered similar, according the results of frequency-matching.

Excluded were: (1) less than 18 years old; (2) subjects with infection, acute or chronic gastrointestinal diseases, autoimmune diseases or malignant tumors; (3) subjects with history of other viral hepatitis, alcoholic liver disease or primary liver cancer; (4) subjects of excessive drinking (alcohol consumption ≥30g/d in males and ≥20g/d in females); (5) subjects who received a liver transplant within the previous year, or had complications of advanced liver disease (varicose veins, ascites, etc.); (6) subjects with drug-induced fatty hepatitis; (7) subjects with history of psychiatric disorders.

By reviewing the literature, we assumed the frequency of gene mutation in the general population was 20%, odds ratio (OR) was 1.5, two-sided test α was 0.05, and power of test (1-β) was 90%. Therefore, the minimum sample size was estimated by NCSS-PASS 11 software (Dawson edition; Kaysville, UT) to be 784. This study had a sample size large enough to guarantee the production of reliable results.

The current study protocol was in accordance with the Declaration of Helsinki, and was approved by the Institutional

Ethics Review Committee of Nanjing Medical University (Nanjing, China). Written informed consent was obtained before blood test and genetic analysis.

Collection of Basic Data and Blood Samples

Self-designed questionnaires and an electronic medical record system were used to collect the demographic and clinical characteristics of all participants. 5-mL ethylene diamine tetraacetic acid (EDTA) anticoagulant venous blood was collected from each subject in the morning after an overnight fast. Within 2 hours, the serum and blood cells in each blood sample were separated and frozen at -80°C until further serological tests and genotyping assays.

Serum 25(OH)D_3 Level Detection

In two groups (gender and age matched at a ratio of 1:1, 336 subjects in the NAFLD group and 336 in the control group), the serum 25(OH)D_3 level was measured by enzyme-linked immunosorbent assay (ELISA) according to the manufacturer's instructions (Human 25-Dihydroxy vitamin D3 (25(OH)D3) ELISA Kit; Jin Yibai Biological Technology Co., Ltd.; Nanjing, China).

SNP Selection and Genotyping

Target SNPs with potential biological function were selected to better identify the susceptibility sites that affect the development of NAFLD. The selection processes were as follows: (1) Downloading the genotype database of *VDR* gene in Han Chinese in Beijing (CHB) from the 1000 Genomes Project database (http://asia.ensembl.org/Homo_sapiens/Info/Index); (2) Importing the genotype database into the Haploview software (version 4.2; Broad Institute, Cambridge, MA, USA). Setting parameters: Hardy-Weinberg *P*-value cutoff = 0.05; minor allele frequency (MAF) = 0.05; r^2 threshold = 0.8. At this point, 56 tagging SNPs (tagSNPs) were captured; (3) Searching for literature in which these potential tagSNPs were associated with NAFLD, hypertension, type 2 diabetes, hyperlipidemia, metabolic syndrome, inflammatory diseases or immune-related disorders. Finally, eight disease-related target SNPs of *VDR* gene were selected, including rs3782905 (C>G), rs3847987 (C>A), rs11574129 (T>C), rs2228570 (C>A), rs11568820 (G>A), rs739837 (G>T), rs7975232 (C>A) and rs11168287 (G>A).

Genomic DNA was isolated from EDTA anticoagulated blood samples using magnetic bead method (blood genomic extraction kit; Pangu Genome Nanotechnology Co., Ltd.; Nanjing, China). The eight SNPs were genotyped using TaqMan allelic discrimination assays on the ABI 9700 system (Applied Biosystems, Foster City, California, USA; catalog numbers: C:_3290647_10, C:_2404006_10, C_175992105_10, C:12060045_20, C:_2880808_10, C:_2404007_10, C:28977635_10, C:_2404006_10). The quality control of experimental data was as follows: (1) blinding was adopted in genotyping, so that all laboratory personnel were unclear about the clinical data of the subjects; (2) 10% of the samples were randomly selected for repeated experiments with a repeatability of 100%. The success rates of genotyping all SNPs were higher than 99% in this study.

Statistical Analysis

All statistical analyses were processed using SPSS (version 22.0, SPSS Inc., Chicago, IL, USA) and MedCalc (Version 19.1, Ostend, Belgium). Distributions of demographic and clinical characteristics of two groups were compared using χ^2-test, student's *t* test or Mann-Whitney U test, wherever appropriate. Logistic regression analysis was used to calculate odds ratio (OR) and 95% confidence interval (95% CI) for quantifying the association of serum 25(OH)D_3 level with the risk of NAFLD. The correlation of serum 25(OH)D_3 level with *VDR* SNPs was assessed using general linear regression model adjusted for gender and age. The Hardy-Weinberg equilibrium (HWE) was tested using a goodness of-fit χ^2 -test among the control subjects. The relationships between *VDR* SNPs and the risk of NAFLD were analyzed by dominant model (heterozygote + mutant homozygote *VS*. wild homozygote), recessive model (mutant homozygote *VS*. wild homozygote + heterozygote), and additive model (mutant homozygote *VS*. heterozygote *VS*. wild homozygote), respectively. For multiple SNPs comparisons, false discovery rate (FDR) correction was used and the P_{FDR} value ≤ 0.25 was regarded as modest confidence that the correlation represented a positive result (30). Subgroup analysis was performed for positive SNPs, and Q test was performed to calculate the heterogeneity between subgroups. The area under the receiver operating curves (AUROCs) was performed to assess the predictive power of the combination of positive SNPs, environmental behavior factors and mainly related clinical factors for NAFLD risk. A two-tailed test with a *P* value < 0.05 was regarded as statistically significant in all analyses.

RESULTS

Basic Characteristics of Participants

The demographic and clinical characteristics of 1120 NAFLD cases and 1903 controls were summarized in **Table 1**. No significant differences were observed in the distribution of gender and age between the two groups (all *P*>0.05). However, there were significant differences in exercise time, body mass index (BMI), waist circumference (WC), systolic blood pressure (SBP), diastolic blood pressure (DBP), triglyceride (TG), total cholesterol (TC), high density lipoprotein-cholesterol (HDL-C), low density lipoprotein-cholesterol (LDL-C), glucose (GLU), γ-glutamyl transpeptidase (γ-GT), alanine aminotransferase (ALT), aspartate aminotransferase (AST), direct bilirubin (DBIL), total bilirubin (TBIL) and serum 25(OH)D_3 levels (all *P*<0.05).

Association Between Serum 25(OH)D_3 Level and NAFLD Risk

According to the level of serum 25(OH)D_3, 672 participants were divided into three categories: VD deficiency (<20ng/mL), VD insufficiency (20ng/mL-30ng/mL) and VD sufficiency (≥30ng/mL) (31). The constituent ratios of three categories were 60.9%

TABLE 1 | Distributions and comparisons of demographic and clinical characteristics between NAFLD case and control groups.

Variables	NAFLD cases (N=1120)	Controls (N=1903)	χ^2/t/Z	P
Gender			2.324	0.127[a]
male	948 (84.6)	1570 (82.5)		
female	172 (15.4)	333 (17.5)		
Age (years)			1.107	0.293[a]
≤40	596 (53.2)	975 (51.2)		
>40	524 (46.8)	928 (48.8)		
mean ± SD	40.48 ± 8.80	39.89 ± 9.78	-1.649	0.099[b]
Exercise time (min/week)			**8.556**	**0.003**[a]
<150	622 (58.6)	995 (53.0)		
≥150	440 (41.4)	883 (47.0)		
mean ± SD	144.09 ± 41.77	150.06 ± 43.82	**3.609**	**<0.001**[b]
BMI (kg/m^2)	25.36 ± 2.53	22.80 ± 2.48	**-27.235**	**<0.001**[b]
WC (cm)	88.47 ± 7.85	81.68 ± 7.59	**-23.462**	**<0.001**[b]
SBP (mmHg)	130.58 ± 15.08	124.70 ± 13.70	**-10.700**	**<0.001**[b]
DBP (mmHg)	79.48 ± 10.86	74.81 ± 9.38	**-12.134**	**<0.001**[b]
TG (mmol/L)	1.96 (1.43, 2.69)	1.06 (0.79, 1.41)	**-23.408**	**<0.001**[c]
TC (mmol/L)	4.84 (4.27, 5.42)	4.45 (4.05, 5.03)	**-7.804**	**<0.001**[c]
HDL-C (mmol/L)	1.00 (0.85, 1.18)	1.27 (1.07, 1.48)	**-18.179**	**<0.001**[c]
LDL-C (mmol/L)	2.82 (2.20, 3.33)	2.63 (2.24, 3.10)	**-4.424**	**<0.001**[c]
GLU (mmol/L)	3.13 (2.39, 5.00)	3.91 (2.32, 4.73)	**-5.754**	**<0.001**[c]
γ-GT (U/L)	35.00 (24.00, 55.00)	17.00 (13.00, 25.00)	**-20.121**	**<0.001**[c]
ALT (U/L)	36.00 (25.00, 54.50)	18.00 (13.25, 25.00)	**-19.872**	**<0.001**[c]
AST (U/L)	24.00 (19.00, 31.00)	19.00 (16.00, 21.00)	**-11.789**	**<0.001**[c]
DBIL (μmol/L)	4.01 (3.21 5.21)	4.20 (3.32, 5.23)	**-5.025**	**<0.001**[c]
TBIL (μmol/L)	13.59 (10.71, 18.39)	13.85 (11.21, 18.21)	**-3.267**	**0.001**[c]
25(OH)D_3 (ng/mL)[d]			**22.575**	**<0.001**[a]
<20	130 (71.0)	167 (49.7)		
20-30	27 (14.8)	97 (28.9)		
≥30	26 (14.2)	72 (21.4)		
median (IQR)	16.06 (12.21, 20.78)	20.00 (16.84, 26.68)	**-7.168**	**<0.001**[c]

NAFLD, non-alcoholic fatty liver disease; SD, standard deviation; BMI, body mass index; WC, waist circumference; SBP, Systolic blood pressure; DBP, Diastolic blood pressure; TG, triglyceride; TC, total cholesterol; HDL-C, high density liptein cholesterol; LDL-C, low density lipoprotein-chesterol; GLU, glucose; γ-GT, γ-glutamyl transpeptidase; ALT, alanine aminotransferase; AST, aspartate aminotransferase; DBIL, direct bilirubin; TBIL, total bilirubin; 25(OH)D_3, 25-hydroxyvitamin D3; IQR, interquartile range.

[a]*χ^2-test among two groups.*

[b]*Student's t test among two groups.*

[c]*Mann-Whitney U test among two groups.*

[d]*serum 25(OH)D_3 levels were measured in 336 NAFLD cases and 336 controls.*

Bold type indicates statistically significant results.

(409/672), 21.4% (144/672), and 17.7% (119/672), respectively. The prevalences of NAFLD in the three categories were 59.2% (242/409), 32.6% (47/144) and 39.5% (47/199), respectively, with significant differences (χ^2 = 36.366, P<0.05). In addition, multiple comparisons showed that the prevalence of NAFLD in patients with VD deficiency was significantly higher than that in patients with VD insufficient or VD sufficient (all $P_{Bonferroni}$<0.017), but there was no significant difference in the prevalence of NAFLD between categories with VD insufficiency and VD sufficiency ($P_{Bonferroni}$>0.017) (**Supplementary Figure 1**).

Further logistic regression analysis suggested that compared to VD deficiency, VD sufficiency (crude OR=0.450, 95% CI=0.297-0.684, P<0.001) and VD insufficiency (crude OR=0.334, 95%CI=0.224-0.499, P<0.001) were associated with a lower risk of NAFLD, and this association was dose-dependent (P_{trend}<0.001) (model 1). After adjusting for gender, age, BMI and SBP (model 2), the subjects with VD sufficiency (adjusted OR=0.477, 95%CI=0.277-0.821, P=0.008) and VD insufficiency (adjusted OR=0.344, 95%CI=0.206-0.573, P<0.001) all had significantly decreased risk of NAFLD compared with those with VD deficiency, and a significant locus-dosage effect of VD level on NAFLD risk was also observed (P_{trend}<0.001). When adjusting for the above factors and TG, HDL-C, GLU (model 3), the risk of NAFLD still decreased significantly with the increase of VD level (VD sufficiency vs. VD deficiency: adjusted OR=0.552, 95%CI=0.305-0.998, P=0.049; VD insufficiency vs. VD deficiency: adjusted OR=0.298, 95%CI=0.165-0.539, P<0.001; P_{trend}=0.005) (**Table 2**).

Associations Between *VDR* SNPs and Serum 25(OH)D_3 Level

Serum 25(OH)D_3 levels were Lg transformed into an approximately normal distribution, and SNPs were coded in an additive genetic model. The general linear regression analysis indicated that there were no significant associations between eight *VDR* SNPs and serum 25(OH)D_3 levels after adjusting for gender and age (all P>0.05) (**Supplementary Table 1**).

Association Between *VDR* SNPs and NAFLD Risk

The genotype distributions of the eight SNPs in both groups were shown in **Table 3**. After adjusting for gender and age, logistic

TABLE 2 | Logistic regression analysis of the associations between serum 25(OH)D_3 levels and risk of NAFLD.

	serum 25 (OH)D_3 levels			P_{trend}
	VD deficiency (N=409)	VD insufficiency (N=144)	VD sufficiency (N=119)	
Model 1	1.00 (Ref)	**0.334 (0.224, 0.499)**	**0.450 (0.297, 0.684)**	**<0.001**
P		**<0.001**	**<0.001**	
Model 2	1.00 (Ref)	**0.344 (0.206, 0.573)**	**0.477 (0.277, 0.821)**	**<0.001**
P		**<0.001**	**0.008**	
Model 3	1.00 (Ref)	**0.298 (0.165, 0.539)**	**0.552 (0.305, 0.998)**	**0.005**
P		**<0.001**	**0.049**	

NAFLD, non-alcoholic fatty liver disease; 25(OH)D_3, 25-hydroxyvitamin D3.
VD deficiency, serum 25(OH)D_3 < 20ng/mL; VD insufficiency, 20ng/mL≤ serum 25(OH)D_3 <30ng/mL; VD sufficiency, serum 25(OH)D_3 ≥30ng/mL.
Model 1, unadjusted; Model 2, adjusted for gender, age, BMI, SBP; Model 3, model 2 with additional adjustment for TG, HDL-C, GLU.
Bold type indicates statistically significant results.

regression analyses showed that *VDR* rs2228570-A variant (AA: adjusted OR=0.782, 95%CI=0.633-0.966, *P*=0.023; dominant model: adjusted OR=0.837, 95%CI=0.710-0.986, *P*=0.034; additive model: adjusted OR=0.883, 95%CI=0.794-0.981, *P*=0.020) and rs11168287-A variant (GA: adjusted OR=0.830, 95%CI=0.707-0.974, *P*=0.022; dominant model: adjusted OR=0.839, 95%CI=0.721-0.976, *P*=0.023) all significantly reduced the risk of NAFLD in different models. Under the premise of FDR threshold ≤ 0.25, FDR revealed with modest confidence that the associations between the two SNPs and a low risk of NAFLD were positive (all P_{FDR}=0.136, in dominant model; **Supplementary Table 2**).

In addition, the combined effects of *VDR* variants rs2228570 and rs11168287 on the risk of NAFLD were estimated by the number of favorable alleles from the two SNPs, as shown in **Supplementary Table 3**. The subjects were first divided into three groups with "0", "1-2" and "3-4" favorable alleles. Compared with those who had 0 favorable alleles, subjects with "3-4" favorable alleles had significantly decreased risk of NAFLD (adjusted OR=0.750, 95%CI=0.577-0.974, *P*=0.031) and the more favorable alleles, the lower NAFLD risk, suggesting a significant locus-dosage effect of the combined alleles on NAFLD risk (P_{trend}=0.039). The subjects were then distributed into two groups with "0" and "1-4" favorable alleles, and we found that the presence of "1-4" alleles was related to a 0.798-fold lower risk of NAFLD (adjusted 95% CI=0.644-0.990, *P*=0.040).

We further performed the stratification analyses to evaluate the combined effects of *VDR* rs2228570-A and rs11168287-A alleles on the risk of NAFLD adjusted with gender and age. As shown in **Supplementary Figure 2**, the combined protective effects of two alleles were more prominent in subjects ≤ 40 years (adjusted OR=0.696, 95%CI=0.515-0.940, *P*=0.018), non-hypertension (adjusted OR=0.770, 95%CI=0.602-0.986, *P*=0.038), non-hyperglycemia (adjusted OR=0.791, 95% CI=0.631-0.991, *P*=0.042) and non-low HDL-C (adjusted OR=0.710, 95%CI=0.536-0.942, *P*=0.018). The heterogeneity test discovered no significant differences among all the subgroups (all *P*>0.05).

Influence Factors of NAFLD

A stepwise regression model were performed with gender, age, visceral obesity, hypertension, hyperglycemia, hypertriglyceridemia, Low HDL-C, ALT, exercise time, rs2228570 and rs11168287. The coding of each variable was described in **Supplementary Table 4**. The results showed that age ≤40 years (OR=0.716, 95%CI=0.583-0.879, *P*=0.001), exercise time ≥150 min/week (OR=0.798, 95% CI=0.661-0.963, *P*=0.019) and rs2228570-A (OR=0.768, 95% CI=0.626-0.942, *P*=0.011) were independent protective factors of NAFLD. Conversely, visceral obesity (OR=3.653, 95%CI=2.984-4.471, *P*<0.001), hypertension (OR=1.654, 95%CI=1.290-2.121, *P*<0.001), hypertriglyceridemia (OR=3.455, 95%CI=2.784-4.288, *P*<0.001), Low HDL-C (OR=1.879, 95%CI=1.536-2.299, *P*<0.001) and ALT > 40U/L (OR=2.729, 95%CI=2.060-3.615, *P*<0.001) were independent risk factors of NAFLD (**Table 4**).

We further constructed combined factors based on the above factors for assessing NAFLD risk, and the combined factor 1 (a combination of clinical factors) = (-1.588) + (-0.229) × age + 1.333 × visceral obesity + 0.484 × hypertension + 1.233 × hypertriglyceridemia + 0.621 × Low HDL-C + 0.939 × ALT. Similarly, combined factor 2 (a combination of clinical factors and exercise time) = (-1.448) + (-0.254) × age + 1.294 × visceral obesity + 0.512 × hypertension + 1.222 × hypertriglyceridemia + 0.610 × low HDL-C + 0.958 × ALT + (-0.220) × exercise time; combined factor 3 (a combination of clinical factors, exercise time and SNP genetic variant) = (-1.519) + (-0.334) × age + 1.296 × visceral obesity + 0.503 × hypertension + 1.240 × hypertriglyceridemia + 0.631 × low HDL-C + 1.004 × ALT + (-0.225) × exercise time + (-0.264) × rs2228570. In **Figure 1**, the AUROCs of these combined factors were 0.770, 0.774, and 0.780, respectively, and the AUROC of combined factor 3 for assessing NAFLD risk was slightly higher than that of combined factor 2 (0.780 vs. 0.774, 95%CI=0.002-0.011, *P*=0.007) and combined factor 1 (0.780 vs. 0.770, 95%CI=0.005-0.016, *P*<0.001).

DISCUSSION

In the current study, our findings suggested that high serum vitamin D level, *VDR* rs2228570-A and rs11168287-A were associated with a decreased risk of NAFLD, and the combination of *VDR* rs2228570 and exercise time was more effective in the risk assessment of NAFLD.

Accumulative evidence suggests that VD deficiency is highly prevalent among the general population in China (32), and low

TABLE 3 | Genotype distributions of *VDR* polymorphisms among the two study groups and association analyses of these eight SNPs and NAFLD.

SNP	NAFLD cases n (%)	Controls n (%)	OR (95% CI)[a]	*P*[a]
rs3782905-CC	756 (69.3)	1328 (71.1)	1.00 (Ref)	
CG	296 (27.1)	475 (25.4)	1.087 (0.922, 1.282)	0.319
GG	39 (3.6)	65 (3.5)	0.980 (0.773, 1.244)	0.870
Dominant model			1.061 (0.909, 1.238)	0.455
Recessive model			0.940 (0.752, 1.175)	0.586
Additive model			1.015 (0.909, 1.133)	0.794
rs3847987-CC	673 (61.5)	1172 (62.7)	1.00 (Ref)	
CA	372 (34.0)	619 (33.1)	1.065 (0.907, 1.252)	0.442
AA	49 (4.5)	79 (4.2)	1.060 (0.728, 1.543)	0.761
Dominant model			1.065 (0.912, 1.244)	0.428
Recessive model			1.037 (0.715,1.503)	0.848
Additive model			1.050 (0.921, 1.197)	0.462
rs11574129-TT	752 (68.6)	1266 (67.2)	1.00 (Ref)	
TC	311 (28.4)	569 (30.2)	0.924 (0.783, 1.090)	0.347
CC	34 (3.1)	48 (2.5)	1.212 (0.777, 1.893)	0.397
Dominant model			0.946 (0.806, 1.111)	0.501
Recessive model			1.241 (0.797, 1.933)	0.338
Additive model			0.979 (0.851, 1.127)	0.769
rs2228570-CC	339 (30.6)	518 (27.5)	1.00 (Ref)	
CA	537 (48.8)	933 (49.6)	0.863 (0.725, 1.028)	0.099
AA	225 (20.4)	431 (22.9)	**0.782 (0.633, 0.966)**	**0.023**
Dominant model			**0.837 (0.710, 0.986)**	**0.034**
Recessive model			0.857 (0.715, 1.028)	0.097
Additive model			**0.883 (0.794, 0.981)**	**0.020**
rs11568820-GG	372 (33.9)	596 (31.7)	1.00 (Ref)	
GA	550 (50.1)	951 (50.6)	0.947 (0.801, 1.118)	0.519
AA	176 (16.0)	331 (17.6)	0.833 (0.664, 1.044)	0.113
Dominant model			0.917 (0.783, 1.075)	0.285
Recessive model			0.861 (0.703, 1.054)	0.148
Additive model			0.919 (0.824, 1.025)	0.128
rs739837-GG	566 (51.7)	983 (52.3)	1.00 (Ref)	
GT	448 (40.9)	767 (40.8)	1.045 (0.893, 1.224)	0.583
TT	81 (7.4)	131 (7.0)	1.097 (0.817, 1.472)	0.540
Dominant model			1.053 (0.906, 1.224)	0.500
Recessive model			1.076 (0.808, 1.433)	0.616
Additive model			1.046 (0.929, 1.179)	0.457
rs7975232-CC	564 (51.4)	978 (51.9)	1.00 (Ref)	
CA	446 (40.6)	770 (40.9)	1.003 (0.857, 1.175)	0.967
AA	88 (8.0)	135 (7.2)	1.118 (0.848, 1.474)	0.428
Dominant model			1.023 (0.880, 1.188)	0.770
Recessive model			1.116 (0.854, 1.459)	0.420
Additive model			1.035 (0.921, 1.162)	0.566
rs11168287-GG	466 (42.6)	730 (38.9)	1.00 (Ref)	
GA	486 (44.5)	903 (48.1)	**0.830 (0.707, 0.974)**	**0.022**
AA	141 (12.9)	243 (13.0)	0.872 (0.689, 1.104)	0.255
Dominant model			**0.839 (0.721, 0.976)**	**0.023**
Recessive model			0.963 (0.773, 1.200)	0.738
Additive model			0.904 (0.810, 1.009)	0.071

VDR, vitamin D receptor; SNPs, single nucleotide polymorphisms; NAFLD, non-alcoholic fatty liver disease; OR, odds ratio; CI, confidence interval.

A pair of alleles such as C/G, if G is a less frequent gene, then dominant model (CG+GG vs. CC), recessive model (GG vs. CG+CC), and additive model (GG vs CG vs. CC).

[a]*Logistic regression model, adjusted for gender and age.*

Bold type indicates statistically significant results.

VD level is a risk factor of NAFLD (33). VD poses protective effects on many other metabolic-related diseases, such as obesity, hypertension, insulin resistance, type 2 diabetes, metabolic syndrome and cardiovascular disease (34–36). Consistently, our study manifested a high prevalence of NAFLD (59.2%) in the subjects with low serum 25(OH)D_3 level (<20ng/mL), and VD deficiency might increase the risk of NAFLD. The regulatory mechanism of VD level and *VDR* activity in the development of NAFDL has not been fully elucidated yet (37, 38). Therefore, the present study provides a new insight into the association between *VDR* genetic mutation and NAFLD risk.

The *VDR* SNPs rs7975232, rs2228570 were reported to be associated with VD deficiency (39, 40). However, other research showed no association of rs7975232, rs11568820, rs11574129 with serum 25(OH)D_3 in a Han Chinese population (41). A case-control study in Caucasian population found no correlation between VD level and rs2228570 genotype (42). In our study, no significant associations were found between eight *VDR*

TABLE 4 | Multivariate stepwise regression analysis for independent factors of NAFLD.

Variables	*β*	SE	Wald	OR (95% CI)	*P*
Age (≤40 *vs.* >40 years)	-0.334	0.105	10.155	**0.716 (0.583, 0.879)**	**0.001**
Visceral obesity	1.296	0.103	157.695	**3.653 (2.984, 4.471)**	**<0.001**
Hypertension	0.503	1.27	15.733	**1.654 (1.290, 2.121)**	**<0.001**
Hypertriglyceridemia	1.240	0.110	126.586	**3.455 (2.784, 4.288)**	**<0.001**
Low HDL-C	0.631	0.103	37.538	**1.879 (1.536, 2.299)**	**<0.001**
ALT (>40 *vs.*≤40U/L)	1.004	0.143	48.990	**2.729 (2.060, 3.615)**	**<0.001**
Exercise time (≥150 *vs.* <150 min/week)	-0.225	0.096	5.511	**0.798 (0.661, 0.963)**	**0.019**
rs2228570 (CA+AA *vs.*CC)	-0.264	0.104	6.422	**0.768 (0.626, 0.942)**	**0.011**

NAFLD, non-alcoholic fatty liver disease; HDL-C, high density liptein cholesterol; ALT, alanine aminotransferase; OR, odds ratio; CI, confidence interval.
Bold type indicates statistically significant results.

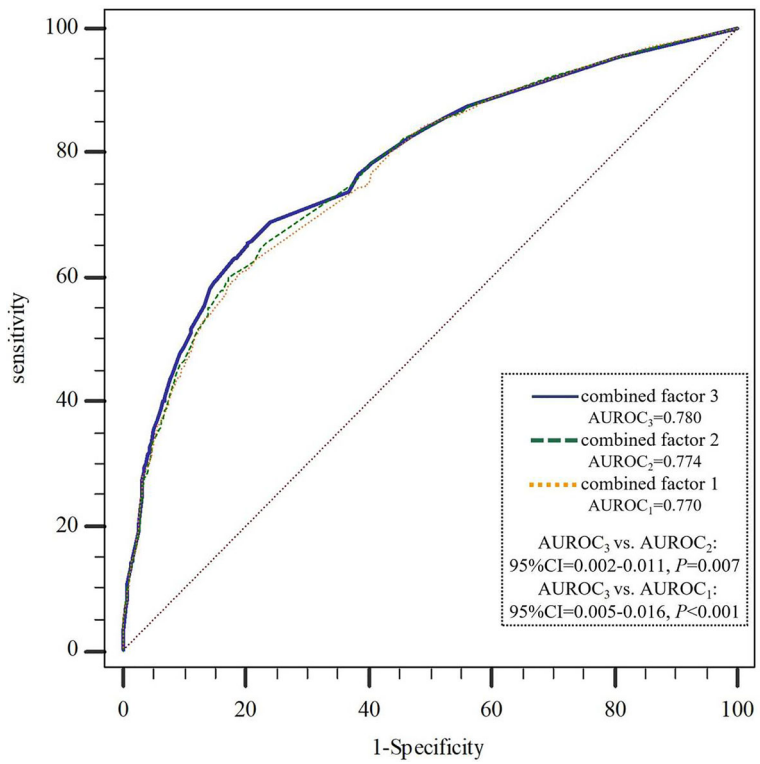

FIGURE 1 | AUROCs comparison of the three combined factors to assess NAFLD risk. NAFLD, non-alcoholic fatty liver disease; AUROC, area under the receiver operating curve. combined factor 1: a combination of age, visceral obesity, blood pressure, TG, HDL-C and ALT; combined factor 2: a combination of combined factor 1 and exercise time; combined factor 3: a combination of combined factor 2 and *VDR*-rs2228570.

polymorphisms and 25(OH)D_3 level either. Possible explanations include geographical location, racial backgrounds and sunlight exposure (43).

Our study suggested that the SNPs of rs2228570-A and rs11168287-A in *VDR* gene exhibited an association with the decrease in NAFLD risk, with an evident gene-gene combined effect. Metabolic impairment and alteration of the glucose-insulinhomeostasis are the primarily pathogenesis of NAFLD (44). Evidence indicated that the rs2228570 polymorphism of *VDR* gene was associated with the risk of fasting glucose in a Chinese Han population (45). It was found that the expression of *VDR* mRNA in the liver of obese individuals with biopsy-proven NAFLD was higher than that of non-NAFLD (46). Study reported that the combination of rs2228570 (*FokI*), rs1544410 (*BsmI*) and rs731236 (*TaqI*) was involved in the risk of T2DM in north Indians (47). However, another study showed that *VDR*-rs2225780 genetic variation was not associated with T2DM in a Caucasian population (42). The possible explanation might have various ethnic groups. The Jackson Heart Study indicated that *VDR* variants are associated with abdominal visceral adipose tissue volume and adiponectin concentrations, but not with BMI or WC in African Americans (48), a finding that is consistent with the stratified analysis of the combined effect of the two positive SNPs in this study. Although there is no research on rs11168287

polymorphisms and NAFLD, we found that rs11168287 is situated in the peak of H3k4me1 and near the peak of transcription levels by searching the UCSC genome browser (https://genome.ucsc.edu), which means that rs11168287 mutation might affect the serum VD level and its biological effects including insulin sensitivity, lipid metabolism as well as immune inflammation by dysregulating the transcription and expression of *VDR* gene, and ultimately affect the risk of NAFLD. Further study is warranted to identify the role and function of these *VDR* polymorphisms in VD metabolism and NAFLD risk.

This study also demonstrated that age ≤40 years, exercise time ≥150 min/week, and rs2228570-A were independent protective factors of NAFLD; visceral obesity, hypertension, hypertriglyceridemia, Low HDL-C and ALT >40U/L were independent risk factors of NAFLD, which is consistent with the results of previous studies (49–52). Based on these independent factors, we constructed combined factors to assess NAFLD risk. The results showed that the assessment efficiency of combined factor 3 (including age, visceral obesity, blood pressure, TG, HDL-C, ALT, exercise time and rs2228570) in NAFLD risk was higher than that of combined factor 2 (including age, visceral obesity, blood pressure, TG, HDL-C, ALT and exercise time) and combined factor 1 (including age, visceral obesity, blood pressure, TG, HDL-C and ALT). There is no research on the combination of genetic and environmental behavioral factors to evaluate the risk of NAFLD in Chinese population so far. A study of NAFLD risk in Italian obese children and adolescents found that combining genetic variants with clinical risk factors improved the predictability of NAFLD (53). For a disease related to heredity and environment, the predictive power of genetic-environmental factors is reasonably stronger than a single one. However, in our study, compared with the AUROC of combined factor 1 or combined factor 2, the AUROC of combined factor 3 only increased slightly, probably due to the weak effect of a single SNP on disease risk (54). In spite of this, we cannot ignore the effect of individual differences in genetic mutation on disease susceptibility. Once the risk of a particular genotype and environmental exposure combination is known, medical interventions, including medical surveillance, lifestyle advice, diet or drug treatment, could then be taken for high-risk groups or individuals to prevent disease (55, 56).

There are a few limitations in our study. Firstly, based on the case-control study, we collected the data of the subjects and measured their VD level, which may not represent the average level of different seasons. A convenient and inexpensive ELISA method was used to detect $25(OH)D_3$ levels in this study. Although it is not as accurate as liquid chromatography tandem mass spectrometry (LC-MS), it can reflect the level of $25(OH)D_3$ to some extent (41, 57). Secondly, only subjects from one community were enrolled, which may not be representative enough. In response to this problem, the frequency-matching of gender and age was used in the design stage, and multivariate analysis and stratified analysis were carried out to control the influence of the confounding factors to a certain extent. Finally, we only selected one key gene in the VD metabolic pathway, which may not be able to fully analyze the relationship between genetic factors and NAFLD risk. It is necessary to further explore the impact of polygenic polyloci and their combination with environmental factors on disease risk in a multicenter population of different races.

In conclusion, our results supported that high serum VD levels and *VDR* variants (rs2228570-A and rs11168287-A) might be involved in a low risk of NAFLD in the Chinese Han population, and a combination of *VDR* SNP and exercise time could improve the efficiency in assessment of NAFLD risk. These findings might provide new insight for risk evaluation of NAFLD and early screening of high-risk population.

DATA AVAILABILITY STATEMENT

The original contributions presented in the study are included in the article/**Supplementary Material**. Further inquiries can be directed to the corresponding author.

ETHICS STATEMENT

The studies involving human participants were reviewed and approved by The Institutional Ethics Review Committee of Nanjing Medical University (Nanjing, China). The patients/participants provided their written informed consent to participate in this study.

AUTHOR CONTRIBUTIONS

JW designed and organized the study. RZ, MXW, MW, LZ, YD, ZT, ZF, HF, and WZ contributed to the planning, designing and analyses of the experiments, data collection and quality control. RZ, MXW, and JW wrote and critical revised the manuscript. All authors contributed to the article and approved the submitted version.

FUNDING

This work was supported by the Natural Science Foundation of Jiangsu Province, China (Grant No. BK20181369) and Priority Academic Program Development of Juangsu Higher Education Institutions (Grant No. PAPD [2018] 87).

ACKNOWLEDGMENTS

Thank you Mr. Yongke Cao for providing article polishing support.

SUPPLEMENTARY MATERIAL

The Supplementary Material for this article can be found online at: https://www.frontiersin.org/articles/10.3389/fendo.2021.648844/full#supplementary-material

REFERENCES

1. Seto WK, Yuen MF. Nonalcoholic Fatty Liver Disease in Asia: Emerging Perspectives. *J Gastroenterol* (2017) 52(2):164–74. doi: 10.1007/s00535-016-1264-3
2. Eslam M, Valenti L, Romeo S. Genetics and Epigenetics of NAFLD and NASH: Clinical Impact. *J Hepatol* (2018) 68(2):268–79. doi: 10.1016/j.jhep.2017.09.003
3. Vernon G, Baranova A, Younossi ZM. Systematic Review: The Epidemiology and Natural History of Non-Alcoholic Fatty Liver Disease and Non-Alcoholic Steatohepatitis in Adults. *Aliment Pharmacol Ther* (2011) 34(3):274–85. doi: 10.1111/j.1365-2036.2011.04724.x
4. Farrell GC, Wong VW, Chitturi S. NAFLD in Asia–as Common and Important as in the West. *Nat Rev Gastroenterol Hepatol* (2013) 10(5):307–18. doi: 10.1038/nrgastro.2013.34
5. Sweet PH, Khoo T, Nguyen S. Nonalcoholic Fatty Liver Disease. *Prim Care* (2017) 44(4):599–607. doi: 10.1016/j.pop.2017.07.003
6. Byrne CD, Targher G. NAFLD: A Multisystem Disease. *J Hepatol* (2015) 62(1 Suppl):S47–64. doi: 10.1016/j.jhep.2014.12.012
7. Zhou JH, Cai JJ, She ZG, Li HL. Noninvasive Evaluation of Nonalcoholic Fatty Liver Disease: Current Evidence and Practice. *World J Gastroenterol* (2019) 25(11):1307–26. doi: 10.3748/wjg.v25.i11.1307
8. Sumida Y, Yoneda M. Current and Future Pharmacological Therapies for NAFLD/NASH. *J Gastroenterol* (2018) 53(3):362–76. doi: 10.1007/s00535-017-1415-1
9. Mazhar K. The Future of Nonalcoholic Fatty Liver Disease Treatment. *Med Clin North Am* (2019) 103(1):57–69. doi: 10.1016/j.mcna.2018.08.005
10. Rinella ME. Nonalcoholic Fatty Liver Disease: A Systematic Review. *JAMA* (2015) 313(22):2263–73. doi: 10.1001/jama.2015.5370
11. Diehl AM, Day C. Cause, Pathogenesis, and Treatment of Nonalcoholic Steatohepatitis. *N Engl J Med* (2017) 377(21):2063–72. doi: 10.1056/NEJMra1503519
12. Giblin RJ, Bennett EJ, Zosky GR, Dwyer RM. The Impact of Sex and 25(OH)D Deficiency on Metabolic Function in Mice. *Nutrients* (2017) 9(9):985. doi: 10.3390/nu9090985
13. Drori A, Rotnemer-Golinkin D, Avni S, Drori A, Danay O, Levanon D, et al. Attenuating the Rate of Total Body Fat Accumulation and Alleviating Liver Damage by Oral Administration of Vitamin D-Enriched Edible Mushrooms in a Diet-Induced Obesity Murine Model Is Mediated by an Anti-Inflammatory Paradigm Shift. *BMC Gastroenterol* (2017) 17(1):130. doi: 10.1186/s12876-017-0688-4
14. Zhu CG, Liu YX, Wang H, Wang BP, Qu HQ, Wang BL, et al. Active Form of Vitamin D Ameliorates Non-Alcoholic Fatty Liver Disease by Alleviating Oxidative Stress in a High-Fat Diet Rat Model. *Endocr J* (2017) 64(7):663–73. doi: 10.1507/endocrj.EJ16-0542
15. Jablonski KL, Jovanovich A, Holmen J, Targher G, McFann K, Kendrick J, et al. Low 25-Hydroxyvitamin D Level Is Independently Associated With Non-Alcoholic Fatty Liver Disease. *Nutr Metab Cardiovasc Dis* (2013) 23(8):792–8. doi: 10.1016/j.numecd.2012.12.006
16. Cimini FA, Barchetta I, Carotti S, Morini S, Cavallo MG. Overview of Studies of the Vitamin D/Vitamin D Receptor System in the Development of Non-Alcoholic Fatty Liver Disease. *World J Gastrointest Pathophysiol* (2019) 10(2):11–6. doi: 10.4291/wjgp.v10.i2.11
17. Pirgon O, Cekmez F, Bilgin H, Eren E, Dundar B. Low 25-Hydroxyvitamin D Level Is Associated With Insulin Sensitivity in Obese Adolescents With Non-Alcoholic Fatty Liver Disease. *Obes Res Clin Pract* (2013) 7(4):e275–83. doi: 10.1016/j.orcp.2012.01.004
18. Lee SM, Jun DW, Cho YK, Jang KS. Vitamin D Deficiency in Non-Alcoholic Fatty Liver Disease: The Chicken or the Egg. *Clin Nutr* (2017) 36(1):191–7. doi: 10.1016/j.clnu.2015.10.017
19. Eliades M, Spyrou E, Agrawal N, Lazo M, Brancati FL, Potter JJ, et al. Meta-Analysis: Vitamin D and Non-Alcoholic Fatty Liver Disease. *Aliment Pharmacol Ther* (2013) 38(3):246–54. doi: 10.1111/apt.12377
20. Yang BB, Chen YH, Zhang C, Shi CE, Hu KF, Zhou J, et al. Low Vitamin D Status Is Associated With Advanced Liver Fibrosis in Patients With Nonalcoholic Fatty Liver Disease. *Endocrine* (2017) 55(2):582–90. doi: 10.1007/s12020-016-1152-x
21. Jaruvongvanich V, Ahuja W, Sanguankeo A, Wijarnpreecha K, Upala S. Vitamin D and Histologic Severity of Nonalcoholic Fatty Liver Disease: A Systematic Review and Meta-Analysis. *Dig Liver Dis* (2017) 49(6):618–22. doi: 10.1016/j.dld.2017.02.003
22. Barchetta I, Del Ben M, Angelico F, Di Martino M, Fraioli A, La Torre G, et al. No Effects of Oral Vitamin D Supplementation on Non-Alcoholic Fatty Liver Disease in Patients With Type 2 Diabetes: A Randomized, Double-Blind, Placebo-Controlled Trial. *BMC Med* (2016) 14:92. doi: 10.1186/s12916-016-0638-y
23. Kumar R, Himani, Gupta N, Singh V, Kumar V, Haq A, et al. Unveiling Molecular Associations of Polymorphic Variants of VDR Gene (FokI, BsmI and ApaI) in Multiple Myeloma Patients of Indian Population. *J Steroid Biochem Mol Biol* (2020) 199:105588. doi: 10.1016/j.jsbmb.2020.105588
24. Pike JW. Vitamin D3 Receptors: Structure and Function in Transcription. *Annu Rev Nutr* (1991) 11:189–216. doi: 10.1146/annurev.nu.11.070191.001201
25. Chen KS, DeLuca HF. Cloning of the Human 1 Alpha,25-Dihydroxyvitamin D-3 24-Hydroxylase Gene Promoter and Identification of Two Vitamin D-Responsive Elements. *Biochim Biophys Acta* (1995) 1263(1):1–9. doi: 10.1016/0167-4781(95)00060-T
26. Haussler MR, Whitfield GK, Kaneko I, Haussler CA, Hsieh D, Hsieh JC, et al. Molecular Mechanisms of Vitamin D Action. *Calcif Tissue Int* (2013) 92(2):77–98. doi: 10.1007/s00223-012-9619-0
27. Ding N, Yu RT, Subramaniam N, Sherman MH, Wilson C, Rao R, et al. A Vitamin D Receptor/SMAD Genomic Circuit Gates Hepatic Fibrotic Response. *Cell* (2013) 153(3):601–13. doi: 10.1016/j.cell.2013.03.028
28. Shen J, Wong GL, Chan HL, Chan RS, Chan HY, Chu WC, et al. PNPLA3 Gene Polymorphism and Response to Lifestyle Modification in Patients With Nonalcoholic Fatty Liver Disease. *J Gastroenterol Hepatol* (2015) 30(1):139–46. doi: 10.1111/jgh.12656
29. Sevastianova K, Kotronen A, Gastaldelli A, Perttilä J, Hakkarainen A, Lundbom J, et al. Genetic Variation in PNPLA3 (Adiponutrin) Confers Sensitivity to Weight Loss-Induced Decrease in Liver Fat in Humans. *Am J Clin Nutr* (2011) 94(1):104–11. doi: 10.3945/ajcn.111.012369
30. Woods NT, Monteiro AN, Thompson ZJ, Amankwah EK, Naas N, Haura EB, et al. Interleukin Polymorphisms Associated With Overall Survival, Disease-Free Survival, and Recurrence in Non-Small Cell Lung Cancer Patients. *Mol Carcinog* (2015) 54 Suppl 1(0 1):E172–84. doi: 10.1002/mc.22275
31. Henry HL, Bouillon R, Norman AW, Gallagher JC, Lips P, Heaney RP, et al. 14th Vitamin D Workshop Consensus on Vitamin D Nutritional Guidelines. *J Steroid Biochem Mol Biol* (2010) 121(1-2):4–6. doi: 10.1016/j.jsbmb.2010.05.008
32. Cheng Q, Du Y, Hong W, Tang W, Li H, Chen M, et al. Factors Associated to Serum 25-Hydroxyvitamin D Levels Among Older Adult Populations in Urban and Suburban Communities in Shanghai, China. *BMC Geriatr* (2017) 17(1):246. doi: 10.1186/s12877-017-0632-z
33. Cho YH, Kim JW, Shim JO, Yang HR, Chang JY, Moon JS, et al. Association Between Vitamin D Deficiency and Suspected Nonalcoholic Fatty Liver Disease in an Adolescent Population. *Pediatr Gastroenterol Hepatol Nutr* (2019) 22(3):233–41. doi: 10.5223/pghn.2019.22.3.233
34. Alvarez JA, Ashraf A. Role of Vitamin D in Insulin Secretion and Insulin Sensitivity for Glucose Homeostasis. *Int J Endocrinol* (2010) 2010:351385. doi: 10.1155/2010/351385
35. Pacifico L, Anania C, Osborn JF, Ferraro F, Bonci E, Olivero E, et al. Low 25(OH)D3 Levels Are Associated With Total Adiposity, Metabolic Syndrome, and Hypertension in Caucasian Children and Adolescents. *Eur J Endocrinol* (2011) 165(4):603–11. doi: 10.1530/EJE-11-0545
36. Motiwala SR, Wang TJ. Vitamin D and Cardiovascular Risk. *Curr Hypertens Rep* (2012) 14(3):209–18. doi: 10.1007/s11906-012-0262-y
37. Kulda V, Elangovan H, Stokes RA. Vitamin D Metabolism. *Vnitr Lek* (2012) 58(5):400–4. doi: 10.3390/nu10040496
38. Bikle DD. Vitamin D Metabolism, Mechanism of Action, and Clinical Applications. *Chem Biol* (2014) 21(3):319–29. doi: 10.1016/j.chembiol.2013.12.016
39. Santos BR, Mascarenhas LP, Satler F, Boguszewski MC, Spritzer PM. Vitamin D Deficiency in Girls From South Brazil: A Cross-Sectional Study on Prevalence and Association With Vitamin D Receptor Gene Variants. *BMC Pediatr* (2012) 12:62. doi: 10.1186/1471-2431-12-62
40. Alnahas Z, Fawzy M, Menyawi M, Shaker O, Ragab G. 25-Hydroxyvitamin D3 Deficiency and Vitamin D Receptor Polymorphisms in Egyptian Patients With Behçet's Disease: A Pilot Study. *Int J Clin Rheumatol* (2017) 12:020. doi: 10.1093/rheumatology/kez060

41. Wu M, Yue M, Huang P, Zhang Y, Xie C, Yu R, et al. Vitamin D Level and Vitamin D Receptor Genetic Variations Contribute to HCV Infection Susceptibility and Chronicity in a Chinese Population. *Infect Genet Evol* (2016) 41:146–52. doi: 10.1016/j.meegid.2016.03.032
42. Bertoccini L, Sentinelli F, Leonetti F, Bailetti D, Capoccia D, Cimini FA, et al. The Vitamin D Receptor Functional Variant Rs2228570 (C>T) Does Not Associate With Type 2 Diabetes Mellitus. *Endocr Res* (2017) 42(4):331–5. doi: 10.1080/07435800.2017.1305965
43. Woo J, Lam CW, Leung J, Lau WY, Lau E, Ling X, et al. Very High Rates of Vitamin D Insufficiency in Women of Child-Bearing Age Living in Beijing and Hong Kong. *Br J Nutr* (2008) 99(6):1330–4. doi: 10.1017/S0007114507844382
44. Barchetta I, Cimini FA, Cavallo MG. Vitamin D and Metabolic Dysfunction-Associated Fatty Liver Disease (MAFLD): An Update. *Nutrients* (2020) 12 (11):3302. doi: 10.3390/nu12113302
45. Jia J, Ding H, Yang K, Mao L, Zhao H, Zhan Y, et al. Vitamin D Receptor Genetic Polymorphism Is Significantly Associated With Risk of Type 2 Diabetes Mellitus in Chinese Han Population. *Arch Med Res* (2015) 46 (7):572–9. doi: 10.1016/j.arcmed.2015.09.006
46. Barchetta I, Cimini FA, Chiappetta C, Bertoccini L, Ceccarelli V, Capoccia D, et al. Relationship Between Hepatic and Systemic Angiopoietin-Like 3, Hepatic Vitamin D Receptor Expression and NAFLD in Obesity. *Liver Int* (2020) 40(9):2139–47. doi: 10.1111/liv.14554
47. Bid HK, Konwar R, Aggarwal CG, Gautam S, Saxena M, Nayak VL, et al. Vitamin D Receptor (FokI, BsmI and TaqI) Gene Polymorphisms and Type 2 Diabetes Mellitus: A North Indian Study. *Indian J Med Sci* (2009) 63(5):187–94. doi: 10.4103/0019-5359.53164
48. Khan RJ, Riestra P, Gebreab SY, Wilson JG, Gaye A, Xu R, et al. Vitamin D Receptor Gene Polymorphisms Are Associated With Abdominal Visceral Adipose Tissue Volume and Serum Adipokine Concentrations But Not With Body Mass Index or Waist Circumference in African Americans: The Jackson Heart Study. *J Nutr* (2016) 146(8):1476–82. doi: 10.3945/jn.116.229963
49. Feng RN, Du SS, Wang C, Li YC, Liu LY, Guo FC, et al. Lean-Non-Alcoholic Fatty Liver Disease Increases Risk for Metabolic Disorders in a Normal Weight Chinese Population. *World J Gastroenterol* (2014) 20(47):17932–40. doi: 10.3748/wjg.v20.i47.17932
50. Wei JL, Leung JC, Loong TC, Wong GL, Yeung DK, Chan RS, et al. Prevalence and Severity of Nonalcoholic Fatty Liver Disease in Non-Obese Patients: A Population Study Using Proton-Magnetic Resonance Spectroscopy. *Am J Gastroenterol* (2015) 110(9):1306–14; quiz 1315. doi: 10.1038/ajg.2015.235
51. Rudwill F, Bergouignan A, Gastebois C, Gauquelin-Koch G, Lefai E, Blanc S, et al. Effect of Enforced Physical Inactivity Induced by 60-Day of Bed Rest on Hepatic Markers of NAFLD in Healthy Normal-Weight Women. *Liver Int* (2015) 35(6):1700–6. doi: 10.1111/liv.12743
52. Fukuda Y, Hashimoto Y, Hamaguchi M, Fukuda T, Nakamura N, Ohbora A, et al. Triglycerides to High-Density Lipoprotein Cholesterol Ratio Is an Independent Predictor of Incident Fatty Liver; A Population-Based Cohort Study. *Liver Int* (2016) 36(5):713–20. doi: 10.1111/liv.12977
53. Zusi C, Mantovani A, Olivieri F, Morandi A, Corradi M, Miraglia Del Giudice E, et al. Contribution of a Genetic Risk Score to Clinical Prediction of Hepatic Steatosis in Obese Children and Adolescents. *Dig Liver Dis* (2019) 51 (11):1586–92. doi: 10.1016/j.dld.2019.05.029
54. Manolio TA, Collins FS, Cox NJ, Goldstein DB, Hindorff LA, Hunter DJ, et al. Finding the Missing Heritability of Complex Diseases. *Nature* (2009) 461 (7265):747–53. doi: 10.1038/nature08494
55. Wallace HM. A Model of Gene-Gene and Gene-Environment Interactions and Its Implications for Targeting Environmental Interventions by Genotype. *Theor Biol Med Model* (2006) 3:35. doi: 10.1186/1742-4682-3-35
56. Collins FS, McKusick VA. Implications of the Human Genome Project for Medical Science. *JAMA* (2001) 285(5):540–4. doi: 10.1001/jama.285.5.540
57. Atsukawa M, Tsubota A, Shimada N, Abe H, Kondo C, Itokawa N, et al. Serum 25(OH)D3 Levels Affect Treatment Outcomes for Telaprevir/Peg-Interferon/Ribavirin Combination Therapy in Genotype 1b Chronic Hepatitis C. *Dig Liver Dis* (2014) 46(8):738–43. doi: 10.1016/j.dld.2014.05.004

Conflict of Interest: The authors declare that the research was conducted in the absence of any commercial or financial relationships that could be construed as a potential conflict of interest.

Publisher's Note: All claims expressed in this article are solely those of the authors and do not necessarily represent those of their affiliated organizations, or those of the publisher, the editors and the reviewers. Any product that may be evaluated in this article, or claim that may be made by its manufacturer, is not guaranteed or endorsed by the publisher.

frontiers in Endocrinology

ORIGINAL RESEARCH
published: 24 September 2021
doi: 10.3389/fendo.2021.637317

Serum Metabolic Profiles of Chinese Women With Perimenopausal Obesity Explored by the Untargeted Metabolomics Approach

*Shanshan Ding[1], Mingyi Chen[1], Ying Liao[1], Qiliang Chen[1,2], Xuejuan Lin[1], Shujiao Chen[1], Yujuan Chai[3], Candong Li[1] and Tetsuya Asakawa[1,4,5]**

[1] Research Base of Traditional Chinese Medicine Syndrome, Fujian University of Traditional Chinese Medicine, Fuzhou, China, [2] School of Basic Medicine, Guangzhou University of Chinese Medicine, Guangzhou, China, [3] School of Medical Engineering, Health Science Center, Shenzhen University, Shenzhen, China, [4] Department of Neurosurgery, Hamamatsu University School of Medicine, Hamamatsu, Japan, [5] Department of Neurology, The Eighth Affiliated Hospital, Sun Yat-Sen University, Shenzhen, China

OPEN ACCESS

Edited by:
Nicholas John William Rattray, University of Strathclyde, United Kingdom

Reviewed by:
Tianlu Chen, Shanghai Jiao Tong University, China
Xin Dong, Shanghai University, China
Christopher Gerner, University of Vienna, Austria

***Correspondence:**
Tetsuya Asakawa
asakawat1971@gmail.com

Specialty section:
This article was submitted to Systems Endocrinology, a section of the journal Frontiers in Endocrinology

Received: *03 December 2020*
Accepted: *22 July 2021*
Published: *24 September 2021*

Citation:
Ding S, Chen M, Liao Y, Chen Q, Lin X, Chen S, Chai Y, Li C and Asakawa T (2021) Serum Metabolic Profiles of Chinese Women With Perimenopausal Obesity Explored by the Untargeted Metabolomics Approach. Front. Endocrinol. 12:637317. doi: 10.3389/fendo.2021.637317

By far, no study has focused on observing the metabolomic profiles in perimenopause-related obesity. This study attempted to identify the metabolic characteristics of subjects with perimenopause obesity (PO). Thirty-nine perimenopausal Chinese women, 21 with PO and 18 without obesity (PN), were recruited in this study. A conventional ultra-high-performance liquid chromatography-quadrupole time-of-flight/mass spectrometry (UHPLC-QTOF/MS) followed by principal component analysis (PCA) and orthogonal partial least-squares discriminant analysis (OPLS-DA) were used as untargeted metabolomics approaches to explore the serum metabolic profiles. Kyoto Encyclopedia of Genes and Genomes (KEGG) and MetaboAnalyst were used to identify the related metabolic pathways. A total of 46 differential metabolites, along with seven metabolic pathways relevant to PO were identified, which belonged to lipid, amino acids, carbohydrates, and organic acids. As for amino acids, we found a significant increase in L-arginine and D-ornithine in the positive ion (POS) mode and L-leucine, L-valine, L-tyrosine, and *N*-acetyl-L-tyrosine in the negative ion (NEG) mode and a significant decrease in L-proline in the POS mode of the PO group. We also found phosphatidylcholine (PC) (16:0/16:0), palmitic acid, and myristic acid, which are associated with the significant upregulation of lipid metabolism. Moreover, the serum indole lactic acid and indoleacetic acid were upregulated in the NEG mode. With respect to the metabolic pathways, the D-arginine and D-ornithine metabolisms and the arginine and proline metabolism pathways in POS mode were the most dominant PO-related pathways. The changes of metabolisms of lipid, amino acids, and indoleacetic acid provided a pathophysiological scenario for Chinese women with PO. We believe that the findings of this study are helpful for clinicians to take measures to prevent the women with PO from developing severe incurable obesity-related complications, such as cardiovascular disease and stroke.

Keywords: perimenopausal obesity, metabolic profiles, the ultra-high performance liquid chromatography-quadrupole time-of-flight/mass spectrometry, metabolic pathway, metabolomics

INTRODUCTION

Perimenopause is a peculiar period before and after menopause in women (approximately 40–55 years). Under the background of weakening ovarian function and declining estrogen level, a battery of physiological and pathological changes may happen. Many women experience various symptoms, such as night sweats, hot flushes, mood swings, menstrual disorder, and vaginal dryness (1). Moreover, perimenopause is closely associated with many diseases, such as metabolic syndrome (MetS) (2), breast cancer (3), osteoporosis (4), and cardiovascular disease (CVD) (5). Of those, perimenopause obesity (PO) is a growing concern because it might result in a spectrum of obesity-related diseases. The pathophysiological state of PO is quite complicated. It is influenced by many pathogenic factors, of which estrogen deficiency plays a key role (6). The complicated interactions among these factors sometimes make the situation intractable. Estrogen deficiency has been known to cause fat accumulation and increase body weight (BW) (7), which are highly associated with MetS, type 2 diabetes (T2D), CVD, and stroke. Thus, clarifying the metabolic characteristics in PO is extremely helpful because understanding the pathophysiological mechanisms and the affecting factors relevant to PO is useful, which contribute to the selection of an appropriate clinical strategy to prevent perimenopause women from progressing to intractable complications.

Alternatively, metabolomics has been developed as a promising technology in achieving the quantitative measurement of dynamic metabolomic profiles of a living subject in a certain pathophysiological state. The commonly used methods for sample analysis are mass spectrometry (MS) or ^{1}H nuclear magnetic resonance (NMR). The main strength of metabolomics approach is that it can conduct simultaneous measurements of many small molecular metabolites (8, 9). It is also effective for diseases with a complicated metabolic response (9, 10). Hence, it has been widely used for early diagnosis, exploring novel biomarkers and treatment targets, and elucidating the mechanisms of certain diseases, particularly for metabolic diseases, such as T2D, MetS, and obesity. Recently, we performed a ^{1}H NMR study to explore the metabolic characteristics of untreated patients with MetS. We found that such untreated patients have peculiar metabolic characteristics, such as ketosis tendency, early kidney damage, activation of oxidative signaling, and inflammatory response, which suggested that the pathophysiological state might worsen if MetS is left untreated (11). The metabolomics approach is also used for metabolomic profile elucidation in obesity. Chen et al. used liquid chromatography/time-of-flight MS (LC–MS) and gas chromatography/quadrupole mass spectrometry (GC-MS) methods to explore the metabolic characteristics in patients with metabolic abnormal obesity and healthy obesity. They found that the metabolic characteristics were different between metabolic abnormal obesity and metabolic healthy obesity. A battery of metabolites, such as L-kynurenine, glycerol 1-phosphate, glycolic acid, tagatose, methyl palmitate, and uric acid, are useful in distinguishing these different types of obesity (12). Another study investigated the relationship between metabolomic profiles and clinical indices in obese children using a ^{1}H NMR technology. Saner et al. found that the body mass index (BMI) and phenylalanine, total body fat % and lipids in medium high-density lipoprotein (HDL), and waist circumference and tyrosine were positively correlated, whereas total body fat % and the ratio of docosahexaenoic acid/total fatty acids and histidine were negatively correlated (13). Rangel-Huerta et al. conducted a systematic review summarizing previous studies using the metabolomics approach to investigate metabolomic profiles in subjects with obesity or obesity-related metabolic changes. They analyzed 33 included literatures and found that these studies could be classified into four types: (1) investigation of metabolic characteristics in an obese subject, (2) comparing the difference of the response to dietary challenges between the obese and nonobese population, (3) using metabolomics to predict weight loss and other interventions, and (4) metabolomic profiles in different dietary patterns (14). Albeit these previous studies investigated the obesity-related metabolomic profiles from different perspectives or in different subjects, they all endorsed that the metabolomics approach is a powerful tool in obesity researches, such as identifying the metabolic characteristics associated with obesity, exploring novel biomarkers/targets for obesity, or observing changes of metabolites induced by interventions against obesity. However, to our knowledge, there is no research that particularly observed the metabolomic profiles in perimenopause-related obesity. This study attempted to identify the metabolic characteristics in subjects with PO. We believe that the findings of this study contribute to a better understanding of the pathophysiological nature of PO, which is beneficial for exploring effective interventions against PO to prevent obesity-related severe complications in perimenopausal women.

METHODS AND MATERIALS

Participants

Participants were recruited from the Third Affiliated Hospital of Fujian Traditional Chinese Medical University between October 2016 and March 2018. A total of 39 perimenopausal women were enrolled based on voluntary participation, including 18 without obesity (PN) and 21 with obesity (PO). Inclusion criteria were listed as follows: (1) perimenopause, women aged 40 to 55 years with menstrual disorders or amenorrhea for ≥3 and <12 months (15), and (2) simple obesity (we used the Guidelines for Prevention and Control of Overweight and Obesity in Chinese Adults) (16). In brief, waist circumference (WC) ≥ 80 cm or BMI ≥ 28 kg/m^2 were included. Exclusion criteria were: (1) type 1 diabetes, gestational diabetes, secondary hypertension, or hyperlipemia; (2) serious heart, liver, kidney, or other complications; (3) psychiatric disorders; (4) secondary or drug-induced obesity; and (5) pituitary tumors or Cushing syndrome. This study was designed and conducted according to the *Declaration of Helsinki of the World Medical Association (2000)* and was approved and supervised by the Ethics Committee of the Fujian University of Traditional Chinese Medicine (approval number: SQ2014-007-01, study period from 2014 to 2019).

The investigation protocol was explained in detail to all participants and their relatives. Informed consent was obtained from each participant before the study initiation.

Clinical Indices and Serum Sample Collection

Clinical indices of participants in a fasting state, including height, BW, WC, serum triglyceride (TG), total cholesterol (TC), high-density lipoprotein cholesterol (HDL-C), and low-density lipoprotein cholesterol (LDL-C), were examined. BMI was calculated as BW/height^2 (kg/m^2). WC was measured with tape as the circumference of the horizontal edge of the midpoint at the lower edge of the costal arch. Elbow venous blood was collected in a fasting state from 8:00 AM to 9:00 AM. For menstruating women, blood samples were collected on the third to fifth day after menstruation. For women whose menstruation had stopped for ≥6 months, it was collected on any day at their convenience. These (5 ml) were collected and centrifuged for 15 min at 3,500 rpm and then were preserved at −80°C for subsequent experiments. Because the estrogen level may be one of the factors affecting the results, the serum estrogen levels were measured using a standard enzyme-linked immunosorbent assay, which was as described in our previous study (6).

Sample Preparation

The serum samples were prepared as per the following procedure introduced in a previous study (17). Briefly, first, the extraction solvent (400 µl, V methanol: V acetonitrile = 1:1) was added to a 100-µl sample, mixed by vortex for 30 s, and treated with sonicate for 10 min in an ice-water bath. The solution was then incubated at −20°C for 1 h and centrifuged at 4°C and 12,000 rpm for 15 min to precipitate the proteins for the aim of preventing the macromolecules from blocking the chromatographic column and electrospray ionization probe. Subsequently, 420 µl of the supernatant was transferred into EP tubes, and the extracts were dried in a vacuum concentrator without heating and then added into a 100-µl extraction liquid (V acetonitrile: V water = 1:1) reconstitution, followed by vortexing for 30 s and sonicating for 10 min (4°C water bath), and centrifuged for 15 min at 12,000 rpm, 4°C. The supernatant was transferred into a fresh 2-ml LC/MS glass vial pending for detection. Equal volumes (10 µl) of supernatant from different individual serum samples were pooled as the quality control (QC) sample for the UHPLC-QTOF/MS analysis. The ionization source of LC–MS is electrospray ionization, including positive ion (POS) and negative ion (NEG) modes. The QC samples were used to assess the reproducibility and reliability of the LC–MS system.

UHPLC-QTOF/MS Conditions

Serum metabolic profiling analysis was performed using a 1290 UHPLC system (Agilent Technologies, Santa Clara, CA, USA) with a Waters UPLC BEH Amide column (1.7 µm; 2.1 × 100 mm) coupled to Triple TOF 6600 (AB Sciex, Framingham, MA, USA) & QTOF 6550 (Agilent) according to a previous study (18). The aim of using the two instruments here was to improve the quality and reliability of the experiments. The mobile phase consisting of 25 mM CH_3COONH_4 and 25 mM NH_4OH in water (pH = 9.75) (A), along with acetonitrile (B), was performed with elution gradient as follows: 0 min, 95% B; 7 min, 65% B; 9 min, 40% B; 9.1 min, 95% B; and 12 min, 95% B at 0.5 ml/min. The injection volume was 2 µl. A Triple TOF mass spectrometer was used for its ability to acquire MS/MS spectra on an information-dependent basis (IDA) during the LC/MS experiment. In this mode, Analyst TF 1.7 software (AB Sciex) collected and triggered the acquisition of MS/MS spectra under the preselected conditions while it continuously evaluated the acquired data. In each cycle, 12 precursor ions, which have a >100 intensity, were chosen for fragmentation at a collision energy of 30 V (15 MS/MS events with product ion accumulation time of 50 msec each). Electrospray ionization (ESI) source conditions were set as follows: ion source gas 1 as 60 Psi, ion source gas 2 as 60 Psi, curtain gas as 35 Psi, source temperature 650°C, and IonSpray Voltage Floating (ISVF) 5000 V or −4000 V in positive or negative modes, respectively (19). The UHPLC-QTOF/MS program was run in POS mode then in NEG mode.

UHPLC-QTOF/MS Data Processing and Statistical Analysis

MS raw data were converted to the mzXML format using the ProteoWizard software and processed with R package XCMS (version 3.2). The preprocessing results generated a data matrix that consisted of the retention time (RT), mass-to-charge ratio (m/z) values, and peak intensity. R package CAMERA was used for the peak annotation after XCMS data processing. In-house MS2 database was applied for metabolite identification. Data matrix was ctr-formatted (mean-centered scaling) and pareto-scaled prior to being imported into the SIMCA V15.0.2 software package (Umetrics, Umea, Sweden). The multivariate data analysis included principal component analysis (PCA) and orthogonal partial least-squares discriminant analysis (OPLS-DA). The unsupervised PCA was implemented to demonstrate the distribution of origin data and general separation. The supervised OPLS-DA, on the other hand, was performed to obtain maximal covariance between the measured data and the response variable and validated using sevenfold cross-validation and 200 permutation tests. The validity of the OPLS-DA model was evaluated using R2Y and Q2, which were parameters for model stability and the ability to explain and predict the raw data. R2Y and Q2 values are closer to 1, suggesting a better model. The results of screening differential metabolites were visualized using a volcano plot. Euclidean distance matrix (EDM) is defined as a matrix of squared Euclidean distances between points in Euclidean space (20). It is the most commonly used distance metric in a metabolomics study (21). For comparisons of the differentially expressed metabolites between PN and PO, the EDM was calculated from the quantitative values of differential metabolites to determine the distances between each object, and then the differential metabolites were clustered by the complete linkage method and presented with a heat map. The structural information of the differential metabolites was identified according to a previous study (22). Briefly, the

retention time (RT), mass-to-charge ratio (m/z), and MS/MS spectrum were rigorously matched with the authentic standards, or verified spectrums in the Mass Bank Database (http://www.massbank.jp/), Metabolite and Tandem MS Database (METLIN, http://metlin.scripps.edu/index.php), or Human Metabolome Database (HMDB, http://www.hmdb.ca/) and confirmed by our self-made m/z database. Because of the complicated nature of the untargeted metabolomics (existence of isomers and the limited accuracy of mass spectrometers) (23). All the metabolites were cautiously identified by comprehensively considering the data of m/s value, retention time, and MS/MS spectra, and finally confirmed by our self-made m/z database.

SPSS 22.0 software (SPSS Inc., Chicago, IL, USA) was used for statistical analysis. Student's *t*-test was selected to compare the normalized integral values (clinical indices and metabolites) between PO and PN groups. The normality of data distributions was verified using the Kolmogorov–Smirnov test. All data were regarded as normally distributed because the values of Kolmogorov–Smirnov test were over 0.05. Then, homogeneity of variances was verified using the Levene's test. The significant difference of metabolites (PO *vs.* PN) was explored. Data were presented as mean ± standard deviation. $P < 0.05$ was considered statistically significant. Metabolites that have a value of variable importance in projection (VIP) >1.0 in the OPLS-DA model and $P < 0.05$ in the Student's t-test were identified as differential metabolites (24). Because of the large number of statistical comparisons, we also calculated the Q value, which was corrected by applying the false discovery rate (FDR) to the p values using R (version 4.0.2, URL https://www.R-project.org/) (25).

Metabolic Pathway Analysis

We searched the Kyoto Encyclopedia of Genes and Genomes (KEGG, http://www.genome.jp/kegg) (26) and MetaboAnalyst (http://www.metaboanalyst.ca/) (27) to explore the key metabolic pathways represented by the differential metabolites identified by the above experiments.

RESULTS

Clinical Characteristics

Table 1 shows the clinical characteristics in the two groups. Evidently, the participants in the PO group suffered from higher BW, BMI, waistline, and serum triglyceride level ($p < 0.05$, *vs.* women with PN). In contrast, no significant difference was found between the two groups in terms of age, height, serum TC, HDL-C, LDL-C, and serum estrogen level (**Table 1**).

TABLE 1 | Clinical characteristics of the participants in two groups.

Characteristics	Perimenopausal normal (PN, n = 18)	Perimenopausal obesity (PO, n = 21)	p value
Age (year)	48.6 ± 4.3	49.0 ± 4.5	0.753
Height (cm)	153.6 ± 6.6	155.9 ± 4.4	0.215
BW (kg)	55.6 ± 5.0	67.7 ± 10.1	<0.001**
BMI (kg/m^2)	23.6 ± 1.8	27.7 ± 3.5	<0.001**
WC (cm)	74.9 ± 3.2	90.8 ± 8.1	<0.001**
TG (mmol/L)	1.3 ± 0.7	1.9 ± 0.6	0.015*
TC (mmol/L)	5.3 ± 0.8	5.7 ± 1.5	0.268
HDL-C (mmol/L)	1.6 ± 0.3	1.6 ± 0.3	0.892
LDL-C (mmol/L)	3.1 ± 0.7	3.3 ± 1.4	0.550
Estrogen (pg/ml)	32.9 ± 36.4	32.7 ± 49.3	0.990

*$p < 0.05$, **$p < 0.01$.

QC of the Present LC–MS Analysis

Figure 1 shows the results of QC of the present LC–MS analysis. The total ion chromatograms show that regardless of whether it is in the POS (**Figure 1A**) or NEG (**Figure 1B**) mode, the peak RT and area of all QC samples exhibited good overlap, indicating a satisfactory stability in the analytical system. The score scatter plot of the PCA model also presents an overlap of all QC samples, in both POS (**Figure 1C**) and the NEG (**Figure 1D**) modes, indicating a satisfactory repeatability in the analytical system, hence validating the quality of this experimental system. Then, 1482 of 1485 peaks in the POS mode and 1317 of 1344 peaks in the NEG mode were preserved after the processes of filtering, normalization, and standardization. The raw data of LC–MS analysis are provided as **Supplementary Materials** (NEG-rawdata.xlsx and POS-rawdata.xlsx).

Multivariate Data Analysis of Serum Metabolites

Figure 2 shows the results of the multivariate data analysis of serum metabolites. As for the PCA model, the distribution of the scatter points in the PCA score plot of the UHPLC-QTOF/MS metabolic profiles of all samples was illustrated. In the POS model, the scatter points were distinctly separated between the PN and PO groups, and all samples in each score scatter plot were within the 95% Hotelling's T-squared ellipse (**Figure 2A**). However, the clustering effect was not obvious in the NEG mode (**Figure 2B**). Then, the OPLS-DA model was constructed to discriminate the differential metabolites between the two groups. Distinct separations were presented between the PN and PO groups in this model in both POS (**Figure 2C**) and NEG (**Figure 2D**) modes. Here, the R2Y and Q2 were 0.904 and 0.762 in the POS mode and 0.851 and 0.360 in the NEG, respectively. To avoid the transition fit of the OPLS-DA mode, we subsequently conducted a permutation test. Results of the permutation test for R2Y and Q2 intercepts were 0.41 and −1.33 in the POS mode (**Figure 2E**) and 0.75 and −0.85 in the NEG mode (**Figure 2F**), demonstrating that the OPLS-DA model had no overfitting. The good quality and reliability of this OPLS-DA model were verified, meaning it was suitable to explore the differences between the two groups in this study. Then, we could perform the identification of the metabolites in the two groups.

Identification of the Serum Metabolites in PO and PN Participants

A total of 474 metabolites were found (of those 262 in POS mode and 212 in NEG mode). Then, 340 qualitative metabolites (of those 202 in POS mode and 138 in NEG mode) were obtained by preliminary screening of all identified metabolites. Under the conditions (t-test $p < 0.05$ and OPLS-DA model VIP > 1), 46

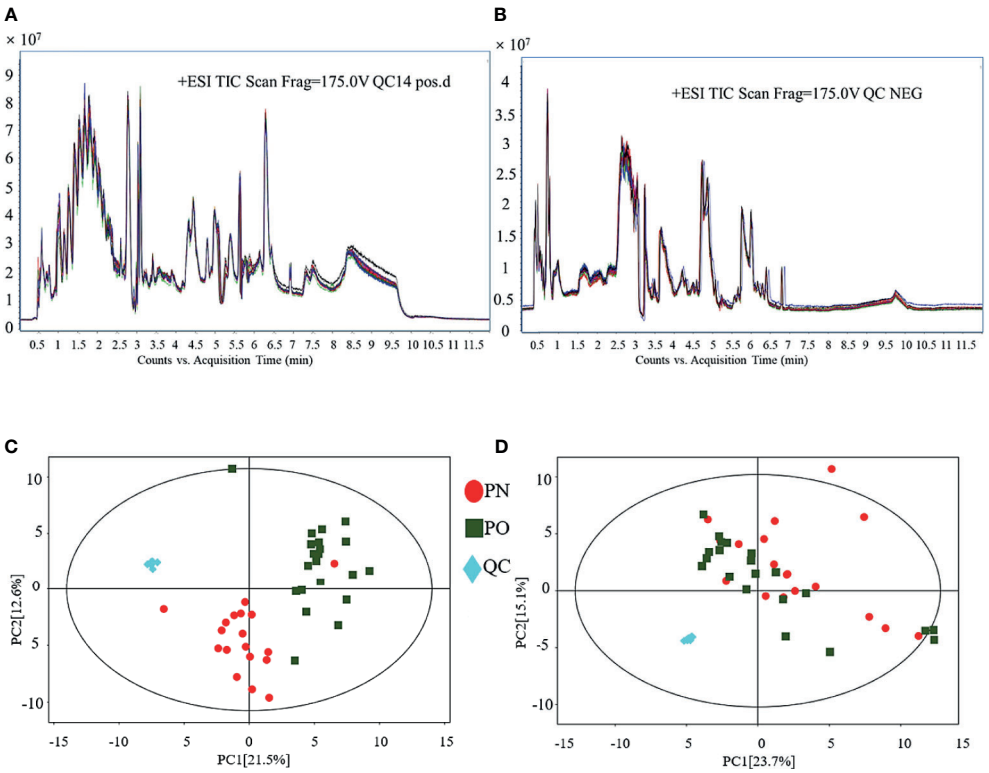

FIGURE 1 | QC of LC–MS analysis. **(A)** TIC (POS); **(B)** TIC (NEG); **(C)** PCA for QC (POS); **(D)** PCA for QC (NEG).

metabolites (of those 19 in POS mode and 27 in NEG mode) were determined, which were different between the PO and PN groups. Metabolites with a significant difference were visualized through volcano plots (**Figure 3**) including carbohydrates, amino acids, organic acids, two peptides, and lipids. **Table 2** summarizes the RT, mz, VIP values, *p* values, and fold change of all these 46 metabolites. EDM was calculated using the quantitative value of a differential metabolite. We used a complete linkage method to cluster these differential metabolites and form a heat map (**Figure 4**), which shows that in the POS mode, PC(16:0/16:0), pseudouridine, L-arginine, α-D-glucose 1-phosphate, and D-ornithine were upregulated, whereas dihydrolipoate, L-proline, Ile-Ala, L-pyroglutamic acid, 3-mercapto-2-butanone, L-pipecolic acid, His-Met, xanthylic acid, N-acetylglutamine, glutaric acid, Leu-Leu, Gly-Glu, myristoleic acid, and D-glucuronate were downregulated in patients with PO. In the NEG mode, thymine, hydrocortisone 21-acetate, dihydrothymine, L-threonate, L-glutamate, atrolactic acid, xanthine, myristic acid, L-valine, azelaic acid, indoleacetic acid, L-leucine, 3,4-dihydroxymandelic acid, palmitic acid, 5-methoxyindoleacetate, DL-lactate, indolelactic acid, L-tyrosine, L-alanine, and *N*-acetyl-L-tyrosine were upregulated, whereas α-*N*-acetyl-L-glutamine, 3-hydroxycapric acid, L-histidinol phosphate, 2-deoxyribose 5-phosphate, *N*-acetyl-D-galactosamine, L-gulonic gamma-lactone, and fructose 1-phosphate were downregulated in the PO group. However, after FDR correction, only Pseudouridine, L-arginine, α-D-glucose 1-phosphate, D-Ornithine, Ile-Ala, Pyroglutamic acid, 3-Mercapto-2-butanone, L-pipecolic acid, His-Met, Xanthylic acid (XMP), Acetylglutamine, Myristoleic acid, and D-Glucuronate in POS mode, and Dihydrothymine, Myristic acid, L-valine, palmitic acid, α-*N*-acetyl-L-glutamine, L-gulonic gamma-lactone, and Fructose 1-phosphate maintained the significance of difference (**Table 2**).

Metabolic Pathway Analysis

KEGG and MetaboAnalyst were comprehensively used in exploring the most relevant metabolic pathways. A total of six metabolic pathways in the POS mode and 19 in the NEG were enriched (**Figure 5**), among which seven pathways exhibited a significant difference ($p < 0.05$) as follows: D-arginine and D-ornithine metabolism, arginine and proline metabolisms, aminoacyl-tRNA biosynthesis, tryptophan metabolism, valine–leucine and isoleucine biosynthesis, valine–leucine and isoleucine degradation, and fatty acid biosynthesis. Two pathways, namely, D-arginine and D-ornithine metabolism pathway and arginine and proline metabolism pathway, in the POS mode had an impact value >0.1, which were 0.50 and 0.23, respectively. Because the present study is an explorative study and for further investigation in the future, we listed all the pathways with significant difference in **Figure 5**, including those with impact value <0.1.

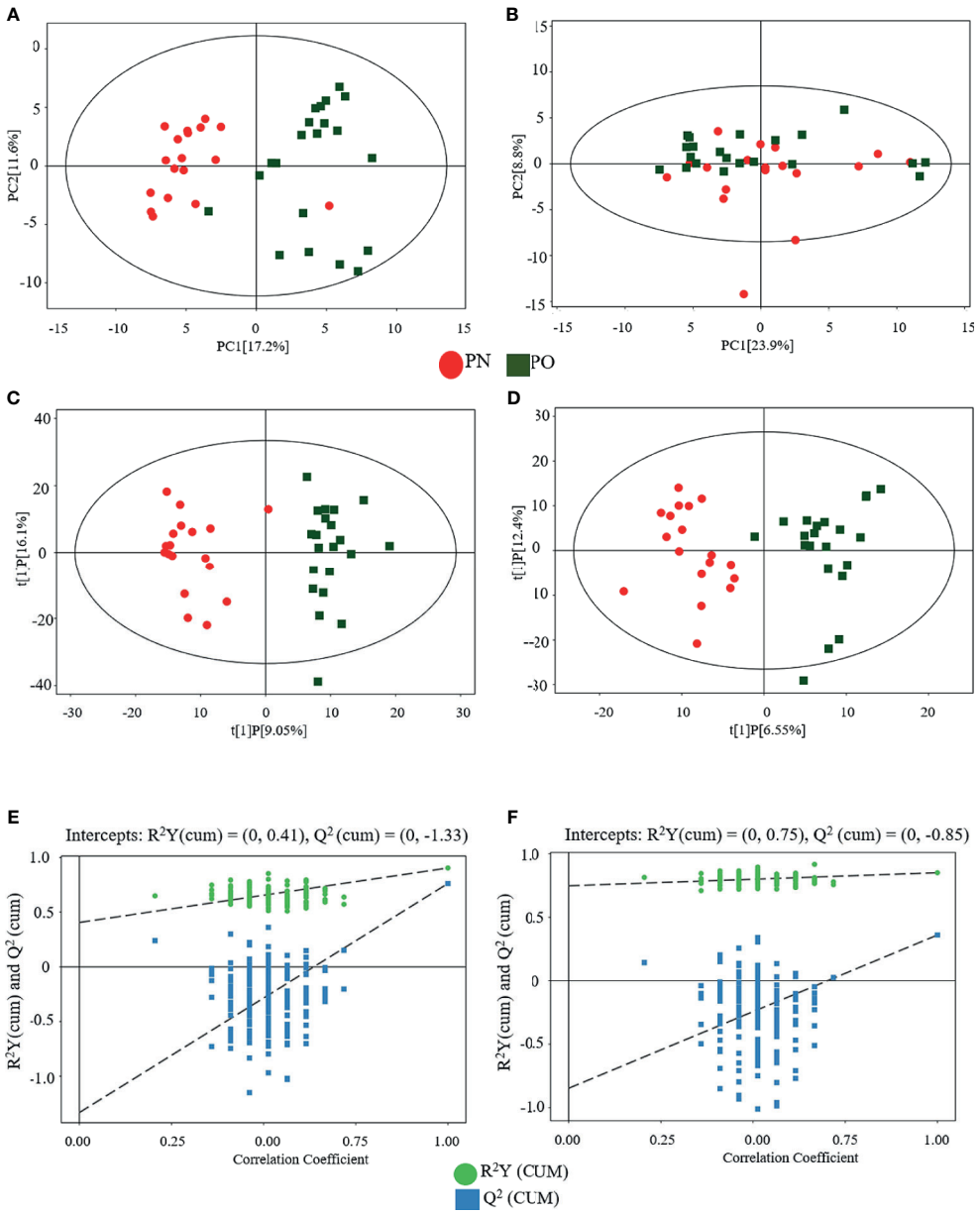

FIGURE 2 | Multivariate analyses of serum metabolites. **(A)** PCA (POS); **(B)** PCA (NEG); **(C)** OPLS-DA (POS); **(D)** OPLS-DA (NEG); statistical validation of OPLS-DA model, **(E)** (POS) and **(F)** (NEG).

DISCUSSION

In this study, we explored the serum differential metabolites in women with PO (*vs.* women with PN) using a conventional UHPLC-QTOF/MS approach, followed by PCA and OPLS-DA. A total of 46 differential metabolites (19, POS mode; 27, NEG mode) were identified. With respect to the key metabolic pathways, a total of seven pathways were identified by KEGG and MetaboAnalyst. To the best of our knowledge, this is the first study to explore the serum metabolic characteristics in women with PO. The findings of the present study are useful to further understand the pathophysiological changes in the PO state, which can provide clues to explore/develop effective therapies in treating these pathophysiological dysfunctions and contribute in preventing the occurrence of severe obesity-related complications.

The POS and NEG Modes in This Study

In the present study, we analyzed the metabolites in POS mode and NEG mode, respectively. POS mode and NEG mode are commonly run to analyze the metabolic profiles of samples during a traditional UHPLC-QTOF/MS approach. Many previous studies indicated that some substances were easily detected in POS mode, whereas others

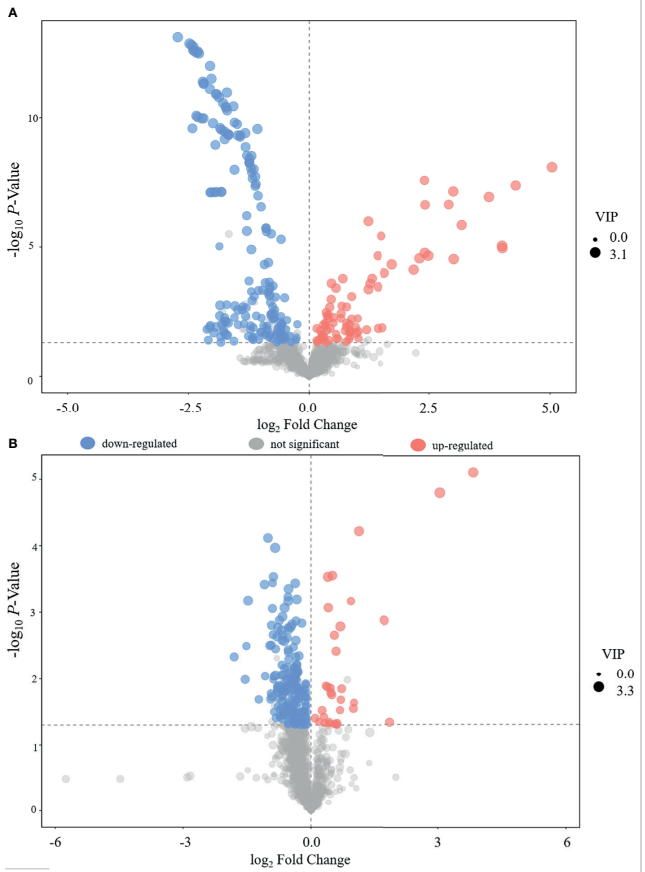

FIGURE 3 | Volcano plot for the differentially expressed metabolites. **(A)** POS; **(B)** NEG.

were easily in NEG mode (28–30). To expand the possibility of identification and determination of the metabolites in the new samples, which have never been previously tested, some authors suggested using a combination of POS and NEG modes in an explorative investigation (30). However, there is a concern that once the metabolites of positive and negative patterns are mixed together for analysis, the metabolites identified in different modes might have the same pathways, which might change the results. In the present study, we did not find any overlapped differential metabolites between these two modes (**Table 2** and **Figures 3**, **4**). Interestingly, the results of pathway analysis display that there is one pathway, namely aminoacyl-tRNA biosynthesis pathway, which was enriched in both POS and NEG models (**Figure 5**). However, this result is acceptable because the metabolites associated with the aminoacyl-tRNA biosynthesis pathway (matching amino acids with tRNAs) (31) were distributed in POS mode and NEG mode, where no overlapped amino acids were found.

The Physiological or Pathological Meanings of the Differential Metabolites

Because of the explorative nature of the present study, we attempted to find more potential differential metabolites for further verification. Albeit there were six metabolites in POS mode and 20 metabolites in NEG mode, which could not maintain the significant difference after FDR correction (**Table 2**), they were still included in the following discussion.

Changes of Metabolisms of Amino Acids

As far as the amino acids, we found a significant increase of L-arginine and D-ornithine in the POS mode and L-leucine, L-valine, L-tyrosine, and *N*-acetyl-L-tyrosine in the NEG mode; a significant decrease of L-proline in the POS mode of the PO group was also noted. L-leucine and L-valine belong to branched-chain amino acids (BCAAs), whereas tyrosine belongs to the amino acid aroma (AAAs). A close association between amino acids and obesity has been noted (32). Our results agree with the previous studies that suggested higher BCAAs and AAAs in subjects with obesity (14, 32–35). The increase of arginine and ornithine suggested that the ornithine cycle might be activated and arginine utilization rate might be suppressed in women with PO. Rangel-Huerta et al. reported that the increase of arginine results from the decreased availability of arginine, which also activates the plasma asymmetric dimethylarginine level. Nevertheless, the increase of asymmetric dimethylarginine might be a marker of endothelial dysfunction (14). The key role of arginine metabolism in the PO state was also verified in our metabolic pathway analysis. We found that D-arginine and D-ornithine metabolism pathways and arginine and proline metabolism pathways in the POS mode exhibited the highest impact value (0.50 and 0.23, respectively, **Figure 5**), which seem to imply that the endothelial dysfunction might be a potentially important pathogenesis involved in women with PO. Although, by far, there is no direct evidence elucidating the intrinsic interaction between endothelial dysfunction, the increase of arginine, and onset of CVD, much indirect evidence strongly implies their close association. It is well known that CVD is one of the main causes of death of perimenopausal women (36), whereas endothelial dysfunction is an important cause of CVD (37). Moreover, arginine might be associated with endothelial dysfunction *via* a nitric oxide synthase (NOS)-related mechanism. Arginine can be catalyzed by NOS to produce NO, which has the following effects: contract and relax the muscle cells in the arteries, dilate the arteries, lower blood pressure, and thus improve blood flow. When the utilization rate of arginine decreases, the synthesis of NO also decreases, thereby resulting in the increased risk of CVD. These mechanisms were summarized as a DDAH/ADMA/NOS/NO pathway (38). A previous study suggested a significant enhancement of proline in subjects with obesity (14), whereas our study presented a converse tendency, probably due to the hindrance of proline synthesis from arginine in the PO state. In the proline–arginine metabolic pathway, synthesizing arginine to proline requires 1-pyrrolin-5-carboxylic acid synthase (P5CS) catalysis (39). Normally, P5CS exists in a circular form in the mitochondria. However, when cells are in a state of senescence and/or oxidative stress, P5CS in the mitochondria may distribute diffusely (39). Nevertheless, cell senescence is one of the most dominant characteristics in the perimenopausal period (40). Thus, we speculate that the P5CS in the cells of subjects with PO might

TABLE 2 | Differential metabolites identified in POS and NEG models.

	MS2 name	RT (min)	m/z	Relative contents		VIP	*p* value	Q value	FC
				PN	PO				
POS mode									
Upregulated	PC (16:0/16:0)	0.76	756.53	0.0057	0.0098	1.05	0.03	0.09	1.72
	Pseudouridine	4.72	245.08	0.1490	0.2238	1.49	<0.001	0.02	1.50
	L-arginine	8.65	175.12	15.1287	22.6698	2.05	<0.001	<0.001	1.50
	α-D-Glucose 1-phosphate	4.72	261.05	0.0402	0.0561	1.33	0.02	0.05	1.40
	D-Ornithine	8.31	133.10	0.1118	0.1537	1.11	0.01	0.03	1.38
Downregulated	Dihydrolipoate	6.30	226.08	0.9609	0.8210	1.48	0.02	0.06	0.85
	L-Proline	5.09	157.10	0.9086	0.7393	1.32	0.04	0.10	0.81
	Ile-Ala	5.98	241.10	0.0164	0.0131	1.43	0.01	0.05	0.79
	L-Pyroglutamic acid	5.31	147.08	0.0820	0.0641	1.77	<0.001	0.02	0.78
	3-Mercapto-2-butanone	4.31	209.07	0.0063	0.0048	1.68	<0.001	0.02	0.76
	L-Pipecolic acid	4.31	171.11	3.8816	2.8309	1.91	<0.001	0.01	0.73
	His-Met	5.07	304.15	0.0105	0.0077	2.20	<0.001	<0.001	0.73
	Xanthylic acid (XMP)	2.80	364.05	0.0059	0.0037	1.35	<0.001	0.01	0.63
	N-Acetylglutamine	5.07	189.09	0.1214	0.0749	2.10	<0.001	<0.001	0.62
	Glutaric acid	5.52	282.11	0.1437	0.0794	1.75	0.02	0.06	0.55
	Leu-Leu	2.62	527.32	0.0099	0.0055	1.28	0.02	0.06	0.55
	Gly-Glu	5.44	246.11	0.0375	0.0190	1.62	0.02	0.07	0.51
	Myristoleic acid	2.22	226.18	0.0238	0.0119	1.12	0.01	0.03	0.50
	D-Glucuronate	4.91	255.07	0.0249	0.0092	1.92	0.01	0.05	0.37
NEG mode									
Upregulated	Thymine	4.96	185.06	0.2174	0.7567	1.79	<0.001	0.08	3.48
	hydrocortisone 21-acetate	0.73	425.20	0.0458	0.0865	2.04	0.02	0.13	1.89
	Dihydrothymine	7.04	165.01	0.2288	0.4273	1.41	<0.001	0.03	1.87
	L-Threonate	6.19	195.05	0.3783	0.6984	1.06	0.01	0.11	1.85
	L-Glutamate	6.30	146.05	0.5866	1.0429	1.65	<0.001	0.07	1.78
	Atrolactic acid	1.73	165.06	0.0215	0.0333	2.53	<0.001	0.06	1.55
	Xanthine	3.45	151.03	0.4823	0.7027	1.14	0.05	0.19	1.46
	Myristic acid	0.73	227.20	0.0257	0.0372	2.35	<0.001	0.04	1.45
	L-Valine	5.56	116.07	0.0715	0.1024	2.00	<0.001	0.05	1.43
	Azelaic acid	5.42	187.10	0.0322	0.0434	1.15	0.04	0.18	1.35
	Indoleacetic acid	2.36	174.06	0.0197	0.0259	1.32	0.05	0.19	1.32
	L-Leucine	4.97	130.09	0.1478	0.1938	1.86	0.01	0.12	1.31
	3,4-Dihydroxymandelic acid	5.50	183.03	0.0306	0.0399	1.68	0.01	0.09	1.30
	Palmitic acid	0.72	255.23	0.5133	0.6636	2.28	<0.001	0.03	1.29
	5-Methoxyindoleacetate	5.57	226.04	0.0024	0.0031	1.21	0.01	0.12	1.28
	DL-lactate	3.67	89.03	14.6582	18.5742	1.39	0.01	0.10	1.27
	Indolelactic acid	2.72	204.07	0.2556	0.3184	1.96	0.04	0.18	1.25
	L-Tyrosine	4.86	180.07	1.0350	1.2788	1.43	0.02	0.12	1.24
	L-Alanine	5.56	88.04	0.5023	0.6196	1.51	0.01	0.12	1.23
	N-acetyl-L-tyrosine	3.53	222.08	0.0952	0.1098	1.58	0.03	0.16	1.15
Downregulated	α-*N*-acetyl-L-glutamine	4.95	187.07	0.6836	0.5187	2.65	<0.001	0.03	0.76
	3-Hydroxycapric acid	0.77	169.12	0.0178	0.0133	1.09	0.05	0.19	0.75
	L-Histidinol phosphate	4.75	280.06	0.0075	0.0054	1.81	0.02	0.12	0.72
	2-Deoxyribose 5-phosphate	2.69	213.02	2.0023	1.3580	1.58	0.05	0.19	0.68
		1.74	242.18	0.0312	0.0205	1.25	0.05	0.19	0.66

(Continued)

TABLE 2 | Continued

	MS2 name	RT (min)	m/z	Relative contents		VIP	*p* value	Q value	FC
				PN	PO				
	N-acetyl-D-galactosamine								
	L-Gulonic gamma-lactone	3.97	237.06	0.0532	0.0160	2.69	<0.001	0.05	0.30
	Fructose 1-phosphate	0.37	259.03	0.3357	0.0406	3.28	<0.001	0.01	0.12

MS, mass spectrometry; m/z, mass-to-charge ratio; NEG, negative ion; PN, perimenopausal women without obesity; PO, perimenopausal women with obesity; POS, positive ion; RT, retention time; VIP, variable importance in projection.

The relative content of each metabolite was calculated by normalization of the contents with the internal standard.

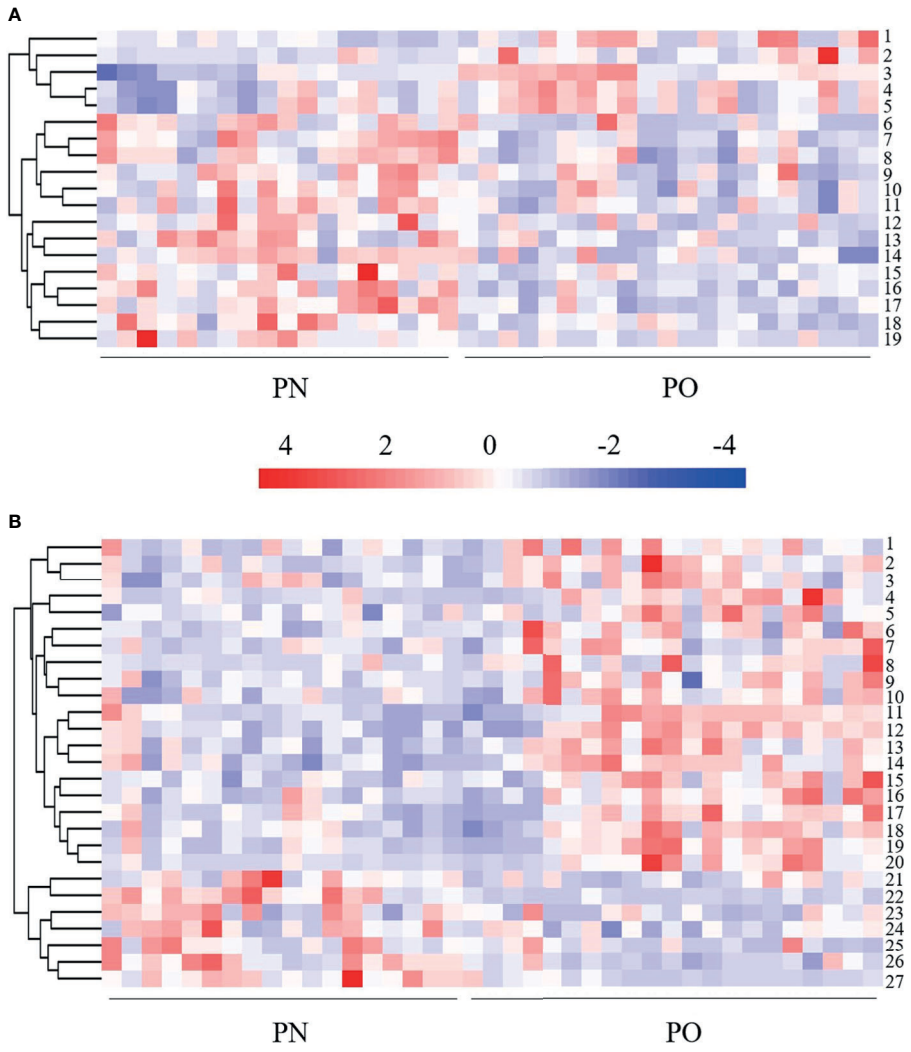

FIGURE 4 | Heat map of hierarchical clustering analysis of the differentially expressed metabolites. **(A)** POS mode. 1 = D-ornithine, 2 = PC (16:0/16:0), 3 = L-arginine, 4 = pseudouridine, 5 = α-D-glucose 1-phosphate, 6 = glutaric acid, 7 = L-pipecolic acid, 8 = 3-mercapto-2-butanone; 9 = L-proline, 10 = dihydrolipoic acid, 11 = Ile-Ala, 12 = Leu-Leu, 13 = myristoleic acid, 14 = xanthylic acid, 15 = Gly-Glu, 16 = *N*-acetylglutamine, 17 = His-Met, 18 = L-pyroglutamic acid, 19 = D-glucuronate. **(B)** NEG mode. 1 = indoleacetic acid, 2 = atrolactic acid, 3 = indolelactic acid, 4 = L-threonate, 5 = 5-methoxyindoleacetate, 6 = 3,4-dihydroxymandelic acid, 7 = azelaic acid, 8 = hydrocortisone 21-acetate; 9 = L-tyrosine, 10 = *N*-acetyl-L-tyrosine, 11 = DL-lactate, 12 = dihydrothymine, 13 = myristic acid, 14 = palmitic acid, 15 = L-valine, 16 = L-leucine, 17 = xanthine, 18 = L-alanine, 19 = L-glutamate, 20 = thymine, 21= *N*-acetyl-D-galactosamine, 22 = fructose 1-phosphate, 23 = 3-hydroxycapric acid, 24 = L-histidinol phosphate, 25 = 2-deoxyribose 5-phosphate, 26 = α-*N*-acetyl-L-glutamine, 27 = L-gulonic gamma-lactone.

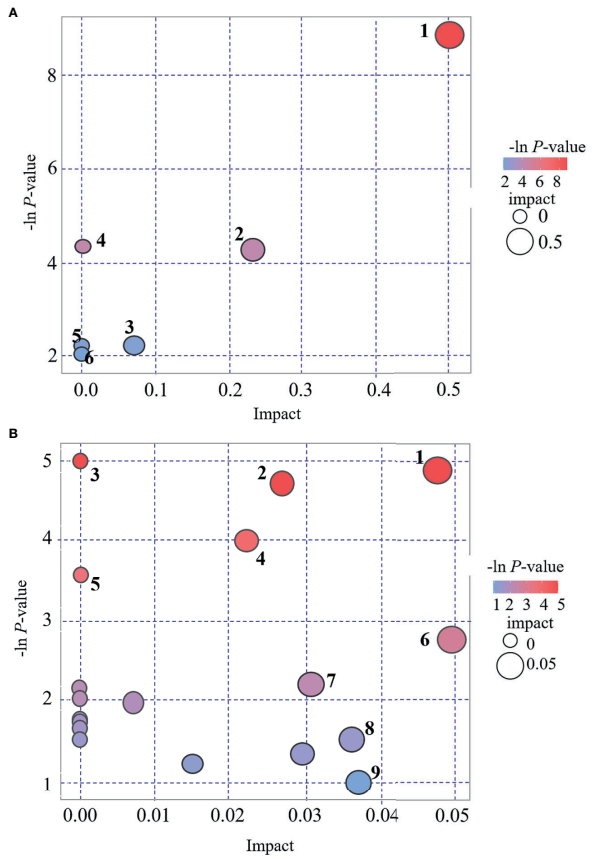

FIGURE 5 | Bubble plot for pathway analysis. **(A)**: POS mode. 1 = D-arginine and D-ornithine metabolism, 2 = arginine and proline metabolism, 3 = lysine degradation, 4 = Aminoacyl-tRNA biosynthesis, 5 = fatty acid metabolism, 6 = pyrimidine metabolism. **(B)**: NEG mode. 1 = tryptophan metabolism, 2 = valine, leucine and isoleucine biosynthesis, 3 = aminoacyl-tRNA biosynthesis, 4 = Valine, leucine and isoleucine degradation, 5 = fatty acid biosynthesis, 6 = tyrosine metabolism, 7 = caffeine metabolism, 8 = fructose and mannose metabolism, 9 = purine metabolism.

be in a diffuse state and cannot synthesize arginine to proline, thereby causing a low serum level of proline. These mechanisms require further verification in our future investigation.

Changes in Lipid Metabolism

PC is one of the main phospholipids in eukaryotic cells, which can hydrolyze to produce fatty acids. It is a major component of many secretory products, such as HDL (41). PC has been reported to be significantly enhanced in postmenopausal women, which is associated with menopausal status (42). Bagheri et al. also reported higher plasma diacyl-PCs in the obesity subjects (32). All available evidence supports that the increase of PC results in the increase of fatty acids in the perimenopausal women. Excessive accumulation of fatty acids in the mitochondria leads to oxidative stress and mitochondrial dysfunction, subsequently causing many perimenopausal disorders, including obesity. Moreover, the changes of PC-related lipoproteins might be affected by hormone levels (43) as well as weight enhancement and insulin resistance (44, 45). In this study, we found that PC (16:0/16:0) is significantly upregulated in women with PO. Available literatures concerning PC (16:0/16:0) and obesity are limited. Previous analogous studies reported an increasing tendency of PC (16:0/16:0) in gestational diabetes mellitus (46) and obese pregnant women (47); however, a significant difference was not noted. Dong et al. reported a significant decrease of PC (16:0/16:0) in the myocardial tissue of diabetic cardiomyopathy rats (48). Sigruener et al. found a positive correlation between plasma PC (16:0/16:0) and mortality of patients with vascular and metabolic diseases (41). The physiological or pathological role of PC (16:0/16:0) in PO requires further investigation.

We found the upregulation of palmitic acid and myristic acid in the PO group of the NEG model, which are consistent with the previous analogous studies, which report that saturated fatty acids, such as palmitic acid and myristic acid, are increased in obese men (49) or adults (including men and women) (50) and in patients with insulin resistance (51) and T2D (52). Myristoleic acid is a desaturation product from myristic acid regulated by stearoyl-CoA desaturase (SCD) gene. In this study, we found the downregulation of myristoleic acid in subjects with PO of the POS mode. The roles of myristic acid and myristoleic acid, along with their interactions in obesity, are not fully understood. Montastier et al. reported a positive correlation between myristoleic acid and BW loss; a lower myristoleic acid means lower BW loss (53). Hence, our data presented a downregulation in the PO group, which may indicate a lower tendency of BW loss in women with PO (*vs.* PN).

Others

Another finding is that the serum indole lactic acid and indoleacetic acid levels are significantly upregulated in the NEG mode of women with PO. Indole lactic acid and indoleacetic acid are products of tryptophan metabolism. Their upregulation seems to imply the activation of tryptophan metabolism in the PO state. The change of tryptophan metabolism may reportedly result in a negative impact on the diversity of intestinal microflora (54), which is associated with dysfunction of the immune system and results in an increased risk of infection, malnutrition, and other functional defects (55).

Limitations

There are several limitations in the present study. First, we did not perform verification of the identified metabolites and pathways. For example, the increase of asymmetric dimethylarginine might be a marker of endothelial dysfunction, however, we did not examine some indicators of endothelial function in these women, although we speculate that the endothelial dysfunction might be a potentially important pathogenesis involved in women with PO. In addition, arginine can be catalyzed by NOS to produce NO; however, we did not check the NOS indicators. Indeed, rigorous verification of the metabolites and pathways, which were explored in this study, can greatly improve the strength of the evidence, which will be performed in our future investigation. Second, in addition to metabolism, many other factors, such as gene, race, diet, and lifestyle, may also contribute to the difference between PO and PN. However, in this study, we only considered age, height, and serum estrogen level and no significant difference was observed between the PO and PN groups, we therefore only performed Student's t-test (PO *vs.* PN). More compelling methods should consider additional factors (gene, race, diet, and

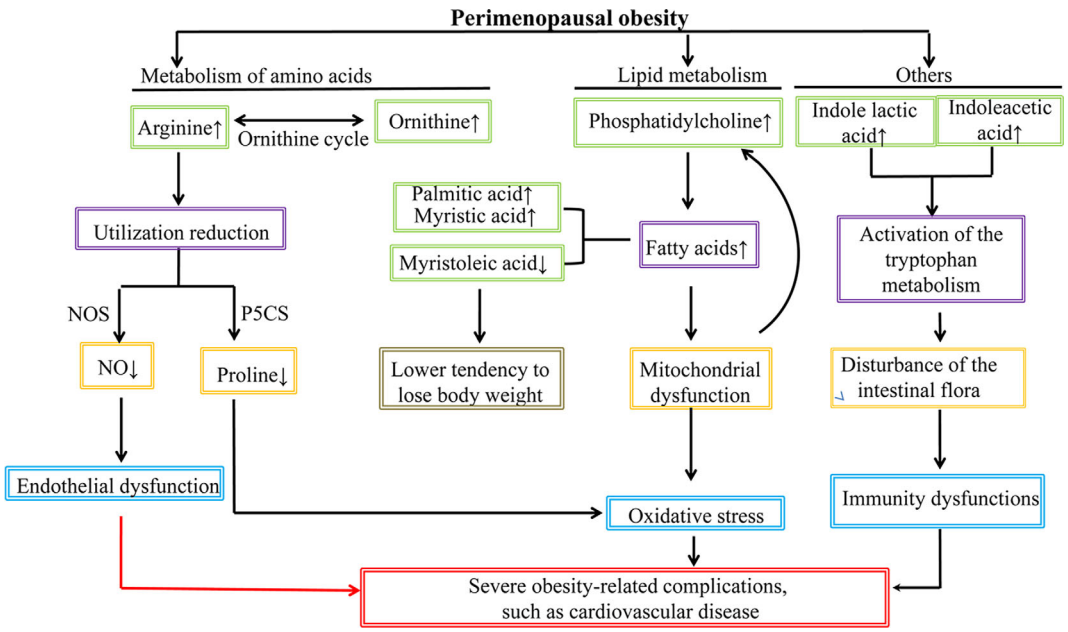

FIGURE 6 | The pathophysiological scenario of perimenopausal obesity summarized in the present study.

lifestyle, etc.) and perform multiple comparisons with post-hoc correction. Third, as an explorative study, for providing a full pathophysiological scenario of PO, we included the data from all samples, including the outlier samples shown in **Figures 1C** and **2A**; however, such data processing methods might potentially cause bias. These issues will be addressed in our future investigation.

This study explored the metabolic characteristics of women with PO by identification of the deferential metabolites using a UHPLC-QTOF/MS approach. A total of 46 differential metabolites, along with seven metabolic pathways, were identified. The differential metabolites can be divided into lipid, amino acids, carbohydrates, and organic acids. The changes of metabolisms of lipid, amino acids, and indoleacetic acid provided a pathophysiological scenario for the perimenopause women with mild obesity (**Figure 6**). Future, deeper investigation will be conducted to further uncover the pathophysiological nature of the PO, which is extremely important in preventing the incurable obesity-related diseases.

CONCLUSIONS

A metabolomics investigation was conducted to identify the differential metabolites in perimenopausal women with mild obesity. Metabolism changes of amino acids indicated a dysfunction of the DDAH/ADMA/NOS/NO pathway, which was related to the onset of CVD; changes of lipid metabolisms indicated the tendency of BW loss and oxidative stress prevention, and the upregulation of serum indole lactic acid and indoleacetic acid levels indicated an intestinal microflora-related immunity dysfunction. Although some mechanisms of these findings require further investigation for the direct evidence, we provided a pathophysiological scenario of PO based on the metabolomic profiles explored by the UHPLC-QTOF/MS approach, which requires further verification. We believe the findings of this study are helpful for the clinicians to take measures in preventing the women with PO from developing severe incurable obesity-related complications, such as CVD.

DATA AVAILABILITY STATEMENT

The original contributions presented in the study are included in the article/**Supplementary Material**. Further inquiries can be directed to the corresponding author.

ETHICS STATEMENT

The studies involving human participants were reviewed and approved by the ethics committee of the Fujian University of Traditional Chinese Medicine (approval number: SQ2014-007-01,study period from 2014 to 2019). The patients/participants provided their written informed consent to participate in this study.

AUTHOR CONTRIBUTIONS

SD and TA fetched the original ideas and designed the study, SD, QC, MC, YL, XL, SC, YC, CL, and TA performed the experiments, SD ran the statistics. SD and TA drew the figures. SD and TA wrote the first draft. TA supervised the study. All authors contributed to the article and approved the submitted version.

FUNDING

This study was supported by Natural Science Foundation of Fujian Province (2020J01740). This study was also supported by the project of Fujian Province Center for Collaborative Innovation of TCM Health Management 2011 (JG2017003). This study was also supported by Fujian Education Department of China: Fujian Provincial universities' incubation project for prominent young scientific researchers (2018). This study was also supported by the scientific research platform project of Fujian University of Traditional Chinese Medicine (X2019018-Platform). This study was also partly supported by grants from the Japan Society for the Promotion of Science (nos. 20791025, 24592157,15k10358, and 18K08991).

ACKNOWLEDGMENTS

The authors would like to thank BIOTREE (http://www.biotree.cn) for the technological support of UHPLC-QTOF/MS; and Enago (www.enago.cn) for the English language review.

SUPPLEMENTARY MATERIAL

The Supplementary Material for this article can be found online at: https://www.frontiersin.org/articles/10.3389/fendo.2021.637317/full#supplementary-material

REFERENCES

1. Marjoribanks J, Farquhar C, Roberts H, Lethaby A, Lee J. Long-Term Hormone Therapy for Perimenopausal and Postmenopausal Women. *Cochrane Database Syst Rev* (2017) 1:CD004143. doi: 10.1002/14651858.CD004143.pub5
2. Christakis MK, Hasan H, De Souza LR, Shirreff L. The Effect of Menopause on Metabolic Syndrome: Cross-Sectional Results From the Canadian Longitudinal Study on Aging. *Menopause* (2020) 27(9):999–1009. doi: 10.1097/GME.0000000000001575
3. Yeo W, Pang E, Liem GS, Suen JJS, Ng RYW, Yip CCH, et al. Menopausal Symptoms in Relationship to Breast Cancer-Specific Quality of Life After Adjuvant Cytotoxic Treatment in Young Breast Cancer Survivors. *Health Qual Life Outcomes* (2020) 18(1):24. doi: 10.1186/s12955-020-1283-x
4. Thangavel P, Puga-Olguin A, Rodriguez-Landa JF, Zepeda RC. Genistein as Potential Therapeutic Candidate for Menopausal Symptoms and Other Related Diseases. *Molecules* (2019) 24(21):3892. doi: 10.3390/molecules24213892
5. Stevenson JC, Tsiligiannis S, Panay N. Cardiovascular Risk in Perimenopausal Women. *Curr Vasc Pharmacol* (2019) 17(6):591–4. doi: 10.2174/1570161116666181002145340
6. Fan H, Chen S, Gao B, Ding S, Zhao Q, Li C, et al. Risk Analysis of Systemic Levels of Estrogen and Adipokines as Well as Estrogen Receptors From PBMCs in Childbearing and Perimenopausal Women With Obesity. *Diabetes Metab Syndr Obes* (2019) 12:1287–95. doi: 10.2147/DMSO.S206069
7. Fernandez-Alonso AM, Cuadros JL, Chedraui P, Mendoza M, Cuadros AM, Perez-Lopez FR. Obesity is Related to Increased Menopausal Symptoms Among Spanish Women. *Menopause Int* (2010) 16(3):105–10. doi: 10.1258/mi.2010.010029
8. Kim HK, Choi YH, Verpoorte R. NMR-Based Metabolomic Analysis of Plants. *Nat Protoc* (2010) 5(3):536–49. doi: 10.1038/nprot.2009.237
9. Sevin DC, Kuehne A, Zamboni N, Sauer U. Biological Insights Through Nontargeted Metabolomics. *Curr Opin Biotechnol* (2015) 34:1–8. doi: 10.1016/j.copbio.2014.10.001
10. Lindon JC, Holmes E, Nicholson JK. Metabonomics: Systems Biology in Pharmaceutical Research and Development. *Curr Opin Mol Ther* (2004) 6(3):265–72.
11. Li Y, Wang Y, Zhuang Y, Zhang P, Chen S, Asakawa T, et al. Serum Metabolomic Profiles Associated With Untreated Metabolic Syndrome Patients in the Chinese Population. *Clin Transl Sci* (2020) 13(6):1271–8. doi: 10.1111/cts.12817
12. Chen HH, Tseng YJ, Wang SY, Tsai YS, Chang CS, Kuo TC, et al. The Metabolome Profiling and Pathway Analysis in Metabolic Healthy and Abnormal Obesity. *Int J Obes (Lond)* (2015) 39(8):1241–8. doi: 10.1038/ijo.2015.65
13. Saner C, Harcourt BE, Pandey A, Ellul S, McCallum Z, Kao KT, et al. Sex and Puberty-Related Differences in Metabolomic Profiles Associated With Adiposity Measures in Youth With Obesity. *Metabolomics* (2019) 15(5):75. doi: 10.1007/s11306-019-1537-y
14. Rangel-Huerta OD, Pastor-Villaescusa B, Gil A. Are We Close to Defining a Metabolomic Signature of Human Obesity? A Systematic Review of Metabolomics Studies. *Metabolomics* (2019) 15(6):93. doi: 10.1007/s11306-019-1553-y
15. Woods NF, Mitchell ES. Symptoms During the Perimenopause: Prevalence, Severity, Trajectory, and Significance in Women's Lives. *Am J Med* (2005) 118(Suppl 12B):14–24. doi: 10.1016/j.amjmed.2005.09.031
16. Chen C, Lu FC. Department of Disease Control Ministry of Health PRC. The Guidelines for Prevention and Control of Overweight and Obesity in Chinese Adults. *BioMed Environ Sci* (2004) 17(Suppl):1–36.
17. Dunn WB, Broadhurst D, Begley P, Zelena E, Francis-McIntyre S, Anderson N, et al. Procedures for Large-Scale Metabolic Profiling of Serum and Plasma Using Gas Chromatography and Liquid Chromatography Coupled to Mass Spectrometry. *Nat Protoc* (2011) 6(7):1060–83. doi: 10.1038/nprot.2011.335
18. Chang R, Zhu Y, Xu J, Chen L, Su G, Kijlstra A, et al. Identification of Urine Metabolic Biomarkers for Vogt-Koyanagi-Harada Disease. *Front Cell Dev Biol* (2021) 9:637489. doi: 10.3389/fcell.2021.637489
19. Wang J, Zhang T, Shen X, Liu J, Zhao D, Sun Y, et al. Serum Metabolomics for Early Diagnosis of Esophageal Squamous Cell Carcinoma by UHPLC-QTOF/MS. *Metabolomics* (2016) 12(7):1–10. doi: 10.1007/s11306-016-1050-5
20. Dokmanic I, Parhizkar R, Ranieri J, Vetterli M. Euclidean Distance Matrices: Essential Theory, Algorithms, and Applications. *IEEE Signal Process Magazine* (2015) 32(6):12–30. doi: 10.1109/MSP.2015.2398954
21. Taylor J, King RD, Altmann T, Fiehn O. Application of Metabolomics to Plant Genotype Discrimination Using Statistics and Machine Learning. *Bioinformatics* (2002) 18(Suppl 2):S241–8. doi: 10.1093/bioinformatics/18.suppl_2.s241
22. Lu X, Nie H, Li Y, Zhan C, Liu X, Shi X, et al. Comprehensive Characterization and Evaluation of Hepatocellular Carcinoma by LC–MS Based Serum Metabolomics. *Metabolomics Off J Metabolomic Soc* (2015) 11(5):1381–93. doi: 10.1007/s11306-015-0797-4
23. Xiao JF, Zhou B, Ressom HW. Metabolite Identification and Quantitation in LC-MS/MS-Based Metabolomics. *Trends Analyt Chem* (2012) 32:1–14. doi: 10.1016/j.trac.2011.08.009
24. Kuhl C, Tautenhahn R, Böttcher C, Larson TR, Neumann S. CAMERA: An Integrated Strategy for Compound Spectra Extraction and Annotation of

Liquid Chromatography/Mass Spectrometry Data Sets. *Anal Chem* (2012) 84 (1):283–9. doi: 10.1021/ac202450g
25. Benjamini Y, Hochberg Y. Controlling the False Discovery Rate: A Practical and Powerful Approach to Multiple Testing. *J R Stat Society: Ser B (Methodological)* (1995) 57(1):289–300. doi: 10.1111/j.2517-6161.1995.tb02031.x
26. Kanehisa M, Goto S. KEGG: Kyoto Encyclopedia of Genes and Genomes. *Nucleic Acids Res* (2000) 28(1):27–30. doi: 10.1093/nar/28.1.27
27. Xia J, Wishart DS. Using MetaboAnalyst 3.0 for Comprehensive Metabolomics Data Analysis. *Curr Protoc Bioinf* (2016) 55:14. doi: 10.1002/cpbi.11
28. Wang X, Lv H, Zhang G, Sun W, Zhou D, Jiao G, et al. Development and Validation of a Ultra Performance LC-ESI/MS Method for Analysis of Metabolic Phenotypes of Healthy Men in Day and Night Urine Samples. *J Sep Sci* (2008) 31(16-17):2994–3001. doi: 10.1002/jssc.200800326
29. Liu W, Li S, Wu YK, Yan X, Zhu YM, Jiang FY, et al. Metabolic Profiling of Rats Poisoned With Paraquat and Treated With Xuebijing Using a UPLC-QTOF-MS/MS Metabolomics Approach. *Anal Methods* (2020) 12(37):4562–71. doi: 10.1039/d0ay00968g
30. Terent'ev A, Morozik YI, Ivanova M, Dudkin A. Identification and Determination of the Molecular Structure of Phosphate Esters by the Joint Application of Positive Ion and Negative Ion Electron Ionization Mass Spectrometry. *J Anal Chem* (2020) 75(2):208–18. doi: 10.1134/S1061934820020161
31. Ibba M, Soll D. The Renaissance of aminoacyl-tRNA Synthesis. *EMBO Rep* (2001) 2(5):382–7. doi: 10.1093/embo-reports/kve095
32. Bagheri M, Djazayery A, Farzadfar F, Qi L, Yekaninejad MS, Aslibekyan S, et al. Plasma Metabolomic Profiling of Amino Acids and Polar Lipids in Iranian Obese Adults. *Lipids Health Dis* (2019) 18(1):94. doi: 10.1186/s12944-019-1037-0
33. Rauschert S, Kirchberg FF, Marchioro L, Koletzko B, Hellmuth C, Uhl O. Early Programming of Obesity Throughout the Life Course: A Metabolomics Perspective. *Ann Nutr Metab* (2017) 70(3):201–9. doi: 10.1159/000459635
34. Newgard C. Metabolomics and Metabolic Diseases: Where Do We Stand? *Cell Metab* (2017) 25(1):43–56. doi: 10.1016/j.cmet.2016.09.018
35. Stroeve JH, Saccenti E, Bouwman J, Dane A, Strassburg K, Vervoort J, et al. Weight Loss Predictability by Plasma Metabolic Signatures in Adults With Obesity and Morbid Obesity of the DiOGenes Study. *Obes (Silver Spring)* (2016) 24(2):379–88. doi: 10.1002/oby.21361
36. Wang Q, Shi H. Progress of the Relationship Between Perimenopausal Hot Hush and Cardiovascular Disease. *J Int Obstetrics Gynecology* (2014) 41(1):29–31.
37. YU FSP, LIU S. Progress in Studies on the Regulation of Exercise Factors in Cardiovascular Function and its Related Mechanisms. *Int J Gynecology Obstetrics* (2014) 41(1):29–31.
38. Zhu ZD, Ye JM, Fu XM, Wang XC, Ye JY, Wu XR, et al. DDAH2 Alleviates Myocardial Fibrosis in Diabetic Cardiomyopathy Through Activation of the DDAH/ADMA/NOS/NO Pathway in Rats. *Int J Mol Med* (2019) 43(2):749–60. doi: 10.3892/ijmm.2018.4034
39. Pérez-Arellano I, Carmona-Alvarez F, Martínez AI, Rodríguez-Díaz J, Cervera J. Pyrroline-5-Carboxylate Synthase and Proline Biosynthesis: From Osmotolerance to Rare Metabolic Disease. *Protein Sci A Publ Protein Soc* (2010) 19(3):372–82. doi: 10.1002/pro.340
40. Ke C, Hou Y, Zhang H, Yang K, Wang J, Guo B, et al. Plasma Metabolic Profiles in Women Are Menopause Dependent. *PloS One* (2015) 10(11): e0141743. doi: 10.1371/journal.pone.0141743
41. Sigruener A, Kleber ME, Heimerl S, Liebisch G, Schmitz G, Maerz W. Glycerophospholipid and Sphingolipid Species and Mortality: The Ludwigshafen Risk and Cardiovascular Health (LURIC) Study. *PloS One* (2014) 9(1):e85724. doi: 10.1371/journal.pone.0085724
42. Cui X, Yu X, Sun G, Hu T, Likhodii S, Zhang J, et al. Differential Metabolomics Networks Analysis of Menopausal Status. *PloS One* (2019) 14(9):e0222353. doi: 10.1371/journal.pone.0222353
43. Mattsson C, Olsson T. Estrogens and Glucocorticoid Hormones in Adipose Tissue Metabolism. *Curr Med Chem* (2007) 14(27):2918–24. doi: 10.2174/092986707782359972
44. Maynar M, Mahedero G, Maynar I, Maynar JI, Tuya IR, Caballero MJ. Menopause-Induced Changes in Lipid Fractions and Total Fatty Acids in Plasma. *Endocr Res* (2001) 27(3):357–65. doi: 10.1081/erc-100106013
45. Milewicz A, Tworowska U, Demissie M. Menopausal Obesity–Myth or Fact? *Climacteric* (2001) 4(4):273–83. doi: 10.1080/cmt.4.4.273.283
46. Uhl O, Demmelmair H, Segura MT, Florido J, Rueda R, Campoy C, et al. Effects of Obesity and Gestational Diabetes Mellitus on Placental Phospholipids. *Diabetes Res Clin Pract* (2015) 109(2):364–71. doi: 10.1016/j.diabres.2015.05.032
47. Gazquez A, Uhl O, Ruiz-Palacios M, Gill C, Patel N, Koletzko B, et al. Placental Lipid Droplet Composition: Effect of a Lifestyle Intervention (UPBEAT) in Obese Pregnant Women. *Biochim Biophys Acta Mol Cell Biol Lipids* (2018) 1863(9):998–1005. doi: 10.1016/j.bbalip.2018.04.020
48. Dong S, Zhang S, Chen Z, Zhang R, Tian L, Cheng L, et al. Berberine Could Ameliorate Cardiac Dysfunction via Interfering Myocardial Lipidomic Profiles in the Rat Model of Diabetic Cardiomyopathy. *Front Physiol* (2018) 9:1042. doi: 10.3389/fphys.2018.01042
49. Kim JY, Park JY, Kim OY, Ham BM, Kim HJ, Kwon DY, et al. Metabolic Profiling of Plasma in Overweight/Obese and Lean Men Using Ultra Performance Liquid Chromatography and Q-TOF Mass Spectrometry (UPLC-Q-TOF Ms). *J Proteome Res* (2010) 9(9):4368–75. doi: 10.1021/pr100101p
50. Soriguer F, Garcia-Serrano S, Garcia-Almeida JM, Garrido-Sanchez L, Garcia-Arnes J, Tinahones FJ, et al. Changes in the Serum Composition of Free-Fatty Acids During an Intravenous Glucose Tolerance Test. *Obes (Silver Spring)* (2009) 17(1):10–5. doi: 10.1038/oby.2008.475
51. Mook S, Halkes Cj C, Bilecen S, Cabezas MC. In Vivo Regulation of Plasma Free Fatty Acids in Insulin Resistance. *Metabolism* (2004) 53(9):1197–201. doi: 10.1016/j.metabol.2004.02.023
52. Pankow JS, Duncan BB, Schmidt MI, Ballantyne CM, Couper DJ, Hoogeveen RC, et al. Fasting Plasma Free Fatty Acids and Risk of Type 2 Diabetes: The Atherosclerosis Risk in Communities Study. *Diabetes Care* (2004) 27(1):77–82. doi: 10.2337/diacare.27.1.77
53. Montastier E, Villa-Vialaneix N, Caspar-Bauguil S, Hlavaty P, Tvrzicka E, Gonzalez I, et al. System Model Network for Adipose Tissue Signatures Related to Weight Changes in Response to Calorie Restriction and Subsequent Weight Maintenance. *PloS Comput Biol* (2015) 11(1):e1004047. doi: 10.1371/journal.pcbi.1004047
54. Gao J, Xu K, Liu H, Liu G, Bai M, Peng C, et al. Impact of the Gut Microbiota on Intestinal Immunity Mediated by Tryptophan Metabolism. *Front Cell Infect Microbiol* (2018) 8:13. doi: 10.3389/fcimb.2018.00013
55. Salazar N, Valdés-Varela L, González S, Gueimonde M, de los Reyes-Gavilán CG. Nutrition and the Gut Microbiome in the Elderly. *Gut Microbes* (2016) 8 (2):82–97. doi: 10.1080/19490976.2016.1256525

Conflict of Interest: The authors declare that the research was conducted in the absence of any commercial or financial relationships that could be construed as a potential conflict of interest.

Publisher's Note: All claims expressed in this article are solely those of the authors and do not necessarily represent those of their affiliated organizations, or those of the publisher, the editors and the reviewers. Any product that may be evaluated in this article, or claim that may be made by its manufacturer, is not guaranteed or endorsed by the publisher.

frontiers in Endocrinology

ORIGINAL RESEARCH
published: 25 November 2021
doi: 10.3389/fendo.2021.730686

The Polymorphism at PLCB4 Promoter (rs6086746) Changes the Binding Affinity of RUNX2 and Affects Osteoporosis Susceptibility: An Analysis of Bioinformatics-Based Case-Control Study and Functional Validation

*Dung-Jang Tsai[1,2], Wen-Hui Fang[3], Li-Wei Wu[3], Ming-Cheng Tai[4], Chung-Cheng Kao[5], Shih-Ming Huang[6], Wei-Teing Chen[7,8], Po-Jen Hsiao[9,10], Chih-Chien Chiu[11], Wen Su[12], Chia-Chun Wu[13] and Sui-Lung Su[1,2]**

[1] Graduate Institute of Life Sciences, National Defense Medical Center, Taipei, Taiwan, [2] School of Public Health, National Defense Medical Center, Taipei, Taiwan, [3] Department of Family and Community Medicine, Tri-Service General Hospital, National Defense Medical Center, Taipei, Taiwan, [4] Department of Ophthalmology, Tri-Service General Hospital, National Defense Medical Center, Taipei, Taiwan, [5] Superintendent's Office, Tri-Service General Hospital Songshan Branch, National Defense Medical Center, Taipei, Taiwan, [6] Department of Biochemistry, National Defense Medical Center, Taipei, Taiwan, [7] Division of Thoracic Medicine, Department of Medicine, Cheng Hsin General Hospital, Taipei, Taiwan, [8] Department of Medicine, Tri-Service General Hospital, National Defense Medical Center, Taipei, ROC, Taiwan, [9] Department of Internal Medicine, Taoyuan Armed Forces General Hospital, Taoyuan, Taiwan, [10] Division of Nephrology, Department of Internal Medicine, Tri-Service General Hospital, National Defense Medical Center, Taipei, Taiwan, [11] Division of Infectious Diseases, Department of Internal Medicine, Taoyuan Armed Forces General Hospital, National Defense Medical Center, Taoyuan, Taiwan, [12] Graduate Institute of Aerospace and Undersea Medicine, National Defense Medical Center, Taipei, Taiwan, [13] Department of Orthopedics, Tri-Service General Hospital, National Defense Medical Center, Taipei, Taiwan

Purpose: Genome-wide association studies have identified numerous genetic variants that are associated with osteoporosis risk; however, most of them are present in the non-coding regions of the genome and the functional mechanisms are unknown. In this study, we aimed to investigate the potential variation in runt domain transcription factor 2 (RUNX2), which is an osteoblast-specific transcription factor that normally stimulates bone formation and osteoblast differentiation, regarding variants within RUNX2 binding sites and risk of osteoporosis in postmenopausal osteoporosis (PMOP).

Methods: We performed bioinformatics-based prediction by combining whole genome sequencing and chromatin immunoprecipitation sequencing to screen functional SNPs in the RUNX2 binding site using data from the database of Taiwan Biobank; Case-control studies with 651 postmenopausal women comprising 107 osteoporosis patients, 290 osteopenia patients, and 254 controls at Tri-Service General Hospital between 2015 and 2019 were included. The subjects were examined for bone mass density and classified into normal and those with osteopenia or osteoporosis by T-scoring with dual-energy X-ray absorptiometry. Furthermore, mRNA expression and luciferase reporter assay were

OPEN ACCESS

Edited by:
Stephen Atkin, Royal College of Surgeons in Ireland, Bahrain

Reviewed by:
Sinan Tanyolac, Istanbul University, Turkey
Yixuan Deng, Chongqing Medical University, China
Yanguo Kong, Peking Union Medical College Hospital (CAMS), China

***Correspondence:**
Sui-Lung Su
a131419@gmail.com

Specialty section:
This article was submitted to Systems Endocrinology, a section of the journal Frontiers in Endocrinology

Received: *23 July 2021*
Accepted: *09 November 2021*
Published: *25 November 2021*

Citation:
Tsai D-J, Fang W-H, Wu L-W, Tai M-C, Kao C-C, Huang S-M, Chen W-T, Hsiao P-J, Chiu C-C, Su W, Wu C-C and Su S-L (2021) The Polymorphism at PLCB4 Promoter (rs6086746) Changes the Binding Affinity of RUNX2 and Affects Osteoporosis Susceptibility: An Analysis of Bioinformatics-Based Case-Control Study and Functional Validation. Front. Endocrinol. 12:730686. doi: 10.3389/fendo.2021.730686

used to provide additional evidence regarding the associations identified in the association analyses. Chi-square tests and logistic regression were mainly used for statistical assessment.

Results: Through candidate gene approaches, 3 SNPs in the RUNX2 binding site were selected. A novel SNP rs6086746 in the PLCB4 promoter was identified to be associated with osteoporosis in Chinese populations. Patients with AA allele had higher risk of osteoporosis than those with GG+AG (adjusted OR = 6.89; 95% confidence intervals: 2.23–21.31, $p = 0.001$). Moreover, the AA genotype exhibited lower bone mass density ($p < 0.05$). Regarding mRNA expression, there were large differences in the correlation between PLCB4 and different RUNX2 alleles (Cohen's $q = 0.91$). Functionally, the rs6086746 A allele reduces the RUNX2 binding affinity, thus enhancing the suppression of PLCB4 expression ($p < 0.05$).

Conclusions: Our results provide further evidence to support the important role of the SNP rs6086746 in the etiology of osteopenia/osteoporosis, thereby enhancing the current understanding of the susceptibility to osteoporosis. We further studied the mechanism underlying osteoporosis regulation by PLCB4.

Keywords: osteoporosis, runt domain transcription factor 2, binding site polymorphism, case-control study, PLCB4

1 INTRODUCTION

Osteoporosis is a systemic bone disease and is characterized by significant decrease in bone mass density (BMD) and damage to bone microstructure (1). This is especially noted in postmenopausal women because the prevalence of osteopenia and osteoporosis increase with age (2). Researchers estimate that there are >200 million osteoporosis patients globally and the risk of fracture in osteoporosis patients is as high as 40% (3, 4). To make the matter worse, the number of osteoporosis patients is expected to increase continuously owing to the effects of global population aging (5). A Taiwanese survey showed that osteoporosis ranks 4th among chronic diseases in elderly people aged >65 years in Taiwan and its prevalence is increasing with population aging (6). In addition, there are 12.3% of adults aged >50 years with at least one site with osteoporosis (the T-score of at least one vertebra or femur ≤ −2.5). Regarding sex, 8.6% and 15.5% of males and females, respectively, have one site with osteoporosis (7).

Genetic and environmental factors may affect osteoporosis progression (8). In addition to aging and other environmental factors, genetics is also an important factor that determines BMD (9). Osteoporosis is considered to be the outcome of interactions among several gene mutations (10). The results of past studies on twins and family data estimated that approximately 50%–85% of osteoporosis causes can be attributed to genetic factors (4, 11). In clinical practice, BMD is an important marker of osteoporosis and is a key marker for the diagnosis and treatment of osteoporosis (12). Therefore, there is a need to comprehensively understand the genetic factors involved in osteoporosis and BMD for the development of effective treatments for osteoporosis. In recent years, with the development of microarray and next-generation sequencing, genome-wide association studies (GWAS) is considered a valuable tool for studying complex genetic diseases. Since 2007, GWAS has confirmed several hundred susceptible loci for osteoporosis and BMD (12–15). However, most genome-wide significant susceptibility loci are located in non-coding regions in the genome and can provide only limited information on the genetic mechanisms of osteoporosis (16, 17). One of the primary molecular mechanisms by which SNPs regulate disease susceptibility is affecting the transcription factor binding, thereby regulating gene expression (18). Among these regions, transcription factor binding sites (TFBSs) on DNA play a central role in gene regulation *via* their sequence-specific interactions with transcription factor proteins (19).

With the recent progress in osteoporosis-related studies, we understood that the effects of osteoclasts and osteoblasts result in an imbalance between bone destruction and formation, which ultimately causes a decrease in bone mass and bone mineral density (20, 21). RUNX2 is one of the most important transcription factors and is also a key transcription regulatory factor in osteoblast differentiation. Therefore, it plays an important role in regulating osteoblast maturation and balance (22, 23). Recent studies showed that RUNX2 expression and BMD are positively correlated (24–28). During the differentiation of mesenchymal stem cells, RUNX2 regulates the gene transcription of key proteins and aid in the cells' differentiation into osteoblasts (29).

Therefore, the aim of this study was to examine the correlation between the potential DNA binding sites of RUNX2 and osteoporosis. Considering the abovementioned facts, we used a bioinformatics-based approach to identify SNPs within osteoporosis-associated TFBSs. These genetic variations, which may directly affect post-transcriptional regulation of gene expression of transcription factors through

SNPs present in the protein sequence, were assessed with respect to their potential association with osteoporosis susceptibility.

2 MATERIALS AND METHODS

2.1 Study Participants

This hospital-based case-control study was conducted between March 2015 and October 2019. In the study cohort, 107 patients with osteoporosis, 290 patients with osteopenia, and 254 healthy controls were enrolled from Tri-Service General Hospital. All subjects included in the study were randomly chosen and excluded osteoporosis patients with ICD-10 M81.8 after consulting the medical records by the orthopedist. The BMD of all subjects was measured using dual-energy X-ray absorptiometry (DEXA) at the lumbar spine (LS1-4), and the diagnosis of osteoporosis was based on the World Health Organization standards. None of the subjects had a history of medication for osteoporosis treatment. The demographic and clinical characteristics of all subjects were obtained from questionnaires and medical records.

2.2 Bone Marrow Density Measurements

BMD (g/cm2) is used as an indicator of osteoporosis and is calculate by dividing the bone mineral content (g) by bone area (cm^2) (30). In our study, BMD were measured by DEXA during health examinations at TSGH using Prodigy Series X-Ray Tube Housing Assembly (GE Medical Systems Lunar 3030 Ohmeda Dr Madison, Wisconsin, USA) (31). Osteoporosis was defined according to World Health Organization criteria that considers BMD measurements at or below −2.5 standard deviation (S.D.) from the optimal peak bone density (T-score) of healthy young adult of the same sex; conversely, BMD measurement at or above −1 S.D. from the optimal peak bone density of healthy young adult of the same sex was considered bone mass loss or normal (32).

2.3 Process of Bioinformatics Analysis of Candidate SNPs in TFBSs

2.3.1 Screen the Genetic Variation in the Genome of Taiwanese Through Quality Control Procedures

First, we used the next-generation sequencing (NGS) data of 1,517 people released by the Taiwan Biobank, which contains 74,861,556 genetic variants. We deleted structural variants (insertion/deletion) because there was no way to use the multifunctional mass spectrometer (mass array) for genotyping. Then, we excluded SNPs with call rate of <90%. Finally, the remaining SNPs were used for further alignment.

2.3.2 Identify Genetic Variants That May Affect RUNX2 Binding Motif Through Bioinformatics Sequence Alignment

Second, we analyzed genetic variants that may affect RUNX2 binding by using bioinformatics sequence alignment techniques and identified the variants located in the TFBS. In the past, the TFBS sequence of the identified transcription factor was 5'-HGHGGK-3' (H = A, C or T; K = G or T). We aligned this motif found 1,672,016 SNPs that may affect the binding affinity.

2.3.3 Chromatin Immunoprecipitation Sequencing Confirms That These Genetic Variants Bind to These Binding Motifs

Third, we used ChIP-Seq data to verify whether these SNPs combine with RUNX2 in the chromatin immunoprecipitation experiment. The study was performed using SAOS-2 cells for ChIP-Seq analysis and analysis of the RUNX2 proteins of TFBS and was published in the JASPAR database (Matrix ID: MA0511.1) (33). Based on 1,062 motifs of RUNX2 Chip-Seq data, three SNPs that affect RUNX2 binding affinity were filtered out.

2.4 Genomic DNA Extraction and SNP Genotyping

Blood samples were obtained from all subjects in the morning while they were in a fasting state. Genomic DNA was isolated from peripheral blood samples using standard procedures for proteinase K (Invitrogen, Carlsbad, CA, USA) digestion and phenol/chloroform method (34). The SNPs in RUNX2 binding site rs6086746, rs7179057 and rs1531268 were genotyped by iPLEX Gold SNP genotyping (35). We used an inter- and intra-replication validation to assess quality of genotyping experiment. Inter-replication validation was performed in 35 replicate samples (approximately 5%), and the concordance rate was 100%.

2.5 Ethical Statement

The study was reviewed and approved by the institutional ethics committee of the Tri-Service General Hospital (TSGH-2-102-05-028). After completely explaining the objectives of the study, written informed consent was obtained from all participants. All clinical and biological samples were collected, and DNA was genotyped after obtaining patient consent.

2.6 Luciferase Reporter Assays

The RUNX2 binding site SNP rs6086746 of PLCB4 luciferase reporter was amplified by polymerase chain reaction from the genomic DNA library of human immortalized myelogenous leukemia K562 cell with the primer pair: 5': 5'-GGGGTACCCAGATACAAGCTACAACATGAATG-3' and 3': 5'-CCCAAGCTTCAATAAAGATATAAATCCTTTATAGCA-3' and subcloned into a pGL3 basal reporter (Promega, USA) cut at KpnI and HidIII sites. After the sequence verification, we further changed the current A allele into G allele using the QuickChange Lightening Site-directed Mutagenesis Kit (Agilent Technology). The construction of pSG5.HA.RUNX2 (isoform 2) was performed by polymerase chain reaction from the K562 cell cDNA library with the primer pair: 5': 5'-AACTCGAGGATGGCATCAAACAGCCTCTTCAGC-3' and 3': 5'-AAAGATCTTCAATATGGTCGCCAAACAGATTC-3' and subcloned into a pSG5.HA vector (Stratagene, USA) cut at XhoI and BglII sites. HEK293 cells were cultured in Dulbecco's modified Eagle's medium supplemented with 10% charcoal/

dextran-treated fetal bovine serum. The cells in each well (24-well plate) were transfected with total 1 μg DNA and jetPEI (PolyPlus-transfection, Illkirch, France) according to the manufacturer's protocol. Luciferase activity was assessed after 24 h post transfection using the Promega Luciferase Assay Kit and expressed as mean relative light units (RLUs) of two transfected sets. Results shown are representative of at least three independent experiments.

2.7 RNA Extraction and qPCR Analysis

Total RNA was extracted from whole blood obtained from 5 osteoporosis participants, 7 osteopenia participants, and 7 controls by the TRIzol reagent method (Invitrogen, Carlsbad, CA) and then reverse transcribed into cDNA with the Script II 1st strand cDNA RT Kit (ACE biolabs, Taiwan). Real-time quantitative PCR (RT-qPCR) was performed to amplify cDNA with the 7500 fast Real-Time PCR System (Applied Biosystems) using the SYBR color qPCR Master Mix (ACE biolabs, Taiwan). Relative expression was analyzed by the comparative threshold cycle (Ct) method, and human glyceraldehyde-3-phosphate dehydrogenase (GAPDH) was used as an internal control. Expression values were calculated by the $2^{-\Delta CT}$ method. The primer sequences used for genotyping of the SNPs and qPCR of RUNX2 and PLCB4 are shown in **Supplementary Table S1**. Melting curve analysis was used to confirm specificity, and three replicate wells were used for each subject.

2.8 Statistical Analysis

Continuous variables were evaluated using Student's *t*-tests and reported as the mean ± S.D. Genotypes and allelic frequencies were compared between cases and controls using $\chi 2$ test or Fisher's exact tests. Logistic regression was used to estimate ORs and 95% confidence intervals (CIs) as a measure of the association with osteopenia/osteoporosis susceptibility, adjusted by sex and age. The analysis was performed using allele type, genotype, dominant, and recessive models. Statistical analyses were performed using SPSS 22.0 (SPSS Inc., Chicago, Ill., USA) and R 3.5.2 (R Project for Statistical Computing, Vienna, Austria). A p-value of <0.05 was considered statistically significant.

3 RESULTS

3.1 Selection of Candidate SNPs

In **Figure 1**, we used data from the NGS database of 1517 individuals from the Taiwan Biobank, which included 74,861,556 genetic variants. After excluding 13,614,966 structural variants (insertion/deletion) and 8,854,320 SNPs with a call rate of <90%, 52,392,270 SNPs were remaining.

With the human reference genome sequence (GRCh37/hg19) from the National Center for Biotechnology Information in combination with the Taiwan Biobank database. RUNX2 contained 9,264,568 potential binding motifs in the human genome based on the sequence of the above binding sites. Of the TFBSs, we compared the remaining 52,392,270 SNPs in the first step and found that 1,672,016 SNPs were in the TFBS of RUNX2. After excluding SNPs with minor allele frequency of <5%, 188,994 SNPs were remaining for further screening by ChIP-Seq analysis.

In the JASPAR database, there were 1062 positions in the TFBS associated with the RUNX2. After validating these SNPs with the results of the ChIP-Seq database of RUNX2, the remaining 3 SNPs are described in **Supplementary Table S2**. In the end, we used bioinformatics sequence alignment method and ChIP-Seq database for verification. Finally, 3 SNPs that may affect the binding ability of RUNX2 were screened to study the association with osteoporosis.

3.2 Population Characteristics

The basic clinical characteristics of the study population are summarized in **Table 1**. Osteoporosis and osteopenia patients had a lower weight than that the control subjects ($p < 0.05$). Osteoporosis and osteopenia patients had a lower BMI than the control subjects ($p < 0.05$).

3.3 Association Between RUNX2 Binding Site Gene Polymorphisms With Susceptibility and Osteoporosis

Our results showed that SNP rs6086746 had a significant association with osteoporosis risk according to genotype ($p < 0.001$; **Table 2**). The minor allele frequency of rs1531268 (allele C), rs6086746 (allele A), and rs7179057 (allele A) in controls was 0.38, 0.21, and 0.13, respectively, which was similar to the frequency noted in Taiwan Biobank data. In the control group, the Hardy–Weinberg equilibrium p-values for rs1531268, rs6086746, and rs71790572 were 0.998, 0.160, and 0.157, respectively, which conforms to the Hardy–Weinberg equilibrium ($p > 0.05$).

In **Table 3**, we used the logistic regression to compare the genotype and allele frequencies of psteopenia patients and control participants. Significant difference was found in the genotype model (GG vs. AA) in all the subjects with adjustment for age and BMI (OR = 3.56; 95% CI = 1.25–10.14; $p = 0.017$). Significant difference was found in the recessive model (GG+AG vs. AA) in all the subjects with adjustment for age and BMI (OR = 3.25; 95% CI = 1.15–9.15; $p = 0.026$). Moreover, a higher T allele frequency was associated with an increased risk of osteopenia (OR = 1.44; 95% CI = 1.05–1.98; $p = 0.025$). In **Table 4**, we used the logistic regression to compare the genotype and allele frequencies of osteoporosis patients and control participants. Significant difference was found in the genotype model (GG vs. AA) in all the subjects with adjustment for age and BMI (OR = 6.26; 95% CI = 1.99–19.68; $p = 0.002$). Significant difference was found in the recessive model (GG+AG vs. AA) in all the subjects with adjustment for age and BMI (OR = 6.89; 95% CI = 2.23–21.31; $p = 0.001$).

3.4 Associations Between rs6086746 SNP and BMD

BMD was also measured in the current study. Patients with osteopenia/osteoporosis exhibited significantly lower total BMD and BMD of L1–L4 vertebrae compared with control subjects

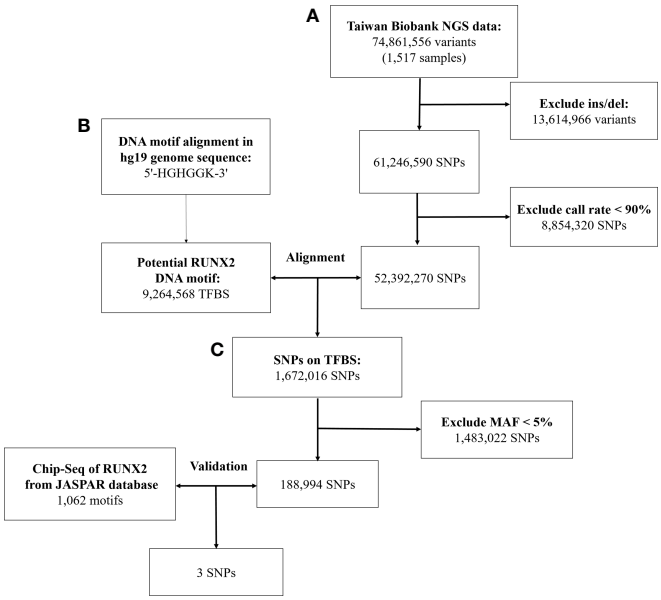

FIGURE 1 | Workflow of the stepwise approach of candidate binding site SNPs. **(A)** Screen the genetic variation in the genome of Taiwanese through quality control procedures. **(B)** Identify genetic variants that may affect RUNX2 binding motif through bioinformatics sequence alignment. **(C)** Chromatin immunoprecipitation sequencing (ChIP-Seq) to confirm that these genetic variants will bind to these binding motifs. NGS, next-generation sequencing; SNP, single-nucleotide polymorphism; Ins/sel, insertion/deletion; TFBS, Transcription factor binding site; MAF, minor allele frequency.

($p < 0.05$, **Table 1**). Significant association was detected for the rs6086746 SNP with BMD levels ($p < 0.05$, **Figures 2**). However, individuals carrying the AA genotype at rs6086746 had significantly lower BMD levels ($p < 0.05$, **Figure 2**).

3.5 mRNA expression of RUNX2 and PLCB4 in whole blood

The RUNX2 transcription factor binds to the promoter of PLCB4 to affect the expression of PLCB4 (**Figure 3**). Therefore, we examined the mRNA levels of RUNX2 and PLCB4 in whole blood extracted from 5 osteopenia patients, 4 osteoporosis patients and 4 controls. **Figure 3** shows the final number of experimental samples. Relative RUNX2 mRNA expression in whole blood was lower in osteoporosis patients than in controls ($p = 0.038$, **Figure 3A**). However, no difference in PLCB4 mRNA expression was found among the groups ($p = 0.737$, **Figure 3B**).

Next, we determined the expression of RUNX2 and PLCB4 in osteopenia/osteoporosis patients and controls with different rs6086746 alleles. In whole blood from controls or osteopenia/osteoporosis patients, no significant differences in RUNX2 and PLCB4 mRNA levels were found in any comparisons (**Figures 3C, D**). Experiments were performed in triplicates.

In addition, we separated the gene expression of different alleles and found that the gene with the G allele showed negative Pearson's correlation coefficient: −0.283, $p = 0.326$ (**Figure S1A**); conversely, gene with the A allele showed positive Pearson's correlation coefficient: −0.283, $p=0.154$ (**Figure S1B**). After testing, the Cohen's q value of the correlation coefficient of the G and A alleles was 0.91, showing that there is a large difference between the two correlation coefficients. The A allele may change the affinity of RUNX2 and prevent it from binding, thereby causing RUNX2 to be unable to inhibit the promoter activity of rs6086746, which in turn increases PLCB4 expression.

TABLE 1 | Characteristics of participants in case-control study.

	Control (n = 254)	Osteopenia (n = 290)	Osteoporosis (n = 107)	P-value
Age (year)	72.95 ± 6.51	72.65 ± 6.43	73.36 ± 6.74	0.619
Age of menopause	49.84 ± 5.40	49.54 ± 4.82	48.77 ± 4.79	0.192
Height (cm)	154.46 ± 5.93	153.94 ± 5.48	153.21 ± 5.69	0.185
Weight (kg)	59.58 ± 9.04	56.36 ± 8.21	51.45 ± 7.63	<0.001*
BMI[a]	25.05 ± 3.74	23.96 ± 3.49	22.47 ± 3.16	<0.001*
BMD (g/cm^2)	1.09 ± 0.15	0.89 ± 0.13	0.77 ± 0.16	<0.001*
T-score	0.11 ± 1.03	−1.73 ± 0.40	−2.96 ± 0.40	<0.001*
eGFR[b]	85.32 ± 21.07	86.61 ± 19.57	89.72 ± 20.94	0.194

p-value < 0.05,

a: BMI, Weight/Height^2,

b: eGFR, (MDRD-Simplify-GFR) (186 creatinine$^{-1.154}$*age$^{-0.203}$*0.742).*

3.6 Comparison of Promoter Activity of G and A Alleles of the PLCB4

To further test our hypothesis and to assess whether these enhancers cause allele-specific promoter activity, we cloned 268 bp regions containing individual allele of rs6086746. Indeed, our luciferase reporter assay data showed dramatic allelic difference of promoter activity. The promoter regions with the A allele (128975 ± 1979.87 RLU) at rs6086746 showed significantly higher activity to drive luciferase gene expression in HEK293 cells than those with the G allele

TABLE 2 | Genotypic characteristics of participants in this study.

	Control (n=254)	Osteopenia (n=290)	Osteoporosis (n=107)	P-value
rs1531268				0.617
TT	97 (38.5%)	106 (36.9%)	46 (43.4%)	
TC	118 (46.8%)	134 (46.7%)	41 (38.7%)	
CC	37 (14.7%)	47 (16.4%)	19 (17.9%)	
rs6086746				<0.001*
GG	151 (60.4%)	156 (54.2%)	59 (55.1%)	
AG	93 (37.2%)	115 (39.9%)	32 (29.9%)	
AA	6 (2.4%)	17 (5.9%)	16 (15.0%)	
rs7179057				0.579
GG	192 (76.5%)	209 (72.8%)	84 (79.2%)	
AG	51 (20.3%)	71 (24.7%)	19 (17.9%)	
AA	8 (3.2%)	7 (2.4%)	3 (2.8%)	

**p-value < 0.05.*

(85478.67 ± 6281.75 RLU) (**Figure 4**). RUNX2 suppressed these promoter reporter activities. These results supported that these regions have allele-dependent enhancer activity, which is highly consistent with genotype-associated gene expression level ($p < 0.05$).

4 DISCUSSION

In the current study, we investigated the association of SNPs in the RUNX2 binding site region with osteoporosis and showed that the rs6086746 polymorphism was significantly associated with osteoporosis. We also investigated the effect of SNPs on the expression level of PLCB4 in whole blood. In addition, luciferase activity of PLCB4 in individuals carrying the rs6086746 A allele was increased, suggesting a functional explanation for the observed association.

Because RUNX2 is a key molecule for osteoblast development, some studies have already been published regarding genomic association. Bustamante et al. (27) showed that the −1025 T/C polymorphism (rs7771980) in promoter 2 of RUNX2 is related to lumbar spine and femoral neck BMD in Spanish postmenopausal women. Auerkari et al. (36) showed that rs59983488 of RUNX2 promoter P1 region have been found to been associated with osteoporosis in postmenopausal Indonesian women. Qui et al. (37) suggested that osteoporosis GWAS-associated lead SNPs and their linked SNPs on the RUNX2 TF binding affinity. Previous studies all identified disease-related SNPs before identifying the transcription factor(s). Therefore, we provided an approach to use a hybrid method comprising candidate gene and epidemiologic approaches by first identifying specific disease-related transcription factors before identifying motif-binding regions.

SNP rs6086746 is located upstream of the PLCB4 gene, a large gene spanning 412 kb and containing 46 coding exons. The PLCB4 gene provides instructions for making one form (the beta 4 isoform) of a protein called phospholipase C. This protein is involved in a signaling pathway within cells known as the phosphoinositide cycle, which helps transmit information from outside the cell to inside the cell. Phospholipase C carries out one particular step in the phosphoinositide cycle: the conversion of a molecule called phosphatidylinositol 4,5-bisphosphate (PIP2) to two smaller molecules, inositol 1,4,5-trisphosphate (IP3) and 1,2-diacylglycerol. These smaller molecules relay messages to the cell that ultimately influence many cellular activities (38).

Study suggest that the beta 4 isoform of phospholipase C contributes to the development of the first and second pharyngeal arches (39). These embryonic structures ultimately develop into the jawbones, facial muscles, middle ear bones, ear canals, outer ears, and related tissues. This protein is also believed to play a role in vision, particularly in the function of the retina, which is a specialized tissue at the back of the eye that detects light and color. Diseases associated with PLCB4 include auriculocondylar syndrome 2 (40) and auriculo-condylar syndrome (41).

rs6140791 polymorphism of the PLCB4 and PLCB1 genes might be involved in the pathogenesis of coronary artery aneurysm in Kawasaki disease (42). In a GWAS study, it was demonstrated that the two genetic loci rs4794822 and rs2072910 (PSMD3–CSF3 locus in 17q21.1 and PLCB4 locus in 20p12) were significantly associated with the regulation of neutrophil count (43). However, to date, there has been no study that examined the correlation between PLCB4 and osteoporosis, and the related pathogenesis remains unclear. In this study, we found that the rs6086746 may affect the binding of the RUNX2 transcription factor to increase PLCB4 expression, thereby increasing the risk of osteoporosis.

In the blood mRNA expression experiment in our study, RUNX2 expression decreases as osteoporosis becomes more severe, which is similar to the results of previous studies (44). Moreover, animal experiments have confirmed that there is low RUNX2 expression in osteoporosis rats model (45). The expression of PLCB4 in blood is low. We searched the GTEx database and AceView (https://www.ncbi.nlm.nih.gov/ieb/research/acembly/av.cgi?db=human&term=PLCB4&submit=Go) and confirmed that PLCB4 gene expression levels in blood are low. Therefore, we recommend the examination of

TABLE 3 | Association of the rs6086746 with osteopenia.

Independent variable	Crude-OR (95% CI)	P-value	Adj-OR (95% CI)[#]	P-value
rs6086746				
GG	1		1	
AG	1.20 (0.84–1.70)	0.319	1.27 (0.85–1.88)	0.243
AA	2.74 (1.05–7.14)	0.039*	3.56 (1.25–10.14)	0.017*
Dominant model				
GG	1		1	
AG+AA	1.29 (0.92–1.82)	0.145	1.40 (0.96–2.06)	0.083
Recessive model				
GG+AG	1		1	
AA	2.55 (0.99–6.57)	0.053	3.25 (1.15–9.15)	0.026*
Allele model				
G	1		1	
A	1.31 (0.99–1.75)	0.061	1.44 (1.05–1.98)	0.025*

**p-value < 0.05; [#]Adjust by age, BMI.*

TABLE 4 | Association of the rs6086746 with osteoporosis.

Independent variable	Crude-OR (95% CI)	P-value	Adj-OR (95% CI)[#]	P-value
rs6086746				
GG	1		1	
AG	0.88 (0.53–1.45)	0.62	0.75 (0.41–1.36)	0.339
AA	6.82 (2.55–18.28)	<0.001*	6.26 (1.99–19.68)	0.002*
Dominant model				
GG	1		1	
AG+AA	1.24 (0.79–1.96)	0.355	1.09 (0.63–1.87)	0.754
Recessive model				
GG+AG	1		1	
AA	7.15 (2.71–18.84)	<0.001*	6.89 (2.23–21.31)	0.001*
Allele model				
G	1		1	
A	1.61 (1.12 - 2.31)	0.011*	1.48 (0.96–2.28)	0.079

*p-value < 0.05; [#]Adjust by age, BMI.

expression levels in other tissues in future studies. Although RNA expression in blood is low and there was no difference, we were unable to find rs60867462 mRNA expression data in the GTEx database. However, we were able to identify the SNP for rs60867462 D'=1 in linkage disequilibrium data, which proved that the expression level of PLCB4 increases as the number of minor alleles increases (**Supplementary Table S3**). Moreover, our reporter gene assay results show that the RUNX2-associated sequence has regulatory activity and that rs6086746 in this binding site is able to affect the binding of this sequence to RUNX2.

In this study, we employed a candidate method that was different from past studies. In our method, we examined the pathogenic contributions of gene mutations in the entire genome based on candidate gene linkage studies and GWAS. From our screening results, many novel SNPs were identified. This was followed by in-depth examination of the biological pathways that are affected by these SNPs and their correlation with diseases. However, only an extremely low number of causal variants were found to be directly related to disease in GWAS (46). Therefore, most of the SNPs found by GWAS are not causal variants and further fine-mapping is required (47). Hence, our whole genome screening method successfully identified 3 RUNX2-associated SNPs. In the future, multiple omics technologies, including genomics, transcriptomics, epigenomics, proteomics, and metabolomics, can be combined to identify the molecular factors contributing to the pathogenesis and thereby address genetic susceptibility to disease development.

Certain potential limitations of this study may have influenced the results, such as the participants in this study were Asians; hence, the inferences may not be generalized to other populations. Secondly, regarding mRNA expression level, we were only able to use whole blood for gene expression experiments because most

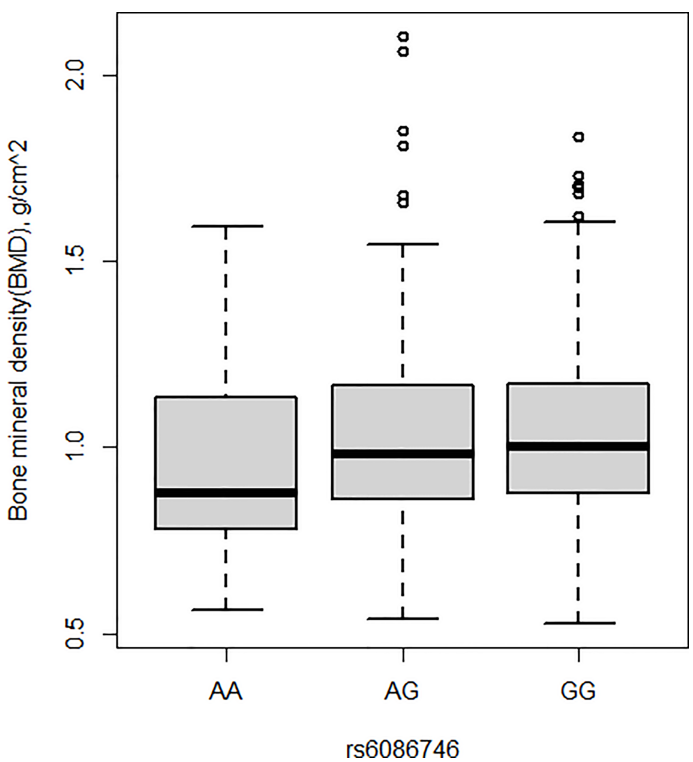

FIGURE 2 | Association of bone mineral density and rs6086746 GG (n = 366), GA (n = 240), AA (n = 39). rs6086746 was determined by G or A in the position of -6363 relative to the PLCB4 gene. Numbers represent the population who has the specified genotype. BMD, expressed as an areal density in grams per square centimeter, was measured in the lumbar spine (L1–L4).

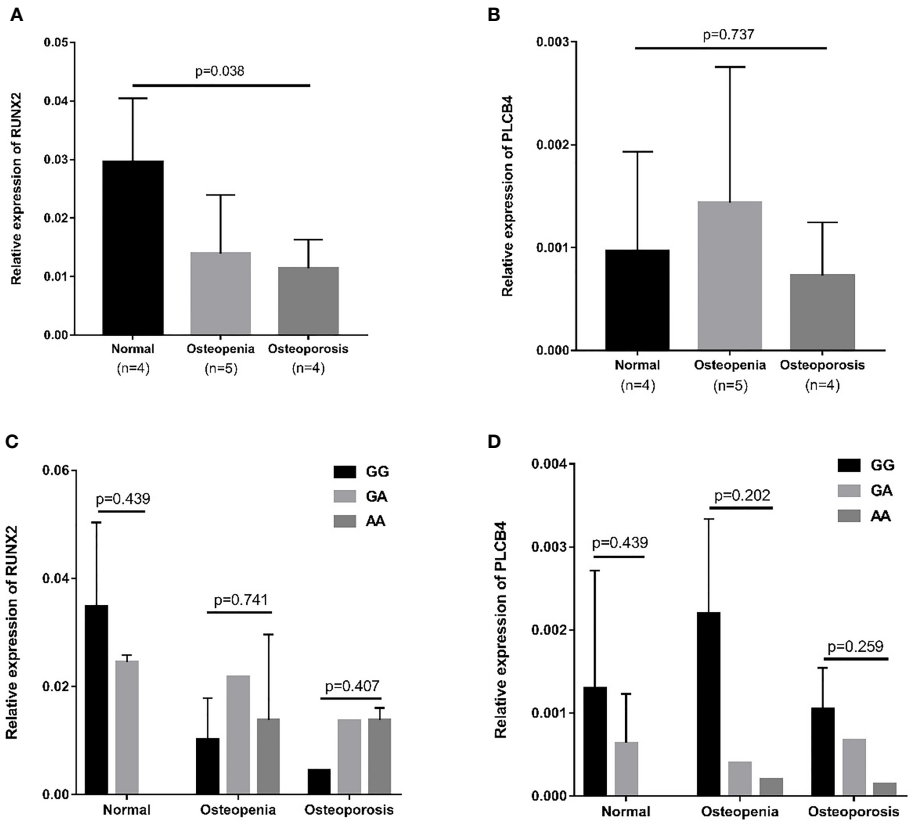

FIGURE 3 | Relative mRNA expression in osteopenia, osteoporosis, and normal groups. **(A)** Relative mRNA expression of RUNX2: osteoporosis patients had lower mRNA expression than normal group (p = 0.008). **(B)** Relative mRNA expression of PLCB4: there is no difference in mRNA expression among the 3 groups (p = 0.737). The effect of the rs6086746 genotypes on the **(C)** RUNX2 and **(D)** PLCB4 mRNA expression level in the normal, osteopenia, and osteoporosis patient groups. There was no association between rs6086746 genotype and mRNA expression in each group. RUNX2, RUNX family transcription factor 2; PLCB4, phospholipase C beta 4.

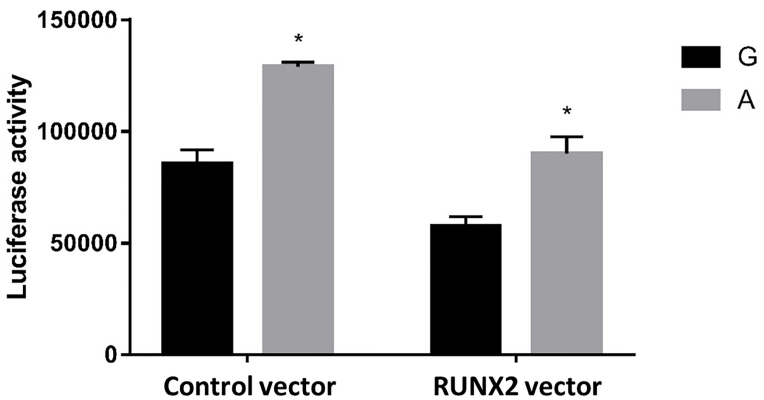

FIGURE 4 | Effects of the rs6086746 genotype on luciferase activity in cultured HEK293cells. HEK293 cells were transfected with 0.5 μg pGL3 basic-LUC luciferase reporter recombinant plasmids containing a PLCB4 promoter sequence with the wild-type G allele or A allele at the rs6086746 SNP in the presence of 0.5 μg pSG5.HA control vector or pSG5.HA.RUNX2 vector. Transfected cells were cultured for 24 h. Luciferase activity in cell extracts was expressed in relative light units (RLUs). Mean ± SEM is given for each construct from three experiments. *p < 0.05.

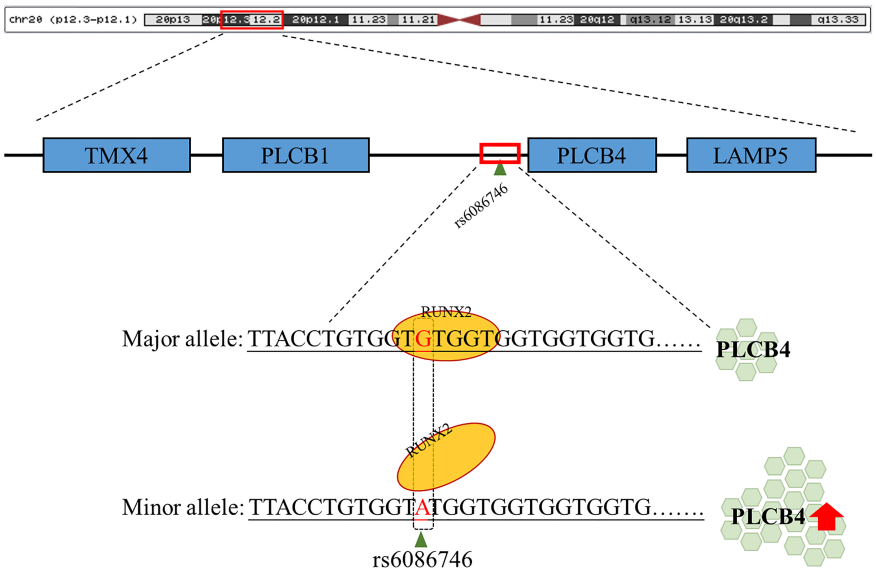

FIGURE 5 | Schematic diagram of the binding of RUNX2 transcription factor to the PLCB4 promoter region. rs6086746 is located in the promoter region of PLCB4, and when G allele is mutated to A allele, it may affect the binding ability of runx2 transcription factors. This prevents the RUNX2 transcription factor from binding to its binding motif, thereby increasing the expression level of the downstream PLCB4 gene.

osteoporosis patients did not undergo invasive treatment. This resulted in very low PLCB4 expression. Third, the etiology of osteoporosis is relatively complex and is jointly affected by several genes. Therefore, the effect of a single gene or a single-nucleotide polymorphism on osteoporosis may be lower. We recommend that the effects of different transcription factors on osteoporosis be examined in the future, which may provide novel information on the genetic background underlying osteoporosis.

5 CONCLUSIONS

In summary, our data demonstrated that rs6086746 plays an important role in postmenopausal women with osteoporosis susceptibility, modulating the epigenetic regulation of a critical osteoporosis-related gene, PLCB4. rs6086746 impairs the binding of RUNX2 to the promoter of PLCB4, which may lead to enhanced expression of the PLCB4 gene(**Figure 5**). However, the impact of the RUNX2 binding site SNP rs6086746 and PLCB4 on the development and function of osteoporosis remains incompletely understood, and further exploration of the regulatory mechanism is warranted.

DATA AVAILABILITY STATEMENT

The datasets presented in this study can be found in online repositories. The names of the repository/repositories and accession number(s) can be found below: European Variation Archive [accession: PRJEB47913].

ETHICS STATEMENT

The study was reviewed and approved by the institutional ethics committee of the Tri-Service General Hospital (TSGH-2-102-05-028). The patients/participants provided their written informed consent to participate in this study.

AUTHOR CONTRIBUTIONS

D-JT, W-HF, and S-LS: Conception and design. D-JT, LW-W, M-CT, C-CK, P-JH, C-CC, and WS: Acquisition of data. D-JT, S-MH, W-TC, and C-CW: Data analysis. D-JT: Drafting the article. D-JT, W-HF, LW-W, M-CT, C-CK, S-MH, W-TC, P-JH, C-CC, WS, C-CW, and S-LS have made substantial contributions in the interpretation of data, revising the article critically, and all approved of the final version for submission. All authors contributed to the article and approved the submitted version.

FUNDING

This study was supported by grants from the Tri-Service General Hospital (TSGH-E-110231, TSGH-E-110232), Ministry of Science and Technology (MOST107-2314-B016-052-MY3, MOST110-2314-B016-006), Taoyuan Armed Forces General Hospital (TYAFGH-D-109009, TYAFGH-E-109052, TYAFGH-D-110032, TYAFGH-A110023), National Defense Medical

Center(MND-MAB-110-105), Cheng Hsin General Hospital (CHNDMC-109-8, CHNDMC-110-16).

SUPPLEMENTARY MATERIAL

The Supplementary Material for this article can be found online at: https://www.frontiersin.org/articles/10.3389/fendo.2021.730686/full#supplementary-material

Supplementary Figure 1 | Scatter plot of RUNX2 and PLCB4 expression levels in whole blood. **(A)** Scatter plot of all the expressed genes in G allele. The red line demonstrates negative correlation between RUNX2 and PLCB4 with Pearson's correlation coefficient of 0.283. **(B)** Scatter plot of all the expressed genes in A allele. The blue line demonstrates positive correlation between RUNX2 and PLCB4 with Pearson's correlation coefficient of 0.554. After the correlation coefficients of the two groups were tested, Cohen's q value was 0.92. Runt-related transcription factor 2 (RUNX2; y-axis) versus phospholipase C beta 4 (PLCB4; x-axis) mRNA expression value. Cohen's q value is used to compare the effect size of the differences between the two correlation coefficients (r). A q value of 0.1 means that there is almost no difference, a q value of 0.3 means moderate difference, and a q value of 0.5 means that there is a large difference.

REFERENCES

1. Dong H, Zhou W, Wang P, Zuo E, Ying X, Chai S, et al. Comprehensive Analysis of the Genetic and Epigenetic Mechanisms of Osteoporosis and Bone Mineral Density. *Front Cell Dev Biol* (2020) 8:194. doi: 10.3389/fcell.2020.00194
2. Cummings SR, Melton LJ. Epidemiology and Outcomes of Osteoporotic Fractures. *Lancet* (2002) 359(9319):1761–7. doi: 10.1016/S0140-6736(02)08657-9
3. Rachner TD, Khosla S, Hofbauer LC. Osteoporosis: Now and the Future. *Lancet* (2011) 377(9773):1276–87. doi: 10.1016/S0140-6736(10)62349-5
4. Al-Barghouthi BM, Farber CR. Dissecting the Genetics of Osteoporosis Using Systems Approaches. *Trends Genet* (2019) 35(1):55–67. doi: 10.1016/j.tig.2018.10.004
5. Aggarwal L, Masuda C. Osteoporosis: A Quick Update. *J Fam Pract* (2018) 67 (2):59–62.
6. *Long-Term Follow-Up Survey on the Physical and Mental Social Life of Middle-Aged and Elderly*. Available at: https://www.hpa.gov.tw/Pages/Detail.aspx?nodeid=1128&pid=1949.
7. Chen F-P, Huang T-S, Fu T-S, Sun C-C, Chao A-S, Tsai T-L. Secular Trends in Incidence of Osteoporosis in Taiwan: A Nationwide Population-Based Study. *Biomedical Journal* (2018) 41(5):314–20.
8. Hendrickx G, Boudin E, Van Hul W. A Look Behind the Scenes: The Risk and Pathogenesis of Primary Osteoporosis. *Nat Rev Rheumatol* (2015) 11(8):462–74. doi: 10.1038/nrrheum.2015.48
9. Boudin E, Fijalkowski I, Hendrickx G, Van Hul W. Genetic Control of Bone Mass. *Mol Cell Endocrinol* (2016) 432:3–13. doi: 10.1016/j.mce.2015.12.021
10. Saad FA. Novel Insights Into the Complex Architecture of Osteoporosis Molecular Genetics. *Ann New York Acad Sci* (2020) 1462(1):37–52. doi: 10.1111/nyas.14231
11. Ralston SH, Uitterlinden AG. Genetics of Osteoporosis. *Endocr Rev* (2010) 31 (5):629–62. doi: 10.1210/er.2009-0044
12. Kemp JP, Morris JA, Medina-Gomez C, Forgetta V, Warrington NM, Youlten SE, et al. Identification of 153 New Loci Associated With Heel Bone Mineral Density and Functional Involvement of GPC6 in Osteoporosis. *Nat Genet* (2017) 49(10):1468. doi: 10.1038/ng.3949
13. Estrada K, Styrkarsdottir U, Evangelou E, Hsu YH, Duncan EL, Ntzani EE, et al. Genome-Wide Meta-Analysis Identifies 56 Bone Mineral Density Loci and Reveals 14 Loci Associated With Risk of Fracture. *Nat Genet* (2012) 44 (5):491–501. doi: 10.1038/ng.2247
14. Richards JB, Zheng H-F, Spector TD. Genetics of Osteoporosis From Genome-Wide Association Studies: Advances and Challenges. *Nat Rev Genet* (2012) 13(8):576–88. doi: 10.1038/nrg3228
15. Morris JA, Kemp JP, Youlten SE, Laurent L, Logan JG, Chai RC, et al. An Atlas of Genetic Influences on Osteoporosis in Humans and Mice. *Nat Genet* (2019) 51(2):258–66. doi: 10.1038/s41588-018-0302-x
16. Manolio TA, Collins FS, Cox NJ, Goldstein DB, Hindorff LA, Hunter DJ, et al. Finding the Missing Heritability of Complex Diseases. *Nature* (2009) 461 (7265):747–53. doi: 10.1038/nature08494
17. Liu G, Hu Y, Han Z, Jin S, Jiang Q. Genetic Variant Rs17185536 Regulates SIM1 Gene Expression in Human Brain Hypothalamus. *Proc Natl Acad Sci* (2019) 116(9):3347–8. doi: 10.1073/pnas.1821550116
18. Huang Q. Genetic Study of Complex Diseases in the Post-GWAS Era. *J Genet Genomics* (2015) 42(3):87–98. doi: 10.1016/j.jgg.2015.02.001
19. Wasserman WW, Sandelin A. Applied Bioinformatics for the Identification of Regulatory Elements. *Nat Rev Genet* (2004) 5(4):276–87. doi: 10.1038/nrg1315
20. Tu KN, Lie JD, Wan CKV, Cameron M, Austel AG, Nguyen JK, et al. Osteoporosis: A Review of Treatment Options. *P t* (2018) 43(2):92–104.
21. Raisz LG. Pathogenesis of Osteoporosis: Concepts, Conflicts, and Prospects. *J Clin Invest* (2005) 115(12):3318–25. doi: 10.1172/JCI27071
22. Ziros PG, Basdra EK, Papavassiliou AG. Runx2: Of Bone and Stretch. *Int J Biochem Cell Biol* (2008) 40(9):1659–63. doi: 10.1016/j.biocel.2007.05.024
23. Ma XL, Liu ZP, Ma JX, Han C, Zang JC. Dynamic Expression of Runx2, Osterix and AJ18 in the Femoral Head of Steroid-Induced Osteonecrosis in Rats. *Orthop Surg* (2010) 2(4):278–84. doi: 10.1111/j.1757-7861.2010.00100.x
24. Vaughan T, Reid DM, Morrison NA, Ralston SH. RUNX2 Alleles Associated With BMD in Scottish Women; Interaction of RUNX2 Alleles With Menopausal Status and Body Mass Index. *Bone* (2004) 34(6):1029–36. doi: 10.1016/j.bone.2004.02.004
25. Xiao Z, Awad HA, Liu S, Mahlios J, Zhang S, Guilak F, et al. Selective Runx2-II Deficiency Leads to Low-Turnover Osteopenia in Adult Mice. *Dev Biol* (2005) 283(2):345–56. doi: 10.1016/j.ydbio.2005.04.028
26. Doecke JD, Day CJ, Stephens AS, Carter SL, van Daal A, Kotowicz MA, et al. Association of Functionally Different RUNX2 P2 Promoter Alleles With BMD. *J Bone Miner Res* (2006) 21(2):265–73. doi: 10.1359/JBMR.051013
27. Bustamante M, Nogués X, Agueda L, Jurado S, Wesselius A, Cáceres E, et al. Promoter 2 -1025 T/C Polymorphism in the RUNX2 Gene is Associated With Femoral Neck Bmd in Spanish Postmenopausal Women. *Calcif Tissue Int* (2007) 81(4):327–32. doi: 10.1007/s00223-007-9069-2
28. Lee HJ, Koh JM, Hwang JY, Choi KY, Lee SH, Park EK, et al. Association of a RUNX2 Promoter Polymorphism With Bone Mineral Density in Postmenopausal Korean Women. *Calcif Tissue Int* (2009) 84(6):439–45. doi: 10.1007/s00223-009-9246-6
29. Xu J, Li Z, Hou Y, Fang W. Potential Mechanisms Underlying the Runx2 Induced Osteogenesis of Bone Marrow Mesenchymal Stem Cells. *Am J Transl Res* (2015) 7(12):2527–35.
30. Nakamura T. [WHO Diagnostic Criteria for Osteoporosis and Trends in Europe and USA]. *Nihon Rinsho* (2004) 62 Suppl 2:235–9.
31. Chen YY, Fang WH, Wang CC, Kao TW, Chang YW, Yang HF, et al. Crosssectional Assessment of Bone Mass Density in Adults With Hepatitis B Virus and Hepatitis C Virus Infection. *Sci Rep* (2019) 9(1):5069. doi: 10.1038/s41598-019-41674-4
32. *The Asia-Pacific Regional Audit Epidemiology, C.a.B.o.O.i., Published by International Osteoporosis Foundation*. Available at: http://www.iofbonehealth.org (Accessed date: 8 September 2015).
33. van der Deen M, Akech J, Lapointe D, Gupta S, Young DW, Montecino MA, et al. Genomic Promoter Occupancy of Runt-Related Transcription Factor RUNX2 in Osteosarcoma Cells Identifies Genes Involved in Cell Adhesion and Motility. *J Biol Chem* (2012) 287(7):4503–17. doi: 10.1074/jbc.M111.287771
34. Tan SC, Yiap BC. DNA, RNA, and Protein Extraction: The Past and the Present. *J BioMed Biotechnol* (2009) 2009:574398. doi: 10.1155/2009/574398
35. Perkel J. SNP Genotyping: Six Technologies That Keyed a Revolution. *Nat Methods* (2008) 5(5):447–53. doi: 10.1038/nmeth0508-447
36. Auerkari EI, Suryandari DA, Umami SS, Kusdhany LS, Siregar TW, Rahardjo TB, et al. Gene Promoter Polymorphism of RUNX2 and Risk of Osteoporosis in Postmenopausal Indonesian Women. *SAGE Open Med* (2014) 2:2050312114531571. doi: 10.1177/2050312114531571
37. Qin L, Liu Y, Wang Y, Wu G, Chen J, Ye W, et al. Computational Characterization of Osteoporosis Associated SNPs and Genes Identified by

Genome-Wide Association Studies. *PloS One* (2016) 11(3):e0150070. doi: 10.1371/journal.pone.0150070
38. Lyon AM, Tesmer JJ. Structural Insights Into Phospholipase C-β Function. *Mol Pharmacol* (2013) 84(4):488–500. doi: 10.1124/mol.113.087403
39. Clouthier DE, Passos-Bueno MR, Tavares AL, Lyonnet S, Amiel J, Gordon CT. Understanding the Basis of Auriculocondylar Syndrome: Insights From Human, Mouse and Zebrafish Genetic Studies. *Am J Med Genet C Semin Med Genet* (2013) 163c(4):306–17. doi: 10.1002/ajmg.c.31376
40. Nabil A, El Shafei S, El Shakankiri NM, Habib A, Morsy H, Maddirevula S, et al. A Familial PLCB4 Mutation Causing Auriculocondylar Syndrome 2 With Variable Severity. *Eur J Med Genet* (2020) 63(6):103917. doi: 10.1016/j.ejmg.2020.103917
41. Rieder MJ, Green GE, Park SS, Stamper BD, Gordon CT, Johnson JM, et al. A Human Homeotic Transformation Resulting From Mutations in PLCB4 and GNAI3 Causes Auriculocondylar Syndrome. *Am J Hum Genet* (2012) 90 (5):907–14. doi: 10.1016/j.ajhg.2012.04.002
42. Lin YJ, Chang JS, Liu X, Tsang H, Chien WK, Chen JH, et al. Genetic Variants in PLCB4/PLCB1 as Susceptibility Loci for Coronary Artery Aneurysm Formation in Kawasaki Disease in Han Chinese in Taiwan. *Sci Rep* (2015) 5:14762. doi: 10.1038/srep14762
43. Okada Y, Kamatani Y, Takahashi A, Matsuda K, Hosono N, Ohmiya H, et al. Common Variations in PSMD3–CSF3 and PLCB4 are Associated With Neutrophil Count. *Hum Mol Genet* (2010) 19(10):2079–85. doi: 10.1093/hmg/ddq080
44. Shi X, Zhang Z. MicroRNA-135a-5p is Involved in Osteoporosis Progression Through Regulation of Osteogenic Differentiation by Targeting RUNX2. *Exp Ther Med* (2019) 18(4):2393–400. doi: 10.3892/etm.2019.7849
45. Cai WL, Zeng W, Zhu BY, Liu HH, Liu JL. MiR-137 Affects Bone Mineral Density in Osteoporosis Rats Through Regulating RUNX2. *Eur Rev Med Pharmacol Sci* (2020) 24(3):1023–9. doi: 10.26355/eurrev_202002_20152
46. Fugger L, McVean G, Bell JI. Genomewide Association Studies and Common Disease–Realizing Clinical Utility. *N Engl J Med* (2012) 367(25):2370–1. doi: 10.1056/NEJMp1212285
47. Schaid DJ, Chen W, Larson NB. From Genome-Wide Associations to Candidate Causal Variants by Statistical Fine-Mapping. *Nat Rev Genet* (2018) 19(8):491–504. doi: 10.1038/s41576-018-0016-z

Conflict of Interest: The authors declare that the research was conducted in the absence of any commercial or financial relationships that could be construed as a potential conflict of interest.

Publisher's Note: All claims expressed in this article are solely those of the authors and do not necessarily represent those of their affiliated organizations, or those of the publisher, the editors and the reviewers. Any product that may be evaluated in this article, or claim that may be made by its manufacturer, is not guaranteed or endorsed by the publisher.

frontiers in Endocrinology

ORIGINAL RESEARCH
published: 18 January 2022
doi: 10.3389/fendo.2021.756785

Exploring the Multi-Tissue Crosstalk Relevant to Insulin Resistance Through Network-Based Analysis

Linlin Yang[1,2], *Linquan Yang*[1,2], *Xing Wang*[1,2], *Hanying Xing*[1,2], *Hang Zhao*[3], *Yuling Xing*[3,4], *Fei Zhou*[3,4], *Chao Wang*[1,2], *Guangyao Song*[1,3]* *and Huijuan Ma*[1,3]*

[1] Hebei Key Laboratory of Metabolic Diseases, Shijiazhuang, China, [2] Clinical Medical Research Center, Hebei General Hospital, Shijiazhuang, China, [3] Department of Endocrinology, Hebei General Hospital, Shijiazhuang, China, [4] Department of Internal Medicine, Hebei Medical University, Shijiazhuang, China

Insulin resistance (IR) is a precursor event that occurs in multiple organs and underpins many metabolic disorders. However, due to the lack of effective means to systematically explore and interpret disease-related tissue crosstalk, the tissue communication mechanism in pathogenesis of IR has not been elucidated yet. To solve this issue, we profiled all proteins in white adipose tissue (WAT), liver, and skeletal muscle of a high fat diet induced IR mouse model *via* proteomics. A network-based approach was proposed to explore IR related tissue communications. The cross-tissue interface was constructed, in which the inter-tissue connections and also their up and downstream processes were particularly inspected. By functional quantification, liver was recognized as the only organ that can output abnormal carbohydrate metabolic signals, clearly highlighting its central role in regulation of glucose homeostasis. Especially, the CD36–PPAR axis in liver and WAT was identified and verified as a potential bridge that links cross-tissue signals with intracellular metabolism, thereby promoting the progression of IR through a PCK1-mediated lipotoxicity mechanism. The cross-tissue mechanism unraveled in this study not only provides novel insights into the pathogenesis of IR, but also is conducive to development of precision therapies against various IR associated diseases. With further improvement, our network-based cross-tissue analytic method would facilitate other disease-related tissue crosstalk study in the near future.

Keywords: network analysis, tissue crosstalk, multi-tissue analysis, glucose homeostasis, insulin sensitivity

OPEN ACCESS

Edited by:
Anna Halama, Weill Cornell Medicine, Qatar

Reviewed by:
Manikandan Narayanan, Indian Institute of Technology Madras, India
Neil G. Docherty, University College Dublin, Ireland

***Correspondence:**
Huijuan Ma
huijuanma76@163.com
Guangyao Song
sguangyao2@163.com

Specialty section:
This article was submitted to Systems Endocrinology, a section of the journal Frontiers in Endocrinology

Received: *11 August 2021*
Accepted: *17 December 2021*
Published: *18 January 2022*

Citation:
Yang L, Yang L, Wang X, Xing H, Zhao H, Xing Y, Zhou F, Wang C, Song G and Ma H (2022) Exploring the Multi-Tissue Crosstalk Relevant to Insulin Resistance Through Network-Based Analysis. Front. Endocrinol. 12:756785. doi: 10.3389/fendo.2021.756785

INTRODUCTION

Insulin resistance (IR) is a precursor event to metabolic syndromes and underpins many metabolic disorders such as obesity, type 2 diabetes (T2D), and cardiovascular disease (1, 2). So far, considerable efforts have been devoted to investigate the pathogenesis of IR, thereby revealing several molecular basis for IR in individual tissues (3, 4). However, as a metabolic disorder affecting multiple organs, the tissue crosstalk mechanism underlying IR has not been elucidated yet.

In physiological conditions, tissues in body are not isolated and their dynamical interplay lays a cornerstone for the maintenance of whole-body homeostasis. Inter-tissue communication is such a

vital mechanism for metabolic regulation (5, 6). Several lines of investigations even pointed a crucial role of tissue communication in metabolic diseases (7, 8). For example, by integrating multi-tissue transcriptomics data, the human metabolic activities in healthy and unhealthy conditions can be precisely predicted (9). By detecting metabolic profiles of eight tissues, circadian metabolic relationships were found to be rewired by nutrient challenges (10). Based on observations from multiple tissues, these outstanding works offered a whole-organism view for the understanding of metabolism. Nevertheless, due to the lack of effective means for crosstalk exploration, the tissue communications related to metabolic regulation were merely researched.

Although previous researchers tried to use the pair of secreted molecules and their receptors to describe inter-tissue connections (5, 11), there is still lack of a systematical characterization for the entire process of tissue crosstalk and related regulatory events. Network analysis is a powerful technology which helps to reproduce all activities within a biological system (12) and hence has been tried to solve multi-tissue problems (13). Theoretically, the tissue communications can be represented in form of the interface across networks of single tissue. Unfortunately, so far, most of the existing multi-network analysis algorithms were developed to mine either conservative motifs or dissimilarities among different networks (14–16). A method targeting interactions across networks, especially multi-organ networks, has not been reported yet.

To solve this issue, we proposed a network-based strategy to explore IR related tissue communications. The protein profiles of insulin sensitive organs, namely, white adipose tissue (WAT), liver, and skeletal muscle were detected in an insulin resistance mouse model *via* proteomics. A network-based method was developed to identify the interface between tissues, by which cross-tissue interactions as well as their up and downstream functions were particularly inspected. The functional interpretation of IR related tissue crosstalk not only provided a novel framework for exploring multilayer network connections, but also would benefit further precision therapies against various IR associated diseases.

METHODS

Animals and Samples

Previous studies have shown strong causative relation between restricted intrauterine growth and adult metabolic reprograming in rodents (17, 18). To reduce the potential impact of uneven intrauterine nutrition accompanied by different litter size, we used a previously developed ICR mouse model (19). Adult (6- to 8-week-old) male and female ICR mice were purchased from Beijing Vital River Laboratory Animal Technology Co., Ltd. and caged. Three-week-old pups were weaned and randomly assigned to insulin resistance (IR) and control (Con) group. Respectively, they were fed *ad libitum* for 19 weeks with either high fat diet (n = 9) composed of 60% Kcal from fat (Beijing HFK Bioscience Co., LTD., H10060) to induce IR or standard chow diet (n = 12, Beijing HFK Bioscience Co., LTD., H10010). All mice were maintained on a 12 h-light/12 h-dark cycle in a specific pathogen-free barrier facility. Mice were fasted overnight before sacrifice. Liver, epididymal fat, quadriceps femoris and gastrocnemius were collected, shock-frozen in liquid nitrogen and stored at −80°C. All animal experiments were performed with the approval of the Animal Ethics Committee of Hebei General Hospital.

Assessment of Insulin Sensitivity

To assess the insulin sensitivity of experimental mice, intraperitoneal glucose tolerance test (IPGTT) was performed. Mice were fasted for 8 h with free access to water before IPGTT. For each mouse, 50% glucose was injected in abdominal cavity at dose of 2 g glucose per kg body weight (2 g/kg BW). Blood glucose of fasting (0), 15, 30, 60, and 120 min were detected from tail vein blood by glucose analyzer (OneTouch® UltraVue™). Fasting level of peripheral insulin was measured by ELISA or according to manufacturers' instructions (80-INSMSU-E01, APLCO).

TMT-Based Proteomics Analysis

A total of 9 subjects/group were selected for TMT-based quantitative proteomics. In this study, technical replicates were used to increase the number of identified peptides and also to improve the quantification. Equal protein extracts from each subject in the same group were pooled together and trypsin digested to perform LC–MS/MS analysis, which was repeated for three times. Details on sample preparation, LC–MS/MS assay and data analysis were provided in **Supplementary Methods**. The proteomics data has been deposited to PRIDE (20) with identifier PXD021046. Proteins with Fold Change ≥1.2 or ≤0.83 and P-value <0.05 (Student's t test of log2 transformed signals) were regarded as differentially expressed proteins (DEPs) between two groups.

Functional Enrichment Analysis

The Gene Ontology annotation about biological process of DEPs were obtained by BINGO (21). Pathway distribution of DEPs was extracted from KEGG (22). For better functional interpretation, disease pathways and global maps in KEGG were excluded and the remaining basic pathways were selected into subsequent enrichment analysis. False discovery rate (FDR) correction of hypergeometric test was used to measure the significance of differential proteins co-existing in a GO term or KEGG pathway. FDR <0.05 was regarded as a sign of significance.

Identification of Metabolic Enzymes and Signaling Proteins

Metabolic enzymes and signaling proteins are two kinds of widely-studied functional proteins. In this study, we identified enzymes from the protein profiles based on whether there was an EC number corresponding to the protein. To exclude kinases which functioned as signaling proteins, metabolic enzymes were further restricted as enzymes that could only be mapped onto a metabolic pathway in KEGG. As many KEGG signaling pathways contain both signaling proteins and their target enzymes, we defined signaling proteins as those could be mapped to signaling pathways but not to metabolic ones.

Chi-square test was used to assess the difference in proportions of enzyme and signal protein within each tissue's protein profile.

Constructing Tissue-Specific Networks of IR

Networks of liver, skeletal muscle, and WAT were separately constructed *via* a developed core network generating strategy (23). Firstly, a Perl script was written to extract all the proteins and their interactions from the *.kgml files of each mouse pathway in KEGG (22). Then, for each tissue, its DEPs were regarded as seed nodes and their connected proteins according to KEGG were screened. Afterwards, the seed nodes and their neighbors were connected to generate a seed net specific to one tissue. Finally, this seed net was simplified by Steiner minimal tree algorism, helping to cut unnecessary branches mainly composed by non-DEPs and keep important nodes bridging seed proteins (24). In order to avoid loss of information, all the connected components in the seed net were traversed during the Steiner tree step. In addition, to reduce the computational complexity, the constructed networks were all undirected. Finally, all trees obtained from the Steiner step were retained to constitute the tissue-specific network.

To assess the goodness of these tissue-specific networks, their topological structures, namely, connected nodes, edges, and density were compared to random situations. Here, density is defined as the ratio of existing edges (E) to all potential ones ($E * (E - 1)/2$), which descripts sparsity of a net. For each tissue, a protein set with the same node number as differential proteins was randomly selected from the background network, thereby generating a random network. In total, 100 random networks were constructed for each tissue-specific network. Compared to corresponding randomizations, tissue-specific network showing all parameters with $|Z| > 2.33$ (25) was supposed to be successfully constructed.

Constructing the Interface of Multi-Tissue Crosstalk Relevant to IR

The interface of tissue crosstalk was constructed to investigate the communications between different tissues involved in IR. As primary proteins responsible for tissue communication, secreted proteins were identified. Based on Uhlén's prediction (26), human secreted proteins were converted to their homologous genes in mouse. Any proteins that cannot be identified as secreted ones were assigned into non-secreted proteins. Then, we used the manually curated information in KEGG PATHWAY (22) as background knowledge for regulatory relationships between proteins. Notably, these collected interactions were directed, which further helped to define the up and downstream processes involved by a given protein. For each secreted DEPs in tissue A, their regulated non-secretory proteins in tissue B were searched in network of tissue B and then regarded as non-secreted receptors. Thus, the cross-tissue interactions between secretory DEPs and their cross-tissue targets were extracted. Afterwards, to find the inner-tissue regulatory events relevant to tissue communication, the (a) connections between secreted DEPs and their upstream neighbor DEPs and (b) those between cross-tissue targets and their downstream neighbor DEPs within one organ were identified. The inter- and intra-tissue connections together constituted the interface of tissue crosstalk.

In addition, for each tissue, to exclude the interference of secreted proteins coming from other organ, their tissue specificity was further estimated according to the Genotype Tissue Expression (GTEx) Project (27). Among the three insulin sensitive tissues, proteins whose mRNA levels were more than 10 times lower than any other tissue were considered to be low-expressed and were excluded from this tissue when constructing the interface.

Functional Analysis of Cross-Tissue Interface

To functionally interpret the interface of tissue crosstalk, the up and downstream regulatory processes of cross-tissue interactions were investigated. Here, the upstream processes were defined as the pathways regulating or interacting with secreted proteins. In the interface of crosstalk, upstream processes can be measured by the pathways enriched by upstream and secreted proteins within one tissue (FDR <0.05). Similarly, downstream processes were defined as the pathways receiving regulation from secreted proteins and can be measured by pathways enriched by non-secreted proteins and their targets on the interface.

Validation

Since pooled samples were used during proteomics detection, which might implicate the significance of DEP signals, the expression of candidate DEPs was further validated by Western blotting (WB) assay of individual subjects. Total protein of each sample was extracted using total protein extraction kit (BC3710, Solarbio) according to the manufacturers' instructions. Western blots were performed by using specific antibody of CD36 (ab133625, Abcam), ACTIN (4970, CST), fatty acid-binding protein 1 (FABP1, 13368, CST), fatty acid-binding protein 3 (FABP3, 10676-1-AP, Proteintech), fatty acid-binding protein 4 (FABP4, 3544, CST), peroxisome proliferators-activated receptor α (PPARα, 15540-1-AP, Proteintech), peroxisome proliferators-activated receptor γ (PPARγ, 2443, CST), and phosphoenolpyruvate carboxykinase 1 (PCK1, 12940, CST). The images were captured *via* Minichemi 610 Plus (Sagecreation, Beijing, China). Serum thrombospondin 4 (THBS4) were measured *via* enzyme-linked immunosorbent assay (ELISA) according to manufacturers' instructions (SED824Mu, Cloud-Clone Corp.).

RESULTS

High Fat Diet Induced Insulin Resistance

Compared with control group, high fat diet fed mice showed significantly higher body weight and body mass index (BMI) ($P < 0.05$, two-tailed Student's t-test, **Supplementary Figures 1A, B**). After 17 weeks of feeding, high fat diet fed mice showed elevated blood glucose at 0.5, 1, and 2 h after injection of glucose ($P < 0.05$, two-tailed Student's t-test, **Figure 1A**). Correspondingly, the area under intraperitoneal glucose tolerance test (IPGTT) curve (AUC) was significantly enlarged as well ($P < 0.05$, two-tailed

Student's t-test, **Figure 1B**). Besides, higher fasting insulin demonstrated hyperinsulinemia in high fat diet fed mice (P <0.05, two-tailed Student's t-test, **Figure 1C**), further confirming insulin resistance in IR group.

Overview of Tissue-Specific Protein Profiles

In total, 5,854, 5,116, and 3,039 proteins were respectively quantified in WAT, liver, and skeletal muscle by proteomics. A total of 1,554, 477, and 219 differential proteins were identified in WAT, liver, and skeletal muscle, which are respectively listed in **Supplementary Tables 1–3**. It was unexpected that only 8 proteins were simultaneously up/downregulated in these tissues (**Figure 2A**), which are listed in **Supplementary Table 4**. Despite the low coincidence rate, the three DEP profiles showed quite similar biological functions. Among the TOP20 most enriched GO terms in the three tissue (see **Supplementary Figure 2**), there were more than 50% were annotated as metabolism-related processes (**Figure 2B**), which was in line with their mission as metabolic organs. Similarly, the three sets of DEPs commonly enriched in 3 KEGG pathways: pyruvate metabolism, PPAR signaling pathway and thermogenesis (**Figure 2C**), which accounted for 12.5, 9.4, and 21.4% of total pathways enriched by WAT, liver, and muscle. Notably, PPAR pathway was the only signaling pathway simultaneously enriched by the three tissues, highlighting its important role in regulation of IR.

Tissue-Specific Networks of IR Showed Widespread Metabolic Alterations

Based on DEPs, tissue-specific networks of WAT, liver, and skeletal muscle were constructed, which were shown in **Figures 3A–C**. Compared to corresponding random networks, significantly larger number of connected nodes, edges and density were found in adipose, liver, and muscle network (**Supplementary Figure 3**), suggesting successful construction of these nets.

It was worthy to note that enzyme-involved interactions dominated 57.9, 83.5, and 62.1% of the adipose, liver, and muscle network (**Figure 3D**), indicating widespread metabolic alterations in these tissues. This might be related to their proportion of metabolic enzymes. Separately, there were 26.8, 41.1, and 37.9% of DEPs in WAT, liver, and skeletal muscle belonging to metabolic enzymes, the proportion of which was consistently higher than signaling proteins (**Figure 3E**). Especially in liver and skeletal muscle, proportions of metabolic enzymes in DEPs were significantly larger than detecting pool (P <0.05, chi-square test, **Figure 3E**). It was strongly suggested that, rather than signaling interactions, wide-ranging metabolic processes were altered during the state of IR.

Cross-Tissue Alterations Were Preferred in State of IR

Considering secreted proteins are important functional vehicle for tissue communication, we screened secreted proteins in insulin sensitive tissues. According to Uhlén's prediction (26), 360, 227, and 158 secreted proteins were identified in WAT, liver, and skeletal muscle (**Figure 4A**). The most secreted proteins were detected in WAT, implying its stronger potential for tissue communication than liver and skeletal muscle. Intriguingly, although secreted proteins in the three tissues only accounted for 5% of detected pool on average (**Figure 4A**), their differential rates were all significantly higher than non-secreted ones (P <0.05, chi-square test, **Figure 4B**). It was suggested that, compared to inner-tissue perturbations, the cross-tissue alterations may be prioritized in state of IR.

The Cross-Tissue Interface of IR Was Featured by Metabolic Processes

To explore tissue communications perturbated in process of IR, we used secreted proteins to trace the connection between networks of different tissues, the rationale of which was shown in **Figure 5A**. To guarantee the correct direction of tissue crosstalk, low-expressed secreted proteins in each tissue were firstly excluded. Then the cross-tissue interactions from secreted DEPs to non-secreted proteins were identified according to protein relationships annotated by KEGG database (22). Finally, the upstream DEP neighbors of secreted DEPs and the downstream DEP neighbors of non-secreted receptors were

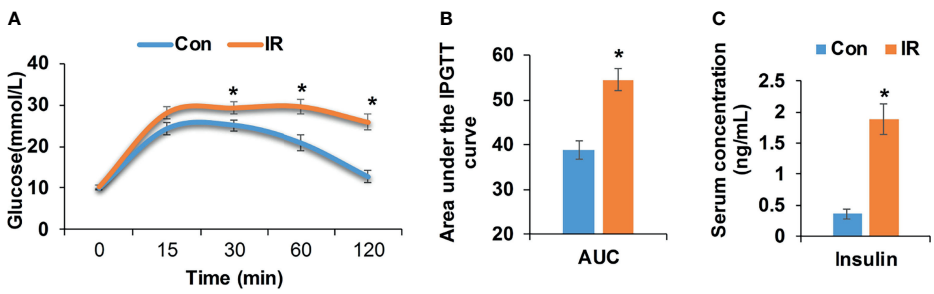

FIGURE 1 | Metabolic measurements of experimental mice. **(A)** Intraperitoneal glucose tolerance test (IPGTT, 2 mg/kg), age 21 weeks (Con, n = 12; IR, n = 9); **(B)** Area under the IPGTT curve; **(C)** Fasting insulin level of experimental mice, age 21 weeks (n = 6/group). *P < 0.05, compared to control group, Student's t-test; the normality of corresponding data was determined by Shapiro–Wilk test (P > 0.05).

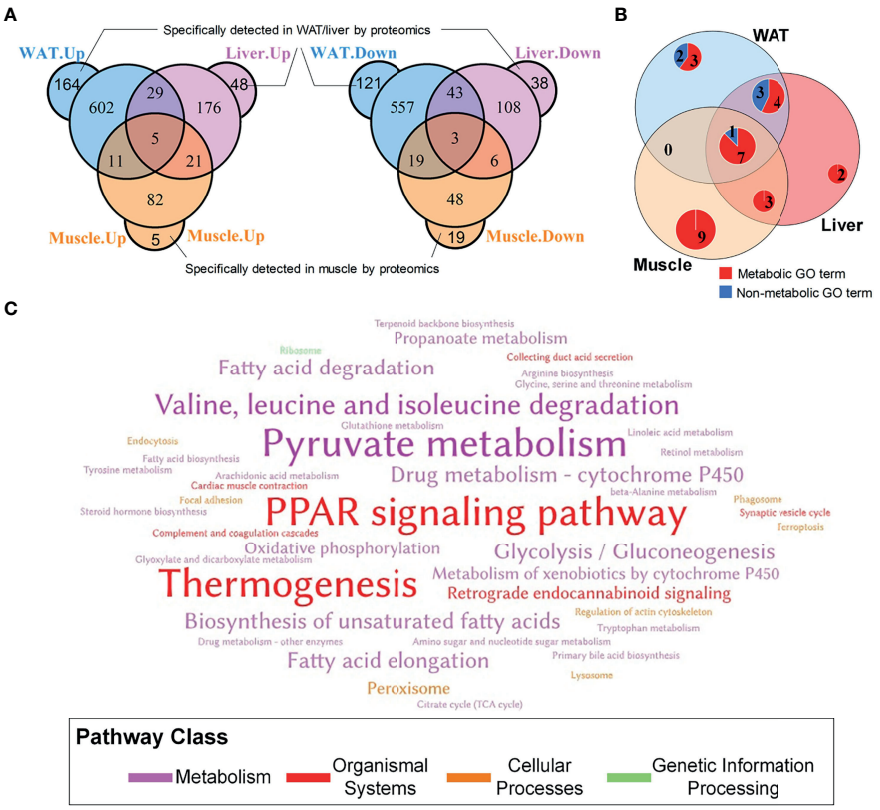

FIGURE 2 | General information of DEPs in WAT, liver and skeletal muscle. **(A)** Overlapping of differential proteins; **(B)** Coincidence of TOP20 enriched GO terms, where the TOP20 GO terms with the lowest FDR in distinct tissue were graphed; **(C)** Word cloud of KEGG pathways enriched by tissue-specific protein profiles. The words with the largest font size represent pathways simultaneously enriched by three tissues; the words with medium font size represent pathways commonly enriched by two tissues; and the words with small font size represent pathways only enriched by one tissue.

extracted to describe the up/down regulatory processes of tissue crosstalk. Together, the secreted DEPs, all possible cross-tissue receptors and their up/downstream DEP neighbors constituted the cross-tissue interface of IR. All involved interactions are listed in **Supplementary Table 5**.

Furthermore, the main function of these elements in the interface was investigated by searching their enriched pathways (FDR <0.05), which are shown in **Figure 5B**. Surprisingly, among the up- and down-stream processes (**Figure 5B**), metabolic pathways dominated an average of 66.08% of all enriched pathways (95% Confidence interval: 53.21–78.95%). This proportion was significantly higher than that in background database (P <0.01, one-sample z-test), where 91 (37.45%) out of 243 basic pathways were annotated as metabolic ones. It was suggested that the metabolism alterations accompanied by IR participated or even drove the communications between WAT, liver, and skeletal muscle. By characterizing the cross-tissue interactions *via* their dominant upstream pathways (**Figure 5B**), the crosstalk from liver to WAT was found as the only tissue communication driven by carbohydrate metabolism during IR. The main reason for this was due to the high proportion of glucose metabolic enzymes in upstream regulatory proteins of liver. Among the 6 differential upstream regulatory proteins in liver (**Supplementary Table 6**), 5 were enzymes related to glucose metabolism: glucosamine-6-phosphate isomerase, transketolase, glucose-6-phosphatase, hexokinase-3, and glucokinase. These enzymes may connect to secreted proteins through a series of linked metabolic reactions, thereby outputting abnormal glucose metabolic signals from liver. Besides, in WAT and skeletal muscle, carbohydrate metabolism accounted for one-third of the processes receiving hepatic signals (**Figure 5B**). It was stressed that liver played a pivotal role in regulation of glucose homeostasis during IR.

CD36-PPAR Axis Was Highlighted as Vital Target for Tissue Crosstalk Relevant to IR

The interface of WAT, liver, and muscle is displayed in detail in **Figure 6**. As shown in **Figure 6**, many of the secreted proteins participating in tissue crosstalk were extracellular matrix (51.9%, see **Supplementary Table 7** for more details), while non-secreted receptors varied a lot. As one of the 5 commonly upregulated proteins in three tissues (**Supplementary Table 4**), CD36 was highlighted as receptor in WAT and liver. It was indicated that adipose and hepatic CD36 might be a vital receptor receiving

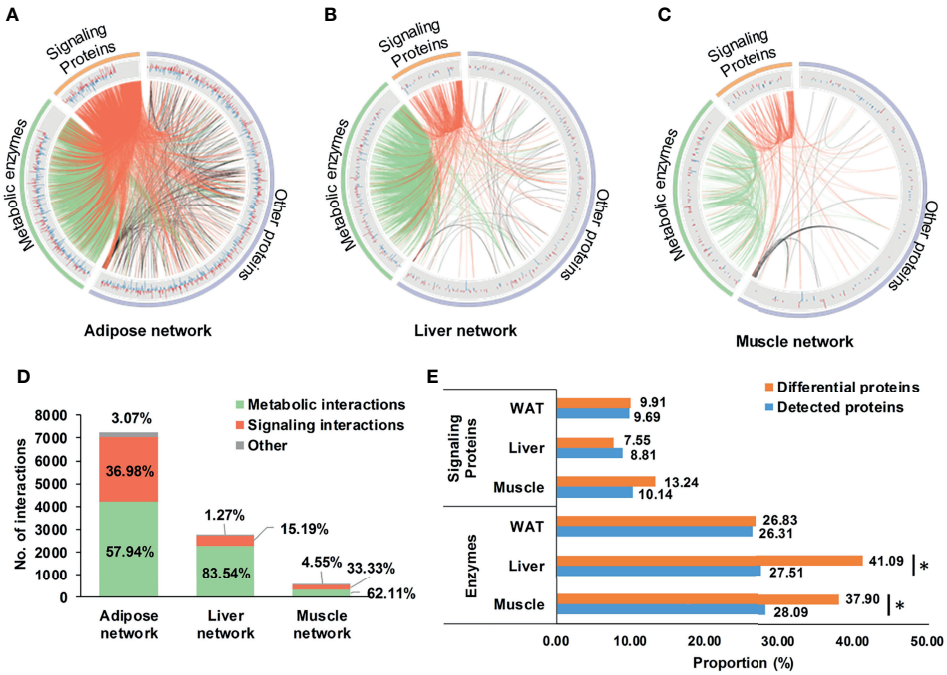

FIGURE 3 | Tissue-specific networks of IR. **(A–C)** tissue-specific networks of IR. Where, fold changes of all differential proteins were shown in bar plots; signaling protein-related and metabolic enzyme-related interactions were respectively highlighted in red and green; **(D)** Distribution of metabolic and signaling interactions in tissue-specific networks; **(E)** Proportion of metabolic enzymes and signaling proteins in differential and detected proteins. *P < 0.05, chi-square test.

cross-tissue signals. WB assay confirmed the elevated CD36 in three tissues (P <0.05, Student's t-test, **Figures 7A, B**). Muscular CD36 was not included in the interface because no corresponding secreted proteins were differentially expressed in WAT and liver.

As it was exhibited in the cross-tissue interface of IR (**Figure 6**), both adipose and hepatic CD36 were linked with muscular thrombospondin-4 (THBS4). According to the proteomics detection, THBS4 in skeletal muscle was significantly increased in IR group (P <0.05, Student's t-test, see **Supplementary Table 3**). Additionally, we also detected elevated THBS4 in serum of IR mice (P <0.05, Student's t-test, **Figure 7C**). In liver and WAT, CD36-mediated lipid uptake could directly regulate the activity of PPAR pathway, which is an important controller for glucose homeostasis (**Figure 7D**). Hence, further effect of CD36–PPAR axis on metabolic regulation was subsequently evaluated. As a target gene of PPAR pathway, PCK1 is a rate-limiting enzyme of glyceroneogenesis in which gluconeogenic precursors such as pyruvate, lactate, and alanine were converted into the glycerol backbone of triglyceride (28, 29). It was identified as downregulated DEP in WAT and liver according to proteomics data. Following WB assay also confirmed decreased PCK1 in WAT and liver (P <0.05, Student's t-test, **Figure 7E**), suggesting impaired metabolic homeostasis in IR group.

In addition, as the only signaling pathway commonly enriched by three tissues, the activity of PPAR pathway was

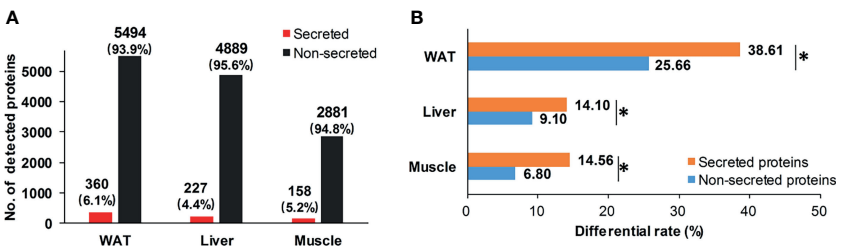

FIGURE 4 | Distribution of secreted proteins. **(A)** Distribution of secretory and non-secretory proteins in detecting pool; **(B)** Differential rate of secretory and non-secretory proteins. *P < 0.05, chi-square test.

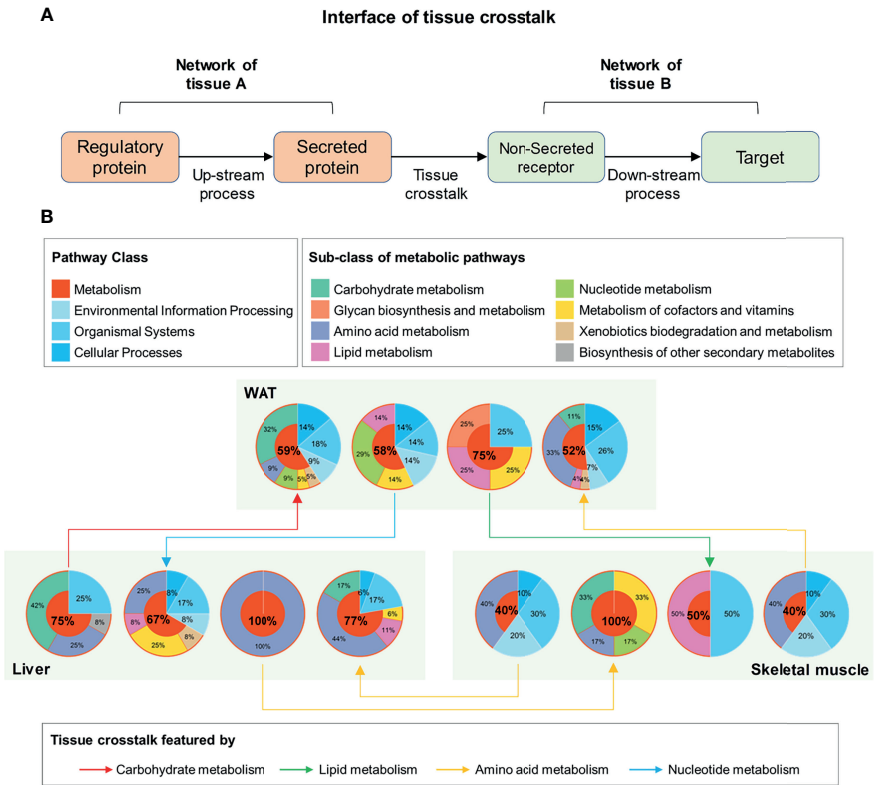

FIGURE 5 | Functional interpretation of tissue crosstalk interface relevant to IR. **(A)** Schematic diagram of cross-tissue interface; **(B)** Functional classification of up and downstream processes in the interface of IR.

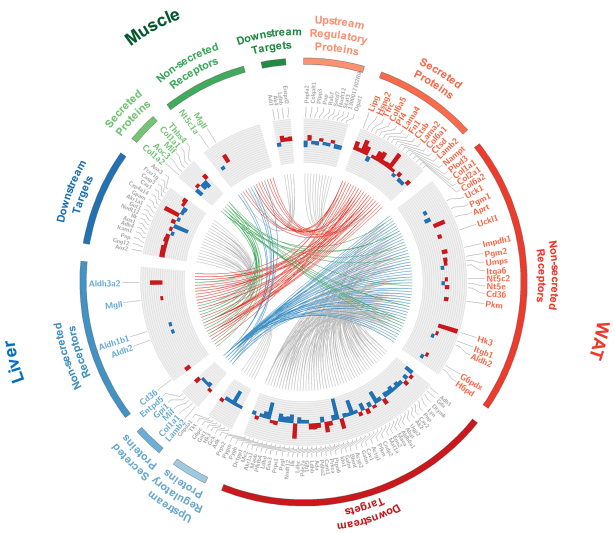

FIGURE 6 | Detailed information of the tissue crosstalk interface relevant to IR. Where, fold changes of all differential proteins were shown in bar plots; the differentially expressed secretory proteins and their differential non-secreted receptors were labeled in color corresponding to each tissue; the up- and down-stream regulators were labeled in gray; the cross-tissue interactions started from WAT, liver, and skeletal muscle were respectively colored in red, blue and green.

examined. FABPs are a class of lipid carrier which binds and delivers ligands to PPAR. Unchanged FABP1 (P = 0.76, Student's t-test) and significantly decreased FABP4 (P <0.05, Student's t-test) was respectively detected in liver and WAT (**Figures 7A, F**), which was in line with the quantification result from proteomics. Although proteomics did not capture signals of PPAR, WB assay showed unchanged PPARα and decreased PPARγ in liver and WAT of IR group (**Figure 7F**). PGC-1α was consistently decreased in liver and WAT of IR group (P <0.05, Student's t-test, **Figure 7F**). Therefore, PPAR pathway was suppressed in WAT and liver, which may resonate with the cross-tissue signals input by CD36. In parallel, the protein level of PPARγ and FABP3 in skeletal muscle was measured to be elevated in IR group (P <0.05, Student's t-test, **Figure 7F**), suggesting enhanced muscular PPAR pathway. But neither proteomics nor WB assay detected protein expression of PCK1 in skeletal muscle, suggesting a rather weak effect of muscular PPAR pathway on PCK1 mediated metabolic dysfunction.

DISCUSSION

The present study developed a network-based strategy for tissue crosstalk identification, which was applied to the protein profiles of WAT, liver, and skeletal muscle in IR mice. From a network perspective, the tissue crosstalk relevant to IR was systematically explored and the potential cross-tissue mechanism was characterized.

As secretory proteins are essential for signal transduction between individual tissues, we screened them in all proteins detected from WAT, liver, and skeletal muscle. It was found that secreted proteins only accounted for a small fraction (5% on average) while presented significantly higher differential rates than non-secretory ones, suggesting a strong tendency of IR group towards impairing tissue communications. In this context, we proposed a secreted protein-based strategy for identifying tissue crosstalk relevant to IR. Inter-tissue connections including secretory proteins and their receptors as well as the inner-tissue up- and down-stream regulatory events were searched from distinct tissue-specific networks, thus generating a multi-tissue interface of IR.

We observed widespread metabolic alterations not only inside tissue-specific networks but also on the cross-tissue interface of IR, highlighting a significant role of metabolism in tissue communication during IR. Extraordinarily, liver was revealed as the only organ outputting abnormal glucose metabolic signals. Approximately 5 out of 6 differentially expressed upstream proteins of hepatic secreted proteins were glucose metabolism related enzymes. It was strongly suggested that, in IR subjects, the transduction of abnormal glucose metabolic signals was probably started from liver. As targets receiving hepatic signals, almost 1/3 downstream processes in WAT and skeletal muscle

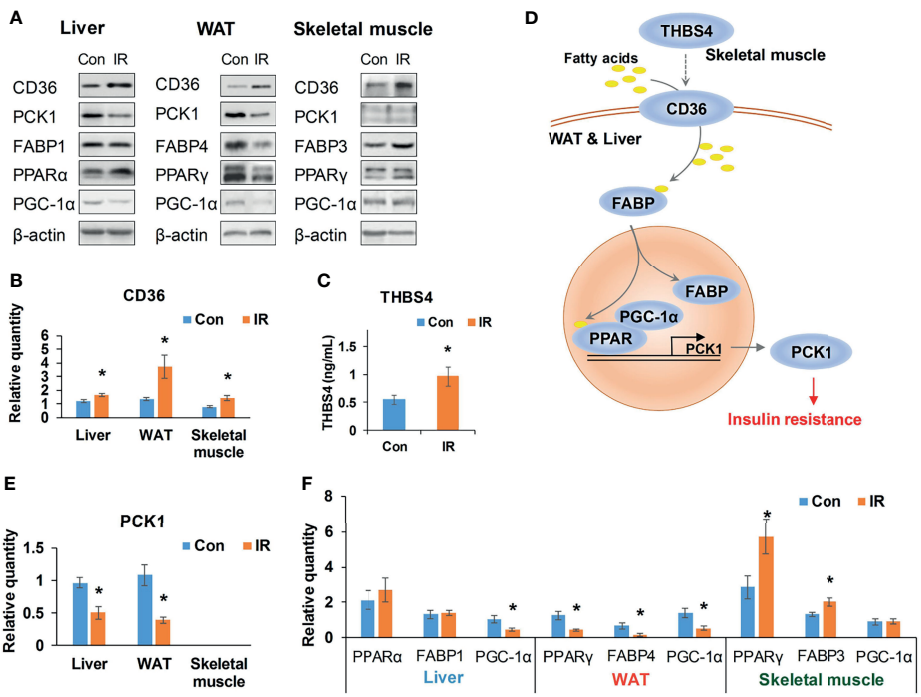

FIGURE 7 | Validation of CD36–PPAR axis. **(A)** Representative WB bands of candidate proteins; **(B)** Relative quantity of CD36 based on WB bands (n =4/group); **(C)** Serum THBS4 level of experimental mice, (n = 9/group); **(D)** A potential cross-tissue mechanism of CD36-PPAR axis; **(E)** Relative quantity of PCK1 based on WB bands (n = 3–4); **(F)** Relative quantity of regulators in PPAR pathway based on WB bands (n = 4). *P < 0.05, compared to control group, Student's t-test; the normality of corresponding data was determined by Shapiro–Wilk test (P > 0.05).

were classified into carbohydrate metabolism, further confirming the pivotal role of liver in regulation of glucose metabolism.

In the extracted cross-tissue interface of IR, we noticed that one of the 5 consistently upregulated proteins in three tissues CD36 was commonly highlighted as crosstalk receptors in both WAT and liver. In metabolic organs, CD36 is a major importer for fatty acids which were then delivered by FABPs to PPAR as ligands (30, 31). Coincidently, PPAR pathway was the only signaling pathway commonly enriched by three tissues, thus emphasizing the significance of CD36–PPAR axis in pathogenesis of IR. In fact, the effect of PPAR pathway in progressing IR was widely confirmed in individual tissues (32, 33), but its role in cross-tissue communications has not been clarified. As PPARs can activate the transcription of many rate-limiting enzymes and control glucose and lipid metabolism (34), we then respectively investigated the upstream cross-tissue signals and downstream metabolic effects of CD36–PPAR axis.

In IR group, both proteomics data and WB assay confirmed elevated CD36 in WAT, liver, and skeletal muscle, which was consistent with previous observations on individual tissues (35–38). As a membrane receptor, CD36 can bind various ligands like fatty acids and thrombospondins (39). In the crosstalk interface of IR, hepatic and adipose CD36 was pointed to receiving external signals from muscular THBS4. THBS4 is a member of thrombospondins which has been identified as secreted proteins regulating cell communications (40). We detected increased THBS4 in skeletal muscle and confirmed elevated THBS4 in serum of IR mice. Consistently, a recent study observed higher peripheral THBS4 levels in patients with type 2 diabetes (41). Conversely, $THBS4^{-/-}$ mice also showed lower fasting glucose level than wild type and relieved hyperinsulinemia in nutrient challenge (42). It was indicated that the altered THBS4 highlighted in the upstream of CD36-PPAR axis may be important regulators for whole-body glucose metabolism.

To further verify the intracellular metabolic effect of CD36–PPAR axis, the protein expression of a PPAR target, PCK1 was examined. PCK1 is a key enzyme controlling the conversion of oxaloacetate into phosphoenolpyruvate, which is further used in glycerol 3-phosphate production for triglyceride synthesis (28, 29). In our study, both proteomics and WB assay detected decreased PCK1 in WAT and liver of IR mice. Low expression of PCK1 in liver and WAT has been implicated with IR through a lipotoxicity mechanism in transgenic mice (43). The reduced PCK1 in WAT can suppress fatty acids re-esterification and cause excessive accumulation of fatty acids derived toxic metabolites, thus resulting in lipotoxicity in ectopic tissues such as liver and skeletal muscle (44). Liver-specific PCK1-knockout experiment also confirmed the peripheral lipotoxicity of reduced hepatic PCK1 in chow-diet condition and its effect on exacerbating IR in high fat diet condition (45). Therefore, the downregulation of PCK1 here may contribute to the impaired glucose metabolism through a lipotoxicity mechanism, mechanically confirming a depressed effect of CD36–PPAR axis on glucose homeostasis in our IR mice.

Meanwhile, interference from the inherent activity of PPAR pathway was assessed by measuring main isotypes of its regulators, namely, FABPs, PPARs, and PGC-1α. FABPs are lipid carriers which bind and deliver ligands to PPAR (46). Our study respectively confirmed unchanged FABP1 and significantly reduced FABP4 in liver and WAT of IR group by proteomics and WB assay. Although proteomics did not capture signals of PPARs and PGC-1α, WB assay showed decreased PPARγ in both liver and WAT and downregulated PGC-1α in WAT of IR group. It was suggested that the activity of PPAR pathway was consistently depressed in liver and WAT of IR group. In parallel, skeletal muscle of IR group showed elevated FABP3 and PPARγ. But no signals of muscular PCK1 were captured by proteomics or WB, indicating a mechanism different from liver and WAT in regulation of glucose homeostasis. Taken together, it can be concluded that adipose and hepatic PPAR pathways are integral channels bridging external signals to intracellular glucose homeostasis in progression of IR.

In addition to the CD36-mediated signals, many extracellular matrix (ECM) related proteins were highlighted in the cross-tissue interface. ECM-related proteins are known as structural support can be released into circulation. A growing body of reports have shown strong correlation between altered ECMs and metabolic disorders (47, 48). Mechanically, ECM attachment has been reported to be required for cell communication (49) and regulation of metabolic processes (50), yet few direct pieces of evidence linking ECMs and tissue crosstalk can be found. In this study, our unbiased proteomics analysis provided a computational clue for the potential role of ECM-related proteins in tissue communication during IR, which may hint an alternative aspect of ECM functions.

This study is not without limitations. Our observation is based on static experiments in freshly isolated mouse organs. Dynamic experiments with further technical supports from conditional knockout animals or *in vivo* tracer techniques would provide more solid evidences for the transduction of cross-tissue signals. As obesity is the most common cause of IR (51), we chose high fat diet fed mice as our subjects. Inevitably, the results here may be specific to dietary fat induced IR. Technically, we used the same database during network construction and functional assessment and performed one sample z-test to reduce the possible circularity. Future random network analysis might be helpful to further improve this issue. Currently, as there was no standard dataset collecting tissue crosstalk interactions, we were not able to evaluate the performance of our approach. Alternatively, the results obtained from network analysis were partially verified by experimental assays. Overall, our systematical analysis of multi-organ proteomics paved a novel way to deciphering inter-tissue communications in dietary fat induced IR.

CONCLUSION

It has been widely accepted that tissue communication underlies pathological basis of many diseases such as obesity, diabetes, metabolic syndromes, and so on. However, due to the lack of effective means to explore and functionally infer cross-tissue

interactions, current study on disease-related tissue crosstalk has been tremendously hindered. To solve this issue, we proposed a network-based approach to explore the interface between multiple tissues, which was then applied to the proteomics data of WAT, liver, and skeletal muscle in IR mice. Interestingly, widespread metabolic alterations not only were observed in tissue-specific networks, but also dominated the cross-tissue interface related to IR, emphasizing their significance in development of IR. By quantifying functional pathways involved in the interface, liver was recognized as the only organ that can output abnormal carbohydrate metabolic signals, clearly highlighting its central role for glucose homeostasis. Especially, CD36–PPAR axis was identified and verified to potentially link inter-tissue signals with intracellular metabolism in liver and WAT, thereby promoting the progression of dietary fat induced IR through a PCK1-mediated lipotoxicity mechanism.

Although this CD36–PPAR axis mediated crosstalk mechanism requires validation from more functional experiments such as conditional transgenic assays, the present study still provides novel insights into understanding the tissue communications in pathogenesis of IR. With further improvement, our network-based function mining method would shed a light on other disease-related tissue crosstalk exploration in the near future.

DATA AVAILABILITY STATEMENT

The datasets presented in this study can be found in online repositories. The names of the repository/repositories and accession number(s) can be found below: https://www.ebi.ac.uk/pride/archive/, PXD021046.

ETHICS STATEMENT

The animal study was reviewed and approved by the Animal Ethics Committee of Hebei General Hospital.

AUTHOR CONTRIBUTIONS

GS and HM conceived this research and designed the analysis. LinlY researched the data and prepared the primary manuscript. LinqY, XW, HX, HZ, YX, FZ, and CW performed the sample preparation and contributed to discussion. GS and HM are the guarantors of this work and, as such, had full access to all the data in the study and takes responsibility for the integrity of the data and the accuracy of the data analysis. All authors contributed to the article and approved the submitted version.

FUNDING

This research was supported by grants from the National Natural Science Foundation of Hebei, China (C2019307081 to LinlY, H2019307108 to HM) and the Government Funded Program for Clinical Medicine Talent Training and Basic Research Project of Hebei, China (2015 to HM, 2017 to LinlY and HX).

SUPPLEMENTARY MATERIAL

The Supplementary Material for this article can be found online at: https://www.frontiersin.org/articles/10.3389/fendo.2021.756785/full#supplementary-material

REFERENCES

1. Saklayen MG. The Global Epidemic of the Metabolic Syndrome. *Curr Hypertens Rep* (2018) 20(2):12. doi: 10.1007/s11906-018-0812-z
2. Yaribeygi H, Farrokhi FR, Butler AE, Sahebkar A. Insulin Resistance: Review of the Underlying Molecular Mechanisms. *J Cell Physiol* (2019) 234(6):8152–61. doi: 10.1002/jcp.27603
3. Ribes-Navarro A, Atef M, Sánchez-Sarasúa S, Beltrán-Bretones MT, Olucha-Bordonau F, Sánchez-Pérez AM. Abscisic Acid Supplementation Rescues High Fat Diet-Induced Alterations in Hippocampal Inflammation and IRSs Expression. *Mol Neurobiol* (2019) 56(1):454–64. doi: 10.1007/s12035-018-1091-z
4. Sun N, Shen C, Zhang L, Wu X, Yu Y, Yang X, et al. Hepatic Krüppel-Like Factor 16 (KLF16) Targets Pparα to Improve Steatohepatitis and Insulin Resistance. *Gut* (2020) 70(11):2183–95. doi: 10.1136/gutjnl-2020-321774
5. Seldin MM, Koplev S, Rajbhandari P, Vergnes L, Rosenberg GM, Meng Y, et al. A Strategy for Discovery of Endocrine Interactions With Application to Whole-Body Metabolism. *Cell Metab* (2018) 27(5):1138–55.e1136. doi: 10.1016/j.cmet.2018.03.015
6. Seldin M, Yang X, Lusis AJ. Systems Genetics Applications in Metabolism Research. *Nat Metab* (2019) 1(11):1038–50. doi: 10.1038/s42255-019-0132-x
7. Shimizu N, Maruyama T, Yoshikawa N, Matsumiya R, Ma Y, Ito N, et al. A Muscle-Liver-Fat Signalling Axis is Essential for Central Control of Adaptive Adipose Remodelling. *Nat Commun* (2015) 6:6693 . doi: 10.1038/ncomms7693
8. Zhang Z, Gallagher T, Scherer PE, Beutler B. Tissue-Specific Disruption of Kbtbd2 Uncovers Adipocyte-Intrinsic and -Extrinsic Features of the Teeny Lipodystrophy Syndrome. *Proc Natl Acad Sci USA* (2020) 117(21):11829–35. doi: 10.1073/pnas.2000118117
9. Martins Conde P, Pfau T, Pires Pacheco M, Sauter T. A Dynamic Multi-Tissue Model to Study Human Metabolism. *NPJ Syst Biol Appl* (2021) 7(1):5. doi: 10.1038/s41540-020-00159-1
10. Dyar KA, Lutter D, Artati A, Ceglia NJ, Liu Y, Armenta D, et al. Atlas of Circadian Metabolism Reveals System-Wide Coordination and Communication Between Clocks. *Cell* (2018) 174(6):1571–85.e1511. doi: 10.1016/j.cell.2018.08.042
11. Samdani P, Singhal M, Sinha N, Tripathi P, Sharma S, Tikoo K, et al. A Comprehensive Inter-Tissue Crosstalk Analysis Underlying Progression and Control of Obesity and Diabetes. *Sci Rep* (2015) 5:12340. doi: 10.1038/srep12340
12. Chen YM, Zheng Y, Yu Y, Wang Y, Huang Q, Qian F, et al. Blood Molecular Markers Associated With COVID-19 Immunopathology and Multi-Organ Damage. *EMBO J* (2020) 39(24):e105896. doi: 10.15252/embj.2020105896
13. Narayanan M. Computational Problems in Multi-Tissue Models of Health and Disease. *J Indian Inst Sci* (2017) 97(3):325–37. doi: 10.1007/s41745-017-0040-6
14. Kuntal BK, Dutta A, Mande SS. CompNet: A GUI Based Tool for Comparison of Multiple Biological Interaction Networks. *BMC Bioinf* (2016) 17(1):185. doi: 10.1186/s12859-016-1013-x
15. Schieber TA, Carpi L, Diaz-Guilera A, Pardalos PM, Masoller C, Ravetti MG. Quantification of Network Structural Dissimilarities. *Nat Commun* (2017) 8:13928. doi: 10.1038/ncomms13928
16. Jo Y, Kim S. Identification of Common Coexpression Modules Based on Quantitative Network Comparison. *BMC Bioinf* (2018) 19(Suppl 8):213. doi: 10.1186/s12859-018-2193-3
17. Pedroso AP, Souza AP, Dornellas AP, Oyama LM, Nascimento CM, Santos GM, et al. Intrauterine Growth Restriction Programs the Hypothalamus of Adult Male Rats: Integrated Analysis of Proteomic and Metabolomic Data. *J Proteome Res* (2017) 16(4):1515–25. doi: 10.1021/acs.jproteome.6b00923

18. Rashid CS, Bansal A, Simmons RA. Oxidative Stress, Intrauterine Growth Restriction, and Developmental Programming of Type 2 Diabetes. *Physiol (Bethesda)* (2018) 33(5):348–59. doi: 10.1152/physiol.00023.2018
19. Ma H, Sales VM, Wolf AR, Subramanian S, Matthews TJ, Chen M, et al. Attenuated Effects of Bile Acids on Glucose Metabolism and Insulin Sensitivity in a Male Mouse Model of Prenatal Undernutrition. *Endocrinology* (2017) 158(8):2441–52. doi: 10.1210/en.2017-00288
20. Perez-Riverol Y, Csordas A, Bai J, Bernal-Llinares M, Hewapathirana S, Kundu DJ, et al. The PRIDE Database and Related Tools and Resources in 2019: Improving Support for Quantification Data. *Nucleic Acids Res* (2019) 47 (D1):D442–50. doi: 10.1093/nar/gky1106
21. Maere S, Heymans K, Kuiper M. BiNGO: A Cytoscape Plugin to Assess Overrepresentation of Gene Ontology Categories in Biological Networks. *Bioinformatics* (2005) 21(16):3448–9. doi: 10.1093/bioinformatics/bti551
22. Kanehisa M, Furumichi M, Sato Y, Ishiguro-Watanabe M, Tanabe M. KEGG: Integrating Viruses and Cellular Organisms. *Nucleic Acids Res* (2021) 49(D1): D545–d551. doi: 10.1093/nar/gkaa970
23. Yang L, Wang X, Guo H, Zhang W, Wang W, Ma H. Whole Transcriptome Analysis of Obese Adipose Tissue Suggests U001kfc.1 as a Potential Regulator to Glucose Homeostasis. *Front Genet* (2019) 10:1133. doi: 10.3389/fgene.2019.01133
24. Klein P, Ravi R. A Nearly Best-Possible Approximation Algorithm for Node-Weighted Steiner Trees. *J Algorithms* (1995) 19(1):104–15. doi: 10.1006/jagm.1995.1029
25. Yang L, Tang K, Qi Y, Ye H, Chen W, Zhang Y, et al. Potential Metabolic Mechanism of Girls' Central Precocious Puberty: A Network Analysis on Urine Metabonomics Data. *BMC Syst Biol* (2012) 6 Suppl 3:S19. doi: 10.1186/1752-0509-6-S3-S19
26. Uhlén M, Fagerberg L, Hallström BM, Lindskog C, Oksvold P, Mardinoglu A, et al. Proteomics. Tissue-Based Map of the Human Proteome. *Science* (2015) 347(6220):1260419. doi: 10.1126/science.1260419
27. eGTEx Project. Enhancing GTEx by Bridging the Gaps Between Genotype, Gene Expression, and Disease. *Nat Genet* (2017) 49(12):1664–70. doi: 10.1038/ng.3969
28. Davies GF, Khandelwal RL, Wu L, Juurlink BH, Roesler WJ. Inhibition of Phosphoenolpyruvate Carboxykinase (PEPCK) Gene Expression by Troglitazone: A Peroxisome Proliferator-Activated Receptor-Gamma (PPARgamma)-Independent, Antioxidant-Related Mechanism. *Biochem Pharmacol* (2001) 62(8):1071–9. doi: 10.1016/s0006-2952(01)00764-x
29. Yu S, Meng S, Xiang M, Ma H. Phosphoenolpyruvate Carboxykinase in Cell Metabolism: Roles and Mechanisms Beyond Gluconeogenesis. *Mol Metab* (2021) 53:101257. doi: 10.1016/j.molmet.2021.101257
30. Hajri T, Hall AM, Jensen DR, Pietka TA, Drover VA, Tao H, et al. CD36-Facilitated Fatty Acid Uptake Inhibits Leptin Production and Signaling in Adipose Tissue. *Diabetes* (2007) 56(7):1872–80. doi: 10.2337/db06-1699
31. Hao JW, Wang J, Guo H, Zhao YY, Sun HH, Li YF, et al. CD36 Facilitates Fatty Acid Uptake by Dynamic Palmitoylation-Regulated Endocytosis. *Nat Commun* (2020) 11(1):4765. doi: 10.1038/s41467-020-18565-8
32. He W, Barak Y, Hevener A, Olson P, Liao D, Le J, et al. Adipose-Specific Peroxisome Proliferator-Activated Receptor Gamma Knockout Causes Insulin Resistance in Fat and Liver But Not in Muscle. *Proc Natl Acad Sci USA* (2003) 100(26):15712–7. doi: 10.1073/pnas.2536828100
33. Koo S-H, Satoh H, Herzig S, Lee C-H, Hedrick S, Kulkarni R, et al. PGC-1 Promotes Insulin Resistance in Liver Through PPAR-α-Dependent Induction of TRB-3. *Nat Med* (2004) 10(5):530–4. doi: 10.1038/nm1044
34. Montaigne D, Butruille L, Staels B. PPAR Control of Metabolism and Cardiovascular Functions. *Nat Rev Cardiol* (2021) 18(12):809–23. doi: 10.1038/s41569-021-00569-6
35. Smith AC, Mullen KL, Junkin KA, Nickerson J, Chabowski A, Bonen A, et al. Metformin and Exercise Reduce Muscle FAT/CD36 and Lipid Accumulation and Blunt the Progression of High-Fat Diet-Induced Hyperglycemia. *Am J Physiol Endocrinol Metab* (2007) 293(1):E172–181. doi: 10.1152/ajpendo.00677.2006
36. Vroegrijk IO, van Klinken JB, van Diepen JA, van den Berg SA, Febbraio M, Steinbusch LK, et al. CD36 is Important for Adipocyte Recruitment and Affects Lipolysis. *Obes (Silver Spring)* (2013) 21(10):2037–45. doi: 10.1002/oby.20354
37. Wilson CG, Tran JL, Erion DM, Vera NB, Febbraio M, Weiss EJ. Hepatocyte-Specific Disruption of CD36 Attenuates Fatty Liver and Improves Insulin Sensitivity in HFD-Fed Mice. *Endocrinology* (2016) 157(2):570–85. doi: 10.1210/en.2015-1866
38. Rada P, González-Rodríguez Á., García-Monzón C, Valverde Á,M. Understanding Lipotoxicity in NAFLD Pathogenesis: Is CD36 a Key Driver? *Cell Death Dis* (2020) 11(9):802. doi: 10.1038/s41419-020-03003-w
39. Zhang X, Fan J, Li H, Chen C, Wang Y. CD36 Signaling in Diabetic Cardiomyopathy. *Aging Dis* (2021) 12(3):826–40. doi: 10.14336/ad.2020.1217
40. Spinale FG. Cell-Matrix Signaling and Thrombospondin: Another Link to Myocardial Matrix Remodeling. *Circ Res* (2004) 95(5):446–8. doi: 10.1161/01.res.0000142315.88477.42
41. Zierfuss B, Höbaus C, Herz CT, Pesau G, Koppensteiner R, Schernthaner GH. Thrombospondin-4 Increases With the Severity of Peripheral Arterial Disease and is Associated With Diabetes. *Heart Vessels* (2020) 35(1):52–8. doi: 10.1007/s00380-019-01453-7
42. Frolova EG, Drazba J, Krukovets I, Kostenko V, Blech L, Harry C, et al. Control of Organization and Function of Muscle and Tendon by Thrombospondin-4. *Matrix Biol* (2014) 37:35–48. doi: 10.1016/j.matbio.2014.02.003
43. Millward CA, Desantis D, Hsieh CW, Heaney JD, Pisano S, Olswang Y, et al. Phosphoenolpyruvate Carboxykinase (Pck1) Helps Regulate the Triglyceride/Fatty Acid Cycle and Development of Insulin Resistance in Mice. *J Lipid Res* (2010) 51(6):1452–63. doi: 10.1194/jlr.M005363
44. Kwon EY, Jung UJ, Park T, Yun JW, Choi MS. Luteolin Attenuates Hepatic Steatosis and Insulin Resistance Through the Interplay Between the Liver and Adipose Tissue in Mice With Diet-Induced Obesity. *Diabetes* (2015) 64 (5):1658–69. doi: 10.2337/db14-0631
45. Ye Q, Liu Y, Zhang G, Deng H, Chen C, Pan X, et al. Deficiency of Gluconeogenic Enzyme PCK1 Promotes Non-Alcoholic Steatohepatitis Progression by Activation of PI3K/AKT/PDGF Axis. *bioRxiv* (2021) 2021.2001.2012.426294. doi: 10.1101/2021.01.12.426294
46. Hofer P, Boeszoermenyi A, Jaeger D, Feiler U, Arthanari H, Mayer N, et al. Fatty Acid-Binding Proteins Interact With Comparative Gene Identification-58 Linking Lipolysis With Lipid Ligand Shuttling. *J Biol Chem* (2015) 290 (30):18438–53. doi: 10.1074/jbc.M114.628958
47. Cohen MP, Lautenslager GT, Shearman CW. Increased Collagen IV Excretion in Diabetes. A Marker of Compromised Filtration Function. *Diabetes Care* (2001) 24(5):914–8. doi: 10.2337/diacare.24.5.914
48. Strieder-Barboza C, Baker NA, Flesher CG, Karmakar M, Patel A, Lumeng CN, et al. Depot-Specific Adipocyte-Extracellular Matrix Metabolic Crosstalk in Murine Obesity. *Adipocyte* (2020) 9(1):189–96. doi: 10.1080/21623945.2020.1749500
49. Zhou C, Zhang D, Du W, Zou J, Li X, Xie J. Substrate Mechanics Dictate Cell-Cell Communication by Gap Junctions in Stem Cells From Human Apical Papilla. *Acta Biomater* (2020) 107:178–93. doi: 10.1016/j.actbio.2020.02.032
50. Sullivan WJ, Mullen PJ, Schmid EW, Flores A, Momcilovic M, Sharpley MS, et al. Extracellular Matrix Remodeling Regulates Glucose Metabolism Through TXNIP Destabilization. *Cell* (2018) 175(1):117–32.e121. doi: 10.1016/j.cell.2018.08.017
51. Johnson AM, Olefsky JM. The Origins and Drivers of Insulin Resistance. *Cell* (2013) 152(4):673–84. doi: 10.1016/j.cell.2013.01.041

Conflict of Interest: The authors declare that the research was conducted in the absence of any commercial or financial relationships that could be construed as a potential conflict of interest.

Publisher's Note: All claims expressed in this article are solely those of the authors and do not necessarily represent those of their affiliated organizations, or those of the publisher, the editors and the reviewers. Any product that may be evaluated in this article, or claim that may be made by its manufacturer, is not guaranteed or endorsed by the publisher.

frontiers in Endocrinology

ORIGINAL RESEARCH
published: 26 January 2022
doi: 10.3389/fendo.2021.757228

Medications Activating Tubular Fatty Acid Oxidation Enhance the Protective Effects of Roux-en-Y Gastric Bypass Surgery in a Rat Model of Early Diabetic Kidney Disease

William P. Martin[1], Yeong H. D. Chuah[1], Mahmoud Abdelaal[1], Anders Pedersen[2], Daniel Malmodin[2], Sanna Abrahamsson[3], Michaela Hutter[1], Catherine Godson[1], Eoin P. Brennan[1], Lars Fändriks[4], Carel W. le Roux[1,5†] and Neil G. Docherty[1†]*

[1] Diabetes Complications Research Centre, School of Medicine, Conway Institute, University College Dublin, Dublin, Ireland, [2] Swedish NMR Centre, University of Gothenburg, Gothenburg, Sweden, [3] Bioinformatics Core Facility, Sahlgrenska Academy, University of Gothenburg, Gothenburg, Sweden, [4] Institute of Clinical Sciences, Sahlgrenska Academy, University of Gothenburg, Gothenburg, Sweden, [5] Diabetes Research Group, Ulster University, Coleraine, United Kingdom

Background: Roux-en-Y gastric bypass surgery (RYGB) improves biochemical and histological parameters of diabetic kidney disease (DKD). Targeted adjunct medical therapy may enhance renoprotection following RYGB.

Methods: The effects of RYGB and RYGB plus fenofibrate, metformin, ramipril, and rosuvastatin (RYGB-FMRR) on metabolic control and histological and ultrastructural indices of glomerular and proximal tubular injury were compared in the Zucker Diabetic Sprague Dawley (ZDSD) rat model of DKD. Renal cortical transcriptomic (RNA-sequencing) and urinary metabolomic (^{1}H-NMR spectroscopy) responses were profiled and integrated. Transcripts were assigned to kidney cell types through *in silico* deconvolution in kidney single-nucleus RNA-sequencing and microdissected tubular epithelial cell proteomics datasets. Medication-specific transcriptomic responses following RYGB-FMRR were explored using a network pharmacology approach. Omic correlates of improvements in structural and ultrastructural indices of renal injury were defined using a molecular morphometric approach.

Results: RYGB-FMRR was superior to RYGB alone with respect to metabolic control, albuminuria, and histological and ultrastructural indices of glomerular injury. RYGB-FMRR reversed DKD-associated changes in mitochondrial morphology in the proximal tubule to a greater extent than RYGB. Attenuation of transcriptomic pathway level activation of pro-fibrotic responses was greater after RYGB-FMRR than RYGB. Fenofibrate was found to be the principal medication effector of gene expression changes following

OPEN ACCESS

Edited by:
Luca Busetto,
Università degli Studi di Padova, Italy

Reviewed by:
Esteban Porrini,
University of La Laguna, Spain
Marina Martín Taboada,
Rey Juan Carlos University, Spain

****Correspondence:***
Neil G. Docherty
neil.docherty@ucd.ie

†These authors have contributed equally to this work and share senior authorship

Specialty section:
This article was submitted to Systems Endocrinology, a section of the journal Frontiers in Endocrinology

Received: *11 August 2021*
Accepted: *23 December 2021*
Published: *26 January 2022*

Citation:
Martin WP, Chuah YHD, Abdelaal M, Pedersen A, Malmodin D, Abrahamsson S, Hutter M, Godson C, Brennan EP, Fändriks L, le Roux CW and Docherty NG (2022) Medications Activating Tubular Fatty Acid Oxidation Enhance the Protective Effects of Roux-en-Y Gastric Bypass Surgery in a Rat Model of Early Diabetic Kidney Disease. Front. Endocrinol. 12:757228. doi: 10.3389/fendo.2021.757228

RYGB-FMRR, which led to the transcriptional induction of PPARα-regulated genes that are predominantly expressed in the proximal tubule and which regulate peroxisomal and mitochondrial fatty acid oxidation (FAO). After omics integration, expression of these FAO transcripts positively correlated with urinary levels of PPARα-regulated nicotinamide metabolites and negatively correlated with urinary tricarboxylic acid (TCA) cycle intermediates. Changes in FAO transcripts and nicotinamide and TCA cycle metabolites following RYGB-FMRR correlated strongly with improvements in glomerular and proximal tubular injury.

Conclusions: Integrative multi-omic analyses point to PPARα-stimulated FAO in the proximal tubule as a dominant effector of treatment response to combined surgical and medical therapy in experimental DKD. Synergism between RYGB and pharmacological stimulation of FAO represents a promising combinatorial approach to the treatment of DKD in the setting of obesity.

Keywords: bariatric surgery, diabetic kidney disease, transcriptome, metabolome, fatty acid oxidation, peroxisome, mitochondria, PPAR-alpha

INTRODUCTION

Diabetic kidney disease (DKD) is the leading cause of end-stage renal disease (ESRD) (1, 2). Obesity is common in people with chronic kidney disease (CKD), with reported prevalence rates ranging from 35-44% (3, 4), and is an independent risk factor for the onset and progression of DKD (5).

Roux-en-Y gastric bypass (RYGB) is the surgical procedure for which the most data on renoprotection in type 2 diabetes exists (6–8). In a randomized study of RYGB in patients with type 2 diabetes and microalbuminuria, remission of albuminuria at 24-month follow-up was greater following RYGB plus medications (82%) compared with medications alone (55%) (9). We demonstrated that RYGB improved glomerular injury whilst also opposing the activation of pro-fibrotic and pro-inflammatory transcriptional programmes in the Zucker Diabetic Fatty (ZDF) rat model (10–13).

Impaired renal tubular fatty acid oxidation (FAO) is implicated as a pathogenic driver of tubulointerstitial fibrosis in CKD (14). Restoration of mitochondrial number and FAO by tubular epithelial-specific overexpression of the rate-limiting fatty acid shuttling enzyme, carnitine palmitoyltransferase 1A, attenuates experimental renal fibrosis (15). We did not detect transcriptomic evidence of FAO induction following RYGB in the ZDF rat (12), suggesting that pharmacotherapy promoting FAO may complement the metabolic benefits of surgery vis-à-vis renoprotection.

We assessed whether drugs routinely used in type 2 diabetes management, and with the potential to stimulate FAO, enhanced renoprotection when added to RYGB in Zucker Diabetic Sprague Dawley (ZDSD) rats (16). Ramipril was included as renin-angiotensin-aldosterone-system (RAAS) blockade is the backbone of DKD management (17). Metformin, rosuvastatin and fenofibrate were included as, by convergent mechanisms, each drug can stimulate FAO (18–20). Metformin activates the energy sensing AMP-activating protein kinase (AMPK) which results in inhibitory phosphorylation of acetyl-CoA carboxylase (ACC), a major regulator of FAO (21). Low ACC activity results in reduced fatty acid synthesis and increased mitochondrial entry of fatty acids leading to increased FAO (22). Inhibitory phosphorylation of ACC to promote FAO has been demonstrated to be essential for the renal anti-fibrotic effects of metformin observed in preclinical models (20). Both rosuvastatin and fenofibrate also promote FAO by activating AMPK (23, 24), and AMPK activation at least partly explains the anti-fibrotic effects of fenofibrate in preclinical models of renal injury (25).

Moreover, fenofibrate is an agonist of peroxisome proliferator-activated receptor-alpha (PPARα) (18), a nuclear transcription factor which promotes FAO in metabolically active tissues such as liver and kidney (26). PPARα is highly abundant in proximal tubular cells (26) and reduced proximal tubular PPARα expression contributes to the impairment of FAO which promotes renal fibrosis (14, 27, 28). Fenofibrate treatment restores tubular FAO *via* PPARα agonism and reduces renal fibrosis in experimental models (14). Statins may synergistically activate PPARα alongside fenofibrate (19), and PPARα-dependent reductions in renal fibrosis have been observed following statin treatment in preclinical models (29). While the most important renoprotective effect of RAAS blockade in DKD is felt to be a reduction in glomerular hypertension (30), metabolic effects of RAAS blockade are increasingly recognised. For example, RAAS inhibition with combined lisinopril and losartan treatment in the db/db mouse model reversed DKD-associated changes in renal cortical triacylglycerol fatty acid composition (31).

While metformin, rosuvastatin, and fenofibrate are primarily indicated to improve metabolic control in patients with type 2 diabetes, data from rat models of hypertensive or diabetic renal injury suggest that these medications, along with ramipril, have renoprotective effects (32–35). Thus, in the present study, these four medications were administered in combination in an effort to maximize reductions in renal injury following RYGB.

MATERIALS AND METHODS

Animal Studies

Experiments were undertaken under governmental project license (Health Products Regulatory Authority – AE18982/P084). Fourteen-week-old adult male ZDSD rats (n=35) and Sprague Dawley (SD, n=6) control rats (Crown BioScience) were provided with water and Purina 5008 rodent chow (Nestle Purina, St. Louis, MO). Body weight and glycaemia-matched ZDSD rats were allocated to either a sham-operated disease control (SHAM, n = 9), or one of two treatment groups: RYGB surgery (RYGB) and RYGB surgery plus fenofibrate, metformin, ramipril, and rosuvastatin (RYGB-FMRR). In total, 26 ZDSD rats underwent RYGB surgery, with 8 dying in the intra- or post-operative periods. RYGB was thus associated with a mortality rate of 30.8%. Causes of death included primary intraoperative gastrointestinal haemorrhage (n=1) and anastomotic complications (n=5, including haemorrhage and leakage). No abdominal pathology was identified on post-mortem of two rats who died after RYGB. Of the 18 remaining RYGB-operated ZDSD rats, n=9 each were assigned to the RYGB alone and RYGB-FMRR groups. No mortalities occurred in the SD or SHAM groups.

Rats treated with RYGB-FMRR received 100 mg/kg fenofibrate (Mylan Pharma, Canonsburg, PA), 300 mg/kg metformin (Teva Pharma, Petah Tikva, Israel), 1 mg/kg ramipril (Sanofi, Paris, France), and 10 mg/kg rosuvastatin (Teva Pharma). After RYGB, rats were transitioned from a liquid to a semi-solid and then to a regular chow diet over a two-week period to allow for anastomotic healing. As the above medications were incorporated into daily chow rations, they were introduced two weeks after RYGB once rats were established on a regular chow diet. Metformin monotherapy was introduced for the first two days to monitor for adverse responses, including anorexia. The remaining medications (fenofibrate, ramipril, and rosuvastatin) were commenced thereafter when no adverse response was observed. Medications were administered at doses which have been shown to be renoprotective in monotherapy in rat models of hypertensive or diabetic renal injury (32–35).

Body weights and mid-morning plasma glucose levels (Freestyle Optium Neo, Abbott Laboratories, Chicago, IL) were examined on a weekly basis before and after intervention. Animals were euthanized and tissue (renal cortex, liver, and epididymal fat) collected after an 8-week post-intervention period. The study design, including timing of interventions and sample collection, is summarised in **Figure 1**.

Roux-en-Y Gastric Bypass and Sham Surgeries

Sham surgeries were performed in ZDSD animals at 25 weeks of age (**Figure 1**). RYGB surgeries were performed at 29 weeks of age in the RYGB-FMRR group and at 30 weeks of age in the RYGB group (**Figure 1**). In light of the animal husbandry requirements in the postoperative setting, as well as the fact that all RYGB surgeries were performed by a single surgeon (M.A.), it was not possible to perform all RYGB surgeries in a single week and the procedures were thus staggered. One week prior to surgery, glycaemic control was optimized with daily subcutaneous injection of insulin degludec (Tresiba®, Novo Nordisk) to achieve a fasting plasma glucose below 12 mmol/L. Animals were anaesthetized with isoflurane and administered a

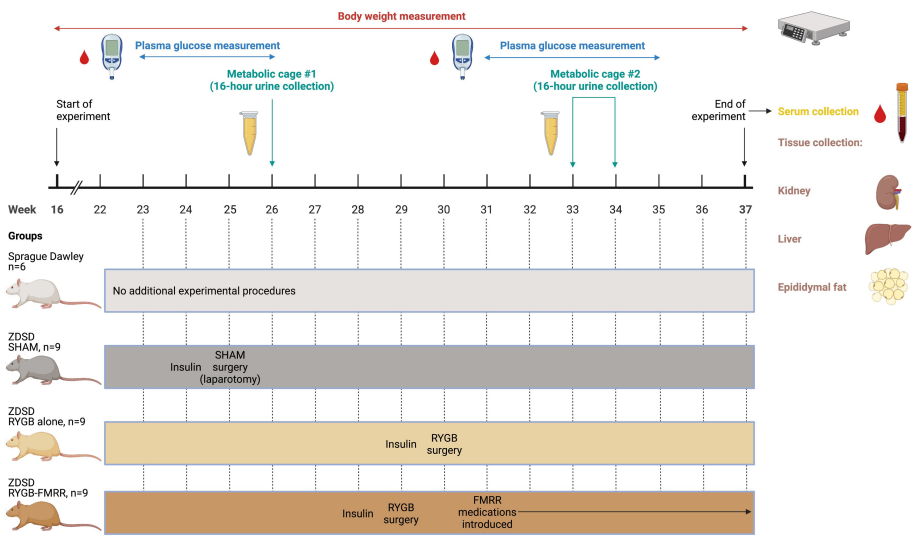

FIGURE 1 | Overview of the study design. Created with BioRender.com. In the SHAM, RYGB, and RYGB-FMRR groups, glycaemic control was optimized for one week prior to surgery with daily subcutaneous injection of insulin degludec (Tresiba®, Novo Nordisk) to achieve a fasting plasma glucose below 12 mmol/L. When introducing medications in the RYGB-FMRR group, metformin monotherapy was introduced for the first two days to monitor for adverse responses, including anorexia. The remaining medications (fenofibrate, ramipril, and rosuvastatin) were commenced thereafter when no adverse response was observed. FMRR, fenofibrate, metformin, ramipril, and rosuvastatin; RYGB, Roux-en-Y gastric bypass; RYGB-FMRR, Roux-en-Y gastric bypass plus fenofibrate, metformin, ramipril, and rosuvastatin; SHAM, sham surgery (laparotomy); ZDSD, Zucker Diabetic Sprague Dawley.

pre-operative prophylactic antibiotic, enrofloxacin 5mg/kg s.c. (Baytril, Bayer). In the SHAM group, a midline laparotomy was performed followed by closure. In RYGB groups, the jejunum was transected 15 cm distal to the duodenum and the proximal stump side-to-side anastomosed to the distal jejunum 25 cm from the ileocaecal valve. The stomach was transected 3 mm from the gastro-esophageal junction, creating a small gastric pouch, which was then end-to-side anastomosed to the distal stump of jejunum. The remnant stomach was closed, forming standardized biliopancreatic and alimentary limbs and a common channel. Buprenorphine (Animalcare Limited) analgesia was provided at 0.01-0.05 mg/kg s.c. every 6 hours for the first 2 post-operative days and as required thereafter.

Biochemical Analyses

As outlined in **Figure 1**, urine samples were collected over a duration of 16 hours at baseline (26 weeks of age) and at 4-week follow-up (33 weeks of age in the RYGB-FMRR group and 34 weeks of age in the RYGB group). Urinary concentrations of albumin were examined by ELISA (K15162C Meso Scale Discovery, Rockville, MD). Serum samples were collected at 8-week follow-up. Serum cholesterol and triglycerides were measured using an Atellica® Solution Immunoassay and Clinical Chemistry Analyser (Siemens Healthineers).

Histological and Immunohistochemical Analyses

Ten-micron thick sections of formalin-fixed paraffin-embedded kidney were used for haematoxylin and eosin staining, while five-micron thick sections were used for immunohistochemical staining. Scanned haematoxylin and eosin-stained sections were used to measure glomerular area in QuPath (36), from which glomerular volume was calculated using the Weibel and Gomez formula (37). Thirty glomerular tufts per sample were manually annotated at random throughout the renal cortex, from a minimum of six animals per experimental group. Kidney sections were stained with anti-ACOX1 antibody (ab184032, Abcam) using the VECTASTAIN Elite ABC-HRP peroxidase kit (PK-6200, Vector Laboratories). An IgG isotype control (ADI-950-231-0025, Enzo Life Sciences) and no antibody control were used to confirm the specificity of staining. All slides were digitized using an Aperio AT2 Digital Slide Scanner (Leica Biosystems).

Transmission Electron Microscopy

Glutaraldehyde-fixed and 1% osmium tetroxide post-fixed renal tissue was dehydrated and infiltrated with EPON™ Epoxy Resin. Ultra-thin sections were prepared and examined by transmission electron microscopy (Tecnai™ G2 12 BioTWIN). Images were analyzed using ImageJ software (NIH, https://imagej.nih.gov/ij/). Data were acquired from both glomeruli and proximal tubules of six rats from each of the four experimental groups.

All glomerular ultrastructural measurements were recorded from six separate capillary loops, representative of at least three separate glomeruli per sample. Podocyte foot process frequency (PFPF) was measured at 9900x by determining the number of podocyte foot processes (FPs) per unit length (8μm) of glomerular basement membrane (GBM). Six measurements were recorded per sample. GBM thickness was measured according to the Haas method at 20500x (38). Podocyte foot process diameter (PFPD) was measured as a reciprocal of PFPF at 20500x. Twenty-four GBM thickness and PFPD measurements were recorded per specimen.

Mitochondrial roundness was assessed as a marker of mitochondrial stress and measured in thirty images of proximal tubular cells per animal, fifteen each from the pars convoluta and pars recta segments. The pars convoluta and pars recta sections of the proximal tubule were distinguished by their ultrastructural morphometry and mitochondria contained therein imaged separately (39, 40). For each of the pars convoluta and pars recta sections, fifteen non-overlapping images from three distinct regions (five images/region) were acquired at 16500x per sample. Each image contained a minimum of five mitochondria for quantification. Images were captured in the basal region of pars convoluta cells for consistency, adjacent to the tubular basement membrane. Longer mitochondria which ran off the edge of the image, and for which less than 2μm of their course was captured by the image window, were excluded from analysis. Mitochondrial parameters (area, perimeter, major and minor axis, roundness, and aspect ratio) were measured using the freehand line selection tool of ImageJ. Roundness is the inverse of the aspect ratio (major axis/minor axis length) and is calculated as: $4^{*}\text{area}/(\pi^{*}\text{major axis}^2)$.

Transcriptomic and Quantitative Real-Time PCR Analyses

RNA was extracted from renal cortex, liver, and epididymal fat pads using an RNeasy Plus Mini Kit (Qiagen). The concentration and purity of RNA samples were determined using a Nanodrop™ 2000 Spectrophotometer (Thermo Fisher Scientific) and RNA sample integrity assessed using Agilent RNA 6000 Nano kits (Agilent Technologies).

For renal cortical RNA sequencing, RNA library preparation was carried out using the TruSeq Stranded Total RNA Library Prep Gold® kit (Cat. No. 20020598, Illumina). Libraries were sequenced on the Illumina NovaSeq 6000® platform in a paired-end fashion at a read length of 2x100bp. Sequencing fastq files and raw counts of aligned reads have been deposited in GEO (accession number GSE147706).

For quantitative reverse-transcription polymerase chain reaction (qRT-PCR) analyses, samples were treated with DNase I and complementary DNA (cDNA) synthesized using SuperScript™ II Reverse Transcriptase Kit (Invitrogen). mRNA expression of *Pdk4* in renal cortex and of *Acox1*, *Ehhadh*, and *Acaa2* in three tissue depots (renal cortex, liver, and epididymal fat) was quantified using beta-actin as the endogenous reference gene (TaqMan® Gene Expression Assays, Thermo Fisher Scientific and QuantStudio 7 Flex System, Applied Biosystems). Comparative analysis was performed using the ΔΔCt method (41), with SD animals serving as calibrators.

RNA-Seq Bioinformatic Analyses

The quality of the raw renal cortical RNA sequencing fastq files was analyzed using FastQC (0.11.2) (42). Quality filtering of

reads and adapter removal was performed using Trim Galore (0.4.0) together with Cutadapt (1.9) (43, 44). The data was mapped with STAR (2.5.2b) towards the rat reference genome, rn5 (45). Read quantification was performed with featureCounts (1.6.4) (46).

Further analysis was performed using the R statistical programming language (4.0.5) (47). Differential expression analysis was performed using DESeq2 (48). The data was normalized by size factors. A negative binomial generalized linear model was fitted to the normalized data, with the Wald statistic used to identify differentially expressed genes. The p-values were adjusted for multiple testing with the Benjamini-Hochberg procedure. A regularized log (rlog) transformation was subsequently applied to gene expression counts.

Clustering by principal component analysis was performed using rlog gene expression counts and plotted by experimental group using the R package factoextra (49). Volcano plots were created to highlight the most strongly changed transcripts between groups. Differentially expressed transcripts between experimental groups, considered as those with an absolute fold-change ≥1.3 and adjusted p-value <0.05, were used as the input for functional enrichment analyses. Pathways (Reactome database) and gene ontology terms over-represented between all experimental groups were examined using the function 'compareCluster' in the R package clusterProfiler (50). Pathway over-representation analysis between the RYGB-FMRR and RYGB groups was performed using the function 'enrichPathway' in the R package ReactomePA (51). Upstream regulator analysis was performed using Ingenuity Pathway Analysis (IPA) (52).

After converting rat ENSEMBL gene identifiers to human ENTREZ gene identifiers using the R package biomaRt (53), the abundance of renal cortical immune and stromal cell populations was estimated by inputting rlog gene expression counts to the function 'MCPcounter.estimate' from the Microenvironment Cell Populations-counter (MCP-counter) R package (54). Cell abundance estimates were subsequently plotted on a heatmap using the R package pheatmap (55).

In Silico Deconvolution of the Predicted Cellular Source of Transcripts

To interrogate localization of transcripts differentially expressed between the RYGB and RYGB-FMRR groups, we accessed a publicly available human kidney single-nucleus RNA-sequencing dataset containing samples from 3 individuals with early DKD (56). Raw gene expression counts and cell assignments were obtained. The data were analyzed according to standard single cell clustering workflows in the R package Seurat, including normalization, identification of variable features between cells, scaling, dimensionality reduction, cell clustering, and ultimately the assignment of identity to clusters of cell types (57). Assignment of cluster identity was cross-checked with the human diabetic kidney dataset on the Kidney Interactive Transcriptomics website (http://humphreyslab.com/SingleCell/), which is the same dataset analyzed herein. Average expression of each transcript across the defined cell types was calculated using the function 'AverageExpression'. Transcripts differentially expressed between the RYGB and RYGB-FMRR groups, after conversion to their human orthologs (53), were intersected with the human diabetic kidney gene expression matrix and plotted on a heatmap to explore their cell-specific expression patterns (55). Violin plots of cell type expression of three transcripts, *Acox1*, *Ehhadh*, and *Acaa2*, were generated with the Seurat function 'VlnPlot'.

Further interrogation of the localisation of transcripts differentially expressed between the RYGB-FMRR and RYGB groups was performed using a proteomics dataset of 14 rat tubular epithelial cell types (58), which offered improved granularity for predicted localisation of transcripts along the renal tubule. The proteomics data was downloaded from the Kidney Tubules Expression Atlas website (https://esbl.nhlbi.nih.gov/KTEA/) and imported into RStudio (47). Transcripts differentially expressed between the RYGB-FMRR and RYGB groups were intersected with the rat tubular epithelial cell protein expression matrix and plotted on a heatmap (55). Line plots of cell type expression of three proteins, ACOX1, EHHADH, and ACAA2, were generated.

In Silico Deconvolution of Medication- and PPAR Isotype-Specific Transcriptomic Responses Using a Network Pharmacology Approach

As the four medications were provided concurrently to rats in the RYGB-FMRR group, we employed a network pharmacology approach to discern contributions of individual medications to transcriptomic differences between the RYGB-FMRR and RYGB groups. We also explored contributions of individual PPAR isotypes in this regard, given the over-representation of PPAR-governed mitochondrial and peroxisomal FAO pathways observed between the two groups.

Genes responsive to FMRR medications (fenofibrate, metformin, ramipril, and rosuvastatin) and PPAR isotypes (alpha, beta/delta, and gamma) were obtained using IPA (52). Separate lists of the four medications, alongside their corresponding cardinal drug targets, as well as the three PPAR isotypes were generated in IPA. For each list, a network was grown using the 'Grow' tool in the 'Build' section of the 'My Pathways' interface. An additional network was grown for all four medications and their cardinal drug targets simultaneously to create a network visualisation of medication-responsive genes contained within the RYGB-FMRR vs RYGB differentially expressed gene (DEG) list. Molecules within the network were limited to RYGB-FMRR vs RYGB DEGs when growing the network in IPA. Only experimentally observed relationships were permitted. Drug, chemical, disease, and function categories were excluded.

The data underlying the individual networks constructed for each medication and PPAR isotype were exported as a.txt file and imported into RStudio (47). Orthologous rat genes were obtained by converting the rat Entrez ID (contained within IPA export) to rat gene symbol using the R packages AnnotationDbi and org.Rn.eg.db (59, 60). The target gene data for each medication and PPAR isotype was intersected with the RYGB-FMRR vs RYGB DEG list on the basis of gene symbol.

Doughnut plots were generated to illustrate the number and percentage of medication- and PPAR-responsive genes identified in IPA, stratified by medication type/PPAR isotype (inner layer) as well as presence in or absence from the RYGB-FMRR vs RYGB DEG list (outer layer). For the subsets of medication- and PPAR-responsive genes present in the RYGB-FMRR vs RYGB DEG list, Venn diagrams were created using the R package ggvenn to illustrate the overlap and separation in transcripts responsive to each of the four medications and each of the three PPAR isotypes (61).

To interrogate cellular localisation along the renal tubule, medication- and PPAR-responsive transcripts contained within the RYGB-FMRR vs RYGB DEGs were intersected with a rat tubular epithelial cell protein expression matrix (58). Protein abundance across all non-proximal tubular cell types was collapsed into a 'Rest of tubule' category by obtaining row-wise means across the relevant cell types. Cell type-specific abundance of medication- and PPAR-responsive transcripts present in the RYGB-FMRR vs RYGB DEGs was plotted on heatmaps (55). Transcripts clustered on the heatmaps based on relative abundance along the renal tubule; this information was extracted from the heatmap dendrograms and transcripts were accordingly classified as belonging to one of two categories, the proximal tubule or the rest of the renal tubule, based on site of maximal abundance. Doughnut plots were subsequently generated for the medication- and PPAR-responsive transcripts present in the RYGB-FMRR vs RYGB DEGs to summarise the number and percentage of transcripts stratified by fenofibrate- or PPARα-responsiveness (inner layers), presence or absence from the tubular epithelial cell proteomics dataset (middle layers), and localisation in either the proximal tubule or the rest of the renal tubule (outer layers).

Pathway over-representation analysis was performed for the subsets of fenofibrate- and PPARα-responsive transcripts present in the RYGB-FMRR vs RYGB DEGs using the function 'enrichPathway' in the R package ReactomePA (51), with results presented on a dotplot.

Metabolomic Analyses: Nuclear Magnetic Resonance Spectroscopy

^{1}H-NMR spectroscopy was performed on timed urine samples obtained at baseline and at 4 weeks after intervention according to standard Bruker *In Vitro* Diagnostics for research (IVDr) methods. Urine samples were thawed at room temperature for 20 min before a brief spin at 2000 g at 4°C for 10 min. NMR samples for 5 mm SampleJet racks were prepared by mixing 9 parts urine with 1 part urine buffer (1.5 M KH_2PO_4 pD 6.95, 0.5% w/v NaN_3, 0.1% w/v 3-trimethylsilyl propionic-2,2,3,3 acid sodium salt D4 (TSP-d4) in 99.8% D_2O) using a SamplePro Tube L liquid handling robot (Bruker BioSpin). The temperature was kept at 279 K throughout the sample preparation process. ^{1}H-^{1}H total correlation spectroscopy (TOCSY) POM balls were added to tube caps in the finished sample tube rack before placing the rack in the cooled SampleJet sample changer on the spectrometer. 1D Nuclear Overhauser Effect Spectroscopy (NOESY), 1D Carr-Purcell-Meiboom-Gill (CPMG) and 2D J-resolved experiments were acquired for each sample with a 600 MHz Bruker Avance III HD spectrometer at 300 K equipped with a 5 mm BBI room temperature probe, using the pulse sequences 'noesygppr1d', 'cpmgpr1d' and 'jresgpprqf', respectively, according to the IVDr SOP. Urine samples were randomised during sample preparation such that samples from each experimental group were evenly distributed during data acquisition. Pooled samples containing aliquots of samples from each of the study groups were included as an internal quality control. TSP-d4 was used for internal chemical shift referencing.

To facilitate metabolite annotation, a set of 2D experiments on four selected samples were acquired on an Oxford 800 MHz magnet equipped with a Bruker Avance III HD console, a 3 mm TCI cryoprobe and a cooled SampleJet sample changer. ^{13}C-HSQCs were acquired using the pulse sequence 'hsqcedetgpsisp2.3' using spectral widths of 20 and 90 ppm in the direct and indirect dimensions, respectively, collecting 64 scans per increment for a total of 512 increments and 2048 data points. The acquisition time was 63.9 and 14 ms for the direct and indirect dimensions, respectively, and the relaxation delay was 1.5 s. ^{1}H-^{1}H-TOCSYs were acquired using the pulse sequence 'dipsi2esgpph' with sweepwidths in both dimensions of 12 ppm, collecting 16 scans per increment into 512 increments and 8192 data points. Acquisition times were 0.426 s and 26.6 ms for the direct and indirect dimensions, respectively. The TOCSY transfer delay was 60 ms and the relaxation delay between scans was 1 s. ^{1}H-^{1}H-COSYs were acquired with the pulse sequence 'cosygpppqfpr'. Sweepwidths were 13.95 ppm in both dimensions; 4 scans per increment were collected to a total of 1024 increments and 2048 data points. The acquisition time was 92 ms and the relaxation delay 2 s. All 2D spectra were referenced to TSP-d4.

^{1}H-NMR Spectral Processing

The 1D NOESY spectra destined for peak picking and multivariate analysis were zero-filled twice before Fourier transformation into 132k data points, including addition of 0.3 Hz exponential line-broadening and referencing to TSP-d4. Spectra were processed in TopSpin3.5pl7 (Bruker BioSpin). The 1D NOESY spectra were loaded into Matlab using RBNMR (62). Baseline correction of the spectra was performed due to the high urinary glucose concentrations present in untreated ZDSD rats using the command 'msbackadj' with window size set to 1000, quantile set to 0.1, and stepsize set to 500 (63). Further analysis of NMR data was performed using the R statistical programming language (4.0.5) (47). Spectra and parts per million (ppm) chemical shift values were imported and processed to a peak intensity matrix according to a standard workflow using the R package Speaq (64). Peak detection was performed using a Mexican hat wavelet method implemented by the function getWaveletPeaks. Detected peaks were aligned and grouped to a single ppm index value using the function PeakGrouper. Illustrative examples of raw spectra, peak detection, and peak grouping/alignment using Speaq for two peaks of interest are presented in **Supplemental Figure 1**. Silhouette values were calculated as a metric of the quality of peak grouping using the function SilhouetR. Peak groupings with a silhouette value less than 0.6 were removed and the peaks

regrouped with the function regroupR – this process was repeated iteratively until all peak groupings had a silhouette value ≥0.6. Peak filling was performed to detect peaks that may have been missed during the first round of peak detection. Finally, a peak intensity matrix was built with grouped peaks (identified by their ppm shift values) as columns and samples as rows. A probabilistic quotient normalisation (PQN) was applied to the peak intensity matrix (65, 66), which was subsequently used as the input for multivariate statistics. Annotation of processed spectra was performed using Chenomx 8.6 software (Chenomx Inc.), the Human Metabolome Database (HMDB), and the Biological Magnetic Resonance Data Bank (BMRB) (67–69).

^{1}H-NMR Clustering Analyses and Classification Modeling

Clustering by principal component analysis was performed using PQN-normalised NMR peak intensities and plotted by phenotype as biplots along principal components 1-4 using the R package factoextra (49). To elucidate differences in the urinary metabolome between RYGB and RYGB-FMRR rats at 4 weeks after intervention, the R package MUVR was used to fit a multivariate random forest (RF) classification model to a PQN-normalised NMR peak intensity matrix for post-intervention samples from RYGB and RYGB-FMRR rats (70). A response vector indicating experimental group assignment was inputted to the supervised model. The MUVR algorithm minimises overfitting in multivariate modelling by performing recursive elimination of the least informative variables in a repeated double cross-validation procedure (70). The following modelling parameters were used as recommended: nOuter=5 (number of outer cross-validation segments, to ensure both classes were present in all model segments), nRep=100 (number of model repetitions), and varRatio=0.85 (proportion of variables maintained in the data per model iteration during variable elimination) (70).

MUVR returns three consensus models (min, mid, and max) with similar fitness (70). The max RF model, which attempts to consider all relevant predictors without compromising classification performance, was selected to identify as many urinary NMR peaks relevant to classifying RYGB and RYGB-FMRR status as possible. Model stability across 100 repetitions was ensured by inspecting the number and proportion of selected variables as well as the number of classifications, per repetition and cumulatively; model convergence occurred by 20 model repetitions. The number of model misclassifications was used to assess model performance. Additional performance metrics (area under the curve, sensitivity, and specificity) were calculated using the R package caret (71). Mean decrease in Gini index was used to rank variable (urinary ^{1}H-NMR peak) importance to RF model classification.

Multi-Omic Integration of RNA-Seq and ^{1}H-NMR Data

Multi-omic integration of the renal cortical transcriptome and urinary metabolome was performed using the DIABLO (data integration analysis for biomarker discovery using latent variable approaches for omics studies) framework in the R package mixOmics (72, 73). A supervised, sparse partial least squares-discriminant analysis (PLS-DA) model was fit to rlog gene expression counts and annotated, PQN-normalized urinary ^{1}H-NMR peaks from 4 weeks after intervention. Lowly expressed transcripts were removed from the gene expression count matrix derived from RNA-Seq to reduce the number of inputted transcripts to ~10,000 as recommended to reduce computational time (72). This was performed by removing transcripts for which all samples had an rlog count value <7.

Several aspects of the sparse DIABLO model were tuned to identify a gene-metabolite signature distinguishing the RYGB-FMRR group from the other experimental groups, including the number of model components, the number of features to select from each omics dataset for each model component, and the design matrix (ranging between 0-1 and specifying the extent to which datasets should be connected to maximise the covariance beween components) (73). The following modelling parameters were used after tuning: ncomp=3 (number of model components); number of transcripts to consider for each of the 3 model components: 50; number of metabolites to consider for each of the 3 model components: 10, 20, and 10; and a design matrix value of 0.3 to maximise discrimination between RYGB-FMRR rats and the other experimental groups. Plots of variable loadings (importance) along the model components were generated. A network visualisation of the gene-metabolite signature distinguishing RYGB-FMRR rats from the other experimental groups was generated in mixOmics and edited in Cytoscape (3.7.2) after export using the R package RCy3 (72, 74, 75).

Correlations Between Kidney Structure, Renal Cortical Transcripts, and Urinary Metabolites

The relationships between changes in kidney structure with changes in renal cortical transcript expression and urinary metabolite abundance were investigated. Pearson correlation matrices between mean values for histological and ultrastructural parameters and rlog gene expression counts as well as PQN-normalised urinary NMR peaks from 4 weeks post-intervention were constructed on a per animal basis. Gene-structure correlations for transcripts which belonged to enriched pathways between RYGB and RYGB-FMRR rats by over-representation analysis were extracted. Metabolite-structure correlations for selected metabolites which were differentially abundant between RYGB and RYGB-FMRR rats were extracted. Correlation matrices were plotted using ggcorrplot (76).

Descriptive and Inferential Statistics

Study endpoints, statistical tests by which they were analyzed, and location within the manuscript are presented in **Table 1**. Percentage delta change in metabolic parameters (body weight and plasma glucose) and urinary albumin excretion rates (natural logarithm-transformed) were calculated. Statistical

analyses were performed using the R package rstatix in RStudio (R version 4.0.5) (47, 77). For tests involving comparisons between more than two groups, a Benjamini-Hochberg multiplicity correction of p–values was applied. P <0.05 was considered statistically significant. Study endpoints are plotted as violin plots or boxplots, with individual data points for each animal superimposed (78). For histological and ultrastructural data, individual measurements for each animal within each group are plotted to provide additional insight into data distribution (78).

RESULTS

Greater Improvements in Metabolic Control and Albuminuria Following RYGB-FMRR Compared With RYGB

Body weight decreased from 570.8±23.0 to 452.7±32.2 g (mean ±SD) following RYGB (p<0.001) and from 564.0±20.4 to 410.0 ±24.2 g following RYGB-FMRR (p<0.001) (**Table 2**). Weight loss was greater in the RYGB-FMRR group compared with the RYGB group (-27.3±3.8 vs -20.7±4.7%, p=0.01).

Comparing pre- and post-intervention plasma glucose concentrations, the SHAM group deteriorated by 84.3 ± 95.9% (13.3±6.4 vs 23.2±11.5 mmol/L, p=0.06). Over the same timeframe, RYGB-operated animals improved by 15.7±25.5% (13.0±4.3 vs 11.7±7.5 mmol/L, p=0.30) and the RYGB-FMRR group improved by 50.5±13.0% (13.4±4.9 vs 6.2±1.7 mmol/L, p=0.007). Improvements in glycaemia were greater in the RYGB-FMRR group compared with RYGB-operated animals (p=0.02). Serum cholesterol and triglycerides were elevated in SHAM compared with SD rats. Compared with SHAM rats, RYGB and RYGB-FMRR lowered both serum cholesterol and serum triglycerides, with no differences observed between both interventions (p=0.33 for cholesterol; p=0.81 for triglycerides).

Comparing pre- and post-intervention log UAER, the SHAM group deteriorated by 37.2±30.3% (4.8±0.8 vs 6.8±2.2 µg/hour, p=0.03). RYGB-operated animals improved by 10.6±22.8% (5.1 ±0.5 vs 4.5±1.2 µg/hour, p=0.32) and the RYGB-FMRR group improved by 36.4±17.5% (5.0±0.8 vs 3.1±0.9 µg/hour, p=0.003). Improvements in albuminuria were greater in the RYGB-FMRR group compared with RYGB-operated animals (p=0.03).

Renal Transcriptome Profiling Identifies Enhanced FAO Following RYGB-FMRR

Principal component analysis of kidney RNA-Seq data identified discrete shifts across groups (**Figure 2A**). RYGB-FMRR altered more transcripts (n=1982 vs n=987) and corrected more disease-associated transcripts (i.e., those that were altered between SD and SHAM, n=871 vs 453) than RYGB. Lists of differentially expressed genes between the study groups are available at: https://osf.io/cf7v5/. Volcano plots emphasize that RYGB-FMRR induced more transcripts than RYGB (**Supplemental Figure 2**).

Both RYGB and RYGB-FMRR downregulated cell cycle and fibrosis pathways while restoring biological oxidation capacity (**Figure 2B**), as seen previously after RYGB in the ZDF rat (12). The magnitude of fibrosis pathway downregulation was greater after RYGB-FMRR compared with RYGB. Using MCP-counter (54), SHAM-operated animals were predicted to have an increased relative abundance of renal cortical fibroblasts compared with SD controls (**Figure 2C**). Congruent with pathway analysis, both RYGB and RYGB-FMRR were

TABLE 1 | Study endpoints and statistical tests by which they were analyzed[a].

Endpoint	Statistical Method	Location	Unit of Analysis
Within-group differences in body weight, plasma glucose, and log UAER from baseline to follow-up[a]	Paired t-test with multiplicity correction (Benjamini-Hochberg)	**Table 2**	Per animal
Between-group differences in percentage delta change in body weight, plasma glucose, and log UAER from baseline to follow-up, and in serum cholesterol and triglycerides at study close	Unpaired t-test with multiplicity correction (Benjamini-Hochberg)	**Table 2**	Per animal
Between-group differences in qRT-PCR data (kidney, liver, and epididymal fat)	Wilcoxon rank-sum test with multiplicity correction (Benjamini-Hochberg)	**Figure 2** **Supplemental Figure 4**	Per animal
Between-group differences in histological (glomerular volume) and ultrastructural (podocyte foot process frequency, podocyte foot process diameter, glomerular basement membrane thickness, and mitochondrial roundness) parameters	Wilcoxon rank-sum test with multiplicity correction (Benjamini-Hochberg)	**Figure 8B** **Figure 9B–D** **Figure 10B–D**	Per individual structural measurement
Correlations between renal cortical transcripts and urinary metabolites with morphometric parameters of glomerular and proximal tubular injury	Pearson correlations	**Figure 8C** **Figure 9E** **Figure 10E**	Per animal
Differences in mitochondrial morphology between the pars convoluta and pars recta proximal tubular sections	Wilcoxon rank-sum test	**Supplemental Figure 5**	Per individual structural measurement
Differences in mitochondrial roundness between RYGB and RYGB-FMRR animals matched for improvements in metabolic control and albuminuria	Wilcoxon rank-sum test	**Figure 11**	Per individual structural measurement

[a]*qRT-PCR, quantitative reverse-transcription polymerase chain reaction; RYGB, Roux-en-Y gastric bypass; RYGB-FMRR, Roux-en-Y gastric bypass plus fenofibrate, metformin, ramipril, and rosuvastatin; UAER, urinary albumin excretion rate.*

TABLE 2 | Changes in body weight, plasma glucose, urinary albumin excretion, and serum lipids by experimental group.[a,b,c]

	Pre-post intervention comparisons (absolute values)[d]											
	SD			SHAM			RYGB			RYGB-FMRR		
	Pre	Post	p	Pre	Post	p	Pre	Post	p	Pre	Post	p
Body weight (g)	564.2 ±28.3	603.5 ±31.5	0.002	592.4 ±35.7	486.7 ±76.8	0.09	570.8±23.0	452.7 ±32.2	<0.001	564.0±20.4	410.0 ±24.2	<0.001
Plasma glucose (mmol/L)	5.3±0.2	6.0±1.0	0.12	13.3±6.4	23.2 ±11.5	0.06	13.0±4.3	11.7±7.5	0.30	13.4±4.9	6.2±1.7	0.007
Log UAER (µg/hour)	3.3±0.4	3.4±0.5	0.47	4.8±0.8	6.8±2.2	0.03	5.1±0.5	4.5±1.2	0.32	5.0±0.8	3.1±0.9	0.003

	Pre-post intervention comparisons (percentage delta change values)[e]							
	Percentage delta change values				P-values for comparisons			
	SD	SHAM	RYGB	RYGB-FMRR	SHAM vs SD	RYGB vs SHAM	RYGB-FMRR vs SHAM	RYGB-FMRR vs RYGB
Δ Body weight (%)	7.0±2.7	-8.3±10.5	-20.7 ±4.7	-27.3±3.8	0.01	0.02	0.008	0.01
Δ Plasma glucose (%)	12.9 ±14.7	84.3±95.9	-15.7 ±25.5	-50.5±13.0	0.10	0.04	0.02	0.02
Δ Log UAER rate (%)	3.3±9.5	37.2±30.3	-10.6 ±22.8	-36.4±17.5	0.03	0.01	0.001	0.03

	Study close comparisons[e]							
	Study close values				P-values for comparisons			
	SD	SHAM	RYGB	RYGB-FMRR	SHAM vs SD	RYGB vs SHAM	RYGB-FMRR vs SHAM	RYGB-FMRR vs RYGB
Serum cholesterol (mmol/L)	1.78 ±0.11	2.66±0.42	2.15 ±0.26	2.26±0.19	0.004	0.04	0.07	0.33
Serum triglycerides (mmol/L)	0.85 ±0.19	2.37±1.43	1.13 ±0.21	1.08±0.38	0.08	0.08	0.08	0.81

[a]*RYGB, Roux-en-Y gastric bypass; RYGB-FMRR, Roux-en-Y gastric bypass plus fenofibrate, metformin, ramipril, and rosuvastatin; SD, Sprague Dawley; SHAM, sham surgery (laparotomy); UAER, urinary albumin excretion rate.*

[b]*Body weight was assessed at 8 weeks after intervention, while plasma glucose and urinary albumin excretion were assessed at 4 weeks post-intervention.*

[c]*Values are given as mean ± SD.*

[d]*Statistical significance of within-group differences are derived from multiplicity-corrected (Benjamini-Hochberg) paired t-tests.*

[e]*Statistical significance of between-group differences are derived from multiplicity-corrected (Benjamini-Hochberg) unpaired t-tests.*

predicted to decrease the relative abundance of renal cortical fibroblasts, with the magnitude of reduction being greater following RYGB-FMRR (**Figure 2C**).

Enrichment of fatty acid metabolism pathways was a unique and dominant transcriptomic response to RYGB-FMRR, which contrasted with decreased fatty acid metabolism, and in particular peroxisomal lipid metabolism, in SHAM-operated rats (**Figure 2B**). Peroxisomal and mitochondrial pathways upregulated by RYGB-FMRR are plotted to illustrate the abundance of peroxisome proliferator-activated receptor-alpha (PPARα)-responsive transcripts (for example, *Acox1, Ehhadh, Acaa2*) causing FAO pathway enrichment (**Figure 2D**). Gene ontology testing reinforced the unique stimulation of long-chain and very-long-chain fatty acid (VLCFA) metabolism, peroxisomal and mitochondrial activity, and fatty acid acyltransferase activity by RYGB-FMRR (**Supplemental Figures 3A–C**).

Activation of PPARα was predicted to increase FAO following RYGB-FMRR by upstream regulator analysis (**Figure 2E**). We validated renal expression of peroxisomal (*Acox1*, *Ehhadh*) and mitochondrial (*Acaa2*) PPARα-responsive transcripts by qRT-PCR (**Figure 2F**). PPARα-response genes were induced by RYGB-FMRR in the liver but not in visceral adipose tissue (**Supplemental Figure 4**). Renal cortical induction of the mitochondrial enzyme pyruvate dehydrogenase kinase 4 (*Pdk4*), which is a sensitive transcriptional marker of increased FAO (79), was also validated by qRT-PCR.

FAO Transcripts Induced by RYGB-FMRR Map to the Proximal Tubule

We assessed cell type-specific expression patterns of transcripts in a human diabetic kidney single-nucleus RNA-sequencing dataset and in a rat tubular epithelial cell proteomics dataset (56, 58). Transcripts differentially regulated between the RYGB and RYGB-FMRR groups were most commonly expressed in the proximal tubule of the human and rat kidney (**Figures 3A, C**), and included PPARα-responsive genes with roles in peroxisomal (*Acox1*, *Ehhadh*) and mitochondrial (*Acaa2*) FAO (**Figures 3B, D**). We validated the proximal tubular enrichment of ACOX1 as well as its induction following RYGB-FMRR by immunohistochemistry (**Figure 3E**).

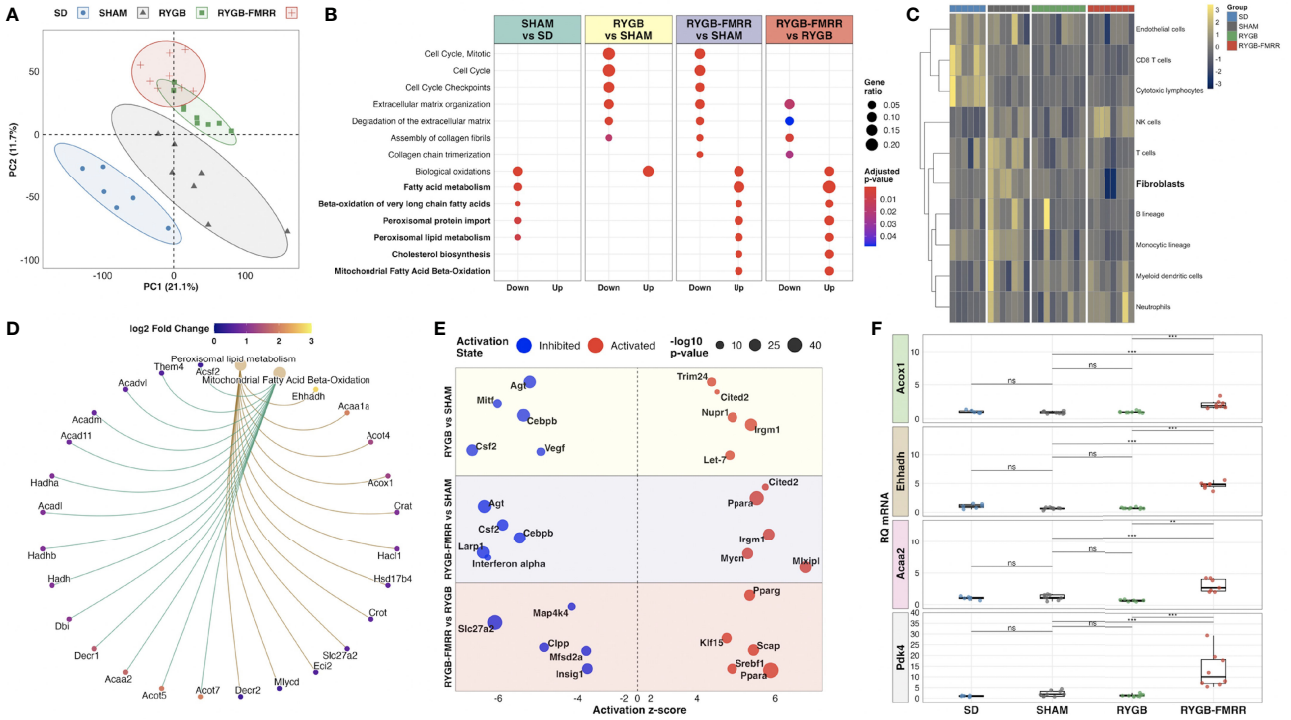

FIGURE 2 | Characterization of renal cortical transcriptomic changes across the experimental groups. **(A)** Principal component analysis of regularized log-transformed gene expression counts demonstrates renal cortical transcriptomic differences according to group assignment. **(B)** Dotplot of Reactome pathway over-representation analysis illustrating pathways commonly changed by both RYGB and RYGB-FMRR, and those uniquely changed by RYGB-FMRR (50). Dot colour represents the adjusted p-value for pathway enrichment while dot size is scaled by the gene ratio. Pathways pertaining to fatty acid metabolism are bolded. **(C)** Heatmap visualization of abundance estimates of eight immune and two stromal cell populations obtained using the Microenvironment Cell Populations-counter (MCP-counter) R package (54). Cell abundance estimates were centred and scaled by heatmap row. Each heatmap row displays abundance of a different cell population. Heatmap columns correspond to individual rats. Gaps between columns as well as the column annotations demarcate the four experimental groups from left to right: SD (blue), SHAM (grey), RYGB (green), and RYGB-FMRR (red). Colouring of heatmap cells reflects relative cell abundance between rats: navy = low relative abundance, yellow = high relative abundance. **(D)** Circular network plot of two fatty acid metabolism pathways uniquely changed by RYGB-FMRR (51). Pathways are represented by the brown nodes at the top of the network. Gene nodes are connected to the brown pathway nodes by coloured edges (gold = peroxisomal; green = mitochondrial). Individual gene nodes are coloured according to magnitude of log2 fold change in transcript abundance in the RYGB-FMRR group relative to the RYGB group. **(E)** Bubble plot of predicted upstream regulators of gene expression changes (Ingenuity Pathway Analysis) (52). Upstream regulator changes are presented for 3 comparisons: RYGB vs SHAM, RYGB-FMRR vs SHAM, and RYGB-FMRR vs RYGB. The predicted status (inhibited or activated) of upstream regulators is plotted according to z-score. Dot size is scaled to reflect the statistical significance of z-score changes. **(F)** Quantitative reverse-transcription PCR validation of renal cortical expression changes in three PPARα-responsive transcripts, both peroxisomal (*Acox1*, *Ehhadh*) and mitochondrial (*Acaa2*), as well as the mitochondrial enzyme *Pdk4*, which is a sensitive transcriptional marker of FAO induction. The full data range in each group is captured in boxplots, with gene expression levels of individual constituent samples superimposed. Statistical significance of between-group differences derived from multiplicity-corrected Wilcoxon rank-sum tests is presented. Statistical significance is denoted as follows: ns = not significant; * = p <0.05; ** = p <0.01; *** = p <0.001; **** = p <0.0001. *Acaa2*, acetyl-Coenzyme A acyltransferase 2; *Acox1*, acyl-CoA oxidase 1; *Ehhadh*, enoyl-CoA hydratase and 3-hydroxyacyl CoA dehydrogenase; PC, principal component; *Pdk4*, pyruvate dehydrogenase kinase 4; RQ mRNA, relative quantification of messenger ribonucleic acid; RYGB, Roux-en-Y gastric bypass; RYGB-FMRR, Roux-en-Y gastric bypass plus fenofibrate, metformin, ramipril, and rosuvastatin; SD, Sprague Dawley; SHAM, sham surgery (laparotomy).

Fenofibrate and PPARα Are the Dominant Regulators of Proximal Tubular FAO Transcripts Following RYGB-FMRR

Using a network pharmacology approach, we assessed the magnitude, cellular localisation, and biological pathways associated with medication- and PPAR isotype-specific transcriptomic responses in rats treated with RYGB-FMRR compared with RYGB alone. Compared with other medications administered to RYGB-FMRR rats, there was a greater number of fenofibrate-responsive genes present in the RYGB-FMRR vs RYGB DEG list, both in absolute numbers (n=115 transcripts) and as a proportion of all genes known to be changed by fenofibrate (13%; **Figure 4A**). Overall, 129 genes in the RYGB-FMRR vs RYGB DEG list were found to be responsive to one or more of the four medications in the FMRR combination, with 115 (89%) of these being fenofibrate-responsive (**Figure 4B**). Of the medication-responsive transcripts present in both the RYGB-FMRR vs RYGB DEG list and a rat tubular epithelial cell proteomics dataset (58), 86% of the fenofibrate-responsive transcripts were found to be proximal tubular-abundant,

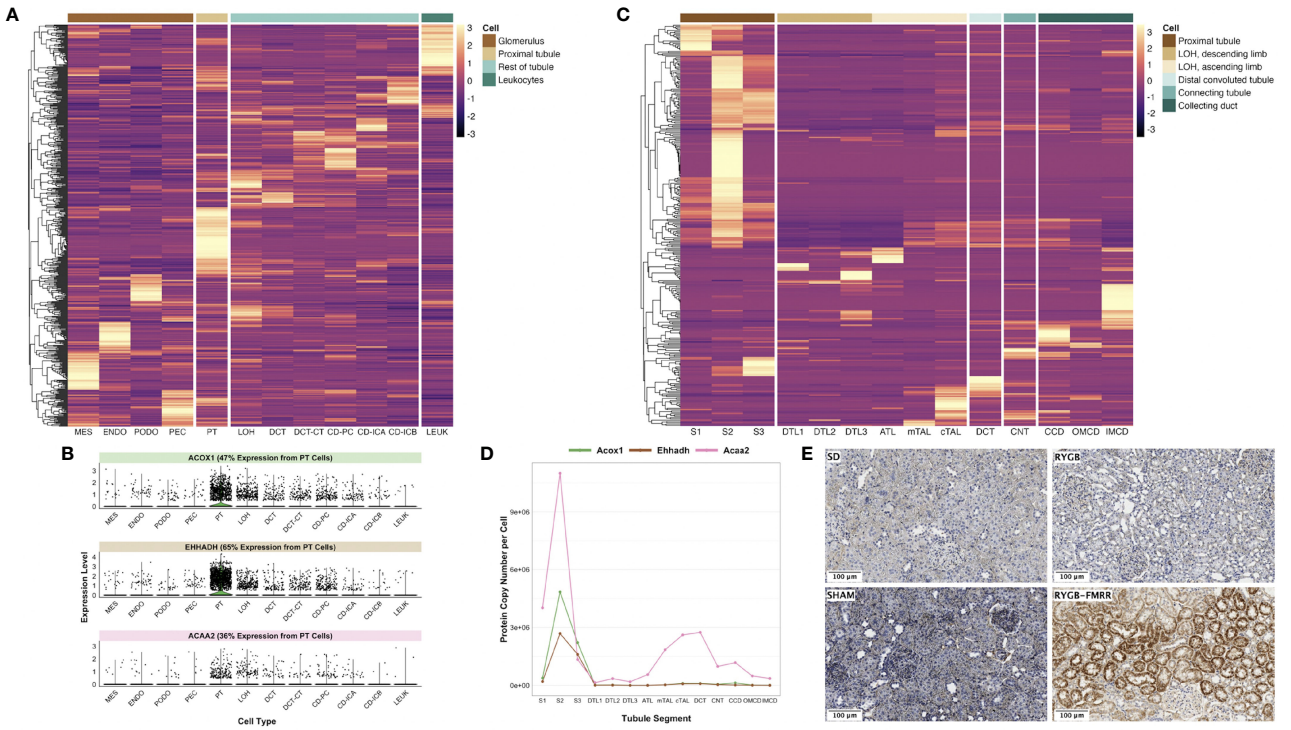

FIGURE 3 | *In silico* deconvolution of the predicted cellular source of transcripts differentially expressed between the RYGB-FMRR and RYGB groups. **(A)** Transcripts identified in the RYGB-FMRR versus RYGB differential expression analysis were intersected with a human diabetic kidney single-nucleus RNA-sequencing dataset (56). Transcript expression levels in the human diabetic kidney, averaged across cell types by the Seurat function 'AverageExpression' and subsequently centred and scaled by row, are plotted on the heatmap. Heatmap rows display the differentially regulated transcripts whilst each column represents 1 of 12 identified renal cell types. Cell groupings of individual cell types in the heatmap columns are indicated in the legend key. An increasingly light colour in a specific cell type reflects an increased relative expression therein relative to other cell types. **(B)** Violin plots of cell-specific expression in the human diabetic kidney of three PPARα-responsive transcripts upregulated by RYGB-FMRR. Kidney cell types are presented on the x-axis with relative transcript expression levels in the human diabetic kidney on the y-axis. Each dot represents a single cell in the human diabetic kidney. The proportion of expression of each transcript by proximal tubular cells as a proportion of all cells identified in the single-nucleus RNA-sequencing dataset is indicated. **(C)** Transcripts identified in the RYGB-FMRR versus RYGB differential expression analysis were intersected with a proteomics dataset of microdissected Sprague Dawley rat kidney tubules (https://esbl.nhlbi.nih.gov/KTEA/) (58). Protein expression (copy number per cell) in rat tubular epithelial cells is plotted on the heatmap, after centering and scaling by row. Heatmap rows display the differentially regulated transcripts between RYGB-FMRR and RYGB whilst each column represents 1 of 14 rat tubular epithelial cell types. Cell groupings of individual cell types in the heatmap columns are indicated in the legend key. An increasingly light colour in a specific cell type reflects an increased relative expression therein relative to other cell types. **(D)** Line plots of cell-specific expression in rat tubular epithelial cells of three PPARα-responsive transcripts upregulated by RYGB-FMRR. Tubular epithelial cell types are presented on the x-axis with protein expression (copy number per cell) in rat tubular epithelial cells on the y-axis. **(E)** Representative images (20x, scale bar 100µm) of kidney immunohistochemical ACOX1 staining across the four experimental groups, validating the proximal tubular localisation of ACOX1 as well as its induction in rats treated with RYGB-FMRR. ACAA2, acetyl-coenzyme A acyltransferase 2; ACOX1, acyl-CoA oxidase 1; ATL, ascending thin limb of Henle's loop; CCD, cortical collecting duct; CD-ICA, collecting duct-intercalated cell type A; CD-ICB, collecting duct-intercalated cell type B; CD-PC, collecting duct-principal cell; CNT, connecting tubule; cTAL, cortical thick ascending limb; DCT, distal convoluted tubule; DCT-CT, distal convoluted tubule-connecting tubule; DTL1, descending thin limb of Henle's loop, short-loop; DTL2, descending thin limb of Henle's loop, long-loop, outer medulla; DTL3, descending thin limb of Henle's loop, long-loop, inner medulla; ENDO, endothelial cell; EHHADH, enoyl-CoA hydratase and 3-hydroxyacyl CoA dehydrogenase; IMCD, inner medullary collecting duct; LEUK, leukocytes; LOH, loop of Henle; MES, mesangial cell; mTAL, medullary thick ascending limb; OMCD, outer medullary collecting duct; PEC, parietal epithelial cell; PODO, podocyte; PPARα, peroxisome proliferator-activated receptor-alpha; PT, proximal tubule; RYGB, Roux-en-Y gastric bypass; RYGB-FMRR, Roux-en-Y gastric bypass plus fenofibrate, metformin, ramipril, and rosuvastatin; S1, S1 region of proximal tubule; S2, S2 region of proximal tubule; S3, S3 region of proximal tubule; SD, Sprague Dawley; SHAM, sham surgery (laparotomy).

compared with only 40% of transcripts responsive to one or more of metformin, ramipril, or rosuvastatin, but not fenofibrate (**Figure 4C**).

Similarly, compared with other PPAR isotypes, there was a greater number of PPARα-responsive genes present in the RYGB-FMRR vs RYGB DEG list, both in absolute numbers (n=95 transcripts) and as a proportion of all genes known to be changed by PPARα (15%; **Figure 4D**). Overall, 133 genes in the RYGB-FMRR vs RYGB DEG list were found to be responsive to one or more PPAR isotypes, with 95 (71%) of these being PPARα-responsive (**Figure 4E**). Of the PPAR isotype-responsive transcripts present in both the RYGB-FMRR vs RYGB DEG list and a rat tubular epithelial cell proteomics dataset (58), 86% of the PPARα-responsive transcripts were

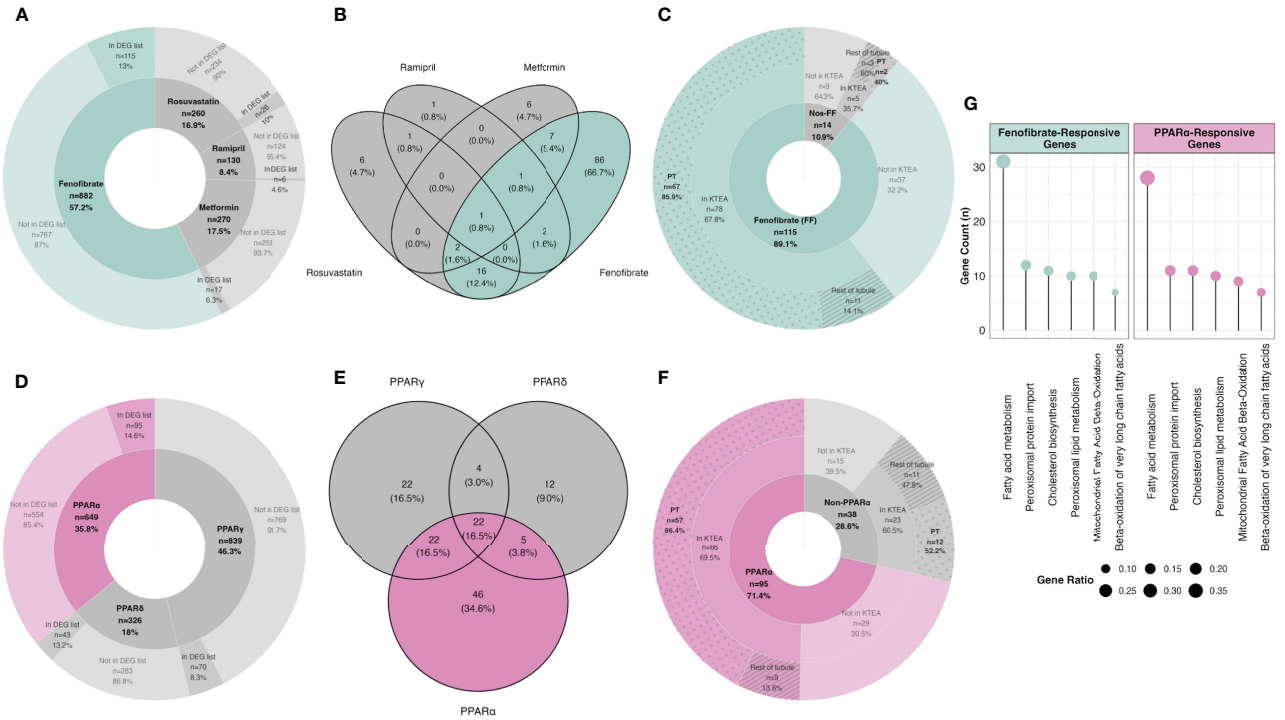

FIGURE 4 | *In silico* deconvolution of medication-specific and PPAR isotype-specific transcriptomic effects following RYGB-FMRR. **(A, D)** Genes responsive to FMRR medications **(A)** and PPAR isotypes **(D)** were retrieved from IPA, intersected with transcripts identified in the RYGB-FMRR versus RYGB differential expression analysis, and presented on doughnut plots with counts and percentages of transcripts in each category outlined. The inner doughnut layers outline all transcripts known to be responsive to each medication **(A)** or PPAR isotype **(D)**. The outer layers stratify transcripts by presence in or absence from the RYGB-FMRR vs RYGB DEG list. **(B, E)** Venn diagram enumeration of the overlap and separation in transcripts present in the RYGB-FMRR vs RYGB DEG list and responsive to one or more of the FMRR medications **(B)** or one or more of the PPAR isotypes **(E)**. These transcripts are labelled as 'In DEG list' in the outer doughnut layers in **(A, D)**, respectively. **(C, F)** Subsets of genes present in the RYGB-FMRR vs RYGB DEG list and found to be responsive to FMRR medications **(C)** or PPAR isotypes **(F)** are presented on doughnut plots with counts and percentages of transcripts in each category outlined. Transcripts are stratified by fenofibrate- **(C)** or PPARα- **(F)** responsiveness (inner layers), presence or absence from Kidney Tubules Expression Atlas (KTEA; middle layers), and localisation in either the proximal tubule or the rest of the renal tubule in KTEA (outer layers). **(G)** Dotplots of over-represented Reactome pathways for fenofibrate- and PPARα-responsive genes present in the RYGB-FMRR vs RYGB DEG list. The size of dots is scaled by the gene ratio. DEG, differentially expressed gene; FF, fenofibrate; FMRR, fenofibrate, metformin, ramipril, and rosuvastatin; KTEA, Kidney Tubules Expression Atlas; PPAR, peroxisome proliferator-activated receptor; PPARα, peroxisome proliferator-activated receptor-alpha; PPARδ, peroxisome proliferator-activated receptor-delta; PPARγ, peroxisome proliferator-activated receptor-gamma; PT, proximal tubule; RYGB, Roux-en-Y gastric bypass; RYGB-FMRR, Roux-en-Y gastric bypass plus fenofibrate, metformin, ramipril, and rosuvastatin.

found to be proximal tubular-abundant, compared with only 52% of transcripts responsive to either PPARδ or PPARγ, but not PPARα (**Figure 4F**).

Furthermore, fenofibrate- and PPARα-responsive transcripts present in the RYGB-FMRR vs RYGB DEG list were confirmed to be functionally involved in stimulation of both peroxisomal and mitochondrial FAO by pathway over-representation analysis (**Figure 4G**). The magnitude of FAO pathway enrichment was similar between fenofibrate- and PPARα- responsive genes, thereby identifying PPARα as the principal mediator of fenofibrate-stimulated FAO. Thus, fenofibrate was found to be the dominant medication effector of gene expression changes following RYGB-FMRR, and *via* its molecular target PPARα, contributed to FAO induction in the proximal tubule. A network visualisation outlining the medication-responsive genes which are differentially expressed between the RYGB-FMRR and RYGB groups emphasises the dominant roles of fenofibrate and PPARα as effectors of gene expression changes following RYGB-FMRR (**Figure 5**), which contributed to FAO induction in the proximal tubule.

Urinary Metabolomics Identifies Increased PPARα-Responsive Nicotinamide Metabolites and Decreased TCA Cycle Intermediates Following RYGB-FMRR

Urinary metabolomic profiles of SHAM rats at baseline and follow-up clustered alongside baseline samples from RYGB and RYGB-FMRR rats, and were collectively designated as untreated ZDSD rats (**Figures 6A, B**). Untreated ZDSD rats separated into two subphenotypes, mild and severe, based on urinary metabolomic changes relating to disease severity. The major sources of variation along principal components 1 and 2

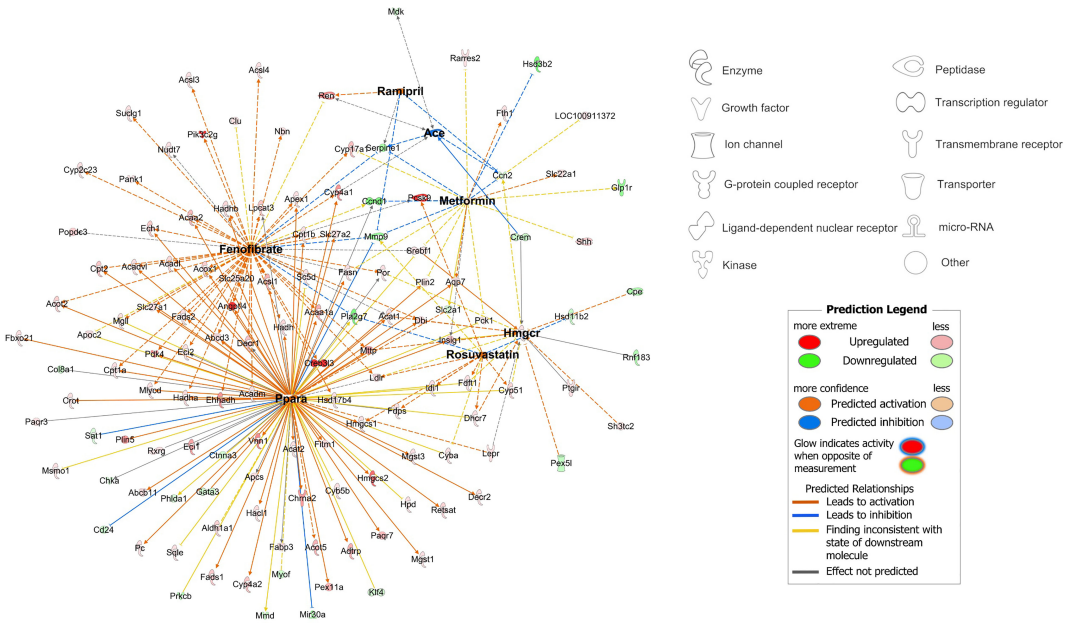

FIGURE 5 | Network visualisation of medication-responsive genes which were differentially expressed between the RYGB-FMRR and RYGB groups. The network was constructed using the 'My Pathways' interface in IPA, and edited using 'PathDesigner' in IPA. The four medications administered to rats treated with RYGB-FMRR, and their corresponding drug targets, are bolded. The legend outlines node symbols corresponding to molecule types contained within the network. The directionality of gene expression change in the RYGB-FMRR vs RYGB DEG list is displayed by node colour (red = upregulated; green = downregulated). Relationships between medications and their gene targets are illustrated by edge colour (orange = predicted activation; blue = predicted inhibition). DEG, differentially expressed gene; IPA, Ingenuity Pathway Analysis; RYGB, Roux-en-Y gastric bypass; RYGB-FMRR, Roux-en-Y gastric bypass plus fenofibrate, metformin, ramipril, and rosuvastatin.

pertained to the untreated severe ZDSD rat phenotype and a post-RYGB phenotype, the latter of which was common to rats in both the RYGB and the RYGB-FMRR groups. Loading vectors in the principal component analysis biplot indicate that increased urinary excretion of sugars (glucose, sucrose, and mannose) and TCA cycle intermediates (citrate, succinate, and 2-oxoglutarate) characterised the untreated severe ZDSD rat phenotype (**Figure 6A**). Given that these rats clustered away from other untreated ZDSD rats on the basis of increased urinary excretion of sugars and TCA cycle intermediates, they were designated as having a more severe phenotype, while those with lower urinary abundance of these metabolites were designated as having a mild phenotype. Increased urinary excretion of host-gut microbial co-metabolites including N-phenylacetylglycine, 3-indoxyl sulfate, and hippurate occurred following both RYGB and RYGB-FMRR.

The RYGB and RYGB-FMRR groups clustered separately along principal components 3 and 4 (**Figure 6B**). The post-RYGB-FMRR urinary metabolome was characterised by increased abundance of PPARα-responsive metabolites involved in nicotinamide and vitamin B metabolism (1-methylnicotinamide, nicotinamide N-oxide, nicotinurate, and methylmalonate).

An RF model effectively classified the RYGB and RYGB-FMRR groups based on urinary metabolomic profiles, with an AUC of 0.97, sensitivity of 0.89, and specificity of 0.88. PPARα-responsive nicotinamide metabolites and TCA cycle intermediates were important to model performance (**Figure 6C**). Increased urinary excretion of PPARα-responsive nicotinamide metabolites occurred following RYGB-FMRR but not RYGB (**Figure 6D**). DKD-associated increases in urinary TCA cycle intermediates were generally reversed by both RYGB and RYGB-FMRR. Reductions in 2-oxoglutarate, fumarate, and malate were greater following RYGB-FMRR compared with RYGB. NMR characteristics of nicotinamide metabolites and TCA cycle intermediates are provided in **Supplemental Table 1**.

Multi-Omic Integration Identifies a Gene-Metabolite Network Distinctive to RYGB-FMRR and Governed by PPARα

Component 1 of a PLS-DA model integrating kidney RNA-Seq and urinary ^{1}H-NMR data selected a highly correlated (Pearson r = 0.93) set of transcripts (n=50) and metabolites (n=10) distinctive to RYGB-FMRR (**Figures 7A, B**). The majority of transcripts selected along component 1 have direct roles in renal cortical FAO, including peroxisomal (*Ehhadh, Acox1*) and mitochondrial (*Acaa2*) PPARα-responsive transcripts (**Figure 7C**). Component 1 metabolites included 1-methylnicotinamide, nicotinamide N-oxide, and 2-oxoglutarate. Network visualisation of the gene-metabolite signature distinctive to RYGB-FMRR illustrates positive correlations between FAO transcripts and urinary nicotinamide metabolites, as well as inverse correlations between FAO transcripts and urinary 2-oxoglutarate (**Figure 7D**).

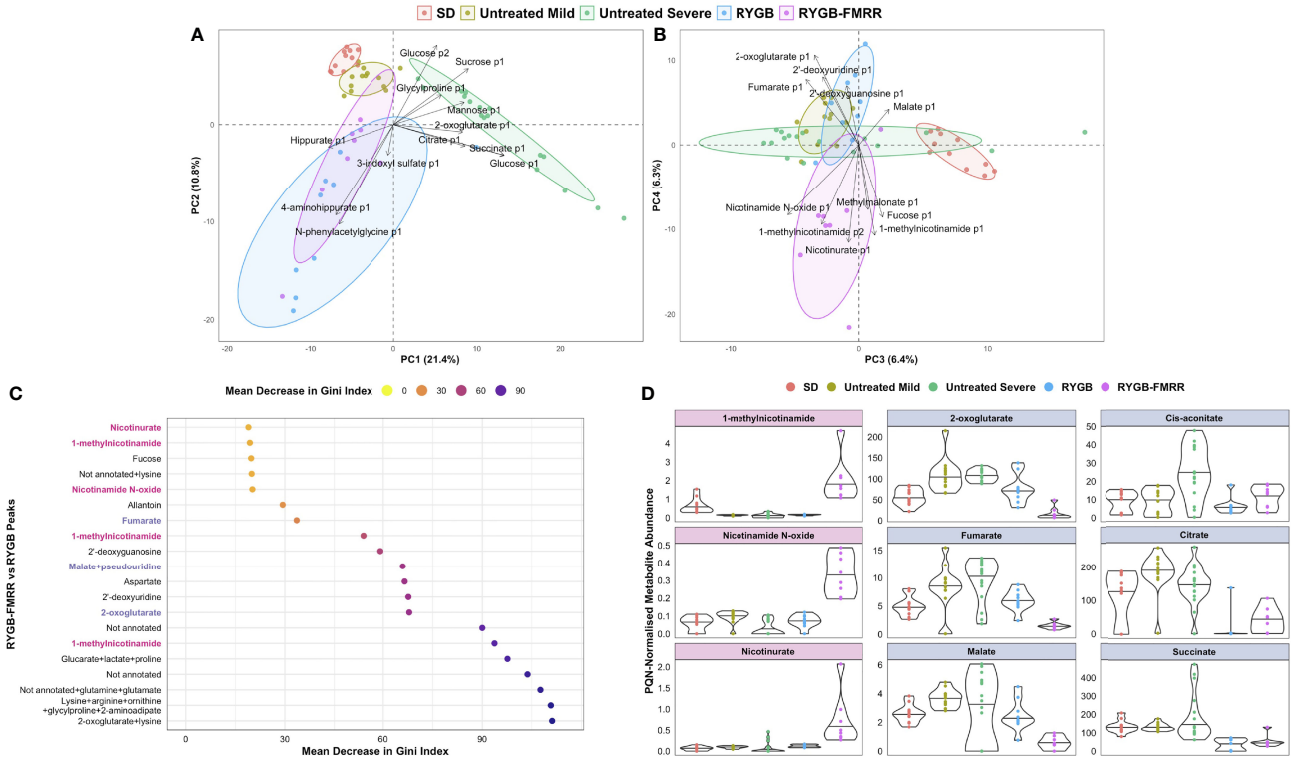

FIGURE 6 | Characterization of urinary metabolomic changes following RYGB and RYGB-FMRR. **(A, B)** Principal component analysis biplots of PQN-normalized urinary ^{1}H-NMR peaks obtained before and at 4 weeks after intervention (A, principal components 1-2; B, principal components 3-4). Baseline and follow-up samples from SD rats were considered together given the lack of change in metabolomic profiles evident in this group. Samples from SHAM rats at baseline and follow-up were considered alongside baseline samples from RYGB and RYGB-FMRR rats, and collectively designated as untreated ZDSD rats. Untreated ZDSD rats clustered based on disease severity into two subphenotypes, mild and severe, rather than by timing of sampling or by experimental group assignment. The definition of disease severity in this context was based on patterns of urinary metabolomic changes influencing subphenotypes observed after clustering of rats by principal component analysis. RYGB and RYGB-FMRR reflect post-intervention values in these two groups. Arrows indicate loading vectors of metabolites driving separation of the groups along principal components 1-4. **(C)** Dotplot of urinary ^{1}H-NMR peaks ranked by importance to classification of RYGB and RYGB-FMRR groups in random forest modelling (70). Peaks are displayed in descending rank order from left to right according to the variable importance metric, mean decrease in Gini index. Variable importance estimates are mean values derived from 100 model repetitions. Multiple peaks were identified for certain metabolites and some peaks remained unannotated despite 2-D NMR analysis. When multiple metabolites are present in a given peak, metabolites are listed in order of relative abundance in the peak, with the most abundant metabolite listed first. PPARα biomarker metabolites involved in nicotinamide metabolism are highlighted in pink; TCA cycle intermediates are highlighted in blue. **(D)**: PQN-normalized abundance of metabolites according to the groups outlined in the PCA biplots in **(A, B)** The first column reflects PPARα biomarker metabolites involved in nicotinamide metabolism (pink panels). The second and third columns reflect TCA cycle intermediates (blue panels). The raw spectra and spectral processing in the R package Speaq was manually reviewed for these metabolites to ensure that the between-group differences highlighted are not artefactual (64). Illustrative examples of the raw spectra and spectral processing in Speaq for the 1-methylnicotinamide and 2-oxoglutarate peaks are presented in **Supplemental Figure 1**. NMR characteristics of the peaks are presented in **Supplemental Table 1**. ^{1}H-NMR, proton nuclear magnetic resonance spectroscopy; 2-D, two-dimensional; p1, peak 1; p2, peak 2; PC, principal component; PQN, probabilistic quotient normalization; RYGB, Roux-en-Y gastric bypass; RYGB-FMRR, Roux-en-Y gastric bypass plus fenofibrate, metformin, ramipril, and rosuvastatin; SD, Sprague Dawley; SHAM, sham surgery (laparotomy); TCA, tricarboxylic acid; ZDSD, Zucker Diabetic Sprague Dawley.

Improvements in Glomerular Volume and Relationship to Renal FAO Transcripts and Urinary Metabolites

Median [IQR] glomerular volume was elevated in SHAM-operated animals relative to the SD group ($1.9x10^6$ [$6.1x10^5$] vs $1.1x10^6$ [$3.6x10^5$] μm^3, p<0.001) (**Figures 8A, B**). Glomerular volume was reduced in RYGB-operated animals (p<0.001) and in animals treated with RYGB-FMRR relative to the SHAM group (p<0.001). Improvements in glomerular volume were greater in the RYGB-FMRR group compared with the RYGB group ($1.3x10^6$ [$4.6x10^5$] vs $1.4x10^6$ [$5.0x10^5$] μm^3, p=0.001).

Glomerular volume was inversely associated with induction of PPARα-responsive FAO transcripts including *Acox1* (r=-0.47), *Ehhadh* (r=-0.47), and *Acaa2* (r=-0.32) as well as urinary nicotinamide metabolites including 1-methylnicotinamide (r=-0.41) and nicotinamide N-oxide (r=-0.40), collectively suggesting that increased renal cortical PPARα activity following RYGB-FMRR was associated with quantitative improvements in glomerular structure (**Figure 8C**). Urinary excretion of TCA cycle intermediates was positively correlated with glomerulomegaly. Correlations with glomerular volume were moderately strong for two TCA cycle intermediates which were diminished to a greater

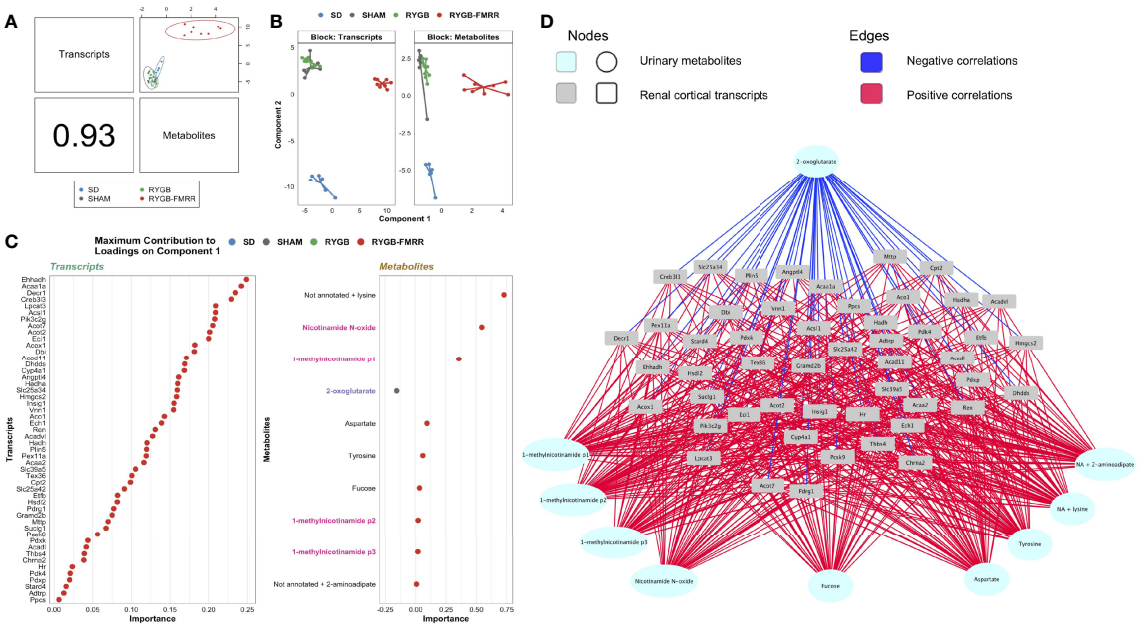

FIGURE 7 | Multi-omic integration of the renal cortical transcriptome and urinary metabolome identifies a distinctive gene-metabolite signature following RYGB-FMRR. **(A)** A supervised, sparse partial least squares-discriminant analysis model was fit to regularized log-transformed gene expression counts and annotated, PQN-normalized urinary ^{1}H-NMR peaks from 4 weeks after intervention using the DIABLO framework in the R package mixOmics (72, 73). An overview of the correlation structure between transcripts and metabolites selected by component 1 of the model, which separated RYGB-FMRR rats from the three other experimental groups, is presented. The left lower panel indicates the Pearson's correlation coefficient between transcripts and metabolites, and the top right panel presents a scatterplot of the correlation structure between the two omics datasets for each sample. Each dot represents an individual rat, with colours indicating experimental group assignment. **(B)** Dimensionality reduction plot of the subspace spanned by the latent variables of the sparse DIABLO model indicating clustering of experimental groups along component 1 (x-axis) and component 2 (y-axis). The plot is facetted by omics modality such that one panel each is presented for transcripts and metabolites. Based on renal cortical transcript expression and urinary metabolite abundance, RYGB-FMRR rats separated from the other experimental groups along component 1. Each dot represents an individual rat, with colours indicating experimental group assignment. **(C)** Dotplots illustrating the contribution of each selected feature (n=50 transcripts, n=10 metabolites) to component 1 of the sparse DIABLO model. Dots are ordered from top to bottom and from right to left according to the loading weight (importance) of the feature. The loading weight can be positive or negative and ranking is by absolute values. The colour of dots corresponds to the group in which the feature is most abundant. Some metabolites in urinary ^{1}H-NMR peaks remained unannotated despite 2-D NMR analysis. When multiple metabolites are present in a given peak, metabolites are listed in order of relative abundance in the peak, with the most abundant metabolite listed first. PPARα biomarker metabolites involved in nicotinamide metabolism are highlighted in pink; TCA cycle intermediates are highlighted in blue. **(D)** Network visualization of the correlation structure between the 50 transcripts and 10 metabolites selected by component 1 of the sparse DIABLO model. Correlations between features with an absolute value greater than 0.5 are presented. Metabolites are presented at the periphery of the network as cyan spherical nodes. Transcripts are presented towards the middle of the network as grey rectangular nodes. Edges are coloured by the directionality of correlation between nodes: blue for negative correlations, red for positive correlations. ^{1}H-NMR, proton nuclear magnetic resonance spectroscopy; DIABLO, data integration analysis for biomarker discovery using latent variable approaches for omics studies; NA, not annotated; p1, peak 1; p2, peak 2; p3, peak 3; PLS-DA, partial least squares-discriminant analysis; PQN, probabilistic quotient normalization; RYGB, Roux-en-Y gastric bypass; RYGB-FMRR, Roux-en-Y gastric bypass plus fenofibrate, metformin, ramipril, and rosuvastatin; SD, Sprague Dawley; SHAM, sham surgery (laparotomy); TCA, tricarboxylic acid.

degree by RYGB-FMRR than RYGB alone: 2-oxoglutarate (r=0.57) and fumarate (r=0.61).

Improvements in Glomerular Ultrastructure and Relationship to Renal FAO Transcripts and Urinary Metabolites

Median [IQR] podocyte foot process frequency (PFPF) was reduced in SHAM-operated animals relative to the SD group (12.5 [4.0] vs 19.4 [4.3] FPs per 8µm GBM, p<0.001) (**Figures 9A, B**). Compared with the SHAM group, PFPF was partially restored by RYGB (15.0 [4.3] FPs, p=0.004) and by RYGB-FMRR (17.0 [3.5] FPs, p<0.001). Restoration of PFPF was greater in the RYGB-FMRR group compared with the RYGB group (p=0.04). Podocyte foot process diameter (PFPD) was higher in the SHAM group relative to the SD group (463 [238.1] vs 330.8 [135.6] nm, p<0.001) (**Figures 9A, C**). PFPD measures were significantly lower in both the RYGB (p=0.001) and RYGB-FMRR (p<0.001) groups relative to the SHAM group. Reduction in PFPD was greater in the RYGB-FMRR group compared with the RYGB group (344.8 [100.8] vs 410.9 [145.7] nm, p<0.001). Increases in GBM thickness were observed in the SHAM group relative to the SD group (330.5 [102.5] vs 219.4 [51.1] nm, p<0.001) (**Figures 9A, D**). GBM thickness was significantly lower in both the RYGB (p<0.001) and RYGB-FMRR (p<0.001) groups relative to the SHAM group. Improvements in GBM thickness were greater in the RYGB-FMRR group

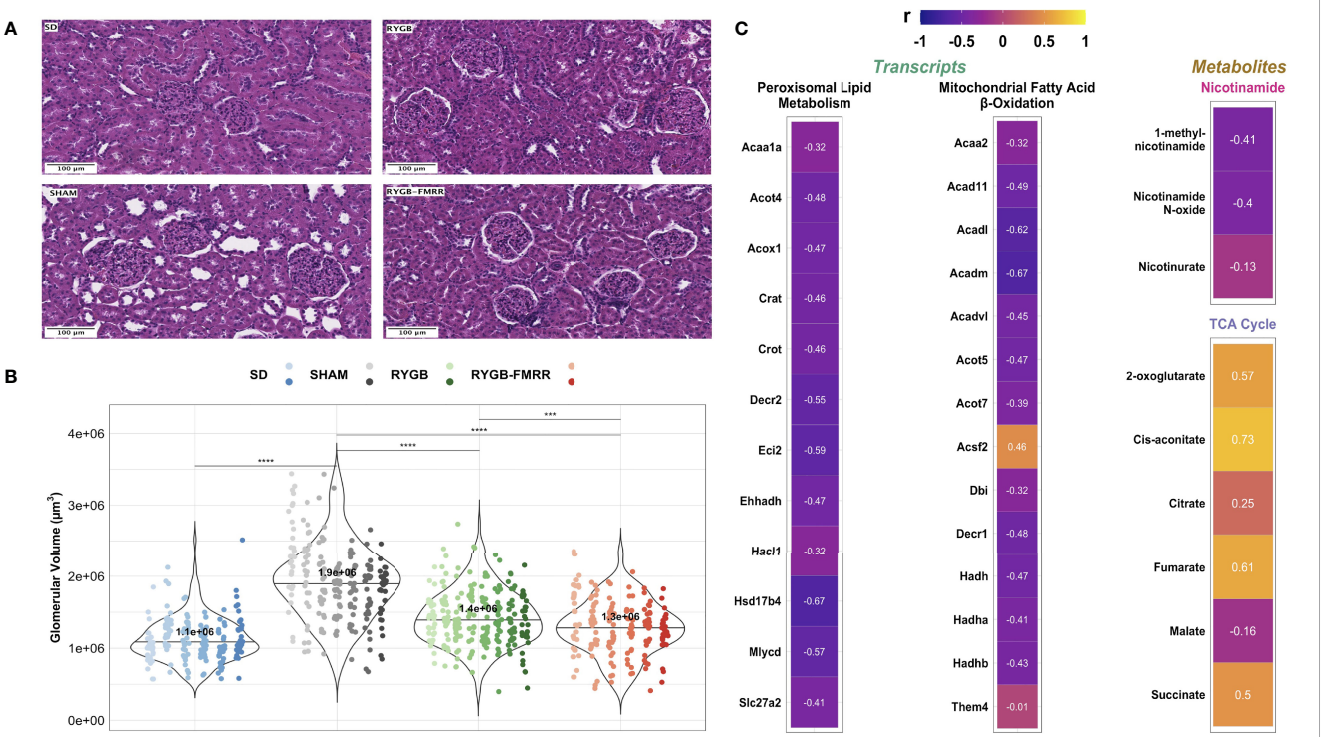

FIGURE 8 | Changes in glomerular volume and their relationship to renal cortical FAO transcripts and urinary nicotinamide and TCA cycle metabolites. **(A)** Representative images (20x, scale bar 100µm) of haematoxylin and eosin-stained kidney sections from the four experimental groups. **(B)** Glomerular volume (μm^3) was assessed in 30 glomeruli from 6-8 animals per group. Data are plotted as violin plots with individual glomerular measurements superimposed. Within each group, each animal is identified as its own column of dots with a unique colour shade. Median group values are identified by the horizontal black line in each violin and printed on each violin. Statistical significance of between-group differences derived from multiplicity-corrected Wilcoxon rank-sum tests is presented. Statistical significance is denoted as follows: ns = not significant; * = p <0.05; ** = p <0.01; *** = p <0.001; **** = p <0.0001. **(C)** Correlation plots highlighting Pearson correlation r values for glomerular volume correlations with renal cortical transcripts and urinary metabolites. Regularized log-transformed gene expression counts were used for gene-structure correlations. Transcripts plotted are those which resulted in enrichment of peroxisomal and mitochondrial lipid metabolism pathways in RYGB-FMRR rats (also highlighted in the circular network plot in **Figure 2D**). PQN-normalized urinary ^{1}H-NMR peaks from samples obtained at 4 weeks after intervention were used for metabolite-structure correlations. Metabolites involved in nicotinamide metabolism (PPARα biomarkers) and TCA cycle intermediates, many of which were differentially abundant between RYGB-FMRR and RYGB rats, are plotted. Individual cells in the correlation plots are scaled by colour indicating strength and directionality of the correlation. PPARα, peroxisome proliferator-activated receptor-alpha; RYGB, Roux-en-Y gastric bypass; RYGB-FMRR, Roux-en-Y gastric bypass plus fenofibrate, metformin, ramipril, and rosuvastatin; SD, Sprague Dawley; SHAM, sham surgery (laparotomy); TCA, tricarboxylic acid.

compared with the RYGB group (263.2 [59.2] vs 273.8 [63.5] nm, p=0.04).

Induction of FAO transcripts and urinary excretion of nicotinamide metabolites by RYGB-FMRR was inversely associated with glomerular ultrastructural injury (PFPD and GBM thickness) (**Figure 9E**). Urinary excretion of TCA cycle intermediates was positively correlated with glomerular ultrastructural injury (PFPD and GBM thickness).

Improvements in Mitochondrial Morphology and Relationship to Renal FAO Transcripts and Urinary Metabolites

Mitochondria in the pars convoluta had a greater two-dimensional area, were longer, and less round compared with mitochondria in the pars recta (**Supplemental Figure 5**), as previously described (40). In the pars convoluta, median [IQR] mitochondrial roundness did not differ between the SD, SHAM, and RYGB groups at 0.36 [0.30], 0.37 [0.33], and 0.38 [0.30], respectively (p>0.05) (**Figures 10A, B**). However, mitochondrial roundness did decrease in the pars convoluta of animals in the RYGB-FMRR group at 0.35 [0.28] (p=0.02 versus SHAM and p=0.008 versus RYGB).

In the pars recta, mitochondrial roundness was increased in SHAM-operated animals relative to the SD group (0.69 [0.27] vs 0.65 [0.30], p<0.001) (**Figures 10C, D**). Mitochondrial roundness was lower in RYGB-operated animals relative to the SHAM group (0.68 [0.30] vs 0.69 [0.27], p=0.02). Mitochondrial roundness was lower in animals treated with RYGB-FMRR at 0.62 [0.32] (p<0.001 versus both SHAM and RYGB).

Increased renal FAO transcript expression and urinary nicotinamide metabolite excretion following RYGB-FMRR inversely correlated with mitochondrial roundness in the proximal tubule (**Figures 10E**), with correlations being greater in magnitude in the pars recta. Urinary excretion of TCA cycle intermediates positively correlated with proximal tubular mitochondrial roundness.

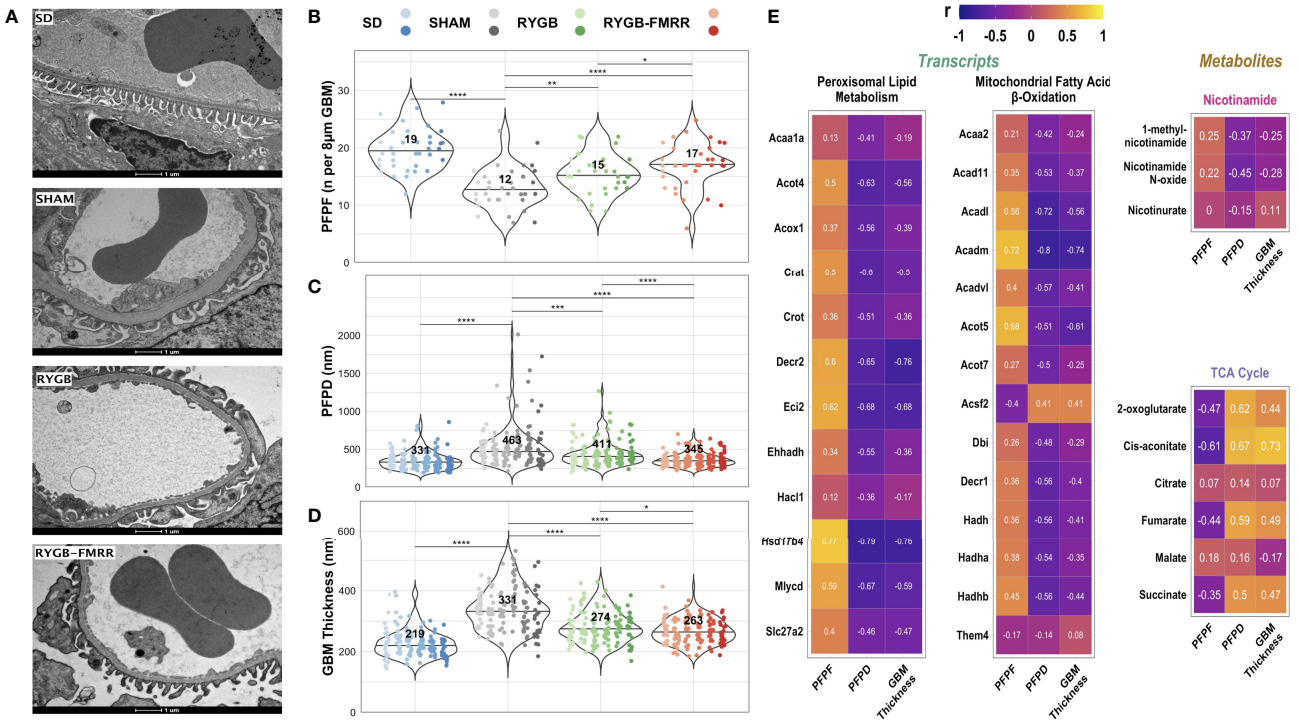

FIGURE 9 | Changes in glomerular ultrastructure and their relationship to renal cortical FAO transcripts and urinary nicotinamide and TCA cycle metabolites. **(A)** Representative images (9900x, scale bar 1µm) of transmission electron microscopy images of glomerular capillary loops from the four experimental groups. **(B–D)** Podocyte foot process frequency (per 8µm of glomerular basement membrane length), podocyte foot process diameter (nm), and glomerular basement membrane thickness (nm) were quantified using transmission electron microscopy images from 6 animals per group. Six determinations of podocyte foot process frequency were made per animal, while twenty-four determinations of podocyte foot process diameter and glomerular basement membrane thickness were made per animal. Data are plotted as violin plots with individual glomerular measurements superimposed. Within each group, each animal is identified as its own column of dots with a unique colour shade. Median group values are identified by the horizontal black line in each violin and printed on each violin. Statistical significance of between-group differences derived from multiplicity-corrected Wilcoxon rank-sum tests is presented. Statistical significance is denoted as follows: ns = not significant; * = p <0.05; ** = p <0.01; *** = p <0.001; **** = p <0.0001. **(E)** Correlation plots highlighting Pearson correlation r values for glomerular ultrastructure (podocyte foot process frequency, podocyte foot process diameter, and glomerular basement membrane thickness) correlations with renal cortical transcripts and urinary metabolites. Regularized log-transformed gene expression counts were used for gene-structure correlations. Transcripts plotted are those which resulted in enrichment of peroxisomal and mitochondrial lipid metabolism pathways in RYGB-FMRR rats (also highlighted in the circular network plot in **Figure 2D**). PQN-normalized urinary ^{1}H-NMR peaks from samples obtained at 4 weeks after intervention were used for metabolite-structure correlations. Metabolites involved in nicotinamide metabolism (PPARα biomarkers) and TCA cycle intermediates, many of which were differentially abundant between RYGB-FMRR and RYGB rats, are plotted. Individual cells in the correlation plots are scaled by colour indicating strength and directionality of the correlation. GBM, glomerular basement membrane; PFPD, podocyte foot process diameter; PFPF, podocyte foot process frequency; PPARα, peroxisome proliferator-activated receptor-alpha; RYGB, Roux-en-Y gastric bypass; RYGB-FMRR, Roux-en-Y gastric bypass plus fenofibrate, metformin, ramipril, and rosuvastatin; SD, Sprague Dawley; SHAM, sham surgery (laparotomy); TCA, tricarboxylic acid.

Comparison of Kidney FAO Parameters Between RYGB and RYGB-FMRR Rats Matched for Metabolic Control and Albuminuria

Enhanced expression of PPARα-responsive transcripts and reduced mitochondrial roundening may have been related to greater improvements in metabolic control after RYGB-FMRR compared with RYGB. We therefore assessed FAO transcript expression and mitochondrial roundness in a pair of rats, one each from the RYGB and RYGB-FMRR groups, that were matched for baseline values and delta improvements in body weight, plasma glucose, and albuminuria. Both animals achieved >20% reduction in body weight, >40% reduction in plasma glucose, and >25% reduction in albuminuria (**Figure 11A**). Despite this, expression of FAO transcripts was higher in the RYGB-FMRR animal (**Figure 11B**). Furthermore, mitochondrial roundness of the RYGB-FMRR animal was lower compared with the matched RYGB animal in both the pars convoluta (0.36 [0.29] vs 0.43 [0.32], p=0.04) and the pars recta (0.56 [0.35] vs 0.64 [0.25], p <0.001) (**Figure 11C**).

DISCUSSION

We interrogated mechanisms underpinning the renoprotective effects of RYGB surgery, alone and in combination with

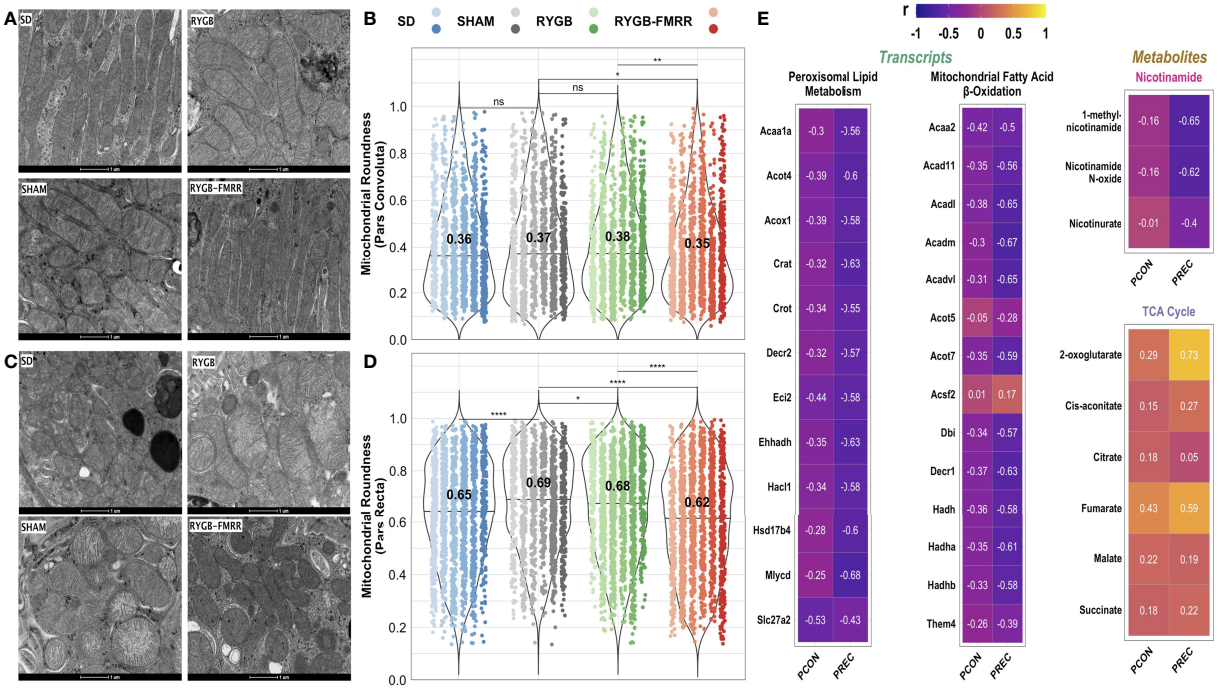

FIGURE 10 | Changes in proximal tubular mitochondrial roundness and their relationship to renal cortical FAO transcripts and urinary nicotinamide and TCA cycle metabolites. **(A, C)** Representative images (16500x, scale bar 1μm) of transmission electron microscopy images of mitochondria in the pars convoluta **(A)** and pars recta **(C)** regions of the proximal tubule from the four experimental groups. **(B, D)** Mitochondrial roundness in the pars convoluta **(B)** and pars recta **(D)** was quantified using transmission electron microscopy images from 6 animals per group. Mitochondria were quantified in 15 non-overlapping images captured from 3 distinct pars convoluta and pars recta regions (5 images/region) for each animal. Data are plotted as violin plots with individual mitochondrial measurements superimposed. Within each group, each animal is identified as its own column of dots with a unique colour shade. Median group values are identified by the horizontal black line in each violin and printed on each violin. Statistical significance of between-group differences derived from multiplicity-corrected Wilcoxon rank-sum tests is presented. Statistical significance is denoted as follows: ns = not significant; * = p <0.05; ** = p <0.01; *** = p <0.001; **** = p <0.0001. **(E)** Correlation plots highlighting Pearson correlation r values for mitochondrial roundness (pars convoluta and pars recta) correlations with renal cortical transcripts and urinary metabolites. Regularized log-transformed gene expression counts were used for gene-structure correlations. Transcripts plotted are those which resulted in enrichment of peroxisomal and mitochondrial lipid metabolism pathways in RYGB-FMRR rats (also highlighted in the circular network plot in **Figure 2D**). PQN-normalized urinary ^{1}H-NMR peaks from samples obtained at 4 weeks after intervention were used for metabolite-structure correlations. Metabolites involved in nicotinamide metabolism (PPARα biomarkers) and TCA cycle intermediates, many of which were differentially abundant between RYGB-FMRR and RYGB rats, are plotted. Individual cells in the correlation plots are scaled by colour indicating strength and directionality of the correlation. PCON, pars convoluta; PPARα, peroxisome proliferator-activated receptor-alpha; PREC, pars recta; RYGB, Roux-en-Y gastric bypass; RYGB-FMRR, Roux-en-Y gastric bypass plus fenofibrate, metformin, ramipril, and rosuvastatin; SD, Sprague Dawley; SHAM, sham surgery (laparotomy); TCA, tricarboxylic acid.

medications (**Figure 12**). Attenuated glomerular injury after RYGB was underpinned by reduced activation of transcriptomic fibrosis pathways, as previously reported (10–13). Improvements in glomerular injury of greater magnitude and lower variability were however achieved by combining RYGB with type 2 diabetes medications (fenofibrate, metformin, ramipril, and rosuvastatin) to stimulate renal FAO, a mechanism of progressive DKD which was not addressed by RYGB alone (80, 81). Fenofibrate was found to be the principal medication effector of gene expression changes following RYGB-FMRR; consequent induction of PPARα-regulated FAO transcripts in the proximal tubule was a dominant response to RYGB-FMRR which strongly correlated with urinary abundance of nicotinamide metabolites and TCA cycle intermediates.

Impaired FAO perpetuates organ fibrosis, and defective renal tubular epithelial cell fatty acid utilization propagates tubulointerstitial fibrosis (14, 82, 83). Studies linking loss of tubular FAO with fibrosis have principally focused on mitochondrial metabolism (84). Our data highlight the possible involvement of peroxisomal dysfunction in tubular FAO impairment (85). Peroxisomes mainly localize to the proximal tubule of the kidney, a site of strategic importance with respect to FAO due to high energy demands in this region (84). Suppression of the rate-limiting, PPARα-responsive peroxisomal enzyme, *Acox1*, has been described in experimental renal fibrosis and after treatment of tubular epithelial cells with TGF-β, a phenomenon reversed by the PPARα agonist fenofibrate (14). Impaired PPARα and *Acox1* activity have been implicated in age-associated renal fibrosis and can be reversed through calorie restriction (28).

Urinary abundance of six TCA cycle intermediates showed a pattern of increasing in SHAM group rats and decreasing in rats

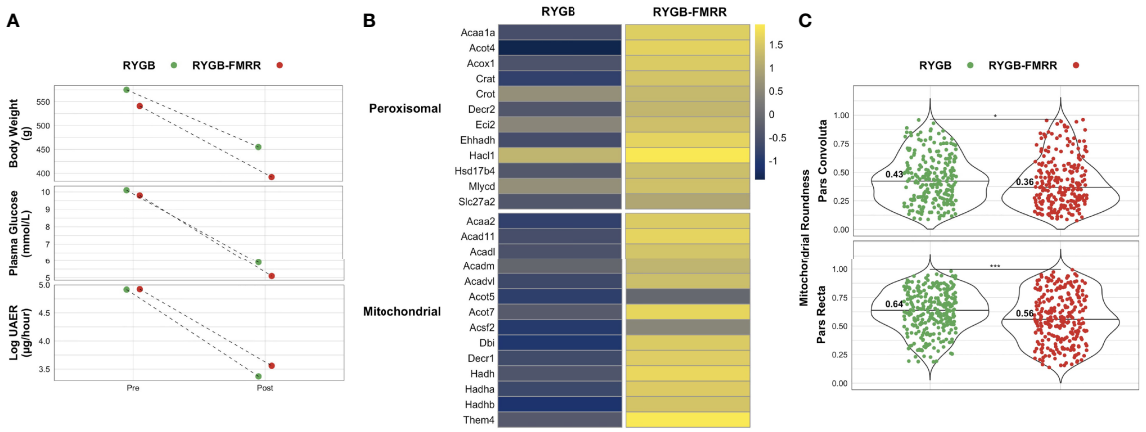

FIGURE 11 | Comparison of renal cortical lipid metabolism parameters between RYGB and RYGB-FMRR rats matched for improvements in metabolic control and urinary albumin excretion. **(A)** One rat each from the RYGB and RYGB-FMRR groups, matched for body weight, plasma glucose, and albuminuria, was used for a comparative analysis of renal cortical lipid metabolism transcript expression and proximal tubular mitochondrial morphology. Body weight, plasma glucose, and log urinary albumin excretion rate values pre- and post-intervention are plotted, highlighting both similar baseline values and magnitude of improvement in these parameters for each rat from the RYGB and RYGB-FMRR groups. **(B)** Heatmap of renal cortical peroxisomal and mitochondrial lipid metabolism transcript expression for the matched RYGB and RYGB-FMRR rats, indicating increased relative expression of lipid metabolism transcripts in the RYGB-FMRR rat. Regularized log-transformed gene expression counts from RNA-sequencing, centred and scaled by row, are plotted. Transcripts plotted are those which resulted in enrichment of peroxisomal and mitochondrial lipid metabolism pathways in RYGB-FMRR rats (also highlighted in the circular network plot in **Figure 2D**). Heatmap rows display individual transcripts while columns reflect values from the matched RYGB and RYGB-FMRR rats. The column gap separates RYGB and RYGB-FMRR rats, while the row gap separates peroxisomal and mitochondrial lipid metabolism transcripts. **(C)** Mitochondrial roundening was lower in both the pars convoluta and pars recta sections of the proximal tubule in the RYGB-FMRR animal compared with the matched RYGB animal. Mitochondrial roundness in the pars convoluta and pars recta was quantified using transmission electron microscopy images from each of the matched animals. Mitochondria were quantified in 15 non-overlapping images captured from 3 distinct pars convoluta and pars recta regions (5 images/region) for each animal. Data are plotted as violin plots with individual mitochondrial measurements superimposed. Median values are identified by the horizontal black line in each violin and printed on each violin. Statistical significance of differences in mitochondrial characteristics between the two animals derived from Wilcoxon rank-sum tests is denoted as follows: ns = not significant; * = p <0.05; ** = p <0.01; *** = p <0.001; **** = p <0.0001. RYGB, Roux-en-Y gastric bypass; RYGB-FMRR, Roux-en-Y gastric bypass plus fenofibrate, metformin, ramipril, and rosuvastatin; UAER, urinary albumin excretion rate.

in the RYGB and RYGB-FMRR groups. Reductions in 2-oxoglutarate, fumarate, and malate were greater following RYGB-FMRR than RYGB. Following multi-omic integration, urinary 2-oxoglutarate was found to be strongly inversely correlated with a range of FAO transcripts induced by RYGB-FMRR suggesting that its decrease may reflect increased consumption in the TCA cycle as a consequence of enhanced renal cortical FAO (86).

Increased urinary excretion of TCA cycle intermediates in preclinical models of DKD has previously been reported (86, 87), and implicates reduced TCA cycle flux and compromised renal bioenergetics in DKD progression. The finding of increased urinary excretion of TCA cycle intermediates in preclinical studies is in contrast to human studies in which reduced urinary TCA cycle intermediate excretion has been reported (88, 89). In a fashion similar to the strong correlations between TCA cycle intermediates and morphometric parameters of renal injury in the current study, urinary citrate and aconitate levels have been found to independently and positively associate with change in eGFR and negatively associate with indices of glomerular structural injury in patients with DKD (88, 90). The directionality of these relationships is the opposite to those observed between TCA cycle intermediates and renal injury parameters in the current study, a discrepancy likely related to differences in DKD stage beween animal and human studies (91). Nevertheless, considering the strong inverse correlations between FAO transcripts and 2-oxoglutarate alongside the positive correlations between TCA cycle intermediates and indices of glomerular and proximal tubular injury provides a functional link between FAO transcript expression, TCA cycle activity, and improvements in kidney structure following RYGB-FMRR.

RYGB-FMRR increased urinary excretion of several PPARα-regulated nicotinamide metabolites, including 1-methylnicotinamide, nicotinamide N-oxide, and nicotinurate (92, 93). Urinary 1-methylnicotinamide levels increase following treatment with a PPARα agonist and positively correlate with hepatic peroxisomal number (94). Increased urinary nicotinamide metabolites following RYGB-FMRR may reflect enhanced nicotinamide adenine dinucleotide (NAD+) biosynthesis to facilitate translation of FAO into reduced intermediates for the electron transport chain (94). Reduced renal NAD+ levels are implicated in the pathogenesis of acute kidney injury and CKD (95); NAD+ augmentation may have contributed to the enhanced renoprotection observed following RYGB-FMRR compared with RYGB.

The strong correlations between FAO transcripts, urinary nicotinamide metabolites, and urinary TCA cycle intermediates

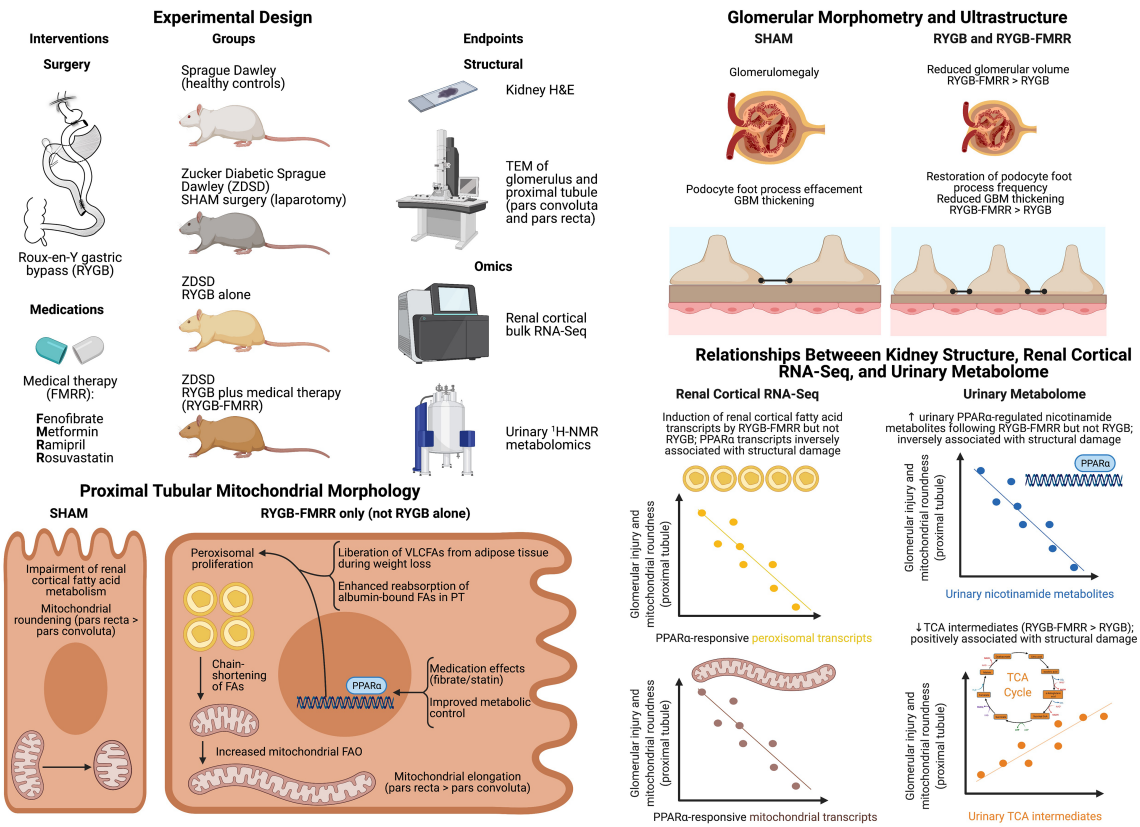

FIGURE 12 | Overview schematic. Created with BioRender.com. ¹H-NMR, proton nuclear magnetic resonance spectroscopy; FA, fatty acid; FAO, fatty acid oxidation; FMRR, fenofibrate, metformin, ramipril, and rosuvastatin; GBM, glomerular basement membrane; H&E, haematoxylin and eosin; PPARα, peroxisome proliferator-activated receptor-alpha; PT, proximal tubule; RNA-Seq, ribonucleic acid next-generation sequencing; RYGB, Roux-en-Y gastric bypass; RYGB-FMRR, Roux-en-Y gastric bypass plus fenofibrate, metformin, ramipril, and rosuvastatin; SD, Sprague Dawley; SHAM, sham surgery (laparotomy); TCA, tricarboxylic acid; TEM, transmission electron microscopy; UAER, urinary albumin excretion rate; VLCFA, very-long-chain fatty acid; ZDSD, Zucker Diabetic Sprague Dawley.

with mitochondrial roundness links increased PPARα activity after RYGB-FMRR with mitochondrial bioenergetic changes opposing renal fibrosis (28, 96). Correlations were strongest in the pars recta, the site of greatest peroxisomal abundance in the rat proximal tubule (39, 97). Using a network pharmacology approach, treatment with the PPARα agonist fenofibrate was found to be a dominant effector of PPARα-stimulated FAO in the proximal tubule following RYGB-FMRR (18). Statins and fibrates do however synergistically activate PPARα (19). Both RYGB and metformin can activate AMPK to restore renal mitochondrial biogenesis (20, 98). RYGB may also enhance peroxisomal activity by liberating VLCFAs from adipose tissue during weight loss (99, 100).

Combining intentional weight loss with pharmacological PPARα agonism in DKD merits further investigation. Fibrates are the obvious candidate drug class for such studies. In a *post-hoc* analysis of the ACCORD Lipid Trial, randomization to fenofibrate (n=2636) was associated with slower eGFR decline and lower incident albuminuria compared with placebo (n=2632) (101). Similar findings were reported in the FIELD study (102). Pemafibrate, a selective PPARα modulator (103), activated PPARα and ameliorated DKD in the db/db mouse (104). A preclinical systematic review and meta-analysis assessing the impact of pharmacological targeting of PPARs in experimental renal injury is underway (105), and may help to inform the design of future studies evaluating PPARα-mediated restoration of FAO in DKD. By liberating fatty acids, intentional weight loss may synergize with PPARα agonism to further enhance renal FAO (84).

Our study findings should be interpreted in the context of certain limitations. The ZDSD rat is a model of early DKD (16), and thus the reversal of renal injury by RYGB and RYGB-FMRR reflects plasticity of the kidney in early diabetic renal injury. The extent to which these findings translate to later stages of DKD, accompanied by more prominent tubulointerstitial fibrosis, is unknown. The absence of marked histological evidence of renal injury in SHAM-operated ZDSD rats makes it unlikely that meaningful differences in the extent of renal fibrosis assessed histologically, which could potentially be attributed to stimulation of FAO, would be observed between rats treated with RYGB-FMRR and RYGB. Nevertheless, upon transcriptomic pathway over-representation analysis, interruption of the early pro-fibrotic

programme of DKD by both RYGB and RYGB-FMRR was observed, with the magnitude of fibrosis pathway downregulation being greater following RYGB-FMRR. Furthermore, reduction in the abundance of renal cortical fibroblasts, estimated using MCP-counter (54), was greater following RYGB-FMRR compared with RYGB. Thus, stimulation of FAO following RYGB-FMRR may have contributed to enhanced abrogation of diabetes-associated renal fibrosis compared with RYGB alone, although future studies in models which manifest more extensive histological renal fibrosis are warranted.

Baseline body weights were not markedly different between Sprague Dawley and ZDSD rats in the present study. The ZDSD rat model is a comprehensive model of diet-induced polygenic obesity (16, 106). However, Sprague Dawley rats are also prone to diet-induced obesity and are frequently used as a preclinical model of obesity after administration of a high-fat diet (107). Thus, ZDSD rats were not compared to a fully lean healthy control group in the present study. Nevertheless, Sprague Dawley rats remain the best healthy control group for ZDSD rats given that the ZDSD model was developed by crossing lean homozygous ZDF rats with a substrain of Sprague Dawley rats selectively bred for high-fat diet-induced obesity (106). Furthermore, interventions in the present study were targeted to their metabolic and renoprotective effects, rather than purely to their weight loss effects. Indeed, reductions in albuminuria occur independently of weight loss following metabolic surgery in patients with DKD (108). Thus, the renal benefits of metabolic surgery may extend to patients with DKD and mild obesity. Such patients with mild obesity (BMI 30-35 kg/m^2) have been selectively recruited to a randomised study of metabolic surgery in early-stage DKD (9). Findings from the present study would appear to be translationally relevant to such studies of metabolic surgery in patients with obesity and early-moderate stage DKD.

Post-intervention urine samples were collected at 4-week follow-up while kidney tissue samples were collected at 8-week follow-up. Thus, correlations between urinary metabolites and both renal cortical transcripts and kidney structural parameters were not time-matched. However, in preclinical models of folic acid nephropathy, unilateral ureteric obstruction, and cisplatin-induced nephrotoxicity, renal induction of the PPARα protein and its responsive transcripts occurred within 5-10 days of treatment with fenofibrate at similar doses to that used in the present study (100 mg/kg/day) (14, 109). As fenofibrate was found to be the dominant medication effector of FAO induction in the present study, it therefore seems probable that gene expression changes in PPARα-governed FAO pathways observed on transcriptomic analysis of renal cortical tissue after 8 weeks of follow-up were already established by the time of the post-intervention urine collection, which occurred 2 weeks after introduction of the FMRR medications post-RYGB. Additionally, the biological coherence of the strong correlations observed between PPARα-governed renal cortical FAO transcripts and urinary nicotinamide metabolites is implicit.

Transcriptomic analysis was performed on whole renal cortex rather than individual cells. However, deconvolution in kidney single-nucleus RNA-sequencing and microdissected tubular epithelial cell proteomics datasets allowed us to assign FAO genes to the proximal tubule (56, 58). We do not report on the extent to which diet-induced weight loss in combination with PPARα-directed pharmacotherapy stimulates renal FAO, but future studies are warranted (110, 111). Furthermore, outside the context of obesity, evaluation of the capacity of the FMRR medication combination to reverse renal injury and to stimulate renal cortical FAO without superimposed weight loss merits further consideration in preclinical models of DKD.

All four medications were provided concurrently to rats in the RYGB-FMRR group in an effort to maximally stimulate FAO with medications routinely used in type 2 diabetes management. As the study design makes it more difficult to discern individual medication contributions, multi-modal pharmacological treatment may be a perceived limitation of the work. However, we propose that this design is more translationally relevant to the clinical setting, given that patients with DKD are usually treated with several medications for control of dysglycaemia, dyslipidaemia, hypertension, and dysregulated glomerular haemodynamics (17). Preclinical studies of RYGB are technically challenging and labor-intensive, particularly with respect to post-operative monitoring (112). The addition of further study groups in which rats were treated with RYGB and each of the four FMRR medications in monotherapy would have rendered the study infeasible in terms of time and cost restraints.

It would have been possible to study gene expression changes in response to components of the FMRR medication regimen, individually and in combination, in a renal cell line *in vitro*. However, this would switch the line of interrogation to an entirely new model system in which it is impossible to directly mimic the effects of RYGB; thus, it would not have been possible to assess synergistic renoprotective effects of RYGB and FAO-directed medications, the primary purpose of this study, *in vitro*. To overcome the limitations of *in vitro* interrogation, we employed a network pharmacology approach in which RYGB-FMRR vs RYGB DEGs were deconvoluted using curated information on medication- and PPAR isotype-responsiveness of genes obtained using IPA (52). This approach allowed us to assess all gene targets of the FMRR medications, as opposed to a limited number of targets selected for validation in a supervised fashion *in vitro*, and also allowed us to explore the cellular localisation within the kidney of medication-specific transcriptomic responses through further deconvolution in a rat microdissected tubular epithelial cell proteomics dataset (58). Using this approach, we identified fenofibrate as the dominant medication effector of gene expression changes following RYGB-FMRR, which in turn contributed to FAO induction in the proximal tubule.

The RYGB-FMRR group achieved greater improvements in body weight, glycaemia, and albuminuria compared with the RYGB group. However, in a sensitivity analysis matching for baseline values and delta improvements in these parameters in one rat each from the RYGB and RYGB-FMRR groups, improvements in kidney FAO parameters remained much greater following RYGB-FMRR. This provides proof-of-

principle that the renal cortical FAO stimulation observed following RYGB-FMRR arose due to synergism between weight loss and directed pharmacological therapy (18–20, 84), rather than as a direct consequence of the greater improvements in metabolic control achieved.

In summary, compared with RYGB alone, combining RYGB with type 2 diabetes medications to stimulate FAO produces greater improvements in metabolic control and diabetic glomerular and proximal tubular damage. Pharmacological PPARα agonism as an adjunct to weight loss and improved glycemic control merits further investigation as a means of attenuating DKD progression.

DATA AVAILABILITY STATEMENT

RNA-sequencing fastq files and raw counts of aligned reads have been deposited in Gene Expression Omnibus and are accessible through GEO Series accession number GSE147706 (https://www.ncbi.nlm.nih.gov/geo/query/acc.cgi?acc=GSE147706; last accessed 21st December 2021). Lists of differentially expressed genes (absolute fold-change ≥1.3, adjusted p-value <0.05) between the study groups are available on Open Science Framework (https://osf.io/cf7v5/; last accessed 21st December 2021). Along with sample metadata, the following urinary ^{1}H-NMR data has also been uploaded to Open Science Framework (https://osf.io/cf7v5/): raw spectra, parts per million (ppm) chemical shift vector, processed peak intensity matrices, and peak annotations. A PDF outlining spectral processing using the R package Speaq (64) as well as peak abundance by experimental group for each annotated peak in the urinary ^{1}H-NMR spectra has also been uploaded to the Open Science Framework repository. All remaining animal data presented in this study are available from the authors upon written request and following agreement on the intended purpose of the request.

ETHICS STATEMENT

This animal study was reviewed and approved by the University College Dublin Animal Research Ethics Committee.

AUTHOR CONTRIBUTIONS

ND, LF and ClR devised and designed the studies. YC, ND, and MA performed surgery and animal husbandry. YC and WM conducted RNA isolation and histological studies. WM and ND conducted immunohistochemical studies. WM conducted transmission electron microscopy imaging. SA performed RNA-Seq raw data processing. Remaining RNA-Seq bioinformatic analyses were performed by WM, with input from SA and EB. Validation of transcriptomic signals at mRNA level was conducted by WM. AP performed urinary ^{1}H-NMR and 2-D NMR analyses, and annotated NMR peaks as metabolites. WM and DM performed urinary ^{1}H-NMR data spectral processing and multivariate modelling. WM performed RNA-Seq and ^{1}H-NMR omics integration. WM analyzed the experimental data. WM, DM, AP, ND, EB, CG, LF, and ClR interpreted the data. WM, ND, and ClR drafted the manuscript with critical input from LF, CG, and EB. ND and ClR are co-guarantors of this work and, as such, had full access to all the data in the study and take responsibility for the integrity of the data and the accuracy of the data analysis. All authors contributed to the article and approved the submitted version.

FUNDING

Funding support from the following agencies is acknowledged; Science Foundation Ireland (12/YI/B2480) to ClR, Swedish Medical Research Council (2015-02733) to LF, ClR, and ND, European Foundation for the Study of Diabetes/Boehringer Ingelheim European Diabetes Research Programme (BI 2017_3) to ClR and ND, and Science Foundation Ireland (15/IA/3152 and 15/US/B3130) to CG and EB. EB is supported by a UCD Ad Astra Fellowship. WM's contribution was performed within the Irish Clinical Academic Training (ICAT) Programme, supported by the Wellcome Trust and the Health Research Board (Grant Number 203930/B/16/Z), the Health Service Executive National Doctors Training and Planning, and the Health and Social Care, Research and Development Division, Northern Ireland.

ACKNOWLEDGMENTS

We acknowledge local support received in the realization of these studies from the UCD Biomedical Facility and the Research Pathology and Genomics Core Facilities at the UCD Conway Institute. We also acknowledge the Genomics and Bioinformatics Core Facility platforms at the Sahlgrenska Academy, University of Gothenburg as well as the Swedish NMR Centre, University of Gothenburg. We thank Dr. Parker Wilson and Dr. Benjamin Humphreys for sharing human kidney single-nucleus RNA-sequencing data with us. **Figures 1** and **12** were created with BioRender.com. We are grateful to Ludmilla Dellatorre Pessanha (ludmilla.pessanha@ucd.ie) for preparing the illustration of Roux-en-Y gastric bypass included in **Figure 12**.

SUPPLEMENTARY MATERIAL

The Supplementary Material for this article can be found online at: https://www.frontiersin.org/articles/10.3389/fendo.2021.757228/full#supplementary-material

REFERENCES

1. Reutens AT. Epidemiology of Diabetic Kidney Disease. *Med Clin North Am* (2013) 97(1):1–18. doi: 10.1016/j.mcna.2012.10.001
2. Johansen KL, Chertow GM, Foley RN, Gilbertson DT, Herzog CA, Ishani A, et al. US Renal Data System 2020 Annual Data Report: Epidemiology of Kidney Disease in the United States. *Am J Kidney Dis* (2021) 77(4, Supplement 1):A7–8. doi: 10.1053/j.ajkd.2021.01.002
3. Martin WP, Bauer J, Coleman J, Dellatorre-Teixeira L, Reeve JLV, Twomey PJ, et al. Obesity is Common in Chronic Kidney Disease and Associates With Greater Antihypertensive Usage and Proteinuria: Evidence From a Cross-Sectional Study in a Tertiary Nephrology Centre. *Clin Obes* (2020) e12402. doi: 10.1111/cob.12402
4. Chang AR, Grams ME, Navaneethan SD. Bariatric Surgery and Kidney-Related Outcomes. *Kidney Int Rep* (2017) 2(2):261–70. doi: 10.1016/j.ekir.2017.01.010
5. Alicic RZ, Rooney MT, Tuttle KR. Diabetic Kidney Disease: Challenges, Progress, and Possibilities. *Clin J Am Soc Nephrol CJASN* (2017) 12 (12):2032–45. doi: 10.2215/cjn.11491116
6. Martin WP, Docherty NG, Le Roux CW. Impact of Bariatric Surgery on Cardiovascular and Renal Complications of Diabetes: A Focus on Clinical Outcomes and Putative Mechanisms. *Expert Rev Endocrinol Metab* (2018) 13(5):251–62. doi: 10.1080/17446651.2018.1518130
7. Docherty NG, le Roux CW. Bariatric Surgery for the Treatment of Chronic Kidney Disease in Obesity and Type 2 Diabetes Mellitus. *Nat Rev Nephrol* (2020) 16(12):709–20. doi: 10.1038/s41581-020-0323-4
8. Martin WP, White J, López-Hernández FJ, Docherty NG, le Roux CW. Metabolic Surgery to Treat Obesity in Diabetic Kidney Disease, Chronic Kidney Disease, and End-Stage Kidney Disease; What Are the Unanswered Questions? *Front Endocrinol* (2020) 11:289(289). doi: 10.3389/fendo.2020.00289
9. Cohen RV, Pereira TV, Aboud CM, Petry TBZ, Lopes Correa JL, Schiavon CA, et al. Effect of Gastric Bypass vs Best Medical Treatment on Early-Stage Chronic Kidney Disease in Patients With Type 2 Diabetes and Obesity: A Randomized Clinical Trial. *JAMA Surg* (2020) 155(8):e200420–e. doi: 10.1001/jamasurg.2020.0420
10. Neff KJ, Elliott JA, Corteville C, Abegg K, Boza C, Lutz TA, et al. Effect of Roux-En-Y Gastric Bypass and Diet-Induced Weight Loss on Diabetic Kidney Disease in the Zucker Diabetic Fatty Rat. *Surg Obes Relat Dis* (2017) 13(1):21–7. doi: 10.1016/j.soard.2016.08.026
11. Canney AL, Cohen RV, Elliott JA, MA C, Martin WP, Docherty NG, et al. Improvements in Diabetic Albuminuria and Podocyte Differentiation Following Roux-En-Y Gastric Bypass Surgery. *Diabetes Vasc Dis Res* (2019) 1479164119879039. doi: 10.1177/1479164119879039
12. Nair M, Martin WP, Zhernovkov V, Elliott JA, Fearon N, Eckhardt H, et al. Characterization of the Renal Cortical Transcriptome Following Roux-En-Y Gastric Bypass Surgery in Experimental Diabetic Kidney Disease. *BMJ Open Diabetes Res & Care* (2020) 8(1):e001113. doi: 10.1136/bmjdrc-2019-001113
13. Martin WP, le Roux CW, Docherty NG. Impact of Metabolic Surgery on Renal Injury in Pre-Clinical Models of Diabetic Kidney Disease. *Nephron* (2021) 146(6):585–94. doi: 10.1159/000511790
14. Kang HM, Ahn SH, Choi P, Ko YA, Han SH, Chinga F, et al. Defective Fatty Acid Oxidation in Renal Tubular Epithelial Cells has a Key Role in Kidney Fibrosis Development. *Nat Med* (2015) 21(1):37–46. doi: 10.1038/nm.3762
15. Miguel V, Tituaña J, Herrero JI, Herrero L, Serra D, Cuevas P, et al. Renal Tubule Cpt1a Overexpression Protects From Kidney Fibrosis by Restoring Mitochondrial Homeostasis. *J Clin Invest* (2021) 131(5). doi: 10.1172/JCI140695
16. Peterson RG, Jackson CV, Zimmerman KM. The ZDSD Rat: A Novel Model of Diabetic Nephropathy. *Am J Trans Res* (2017) 9(9):4236–49.
17. de Boer IH, Caramori ML, Chan JCN, Heerspink HJL, Hurst C, Khunti K, et al. KDIGO 2020 Clinical Practice Guideline for Diabetes Management in Chronic Kidney Disease. *Kidney Int* (2020) 98(4):S1–S115. doi: 10.1016/j.kint.2020.06.019
18. Schoonjans K, Staels B, Auwerx J. Role of the Peroxisome Proliferator-Activated Receptor (PPAR) in Mediating the Effects of Fibrates and Fatty Acids on Gene Expression. *J Lipid Res* (1996) 37(5):907–25.
19. Inoue I, Itoh F, Aoyagi S, Tazawa S, Kusama H, Akahane M, et al. Fibrate and Statin Synergistically Increase the Transcriptional Activities of PPARalpha/RXRalpha and Decrease the Transactivation of NFkappaB. *Biochem Biophys Res Commun* (2002) 290(1):131–9. doi: 10.1006/bbrc.2001.6141
20. Lee M, Katerelos M, Gleich K, Galic S, Kemp BE, Mount PF, et al. Phosphorylation of Acetyl-CoA Carboxylase by AMPK Reduces Renal Fibrosis and Is Essential for the Anti-Fibrotic Effect of Metformin. *J Am Soc Nephrol JASN* (2018) 29(9):2326–36. doi: 10.1681/asn.2018010050
21. Zhou G, Myers R, Li Y, Chen Y, Shen X, Fenyk-Melody J, et al. Role of AMP-Activated Protein Kinase in Mechanism of Metformin Action. *J Clin Invest* (2001) 108(8):1167–74. doi: 10.1172/jci13505
22. Angin Y, Beauloye C, Horman S, Bertrand L. Regulation of Carbohydrate Metabolism, Lipid Metabolism, and Protein Metabolism by AMPK. *Exp Suppl* (2016) 107:23–43. doi: 10.1007/978-3-319-43589-3_2
23. Munday MR, Hemingway CJ. The Regulation of Acetyl-CoA Carboxylase–A Potential Target for the Action of Hypolipidemic Agents. *Adv Enzyme Regul* (1999) 39:205–34. doi: 10.1016/s0065-2571(98)00016-8
24. Rajani R, Pastor-Soler NM, Hallows KR. Role of AMP-Activated Protein Kinase in Kidney Tubular Transport, Metabolism, and Disease. *Curr Opin Nephrol Hypertension* (2017) 26(5):375–83. doi: 10.1097/mnh.0000000000000349
25. Sohn M, Kim K, Uddin MJ, Lee G, Hwang I, Kang H, et al. Delayed Treatment With Fenofibrate Protects Against High-Fat Diet-Induced Kidney Injury in Mice: The Possible Role of AMPK Autophagy. *Am J Physiol Renal Physiol* (2017) 312(2):F323–f34. doi: 10.1152/ajprenal.00596.2015
26. Braissant O, Foufelle F, Scotto C, Dauça M, Wahli W. Differential Expression of Peroxisome Proliferator-Activated Receptors (PPARs): Tissue Distribution of PPAR-Alpha, -Beta, and -Gamma in the Adult Rat. *Endocrinology* (1996) 137(1):354–66. doi: 10.1210/endo.137.1.8536636
27. Li S, Nagothu KK, Desai V, Lee T, Branham W, Moland C, et al. Transgenic Expression of Proximal Tubule Peroxisome Proliferator-Activated Receptor-Alpha in Mice Confers Protection During Acute Kidney Injury. *Kidney Int* (2009) 76(10):1049–62. doi: 10.1038/ki.2009.330
28. Chung KW, Lee EK, Lee MK, Oh GT, Yu BP, Chung HY. Impairment of Pparα and the Fatty Acid Oxidation Pathway Aggravates Renal Fibrosis During Aging. *J Am Soc Nephrol JASN* (2018) 29(4):1223–37. doi: 10.1681/asn.2017070802
29. Chen HH, Chen TW, Lin H. Pravastatin Attenuates Carboplatin-Induced Nephrotoxicity in Rodents *via* Peroxisome Proliferator-Activated Receptor Alpha-Regulated Heme Oxygenase-1. *Mol Pharmacol* (2010) 78(1):36–45. doi: 10.1124/mol.109.061101
30. Karalliedde J, Viberti G. Evidence for Renoprotection by Blockade of the Renin–Angiotensin–Aldosterone System in Hypertension and Diabetes. *J Hum Hypertension* (2006) 20(4):239–53. doi: 10.1038/sj.jhh.1001982
31. Sas KM, Lin J, Wang CH, Zhang H, Saha J, Rajendiran TM, et al. Renin-Angiotensin System Inhibition Reverses the Altered Triacylglycerol Metabolic Network in Diabetic Kidney Disease. *Metabolomics* (2021) 17 (7):65. doi: 10.1007/s11306-021-01816-0
32. Al-Rasheed NM, Al-Rasheed NM, Al-Amin MA, Hasan IH, Al-Ajmi HN, Mohammad RA, et al. Fenofibrate Attenuates Diabetic Nephropathy in Experimental Diabetic Rat's Model *via* Suppression of Augmented TGF-β1/Smad3 Signaling Pathway. *Arch Physiol Biochem* (2016) 122(4):186–94. doi: 10.3109/13813455.2016.1164186
33. Zhai L, Gu J, Yang D, Wang W, Ye S. Metformin Ameliorates Podocyte Damage by Restoring Renal Tissue Podocalyxin Expression in Type 2 Diabetic Rats. *J Diabetes Res* (2015) 2015:231825–. doi: 10.1155/2015/231825
34. Thallas-Bonke V, Coughlan MT, Bach LA, Cooper ME, Forbes JM. Preservation of Kidney Function With Combined Inhibition of NADPH Oxidase and Angiotensin-Converting Enzyme in Diabetic Nephropathy. *Am J Nephrol* (2010) 32(1):73–82. doi: 10.1159/000314924
35. Bae EH, Kim IJ, Park JW, Ma SK, Lee JU, Kim SW. Renoprotective Effect of Rosuvastatin in DOCA–salt Hypertensive Rats. *Nephrol Dialysis Transplant* (2009) 25(4):1051–9. doi: 10.1093/ndt/gfp604
36. Bankhead P, Loughrey MB, Fernández JA, Dombrowski Y, McArt DG, Dunne PD, et al. QuPath: Open Source Software for Digital Pathology Image Analysis. *Sci Rep* (2017) 7(1):16878. doi: 10.1038/s41598-017-17204-5
37. Lane PH, Steffes MW, Mauer SM. Estimation of Glomerular Volume: A Comparison of Four Methods. *Kidney Int* (1992) 41(4):1085–9. doi: 10.1038/ki.1992.165
38. Haas M. Thin Glomerular Basement Membrane Nephropathy: Incidence in 3471 Consecutive Renal Biopsies Examined by Electron Microscopy. *Arch Pathol Lab Med* (2006) 130(5):699–706. doi: 10.1043/1543-2165(2006)130[699:Tgbmni]2.0.Co;2

39. Maunsbach AB, Christensen EI. "Functional Ultrastructure of the Proximal Tubule". *Comprehensive Physiology*. John Wiley & Sons, Ltd (2011) pp. 41–107. doi: 10.1002/cphy.cp080102
40. Caulfield JB, Trump BF. Correlation of Ultrastructure With Function in the Rat Kidney. *Am J Pathol* (1962) 40(2):199–218.
41. Livak KJ, Schmittgen TD. Analysis of Relative Gene Expression Data Using Real-Time Quantitative PCR and the 2(-Delta Delta C(T)) Method. *Methods* (2001) 25(4):402–8. doi: 10.1006/meth.2001.1262
42. Andrews S. *FastQC: A Quality Control Tool for High Throughput Sequence Data [Online]* (2010). Available at: http://www.bioinformatics.babraham.ac.uk/projects/fastqc/.
43. Krueger F. *TrimGalore [Online]* (2021). Available at: https://www.bioinformatics.babraham.ac.uk/projects/trim_galore/.
44. Martin M. Cutadapt Removes Adapter Sequences From High-Throughput Sequencing Reads. *EMBnet J* (2011) 17(1):3. doi: 10.14806/ej.17.1.200
45. Dobin A, Davis CA, Schlesinger F, Drenkow J, Zaleski C, Jha S, et al. STAR: Ultrafast Universal RNA-Seq Aligner. *Bioinformatics* (2012) 29(1):15–21. doi: 10.1093/bioinformatics/bts635
46. Liao Y, Smyth GK, Shi W. Featurecounts: An Efficient General Purpose Program for Assigning Sequence Reads to Genomic Features. *Bioinformatics* (2013) 30(7):923–30. doi: 10.1093/bioinformatics/btt656
47. R Core Team. *R: A Language and Environment for Statistical Computing*. Vienna, Austria: R Foundation for Statistical Computing (2021). Available at: https://www.r-project.org/.
48. Love MI, Huber W, Anders S. Moderated Estimation of Fold Change and Dispersion for RNA-Seq Data With Deseq2. *Genome Biol* (2014) 15(12):550. doi: 10.1186/s13059-014-0550-8
49. Kassambara A, Mundt F. *Factoextra: Extract and Visualize the Results of Multivariate Data Analyses. R Package Version 1.0.7* (2020). Available at: https://cran.r-project.org/package=factoextra.
50. Yu G, Wang L-G, Han Y, He Q-Y. Clusterprofiler: An R Package for Comparing Biological Themes Among Gene Clusters. *OMICS* (2012) 16 (5):284–7. doi: 10.1089/omi.2011.0118
51. Yu G, He QY. ReactomePA: An R/Bioconductor Package for Reactome Pathway Analysis and Visualization. *Mol Biosyst* (2016) 12(2):477–9. doi: 10.1039/c5mb00663e
52. Krämer A, Green J, Pollard JJr., Tugendreich S. Causal Analysis Approaches in Ingenuity Pathway Analysis. *Bioinformatics* (2014) 30(4):523–30. doi: 10.1093/bioinformatics/btt703
53. Durinck S, Spellman PT, Birney E, Huber W. Mapping Identifiers for the Integration of Genomic Datasets With the R/Bioconductor Package biomaRt. *Nat Protoc* (2009) 4(8):1184–91. doi: 10.1038/nprot.2009.97
54. Becht E, Giraldo NA, Lacroix L, Buttard B, Elarouci N, Petitprez F, et al. Estimating the Population Abundance of Tissue-Infiltrating Immune and Stromal Cell Populations Using Gene Expression. *Genome Biol* (2016) 17 (1):218. doi: 10.1186/s13059-016-1070-5
55. Kolde R. *Pheatmap: Pretty Heatmaps. R Package Version 1.0.12* (2019). Available at: https://cran.r-project.org/package=pheatmap.
56. Wilson PC, Wu H, Kirita Y, Uchimura K, Ledru N, Rennke HG, et al. The Single-Cell Transcriptomic Landscape of Early Human Diabetic Nephropathy. *Proc Natl Acad Sci United States America* (2019) 116 (39):19619–25. doi: 10.1073/pnas.1908706116
57. Stuart T, Butler A, Hoffman P, Hafemeister C, Papalexi E, Mauck WM3rd, et al. Comprehensive Integration of Single-Cell Data. *Cell* (2019) 177 (7):1888–902.e21. doi: 10.1016/j.cell.2019.05.031
58. Limbutara K, Chou CL, Knepper MA. Quantitative Proteomics of All 14 Renal Tubule Segments in Rat. *J Am Soc Nephrol JASN* (2020) 31(6):1255–66. doi: 10.1681/asn.2020010071
59. Pagès H, Carlson M, Falcon S, Li N. *AnnotationDbi: Manipulation of SQLite-Based Annotations in Bioconductor. R Package Version 1.56.1* (2021). Available at: https://bioconductor.org/packages/AnnotationDbi.
60. Carlson M. *Org.Rn.eg.db: Genome Wide Annotation for Rat. R Package Version 3.13.0.* (2021).
61. Yan L. *Ggvenn: Draw Venn Diagram by 'Ggplot2'. R Package Version 0.1.8.* (2021). Available at: https://CRAN.R-project.org/package=ggvenn.
62. Nyberg N. *RBNMR*. MATLAB Central File Exchange. Available at: https://www.mathworks.com/matlabcentral/fileexchange/40332-rbnmr. Retrieved January 6, 2022.
63. MATLAB. *The MathWorks Inc.: MATLAB (R2021a)*. Massachusetts: The MathWorks, Inc. (2021).
64. Beirnaert C, Meysman P, Vu TN, Hermans N, Apers S, Pieters L, et al. Speaq 2.0: A Complete Workflow for High-Throughput 1D NMR Spectra Processing and Quantification. *PLoS Comput Biol* (2018) 14(3):e1006018. doi: 10.1371/journal.pcbi.1006018
65. Dieterle F, Ross A, Schlotterbeck G, Senn H. Probabilistic Quotient Normalization as Robust Method to Account for Dilution of Complex Biological Mixtures. Application in 1H NMR Metabonomics. *Anal Chem* (2006) 78(13):4281–90. doi: 10.1021/ac051632c
66. Hedjazi L, Cazier J-B. *mQTL: Metabolomic Quantitative Trait Locus Mapping. R Package Version 1.0* (2013). Available at: https://cran.r-project.org/package=mQTL.
67. Weljie AM, Newton J, Mercier P, Carlson E, Slupsky CM. Targeted Profiling: Quantitative Analysis of 1H NMR Metabolomics Data. *Anal Chem* (2006) 78(13):4430–42. doi: 10.1021/ac060209g
68. Wishart DS, Feunang YD, Marcu A, Guo AC, Liang K, Vázquez-Fresno R, et al. HMDB 4.0: The Human Metabolome Database for 2018. *Nucleic Acids Res* (2018) 46(D1):D608–d17. doi: 10.1093/nar/gkx1089
69. Ulrich EL, Akutsu H, Doreleijers JF, Harano Y, Ioannidis YE, Lin J, et al. BioMagResBank. *Nucleic Acids Res* (2008) 36(Database issue):D402–8. doi: 10.1093/nar/gkm957
70. Shi L, Westerhuis JA, Rosén J, Landberg R, Brunius C. Variable Selection and Validation in Multivariate Modelling. *Bioinf (Oxford England)* (2019) 35 (6):972–80. doi: 10.1093/bioinformatics/bty710
71. Kuhn M. *Caret: Classification and Regression Training. R Package Version 6.0-86* (2020). Available at: https://cran.r-project.org/package=caret.
72. Rohart F, Gautier B, Singh A, KA LC. Mixomics: An R Package for 'Omics Feature Selection and Multiple Data Integration. *PLoS Comput Biol* (2017) 13(11):e1005752. doi: 10.1371/journal.pcbi.1005752
73. Singh A, Shannon CP, Gautier B, Rohart F, Vacher M, Tebbutt SJ, et al. DIABLO: An Integrative Approach for Identifying Key Molecular Drivers From Multi-Omics Assays. *Bioinformatics* (2019) 35(17):3055–62. doi: 10.1093/bioinformatics/bty1054
74. Shannon P, Markiel A, Ozier O, Baliga NS, Wang JT, Ramage D, et al. Cytoscape: A Software Environment for Integrated Models of Biomolecular Interaction Networks. *Genome Res* (2003) 13(11):2498–504. doi: 10.1101/gr.1239303
75. Gustavsen JA, Pai S, Isserlin R, Demchak B, Pico AR. RCy3: Network Biology Using Cytoscape From Within R. *F1000Res* (2019) 8:1774. doi: 10.12688/f1000research.20887.2
76. Kassambara A. *Ggcorrplot: Visualization of a Correlation Matrix Using 'Ggplot2'. R Package Version 0.1.3* (2019). Available at: https://cran.r-project.org/package=ggcorrplot.
77. Kassambara A. Rstatix: Pipe-Friendly Framework for Basic Statistical Tests. R Package Version 0.6.0(2020). Available at: https://cran.r-project.org/package=rstatix.
78. Wickham H. *Ggplot2: Elegant Graphics for Data Analysis*. New York: Springer-Verlag (2016).
79. Pettersen IKN, Tusubira D, Ashrafi H, Dyrstad SE, Hansen L, Liu X-Z, et al. Upregulated PDK4 Expression is a Sensitive Marker of Increased Fatty Acid Oxidation. *Mitochondrion* (2019) 49:97–110. doi: 10.1016/j.mito.2019.07.009
80. Afshinnia F, Nair V, Lin J, Rajendiran TM, Soni T, Byun J, et al. Increased Lipogenesis and Impaired β-Oxidation Predict Type 2 Diabetic Kidney Disease Progression in American Indians. *JCI Insight* (2019) 4(21). doi: 10.1172/jci.insight.130317
81. Forbes JM, Thorburn DR. Mitochondrial Dysfunction in Diabetic Kidney Disease. *Nat Rev Nephrol* (2018) 14(5):291–312. doi: 10.1038/nrneph.2018.9
82. Afshinnia F, Rajendiran TM, Soni T, Byun J, Wernisch S, Sas KM, et al. Impaired β-Oxidation and Altered Complex Lipid Fatty Acid Partitioning With Advancing CKD. *J Am Soc Nephrol* (2018) 29(1):295–306. doi: 10.1681/asn.2017030350
83. Zhang J, Muise ES, Han S, Kutchukian PS, Costet P, Zhu Y, et al. Molecular Profiling Reveals a Common Metabolic Signature of Tissue Fibrosis. *Cell Rep Med* (2020) 1(4):100056. doi: 10.1016/j.xcrm.2020.100056
84. Vasko R. Peroxisomes and Kidney Injury. *Antioxid Redox Signal* (2016) 25 (4):217–31. doi: 10.1089/ars.2016.6666

85. Wanders RJA, Waterham HR, Ferdinandusse S. Metabolic Interplay Between Peroxisomes and Other Subcellular Organelles Including Mitochondria and the Endoplasmic Reticulum. *Front Cell Dev Biol* (2016) 3:83(83). doi: 10.3389/fcell.2015.00083
86. Li M, Wang X, Aa J, Qin W, Zha W, Ge Y, et al. GC/TOFMS Analysis of Metabolites in Serum and Urine Reveals Metabolic Perturbation of TCA Cycle in Db/Db Mice Involved in Diabetic Nephropathy. *Am J Physiol Renal Physiol* (2013) 304(11):F1317–24. doi: 10.1152/ajprenal.00536.2012
87. You YH, Quach T, Saito R, Pham J, Sharma K. Metabolomics Reveals a Key Role for Fumarate in Mediating the Effects of NADPH Oxidase 4 in Diabetic Kidney Disease. *J Am Soc Nephrol JASN* (2016) 27(2):466–81. doi: 10.1681/asn.2015030302
88. Sharma K, Karl B, Mathew AV, Gangoiti JA, Wassel CL, Saito R, et al. Metabolomics Reveals Signature of Mitochondrial Dysfunction in Diabetic Kidney Disease. *J Am Soc Nephrol JASN* (2013) 24(11):1901–12. doi: 10.1681/asn.2013020126
89. Hallan S, Afkarian M, Zelnick LR, Kestenbaum B, Sharma S, Saito R, et al. Metabolomics and Gene Expression Analysis Reveal Down-Regulation of the Citric Acid (TCA) Cycle in Non-Diabetic CKD Patients. *EBioMedicine* (2017) 26:68–77. doi: 10.1016/j.ebiom.2017.10.027
90. Saulnier PJ, Darshi M, Wheelock KM, Looker HC, Fufaa GD, Knowler WC, et al. Urine Metabolites are Associated With Glomerular Lesions in Type 2 Diabetes. *Metabolomics* (2018) 14(6):84. doi: 10.1007/s11306-018-1380-6
91. Darshi M, Van Espen B, Sharma K. Metabolomics in Diabetic Kidney Disease: Unraveling the Biochemistry of a Silent Killer. *Am J Nephrol* (2016) 44(2):92–103. doi: 10.1159/000447954
92. Lysne V, Bjørndal B, Grinna ML, Midttun Ø, Ueland PM, Berge RK, et al. Short-Term Treatment With a Peroxisome Proliferator-Activated Receptor α Agonist Influences Plasma One-Carbon Metabolites and B-Vitamin Status in Rats. *PloS One* (2019) 14(12):e0226069. doi: 10.1371/journal.pone.0226069
93. Lysne V, Strand E, Svingen GFT, Bjørndal B, Pedersen ER, Midttun Ø, et al. Peroxisome Proliferator-Activated Receptor Activation is Associated With Altered Plasma One-Carbon Metabolites and B-Vitamin Status in Rats. *Nutrients* (2016) 8(1):26. doi: 10.3390/nu8010026
94. Ringeissen S, Connor SC, Brown HR, Sweatman BC, Hodson MP, Kenny SP, et al. Potential Urinary and Plasma Biomarkers of Peroxisome Proliferation in the Rat: Identification of N-Methylnicotinamide and N-Methyl-4-Pyridone-3-Carboxamide by 1H Nuclear Magnetic Resonance and High Performance Liquid Chromatography. *Biomarkers* (2003) 8(3-4):240–71. doi: 10.1080/1354750031000149124
95. Ralto KM, Rhee EP, Parikh SM. NAD+ Homeostasis in Renal Health and Disease. *Nat Rev Nephrol* (2020) 16(2):99–111. doi: 10.1038/s41581-019-0216-6
96. Coughlan Melinda T, Nguyen T-V, Penfold Sally A, Higgins Gavin C, Thallas-Bonke V, Tan Sih M, et al. Mapping Time-Course Mitochondrial Adaptations in the Kidney in Experimental Diabetes. *Clin Sci* (2016) 130 (9):711–20. doi: 10.1042/cs20150838
97. Beard ME, Novikoff AB. Distribution of Peroxisomes (Microbodies) in the Nephron of the Rat: A Cytochemical Study. *J Cell Biol* (1969) 42(2):501–18. doi: 10.1083/jcb.42.2.501
98. Wei X, Lu Z, Li L, Zhang H, Sun F, Ma H, et al. Reducing NADPH Synthesis Counteracts Diabetic Nephropathy Through Restoration of AMPK Activity in Type 1 Diabetic Rats. *Cell Rep* (2020) 32(13):108207. doi: 10.1016/j.celrep.2020.108207
99. Wijayatunga NN, Sams VG, Dawson JA, Mancini ML, Mancini GJ, Moustaid-Moussa N. Roux-En-Y Gastric Bypass Surgery Alters Serum Metabolites and Fatty Acids in Patients With Morbid Obesity. *Diabetes Metab Res Rev* (2018) 34(8):e3045. doi: 10.1002/dmrr.3045
100. Duncan RE, Ahmadian M, Jaworski K, Sarkadi-Nagy E, Sul HS. Regulation of Lipolysis in Adipocytes. *Annu Rev Nutr* (2007) 27:79–101. doi: 10.1146/annurev.nutr.27.061406.093734
101. Frazier R, Mehta R, Cai X, Lee J, Napoli S, Craven T, et al. Associations of Fenofibrate Therapy With Incidence and Progression of CKD in Patients With Type 2 Diabetes. *Kidney Int Rep* (2018) 4(1):94–102. doi: 10.1016/j.ekir.2018.09.006
102. Davis TM, Ting R, Best JD, Donoghoe MW, Drury PL, Sullivan DR, et al. Effects of Fenofibrate on Renal Function in Patients With Type 2 Diabetes Mellitus: The Fenofibrate Intervention and Event Lowering in Diabetes (FIELD) Study. *Diabetologia* (2011) 54(2):280–90. doi: 10.1007/s00125-010-1951-1
103. Fruchart J-C, Hermans MP, Fruchart-Najib J. Selective Peroxisome Proliferator–Activated Receptor Alpha Modulators (Spparmα): New Opportunities to Reduce Residual Cardiovascular Risk in Chronic Kidney Disease? *Curr Atheroscl Rep* (2020) 22(8):43. doi: 10.1007/s11883-020-00860-w
104. Maki T, Maeda Y, Sonoda N, Makimura H, Kimura S, Maeno S, et al. Renoprotective Effect of a Novel Selective Pparα Modulator K-877 in Db/Db Mice: A Role of Diacylglycerol-Protein Kinase C-NAD(P)H Oxidase Pathway. *Metabol: Clin Exp* (2017) 71:33–45. doi: 10.1016/j.metabol.2017.02.013
105. Martin WP, Chuah YHD, Conroy E, Reynolds AL, Judge C, López-Hernández FJ, et al. Protocol for a Preclinical Systematic Review and Meta-Analysis of Pharmacological Targeting of Peroxisome Proliferator-Activated Receptors in Experimental Renal Injury. *BMJ Open Sci* (2021) 5(1): e100240. doi: 10.1136/bmjos-2021-100240
106. Peterson RG, Jackson CV, Zimmerman K, de Winter W, Huebert N, Hansen MK. Characterization of the ZDSD Rat: A Translational Model for the Study of Metabolic Syndrome and Type 2 Diabetes. *J Diabetes Res* (2015) 2015:10. doi: 10.1155/2015/487816
107. Marques C, Meireles M, Norberto S, Leite J, Freitas J, Pestana D, et al. High-Fat Diet-Induced Obesity Rat Model: A Comparison Between Wistar and Sprague-Dawley Rat. *Adipocyte* (2016) 5(1):11–21. doi: 10.1080/21623945.2015.1061723
108. Scheurlen KM, Probst P, Kopf S, Nawroth PP, Billeter AT, Muller-Stich BP. Metabolic Surgery Improves Renal Injury Independent of Weight Loss: A Meta-Analysis. *Surg Obes Relat Dis* (2019) 15(6):1006–20. doi: 10.1016/j.soard.2019.03.013
109. Helmy MM, Helmy MW, El-Mas MM. Additive Renoprotection by Pioglitazone and Fenofibrate Against Inflammatory, Oxidative and Apoptotic Manifestations of Cisplatin Nephrotoxicity: Modulation by PPARs. *PloS One* (2015) 10(11):e0142303. doi: 10.1371/journal.pone.0142303
110. Alemán JO, Iyengar NM, Walker JM, Milne GL, Da Rosa JC, Liang Y, et al. Effects of Rapid Weight Loss on Systemic and Adipose Tissue Inflammation and Metabolism in Obese Postmenopausal Women. *J Endocrine Soc* (2017) 1 (6):625–37. doi: 10.1210/js.2017-00020
111. Rossmeislová L, Mališová L, Kračmerová J, Štich V. Adaptation of Human Adipose Tissue to Hypocaloric Diet. *Int J Obes (2005)* (2013) 37(5):640–50. doi: 10.1038/ijo.2012.80
112. Bueter M, Abegg K, Seyfried F, Lutz TA, le Roux CW. Roux-En-Y Gastric Bypass Operation in Rats. *J Visualized Experiments JoVE* (2012) 64):e3940–e. doi: 10.3791/3940

Conflict of Interest: ClR discloses personal fees outside of the submitted work from Novo Nordisk, GI Dynamics, Eli Lilly, Johnson and Johnson, Sanofi, Aventis, Astra Zeneca, Janssen, Bristol-Myers Squibb and Boehringer-Ingelheim.

The remaining authors declare that the research was conducted in the absence of any commercial or financial relationships that could be construed as a potential conflict of interest.

Publisher's Note: All claims expressed in this article are solely those of the authors and do not necessarily represent those of their affiliated organizations, or those of the publisher, the editors and the reviewers. Any product that may be evaluated in this article, or claim that may be made by its manufacturer, is not guaranteed or endorsed by the publisher.

frontiers in Endocrinology

ORIGINAL RESEARCH
published: 17 March 2022
doi: 10.3389/fendo.2022.785605

Transcriptome Analysis Reveal Candidate Genes and Pathways Responses to Lactate Dehydrogenase Inhibition (Oxamate) in Hyperglycemic Human Renal Proximal Epithelial Tubular Cells

Zhimin Wang[1], Dan Hao[2], Dong Fang[3], Jiating Yu[4], Xiao Wang[5] and Guijun Qin[1]**

[1] Division of Endocrinology and Metabolic Diseases, The First Affiliated Hospital of Zhengzhou University, Zhengzhou, China, [2] Shaanxi Key Laboratory of Animal Genetics, Breeding and Reproduction, College of Animal Science and Technology, Northwest A&F University, Yangling, China, [3] Department of Urology, Peking University First Hospital, Institute of Urology, Peking University, Beijing, China, [4] Division of Pediatric Surgery, The First Affiliated Hospital of Zhengzhou University, Zhengzhou, China, [5] Konge Larsen ApS, Kongens Lyngby, Denmark

OPEN ACCESS

Edited by:
Anna Halama,
Weill Cornell Medicine, Qatar

Reviewed by:
Chen Qi Liang,
Fujian University of Traditional Chinese Medicine, China
Wenhu Liu,
Capital Medical University, China

***Correspondence:**
Xiao Wang
xiaowangzntc@163.com
Guijun Qin
hyqingj@zzu.edu.cn

Specialty section:
This article was submitted to Systems Endocrinology, a section of the journal Frontiers in Endocrinology

Received: 29 September 2021
Accepted: 21 February 2022
Published: 17 March 2022

Citation:
Wang Z, Hao D, Fang D, Yu J, Wang X and Qin G (2022) Transcriptome Analysis Reveal Candidate Genes and Pathways Responses to Lactate Dehydrogenase Inhibition (Oxamate) in Hyperglycemic Human Renal Proximal Epithelial Tubular Cells. Front. Endocrinol. 13:785605. doi: 10.3389/fendo.2022.785605

Diabetic kidney disease (DKD) is the leading cause of both chronic kidney disease (CKD) and end-stage renal disease (ESRD). Previous studies showed that oxamate could regulate glycemic homeostasis and impacted mitochondria respiration in a hyperglycemia-dependent manner in the rat proximal tubular cells. To explore the transcriptome gene expression profiling of kidney tissues in human renal proximal epithelial tubular cell line (HK-2), we treated HK-2 cells with high D-glucose (HG) for 7 days before the addition of 40 mM oxamate for a further 24 hours in the presence of HG in this study. Afterwards, we identified 3,884 differentially expressed (DE) genes based on adjusted *P*-value ≤ 0.05 and investigated gene relationships based on weighted gene co-expression network analysis (WGCNA). After qRT-PCR validations, *MAP1LC3A*, *MAP1LC3B* (*P*-value < 0.01) and *BECN1* were found to show relatively higher expression levels in the treated groups than the control groups, while *PGC1α* (*P*-value < 0.05) showed the lower expressions. Accordingly, enrichment analyses of GO terms and KEGG pathways showed that several pathways [e.g., lysosome pathway (hsa04142) and p53 signaling pathway (hsa04115)] may be involved in the response of HK-2 cells to oxamate. Moreover, *via* WGCNA, we identified two modules: both the turquoise and blue modules were enriched in pathways associated with lysosome. However, the p53 signaling pathway was only found using all 3,884 DE genes. Furthermore, the key hub genes *IGFBP3* (adjusted *P*-value = 1.34×10^{-75} and $\log_2$(FC) = 2.64) interacted with 6 up-regulated and 12 down-regulated DE genes in the network that were enriched in the p53 signaling pathway. This is the first study reporting co-expression patterns of a gene network after lactate dehydrogenase inhibition in HK-2 cells. Our results may contribute to our understanding of the underlying

molecular mechanism of *in vitro* reprogramming under hyperglycemic stress that orchestrates the survival and functions of HK-2 cells.

Keywords: diabetic kidney disease, HK-2 cells, high D-glucose, oxamate, transcriptomics, WGCNA, biological enrichment

INTRODUCTION

Diabetic kidney disease (DKD) is the leading cause of chronic kidney disease (CKD) and end-stage renal disease (ESRD) worldwide. Globally, due to the increasing incidence of diabetes and aging, DKD continues to increase stably and imposes the highest burden and the strongest correlation with mortality in patients with diabetes (1, 2). However, the pathological pathways that precipitate the development and/or progression of DKD remain to be fully elucidated. In the kidney, proximal tubular epithelial cells (PTECs), which represent ~90% of the outer kidney cortex and ~50% of the entire kidney mass, present more mitochondria than other renal cell types, because they reabsorb 80% of the filtrate that passes through the glomerulus, including large amounts of water, electrolytes, glucose, and other small molecules (3). Increased glucose reabsorption of PTECs under hyperglycemic stress triggers the initial period of hyperfiltration and tubule-glomerular feedback, exacerbates hypoxia and drives a poorly understood dominos of renal injuries including atrophy of proximal tubular, atubular glomeruli and tubulointerstitial fibrosis that associate with culminating in renal failure and further contributes to the emergence of proximal tubulocentric research (4, 5).

Recently, both *in vivo* and *in vitro* tracer studies have demonstrated an increased glycolysis-driven lactate production, or pyruvate-to-lactate production, in early renal changes associated with diabetes in rat kidney and PTECs (6). Lactic acid is the sink for three-carbon compounds, and the hub of glycolysis, mitochondrial energy metabolism and gluconeogenesis in PTECs (7). Pyruvate-to-lactate process reflects the redox buffer of NADH/NAD^+ ratio across cells (7). Exploration of the pathophysiology involved mechanisms of lactate metabolic adaptation to reshape the field of metabolic reprogramming in hyperglycemic PTECs could offer a comprehensive update on strategies targeting renal tubules.

Oxamate is an isosteric and isoelectronic analogue of pyruvate, i.e., a lactate dehydrogenase (LDH) inhibitor wildly used in tumor cells or in tumor cell energy metabolism and apoptosis research. Recent studies found that oxamate could regulate glycemic homeostasis from both central and peripheral tissues (8). The previous results showed that oxamate, in rat proximal tubular cells line NRK-52E, impacted mitochondria respiration in a hyperglycemia-dependent manner (6). The flexibility of mitochondrial respiration adapting to nutrient stress is dependent on mitophagy and mitochondrial biogenesis; expressions of the mitophagy or mitochondrial biogenesis related genes and their encoded proteins might be involved, e.g., *BCL2*, *BECN1*, *MAP1LC3A*, *MAP1LC3B* and *PGC1α*. Therefore, we aim to explore the transcriptomics of human PTECs cultured with high D-glucose (HG) combined with oxamate *in vitro* to uncover the unexplored *in vitro* reprogramming under hyperglycemic stress and the underlying mechanism for this reprogramming that orchestrates the survival and functions of HK-2 cells (human cortex proximal tubular immortalized cell line), and the therapeutic potentials of targeting the pathways to reprogram the DKD.

The weighted gene co-expression network analysis (WGCNA) is widely used for gene co-expression networks that are constructed by genes with the significant co-expression relationships (9). It shows the co-expressed genes with the similar expression patterns across samples that are controlled by the same transcriptional regulatory programs (10, 11), which has been used in the integrated meta- and microRNA- analysis (12, 13); therefore it can be potentially used in the co-expression analysis of HK-2 cells after oxamate treatment. In this study, three independent replicates of human HK-2 cells with oxamate treatment and three independent replicates of control groups were used. The main objectives of our study are as follows:

1. Conduct a genome-wide transcriptome study on HK-2 cells in the absence and presence of oxamate treatment under HG condition to reveal differentially expressed (DE) genes.
2. Co-expressions analysis for HK-2 cells and construct the weighted gene co-expression networks.
3. Perform the enrichment analysis and identify the potential biological functions for the DE genes on HK-2 cells.
4. Reveal the candidate biomarkers to affect protein levels on HK-2 cells in the network.

MATERIALS AND METHODS

HK-2 Cell Culture

HK-2 cells, the human renal proximal tubular epithelial cell line, were obtained from Beijing Beina Chuanglian Biotechnology Research Institute. HK-2 cells were cultured in Dulbeccos modified eagles medium (DMEM) with the low glucose (Sigma-Aldrich Inc, St. Louis, USA) supplemented with 10% fetal bovine serum (Sigma-Aldrich, St. Louis, USA), 10 units/ml penicillin and 10 mg/ml streptomycin. They were maintained in the continuous culture at 37°C in a humidified atmosphere (5% CO_2) in an incubator. Growth medium was changed every second day, and cells were sub-cultured until further measurements at 80% colony confluency.

Oxamate could induce apoptosis in a dose-dependent manner (14); therefore, the xCELLigence real-time cell analyzer (RTCA) S16 system (Agilent Technologies, Santa Clara, USA) was used to monitor the dynamic real-time cell viability to explore a tolerable dose of oxamate. We exposed HK-2 cells to 5.5 mM low D-glucose (LG) medium or 25 mM HG medium with different

concentrations of oxamate (i.e., 0 mM, 20 mM, 40 mM, 60 mM, 80 mM and 100 mM) for 24-hour intervention. One day prior cells were seeded at a density of 1×10^3 cells per well, respectively, in the 16-well assay plate in medium containing 5.5 mM (LG) or 25 mM (HG) D-glucose. The medium was replaced by 5.5 mM LG medium or 25 mM HG medium with different concentrations of oxamate (i.e., 0 mM, 20 mM, 40 mM, 60 mM, 80 mM and 100 mM). Accordingly, we normalized the starting point 2 hours later after introducing the experimental variables and allowed the cells to grow for the oxamate intervening 24 hours *via* monitoring every 30 minutes. Here, each experiment was carried out in triplicate.

Western Blot Analysis

The radioimmunoprecipitation assay lysis buffer (RIPA buffer) and phenylmethylsulfnoyl fluoride (PMSF) (Servicebio, Wuhan, China) were used to extract proteins at 4°C from the HK-2 cells treated with HG (25 mM) combined with or without different concentrations of oxamate (e.g., 0 mM, 20 mM, 40 mM, 80 mM) for 24 hours. We used BCA protein assay kit (Servicebio, Wuhan, China) to measure and adjust the protein concentrations. The proteins were denatured with 5 × SDS loading buffer (Servicebio, Wuhan, China) at 98°C for 15 min. Then, the prepared proteins were separated by SDS-polyacrylamide gel electrophoresis and concreted with 5% concentrated gel. Polyvinylidene fluoride membranes were used to transfer the proteins at 25 Voltage overnight. We used 5% skim milk solution to block the protein, incubated the membranes with the specific primary antibodies and the secondary antibodies, and visualized the membranes by ECL Plus reagents (Servicebio, Wuhan, China). The primary antibodies [Anti-PGC1α (ab54481), Anti-CASP3 (9665), Anti-BCL2 (ab59348), Anti-BAX (GB11690), Anti-BECN1 (bs-1353R), Anti-MAP1LC3 (14600-1-ap) and Anti-β-actin (GB12001)] and all secondary antibodies were purchased from abcom (Cambridge, MA, USA), Proteintech (Wuhan, China), BIOSS (Boston, Massachusetts, USA) and Servicebio (Wuhan, China), respectively. All primary antibodies were included at the ratio of 1: 3000. AlphaEaseFC software (Alpha Innotech, Miami, USA) was used to calculate the grayscale value of the proteins, and the protein images were processed by the Adobe software.

RNA Sequencing, Read Quality Control and Alignment to Reference Genome

After HK-2 cell culture exposed to different concentrations of oxamate and western blot analysis, 40 mM was chosen as the appropriate oxamate treatment concentration. Thus, six replicates of cells were firstly exposed to HG treatments for seven days, then three replicates of them were exposed to 40 mM oxamate (case group), while the other three replicates were still under the same HG condition but 40 mM oxamate expose (control group). Unfortunately, one replicate of case group failed in RNA sample preparation, so five replicates of cells were finally chosen for RNA sequencing in this study. A total amount of 2 μg RNA per sample was used for RNA sample preparation. The sequencing libraries were generated using NEBNext Library Prep Kit (NEB, USA) for Illumina following the manufacturer's recommendations. Then, they were sequenced on the Illumina Hiseq X ten platform to generate the 150 bp paired-end reads.

In order to guarantee the data quality, raw data was filtered for the clean reads by removing the contaminated reads for adapters (> 5 bp adapter sequences), low quality reads (Phred quality value <= 19 more than 15%) and reads with Ns (Ns > 5%). Afterwards, clean reads were aligned to the human reference genome GRCh38.p13 (Genome Reference Consortium Human Build 38) using HISAT2 software (version 2.1.0) (15) that uses a modified BWT algorithm to convert reference genome to index for faster speed and fewer resources.

FPKM Calculation and Differentially Expressed Gene Analysis

We used HTSeq software (version 0.6.0) (16) to calculate the read counts for each gene. Then, the fragments per kilobase million mapped reads (FPKM) (**Supplementary File 1**) was calculated to estimate the expression levels of genes in each sample, following the formula

$$\mathrm{FPKM} = \frac{10^6 * F}{NL/10^3}$$

where F is the number of fragments in a certain sample that is assigned to a certain gene, N is the total number of mapped reads in the certain sample and L is the length of the certain gene. FPKM could eliminate the effect of sequencing depth and gene length on gene expression levels, so it was most commonly used in the previous studies (17, 18).

DE gene analysis between two groups was performed using R package DESeq2 (version 1.30.0) that was designed for differential gene expression analysis between two groups with biological replicate samples under the theoretical basis following the hypothesis of negative binomial distribution (19–21). DESeq2 estimates the expression level of each gene for each sample by the linear regression model to consider the genes of the same expression levels that share the similarity deviations or own the expression characteristics. It calculates the *P*-value by Wald test and corrects the multiple testings by Benjamini–Hochberg (BH) procedure to achieve the adjusted *P*-value. Here, genes with thresholds of adjusted *P*-value ≤ 0.05 are identified as DE genes. In addition, fold change (FC) of each gene was calculated based on the averaged FPKM value for case group and control group; thus, the up-regulated and down-regulated genes were defined when the $\log_2$(FC) values were positive and negative, respectively.

All genes were visualized in a volcano plot by the R function *plot* based on FCs and adjusted *P*-values. The DE genes were clustered in a heat map by the R function *heatmap* based on the transforms of $\log_{10}$(FPKM + 1) values, where the transforms were scaled for each gene and clustered using the default complete hierarchical clustering method.

Differentially Expressed Gene Validation by qRT-PCR Experiment

The approach of qualitative reverse transcription polymerase chain reaction (qRT-PCR) was applied to validate five genes that are B-cell lymphoma 2 apoptosis regulator (*BCL2*), beclin1

(*BECN1*), microtubule-associated proteins 1A/1B light chain 3A (*MAP1LC3A*), microtubule-associated proteins 1A/1B light chain 3B (*MAP1LC3B*) and peroxisome proliferator-activated receptor-g coactivator 1α (*PGC1α*), using the re-cultured and re-treated cells. The selected genes might be involved in mitophagy and mitochondrial biogenesis for the flexibility of mitochondrial respiration adapting to nutrient stress. Glyceraldehyde-3-phosphate dehydrogenase (*GAPDH*) was chosen as the internal gene for qRT-PCR experiments and 2×SYBR Green qPCR Master Mix (High ROX) (Servicebio, Wuhan, China) was used to perform qRT-PCR experiments. The method of $2^{-\Delta\Delta Ct}$ was used to calculate the relative gene expression levels. All the primers for qRT-PCR experiments are shown in the **Table 1**.

Gene Co-Expression Network of Differentially Expressed Genes and Their Associations With Oxamate Treatment

The gene co-expression network was constructed by R package WGCNA (9) for the similarity measurement between the gene expression profiles by Pearson correlation coefficients of matrix. It transformed the similarity matrix into an adjacency matrix (A) raised to a β exponent (soft threshold) based on the free-scale topology model. A total of 20,377 genes were filtered out of 29,483 genes based on the median absolute deviation (MAD) ≥ 0.01 in this study. The β power parameter (soft threshold) was equal to 8 when the R^2 of the free-scale topology was equal to 0.8 (**Supplementary Figure 1**).

In the network construction, we set the minimum module size equal to 30 for detection with the unsigned TOM type. Additionally, we set the dendrogram cut height for modules merging at 0.25 by clustering module eigengenes using the dissimilarity, so the modules whose eigengenes are highly correlated above 0.75 would be merged on each branch.

Module association between the module eigengenes (MEs) (i.e., the first principle component to represent the overall expression level of the module) and the oxamate treatment status (i.e., 0, 0, 0, 1, 1 for the control and case groups, respectively) was calculated for the relevant module identifications. We calculated the module significance (MS) to evaluate the correlations. Normally, modules with the highest MS score are considered as the key modules (9), thus MS genes in the association analysis (*P*-value < 0.1) were assigned for functional enrichment analysis.

Gene Ontology and Pathway Enrichment Analysis

Both Gene Ontology (GO) terms and Kyoto Encyclopedia of Genes and Genomes (KEGG) pathways analysis were conducted to investigate the important enrichments for the associations between the identified DE genes and gene-related biological functions. We used R package clusterProfiler (version 3.6) (22) to test the statistical enrichments of GO terms and KEGG pathways using DE genes (adjusted *P*-value < 0.05) and DE genes in the key modules with high MS scores, where the GO and pathway enrichments were both based on over-representation analysis (ORA).

Protein-Protein Interactive Analysis of Differentially Expressed Genes

In this study, protein-protein interactions (PPIs) were predicted for the top DE genes based on the STRING database (https://string-db.org). Blastx software (version 2.2.28) (https://blast.ncbi.nlm.nih.gov/Blast.cgi) was used to align the target gene sequences to the selected reference protein sequences using the default settings and the protein networks were built according to the known interactions of human species. Afterwards, we used Cytoscape software (version 3.5.1) to visualize the networks of PPIs (23).

RESULTS

HK-2 Cell Culture and Tolerable Dose Exploration

Comparing with the cells cultured without oxamate (0 mM concentration), the cells treated with 20 mM or 40 mM oxamate retained the proliferation and viability either under LG or HG conditions. However, the cell viability progressively decreased after treating with even higher concentrations of oxamate (i.e., 60 mM, 80mM and 100mM) for 24 hours in both LG medium (**Figure 1A**) and HG medium (**Figure 1B**). It was suggested that oxamate affected the cell viability in a dose-dependent manner in either LG or HG culture condition within 24 hours (**Figure 1**).

Further western blot assay was used to detect the protein expressions of PGC1α, CASP3, BCL2, BAX, BECN1 and MAP1LC3 (**Supplementary Figure 2**). The results showed that oxamate significantly decreased the protein expression levels of PGC1α and BAX under the culture of LGOXA-40mM comparing with the cells cultured without oxamate (0 mM concentration), whereas their expressions remained stable under the treatment of HGOXA-40mM (**Figures 2A, B**). Culturing HK-2 cells in 25 mM HG medium with 40 mM oxamate for 24 hours is suggested to prompt a diabetic state

TABLE 1 | The primers used in the qRT-PCR experiments.

Gene name	Forward Primer	Reverse Primer	Length
BCL2	GAGGAAGTCCAATGTCCAGCC	GCATCCCAGCCTCCGTTATC	157
BECN1	ACATGAGCGAGTTGGTCAAGATC	CCCAGTGACCTTCAGTCTTCG	162
MAP1LC3A	ACATGAGCGAGTTGGTCAAGATC	ACATGAGCGAGTTGGTCAAGATC	141
MAP1LC3B	GTTGGCACAAACGCAGGGTA	ACACTGCTGCTTTCCGTAACAA	305
PGC1α	ACCCAGAACCATGCAAATCACA	ACCCAGAACCATGCAAATCACA	166
GAPDH	ACCCAGAACCATGCAAATCACA	ACCCAGAACCATGCAAATCACA	168

affiliated metabolic reprogramming without disrupting cell growth ability.

Statistics of Alignment to Human Reference Genome

On average, 46,017,884 (97.14%) clean reads were retained from 47,372,938 raw reads after quality control by removing 251,576 low-quality reads, 110,726 ploy-N reads and 992,752 adapter polluted reads. Afterwards, 44,710,680 of them were uniquely mapped to the human reference genome with mapping rate of 97.16% (**Table 2**).

Differentially Expressed Gene in Up/Down Regulation Status and Their Experimental Validations

In this study, we identified 3,884 DE genes (adjusted *P*-value ≤ 0.05) including 1,664 up-regulated DE genes and 2,220 down-regulated DE genes. All the details of 3,884 DE genes with gene names, read counts for each gene along different samples, $\log_2$(FC) values, *P*-values, adjusted *P*-values and regulation status are listed in **Supplementary File 2**. The top ten up-regulated DE genes and down-regulated DE genes were shown in **Table 3**. We found that the most up-regulated DE gene was *SAT1* (adjusted *P*-value = 5.57×10^{-83} and $\log_2$(FC) = 1.75), while the most down-regulated DE gene was *DYNC1H1* (adjusted *P*-value = 3.66×10^{-41} and $\log_2$(FC) = -1.14). In addition, the $\log_2$(FC) values varied from -1.68 to 3.16 among the top ten up-regulated DE genes and ten down-regulated DE genes (**Table 3**).

Figure 3 displayed the obvious division between up-regulated DE genes and down-regulated DE genes based on $\log_2$(FC) values. The range of $\log_2$(FC) values reached to -5 for down-regulated DE genes and 5 for up-regulated DE genes (**Figure 3A**). After the clustering of transformed FPKM values, we found that the DE genes with high expression levels (red color) in two samples (HGOXA2 and HGOXA3) from case group were clustered together, and vice versa (low expression levels in yellow color); thus, the gene expression levels showed an apparent partition between two treatment groups (**Figure 3B**). After the qRT-PCR experiment validations, we found that *MAP1LC3A*, *MAP1LC3B* (*P*-value < 0.01) and *BECN1* had relatively higher expression levels in the 40 mM oxamate treated groups than the control groups, while *PGC1α* (*P*-value < 0.05) showed the lower expressions (**Figure 3C**).

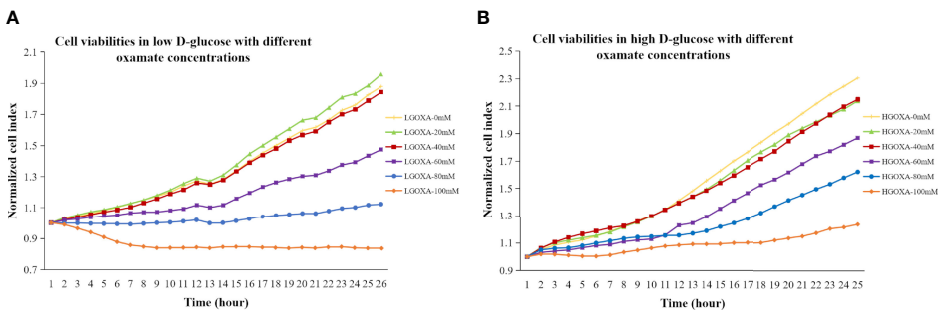

FIGURE 1 | **(A)** Cell viabilities in low D-glucose (LG) with different concentrations of oxamate (LGOXA-0mM, LGOXA-20mM, LGOXA-40mM, LGOXA-60mM, LGOXA-80mM and LGOXA-100mM) for 24 hours. **(B)** Cell viabilities in high D-glucose (HG) with different concentrations of oxamate (HGOXA-0mM, HGOXA-20mM, HGOXA-40mM, HGOXA-60mM, HGOXA-80mM and HGOXA-100mM) for 24 hours.

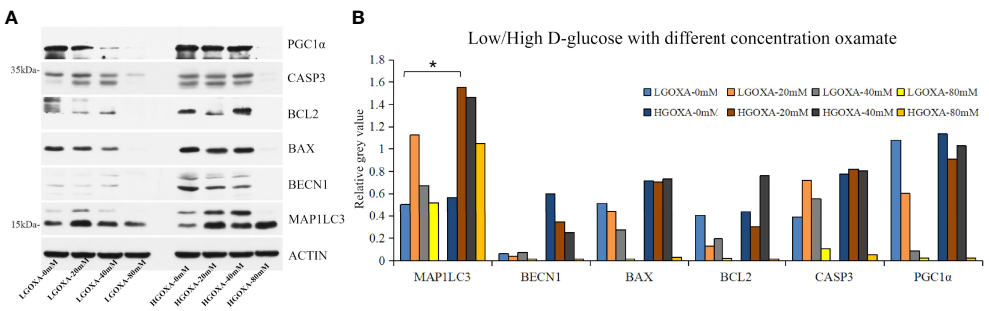

FIGURE 2 | The protein expression levels of peroxisome proliferator-activated receptor-g coactivator 1α (PGC1α), caspase 3 (CASP3), B-cell lymphoma 2 apoptosis regulator (BCL2), BCL2 associated X apoptosis regulator (BAX), beclin1 (BECN1) and microtubule-associated proteins 1A/1B light chain 3 (MAP1LC3) in HK-2 cells treated with low D-glucose (LG) with different concentrations of oxamate (LGOXA-0mM, LGOXA-20mM, LGOXA-40mM and LGOXA-80mM) and high D-glucose **(HG)** with different concentrations of oxamate (HGOXA-0mM, HGOXA-20mM, HGOXA-40mM and HGOXA-80mM) for 24 hours. **(A)** Western blot gels. **(B)** Relative grey values. * indicates *P*-value < 0.05 after student's *t*-test.

TABLE 2 | Statistics of quality control and alignment to human reference genome (GRCh38.p13).

Sample	Raw read number	Low-quality read number (%)	Ploy-N read number (%)	Adapter polluted read number (%)	Clean read number (%)	Mapped read (%)
HG1	48,909,654	219,180 (0.45)	70,820 (0.14)	732,722 (1.50)	47,886,932 (97.91)	46,597,334 (97.31)
HG2	47,359,384	337,124 (0.71)	83,178 (0.18)	675,864 (1.43)	46,263,218 (97.69)	44,866,400 (96.98)
HG3	47,542,838	192,338 (0.41)	261,400 (0.55)	2,126,872 (4.47)	44,962,228 (94.57)	43,678,133 (97.14)
HGOXA2	46,419,566	243,330 (0.52)	60,204 (0.13)	698,242 (1.50)	45,417,790 (97.84)	44,197,980 (97.31)
HGOXA3	46,633,246	265,908 (0.57)	78,028 (0.17)	730,058 (1.57)	45,559,252 (97.70)	44,213,554 (97.05)
Mean	47,372,938	251,576 (0.53)	110,726 (0.23)	992,752 (2.09)	46,017,884 (97.14)	44,710,680 (97.16)
SD	980,639	55,115 (0.12)	84,669 (0.18)	634,430 (1.33)	1,144,377 (1.44)	1,135,766 (0.15)

% indicates the percentage. HGOXA2 and HGOXA3 indicate the case group that were treated with 40 mM oxamate in 25 mM HG medium. HG1, HG2 and HG3 indicate the control groups that were only treated with 25 mM HG medium without oxamate.

Co-Expression Network of Differentially Expressed Genes and the Key Modules Associated With Oxamate Treatment

Using 3,884 DE genes for the sample clustering, we found the samples with oxamate treatment were clustered together (**Figure 4A**). The eigengene adjacency heatmap indicated that these modules of DE genes could be clustered further together into groups, where treatment status was grouped with blue pattern (**Figure 4B**). The weighted DE gene network construction was visualized in the topological overlap matrix (TOM) clusters that showed a high level of overlap densities among the two clusters (**Figure 4C**). Obviously, DE genes were grouped into 2 modules that had similar co-expressions using the average linkage hierarchical clustering algorithm (**Figures 4B, C**), where 3,087 DE genes were grouped into turquoise module as the key module, followed by 797 DE genes into blue module. The module-trait relationship results revealed that oxamate treatment had high correlations with the turquoise module (correlation coefficient = -0.97, *P*-value < 0.01) and blue module (correlation coefficient = 0.96, *P*-value < 0.01) (**Figure 4D**).

Significant Enrichments of GO Term and Pathway

Based on 3,884 DE genes, a total of 1,556 significant GO terms were derived for three domains including 998 biological process (BP), 336 cellular component (CC) and 222 molecular function (MF) ontologies (**Figure 5A**). Based on the regulation status of DE genes, 430 up-regulated and 1126 down-regulated significant GO terms (**Figure 5A**), and 22 up-regulated and 58 down-regulated significant pathways (**Figure 5B**) were achieved respectively.

We found that the three most significant GO terms were chromosome segregation (GO:0007059, adjusted *P*-value =

TABLE 3 | Top ten up-regulated and ten down-regulated differentially expressed genes.

Ensembl gene ID	*Gene name*	Full description	Log_2 (FC)	Adjusted *P*-value	Regulation status
ENSG00000130066	*SAT1*	Spermidine/spermine N1-acetyltransferase 1	1.75	5.57×10^{-83}	Up-regulated
ENSG00000146674	*IGFBP3*	Insulin like growth factor binding protein 3	2.64	1.34×10^{-75}	Up-regulated
ENSG00000165272	*AQP3*	Aquaporin 3 (Gill blood group)	1.97	1.40×10^{-59}	Up-regulated
ENSG00000126709	*IFI6*	Interferon alpha inducible protein 6	2.04	1.15×10^{-53}	Up-regulated
ENSG00000163220	*S100A9*	S100 calcium binding protein A9	3.16	5.50×10^{-51}	Up-regulated
ENSG00000187134	*AKR1C1*	Aldo-keto reductase family 1 member C1	2.12	8.45×10^{-50}	Up-regulated
ENSG00000019186	*CYP24A1*	Cytochrome P450 family 24 subfamily A member 1	1.57	5.53×10^{-49}	Up-regulated
ENSG00000169715	*MT1E*	Metallothionein 1E	1.42	1.07×10^{-48}	Up-regulated
ENSG00000198886	*MT-ND4*	Mitochondrially encoded NADH dehydrogenase 4	1.04	2.15×10^{-44}	Up-regulated
ENSG00000151632	*AKR1C2*	Aldo-keto reductase family 1 member C2	2.82	9.21×10^{-43}	Up-regulated
ENSG00000197102	*DYNC1H1*	Dynein cytoplasmic 1 heavy chain 1	-1.14	3.66×10^{-41}	Down-regulated
ENSG00000167548	*KMT2D*	Lysine methyltransferase 2D	-1.68	9.12×10^{-38}	Down-regulated
ENSG00000109971	*HSPA8*	Heat shock protein family A (Hsp70) member 8	-1.03	1.58×10^{-37}	Down-regulated
ENSG00000148773	*MKI67*	Marker of proliferation Ki-67	-1.38	6.53×10^{-37}	Down-regulated
ENSG00000243156	*MICAL3*	Microtubule associated monooxygenase, calponin and LIM domain containing 3	-1.39	1.46×10^{-35}	Down-regulated
ENSG00000149503	*INCENP*	Inner centromere protein	-1.36	5.14×10^{-33}	Down-regulated
ENSG00000178209	*PLEC*	Plectin	-0.92	6.87×10^{-33}	Down-regulated
ENSG00000127481	*UBR4*	Ubiquitin protein ligase E3 component n-recognin 4	-1.10	1.11×10^{-30}	Down-regulated
ENSG00000113810	*SMC4*	Structural maintenance of chromosomes 4	-1.43	3.91×10^{-29}	Down-regulated
ENSG00000130723	*PRRC2B*	Proline rich coiled-coil 2B	-1.10	1.44×10^{-27}	Down-regulated

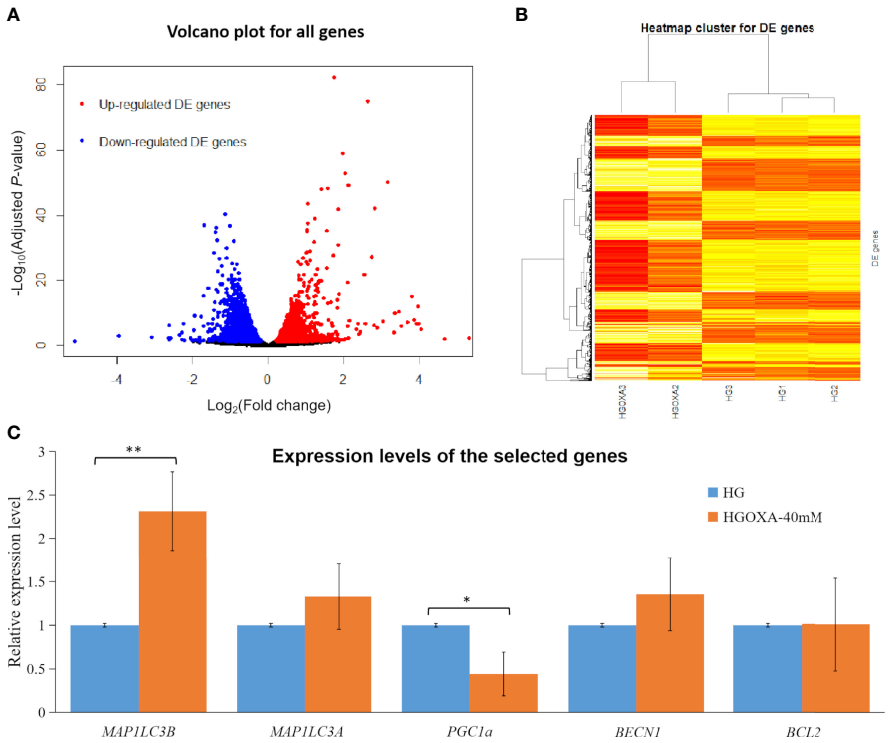

FIGURE 3 | Differentially expressed (DE) analysis results. **(A)** Volcano plots for all genes based on fold change (FC) values and adjusted *P*-values. Note: Genes with thresholds of adjusted *P*-value ≤ 0.05 are identified as DE genes. **(B)** Heatmap plots for all DE genes. Note: The color from yellow to red indicates the gene expression levels from low to high after the transforms of $\log_{10}$(FPKM + 1) values. HGOXA2 and HGOXA3 indicate the case group that were treated with 40 mM oxamate in 25 mM HG medium. HG1, HG2 and HG3 indicate the control groups that were only treated with 25 mM HG medium without oxamate. **(C)** Relative expression levels of the selected genes validated by qRT-PCR experiments. Note: HGOXA-40mM indicates the case group that was treated with 40 mM oxamate in 25 mM HG medium. ** and * indicate the *P*-value < 0.01 and *P*-value < 0.05, respectively, after the student's *t*-test.

2.95×10^{-30}) with 115 DE genes, mitotic nuclear division (GO:0140014, adjusted *P*-value = 2.33×10^{-28}) with 104 DE genes and DNA replication (GO:0006260, adjusted *P*-value = 2.33×10^{-28}) with 102 DE genes in the BP ontology of down-regulated category (**Figure 6A**). Similarly, the three most significant pathways were also in the down-regulated category including RNA transport (hsa03013, adjusted *P*-value = 1.43×10^{-9}) with 55 DE genes, cell cycle (hsa04110, adjusted *P*-value = 2.04×10^{-9}) with 42 DE genes and spliceosome (hsa03040, adjusted *P*-value = 1.27×10^{-6}) with 42 DE genes (**Figure 6B**). Based on 3,087 DE genes in the turquoise module after WGCNA analysis, the three most significant GO terms and pathways (**Figures 7A, B**) were similar to the enrichment results based on 3,884 DE genes, except the longevity regulating pathway - multiple species (hsa04213, adjusted *P*-value = 3.46×10^{-6}) with 22 DE genes (**Figure 7B**) only in the turquoise module. However, enrichment results of 797 DE genes in the blue module were quite different from those in the turquoise module (**Figures 8A, B**), where only RNA transport was still one of the three most significant pathways (**Figure 8B**).

In the up-regulated category, protein localization to endoplasmic reticulum (GO:0070972, adjusted *P*-value = 6.26×10^{-18}, DE gene = 51), neutrophil mediated immunity (GO:0002446, adjusted *P*-value = 1.14×10^{-17}, DE gene = 102) and cotranslational protein targeting to membrane (GO:0006613, adjusted *P*-value = 1.36×10^{-17}, DE gene = 43) in the BP ontology were the most significant GO terms based on 3,884 DE genes (**Figure 6A**). Meanwhile, lysosome (hsa04142, adjusted *P*-value = 2.30×10^{-13}, DE gene = 45), ribosome (hsa03010, adjusted *P*-value = 3.54×10^{-11}, DE gene = 47) and coronavirus disease - COVID-19 (hsa05171, adjusted *P*-value = 5.07×10^{-8}, DE gene = 53) were the most significant pathways (**Figure 6B**). Moreover, we found that p53 signaling pathway with 16 DE genes (hsa04115, adjusted *P*-value = 1.73×10^{-2}) was also involved in the top significant pathways (**Figure 6B**). Based on 3,087 DE genes in the turquoise module, the three most significant GO terms and pathways (**Figures 7A, B**) were similar to the enrichment results based on 3,884 DE genes, but enrichment results of 797 DE genes in the blue module were still different (**Figures 8A, B**).

Protein-Protein Interaction Networks of Differentially Expressed Genes

The PPI network results were visualized using the top eight up-regulated DE genes (*SAT1*, *IGFBP3*, *AQP3*, *IFI6*, *S100A9*, *AKR1C1*, *CYP24A1* and *AKR1C2*) and the top six down-regulated DE genes (*DYNC1H1, KMT2D, INCENP, SMC4, MKI67* and *PRRC2B*). It showed that most DE genes had the PPIs with at least two other DE genes (**Figure 9**). For example,

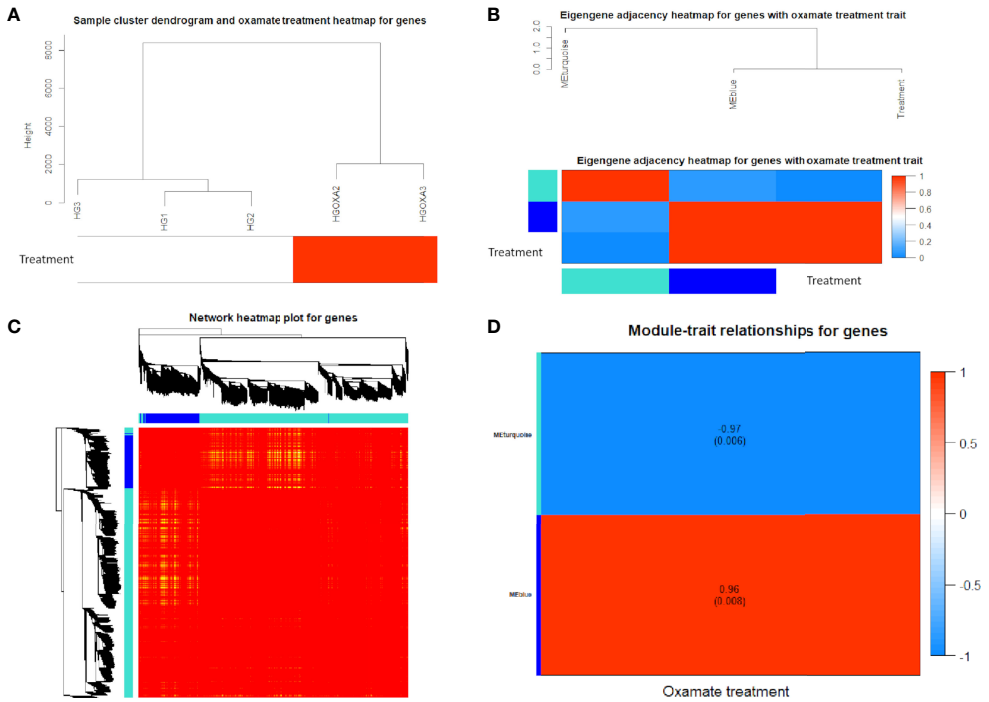

FIGURE 4 | Co-expression network results of differentially expressed (DE) genes. **(A)** Sample cluster heatmap with oxamate treatment for DE genes. **(B)** Eigengene dendrogram and adjacency heatmap of different co-expression modules for DE genes. **(C)** Weighted DE gene network heatmap of the co-expression interactions based on the topological overlap matrix (TOM) dissimilarity. Note: The gene dendrogram and module assignment are shown along the left side and the top, where the axe colors indicate the different modules. The color intensity inside the heatmap represents the overlap degree, where light color represents low overlap and darker red color represents higher overlap. **(D)** Module-trait relationship heatmap between oxamate treatment and control groups for DE genes. Each row indicates module eigengenes (the first principle component of the module) with the correlation coefficients (*P*-values in the brackets), where red color represents positive correlation and blue color represents negative correlation.

the up-regulated *IGFBP3* had the PPIs with the other 6 up-regulated DE genes (*CSF2*, *MT1F*, *RAD54B*, *MKI67*, *CCNE2* and *DDIT3*) and 12 down-regulated DE genes (*STEAP1*, *ANGPTL4*, *FOS*, *PRR15*, *HTRA1*, *LCN2*, *C1R*, *MUC1*, *SAA1*, *NDUFA4L2*, *MX1* and *C1S*) (**Figure 9A**). The down-regulated *KMT2D* had the PPIs with the other 13 up-regulated DE genes (*RP11-313J2.1*, *ZNF699*, *CCNE2*, *ZNF488*, *ZNF770*, *RAD548*, *SZT2*, *EP400*, *MICAL3*, *TRRAP*, *DYNC1H1*, *ZIC4* and *PHC1P1*) and 6 down-regulated DE genes (*HIST2H2AA3*, *ZSCAN16*, *HIST1H1C*, *ZNF880*, *HIST1H2AC* and *IFIT1*) (**Figure 9B**).

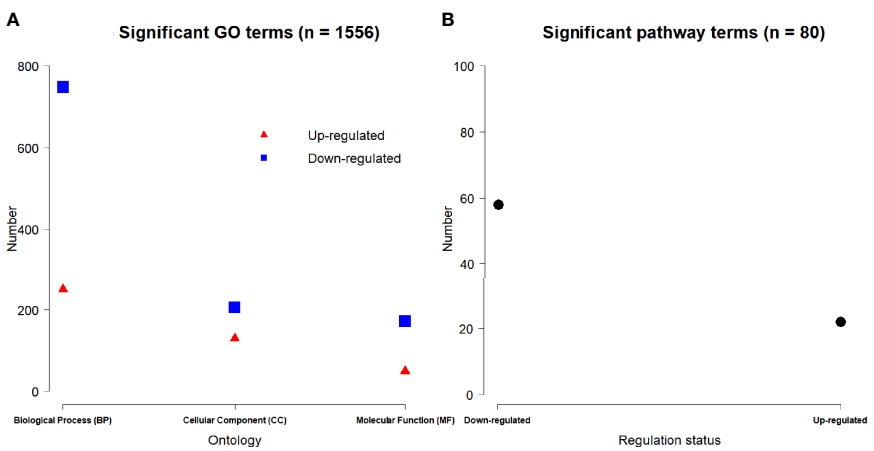

FIGURE 5 | Number of the significant up-regulated and down-regulated **(A)** GO terms and **(B)** pathways.

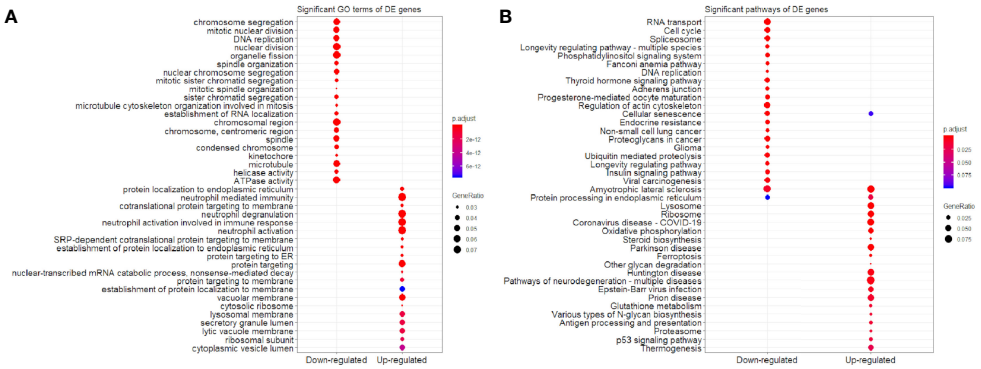

FIGURE 6 | Significant **(A)** GO terms and **(B)** pathways for differentially expressed (DE) genes (n = 3,884) in the down-regulated and up-regulated categories.

DISCUSSION

Proximal tubules present a very high density of mitochondria required for energy consumption (24). Mitochondria occupy about 16.3% relative volume of the human cross-sectioned proximal convoluted tubules (S1 and S2 combined) (25). Mitochondrial dysfunction, with persistent energy depletion and deficiency of oxygen utilization efficiency, is the main driver in the progression of hyperglycemic proximal tubules (24). The process of selective removal of dysfunctional and depolarized mitochondria, known as mitophagy, interfaces and coordinates with mitochondrial biogenesis to maintain mitochondrial homeostasis. Previous studies showed that oxamate could impact mitochondria respiration in a hyperglycemia-dependent manner in the rat proximal tubular cells (6). Here, our results further suggested that under diabetic state, this metabolic reprogramming caused by oxamate was related to its impact on the resilience in both mitophagy and mitochondrial biogenesis, in which MAP1LC3 (MAP1LC3A and MAP1LC3B), BECN1 and PGC1α were involved.

Oxamate Features on Cell Viability/ Survival and Mitochondrial Biogenesis

In mammals, lactate and pyruvate as two sinks for three-carbon compounds, enable the crosstalk between glycolytic flux and mitochondrial respiratory function, and serve as a circulating redox buffer that equilibrates the NADH/NAD+ ratio across cells and tissues together (7). For a long time, oxamate had been considered as a classic LDH enzyme inhibitor. Later, the kinetic modeling results revealed the multiple sites targeting of oxamate (14). Besides LDH inhibition function, oxamate strongly blocked pyruvate kinase (PYK) and enolase (ENO) activities, and slightly inhibited hexosephosphate isomerase (HPI), aldolase (ALD) and glucose-6-phosphate dehydrogenas (Glc6PDH) activities (14). Oxamate effect on cell fate in a dose-dependent manner depended on its cumulative influences on multiple combinations of metabolic enzymes and metabolites. Heretofore, we found that treating hyperglycemic NRK-52E with a relatively high concentration of oxamate (e.g., 100mM) significantly reduced the cell proliferations and survivals (6). To avoid the bias related to cell death caused by excessive drug

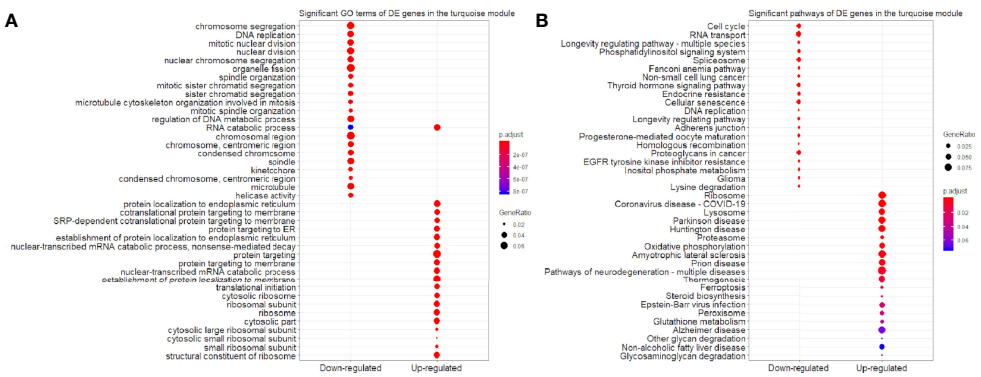

FIGURE 7 | Significant **(A)** GO terms and **(B)** pathways for differentially expressed (DE) genes in the turquoise module (n = 3,087) in the down-regulated and up-regulated categories.

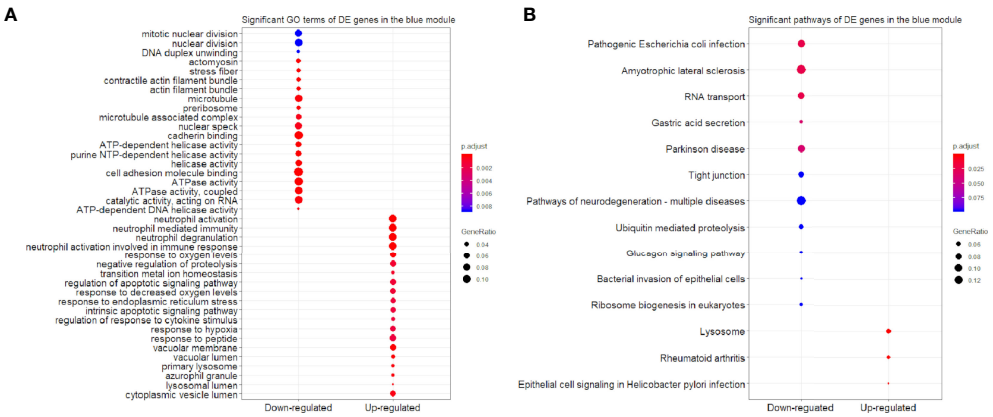

FIGURE 8 | Significant **(A)** GO terms and **(B)** pathways for differentially expressed (DE) genes in the blue module (n = 797) in the down-regulated and up-regulated categories.

concentration, we explored the dose-dependent manner of oxamate on cell viability/survival and mitochondrial biogenesis. Finally, cells treated with 40mM oxamate under HG condition that retained cell viability/survival is suggested to abrogate the PGC1α inhibiting properties caused by oxamate (**Figures 1**, **2**); thus, 40mM oxamate is considered as a plausible concentration for our transcriptomic study.

Differentially Expressed and Co-Expressed Genes After Oxamate Treatment

Oxamate was found to downregulate the expression of *IL6* and upregulate the expression of *PDE3B* in the skeletal muscle of *db/db* mice (26). However, *IL6* (adjusted *P*-value = 2.43×10^{-2} and $\log_2$(FC) = 0.54) was identified as one up-regulated DE gene, whereas *PDE3B* (adjusted *P*-value = 1.80×10^{-2} and $\log_2$(FC) = -0.52) as one down-regulated DE gene in our study (**Supplementary File 2**). As a B-cell differentiation factor, interleukin 6 (IL6) is a multifunctional cytokine to regulate the hematopoiesis, immune and acute-phase responses, and inflammations of interleukin 1 (IL1), tumor necrosis factor alpha (TNF-α), and lipopolysaccharide (LPS) as the stimuli (27–30). *PDE3B* with *PDE3A* from the PDE3 family hydrolyze cAMP and cGMP, and its isoforms are in higher expressions than *PDE3A* in tissues that regulate energy homeostasis, including adipose tissue, liver and pancreatic β cells (31, 32). Ahmad et al. (33) demonstrated that the role of *PDE3B* regulated NLRP3 inflammasome in modulating inflammatory responses to contribute to a reduced inflammatory state in adipose tissue. In addition, our study found *SAT1* (Spermidine/spermine N1-acetyltransferase 1) was the most up-regulated DE gene (adjusted *P*-value = 5.57×10^{-83} and $\log_2$(FC) = 1.75) (**Table 3**). It is reported that *SAT1* is an important transporter involved in sulfate homeostasis as an anion exchanger and regulates the expression of the hepatocellular sulfate by glyoxylate that could be a metabolic link between liver and kidney (34).

The HIF inhibiting properties were removed using oxamate in the hyperglycemic rat proximal tubular cells (6). Studies have

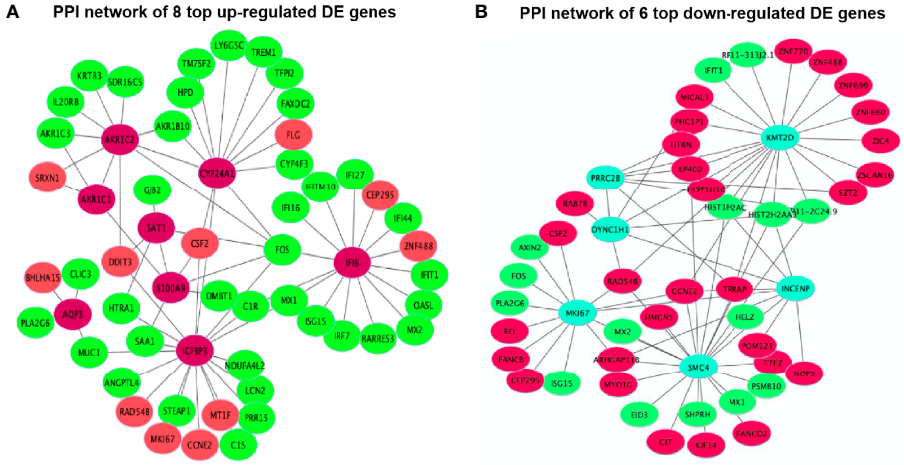

FIGURE 9 | Protein-protein interactions (PPIs) network of 14 top DE genes including **(A)** 8 top up-regulated DE genes and **(B)** 6 top down-regulated DE genes.

been reported that oxamate could induce autophagy *via* downregulation HIF-1α through inhibiting the Akt-mTOR signaling pathway in cancer cells (35, 36). *BECN1* is a haploinsufficient tumor suppressor gene as a core component of the class III phosphatidylinositol 3-kinase that is involved in autophagosome formation and vesicular trafficking (37). It has been suggested that *BECN1* was required for mitophagy completion, and suppressed mitophagy by *BECN1* deficiency could cause aberrant mitochondria quality control in adipocyte to cause lipodystrophy and metabolic dysregulation (38). The qRT-PCR experiment results of *MAP1LC3A* (adjusted *P*-value = 1.30×10^{-3} and $\log_2$(FC) = 0.71) and *MAP1LC3B* (adjusted *P*-value = 8.47×10^{-4} and $\log_2$(FC) = 0.35) showed higher expression levels in the 40 mM oxamate treated groups than the non-treated groups after validations (*P*-value < 0.01 after student's *t*-test) (**Figure 3C**), which is consistent with the transcriptome results in the up-regulated status (**Supplementary File 2**). Matboli et al. (2017) (39) revealed *MAP1LC3A* with the high diagnostic power for detection of DKD, as the urinary expression level of *MAP1LC3A* was significantly lower in DKD than the control group. The mRNA expressions of *MAP1LC3B* were also down-regulated in the DKD group (40). MAP1LC3 is essential in autophagosome mature and selective engulfment of damaged mitochondria fusing with lysosomes and processing mitophagy (41, 42). Therefore, oxamate could be involved in reprogramming the DKD *via* the influence of some potential therapeutic pathways, where the DE *MAP1LC3A* and *MAP1LC3B* are involved.

Significant Pathways and Protein-Protein Interaction Networks in Human Proximal Tubular Cells

Lysosome (hsa04142) was identified as one of the common significant pathways based on 3,884 DE genes, 3,087 DE genes in the turquoise module and 797 DE genes in the blue module (**Figures 6B**, **7B**, **8B**), where *ACP2*, *AGA*, *ARSA*, *ASAH1*, *ATP6AP1*, *CD63*, *CTNS*, *CTSA*, *CTSB*, *CTSC*, *CTSD*, *CTSF*, *CTSH*, *CTSL*, *CTSS*, *CTSZ*, *DNASE2*, *FUCA1*, *FUCA2*, *GAA*, *GLA*, *GNPTG*, *GUSB*, *HEXA*, *HEXB*, *HGSNAT*, *HYAL3*, *LAMP1*, *LAPTM4A*, *LAPTM4B*, *LGMN*, *LIPA*, *LITAF*, *MAN2B1*, *NAGLU*, *NAGPA*, *NAPSA*, *NEU1*, *NPC2*, *PPT1*, *PSAP*, *SLC11A2*, *SMPD1* and *TPP1* were enriched in. Lysosome, known as the place for autophagy, has been recognized as a highly dynamic organelle that bidirectionally contact with mitochondria, to sense nutrient stress and control the switch between anabolism and catabolism by regulating mitochondrial biogenesis and autophagy (43, 44).

There is one pathway, p53 signaling pathway (hsa04115), only found in all 3,884 DE gene enrichment (**Figure 6B**), where *AIFM2*, *BBC3*, *BCL2L1*, *BID*, *CCNE1*, *CDKN1A*, *CHEK2*, *COP1*, *GADD45A*, *GADD45B*, *IGFBP3*, *PERP*, *SHISA5*, *SIAH1*, *TP53* and *TP53I3* were enriched. Chen et al. (45) revealed that MPC-5 cells from the high glucose-induced proliferation-inhibition and apoptosis-promotion *via* p53 signaling pathway can be protected by silencing the CCNG1 (45). Here, *IGFBP3*, as one of the key genes, interacted with 6 up-regulated and 12 down-regulated DE genes in the PPI networks (**Figure 9A**). It is reported that increased oxidative stress from high glucose enhances IGFBP3 expression to induce apoptosis; however, increased IGFBP3 expression by high glucose mediates high-glucose-induced apoptosis in PTECs and induces additional oxidative stress, which may result in amplification of hyperglycemic damage (46–48). The inhibition of LDH in hyperglycemic proximal tubular increased aerobic glycolysis (6), and changes in the extramitochondrial-free NADH/NAD+ ratio signal associated with aerobic glycolysis could control the abundance and activity of p53 by the C-terminal binding protein (CtBP) family of NADH-sensitive transcriptional regulators (49). Previous studies showed increased NADH/NAD+ ratio in response to the oxamate treatment in hyperglycemic rat proximal tubular cells (6). Here, we propose that the NADH-CtBP-p53 pathway may present as one of the hyperglycemia-dependent metabolic reprogramming caused by oxamate.

CONCLUSIONS

In summary, our study conducted the genome-wide transcriptome and co-expression analysis for HK-2 cells to identify 3,884 DE genes (adjusted *P*-value ≤ 0.05), where 1,664 of them were up-regulated and 2,220 of them were down-regulated. In addition, two modules of co-expression patterns were constructed to perform GO terms and pathways. We found that lysosome (hsa04142) can be enriched in DE genes of all, turquoise and blue modules, but p53 signaling pathway (hsa04115) was only detected in all DE genes. *IGFBP3* (adjusted *P*-value = 1.34×10^{-75} and $\log_2$(FC) = 2.64), one of the key genes in p53 signaling pathway (hsa04115), interacted with several DE genes in the PPI networks and could be considered as the candidate biomarker due to its impact in high glucose conditions, after further validations. Together, our results highlight a possibility that anaerobic glycolysis-induced lactate in hyperglycemic HK-2 cells might integrate metabolic signals to mitochondria-lysosome contacts through some unexplored mechanism, which oscillates the coupling of mitochondrial biogenesis and mitophagy, and prolongedly compromises stress resistance.

DATA AVAILABILITY STATEMENT

The raw RNA sequencing data were deposited in the Gene Expression Omnibus (GEO) of National Center for Biotechnology Information (NCBI) with the accession number GSE182138 at https://www.ncbi.nlm.nih.gov/geo/query/acc.cgi?acc=GSE182138.

AUTHOR CONTRIBUTIONS

ZW, XW, and GQ conceived and designed the experiments. ZW and JY performed the experiments. XW, DH, and ZW analyzed the data and wrote the manuscript. ZW, DH, DF, XW, and GQ improved the manuscript. All authors read and approved the final manuscript.

FUNDING

This study was supported by the Overseas Research Project of Scientific and Technological Talents in Health and Family Planning of Henan Province (No. 2015013) and National Natural Science Foundation of China (No. 82100896).

SUPPLEMENTARY MATERIAL

The Supplementary Material for this article can be found online at: https://www.frontiersin.org/articles/10.3389/fendo.2022.785605/full#supplementary-material

Supplementary Figure 1 | R^2 of the free-scale topology and mean connectivity with soft threshold (power) for 20,377 genes.

Supplementary Figure 2 | The original Western blot gels of protein levels of peroxisome proliferator-activated receptor-g coactivator 1α (PGC1α), caspase 3 (CASP3), B-cell lymphoma 2 apoptosis regulator (BCL2), BCL2 associated X apoptosis regulator (BAX), beclin1 (BECN1) and microtubule-associated proteins 1A/1B light chain 3 (MAP1LC3) in HK-2 cells treated with low D-glucose (LG) with different concentrations of oxamate (LGOXA-0mM, LGOXA-20mM, LGOXA-40mM and LGOXA-80mM) and high D-glucose (HG) with different concentrations of oxamate (HGOXA-0mM, HGOXA-20mM, HGOXA-40mM and HGOXA-80mM) for 24 hours.

Supplementary File 1 | The fragments per kilobase million mapped reads (FPKM) for each gene (n = 29,483) along five different samples.

Supplementary File 2 | All 3,884 differentially expressed (DE) genes with gene names, read counts, log_2(FC) values, *P*-values, adjusted *P*-values and regulation status along five different samples.

REFERENCES

1. Anders HJ, Huber TB, Isermann B, Schiffer M. CKD in Diabetes: Diabetic Kidney Disease Versus Nondiabetic Kidney Disease. *Nat Rev Nephrol* (2018) 14:361–77. doi: 10.1038/s41581-018-0001-y
2. Bonner R, Albajrami O, Hudspeth J, Upadhyay A. Diabetic Kidney Disease. *Primary Care - Clinics Office Pract* (2020) 47:645–59. doi: 10.1016/j.pop.2020.08.004
3. Bhargava P, Schnellmann RG. Mitochondrial Energetics in the Kidney. *Nat Rev Nephrol* (2017) 13:629–46. doi: 10.1038/nrneph.2017.107
4. Vallon V, Thomson SC. The Tubular Hypothesis of Nephron Filtration and Diabetic Kidney Disease. *Nat Rev Nephrol* (2020) 16:317–36. doi: 10.1038/s41581-020-0256-y
5. Duan S, Lu F, Song D, Zhang C, Zhang B, Xing C, et al. Current Challenges and Future Perspectives of Renal Tubular Dysfunction in Diabetic Kidney Disease. *Front Endocrinol* (2021) 12:661185. doi: 10.3389/fendo.2021.661185
6. Wang Z, Nielsen PM, Laustsen C, Bertelsen LB. Metabolic Consequences of Lactate Dehydrogenase Inhibition by Oxamate in Hyperglycemic Proximal Tubular Cells. *Exp Cell Res* (2019) 378:51–6. doi: 10.1016/j.yexcr.2019.03.001
7. Rabinowitz JD, Enerbäck S. Lactate: The Ugly Duckling of Energy Metabolism. *Nat Metab* (2020) 2:566–71. doi: 10.1038/s42255-020-0243-4
8. Lam TK, Gutierrez-Juarez R, Pocai A, Rossetti L. Regulation of Blood Glucose by Hypothalamic Pyruvate Metabolism. *Science* (2005) 309(5736):943–7.
9. Langfelder P, Horvath S. WGCNA: An R Package for Weighted Correlation Network Analysis. *BMC Bioinf* (2008) 9:559. doi: 10.1186/1471-2105-9-559
10. Stuart JM, Segal E, Koller D, Kim SK. A Gene-Coexpression Network for Global Discovery of Conserved Genetic Modules. *Science* (2003) 302 (5643):249–255. doi: 10.1126/science.1087447
11. Weirauch MT. Gene Coexpression Networks for the Analysis of DNA Microarray Data. *Appl Stat Netw Biol: Methods Syst Biol* (2011) 1:215–50. doi: 10.1002/9783527638079.ch11
12. Farhadian M, Rafat SA, Panahi B, Mayack C. Weighted Gene Co-Expression Network Analysis Identifies Modules and Functionally Enriched Pathways in the Lactation Process. *Sci Rep* (2021) 11:1–15. doi: 10.1038/s41598-021-81888-z
13. Hao D, Wang X, Yang Y, Thomsen B, Holm L-E, Qu K, et al. Integrated Analysis of mRNA and MicroRNA Co-Expressed Network for the Differentiation of Bovine Skeletal Muscle Cells After Polyphenol Resveratrol Treatment. *Front Vet Sci* (2021) 8:777477. doi: 10.3389/fvets.2021.777477
14. Moreno-Sánchez R, Marín-Hernández Á., Del Mazo-Monsalvo I, Saavedra E, Rodríguez-Enríquez S. Assessment of the Low Inhibitory Specificity of Oxamate, Aminooxyacetate and Dichloroacetate on Cancer Energy Metabolism. *Biochim Biophys Acta - Gen Subj* (2017) 1861:3221–36. doi: 10.1016/j.bbagen.2016.08.006
15. Kim D, Langmead B, Salzberg SL. HISAT: A Fast Spliced Aligner With Low Memory Requirements. *Nat Methods* (2015) 12:357–60. doi: 10.1038/nmeth.3317
16. Anders S, Pyl PT, Huber W. HTSeq-A Python Framework to Work With High-Throughput Sequencing Data. *Bioinformatics* (2015) 31:166–9. doi: 10.1093/bioinformatics/btu638
17. Trapnell C, Williams BA, Pertea G, Mortazavi A, Kwan G, Van Baren MJ, et al. Transcript Assembly and Quantification by RNA-Seq Reveals Unannotated Transcripts and Isoform Switching During Cell Differentiation. *Nat Biotechnol* (2010) 28:511–5. doi: 10.1038/nbt.1621
18. Dan Hao, Wang X, Wang X, Thomsen B, N.Kadarmideen H, Lan X, et al. Transcriptomic Changes in Bovine Skeletal Muscle Cells After Resveratrol Treatment. *Gene* (2020) 754:144849. doi: 10.1016/j.gene.2020.144849
19. Wang L, Feng Z, Wang X, Wang X, Zhang X. DEGseq: An R Package for Identifying Differentially Expressed Genes From RNA-Seq Data. *Bioinformatics* (2009) 26:136–8. doi: 10.1093/bioinformatics/btp612
20. Anders S, Huber W. Differential Expression Analysis for Sequence Count Data. *Genome Biol* (2010) 11:R106. doi: 10.1186/gb-2010-11-10-r106
21. Love MI, Huber W, Anders S. Moderated Estimation of Fold Change and Dispersion for RNA-Seq Data With Deseq2. *Genome Biol* (2014) 15:550. doi: 10.1186/s13059-014-0550-8
22. Yu G, Wang LG, Han Y, He QY. Clusterprofiler: An R Package for Comparing Biological Themes Among Gene Clusters. *Omics A J Integr Biol* (2012) 16:284–7. doi: 10.1089/omi.2011.0118
23. Shannon P, Markiel A, Ozier O, Baliga NS, Wang JT, Ramage D, et al. Cytoscape: A Software Environment for Integrated Models of Biomolecular Interaction Networks. *Genome Res* (2003) 13:2498–504. doi: 10.1101/gr.1239303
24. Forbes JM, Thorburn DR. Mitochondrial Dysfunction in Diabetic Kidney Disease. *Nat Rev Nephrol* (2018) 14:291–312. doi: 10.1038/nrneph.2018.9
25. Møller JC, Skriver E. Quantitative Ultrastructure of Human Proximal Tubules and Cortical Interstitium in Chronic Renal Disease (Hydronephrosis). *Virchows Archiv A Pathological Anat Histopathol* (1985) 406:389–406. doi: 10.1007/BF00710231
26. Ye W, Zheng Y, Zhang S, Yan L, Cheng H, Wu M. Oxamate Improves Glycemic Control and Insulin Sensitivity *via* Inhibition of Tissue Lactate Production in Db/Db Mice. *PloS One* (2016) 11:1–19. doi: 10.1371/journal.pone.0150303
27. Boswell RN, Yard BA, Schrama E, Van Es LA, Daha MR, van der Woude FJ, et al. Interleukin 6 Production by Human Proximal Tubular Epithelial Cells *In Vitro*: Analysis of the Effects of Interleukin-1α (IL-1α) and Other Cytokines. *Nephrol Dialysis Transplant* (1994) 9:599–606. doi: 10.1093/ndt/9.6.599
28. Hirano T. Interleukin 6 and Its Receptor: Ten Years Later. *Int Rev Immunol* (1998) 16:249–84. doi: 10.3109/08830189809042997
29. Leonard M, Ryan MP, Watson AJ, Schramek H, Healy E. Role of MAP Kinase Pathways in Mediating IL-6 Production in Human Primary Mesangial and Proximal Tubular Cells. in. *Kidney Int* (1999) 56(4):1366–77. doi: 10.1046/j.1523-1755.1999.00664.x
30. Kamimura D, Hirano T, Murakami M. Interleukin-6. In: *The Curated Reference Collection in Neuroscience and Biobehavioral Psychology*. Elsevier Science Ltd., (2016). pp. 430–9.

31. Degerman E, Ahmad F, Chung YW, Guirguis E, Omar B, Stenson L, et al. From PDE3B to the Regulation of Energy Homeostasis. *Curr Opin Pharmacol* (2011) 11:676–82. doi: 10.1016/j.coph.2011.09.015
32. Maurice DH, Ke H, Ahmad F, Wang Y, Chung J, Manganiello VC. Advances in Targeting Cyclic Nucleotide Phosphodiesterases. *Nat Rev Drug Discov* (2014) 13:290–314. doi: 10.1038/nrd4228
33. Ahmad F, Chung YW, Tang Y, Hockman SC, Liu S, Khan Y, et al. Phosphodiesterase 3b (PDE3B) Regulates NLRP3 Inflammasome in Adipose Tissue. *Sci Rep* (2016) 6:28056. doi: 10.1038/srep28056
34. Stieger B. Regulation of the Expression of the Hepatocellular Sulfate-Oxalate Exchanger SAT-1 (SLC26A1) by Glyoxylate: A Metabolic Link Between Liver and Kidney? *J Hepatol* (2011) 54:406–7. doi: 10.1016/j.jhep.2010.09.011
35. Zhao Z, Han F, Yang S, Wu J, Zhan W. Oxamate-Mediated Inhibition of Lactate Dehydrogenase Induces Protective Autophagy in Gastric Cancer Cells: Involvement of the Akt-mTOR Signaling Pathway. *Cancer Lett* (2015) 358:17–26. doi: 10.1016/j.canlet.2014.11.046
36. Coronel-Hernández J, Salgado-García R, Cantú-De León D, Jacobo-Herrera N, Millan-Catalan O, Delgado-Waldo I, et al. Combination of Metformin, Sodium Oxamate and Doxorubicin Induces Apoptosis and Autophagy in Colorectal Cancer Cells *via* Downregulation HIF-1α. *Front Oncol* (2021) 11:594200. doi: 10.3389/fonc.2021.594200
37. Wirawan E, Lippens S, Berghe TV, Romagnoli A, Fimia GM, Piacentini M, et al. Beclin 1: A Role in Membrane Dynamics and Beyond. *Autophagy* (2012) 8:6–17. doi: 10.4161/auto.8.1.16645
38. Jin Y, Ji Y, Song Y, Choe SS, Jeon YG, Na H, et al. Depletion of Adipocyte Becn1 Leads to Lipodystrophy and Metabolic Dysregulation. *Diabetes* (2021) 70:182–95. doi: 10.2337/db19-1239
39. Matboli M, Azazy AEM, Adel S, Bekhet MM, Eissa S. Evaluation of Urinary Autophagy Transcripts Expression in Diabetic Kidney Disease. *J Diabetes Complications* (2017) 31:1491–8. doi: 10.1016/j.jdiacomp.2017.06.009
40. Matboli M, Eissa S, Ibrahim D, Hegazy MGA, Imam SS, Habib EK. Caffeic Acid Attenuates Diabetic Kidney Disease via Modulation of Autophagy in a High-Fat Diet/Streptozotocin- Induced Diabetic Rat. *Sci Rep* (2017) 7:2263. doi: 10.1038/s41598-017-02320-z
41. Nguyen TN, Padman BS, Usher J, Oorschot V, Ramm G, Lazarou M. Atg8 Family LC3/GAB ARAP Proteins Are Crucial for Autophagosome-Lysosome Fusion But Not Autophagosome Formation During PINK1/Parkin Mitophagy and Starvation. *J Cell Biol* (2016) 215:857–74. doi: 10.1083/jcb.201607039
42. Sun A, Wei J, Childress C, Shaw JH, Peng K, Shao G, et al. The E3 Ubiquitin Ligase NEDD4 is an LC3-Interactive Protein and Regulates Autophagy. *Autophagy* (2017) 13:522–37. doi: 10.1080/15548627.2016.1268301
43. Rambold AS, Pearce EL. Mitochondrial Dynamics at the Interface of Immune Cell Metabolism and Function. *Trends Immunol* (2018) 39:6–18. doi: 10.1016/j.it.2017.08.006
44. Ballabio A, Bonifacino JS. Lysosomes as Dynamic Regulators of Cell and Organismal Homeostasis. *Nat Rev Mol Cell Biol* (2020) 21:101–18. doi: 10.1038/s41580-019-0185-4
45. Chen Y, Yan R, Li B, Liu J, Liu X, Song W, et al. Silencing CCNG1 Protects MPC-5 Cells From High Glucose-Induced Proliferation-Inhibition and Apoptosis-Promotion *via* MDM2/p53 Signaling Pathway. *Int Urol Nephrol* (2020) 52:581–93. doi: 10.1007/s11255-020-02383-4
46. Yoo EG, Lee WJ, Kim JH, Chae HW, Hyun SE, Kim DH, et al. Insulin-Like Growth Factor-Binding Protein-3 Mediates High Glucose-Induced Apoptosis by Increasing Oxidative Stress in Proximal Tubular Epithelial Cells. *Endocrinology* (2011) 152:3135–42. doi: 10.1210/en.2010-1122
47. Palikaras K, Lionaki E, Tavernarakis N. Coordination of Mitophagy and Mitochondrial Biogenesis During Ageing in C. Elegans. *Nature* (2015) 521:525–8. doi: 10.1038/nature14300
48. Padman BS, Nguyen TN, Lazarou M. Autophagosome Formation and Cargo Sequestration in the Absence of LC3/GABARAPs. *Autophagy* (2017) 13:772–4. doi: 10.1080/15548627.2017.1281492
49. Birts CN, Banerjee A, Darley M, Dunlop CR, Nelson S, Nijjar SK, et al. P53 Is Regulated by Aerobic Glycolysis in Cancer Cells by the CtBP Family of NADH-Dependent Transcriptional Regulators. *Sci Signaling* (2020) 13:1–29. doi: 10.1126/scisignal.aaz1854

Conflict of Interest: XW was employed by company Konge Larsen ApS.

The remaining authors declare that the research was conducted in the absence of any commercial or financial relationships that could be construed as a potential conflict of interest.

Publisher's Note: All claims expressed in this article are solely those of the authors and do not necessarily represent those of their affiliated organizations, or those of the publisher, the editors and the reviewers. Any product that may be evaluated in this article, or claim that may be made by its manufacturer, is not guaranteed or endorsed by the publisher.

Advantages of publishing in Frontiers

OPEN ACCESS
Articles are free to read for greatest visibility and readership

FAST PUBLICATION
Around 90 days from submission to decision

HIGH QUALITY PEER-REVIEW
Rigorous, collaborative, and constructive peer-review

TRANSPARENT PEER-REVIEW
Editors and reviewers acknowledged by name on published articles

Frontiers
Avenue du Tribunal-Fédéral 34
1005 Lausanne | Switzerland

Visit us: www.frontiersin.org
Contact us: frontiersin.org/about/contact

REPRODUCIBILITY OF RESEARCH
Support open data and methods to enhance research reproducibility

DIGITAL PUBLISHING
Articles designed for optimal readership across devices

FOLLOW US
@frontiersin

IMPACT METRICS
Advanced article metrics track visibility across digital media

EXTENSIVE PROMOTION
Marketing and promotion of impactful research

LOOP RESEARCH NETWORK
Our network increases your article's readership